ASME
SETTING THE STANDARD

Journal of Engineering for Gas Turbines and Power

Published Bimonthly by ASME

VOLUME 130 • NUMBER 4 • JULY 2008

Transactions of the ASME, Journal of Engineering for Gas Turbines and Power (ISSN 0742-4795) is published bimonthly (Jan., Mar., May, July, Sep, Nov.) by The American Society of Mechanical Engineers, Three Park Avenue, New York, NY 10016. Periodicals postage paid at New York, NY and additional mailing offices.
POSTMASTER: Send address changes to Transactions of the ASME, Journal of Engineering for Gas Turbines and Power, c/o THE AMERICAN SOCIETY OF MECHANICAL ENGINEERS, 22 Law Drive, Box 2300, Fairfield, NJ 07007-2300.
CHANGES OF ADDRESS must be received at Society headquarters seven weeks before they are to be effective. Please send old label and new address.
STATEMENT from By-Laws. The Society shall not be responsible for statements or opinions advanced in papers or ... printed in its publications (B7.1, par. 3).

RESEARCH PAPERS

(Contents continued on inside back cover)

This journal is printed on acid-free paper, which exceeds the ANSI Z39.48-1992 specification for permanence of paper and library materials. ♾™
♻ 85% recycled content, including 10% post-consumer fibers.

Journal of Engineering for Gas Turbines and Power JULY 2008

Volume 130, Number 4

TECHNICAL BRIEFS

The ASME Journal of Engineering for Gas Turbines and Power is abstracted and indexed in the following:

AESIS (Australia's Geoscience, Minerals, & Petroleum Database), Applied Science & Technology Index, Aquatic Sciences and Fisheries Abstracts, Civil Engineering Abstracts, Compendex (The electronic equivalent of Engineering Index), Computer & Information Systems Abstracts, Corrosion Abstracts, Current Contents, Engineered Materials Abstracts, Engineering Index, Enviroline (The electronic equivalent of Environment Abstracts), Environment Abstracts, Environmental Science and Pollution Management, Fluidex, INSPEC, Mechanical & Transportation Engineering Abstracts, Mechanical Engineering Abstracts, METADEX (The electronic equivalent of Metals Abstracts and Alloys Index), Pollution Abstracts, Referativnyi Zhurnal, Science Citation Index, SciSearch (The electronic equivalent of Science Citation Index), Shock and Vibration Digest

Effects of Inlet Flow Distortion on the Performance of Aircraft Gas Turbines

Joachim Kurzke
Gas Turbine Performance Simulation Software,
85221 Dachau,
Max Feldbauer Weg 5, Germany
e-mail: joachim.kurzke@t-online.de

This paper describes how the fundamental effects of inlet flow distortion on the performance of gas turbines can be evaluated with any engine performance program that employs an integrated parallel compressor model. In this simulation method, both pressure and temperature distortions are quantified with coefficients, which relate the pressure (respectively temperature) in the spoiled sector to the value in the clean sector. In single spool compressor engines, the static pressure at the exit of the clean sector equals that of the distorted sector. This hypothesis does not hold true with multispool compressor engines because the short intercompressor ducts, which often contain struts or vanes, do not allow the mass flow transfer over the sector borders, which would be required for balancing the static pressures. The degree of aerodynamic coupling of compressors in series can be described in the performance simulation program by the simple coupling factor introduced in this paper. There are two fundamentally different reasons for the change in engine performance: First, there is the impact of the flow distortion on the component efficiencies and thus the thermodynamic cycle and second there are performance changes due to the actions of the control system. From the engine system simulation results, it becomes clear why inlet flow distortion has only a minor impact on the thermodynamic cycle if the comparison of the two operating conditions (with clean and distorted inlet flow) is made at the properly averaged engine inlet conditions. For each compressor, the parallel compressor theory yields two operating points in the map, one for the clean sector and one for the spoiled sector. The performance loss due to the distortion is small since the efficiency values in the two sectors are only a bit lower than the efficiency at a comparable operating point with clean inlet flow. However, the control system of the engine can react to the inlet flow distortion in such a way that the thrust delivered changes significantly. This is particularly true if a compressor bleed valve or a variable area nozzle is opened to counteract compressor stability problems. Especially, using recirculating bleed air for increasing the surge margin of a compressor affects the performance of the engine negatively. Two examples show clearly that the pros and cons of recirculating bleed can only be judged with a full system simulation; looking at the surge line improvement alone can be misleading. [DOI: 10.1115/1.2901190]

Introduction

Most publications about inlet flow distortion discuss only the effect on compression system stability; the impact on engine performance is ignored. Of course, compressor surge is a much more dangerous event than a limited loss of thrust. Nevertheless, it is of interest how much the performance of an engine is affected by inlet flow distortion.

AIR1419 [1] contains engine performance data from a test in which distortion was simulated by a screen. The total pressure losses of the screen were properly taken into account in the test analysis, which led to the following conclusion: "No significant trends in the corrected gross thrust and fuel flow changes due to the distortion were observed in the data range of 70–100% corrected fan speed for this limited sample test case. Airflow changes were in the order of 0.5%."

Also, Williams [2] stated that the effect of distortion on performance is minimal at important aircraft operational conditions. However, performance changes can be large if control system input signals are affected by the distortion. An example for that is reported by Williams [2] about an engine that was controlled by a local turbine temperature sensor. In the test, the distortion was generated by a screen, which could be rotated. The pressure distortion was converted by the compressor into a temperature distortion at the inlet to the combustor, which in turn produced circumferential turbine inlet and exit temperature profiles. The control system employed a single turbine exit temperature probe and kept its indicated value constant. This resulted in significant spool speed changes when the distortion screen was rotated.

This paper describes how changes in performance due to the inlet pressure and temperature distortion can be calculated with an overall engine simulation.

Performance Methodology

AIR1419 [1] suggested for performance synthesis the use of compressor rig data, which are from tests with distorted inlet flow, generated by screens. Such rig test results are directly applicable for low pressure compressors. Core compressors, however, will see a combination of pressure and temperature distortion and this sort of distortion is nearly impossible to simulate on a compressor rig.

In practice, representative compressor rig test data are seldom available. Williams [2] suggested as an alternative the use of flow and efficiency "deltas" as inputs into a performance model, which is calibrated with data from tests with clean inlet flow.

A methodology is described here that employs compressor

Contributed by the International Gas Turbine Institute of ASME for publication in the JOURNAL OF ENGINEERING FOR GAS TURBINES AND POWER. Manuscript received July 22, 2007; final manuscript received July 24, 2007; published online April 28, 2008. Review conducted by Dilip R. Ballal.

maps generated for clean inlet flow. Flow distortion is taken into account by a parallel compressor model integrated into the performance program.

Types of Inlet Flow Distortion

Pressure Distortion. The engine intake, especially in the case of a fighter aircraft, produces a quite complex total pressure distribution. Such a flow field can be described in different detail and accuracy by various distortion indices, see Cousins [3]. The simplest way for characterizing the reality is to divide the flow field in two sectors with different but uniform total pressure.

The intensity of the flow nonuniformity is described with a distortion coefficient, which takes into account the distorted sector width and the total pressure difference. In a 60 deg sector with the total pressure lower than average, for example, the pressure distortion coefficient DC_{60}, is defined as

$$DC_{60} = \frac{P_{\text{mean}} - P_{60\ \text{deg sector}}}{\frac{\rho}{2} V_{\text{mean}}^2}$$

Thus, the total pressure difference is related to the mean dynamic head $\rho V^2/2$ in the aerodynamic interface plain AIP. Note that with this description, the distortion intensity has no influence on the mean intake recovery. Simulations with various DC_{60} values yield only the effect of distortion and not a mixture of distortion and inlet pressure recovery effects.

Temperature Distortion. Inlet temperature distortion is relevant for military applications where gun or missile gas ingestion needs to be considered. Carrier airplanes are subjected to steam ingestion from the catapult and vertical take-off planes can ingest hot exhaust gases. Commercial aircraft may ingest the exhaust from other aircraft or, during thrust reverser operation, their own exhaust gases.

The temperature distortion coefficient for a sector width of 60 deg is defined in Ref. [4] analogous to the definition mentioned by Cousins [3] as

$$DT_{60} = \frac{T_{2,60} - T_2}{T_2}$$

The spoiled sector has a higher inlet temperature than the total temperature of the air originating from the unspoiled atmosphere. Thus, in the simulation, the average inlet total temperature increases with the temperature distortion level.

Swirl. Swirl can exist in three variations: bulk swirl, peak swirl, and vortex swirl (Cousins [3]). Only bulk swirl is addressed in this paper; it is characterized by the rotation of the complete flow field entering the engine and is thus similar to swirl created deliberately by inlet guide vanes.

Bulk inlet swirl can be created by s-shaped inlet ducts of military aircraft such as the Panavia Tornado. In this case, for one of the two engines, the swirl is in the direction of the rotor rotation (preswirl) and for the other engine opposite (counterswirl).

The intensity of bulk swirl can be described by a representative circumferential flow angle.

Parallel Compressor Model. The application of the parallel compressor theory to problems with inlet pressure distortion was first proposed in 1959 by Pearson [5].

In its simplest application, the distorted flow field upstream of the compressor is characterized by two streams with different, but uniform, total pressures. Each stream enters one of two imaginary compressors working in parallel. Both compressors have the same map—the one measured on the rig with clean inlet flow—except for the flow capacity. If the spoiled sector width is 60 deg, for example, the flow capacity of the first imaginary compressor is 60 deg/360 deg=1/6 (the spoiled sector). The second compressor covers a 300 deg sector and has 300 deg/360 deg=5/6 of the real compressor's capacity, see Fig. 1.

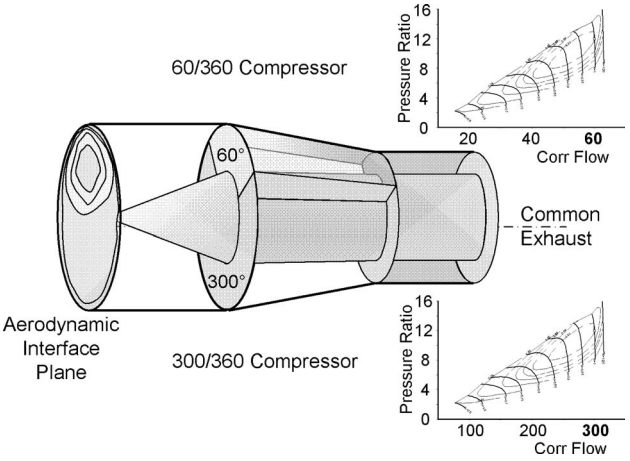

Fig. 1 Parallel compressor model

The original hypothesis of the parallel compressor theory suggests that both compressors discharge to the same static pressure in the downstream duct. This condition allows calculating the position of the operating points in the respective maps.

Figure 2 shows sectors of 180 deg, which implies compressor flow capacities of equal size. As can be seen in the upper part of the figure (total pressure distortion), the compressor dealing with the low inlet pressure operates with a higher than average pressure ratio and for the other compressor the opposite holds true. Both operating points are on the same speed line because both sectors have the same inlet total temperature.

The two operating points move away from each other when the distortion intensity increases. As soon as the point marked L reaches the surge line, the stability boundary of the total compressor is reached according to the parallel compressor theory. The compressor is predicted to surge in spite of the fact that the mean operating point *M* is still far from the (clean) surge line.

The parallel compressor theory can be applied also to temperature distortion simulation. In this case, the pressure ratios of the two compressors are similar, but the operating points are on different speed lines, see lower part of Fig. 2.

Integrating the parallel compressor theory into a performance

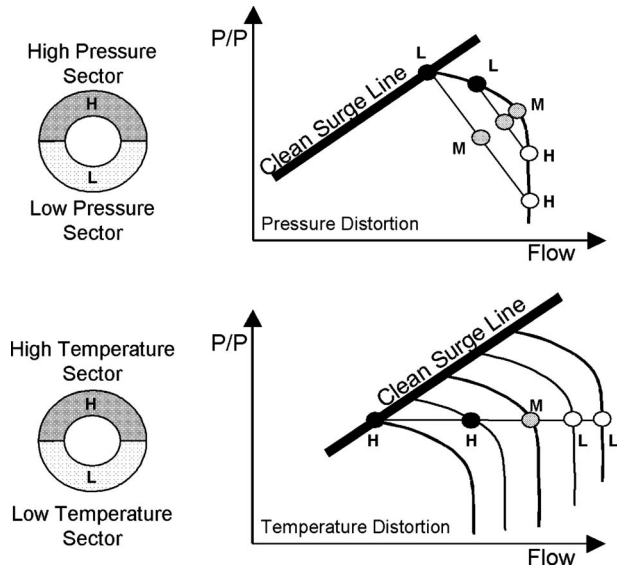

Fig. 2 Operating points in the compressor map

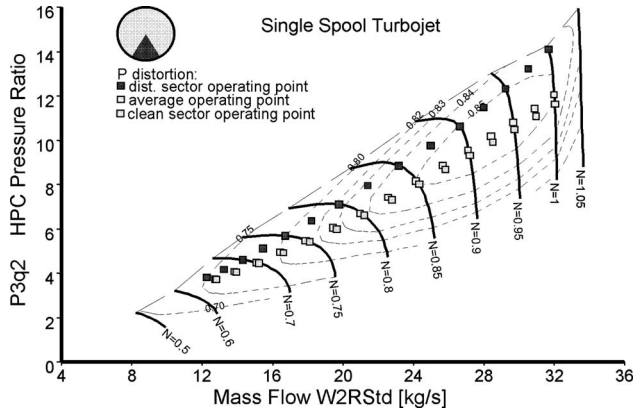

Fig. 3 Operating points for constant DC_{60}

program poses no major problem. For off-design simulations, two operating points must be located in the compressor map, which means one additional variable shows up for each compressor in the standard Newton–Raphson iteration. The corresponding additional conditions are the static pressure balances downstream of the compressors. Note that convergence problems are encountered if the operating point of the distorted sector is in a map region in which, at constant speed, the pressure ratio increases with flow.

Figure 3 shows the average compressor operating points of a turbojet engine together with those in the clean and the distorted sector over a wide power range for constant DC_{60}. Since this distortion descriptor relates the total pressure difference between the sectors to the dynamic head in the AIP, the distance between the two sector operating points is proportional to their compressor mass flow.

The parallel compressor theory has been developed for an isolated compressor and predicts the loss in surge margin due to the inlet flow distortion. When integrated in a performance program, it yields automatically the impact of flow distortion both on the surge margin and on the performance of the engine.

The original theory yields approximate answers for the loss of compression system stability only. The quality of the results can be improved by more or less sophistical corrections; see, for example, the paper of Korn [6]. Moreover, the model may be extended to multiple parallel segments, which allows handling more complex flow field descriptors.

With respect to performance, the parallel compressor theory has some deficits. If the speed lines are vertical, the parallel compressor model does not yield the mass flow decrease, which is evident from compressor rig tests, see, for example, Fig. 83 in AIR1419 [1]. This problem can be solved with an empirical correction factor, which is a function of the distortion intensity and corrected speed. Similarly, efficiency corrections may be applied to the maps that were created for clean inlet flow.

Compressor Coupling. The parallel compressor model as presented above can lead to serious errors in engine distortion tolerance estimates and in the diagnosis of the "critical" compressor with multispool engines. The compressors are connected either with no ducts in between or with short swan neck shaped ducts that contain many vanes or struts. There is no room for circumferentially balancing the static pressure and the static pressure field of the downstream compressor affects the upstream compressor: the compressors are *close coupled*, Ham [7].

Table 1 shows the data from a two-spool turbojet performance calculation for a total pressure distortion in a 60 deg sector. At the HPC inlet, the static pressures are assumed to be equal, which implies that the intercompressor duct is straight and of constant area. In other words, the compressors are considered as *uncoupled*.

In the last column, one can see that in the interduct some air

Table 1 Two spool turbojet distortion details (uncoupled compressors)

Booster	Inlet P (press)	Inlet T (temp)	Corrected flow	Press ratio	Absolute flow
Clean	101.14	288.15	83.54	3.94	83.38
Distorted	84.01	288.15	16.69	4.51	13.84
Average	98.29	288.15	100.22	4.03	97.22
HPC					
Clean	390.40	451.8	26.62	6.93	81.90
Distorted	372.85	459.5	5.26	7.23	15.32
Average	387.90	453.0	31.80	6.97	97.22

(83.38−81.90=1.48 kg/s) must go from the clean sector of the first compressor (the booster) to the distorted sector of the second compressor (the HPC), see Fig. 4.

However, in aircraft gas turbines with short intercompressor ducts, there is limited opportunity for the mass transfer between the sectors and for making the static pressures equal circumferentially and therefore these compressors are closecoupled. It is quite simple to take close coupling of compressors into account in the performance program: In any inter compressor duct, the condition of "equal static pressures" (no coupling) is replaced by the condition "no mass flow between sectors" (full coupling).

For describing any sort of intercompressor duct (short, long, with and without vanes), it is convenient to introduce a coupling factor CF, which allows using a linear combination of the conditions equal static pressures and no flow between sectors for solving the off-design iteration problem.

Figure 5 shows the importance of the coupling factor assumption on the stability assessment for a two spool turbojet. The big yellow area marks under which conditions the HPC surge margin is negative while the surge margin of the LPC is positive. Similarly, the small yellow area marks conditions with negative LPC and positive HPC surge margins.

If no or limited coupling ($CF<0.5$) is assumed, then with $DC_{60}=2.4$ the surge critical component is the LPC (booster), while for full coupling ($CF=1$), the HPC is predicted to surge even with DC_{60} as low as 1.2. Thus the magnitude of the coupling factor decides which of the two compressors will trigger surge of the overall compression system.

The coupling factor CF introduced here corresponds to the coupling number CN developed by Ham and Williams [7]. CN relates the influence of the downstream component on the size of the nonuniformity at the exit of the upstream component. CN varies between 0, representing no static pressure field interaction, and 1, where a strong static pressure interaction is present. With higher values of CN, the two operating points for the upstream compressor are closer together so there is a decreased loss in upstream

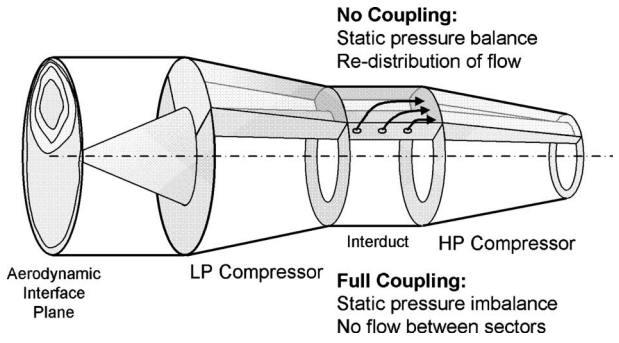

Fig. 4 Compressor coupling

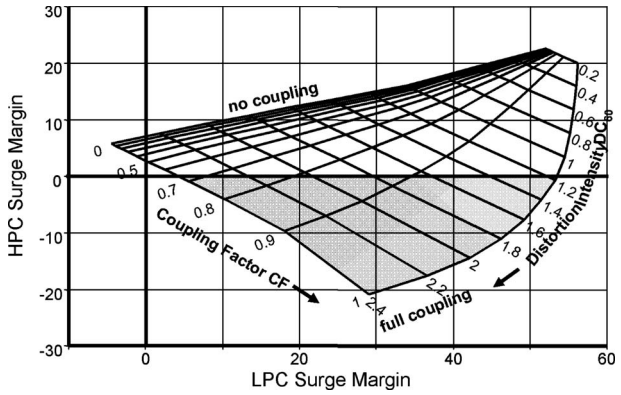

Fig. 5 Influence of the coupling factor on the surge margin assessment ($DC_{60}=0.2,\ldots,2,4$)

compressor surge margin.

Both the coupling factor CF introduced here and the coupling number CN from Ham and Williams [7] lead to similar conclusions to identify the critical compressor from a stability point of view.

Parallel Turbine Model. If the pressure ratios in the spoiled and the clean sector are different, then also the sector exit temperatures will differ. Thus a pressure distortion at the inlet of a compression system is converted into a combined pressure and temperature distortion at the exit of the system. If uniform fuel distribution in the burner is assumed, then the circumferential temperature profile at the burner inlet leads to a circumferential burner exit temperature distribution.

A parallel turbine model was proposed by Kurzke [8] for the assessment of efficiency losses due to a circumferential turbine inlet temperature distribution. When locating the operating point in the temperature distorted sector, two cases must be differentiated:

- The turbine expands to a duct in which static pressure balance between the sectors is feasible.
- A further turbine is following directly. Corrected turbine exit flow must be the same for the turbine sectors operating in parallel.

In both cases, the turbine operating points in the map have different corrected speeds but equal (HP turbines of multispool engines) or nearly equal pressure ratios in both sectors. The efficiencies in both sectors are slightly lower than that from an operating point calculated without the parallel turbine model.

Besides the small efficiency loss due to the inlet temperature distortion, there is a flow angle difference between the sectors downstream of the turbine. This can cause additional losses if there is an incidence sensitive exhaust guide vane.

Zilli [9] has studied the influence of temperature distortion on the performance on a high pressure turbine with CFD simulations and came essentially to the same conclusion as above: It does not have a significant effect on the performance apart from a small reduction in efficiency.

Inlet Swirl. If the engine has inlet guide vanes, then these will eliminate inlet swirl if it is not so big that the flow separates. For engines without inlet guide vanes, incoming bulk swirl is equivalent to the swirl created by an imaginary inlet guide vane.

Changing the setting of an inlet guide vane shifts the speed lines in a compressor map in such a way that both pressure ratio and mass flow change simultaneously in the same direction. The effect on efficiency is typically small; no generally valid statement can be made about the surge line shift due to the inlet guide vane variations.

Thus the basic effect of bulk inlet swirl on the performance of engines without inlet guide vanes can be simulated by applying mass flow and pressure ratio modifiers to the basic compressor map, which are proportional to the swirl angle. Additionally, an efficiency modifier (derived from test data) may be applied.

Impact of Distortion on Thermodynamics

In the following, only the changes of the thermodynamic cycle due to the inlet flow distortion are considered. Compression system stability assessment is beyond the scope of this paper.

Change in Efficiency

Data From Measurements and Simulations. How much the compression efficiency is affected by inlet distortion is not quite clear. Figure 80 of AIR1419 [1] shows a compressor map example in which flow and efficiency losses were less than 1%, the order of the measurement accuracy. Figure 83 of the same reference shows a compressor rig test result with efficiency decrements between 1% and 5% caused by a distortion generating screen. Gostelow [10] showed a test result from a single rotor with an efficiency loss due to the distortion of approximately 5%.

Charalambous [11] presented the theoretical results for the effect of inlet flow distortion on axial compressor efficiency. For circumferential distortion, he shows essentially no efficiency loss as long as no large separation zones appear. In the region near to the surge line—where local flow separation appears—the efficiency loss is less than 1%.

These examples from literature, however, are not representative because the magnitude of the inlet flow distortion, which caused these efficiency decrements, was not comparable.

Conclusions From the Parallel Compressor Model. When a compressor map, which is valid for clean inlet flow, is employed within the parallel compressor model, then one gets three operating points in the map: one for each sector and the average operating point. The latter becomes identical to the operating point found by a performance program without parallel compressor model when DC_{60} values near to zero are considered.

In Fig. 3, the average operating points are located in the map along the peak efficiency ridge. The operating points of the distorted sector are in a region with lower efficiencies than those of the average operating points. Similarly, the efficiencies, read from the map for the clean sector operating point are also lower than the one of the average operating points. Therefore, the mass weighted efficiency of the two parallel compressors is lower than the efficiency calculated by a performance program, which employs no parallel compressor model, because such a simulation considers the average operating point only.

The efficiency loss due to the distortion is proportional to the distortion intensity, but never very large since the efficiency islands in any compressor map are flat. The efficiency decrement caused by inlet temperature distortion for turbines is even smaller since the efficiency islands in turbine maps are generally broader, at least in the normal operating range.

Figure 6 shows the efficiencies of the compressors for the two spool turbojet example, which was already employed for the creation of Fig. 5. The high pressure spool speed is held constant, and the distortion level and the coupling factor are the variables of the parametric study. The thrust change is indicated by the colors and varies between −0.2% and +0.5% in this exercise.

An increase of thrust is observed if the cycle efficiency decreases, which requires a higher burner temperature for keeping the HP spool speed constant as postulated for Fig. 6. The higher burner temperature yields in turn a higher nozzle temperature and therefore gross thrust increases, provided the nozzle mass flow is not or only a little bit affected by the inlet flow distortion.

Rematching Effects. When the efficiency changes are small, rematching effects are equivalently small. Any efficiency loss of the

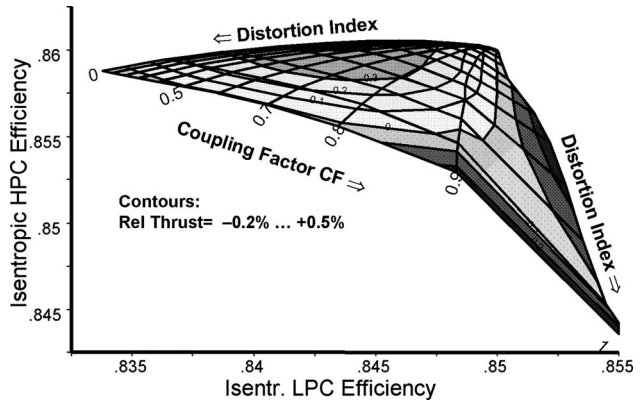

Fig. 6 Efficiency and thrust changes due to distortion

gas generator components will raise the compressor operating line and thus will cause a small additional loss in surge margin.

Effect of Efficiency on Thrust and SFC. However, if there are efficiency and flow capacity losses larger than those resulting from the parallel compressor theory, then the thrust changes might be no longer negligible. Therefore, Fig. 7 was calculated assuming the additional flow capacity and the efficiency losses are directly proportional to the distortion index. That means that with the highest distortion level considered here, in the simulation, the compressor efficiency was decreased by 2.4% and the flow capacity of the compressor was reduced by the same amount.

As in the calculations for Fig. 6, the engine is assumed to run at constant gas generator spool speed. As can be seen from Fig. 7, the thrust loss does not exceed 1%, but the SFC increases 2% with the highest distortion level considered.

This result is in line with the statements of Williams [2] and the remarks in AIR1419 [1]: The impact of inlet flow distortion on the thermodynamics is generally small.

Changes Due to Control System Actions

Figure 7 was calculated for constant high pressure spool speed. The results show that N_L and T_5 increase with the level of distortion. If the calculation would have been performed with constant N_L or constant T_5, then the thrust losses would come out larger.

There is no single answer how large the thrust change is; the answer depends on the engine control logic.

Unintended Reactions. Sometimes engines react to inlet flow distortion in an unintended way because either the control system is unaware of the distortion or there is no actuator available, which can counteract.

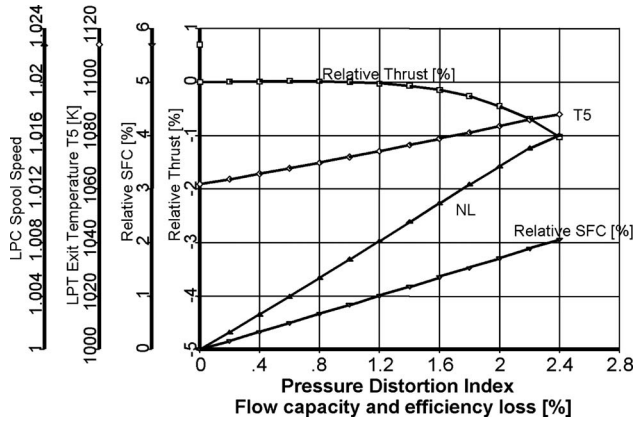

Fig. 7 Performance with increased losses

If a multispool engine is controlled to N_L, then any flow capacity loss of the low pressure compressor due to the inlet flow distortion will lead to a loss of thrust. Turbofan engines that are controlled to a pressure measured downstream of the core compressors are less sensitive to inlet flow distortion provided the distortion does not affect the indicated value of the average engine inlet pressure.

Local Sensors. In the hot end of the engine, the use of many temperature sensors is common. Thus a reasonably averaged output signal is available for the engine control even with inlet flow distortion. In the cold end, however, single flow parameter sensing of engine inlet and compressor exit temperature is frequently employed. That can affect the rated performance when inlet flow distortion (especially temperature distortion) is present.

Regard, for example, variable guide vanes that are usually adjusted following a function of corrected spool speed. The temperature signal needed for calculating the corrected speed will be affected by inlet temperature distortion. Another example is the nozzle area control of mixed flow turbofans with afterburner, which can be a scheduled function of N_L, P_2, and T_2. Any disturbance of the signals employed will affect the scheduled nozzle area and consequently also the thrust.

Reaction to Inlet Swirl. When the engine has no inlet guide vanes and the engine is controlled to N_L, then thrust will be affected by bulk swirl. As mentioned already above, the effect of bulk swirl can be regarded as a modulation of an imaginary inlet guide vane.

Intended Actions. If the engine control system is aware of inlet flow distortion, then compression system stabilizing actions can be commanded.

Bleed to Overboard or to the Bypass. Bleed from the HPC is a means to lower its operating line and thus creates additional surge margin. If the air is injected into the bypass channel, then the performance loss is smaller than with overboard bleed. Air injected into the bypass, however, will reduce the surge margin of the fan. The size of this effect depends on the bypass ratio and whether it is a mixed or an unmixed flow engine.

Nozzle Area Trim. Low bypass mixed flow turbofan engines with afterburner are equipped with a variable area nozzle. During dry operation, the nozzle area need not necessarily to be modulated; however, opening the nozzle may help the low pressure compressor if it encounters inlet flow distortion. This opening generally results in a loss of thrust or an increase in specific fuel consumption.

Recirculating Bleed. Recirculating bleed air is a method for improving the surge line; see, for example, Strazisar [12], Roy [13], and Leinhos [14]. While the first two papers report about compressor rig testing only, the third paper describes experiments with injection of air upstream of a two-spool turbofan, which are complemented by a simulation of the compression system. This simulation, however, did not include the engine components downstream of the two compressors and therefore no valid conclusions about engine performance or operating line shifts could be made.

The order of magnitude for the recirculating air flow needed for a significant surge line shift is typically 3–8% of the total flow. The highest gain in stall margin was observed by Strazisar [12] when the pressure of the recirculated air was high enough to choke the injection slots. Therefore, in a multistage application, the maximum increase in part-speed stability could be achieved by feeding the injectors from a bleed located several stages downstream of the injector.

Strazisar [12] discusses both the influence of the pressure and the temperature of the injected air. Scheidler [15] and Roy [13] do not mention the temperature; they used air from an external

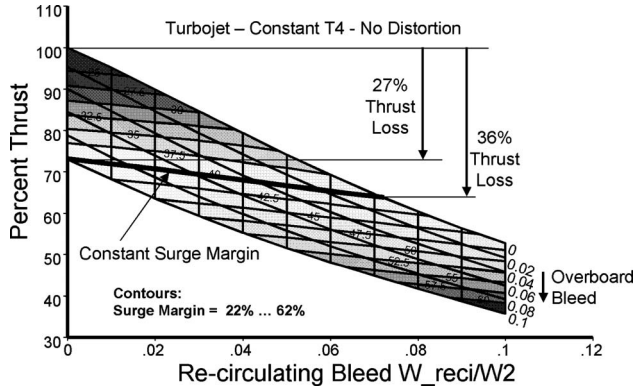

Fig. 8 Effect of bleed, turbojet with T_4=const, no inlet flow distortion

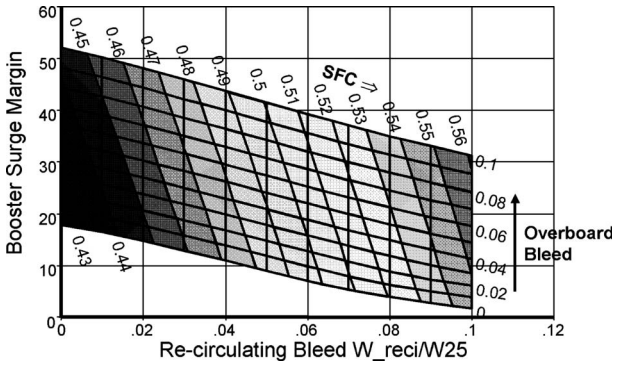

Fig. 10 Three spool turboshaft at constant part power, no inlet flow distortion

source. From a stability improvement point of view, there is no influence of temperature reported by Strazisar [12]. However, from an overall engine simulation point of view, the temperature of the recirculating air is important.

A compressor rig test is representative for the use of recirculation in the compressor of a straight turbojet engine. As any bleed downstream of the compressor, recirculating bleed lowers the compressor operating line and thus creates more surge margin. However, when at rated power the temperature limited performance is considered, then one can see that the thrust loss caused by the recirculating bleed is larger than the one caused by simply blowing the air overboard (compared to the same surge margin, see Fig. 8). The surge line shift achieved with recirculating bleed must significantly overcompensate that effect; otherwise the overboard bleed solution is the better choice.

Another potential application of recirculating bleed is the three spool turboshaft (Fig. 9) with its inherent part power operating problem: The booster operating line tends to run into the surge line at low power. The standard solution to this problem is a handling bleed valve downstream of the booster. Would the recirculating air with its positive influence on the surge line be a better solution?

As mentioned above, Strazisar [12] found out that the maximum benefit from injecting air in front of the compressor is gained when the pressure of the injected air is high enough to choke the injectors. If there is a stability problem of a booster at low power, recirculating booster air will not have sufficient pressure; bleed air from the HPC is needed.

Figure 10 was calculated for constant shaft power, approximately 20% of the rated take-off power. It shows that recirculating air originating from the high pressure compressor not only reduces the booster surge margin; it also increases the specific fuel consumption much more than the conventional overboard bleed. Recirculating high pressure air will be superior only if injecting a small amount of it upstream of the booster yields a very significant shift of the surge line.

The reason for the unfavorable results with recirculating high pressure air shown in Figs. 8 and 10 is the temperature increase caused by the injection of hot air upstream of the engine.

Summary and Conclusions

A parallel compressor model integrated into the performance program yields—besides the compression system stability assessment—also the effect of inlet flow distortion on the performance of an engine. When compressors are connected by ducts, then the static pressure balance in that duct, which is postulated by the parallel compressor theory, cannot happen if the duct is short or contains struts. This effect can be described in the performance program by a coupling factor, which is 0 for full static pressure balance (no aerodynamic coupling of the compressors) and 1 for no mass flow between sectors in the duct (full aerodynamic coupling). Intermediate degrees of aerodynamic coupling can be modeled by employing a weighted mean of the two conditions "static pressure balance" and no mass flow between sectors for finding the compressor operating points. This new methodology is analytically simple, inexpensive, and easy to implement in any performance program.

Engine performance is primarily affected by inlet flow distortion if the control system reacts unintentionally or takes deliberately actions, opening a bleed valve, for example. If that is not the case and as long as the distortion intensity does not affect the flow field within the compressor significantly by large local flow sepa-

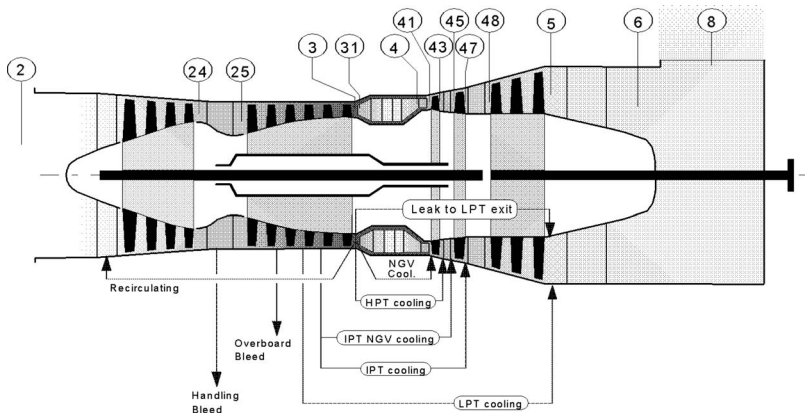

Fig. 9 Three spool turboshaft

ration zones, its effect on the average component efficiencies remains small and the thermodynamic performance will suffer only marginally.

The use of recirculating bleed for stabilizing the compression system causes severe performance penalties. Only if a small amount of recirculating air shifts the surge line considerably, this stabilization method may be superior to the use of a simple overboard bleed valve. For assessing the potential advantage of using recirculating bleed, an overall system simulation is indispensable.

Nomenclature

- AIP = aerodynamic interface plane
- CF = coupling factor
- CN = coupling number (Ham and Williams [7])
- DC_{60} = pressure distortion coefficient, 60° sector
- DT_{60} = temperature distortion coefficient, 60° sector
- HPC = high pressure compressor
- HPT = high pressure turbine
- LPC = low pressure compressor (booster)
- LPT = low pressure turbine
- N_L = low pressure spool speed
- P = total pressure
- P_s = static pressure
- SFC = specific fuel consumption
- T_2 = total temperature at the engine face
- T_5 = exhaust temperature
- V = velocity
- ρ = density

References

[1] 1999, "Inlet Total-Pressure-Distortion Considerations for Gas-Turbine Engines," SAE AIR 1419, Rev. A.

[2] Williams, D. D., 1986, "Review of Current Knowledge on Engine Response to Distorted Inflow Conditions," AGARD-CP-400.

[3] Cousins, W. T., 2004, "History, Philosophy, Physics, and Future Directions of Aircraft Propulsion System/Inlet Integration," ASME Paper No. GT2004–54210.

[4] Kurzke, J., GasTurb 10 User Manual, www.gasturb. de

[5] Pearson, H., McKenzie, A. B., 1959, "Wakes in Axial Compressors," J. R. Aeronaut. Soc., July.

[6] Korn, J. A., 1974, "Estimated Effect of Circumferential Distortion on Axial Compressors Using Parallel Compressor Theory and Dynamic Stall Delay," AIAA Paper No. 74–233.

[7] Ham, C. J., and Williams, D. D., 1993, "Some Applications of Actuator and Semi-Actuator Disk Theory to the Problem of Intake/Engine Compatibility," *JSME Tokyo Gas Turbine Conference 83-Tokyo-IGTC-50*.

[8] Kurzke, J., 1992, "Calculation of Installation Effects Within Performance Computer Programs," *AGARD Lecture Series* 183.

[9] Zilli, A., Pachidis, V., Jackson, A., and Pilidis, P., 2005, "CFD Investigation of the Performance of a Military HP Axial Turbine Subjected to Inlet Temperature Distortion," ASME Paper No. GT2005–68503.

[10] Gostelow, J. P., and Krabacher, K. W., 1967, "Single Stage Experimental Evaluation of High Mach Number Compressor Blading. Part 5—Performance of Rotor 2B," NASA CR-54585.

[11] Charalambous, N., Ghisu, T., Iurisci, G., Pachidis, V., and Pilidis, P., 2004, "Axial Compressor Response to Inlet Flow Distortions by a CFD Analysis," ASME Paper No. GT2004–53846.

[12] Strazisar, A. J., Bright, M. M., Thorp, S., Culley, D. E., and Suder, K. L., 2004, "Compressor Stall Control Through Endwall Recirculation," ASME Paper No. GT2004–54295.

[13] Roy, B., Chouhan, M., and Kaundinya, K. V., 2005, "Experimental Study of Boundary Layer Control Through Tip Injection on Straight and Swept Compressor Blades," ASME Paper No. GT2005–68304.

[14] Leinhos, D. C., Scheidler, S. G., Fottner, L., Grauer, F., Hermann, J., Mettenleiter, M., and Orthmann, A., 2002, "Experiments in Active Stall Control of a Twin-Spool Turbofan Engine," ASME Paper No. GT2002–30002.

[15] Scheidler, S. G., and Fottner, L., 2004, "Experimental Operating Range Extension of a Twin-Spool Turbofan Engine by Active Stability Control Measures," ASME Paper No. GT2004–53077.

F. Zheng
Graduate student
e-mail: fzheng@ncsu.edu

R. L. Ordon
Graduate student

T. D. Scharton
Adjunct Professor

A. V. Kuznetsov
Associate Professor
Mem.ASME

W. L. Roberts
Professor
Mem. ASME

Department of Mechanical and Aerospace Engineering,
North Carolina State University,
Campus Box 7910,
Raleigh, NC 27606

A New Acoustic Model for Valveless Pulsejets and Its Application to Optimization Thrust

Due to its simplicity, the valveless pulsejet may be an ideal low cost propulsion system. In this paper, a new acoustic model is described, which can accurately predict the operating frequency of a valveless pulsejet. Experimental and computational methods were used to investigate how the inlet and exhaust area and the freestream velocity affect the overall performance of a 50 cm pulsejet. Pressure and temperature were measured at several axial locations for different fuel flow rates and different geometries. Computer simulations were performed for exactly the same geometries and fuel flow rates using a commercial CFD package (CFX) to develop further understanding of the factors that affect the performance of a valveless pulsejet. An acoustic model was developed to predict the frequency of these valveless pulsejets. The new model treats the valveless pulsejet engine as a combination of a Helmholtz resonator and a wave tube. This new model was shown to accurately predict geometries for maximum thrust. The model was further extended to account for the effect of freestream velocity. Evidence is provided that valveless pulsejet generates the highest thrust when the inherent inlet frequency matches the inherent exhaust frequency. [DOI: 10.1115/1.2900730]

Keywords: pulsejet, valveless, thermoacoustics

Introduction

The pulsejet is an unsteady propulsion device that generates intermittent thrust [1]. The reactants enter the combustion chamber when the pressure in the combustion chamber is lower than the ambient pressure. Residual hot gases and heat transfer from the hot walls raise the reactants' temperature to the autoignition temperature, initiating combustion of the reactants. The ensuing heat release increases the pressure, and the combustion gases then expand down the exhaust duct and exit at high velocity, generating thrust. Once the combustion gases at the exit have expanded to nearly atmospheric pressure, overexpansion due to the momentum of the combustion products causes the combustion chamber pressure to decrease to subatmospheric, causing fresh reactants to be pulled into the combustion chamber, and the process to begin again.

Simultaneously, there is an acoustic wave propagating down the exhaust duct, reflecting off the exhaust exit, traveling back up to exhaust duct as an expansion wave. The expansion wave reflects off the inlet and travels back down the exhaust, reflecting off the exhaust exit (now as a compression wave) and propagating back to the combustion chamber. When the reflected wave reaches the chamber, the combustion chamber pressure increases again, the autoignition occurs, and the cycle repeats itself.

The primary reason for the development of a valveless pulsejet is that in most designs, the use of reed valves limits the reliability and longevity of the engine, and renders the pulsejet difficult to scale down in size. In the valved pulsejet, the function of the reed valves is to prevent a reversal of the flow at the inlet—and therefore negative momentum transport—when the combustion chamber pressure exceeds the freestream stagnation pressure. By proper utilization of wave processes in an inlet duct of adequate length, the amount of negative thrust can be minimized in a valveless pulsejet [2].

In 1909, Georges Marconnet developed the first pulsating combustor without valves (Fig. 1(*a*)), and it is the grandfather of all valveless pulsejets. The US government made considerable advances in valveless pulsejet technology in the 1950s and early 1960s. Project Squid [3–7], a collaboration between the United States Navy and Air Force to research and develop all potential sources of jet propulsion available at that time, became greatly involved in the investigation of valveless pulsejets.

Another project supported by the US government focusing on the investigation of valveless pulsejet reactors was also conducted between 1961 and 1963 [8]. Numerous valveless designs were developed, produced, and tested in the course of the project. The most well known of these designs was the Lockwood–Hiller pulsejet shown in Fig. 1(*b*). It uses the same principles of the Marconnet design; however, the entire tube was bent into a U-shape to have thrust going in the same direction from both the inlet and exhaust.

Due to their relatively low efficiency, pulsejets were surpassed by the much more efficient turbojets and were put aside for decades following their development into the early 1960s. As the scale of turbomachinery is reduced, the compressor efficiency decreases and, therefore, the efficiency of a turbojet nonlinearly drops with its size when it is utilized in a micropropulsion system [9]. Therefore, there may be applications where small scale, simplicity, low cost, and high thrust-to-weight ratio make the pulsejet attractive.

Recently, pulsejets have been studied utilizing modern numerical techniques [10–12]. Geng et al. [12] performed a combined experimental and computational study on a small scale valveless pulsejet. In Ref. [12], the area ratio of the inlet to that of the combustion chamber and the length ratio of the inlet and exhaust pipes were used to evaluate the scalability of the valveless pulsejet. However, the physical reasons why the inlet area is related to the length ratio of inlet and exhaust pipe length were not investigated.

The purpose of this paper is to develop a model to predict the operating frequency of a valveless pulsejet and suggest how inlet geometry affects the performance of a valveless pulsejet. This is accomplished by comparing the performance of a valveless pulsejet with different geometries to determine how inlet and exhaust

Manuscript received May 2, 2007; final manuscript received January 7, 2008; published online April 28, 2008. Review conducted by Thomas Sattelmayer.

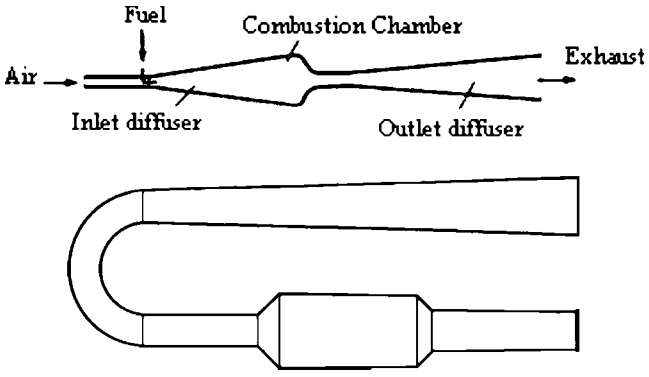

Fig. 1 Earlier pulsejet designs: (*a*) Marconnet and (*b*) Lockwood–Hiller

geometry affects frequency, temperature, and thrust of the valveless pulsejet, leading to an optimization of the design and a set of design rules.

Experimental Setup

The pulsejet discussed in this paper is a modified version of the Bailey machining service (BMS) hobby-scale (50 cm in length) pulsejet where the original valved inlet is replaced with a straight pipe (Fig. 2(*a*)).

As shown in Fig. 2(*a*), the pulsejet is composed of three parts: the valveless head, body, and extension. Ports 1–5 were added to allow temperature and pressure measurements (Fig. 2(*a*)). (Figure 2(*b*) shows the structure of the temperature and pressure sensor on the pulsejet and how the fuel was injected into the combustion chamber.) The pulsejet was secured to a low-friction linear bearing assembly. Four valveless heads were made with different diameters (1.3 cm, 1.6 cm, 2.2 cm, and 2.5 cm) and different lengths (2.54 cm, 5.08 cm, and 7.62 cm) to determine how inlet geometry affects performance. Fuel was continuously fed into the combustion chamber via a 3 mm stainless steel tube with eight small holes drilled into it and located at the same axial position as Port 1, but orthogonal to it, as shown in Fig. 2(*b*). Various extensions were added to the exhaust to evaluate the contribution of exhaust duct length to the valveless pulsejet.

Propane was used as the fuel to run the pulsejet for all tests. This was done to simplify the comparison between the test results and the simulations by eliminating the need for multiphase modeling. Fuel was directly fed into the combustion chamber at a constant flow rate of 0.47 g/s during all experiments. Three Type B (platinum and platinum/rhodium) thermocouples were used to measure the time-averaged temperature simultaneously at Ports 1, 3, and 5 along the jet axis. These thermocouples (TCs) were custom made, and run through ceramic material, thus placing the TC junction at the centerline of the pulsejet. The voltage was measured with a Pentium 4 computer via a data acquisition card with a maximum input of 4 Hz per channel. This measured temperature is a time-averaged value due to the high operation frequency of the pulsejet and thermal inertia of the thermal couples. Also, (time-averaged) inlet and exhaust temperatures were measured at the inlet plane and exhaust exit plane, respectively. Both time-averaged and instantaneous pressures were measured at Ports 1, 3, and 5 on the jets. To measure the time-averaged pressure in the combustion chamber, a mercury manometer was used. For instantaneous pressure, a Kulite XTE-190-5G pressure transducer was used. This transducer has a peak pressure reading ability of 350 kPa with 0.1 kPa resolution and 300 kHz sampling frequency. The operating frequency of the pulsejet was determined from the oscillation frequency of the instantaneous pressure [13].

Numerical Model

Numerical simulations of acoustic resonators are addressed in numerous publications [10–12,14,15]. In this paper, the commer-

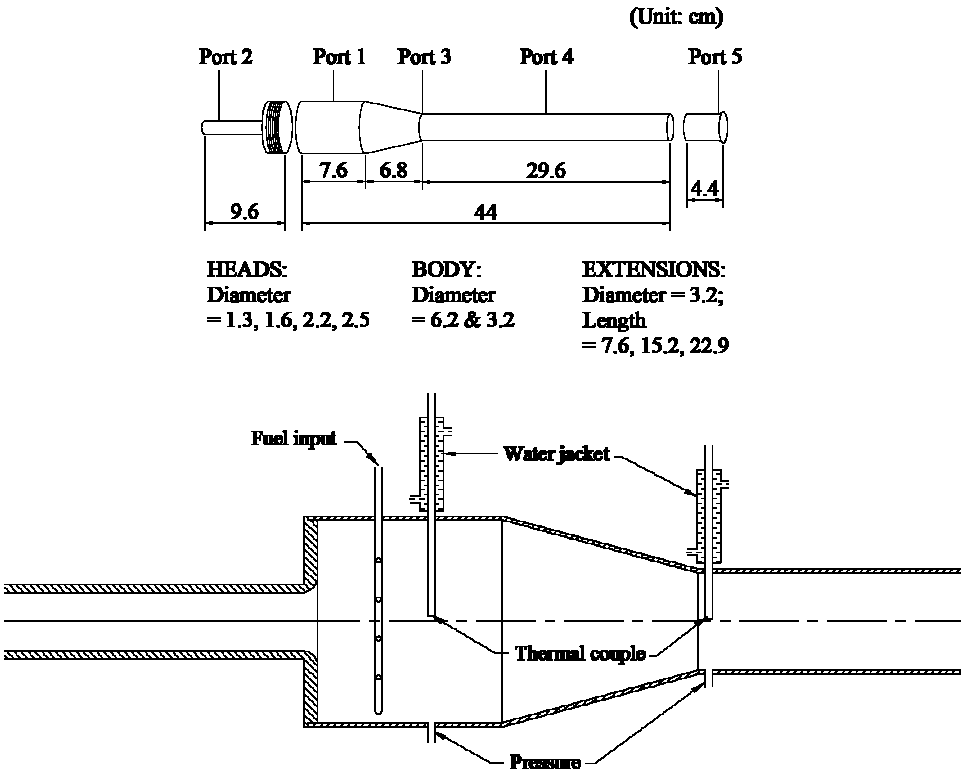

Fig. 2 (*a*) Dimensions of the experimental valveless pulsejet (in cm) and (*b*) pulsejet cross section showing details of fuel injection, pressure, and temperature measurements

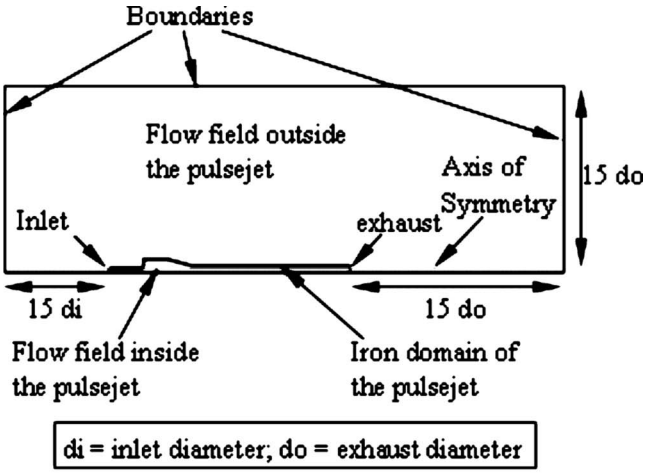

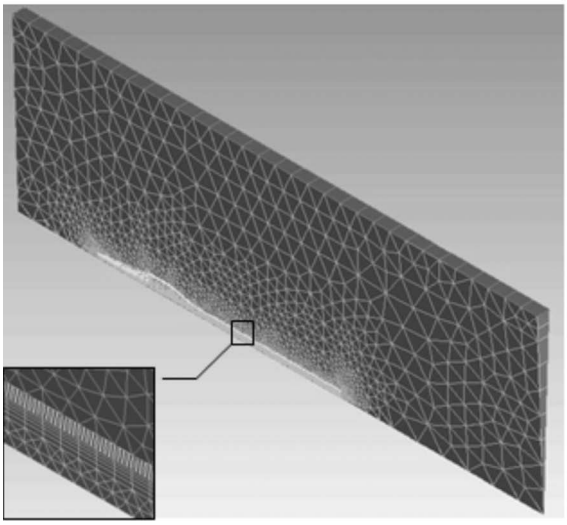

Fig. 3 Numerical model for the pulsejet

cially available CFD software, CFX™ 5.7 package, was used to model the combustion and flow inside and outside of the pulsejet. Because the pulsejet is symmetric about the axis, the geometry was simplified to two-dimensional axisymmetric to save computational time. The mesh was generated in a 4 deg slice instead of the full 360 deg region. In Fig. 3, the computational domain is different from Ref. [13], which only simulated the flow field inside the pulsejet. In this paper, as shown in Fig. 3, the computational domain includes not only the interior of the pulsejet but also an extended domain to compute the flow field around the pulsejet. Because the boundaries were set far from the pulsejet, effects from pulsejet operation were negligible at the boundaries, and the boundary condition was set to temperature T_0 equals to 300 K and pressure P_0 equals to 10^5 Pa.

A much smaller node distance was used for the flow field inside the pulsejet, shown in Fig. 3, than for the flow field outside the pulsejet, with the total number of nodes in this model being about 18,000. The code was also tested with a double mesh density case. However, results showed that further increasing the density of nodes does not affect the results. The computations were performed on the NCSU IBM Blade Center utilizing a single 3.0 GHz Inter Xeon processor. Typical computational time for one cycle of the pulsejet was about 18 CPU hours.

A k-ε model based on the Reynolds averaged Navier–Stokes (RANS) equations was used because it offers a good compromise in terms of accuracy and robustness [16,17]. The eddy dissipation model was chosen as the combustion model. A propane-air five

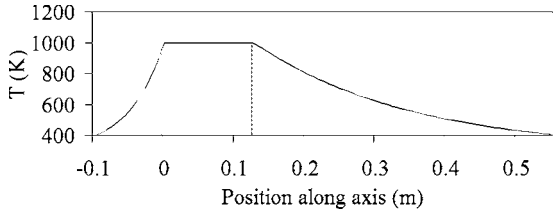

Fig. 4 Temperature distribution along the pulsejet wall

step reaction mechanism (propane oxidation, hydrogen oxidation, CO oxidation, and both directions of water-gas shift reaction) provided by CFX 5.7 was used to simulate the combustion process.

There is a significant heat flux between the pulsejet walls and fluid inside the pulsejet. However, the frequency is high enough and the thermal inertia is large enough so that the wall temperature distribution can be assumed to be steady. To find the steady temperature distribution, a steady state simulation was performed, where boundary conditions were based on the average gas temperature in a transit simulation. This temperature distribution was further simplified to what is shown in Fig. 4, where the region between two dashed lines represents the combustion chamber, with a constant temperature of 1000 K along the combustion chamber and then an exponential decay toward both the inlet and exit planes, which are at 400 K.

The computational procedure for the pulsejet was initiated by setting the velocity to 0 m/s and temperature to 300 K everywhere in the computational domain. A stoichiometric mixture of air and propane was then injected into the combustion chamber and ignited. This generated a high pressure, and pulsed operation of the jet was initiated. This process is quite similar to pulsejet start-up in the analogous experiments.

It was also of interest to understand how the freestream velocities affected the operation of valveless pulsejets. Pulsejets flying at different forward flight speeds were modeled by changing the boundary condition at the inlet of the enclosure flow field. The freestream velocity was varied between 0 m/s zero and 80 m/s.

Monitors for pressure and temperature were set at precisely the same locations as in experiments along the centerline of the pulsejet. Data were acquired at every time step (10^{-5} s) during the simulation. Time-averaged temperature values were calculated by averaging the temperature over a cycle for comparison with experimental (TC) data.

Acoustic Model

Self-compression is one of the most important characteristics of pulsejets, so understanding this phenomenon is of considerable interest. Pressure oscillations in a pulsejet are amplified by an acoustic resonance. Traditionally, a valved pulsejet is modeled as a tube closed at the valve end and open at the exhaust end, so the fundamental resonance occurs when the total length of the pulsejet is equal to one-quarter of an acoustic wavelength. However, an acoustic investigation of valved pulsejets revealed that, because of the increased diameter of the combustion chamber, the frequency of a valved pulsejet obeys the following equation [18,19]:

$$\frac{\omega_e V}{S_e c_e} \tan \frac{\omega_e L_e}{c_e} = 1 \tag{1}$$

where $\omega_e = 2\pi f_e$, f_e is the resonate frequency associated with the exhaust pipe, c_e is the average speed of sound in the exhaust tube (spatial and temporal average), S_e is the cross section area of the exhaust pipe, V is the volume of the combustion chamber, and L_e is the length of the exhaust pipe.

The inlet length was much shorter than the exhaust, only a few diameters long, and thus much shorter than the sound wavelength. The volume of the inlet is also small compared to the volume of the combustion chamber. Therefore, the combination of this short

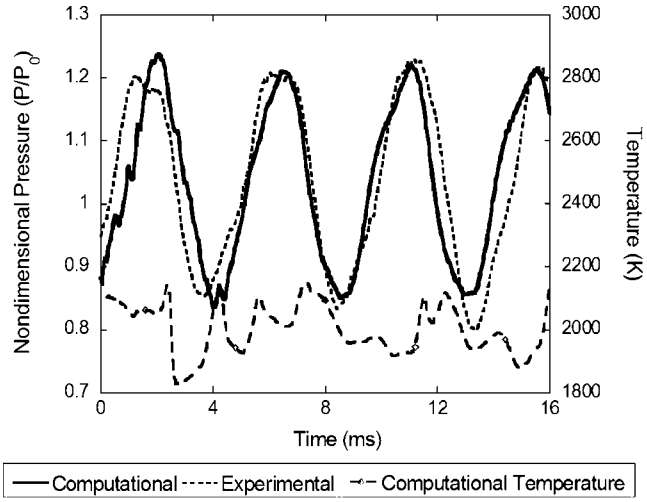

Fig. 5 Chamber pressure and temperature at Port 3 for 1.6 cm inlet diameter and 50 cm exhaust duct length

inlet and combustion chamber is modeled as a Helmholtz resonator. The frequency of a Helmholtz resonator is calculated as [19]

$$f_i = [c_i/(2\pi)][S_i/(VL_i)]^{0.5} \quad (2)$$

where f_i is the resonate frequency associated with the inlet, c_i is the average speed of sound in the inlet and combustion chamber, S_i is the cross section area of the inlet, V is the volume of the combustion chamber, and L_i is the length of the inlet. Since the reactant mixture in the pulsejet has similar heat ratio and specific gas constant to that of air, in this paper, the speed of sound was calculated by assuming a γ (at the appropriate average temperature) and R for air.

Since the operating frequency of the pulsejet is affected by both the inlet and exit tubes, it is expected to be a function of a compound variable that combined both the inlet and exhaust frequencies. In this research, the operating frequency of a pulsejet f was postulated to be the average value of the inlet and exhaust frequency:

$$f = (f_i + f_e)/2 \quad (3)$$

where f_i and f_e are inlet and exhaust frequencies defined in Eqs. (1) and (2), respectively.

Results and Discussion

Static Environment. The instantaneous pressure at Port 3 is shown in Fig. 5 for a pulsejet with a 1.6 cm inlet diameter and 50 cm exhaust duct length. From this comparison between experimental and computational results, two effects are observed. First, the amplitude of pressure variation is almost the same in experimental and computational data. Second, the frequency observed in computational data is a little larger than that in experimental data. Figure 5 also shows computationally obtained temperature at Port 3; the time-averaged temperature at Port 3 is 2000 K.

Operational frequencies for both experimental and computational are relatively accurately obtained by taking the average value for several cycles. This frequency is generated by both the acoustic waves traveling in the tube and the gases flowing into and out of the tube due to the large pressure differences. Therefore, the pulsejet frequency contains information about all the properties relative to combustion, flow, and heat transfer. As shown in Fig. 6, both experimental and computational results show a frequency increase with an increase of inlet diameter and decrease with an increase of the exhaust duct length. Both of these trends are consistent with our modeling of the inlet as a Helmholtz resonator and exhaust as a wave tube.

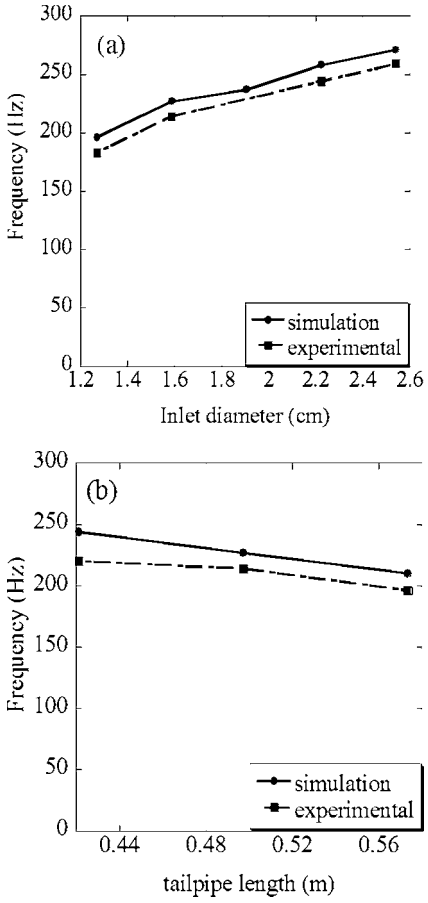

Fig. 6 Frequency comparison between computational and experimental results: (*a*) frequency versus inlet diameter for 50 cm exhaust duct pulsejet and (*b*) frequency versus exhaust duct length for 1.6 cm inlet diameter

As seen from Fig. 6, the frequencies obtained from simulations are 5–10% higher than those from experiments. These disagreements are explained by considering the temperature difference between experiments and simulations. The higher the temperature, the higher the speed of sound and thus the higher the frequency. As shown in Table 1 (unfortunately, experimental temperature for 2.2 cm inlet diameter pulsejet was not acquired), it was found that the average temperature from the simulations at Port 3 was much higher than measured. There are two reasons for this. First, in the two-dimensional simulations, one source point was set in a 4 deg wedge, which equates to 90 point fuel sources for the whole pulsejet; however, in the experiments, there were only eight small holes in the fuel injector. Since the reaction is controlled by fuel-air mixing, this led to a significantly shorter combustion time and thus higher temperature in the simulations than in the experiments. This is the result of the compromise between precision and simulation time expense. Second, there is always heat transfer

Table 1 Chamber temperature from simulations and experimental data

Inlet diameter (cm)	Simulation temperature (K)	Experimental temperature (K)
1.3	1711	1593
1.6	2000	1423
2.2	1826	N/A
2.5	1807	1343

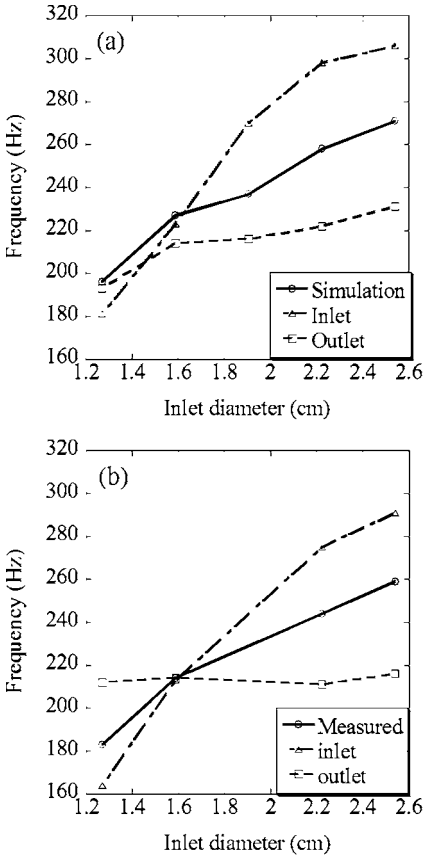

Fig. 7 Calculated inlet and exhaust frequency compared to pulsejet running frequency for 50 cm tail pipe: (*a*) computational data and (*b*) experimental data

from the junction of the thermal couple through the wire. At Port 3, this temperature difference is quite large, and the distance from the centerline to the water jacket is quite small. This causes lower experimental temperature reading than real temperature at Port 3. However, since temperature has the same effect on inlet and exhaust frequencies, this difference will not affect on the inlet-exhaust frequency matching discussed (Eq. (3)) in this paper.

Figure 7 compares the inlet frequency calculated by Eq. (2) and the exhaust frequency calculated by Eq. (1) with operating frequency obtained in either simulations or experiments. In Fig. 7(*a*), the inlet and exhaust frequencies are calculated by using temperature from the computational results, and in Fig. 7(*b*), these are calculated by using experimental temperature results. From these figures, it is clear that the frequencies obtained from both simulations and experiments compare well to the average frequency calculated by the two analytical acoustic models. Moreover, at small inlet diameters, the wave tube (exhaust) model overpredicts the operating frequency while the Helmholtz (inlet) model underpredicts the frequency. This then flips as the inlet diameter increases.

Table 2 shows a comparison of calculated frequencies with the actual measured frequencies for all available experimental results. The inlet frequency was calculated by Eq. (2), the exhaust frequency was calculated by Eq. (1), and the overall operating frequency was calculated by our new acoustic model, Eq. (3). As shown, the new acoustic model frequencies compare very well to the measured frequencies, with the difference between them being less than 5% for all tested cases. Simulation results for the same geometries are summarized in Table 3. It is evident that frequencies obtained using the computational model compare well to frequencies obtained using the analytical model, the difference being less than 10% for all cases. This suggests that the new analytical acoustic model given by Eq. (3) captures the relevant physics and yields correct results.

The frequencies obtained from the analytical acoustic model depend on both inlet and exhaust temperatures through the speed of sound. Average temperatures at the inlet and exhaust provide some information about the relative amount of time during each cycle when the air flows into the pulsejet (i.e., at 300 K), from both ends, and when combustion products flow out (i.e., ~1500 +K), also from both ends. As shown in Fig. 8, for a small inlet diameter, the average temperature of the fluid moving through the pulsejet at the inlet is higher than at the exhaust. As the inlet diameter increases, the average inlet temperature decreases while the exhaust average temperature increases. Computations and experiments agree quite well; however, this result is counterintuitive, as one would expect a small diameter inlet to force more hot products out the exhaust.

To validate the external flow field simulation, computed temperatures at the exit and at several points downstream are compared to measured temperatures. As shown in Fig. 9, simulation and experimental results compare reasonably well. The numerical model is thus validated by comparing with experimental data for the temperature (both inside and outside the pulsejet) and pressure at various locations, as well as for the operating frequency.

Thrust was not experimentally measured, but was calculated

Table 2 Frequencies obtained from experimental data versus those obtained from the analytical model

Tail pipe length (cm)	Inlet length (cm)	Inlet diameter (cm)	Inlet frequency (Eq. (2)) (Hz)	Exhaust frequency (Eq. (1)) (Hz)	Acoustic model (Eq. (3)) (Hz)	Measured jet freq (Hz)
42	10	1.6	208	254	231	220
		2.2	247	258	253	253
50	7	1.3	196	216	206	200
	10	1.3	164	212	188	183
		1.6	213	214	214	214
		2.2	275	211	243	244
		2.5	291	216	253	259
58	7	1.3	192	187	189	198
	10	1.3	158	181	169	178
		1.6	212	183	198	196
		2.2	275	176	226	223
		2.5	297	202	249	246

Table 3 Frequencies obtained from a computer simulation versus those obtained from the analytical model

Tail pipe length (cm)	Inlet length (cm)	Inlet diameter (cm)	Inlet frequency (Eq. (2)) (Hz)	Exhaust frequency (Eq. (1)) (Hz)	Acoustic model (Eq. (3)) (Hz)	Simulation jet freq (Hz)
42	10	1.6	222	238	230	244
		2.2	323	255	289	265
50	7	1.3	212	208	210	218
	10	1.3	181	193	187	196
		1.6	223	214	219	227
		2.2	298	222	260	258
		2.5	306	231	269	271
58	7	1.3	211	184	198	208
	10	1.3	171	179	175	190
		1.6	227	189	208	210
		2.2	316	196	256	250
		2.5	300	214	257	242

based on the momentum flux through the inlet and exhaust. Thrust generated by the momentum flux through the inlet and exhaust planes was separately calculated, and the total thrust was calculated by deducting the inlet thrust from the exhaust thrust. Studying the dependence of the total thrust on the inlet diameter suggests that the maximum thrust occurs for the inlet diameter at which the inlet and exhaust frequencies coincide. To confirm this assumption, a new case with the inlet diameter determined by the intersection of the curves corresponding to inlet and exhaust frequencies in Fig. 7(*a*) was computationally investigated to obtain the thrust for the geometry where the inlet and exhaust frequencies coincide.

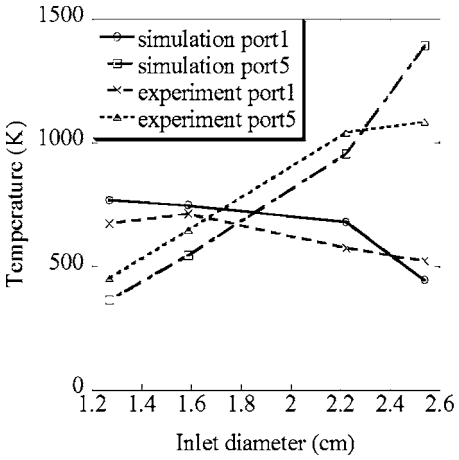

Fig. 8 Inlet and exit temperatures versus the inlet diameter for a 50 cm exhaust duct pulsejet

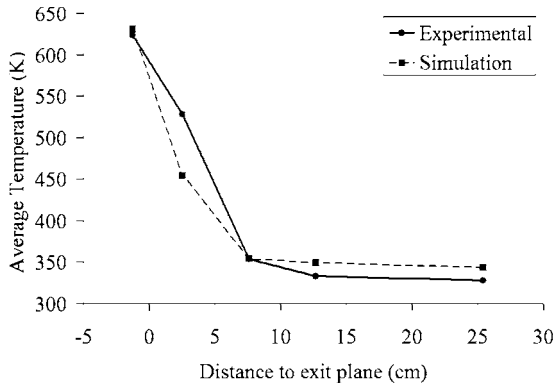

Fig. 9 Temperature at the exit

For the base line exhaust duct length of 50 cm, the inlet thrust, exhaust thrust, and net thrust were calculated as a function of inlet diameter and the results are shown in Fig. 10. The inlet thrust (in the negative x direction) increases with inlet diameter. The exhaust thrust initially increases, is reasonably constant, and then drops as the inlet diameter increases. The net thrust (exhaust thrust minus inlet thrust) is observed to peak at an inlet diameter corresponding to the inlet-exhaust frequency matching condition. It is also clear that as the inlet diameter gets large, the net thrust becomes negative, as expected.

The same simulations were also carried out for 42 cm and 58 cm exhaust duct lengths. The results are displayed in Fig. 11. The pulsejet with 1.70 cm inlet diameter and 42 cm exhaust duct length and 1.32 cm inlet diameter with the 58 cm exhaust duct length generate the greatest net thrust. These are also the inlet diameters, which make the inlet frequencies coincide with exhaust frequencies.

Figures 10 and 11 also show that there is a strong correlation between the peak pressure in the combustion chamber and the matching condition of inlet and exhaust frequencies. The correlation is most obvious for a pulsejet with a shorter exhaust duct. For

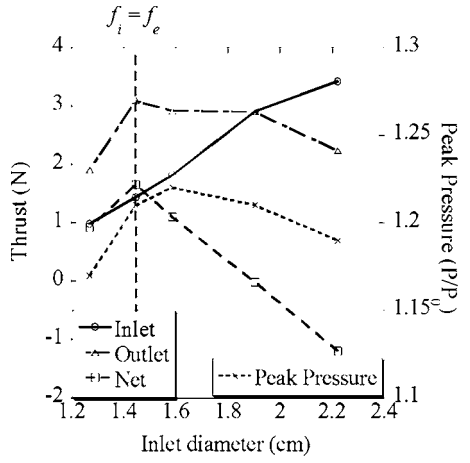

Fig. 10 Thrust versus inlet diameter for 50 cm exhaust duct pulsejet

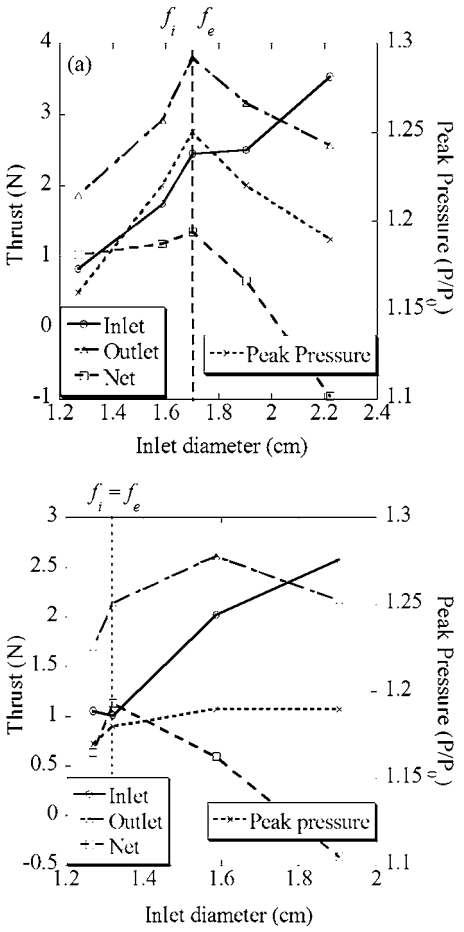

Fig. 11 Thrust versus inlet diameter: (*a*) 42 cm exhaust duct pulsejet and (*b*) 58 cm exhaust duct pulsejet

a 42 cm exhaust duct pulsejet (see Fig. 11(*a*)), the peak combustion chamber pressure takes on a maximum value when the inlet and exhaust frequencies are coincident, and is less sensitive at longer lengths. As expected, the net thrust is correlated with peak chamber pressure.

From the inlet frequency equation (Eq. (2)), it is clear that another way to change the inlet frequency is to change the inlet length. For a pulsejet with a 58 cm exhaust duct length and inlet diameter of 1.6 cm, the inlet-exhaust frequency match condition yields a length of 14 cm. Simulations were performed for this pulsejet as well as for inlet lengths of 10 cm and 17 cm. Results are shown in Fig. 12. Again, the greatest net thrust is obtained for the case when the inlet frequency is equal to exhaust frequency.

These results lead to a conclusion that the total thrust of a valveless pulsejet is maximized when the inlet frequency is equal to the exhaust frequency. This is explained by the resonance between the inlet and exit ducts that enhances waves traveling through the pulsejet, thus improving the pulsejet performance.

The obtained results also suggest that when the difference between the inlet and exhaust frequencies exceeds a certain critical value, pulsejet operation becomes impossible. Table 4 gives the smallest and largest inlet diameters of the pulsejet for which sustainable operation is observed. Although these values do not provide exact boundaries of the region when pulsejet operation is possible, they reflect the relationship between the frequency and operation possibility. Figure 13 shows the simulated chamber pressure for a pulsejet with 2.54 cm inlet diameter and 42 cm exhaust duct length. The inlet frequency increases with the inlet diameter and in this case, it exceeds a tolerable inlet and exhaust

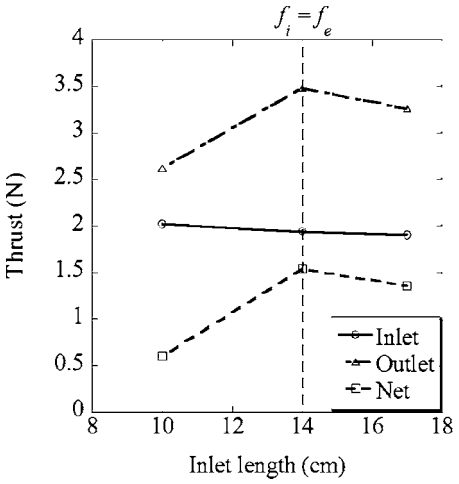

Fig. 12 Thrust versus inlet length for 58 cm exhaust duct pulsejet

frequency difference. As shown in Fig. 13, the amplitude of the pressure oscillation in the pulsejet decays and operation ceases.

Pulsejet in Convective Stream. Simulations were also performed for pulsejets in a freestream. Results are shown for a 42 cm exhaust duct pulsejet with 1.0–2.2 cm inlet diameter and 0.47 g/s fuel flow rate at 0 (static) m/s, 30 m/s, 50 m/s, and 80 m/s freestream velocities in Fig. 14. As seen in this figure, as the inlet diameter increases, the net thrust initially slightly increases before dramatically falling off. Also notable is that as the free stream velocity increases, the inlet diameter corresponding to the maximum net thrust decreases.

To determine the inlet diameter yielding the maximum net thrust, inlet and exhaust frequencies were compared. Simulation results suggest that the higher the freestream velocity, the larger the difference between the inlet diameter for the maximum net thrust and the inlet diameter that makes the inlet and exhaust frequencies equal.

Since pulsejet frequencies are determined by acoustic waves traveling through the pipe, an explanation of this phenomenon is that the freestream velocity changes the inlet frequency. It is ex-

Table 4 Simulation results for smallest and largest diameters for 42 cm exhaust duct pulsejet

Inlet diameter (cm)	Inlet frequency (Hz)	Exhaust frequency (Hz)	Inlet frequency/exhaust frequency
1.27	168	215	0.78
2.22	323	255	1.27

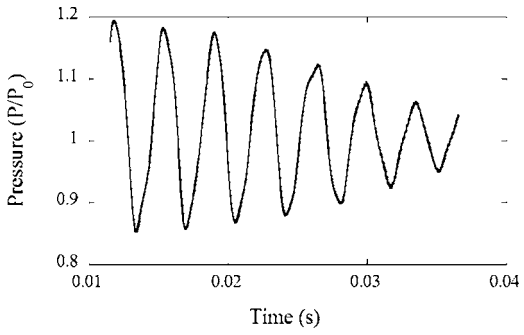

Fig. 13 Chamber pressure 2.54 cm inlet diameter, 0.42 m exhaust duct pulsejet

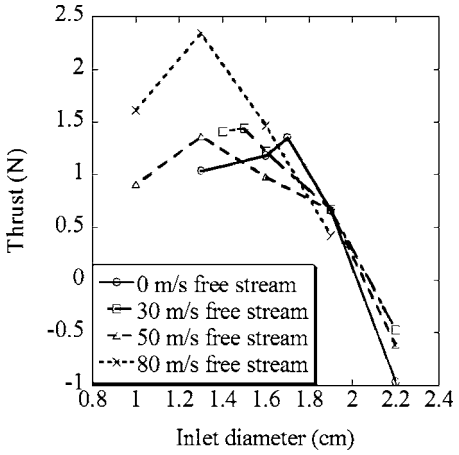

Fig. 14 Thrust versus inlet diameter for different freestream speeds

pected that this change is related to the Mach number M of the freesteam. It is hypothesized that the freestream velocity increases the inlet frequency by the factor of $(1-\mathrm{M})^a$. Table 5 shows the simulation results used to evaluate the power a by using the data for 50 m/s and 80 m/s convective streams. These simulations suggest that a is equal to approximately −1.5. Equation (2) is then modified to account for the inlet flow velocity as follows:

$$f_i = [c_i/(2\pi)][S_i/(VL_i)]^{0.5}(1-\mathrm{M})^{-1.5} \quad (4)$$

This new equation for f_i is used to determine the inlet diameter for the maximum thrust for the inlet flow velocities of 30 m/s and 120 m/s. The predicted inlet diameters for these two cases are 1.5 cm and 1.1 cm, respectively. Figure 15 shows thrust versus inlet diameter for the inlet flow velocities of 30 m/s and 120 m/s. The maximum net thrust is observed to exactly occur at the diameter predicted by Eq. (4) in each case.

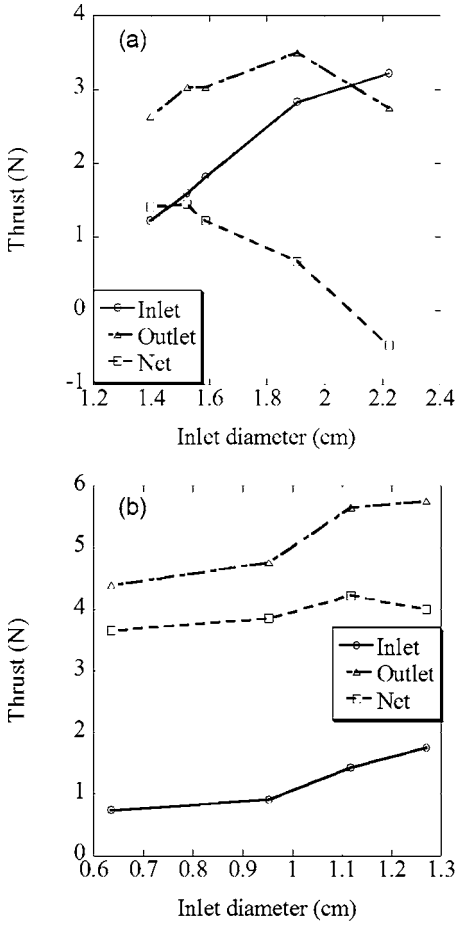

Fig. 15 Thrust versus inlet diameter: (*a*) 30 m/s freestream and (*b*) 120 m/s freestream

Conclusions

From the coupled experimental and computational investigation, the following conclusions are obtained.

1. The operating frequency of the valveless pulsejet depends on the average sound speed (dictated by temperature) and the geometry of both the inlet and exhaust. The average of the frequencies calculated with the one-sixth wavelength equation for the exhaust duct and the Helmholtz resonator equation for the inlet tube predicts the operating frequency of the pulsejets observed in both simulations and experiments within an uncertainty of 10%. The operating frequency increases when the inlet diameter increases, the inlet length decreases, and when the exhaust duct length decreases.
2. The two-dimensional model simulates the experiment reasonably well. Different fuel supply configurations result in the chamber temperature and frequency in the simulation being 5–10% higher than in the experiment.
3. Increasing inlet diameter results in decreasing average inlet temperature, increasing average exhaust temperature, and increasing net mass flow traveling through the pulsejet. The decrease in average inlet temperature suggests that fewer combustion products leave through the inlet with increasing inlet diameter, contrary to intuition.
4. A new analytical acoustic model, where the inlet is treated as a Helmholtz resonator and the exhaust duct is treated as a wave tube, is shown to accurately predict the operating frequency.
5. The difference between inlet (Helmholtz) and exhaust (wave tube) frequencies has a great effect on the operation of a pulsejet. When the inlet frequency is equal to the exhaust frequency, the maximum net thrust is obtained. Conversely,

Table 5 Factor *a* get from 50 m/s and 80 m/s results

Freestream speed (m/s)	Values near peak thrust: Inlet frequency (Hz)	Values near peak thrust: Exhaust frequency (Hz)	ln (exhaust /inlet frequency)	ln(1−M)	*a*
50	164	213	0.261	−0.1556	−1.68
80	154	230	0.401	−0.2620	−1.53

if the difference between the inlet and exhaust frequencies exceeds a critical value, pulsejet operation ceases.

6. A freestream significantly changes the operation of the pulsejet. As the freestream velocity increases, the peak thrust occurs at smaller inlet diameters (or longer inlet lengths). This smaller inlet diameter is predicted by taking into account the freestream Mach number, and modifying the inlet frequency by the factor of $(1-M)^{-1.5}$.

References

[1] Putnam, A. A., Belles, F. E., and Kentfield, J. A. C., 1986, "Pulse Combustion," Prog. Energy Combust. Sci., **12**, pp. 43–79.

[2] Foa, J. V., 1960, *Elements of Flight Propulsion*, Wiley, New York, pp. 368–389.

[3] Logan, Jr., J. G., 1951, "Summary Report on Valveless Pulsejet Investigation," Cornell Aeronautics Laboratory, Project SQUID Technical Memorandum No. CAL-42.

[4] Logan, Jr., J. G., 1949, "Valveless Pulse Jet Investigations, Part I, Test of Small Scale Models," Cornell Aeronautics Laboratory, Project SQUID Technical Memorandum No. CAL-27.

[5] Logan, Jr., J. G., and Finamore, O. B., 1948, "Suggested Forms for Air Duct Motors Utilizing Intermittent Combustion, Part IV, Intermittent Combustion Experiments," Cornell Aeronautics Laboratory, Project SQUID Technical Memorandum No. CAL-20.

[6] Rudinger, G., 1951, "On the Performance Analysis of the Ducted Pulsejet," Cornell Aeronautics Laboratory, Project SQUID Technical Memorandum No. CAL-36.

[7] Wilder, Jr., J. G., 1949, "An Experimental Investigation of the Effect of Inlet Ducts on the Performance Characteristics of a Pulse Jet," Cornell Aeronautics Laboratory, Project SQUID Technical Memorandum No. CAL-29.

[8] Lockwood, R. M., 1963, "Pulse Reactor Lift-Propulsion System Development Program, Final Report," Hiller Aircraft Co., Advanced Research Division Report No. 508.

[9] Jacobson, S. A., 1998, "Aerothermal Challenges in the Design of a Microfabricated Gas Turbine Engine," *29th AIAA Fluid Dynamics Conference*, Albuquerque, NM, Paper No. AIAA 98-2545.

[10] Wan, Q., Roberts, W. L., and Kuznetsov, A. V., 2005, "Computational Analysis of the Feasibility of a Micro-Pulsejet," Int. Commun. Heat Mass Transfer, **32**, pp. 19–26.

[11] Geng, T., Kiker, A., Ordon, R., Schoen, M., Kuznetsov, A. V., Scharton, T., and Roberts, W. L., 2005, "Experimentation and Modeling of Pulsed Combustion Engines," *Four Joint Meeting of the US Sections of the Combustion Institute*, Philadelphia.

[12] Geng, T., Schoen, M. A., Kuznetsov, A. V., and Roberts, W. L., 2007, "Combined Numerical and Experimental Investigation of a 15-cm Valveless Pulsejet," Flow, Turbul. Combust., **78**, pp. 17–33.

[13] Ordon, R. L., 2006, "Experimental Investigation of 50 cm Class Valveless Pulsejet Engines," MS, thesis, North Carolina State University, Raleigh, NC.

[14] Kailasanath, K., Gardner, J., Oran, E., and Boris, J., 1991, "Numerical Simulations of Unsteady Reactive Flows in a Combustion Chamber," Combust. Flame, **86**, pp. 115–134.

[15] Chun, Y., and Kim, Y., 2000, "Numerical Analysis for Nonlinear Resonant Oscillations of Gas in Axisymmetric Closed Tubes," J. Acoust. Soc. Am., **108**, pp. 2765–2774.

[16] CFX 5.7.1 Help Documents, 2004, "Turbulence Models," CFX-5 Solver Modeling, pp. 103–118.

[17] CFX 5.7.1 Help Documents, 2004, "Eddy Viscosity Turbulence Models," CFX-5 Solver theory, pp. 63–74.

[18] Travis, T., Scharton, T. D., Kuznetsov, A. V., and Roberts, W. L., 2006, "The Principles of Operation of a Pulsejet With Valves," *13th International Congress on Sound and Vibration*, Vienna, Austria.

[19] Rossing, T. D., and Fletcher, N. H., 2004, *Principles of Vibration and Sound*, Springer-Verlag, New York, pp. 216–219.

Oxidation of Natural Gas, Natural Gas/Syngas Mixtures, and Effect of Burnt Gas Recirculation: Experimental and Detailed Kinetic Modeling

T. Le Cong

P. Dagaut
e-mail: dagaut@cnrs-orleans.fr

G. Dayma

Centre National de la Recherche Scientifique 1C,
Avenue de la Recherche Scientifique,
45071 Orléans Cedex 2, France

The oxidation of methane-based fuels was studied experimentally in a fused-silica jet-stirred reactor (JSR) operating at 1–10 atm, over the temperature range of 900–1450 K, from fuel-lean to fuel-rich conditions. Similar experiments were performed in the presence of carbon dioxide or syngas (CO/H_2). A previously proposed kinetic reaction mechanism updated for modeling the oxidation of hydrogen, CO, methane, methanol, formaldehyde, and natural gas over a wide range of conditions including JSR, flame, shock tube, and plug flow reactor was used. A detailed chemical kinetic modeling of the present experiments was performed yielding a good agreement between the modeling, the present data and literature burning velocities, and ignition data. Reaction path analyses were used to delineate the important reactions influencing the kinetic of oxidation of the fuels in the presence of variable amounts of CO_2. The kinetic reaction scheme proposed helps understand the effect of the additives on the oxidation of methane.
[DOI: 10.1115/1.2901181]

1 Introduction

Flameless combustion is an interesting emerging combustion concept that can be used for reducing pollutant emissions, particularly NO_x, and improving combustion efficiency. Its application to gas turbine is currently studied [1]. In this new type of combustor, reactants are preheated and diluted by exhaust gases, mainly CO, CO_2, H_2O, and traces of NO_x. Also, the interest for using syngas (CO/H_2) in gas turbines is increasing [2]. Therefore, it is important to study the effect of such compounds on the kinetics of oxidation of conventional fuels, such as natural gas under gas turbine operating conditions. Well-stirred reactors such as that used here are very valuable tools for studying fuel oxidation and providing a database for detailed kinetic modeling. The effects of NO_x recirculation were previously addressed [3–5], whereas those of the other components of recycled gases were not.

In this paper, we present new experimental results obtained for the oxidation of natural gas blends in a JSR at 1–10 atm, over a wide range of equivalence ratio (0.1–1.5), for temperatures in the range of 900–1450 K. Also, the oxidation of methane-based fuels under JSR, shock-tube, and premixed flame conditions is modeled using an updated kinetic scheme. Kinetic analyses including sensitivity analyses and reaction path analyses were used to rationalize the results and propose an improved kinetic combustion model for the $H_2/CO/CH_2O/CH_3OH/CH_4$ systems [6].

2 Experimental Setup

The experimental setup used here is that used earlier [3–8]. The jet-stirred reactor (JSR) consisted of a small sphere of 4 cm diameter (30 cm^3) made of fused-silica (to minimize wall catalytic reactions), equipped with four nozzles of 1 mm inside diameter (i.d.) for the admission of the gases, which achieve the stirring (Fig. 1). A nitrogen flow of 100 l/h was used to dilute the fuel. As before [3–8], all the gases were preheated before injection to minimize temperature gradients inside the reactor. The flow rates were measured and regulated by thermal mass-flow controllers. The fuel and oxygen flowed separately until they reach the mixing point at the entrance of the injectors. Previous residence time distribution studies showed that this reactor operates under macromixing conditions. The JSR operated under steady-state conditions and, due to the high-dilution of the reactants, no flame occurred and the temperature rise due to the reaction was generally <30 K. Thus, a perfectly stirred-reactor model could be used. As before [3–8], a good thermal homogeneity was observed along the vertical axis of the reactor by thermocouple measurements. A Pt/Pt–Rh 10% thermocouple, located inside a thin-wall (<0.5 mm) fused-silica tube to prevent catalytic reactions on the metallic wires of 0.1 mm in diameter, was used. Typical temperature variations of <10 K along the vertical axis of the reactor were measured. Low pressure samples of the reacting mixtures were taken by sonic probe sampling and collected in 1 l Pyrex bulbs at $\sim$50 mbars for immediate gas chromatography (GC) analyses as in Refs. [3–7]. In order to improve the GC detection, these samples were pressurized at 0.8 bar before injection into the GC column, using a glass home-made piston. Capillary columns of 0.53 mm i.d. (Poraplot U and Molecular sieve 5A) were used with a thermal conductivity detector (TCD) and a flame ionization detector (FID) for the measurements of gases, except hydrogen measured on another system. Helium was used as a carrier gas. For hydrogen measurements, a GC operating with nitrogen as carrier gas, a Carboplot (0.53 mm i.d.) and a TCD were used. On-line Fourier transform infrared (FTIR) analyses of the reacting gases were also performed by connecting the sampling probe to a temperature controlled (140°C) gas cell (2 m or 10 m path length) via a Teflon heated line (130°C). The present analytical system allowed the measurements of methane, ethane, ethylene, acetylene, H_2, O_2, H_2O, CO, CH_2O, and CO_2. Very good agreement between the GC and FTIR analyses was found for the compounds measured by both techniques (methane, ethylene, acety-

Contributed by the International Gas Turbine Institute of ASME for publication in the JOURNAL OF ENGINEERING FOR GAS TURBINES AND POWER. Manuscript received July 19, 2007; final manuscript received July 31, 2007; published online April 29, 2008. Review conducted by Dilip R. Ballal.

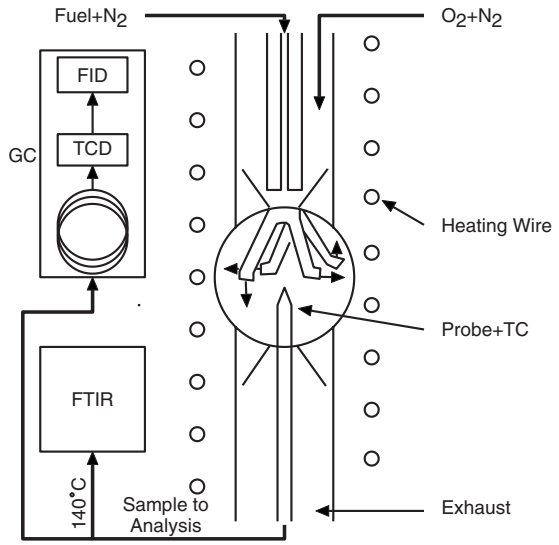

Fig. 1 Schematic representation of the JSR setup used in this work

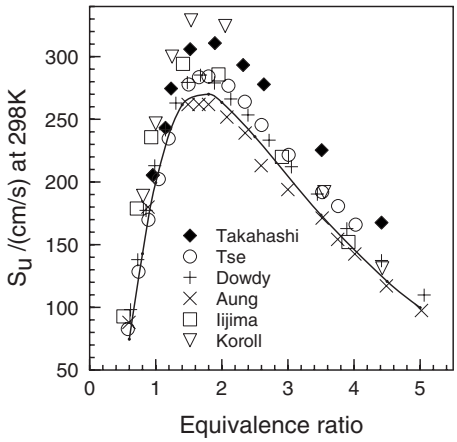

Fig. 2 The burning velocities of H_2/Air at 1 atm and 298 K. The data (symbols: ♦ [12], ○ [13], + [14], × [15], □ [16], ▽ [17]) are compared to this modeling (line)

lene, CO, and CO_2). The reported profiles for hydrocarbons were obtained by GC-FID and those for CO and CO_2 where measured by FTIR. The reported mole fractions were above the detection limits. Quantitative measurements were limited to 1 ppm for hydrocarbons, and 20 ppm for oxygen, hydrogen, water, CO, formaldehyde, and CO_2. Carbon balance was checked for every sample and found generally good within $100 \pm 8\%$.

3 Modeling

For the kinetic modeling of premixed flames, we used the PREMIX computer code [9]. For simulating the ignition delays, we

Table 1 Conditions for present model validation

Mixture	Su[a]	Ignition delays[a]	Flame structures	JSR[b]	PFR	ST	Refs.
H_2-O_2-diluent (N_2;Ar;He)	1–20 atm; 298 K; Φ=0.6–5	1–87 atm; 983–1930 K	0.0467 atm; Φ=1.92; T_o=570 K	1–10 atm; Φ=0.2–2; 700–1150 K	0.6–15.7 atm; 884–943 K		[12–17], [19,40,41]
$H_2-O_2-CO_2-N_2$	1 atm; 300 K; Φ=1–1.8			1 atm; Φ=0.2–2; 900–1050 K			[18]
$H_2-O_2-H_2O-N_2$	1 atm; 373 K; Φ=0.2–0.6			1 atm; Φ=0.2–2; 850–1050 K			[42]
H_2-CO-O_2-diluent (N_2;Ar;He)	1–20 atm; 292–700 K; Φ=0.6–5	1.05–1.13 atm; 850–1350 K	0.0526 atm; Φ=0.13; T_o=328 K	1 atm; Φ=0.1–2; 850–1400 K		24–43 atm; Φ=0.5–1; 1044–1456 K	[20–22], [24,27], [43]
$H_2-CO-H_2O-O_2-N_2$	1 atm; 298 K; 38–90%CO				1–9.6 atm; 1032–1041 K		[44,45]
$H_2-CO-CO_2-O_2$-diluent (N_2;He)	1–10 atm 298 K; Φ=0.6–1						[22,23]
CH_4-O_2-diluent (N_2;Ar)	1–12 atm; 298 K and 615 K; Φ=0.6–1,5	1–60 atm; 1400–2000 K	0.0263–1 atm; Φ=0.8–1.2	1–10 atm; Φ=0.1–1.5; 1000–1450 K	1.2 atm; 1100 K		[28–32], [46–49]
$CH_4-O_2-CO_2-N_2$	1 atm; 298 K; Φ=0.6–1.5			1; Φ=0.1–1.5; 1026–1452 K			[33]
$CH_4-H_2-O_2-N_2$	1 atm; 298 K; Φ=0.6–1.2	10–23 atm; 1440–1553 K		1–10 atm; Φ=0.1–1.5; 925–1277 K			[31,37,38]
$CH_4-H_2-CO-O_2-N_2$				1 atm; Φ=0.1–1.5; 950–1400 K			
$CH_4-H_2-CO_2-O_2-N_2$				1–10 atm; Φ=0.1–1.5; 925–1450 K			

[a]Global parameter.
[b]New data.

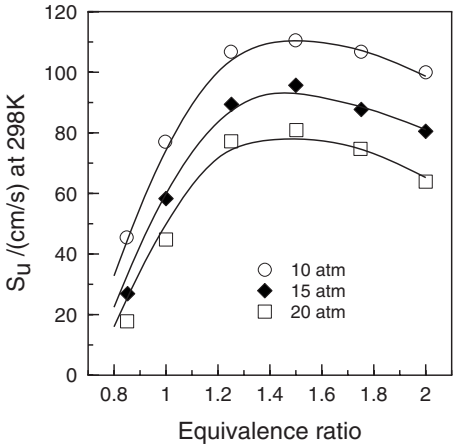

Fig. 3 The burning velocities of $H_2/O_2/He$ ($O_2/(O_2+He)$ =0.08) at 10–20 atm and 298 K (data from Ref. [13])

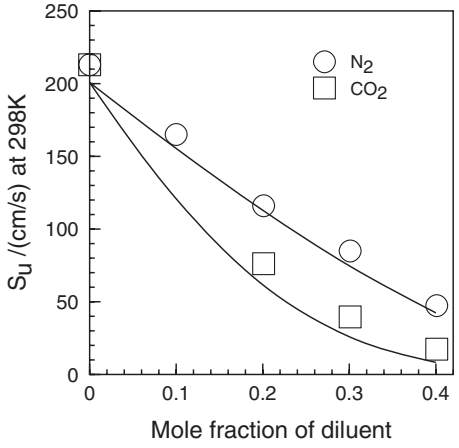

Fig. 4 The burning velocities of H_2/Air/diluent (N_2 and CO_2) at 1 atm, 298 K, and Φ=1.0 (data from Ref. [18])

used the SENKIN code [10]. For the JSR computations, we used the PSR computer code [11] that computes species concentrations from the balance between the net rate of production of each species by chemical reactions and the difference between the input and output flow rates of species. These rates are computed from the kinetic reaction mechanism and the rate constants of the elementary reactions calculated at the experimental temperature, using the modified Arrhenius equation. The reaction mechanism used here has a strong hierarchical structure. It is based on the comprehensive hydrocarbon oxidation mechanisms [3,4,7] developed earlier. The H_2/O_2 and C_1 subschemes were updated resulting in an improved modeling of the $H_2/CO/CH_2O/CH_3OH/CH_4$ combustion systems, as briefly presented in the next paragraph. The reaction mechanism used here consisted of 99 species and 485 reversible reactions. The main updates concern the thermochemistry of the OH radical, and the kinetics of the following reactions: $H+H+M=H_2+M$, $H+OH+M=H_2O+M$, $HO_2+OH=H_2O+O_2$, $HO_2+O=OH+O_2$, $H+HO_2=H_2+O_2$, $H+HO_2=OH+OH$, $HO=+HO_2=H_2O_2+O_2$, $OH+OH(+M)=H_2O_2(+M)$, $CO+HO_2=CO_2+OH$, $HCO+O_2=CO+HO_2$, $CH_2O+M=HCO+H+M$, $CH_3+CH_3(+M)=C_2H_6(+M)$. This mechanism, including references and thermochemical data, is available from the authors. The rate constants for reverse reactions are computed from the corresponding forward rate constants and the appropriate equilibrium constants, $K_c=k_{\text{forward}}/k_{\text{reverse}}$ calculated using thermochemical data [3–8].

The updated kinetic scheme was successfully validated against a large set of data (Table 1). Examples of the kinetic model validation for H_2 combustion are given in Figs. 2–5. As can be seen from Figs. 2 and 3, the burning velocities of hydrogen are well predicted by the model over a wide range of equivalence ratios and pressures (up to 20 atm). Also, the decrease in flame speed due to the dilution by nitrogen or carbon dioxide is well simulated (Fig. 4). The kinetics of hydrogen oxidation was measured by Mueller et al. [19] in a turbulent flow reactor at pressures up to ~16 atm. The present model represents well these data (Fig. 5).

Since one of the objectives of the present study is to provide a validated kinetic model for the combustion of fuel mixtures containing syngas, further tests were performed for the combustion of CO/H_2 mixtures. Thus, the presently updated kinetic scheme was successfully validated against a large set of data (Table 1) for CO and CO/H_2 combustion, as shown in Figs. 6–14. The effect of total pressure and equivalence ratio on flame speeds is well predicted as is the increase in flame speed resulting from the increased fraction of hydrogen in a syngas fuel (Figs. 6–8). Also, the reduction in flame speed by addition of carbon dioxide is well predicted (Fig. 8) by the present model. Figure 10 shows that the model predicts well the activating effect on ignition of increased hydrogen fraction in a syngas fuel. Also, the kinetics of oxidation of CO and hydrogen/CO mixtures were previously measured in a turbulent flow reactor and a JSR. The present model represents

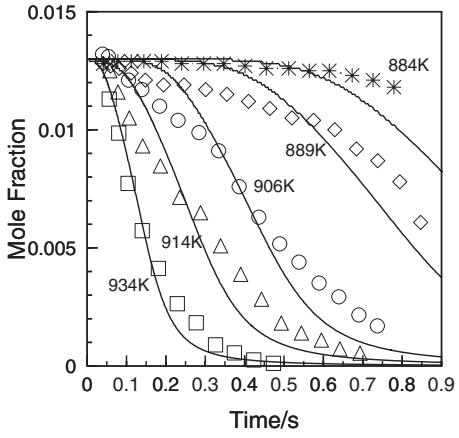

Fig. 5 Oxidation of hydrogen in a "plug" flow reactor (1.3%H_2+2.2%O_2+N_2 at 6.5 atm). The experimental mole fractions of hydrogen (symbols) are compared to the modeling (lines). The data are from Ref. [19].

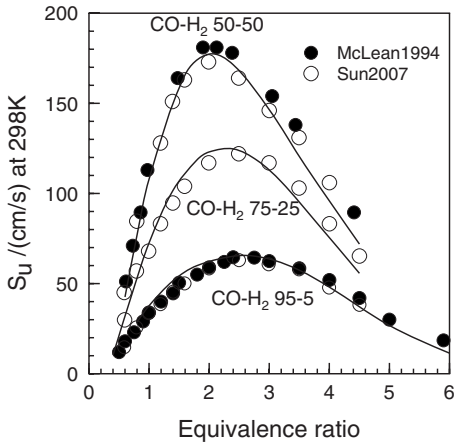

Fig. 6 The burning velocities of CO/H_2/air at 1 atm and 298 K. The data (symbols:● [20], ○ [21]) are compared to this modeling.

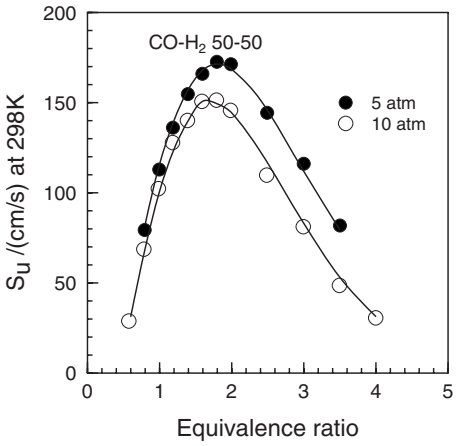

Fig. 7 The burning velocities of CO/H_2/He at 5–10 atm and 298 K. The data were taken from Ref. [21].

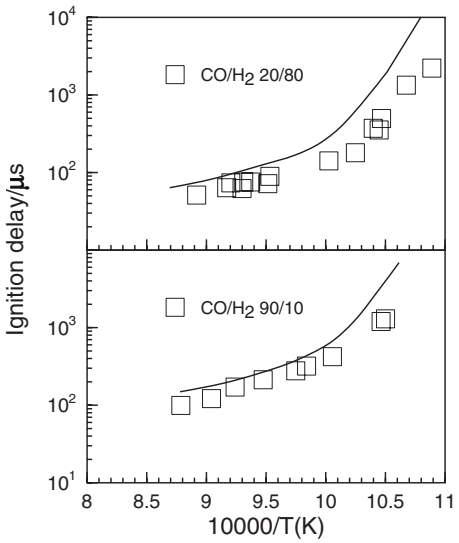

Fig. 10 The ignition of hydrogen-CO-air mixtures. Top: CO/H_2 20/80, Φ=0.5, 1.05 atm; Bottom: CO/H_2 90/10, Φ=0.5, 1.13 atm. The data are from Kalitan and Petersen [24].

well these data (Figs. 11 and 12). Finally, the high-pressure shock-tube experiments on CO/H_2 ignition [27] have been successfully simulated using the present kinetic scheme (Figs. 13 and 14). Besides the kinetic of methane oxidation under JSR conditions,

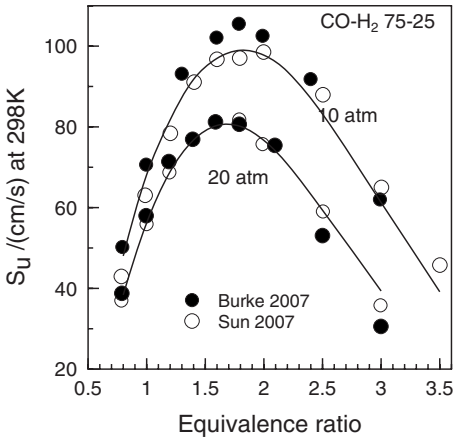

Fig. 8 The burning velocities of hydrogen CO/H_2/He at 10–20 atm and 298 K. The data are from Sun [21] and Burke [22].

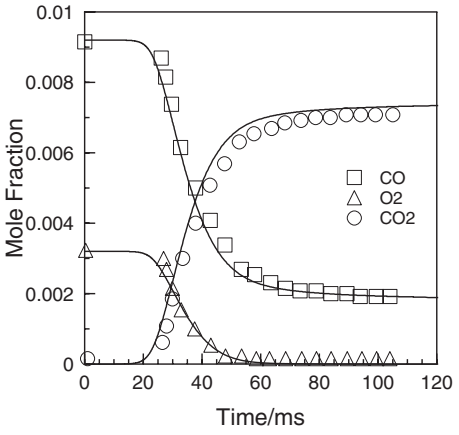

Fig. 11 The oxidation of CO in a PFR at 1 atm (0.92% CO, 0.32% O_2, 0.59% H_2O, N_2 diluent). The data are from Yetter et al. [25].

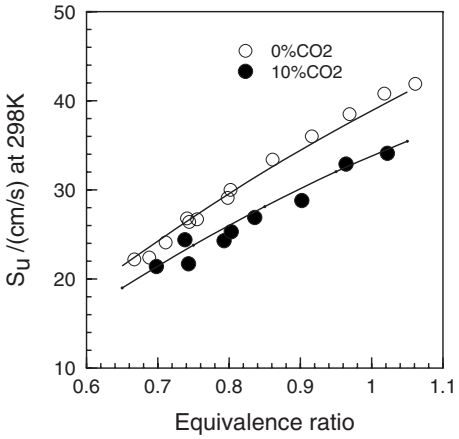

Fig. 9 Effect of CO_2 on the burning velocities of CO/H_2 95/5 at 1 atm and 298 K. The data are from Ref. [23].

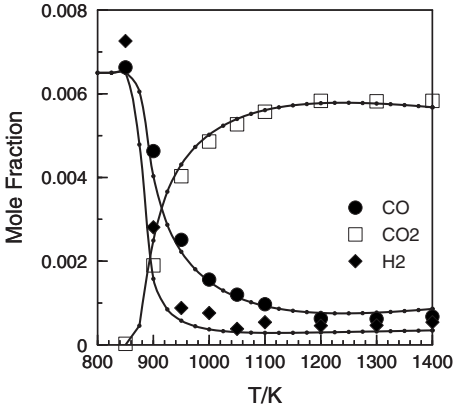

Fig. 12 The oxidation of a hydrogen-CO 50/50 mixture in a JSR at 1 atm and Φ=1 (6500 ppm of CO, 6500 ppm of H_2, 120 ms). The data are from Dagaut et al. [26].

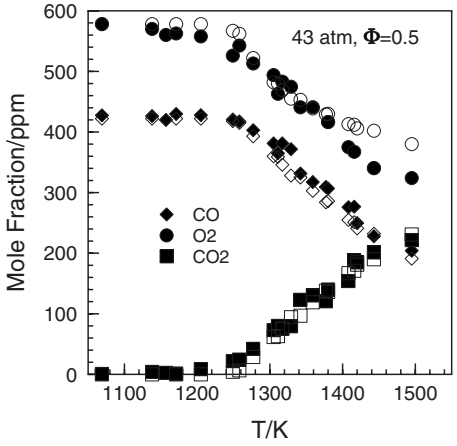

Fig. 13 The oxidation of hydrogen-CO−O_2−Ar mixtures in a single pulse ST at high pressure. Comparison between data (closed symbols) and modeling (open symbols): B: 43 atm, Φ =0.5 (data form Sivaramakrishnan et al. [27]).

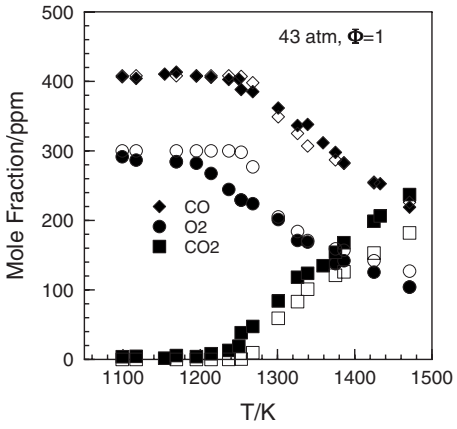

Fig. 14 The oxidation of hydrogen-CO−O_2−Ar mixtures in a single pulse ST at high pressure. Comparison between data (closed symbols) and modeling (open symbols): 43 atm, Φ=1 (data from Ref. [27]).

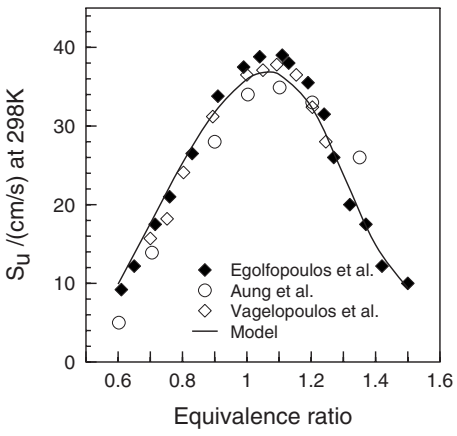

Fig. 15 The laminar burning velocities of methane-air mixtures at 1 atm and 298 K. The present modeling (dashed line) is compared to data taken from Ref. [28–30] (symbols).

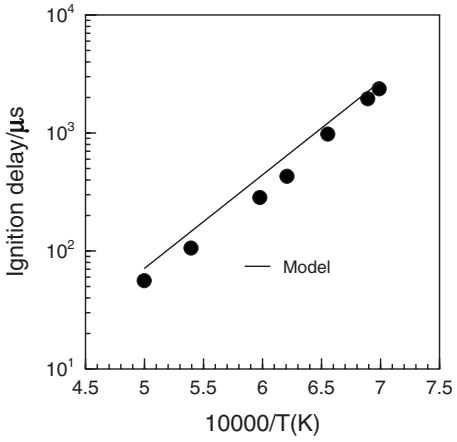

Fig. 16 The ignition of CH_4−O_2−N_2 (5.25% CH_4, 20.98% O_2, 73.77% N_2) at 0.5–0.9 atm. The data are from Petersen et al. [31].

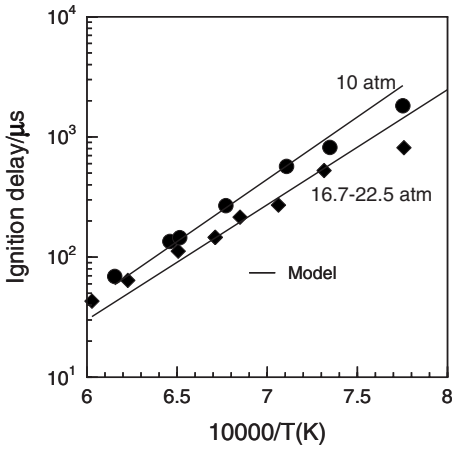

Fig. 17 The ignition of CH_4−O_2−N_2 (5% CH_4, 20% O_2, 75% N_2) at 10 atm and 16.7–22.5 atm. The data are from Petersen et al.

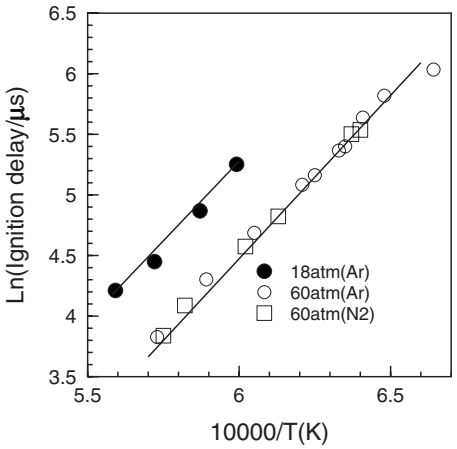

Fig. 18 The ignition of CH_4−O_2-diluent (N_2 or Ar) at 18 and 60 atm. The data are from Petersen et al. [32].

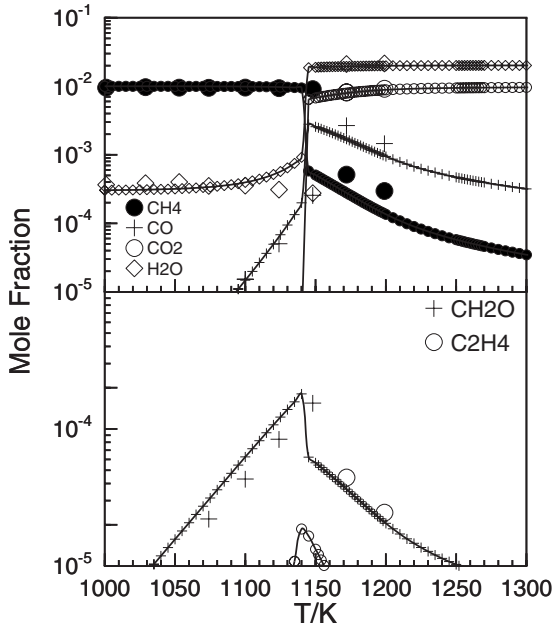

Fig. 19 The oxidation of methane in a JSR (1 atm, τ=120 ms, 1% CH_4, φ=0.3, dilution by nitrogen). The data (large symbols) are compared to the modeling (lines and small symbols).

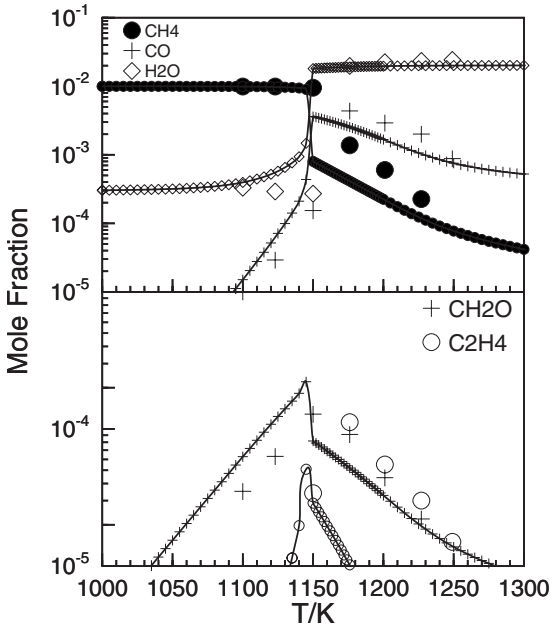

Fig. 20 The oxidation of methane with CO_2 in a JSR (1 atm, τ=120 ms, 1% CH_4, 20% CO_2, φ=0.3, dilution by nitrogen). The data (large symbols) are compared to the modeling (lines and small symbols).

the kinetic model was validated against the methane/air burning velocities (Fig. 15). As can be seen from this figure, the modeling results agree very well with the data of Refs. [28,30] for the methane-air flame speeds. The high-pressure ignition delays (up to 60 atm) of Petersen et al. [31,32] (Figs. 16–18) are of particular interest for validating such a kinetic scheme for gas turbine applications. As can be seen from Figs. 16–18, the present model (lines) performs well simulating this set of data (symbols).

4 Results and Discussion

This study yielded a large set of experimental results for the oxidation of methane-based fuel mixtures over the temperature range of 900–1450 K, for equivalence ratios ranging from 0.1 to 1.5, and for various mole fractions of methane, hydrogen, carbon monoxide, and carbon dioxide. The experiments were performed at a constant residence times of 120 ms at 1 atm and 250 ms at 10 atm. The reaction was studied by varying stepwise the operating temperature in the JSR. Concentration profiles for the reactants, stable intermediate compounds, and final products (O_2, H_2, H_2O, CO, CO_2, CH_2O, CH_4, C_2H_6, C_2H_4, and C_2H_2) were obtained. The proposed kinetic reaction mechanism was used to simulate the present experiments.

4.1 Methane and Methane-CO_2 Oxidation. The examination of the present results allows a comparison of the kinetics of the neat oxidation of methane with that of methane-carbon dioxide mixtures (Figs. 19 and 20). As can be seen from these figures, the presence of 20% carbon dioxide tends to slightly inhibit the oxidation of the fuel: A shift of the concentration toward higher temperatures is observed in the experiments, in agreement with the computations. Table 2 gives the temperature at which 50% methane is consumed, showing the inhibiting effect of CO_2 (the 50% methane consumption is observed at higher temperatures in presence of CO_2). A good agreement between the data and the model is observed. The kinetic modeling shows that CO_2 has an inhibiting effect via the reaction $CO_2+H \Rightarrow CO+OH$ that competes with the H-abstraction reaction $CH_4+H \Rightarrow CH_3+H_2$, decreasing the consumption rate of methane. Since the concentration of H increases with equivalence ratio, the effect is more pronounced under fuel-rich conditions. Also, the H atoms converted by the reaction CO_2 are not available for the main branching reaction $H+O_2 \Rightarrow OH+O$. The model was further tested by simulating the flame speeds of methane-oxygen mixtures in the presence of increasing quantities of carbon dioxide (Fig. 21) reported

Table 2 Summary of the effects of H_2, H_2/CO, CO_2, and pressure on methane oxidation under present JSR experimental conditions

Reactants	T (K)	P (atm)	τ (ms)	T/K at 50% consumption of CH_4				
				ϕ=0.1	ϕ=0.3	ϕ=0.6	ϕ=1	ϕ=1.5
1%CH_4+O_2+N_2 (a)	1000–1450	1	120	1066	1160	1238	1295	1337
1%CH_4+O_2+20%CO_2+N_2	1000–1450	1	120	**1080**	**1163**	—	**1325**	**1375**
0.8%CH_4+0.8%H_2+O_2+N_2	925–1400	1	120	*985*	*1020*	*1055*	*1105*	*1178*
0.8%CH_4+0.8%H_2+O_2+20%CO_2+N_2	925–1450	1	120	*1000*	*1030*	*1070*	*1126*	*1201*
0.8%CH_4+0.4%H_2+0.4%CO+O_2+N_2	950–1400	1	120	*1005*	*1035*	*1090*	*1149*	*1200*
1%CH_4+O_2+N_2 (b)	900–1300	10	250	964	1075	1125	1173	1188
0.8%CH_4+0.8%H_2+O_2+N_2	900–1250	10	250	*960*	*987*	*1024*	*1075*	*1125*
0.8%CH_4+0.8%H_2+O_2+20%CO_2+N_2	900–1225	10	250	*975*	*1010*	*1038*	*1074*	*1125*

Note: Italics: increased reactivity relative to (a) or (b); bold: reduced reactivity relative to (a) or (b).

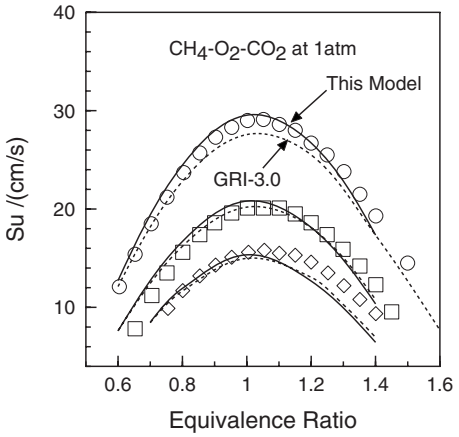

Fig. 21 The laminar burning velocities of methane-oxygen premixed flames in the presence of CO_2 (1 atm, dilution ratio $O_2/(O_2+CO_2)=R$ varied). The conditions were O, $R=0.35$; □, $R=0.3155$; ◇, $R=0.29$ [33]. The data (symbols) are compared to the present modeling (dashed lines) and using GRI-mech 3.0 (continuous line) [34].

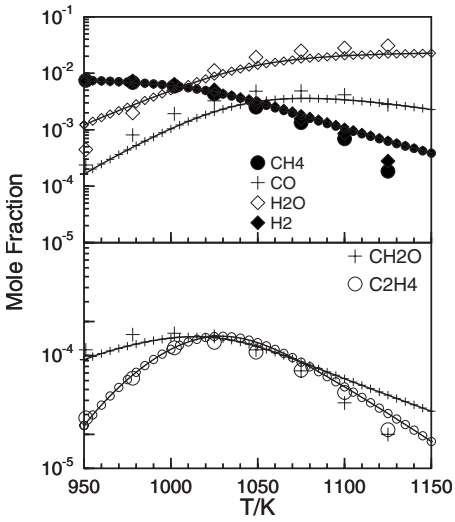

Fig. 23 The oxidation of methane-hydrogen in a JSR with 20% CO_2 (1 atm, $\tau=120$ ms, 0.8% CH_4, 0.8% H_2, $\varphi=0.3$, dilution by nitrogen). The data (large symbols) are compared to the modeling (lines and small symbols).

recently [12]. As can be seen from Fig. 21, the proposed model performs well predicting the inhibition by CO_2 and fits fairly well the data of [33]. One can also note the present model performs better than that of Ref. [34].

4.2 Methane-Hydrogen and Methane-H_2–CO_2 Oxidation. As demonstrated earlier [35,36], the reactivity of methane-hydrogen mixtures is higher than that of methane. The effect of carbon dioxide on the kinetics of oxidation of such mixtures was studied. The examination of the present results clearly confirms that the CH_4–H_2 mixtures (Fig. 22) are more reactive than neat methane mixtures (Fig. 19). Table 2 gives the temperature at which 50% methane is consumed, showing the increase of reactivity due to hydrogen.

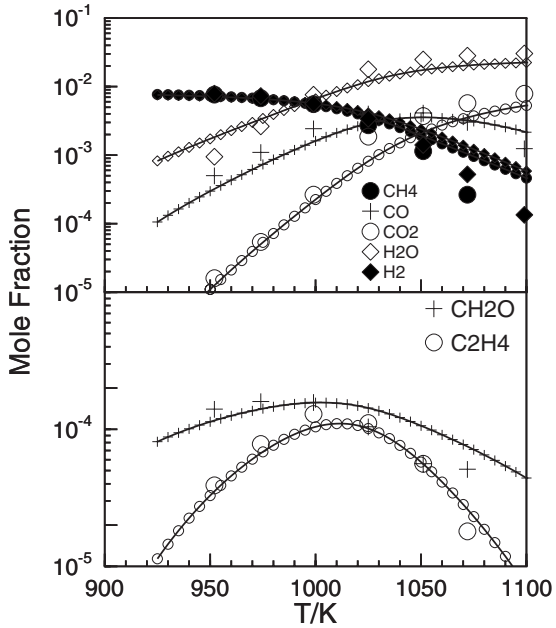

Fig. 22 The oxidation of methane-hydrogen in a JSR (1 atm, $\tau=120$ ms, 0.8% CH_4, 0.8% H_2, $\varphi=0.3$, dilution by nitrogen). The data (large symbols) are compared to the modeling (lines and small symbols).

The effect of carbon dioxide on the kinetics of oxidation of methane-hydrogen mixtures was studied. The examination of the present results (Fig. 23) reveals an inhibition of the fuel oxidation due to CO_2, increasing with equivalence ratio. Temperature shifts of ~10 K, 20 K, and 70 K are observed at, respectively, $\varphi=0.1$, 0.3, and 0.6. Table 2 gives the temperature at which 50% methane is consumed, further showing the inhibiting effect of CO_2. Again, the kinetic modeling shows that CO_2 has an inhibiting effect via the reaction $CO_2+H \Rightarrow CO+OH$ that competes with the H-abstraction reaction $CH_4+H \Rightarrow CH_3+H_2$, reducing the consumption of methane. Since the importance of the reaction of methane with H atoms is increasing with increasing equivalence ratio, the inhibiting effect of carbon dioxide is more pronounced when the equivalence ratio increases, as observed in the present experiments and modeling. Also, one should note that the maximum mole fraction of intermediates increases in the presence of CO_2. This is the case for carbon monoxide and ethylene. This is actually an indication of inhibition: Since the oxidation of the intermediates is slower, they accumulate further.

The model was further tested simulating the burning velocities [37–39] and ignition delays [31] of methane-hydrogen mixtures (Fig. 26). As can be seen from these figures, the model represents fairly well the experimental data taken from the literature. In Fig. 24, we can see that the model predicts well the data of Halter et al. [38], whereas the computed burning velocities at $\varphi \geqslant 1$ are slightly lower than computed before [36] as a result of the use of an updated H_2/O_2 scheme. The measured and experimental burning velocities show a strong increase with increasing concentration of hydrogen in the fuel mixture (Fig. 25). The high pressure ignition delay measurements of Petersen et al. [31] represent an interesting set of data to simulate since they were obtained under conditions representative of gas turbine operation and could be used to extend the validation range of the proposed kinetic scheme. The data and the modeling (Fig. 26) show the strong increase in reactivity resulting from the increased initial concentration of hydrogen in the fuel mixture.

Complementary experiments were performed in a JSR at 10 atm using similar gas mixtures. The experimental results are compared to the simulations in Figs. 27–29. As can be seen there, due to the increased mole concentration from the 1 atm to the 10 atm cases (the initial reactants mole fractions are the same), the fuel reacts at lower temperature at 10 atm than at 1 atm. The data

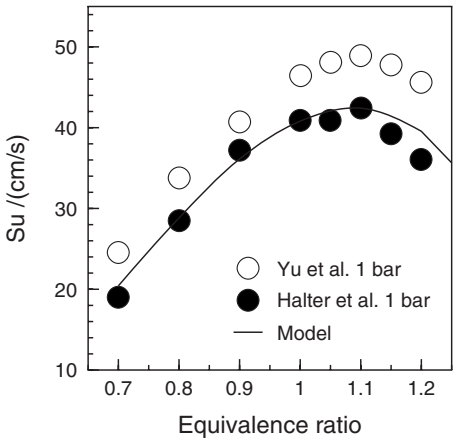

Fig. 24 The laminar burning velocities of methane-hydrogen (20%) mixtures at atmospheric pressure. The data [37,38] (symbols) are compared to the modeling (line).

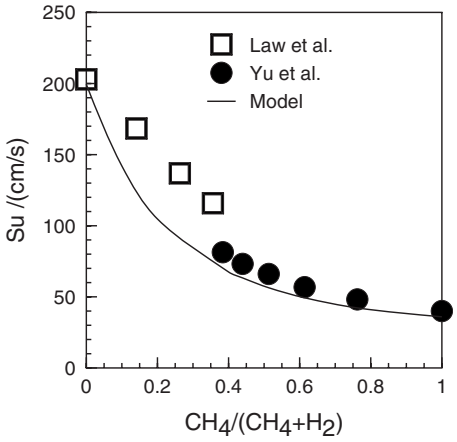

Fig. 25 The laminar burning velocities of φ=1 methane-hydrogen mixtures at atmospheric pressure. The data [37,39] (symbols) are compared to the modeling (line).

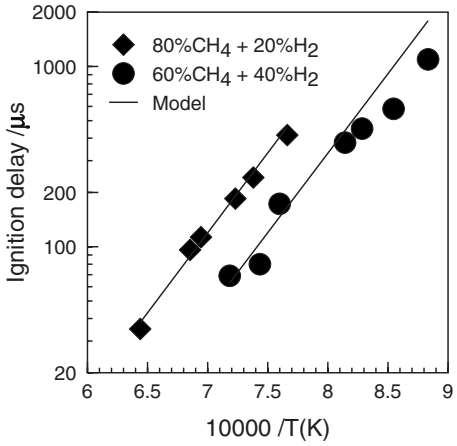

Fig. 26 Ignition delay of methane-hydrogen mixtures at 20–23 atm. The data [31] (symbols) are compared to the modeling (lines).

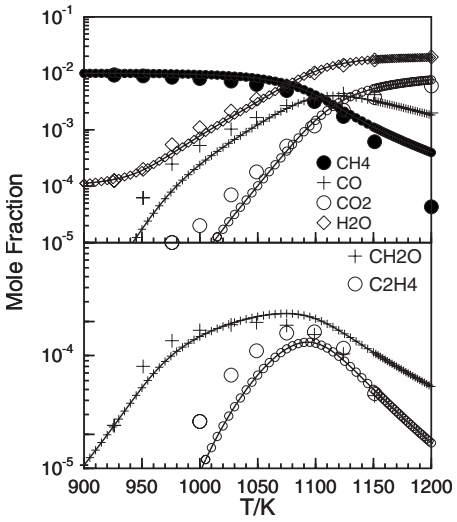

Fig. 27 The oxidation of methane in a JSR (10 atm, τ =250 ms, 1% CH_4, φ=0.3, dilution by nitrogen). The data (large symbols) are compared to the modeling (lines and small symbols).

and the model still indicate the increased reactivity of the methane-hydrogen mixtures compared to that of neat methane (Figs. 27 and 28). The presence of 20% CO_2 still reduces the reactivity of methane, based on the ethylene experimental profiles that show increased maximum mole fractions in the presence of carbon dioxide: 19%, 35%, 29% ($\pm$4%) increases are observed at, respectively, φ=0.1, 0.3, and 0.6. Table 2 gives the temperature at which 50% methane is consumed, confirming the inhibiting effect of CO_2. The kinetic model indicated a reduced inhibition by CO_2 at 10 atm in stoichiometric to fuel-rich conditions. This is due to a partial compensation of the reduction of H concentration, occurring via $CO_2+H \Rightarrow CO+OH$, by the H-atom production reaction $CH_3+H_2 \Rightarrow CH_4+H$, whereas methane is mainly consumed by OH whether hydrogen is present in the fuel or not.

4.3 Methane-Hydrogen-CO (Methane-Syngas) Oxidation. The final set of experiments presented here concerns the oxidation

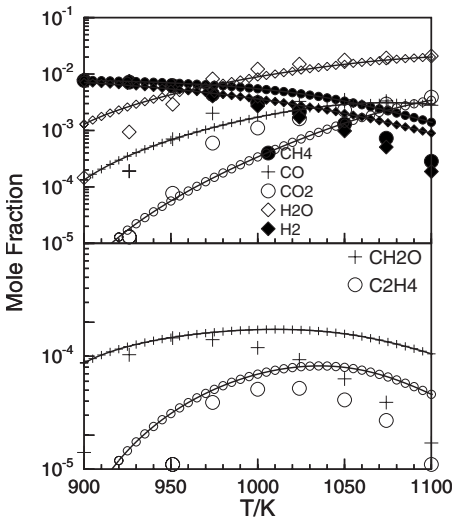

Fig. 28 The oxidation of methane-hydrogen in a JSR (10 atm, τ=250 ms, 0.8% CH_4, 0.8% H_2, φ=0.3, dilution by nitrogen). The data (large symbols) are compared to the modeling (lines and small symbols).

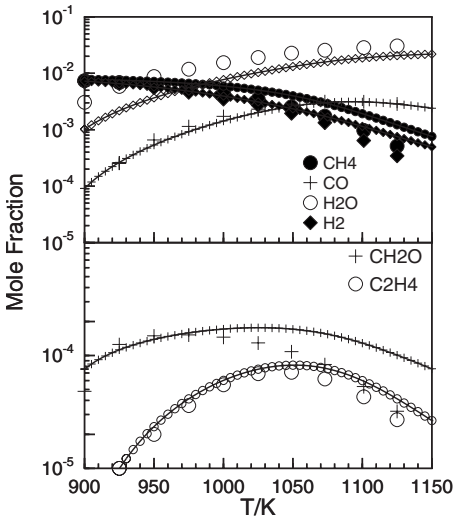

Fig. 29 The oxidation of methane-hydrogen with 20% CO_2 in a JSR (10 atm, τ=250 ms, 0.8% CH_4, 0.8% H_2, φ=0.3, dilution by nitrogen). The data (large symbols) are compared to the modeling (lines and small symbols).

of methane-syngas mixtures in a JSR. The examination of the present results allows a comparison of the kinetics of oxidation of methane-hydrogen with that of methane-carbon monoxide mixtures (Fig. 30). Table 2 gives the temperature at which 50% methane is consumed, showing that the methane-CO-H_2 mixtures are more reactive than the corresponding neat methane mixtures. When CO is added to a $CH_4+H_2/O_2/N_2$ mixture, the formation of OH is mainly due to the reactions of the H_2/O_2 system: $H+O_2 \Rightarrow OH+O$ and $HO_2+H \Rightarrow 2OH$. The competition between $CH_4+OH \Rightarrow CH_3+H_2O$ and $CO+OH \Rightarrow CO_2+H$ does not affect the production of OH, as observed in the absence of H_2. The reaction $CO+OH \Rightarrow CO_2+H$ promotes the oxidation of the fuel through the production of H atoms.

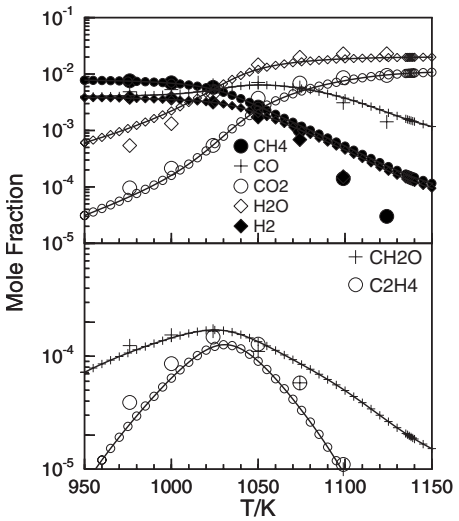

Fig. 30 The oxidation of methane-H_2–CO in a JSR (1 atm, τ =120 ms, 0.8% CH_4, 0.4% H_2, 0.4% CO, φ=0.3, dilution by nitrogen). The data (large symbols) are compared to the modeling (lines and small symbols).

5 Conclusion

New experimental results were obtained for the oxidation of methane-based fuels (CH_4, CH_4/CO_2, CH_4/H_2, $CH_4/CO/H_2$/, and $CH_4/H_2/CO_2$) in conditions relevant to gas turbines operating using a JSR operating at 1–10 atm, over the temperature range of 900–1450 K, from fuel-lean to fuel-rich conditions,. An updated kinetic reaction mechanism was used. The detailed chemical kinetic modeling of these experiments was performed yielding a good agreement with the present data and experimental results taken from the literature (burning velocities and ignition delays in conditions relevant to gas turbines operating conditions, i.e., 1–60 atm, 800–2000 K). Reaction path analyses were used to delineate the important reaction influencing the kinetic of oxidation of the fuels in the presence of variable amounts of CO_2. The kinetic modeling indicates the effect of carbon dioxide addition mainly results from the perturbation of the equilibrium of the reaction $CO+OH=CO_2+H$. The presently proposed scheme should be useful for gas turbine combustion modeling.

Acknowledgments

The authors are grateful to the "Energie" research program of CNRS for financial support through the contract "HyTAG." T.L.C. thanks the Ministère de la Recherche for a doctoral grant. They thank Dr. A. Nicolle for helpful discussions

Nomenclature

φ = equivalence ratio
PFR = plug flow reactor
ST = shock tube
τ = residence time in the JSR
S_u = laminar flame speed

References

[1] Lückerath, R., Meier, W., and Aigner, M., 2007, "FLOX® Combustion at High Pressure With Different Fuel Compositions," ASME Paper No. GT2007-27337.
[2] Wu, J., Brown, P., Diakunchak, I., Gulati, A., Lenze, M., and Koestlin, B., 2007, "Advanced Gas Turbine Combustion System Development for High Hydrogen Fuels," ASME Paper No. GT2007-28337.
[3] Dagaut, P., and Nicolle, A., 2005, "Experimental and Detailed Kinetic Modeling Study of the Effect of Exhaust Gas on Fuel Combustion: Mutual Sensitization of the Oxidation of Nitric Oxide and Methane Over Extended Temperature and Pressure Ranges," Combust. Flame, **140**, pp. 161–171.
[4] Dagaut, P., Mathieu, O., Nicolle, A., and Dayma, G., 2005, "Experimental and Detailed Kinetic Modeling Study of the Mutual Sensitization of the Oxidation of Nitric Oxide, Ethane and Ethylene," Combust. Sci. Technol., **177**, pp. 1767–1791.
[5] Nicolle, A., and Dagaut, P., 2006, "Occurrence of NO-Reburning in MILD Combustion Evidenced via Chemical Kinetic Modeling," Fuel, **85**, pp. 2469–2478.
[6] Le Cong, T., 2007, Doctoral thesis, Orleans, France, in French.
[7] Dagaut, P., 2002, "On the Kinetics of Hydrocarbons Oxidation From Natural Gas to Kerosene and Diesel Fuel," Phys. Chem. Chem. Phys., **4**, pp. 2079–2094.
[8] Tan, Y., Dagaut, P., Cathonnet, M., and Boettner, J.-C., 1994, "Acetylene Oxidation in a JSR From 1 to 10 atm and Comprehensive Kinetic Modeling," Combust. Sci. Technol., **102**, pp. 21–55.
[9] Kee, R. J., Grcar, J. F., Smooke, M. D., and Miller, J. A., 1985, "Premix: A Fortran Program for Modeling Steady Laminar One-Dimensional Premixed Flame," Sandia Report No. SAND85-8240.
[10] Lutz, A. E., Kee, R. J., and Miller, J. A., 1988, "Senkin: A Fortran Program for Predicting Homogeneous Gas Phase Chemical Kinetics With Sensitivity Analysis," Sandia Report No. SAND87-8248.
[11] Glarborg, P., Kee, R. J., Grcar, J. F., and Miller, J. A., 1986, "PSR: A FORTRAN Program for Modeling Well-Stirred Reactors," Sandia Report No. SAND86-8209.
[12] Takahashi, F., Mizomoto, M., and Ikai, S., 1983. "Laminar Burning Velocities of Hydrogen/Oxygen/Inert Gas Mixtures," *Alternative Energy Sources III*, T. Nejat Veziroglu, ed., Nuclear Energy/Synthetic Fuels, Vol. 5, pp. 447–457, McGraw-Hill, New York.
[13] Tse, S. D., Zhu, D. L., and Law, C. K., 2000, "Morphology and Burning Rates of Expanding Spherical Flames in H2/O2/Inert Mixtures Up to 60 Atmospheres," Proc. Combust. Inst., **28**, pp. 1793–1800.
[14] Dowdy, D. R., Smith, D. B., Taylor, S. C., and Williams, A., 1990, "The Use of the Expanding Spherical Flames to Determine Burning Velocities and Stretch Effects in Hydrogen/Air Mixtures," Sym. (Int.) Combust., [Proc.], **23**,

pp. 325–332.
[15] Aung, K. T., Hassan, M. I., and Faeth, G. M., 1997, "Flame Stretch Interactions of Laminar Premixed Hydrogen/Air Flames at Normal Temperature and Pressure," Combust. Flame, **109**, pp. 1–24.
[16] Iijima, T., and Takeno, T., 1986, "Effects of Temperature and Pressure on Burning Velocity," Combust. Flame, **65**, pp. 35–43.
[17] Koroll, G. W., Kumar, R. K., and Bowles, E. M., 1993, "Burning Velocities of Hydrogen-Air Mixtures," Combust. Flame, **94**, pp. 330–340.
[18] Qiao, L., Kim, C. H., and Faeth, G. M., 2005, "Suppression Effects of Diluents on Laminar Premixed Hydrogen/Oxygen/Nitrogen Flames," Combust. Flame, **143**, pp. 79–96.
[19] Mueller, M. A., Kim, T. J., Yetter, R. A., and Dryer, F. L., 1999, "Flow Reactor Studies and Kinetic Modeling of the H_2/O_2 Reaction," Int. J. Chem. Kinet., **31**, pp. 113–125.
[20] McLean, I. C., Smith, D. B., and Taylor, S. C., 1994, "The Use of Carbon Monoxide/Hydrogen Burning Velocities to Examine the Rate of the CO+OH Reaction," Sym. (Int.) Combust., [Proc.], **25**, pp. 749–757.
[21] Sun, H., Yang, S. I., Jomaas, G., and Law, C. K., 2007, "High-Pressure Laminar Flame Speeds and Kinetic Modeling of Carbon Monoxide/Hydrogen Combustion," Proc. Combust. Inst., **31**, pp. 439–446.
[22] Burke, M. P., Xin, X., Ju, Y., and Dryer, F. L., 2007, "Measurements of Hydrogen Syngas Flame Speeds at Elevated Pressures," *Proceedings of the Fifth US Combustion Meeting*, San Diego, CA, Mar. 25–28, Paper No. A16.
[23] Natarajan, J., Lieuwen, T., and Seitzman, J., 2007, "Laminar Flame Speeds of H2/CO Mixtures: Effect of CO2 Dilution, Preheat Temperature, and Pressure," Combust. Flame, **151**, pp. 104–119.
[24] Kalitan, D. M., and Petersen, E. L., 2005, "Ignition and Oxidation of Lean CO/H2 Fuel Blends in Air," AIAA Paper No. 2005-3767.
[25] Yetter, R. A., Dryer, F. L., and Rabitz, H., 1991, "A Comprehensive Reaction-Mechanism for Carbon-Monoxide/Hydrogen/Oxygen Kinetics," Combust. Sci. Technol., **79**, pp. 97–128.
[26] Dagaut, P., and Lecomte, F., 2003, "Experimental and Kinetic Modeling Study of the Reduction of NO by Hydrocarbons and Interactions With SO2 in a JSR at 1 atm," Fuel, **82**, pp. 1033–1040.
[27] Sivaramakrishnan, R., Comandini, A., Tranter, R. S., Brezinsky, K., Davis, S. G., and Wang, H., 2007, "Combustion of CO/H2 Mixtures at Elevated Pressures," Proc. Combust. Inst., **31**, pp. 429–437.
[28] Vagelopoulos, C. M., Egolfopoulos, F. N., and Law, C. K., 1994, "Further Considerations on the Determination of Laminar Flame Speeds With the Counterflow Twin-Flame Technique," Proc. Combust. Inst., **25**, pp. 1341–1347.
[29] Aung, K. T., Tseng, L. K., Ismail, M. A., and Faeth, G. M., 1995, "Response to Comment by S.C. Taylor, and D.B. Smith on 'Laminar Burning Velocities and Markstein Numbers of Hydrocarbon/Air Flames'," Combust. Flame, **102**, pp. 526–530.
[30] Egolfopolous, F. N., Cho, P., and Law, C. K., 1989, "Laminar Flame Speeds of Methane-Air Mixtures Under Reduced and Elevated Pressures," Combust. Flame, **76**, pp. 375–391.
[31] Petersen, E. L., Schuyler, J. M., Smith, S. D., de Vries, J., Amadio, A., and Crofton, M. W., 2005, "Ignition of Lean Methane-Based Fuel Blends at Gas Turbine Pressures," ASME Paper No. GT2005-68517.
[32] Petersen, E. L., Rohrig, M., Davidson, D. F., Hanson, R. K., and Bowman, C. T., 1996, "High-Pressure Methane Oxidation Behind Reflected Shock Waves," Sym. (Int.) Combust., [Proc.], **26**, pp. 799–806.
[33] Dyakov, I. V., Konnov, A. A., and De Ruyck, J., 2004, "Sampling Measurements of Nitric Oxide in Methane—Oxygen—Carbon Dioxide Flames With Ammonia Admixture," Khim. Fiz., **23**(8), pp. 19–24.
[34] Smith, G. P., Golden, D. M., Frenklach, M., Moriarty, N. W., Eiteneer, B., Goldenberg, M., Bowman, C. T., Hanson, R. K., Song, S., Gardiner, W. C., Jr., Lissianski, V. V., and Qin, Z., 1999, http//www.berkeley.edu/gri-mech/
[35] Dagaut, P., and Nicolle, A., 2005, "Experimental and Detailed Kinetic Modeling Study of Hydrogen-Enriched Natural Gas Blend Oxidation Over Extended Temperature and Equivalence Ratio Ranges," Proc. Combust. Inst., **30**, pp. 2631–2638.
[36] Dagaut, P., and Dayma, G., 2006, "Hydrogen-Enriched Natural Gas Blend Oxidation Under High Pressure Conditions: Experimental and Detailed Chemical Kinetic Modeling," Int. J. Hydrogen Energy, **31**, pp. 505–515.
[37] Yu, G., Law, C. K., and Wu, C. K., 1986, "Laminar Flame Speeds of Hydrogen+Air Mixtures With Hydrogen Addition," Combust. Flame, **63**, pp. 339–347.
[38] Halter, F., Chauveau, C., Djebaïli-Chaumeix, N., and Gökalp, I., 2005, "Characterization of the Effects of Pressure and Hydrogen Concentration on Laminar Burning Velocities of Methane-Hydrogen-Air Mixtures," Proc. Combust. Inst., **30**, pp. 201–208.
[39] Law, C. K., and Kwon, O. C., 2004, "Effects of Hydrocarbon Substitution on Atmospheric Hydrogen-Air Flame Propagation," Int. J. Hydrogen Energy, **29**, pp. 867–879.
[40] Petersen, E. L., Davidson, D. F., Rohrig, M., and Hanson, R. K., 1995, "Shock-Induced Ignition of High-Pressure H2-O2-Ar and CH4-O2-Ar Mixtures," AIAA Paper No. 95-3113.
[41] Vandooren, J., and Bian, J., 1990, "Validation of H2/O2 Reaction Mechanism by Comparison With the Experimental Structure of a Rich Hydrogen-Oxygen Flame," Sym. (Int.) Combust., [Proc.], **23**, pp. 341–346.
[42] Koroll, G. W., and Mulpuru, S. R., 1986, "The Effect of Dilution With Steam on the Burning Velocity and Structure of Premixed Hydrogen Flames," Sym. (Int.) Combust., [Proc.], **21**, pp. 1811–1819.
[43] Vandooren, J., Peeters, J., and Van Tiggelen, P. J., 1975, "Rate Constant of the Elementary Reaction of Carbon Monoxide With Hydroxyl Radical," Sym. (Int.) Combust., [Proc.], **15**, pp. 745–753.
[44] Lewis, B., and von Elbe, G., 1987, *Combustion, Flames and Explosions of Gases*, 3rd ed., Academic, Orlando, FL.
[45] Kim, T. J., Yetter, R. A., and Dryer, F. L., 1994, "New Results on Moist CO Oxidation: High Pressure, High Temperature Experiments and Comprehensive Kinetic Modeling," Proc. Combust. Inst., **25**, pp. 759–766.
[46] Hennessy, R. J., Robinson, C., and Smith, D. B., 1986, "A Comparative Study of Methane and Ethane Flame Chemistry by Experimental and Detailed Modelling," Sym. (Int.) Combust., [Proc.], **21**, pp. 761–772.
[47] Bernstein, J. S., Fein, A., Choi, J. B., Cool, T. A., Sausa, R. C., Howard, S. L., Locke, R. J., and Miziolek, A. W., 1993, "Laser-Based Flame Species Profile Measurements—A Comparison With Flame Model Predictions," Combust. Flame, **92**, pp. 85–105.
[48] Bechtel, J. H., Blint, R. J., Dasch, C. J., and Weinberger, D. A., 1981, "Atmospheric Pressure Premixed Hydrocarbon-Air Flames: Theory and Experiment," Combust. Flame, **42**, pp. 197–218.
[49] Konnov, A. A., Zhu, J. N., Bromly, J. H., and Zhang, D.-K., 2004, "Noncatalytic Partial Oxidation of Methane Into Syngas Over a Wide Temperature Range," Combust. Sci. Technol., **176**, pp. 1093–1116.

A Comparison of Two Trending Strategies for Gas Turbine Performance Prediction

Rajat Sekhon

Hany Bassily

John Wagner
e-mail: jwagner@clemson.edu

Energy Systems Laboratory,
Department of Mechanical Engineering,
Clemson University,
Clemson, SC 29634

Complex multidomain dynamic systems demand reliable health monitoring to minimize breakdowns and downtime, thereby enabling cost savings and increased operator safety. Diagnostic and prognostic strategies monitor a system's transient and steady-state operations, detecting deviations from normal operating scenarios and warning operators of potential system anomalies. System diagnostics detect, identify, and isolate a system fault while prognostics offer strategies to predict system behavior at a future operating time to define the useful period before failure criterion is reached. This paper presents the development and the experimental application of two methods to predict the system behavior based on trends in performance. Statistical regression concepts have been used to analyze dynamic plant signals, and based on these results, future plant operation was estimated. Wavelet transforms were used to condition the signal, and the denoised signals were subsequently forecast. The case study presented here applies the two methodologies to the operational data from a simple cycle 85 MW General Electric gas turbine. Those operating data were used to train and validate the algorithms. A comparison of the two methodologies reveals that the wavelet forecast is better than the statistical strategy with lower forecasting error. The developed approaches may be used in parallel with a diagnostic algorithm to monitor gas turbine system behavior. [DOI: 10.1115/1.2898838]

Keywords: health monitoring, wavelets, statistics, gas turbines, experimental data

1 Introduction

Health monitoring strategies estimate the current and future conditions of a system to increase performance and reliability, as well as reduce maintenance and replacement costs. Prognostics, a key component of these strategies, analyzes system health and predicts remaining useful life based on past and current system operation data, individual system histories, and system response characteristics. The feasibility of installing a reliable health monitoring methodology resides in the availability of digital/analog sensors that permit extensive data logging for dynamic systems (Refs. [1,2]). Using a model-free prognostics framework, these raw data can then be processed and utilized to identify short and long term trends, and monitor for system degradations. This strategy offers an alternative to the traditional model-based prediction algorithms since these physical models often require extensive validation and may not capture all the system dynamics.

Initial work on a combined diagnostics and prognostics technique for condition assessment, based on analysis of vibrations from mechanical systems, was investigated by LeBold et al. [3]. Similar work was performed by Atlas et al. [4] on the integration of anomaly, prognostics, and diagnostic "reasoners" for system health monitoring. Neural networks based techniques, which use data based models for fault recognition and prognostics, were introduced by Brotherton et al. [5]. The application of these dynamic neural network techniques was further investigated by Wang and Vachtsevanos [6]. These authors developed robust prediction modules using virtual sensors for condition based maintenance of critical machine components. The virtual sensors were used to measure signals or signal derivatives, which were then processed to obtain signal patterns. To verify the accuracy of model-based prognostics processes, Schwabacher [7] compared nominal and degraded system operating scenarios by integrating model-based life predictions with model probabilities to derive predictions.

Gulen et al. [8] investigated an online real time prognostic strategy, which can manage maintenance (e.g., washing) costs to reduce gas turbine compressor deterioration by up to 20%. Similar work has also been performed for offshore gas turbines by Veer et al. [9]. Some efforts have been undertaken to apply real time gas turbine prognostics techniques to diesel engines [10]. Jardim et al. [11] have used stochastic autoregressive integrated moving average models to develop real time prognostic systems for computer numeric machines. The integration of intelligent processing and data fusion to obtain valuable information for system diagnostics and prognostics has been demonstrated by Greitzer and Ferryman [12]. In their work, correlation of data from key sensors was used to derive the actual life consumed and the remaining useful life. Finally, prediction is always associated with uncertainties. A probability based method to reduce the prognostic uncertainties in real time has been presented by Barlas et al. [13].

Two model-free performance prediction strategies to monitor and predict dynamic system behavior are shown in Fig. 1. The information presented in this diagram will be discussed. First, the plant signals are conditioned (i.e., concatenated and filtered). Second, a correlation analysis of the input/output signals may be performed for signal selection followed by the application of the two proposed strategies. The first approach, the statistical methodology, involves multiregression to identify system behavior from the selected signals. The identified trend is forecasted to describe future system operation; the forecast error may be computed. For the second method, a wavelet transform is performed for processing and downsampling the signals using Daubechies wavelet transforms to obtain approximation coefficients. These coefficients reveal the system trends. A least squares regression fit may be performed on the coefficients followed by inverse wavelet transforms to forecast future system operation. Finally, health evaluations are made based on the predicted system behavior. It

Submitted to ASME for publication in the JOURNAL OF ENGINEERING FOR GAS TURBINES AND POWER. Manuscript received March 8, 2007; final manuscript received September 24, 2007; published online April 29, 2008. Review conducted by Allan Volponi.

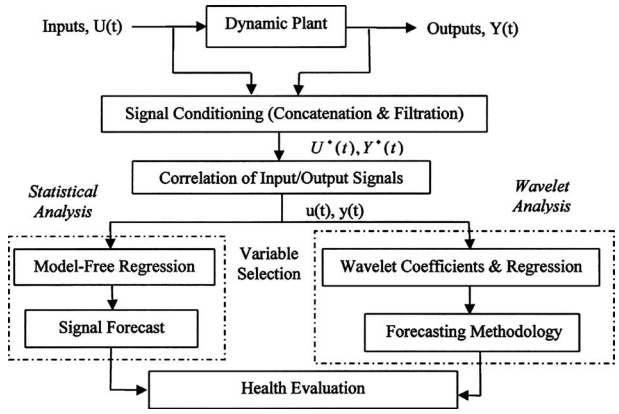

Fig. 1 Statistical and wavelet prediction strategies with forecasting

should be noted that a frequency domain approach was not pursued due to low data logging rates often encountered in plant equipment.[1]

In this paper, two prediction strategies are presented and applied to a simple cycle natural gas turbine for performance evaluation. This paper is organized as follows. The statistical and wavelet prediction approaches are described in Secs. 2 and 3, respectively. A case study is presented in Sec. 4, which examines the operational data for a General Electric 7EA gas turbine to forecast future system behavior. The summary is contained in Sec. 5. A complete nomenclature list was provided.

[1]For the GE 7EA gas turbine, over 180 signals were collected at $\Delta t=60$ s during system operation. Faster data logging would exceed electronic storage capacity.

2 Statistical Prediction Strategy

A variety of statistical methods have been applied to predict the useful life of plant equipment and general dynamic systems (e.g., Refs. [14–16]). In general, methods such as statistical techniques rely on historical data to identify system trends and predict future behavior. The key system characteristics may be described using regression analysis methods and extended in time to forecast future plant behavior. A three step process is recommended for this prediction method: signal selection, multiregression statistics, and signal forecasting.

2.1 Signal Selection Using a Correlation Method. Dynamic systems may have a variety of input (e.g., force, heat, and voltage) and output (e.g., acceleration, vibration, and current) signals that can be measured using appropriate sensors. Let these input and output vectors be represented by $U(t) \in R^g$ and $Y(t) \in R^h$, respectively. It is likely that these signals may be discontinuous or arise from different operating modes. Hence, the system sensor data may need to be filtered, concatenated, and normalized such that the input and output vectors become $U^*(t) \in R^g$ and $Y^*(t) \in R^h$. A smaller set of input and output vectors, $u(t) \in R^n$ and $y(t) \in R^p$, may be selected to investigate the system health based on a correlation analysis. For this study, the correlation between the system inputs and outputs may be stated as

$$\Re_{jk} = \frac{\sum_{i=1}^{m} Y_j^*(t_i)U_k^*(t_i) - \left(\sum_{i=1}^{m} Y_j^*(t_i)\right)\left(\sum_{i=1}^{m} U_k^*(t_i)\right)/m}{\left(\sum_{i=1}^{m} (Y_j^*(t_i))^2 - \left(\sum_{i=1}^{m} Y_j^*(t_i)\right)^2/m\right)^{0.5}\left(\sum_{i=1}^{m} (U_k^*(t_i))^2 - \left(\sum_{i=1}^{m} U_k^*(t_i)\right)^2/m\right)^{0.5}} \tag{1}$$

As a general rule, the system outputs (i.e., the signals being forecasted) with a correlation $|\Re_{jk}| > 0.80$ for the given inputs were selected.

2.2 Model-Free Regression Description. A multiregression empirical model, based on the selected sensor signals, may be created to describe the system's behavior. Although these signals may be affected by noise, it has been assumed that the noise may be neglected. However, this assumption will be removed in Sec. 3 with the wavelet prediction method. For degraded plant operation, the system's steady-state output should change so that time dependent trends may be observed while the system's inputs remain constant [17]. Hence, time will be included in the prediction model. A Euclidian norm, $|\mathbf{Z}_{ji}|$, for the jth signal of the plant output vector $y(t)$ may be expressed as

$$|\mathbf{Z}_{ji}| = \left(\sum_{k=1}^{n}\left(\sum_{q=0}^{r} a_{j_{qk}} t_i^q\right)^2\right)^{0.5} \quad (i = 1,2,\ldots,m) \tag{2}$$

where the parameters n and r denote the number of selected independent variables (input signals) and the regression order. The polynomial coefficients $a_{j_{0k}}, a_{j_{1k}}, \ldots, a_{j_{rk}}$ correspond to of the rth regression order for the kth signal.

Consequently, the Euclidian norm of the deviations, $|\mathbf{D}_j|$, between m time samples in the composite sample data, $V_{j_k}(t_i) = [y_j(t_i)u_k(t_i)]^T$, and the regression curve, $\mathbf{Z}_{ji}$, becomes

$$|\mathbf{D}_j| = \sum_{i=1}^{m}\left[\left(\sum_{k=1}^{n}(V_{j_k}(t_i))^2\right)^{0.5} - |\mathbf{Z}_{ji}|\right]^2 = \sum_{i=1}^{m}\left[\left(\sum_{k=1}^{n}(V_{j_k}(t_i))^2\right)^{0.5} - \left(\sum_{k=1}^{n}\left(\sum_{q=0}^{r} a_{j_{qk}} t_i^q\right)^2\right)^{0.5}\right]^2 \tag{3}$$

A least square method can be based on minimizing the scalar quantity $|\mathbf{D}_j|$. To this end, one can apply the derivative minimization principle, $\partial|\mathbf{D}_j|/\partial a_{j_{qk}} = 0$ for $q = (0,1,\ldots,r)$, to obtain the regression coefficients [18] by solving the $(r+1)$ equations numerically as

$$\frac{\partial}{\partial a_{j_{q\in[0,r]k}}}\left\{\sum_{i=1}^{m}\left[\left(\sum_{k=1}^{n}(V_{j_k}(t_i))^2\right)^{0.5} - \left(\sum_{k=1}^{n}\left(\sum_{q=0}^{r} a_{j_{qk}} t_i^q\right)^2\right)^{0.5}\right]^2\right\} = 0 \tag{4}$$

2.3 Signal Forecasting. The regression model can predict a dependent variable's value both inside and outside the estimation time interval. The regression coefficients, $a_{j_{qk}}$, describe the signal trend so that the time extension of the regression curve may esti-

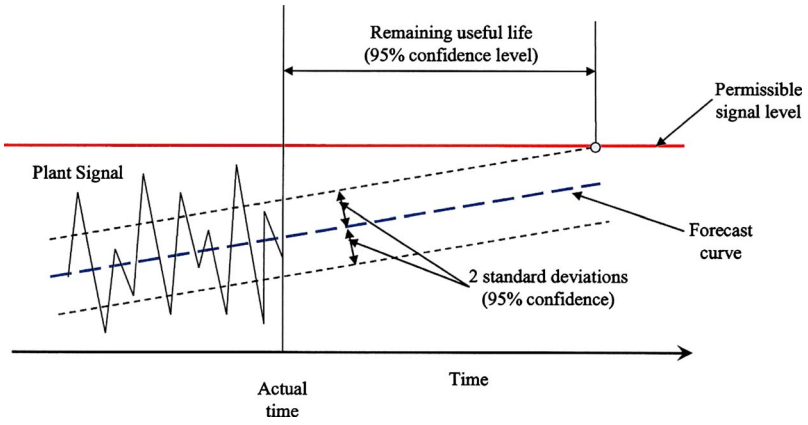

Fig. 2 Application of the statistical trending strategy to estimate a useful remaining time based on a selected threshold of two standard deviations satisfying a 95% confidence limit

mate the system's future behavior. In general, the meaningful prediction time for the regression curve depends on the estimation data. The larger the estimation data sample size, the better the forecast since the curve would be termed "well trained." The dependent variable trends represent the long term signal behavior, rather than fluctuations caused by plant disturbances and load changes. The forecasted signal curve, $\mathbf{Z}_{ji}$, can be obtained from Eq. (2), once the regression coefficients are determined as

$$|\mathbf{Z}_{ji}| = \left(\sum_{k=1}^{n} \left(\sum_{q=0}^{r} a_{j_{qk}} t_i^q \right)^2 \right)^{0.5} \quad (i = m+1, m+2, \ldots, m+f) \tag{5}$$

where $m+f$ denotes the final time value. This forecast has an error of $\varepsilon_j = (|\Sigma_{i=m}^{m+f} \mathbf{Z}_{ji}| - |\Sigma_{i=m}^{m+f} y_j(t_i)|) / |\Sigma_{i=m}^{m+f} y_j(t_i)|$, which can be used for comparison purposes.

2.4 Health Evaluation. A useful application of this trending strategy is to statistically infer either a behavior abnormality or the useful remaining life for an existing performance trend. An adjustable set of thresholds may be established for the forecasted signals, which can be termed acceptable if they lie within the established thresholds. For a normally distributed steady-state signal, 95% of the observed data should lie within two standard deviations, $\sigma_j = [1/m \Sigma_{i=1}^{m} (y_j(t_i) - \bar{y}_j)^2]^{0.5}$, of the sample mean, $\bar{y}_j$. If the system forecast predicts a threshold violation, $|\mathbf{Z}_j| > 2\sigma_j$, then the remedial action should be dependent on the rate and severity of the threshold violation. In some instances, the thresholds may need to be continually violated to minimize false evaluations.

For signals exhibiting an obvious trend, the remaining useful life can be forecasted by estimating the time remaining for the statistical thresholds to reach a preset acceptable signal level. In this case, the prediction of the useful life will have a confidence level similar to the 95% defined in selecting the adjustable thresholds. Figure 2 illustrates the application of the proposed trending technique in estimating the useful remaining time based on the threshold selection.

3 Wavelet Prediction Strategy

Wavelet transforms can be applied to time domain plant signals that contain noisy, intermittent, and transient behavior [19]. A wavelet is a waveform of limited duration with a zero average that converts a time domain signal into a magnitude and time function Refs. [20,21]. Wavelet transforms can be used for multidimensional analyses which make them a powerful tool in analyzing and monitoring dynamic systems [22]. For instance, wavelet transforms with neural networks can remove signal noise and predict nonlinear system behavior [23]. The wavelet transform can also be used to investigate dominant system trends and derive the mean time between hard failures [24] within the context of the diagnostic methods.

In this study, the wavelet technique will predict dynamic system operation again using a three step procedure. First, wavelet transforms of the data will compute the given system signal wavelet coefficients. Second, a regression analysis of these coefficients will forecast the wavelet coefficients for the desired prediction time. Third, the new set of wavelet coefficients may then be used to reconstruct the signal and, hence, obtain a prediction.

3.1 Wavelet Description. Any wave form function, $\psi(t)$, can be selected for a wavelet transform if it satisfies the condition of finite energy and admissibility. The finite energy condition [25] states that the energy, ϑ, of the wavelet function, $\psi(t)$, should be limited as

Table 1 Comparison of statistical and wavelet forecast for five GE 7EA gas turbine output signals based on the three input signals power generated (PG), fuel flow (FF), and inlet guide vane angle (IGVA) over a 10,000 min forecast validation window

Signal No.	Signal description	Correlation ($\|\Re_{jk}\|$)			Forecast error (%ε)	
		PG	FF	IGVA	Statistical	Wavelet
1	Turbine inlet temperature (T_{TT})	0.83	0.83	0.88	11.47	9.23
2	Generator temperature (T_G)	0.83	0.83	0.87	10.40	8.87
3	Exhaust temperature (T_{ex})	0.99	0.99	0.98	9.49	5.24
4	Generator maximum vibration (A_{GV})	0.89	0.89	0.87	10.43	9.69
5	Gas turbine maximum vibration (A_{TV})	0.82	0.82	0.56	10.89	9.01

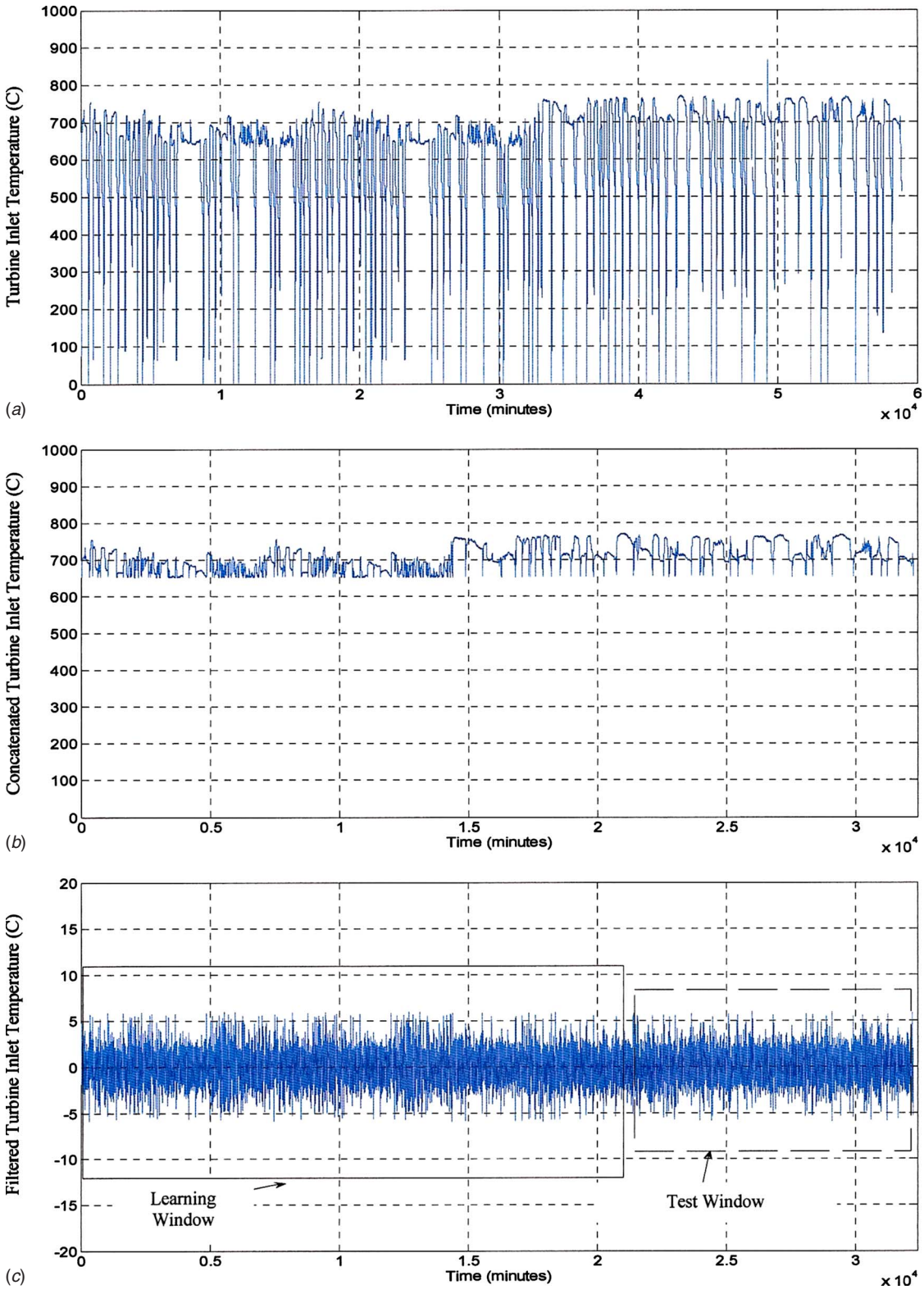

Fig. 3 GE 7EA stationary gas turbine inlet temperature profile: (*a*) raw data signal for $0<t<59{,}000$, (*b*) restricted operating range of 600–800°C for $0<t<32{,}200$ min and (*c*) filtered data showing the learning $0<t<22{,}200$ min and validation windows $22{,}200<t<32{,}200$ min

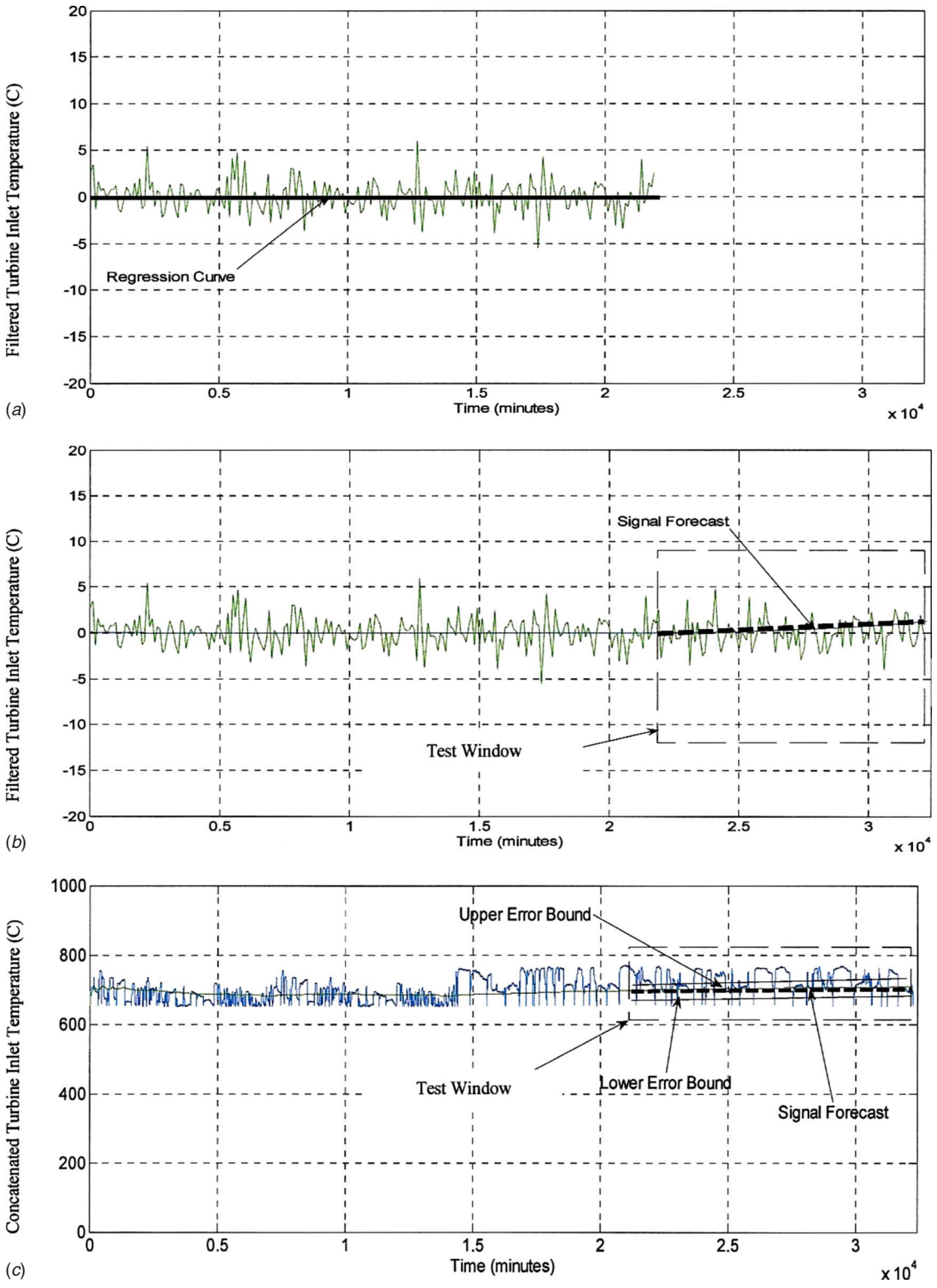

Fig. 4 Statistical prediction strategy: (*a*) regression curve for turbine inlet temperature during learning window (0<*t*<22,200 min) minutes with reduced display intensity, (*b*) statistical signal forecast (22,200<*t*<32,200 min) minutes with reduced display intensity, and (*c*) signal and statistical forecast mapped back into the operating domain for 0<*t*<32,200 min

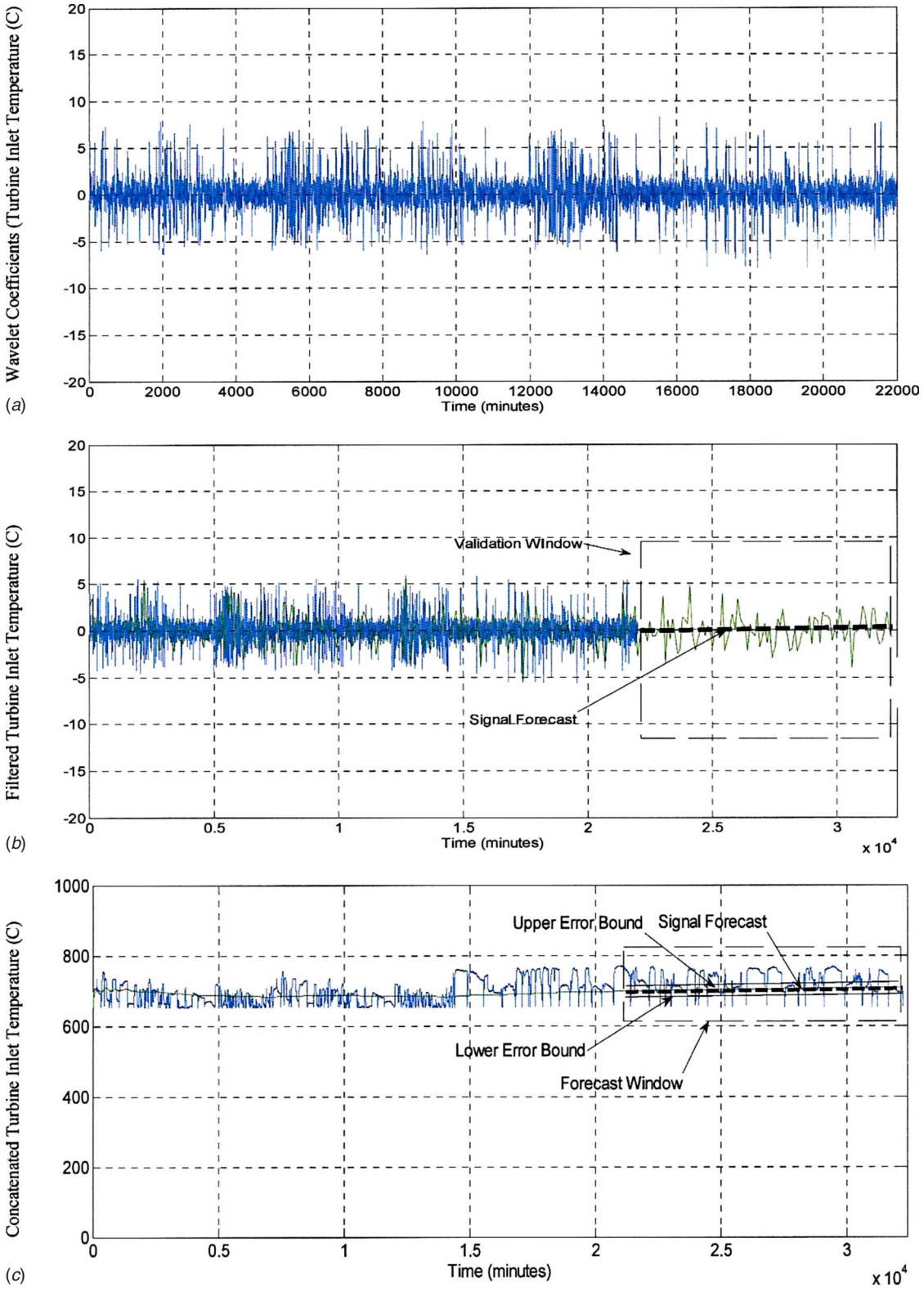

Fig. 5 Wavelet prediction strategy: (*a*) approximation coefficients for turbine inlet temperature for learning window (0<*t*<22,200 min), (*b*) wavelet signal forecast (22,200<*t*<32,200 min) with reduced display density, and (*c*) signal and wavelet forecast mapped back into the operating domain for 0<*t*<32,200 min

$$\vartheta = \int_{-\infty}^{\infty} |\psi(t)|^2 dt < \infty \quad (\vartheta < \infty) \tag{6}$$

The admissibility condition states that the wavelet function has a zero mean, $E(\psi(t))=0$, and that the Fourier transform of the wavelet function with frequency F cannot be zero, $\hat{\psi}(F) \neq 0$. The admissibility constant for the wavelet function has a finite value

$$\varsigma = \int_0^{\infty} \frac{|\hat{\psi}(F)|^2}{F} dF \quad (\varsigma < \infty) \tag{7}$$

In this expression, $\hat{\psi}(F)=\int_{-\infty}^{\infty}\psi(t)e^{-i(2\pi F)t}dt$ represents the Fourier transform of $\psi(t)$. The value of the admissibility constant is dependent on the wavelet function. A discrete wavelet transform uses an orthonormal wavelet basis with the wavelet function, $\psi(t)$, to obtain the wavelet function, $\psi_{\chi,\eta}(t)$, at a given scale and time as

$$\psi_{\chi,\eta}(t) = \frac{1}{\sqrt{u_0^{\chi}}}\psi\left(\frac{t - \eta v_0 u_0^{\chi}}{u_0^{\chi}}\right) \tag{8}$$

The parameters $\chi \in R$ and $\eta \in R$ denote the dilation (scale) and translation (time) variables, respectively. The symbols u_0 and v_0 are wavelet control parameters.

The term "translation" refers to delaying or hastening the onset of a wavelet (i.e., a shift in time). The term "dilation" denotes wavelet scaling (i.e., stretching or compressing). Low and high scales are associated with compressed and stretched wavelets. The scaling function, $\phi(t)$, is any wave form function that satisfies the condition $\int_{-\infty}^{\infty}\phi(t)dt=1$. The orthonormal scaling function at a given scale and time becomes

$$\phi_{\chi,\eta}(t) = \frac{1}{\sqrt{u_0^{\chi}}}\phi\left(\frac{t - \eta v_0 u_0^{\chi}}{u_0^{\chi}}\right) \tag{9}$$

3.2 Wavelet Coefficient Signal Processing. In some instances, the plant output signals may be affected by disturbances, κ_d, and noise, κ_n. For example, consider $y_j(t)=s(t)+\kappa_d+\kappa_n$, which is composed of signal characteristics, $s(t)$, and additive components κ_d and κ_n. A wavelet transform addresses signal noise by computing two sets of wavelet coefficients: detail and approximate. Signal details refer to the high frequency content of the signal, which may be noise and disturbances. Signal approximations are the low frequency signal content. If the high frequency components of the signal are removed, then the signal still retains some characteristics, which can be forecasted. However, if the signal approximations are removed, then the signal may loose its primary characteristic and the residual would likely be noise.

The detail and approximation coefficients, $\hat{\gamma}_{\chi,\eta_j}$ and $\hat{\xi}_{\chi,\eta_j}$, were generated on a dyadic scale (i.e., based on powers of 2). The given discrete wavelet transform of the learning window may be computed to obtain the detail and the approximation coefficients as

$$\hat{\gamma}_{\chi,\eta} = \int_{-\infty}^{\infty} y_j(t)\frac{1}{\sqrt{u_0^{\chi}}}\psi\left(\frac{t - \eta v_0 u_0^{\chi}}{u_0^{\chi}}\right)dt = \langle y_j(t), \psi(t)\rangle \tag{10a}$$

$$\hat{\xi}_{\chi,\eta} = \int_{-\infty}^{\infty} y_j(t)\frac{1}{\sqrt{u_0^{\chi}}}\phi\left(\frac{t - \eta v_0 u_0^{\chi}}{u_0^{\chi}}\right)dt = \langle y_j(t), \phi(t)\rangle \tag{10b}$$

Note that the detail and approximation coefficients are obtained by the convolution of the system signal with the wavelet and scaling functions. The similar analysis of the input signal provides the corresponding detail, $\gamma_{\chi,\eta}$, and approximation, $\xi_{\chi,\eta}$, coefficients as

$$\gamma_{\chi,\eta} = \langle u_k(t), \psi(t)\rangle, \quad \xi_{\chi,\eta} = \langle u_k(t), \phi(t)\rangle \tag{11}$$

From a practical perspective, the signal vectors $y(t)$ and $u(t)$ may be filtered using the complementary filters in Eqs. (10*a*), (10*b*), and (11), to realize low and high frequency coefficients. The next step for the algorithm is a least square fit to obtain a regression model of the signal approximation coefficients.

3.3 Forecasting Methodology. The prediction algorithm eliminates high frequency signal noise, through wavelet transforms, to predict system behavior. The wavelet coefficient regression model for the selected output variable may be derived from the approximation coefficients. This regression model forecasts the system's approximation coefficients by performing a one dimensional inverse wavelet transform on the coefficients so that

$$A_{\chi}(t) = \sum_{\eta=-\infty}^{\infty} \xi_{\chi,\eta}\phi_{\chi,\eta}(t) \tag{12}$$

The algorithm uses Daubechies wavelets with four scaling coefficients [25] for both the wavelet and inverse wavelet transforms. The corresponding wavelet and scaling function for these Daubechies wavelets become

$$\psi(t) = \sum_{e=1,3} d_e\phi[2t-(e-3)] - \sum_{e=0,2} d_e\phi[2t-(3-e)],$$

$$\phi(t) = \sum_{e=0}^{3} d_e\phi(2t-e) \tag{13}$$

where the parameters d_e and e represent the scaling coefficient and the scaling coefficient index. The selected wavelet coefficient order depends on the data being analyzed. For instance, high and low frequency signals need higher and lower order wavelet coefficients, respectively [20]. The coefficients in Eq. (13) can be obtained from the moment condition for compactly supported wavelets as

$$\sum_{e=0}^{3} d_e = 2, \quad \sum_{e=0}^{3} d_e^2 = 2, \quad \sum_{e=0,2} d_e - \sum_{e=1,2} d_e = 0 \tag{14}$$

4 Case Study: Simple Cycle Natural Gas Turbine Performance Prediction

The prediction methodologies presented in Secs. 2 and 3 may be applied to dynamic systems, which feature extensive sensory data. For example, simple cycle gas turbines are increasingly deployed throughout the world to provide electrical and mechanical power for consumer and industrial needs. The efficiency of these complex multidomain systems is dependent on the turbine's design, established operating envelope, environmental conditions, and maintenance schedule. In this section, the prediction strategies will analyze a natural gas turbine to enhance overall plant reliability through operations monitoring.

4.1 Gas Turbine Description. A General Electric 7EA natural gas turbine, located at the Santee Cooper John S. Rainey power generating station, served as the basis to evaluate the two prediction methods. The turbine has a power production capacity of 85 MW with a nominal rotational speed of 3600 RPM. The turbine features a single shaft, 16 stage compressor with a 12.6:1 compression ratio. The heat rate is $Q=10{,}991$ kJ/kW h with an approximate mass flow rate of $\dot{m}_f=292$ kg/s. The available turbine sensors were sampled at $\Delta t=60$ s. The run time for the gas turbine was based on the power generation needs; operating data for two years were available.

The GE 7EA input signals included power generated (PG), fuel flow (FF) rate, and inlet guide vane angle (IGVA). The set of output signals selected to forecast system health consisted of turbine inlet temperature (T_{TT}), generator temperature (T_G), exhaust temperature (T_{ex}), generator maximum vibration (A_{GV}), and gas turbine maximum vibration (A_{TV}). The output signals were selected based on their high correlations with the three input signals,

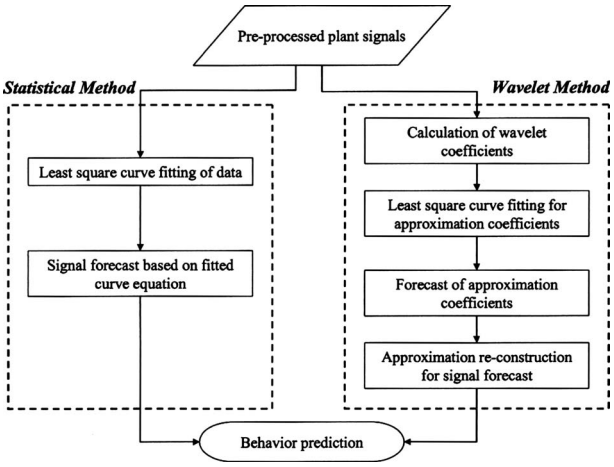

Fig. 6 Comparison between the calculation complexity of the statistical and wavelet methods

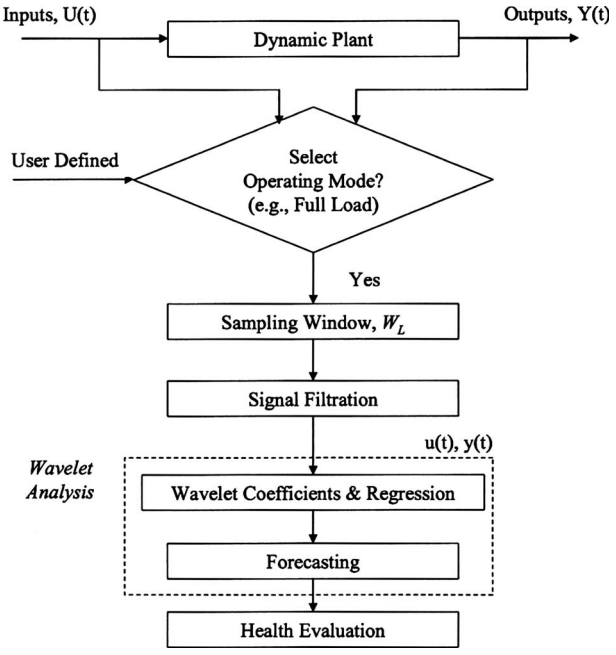

Fig. 7 Application of the wavelet prediction methodology

as shown in Table 1. For instance, the turbine inlet temperature has correlation values of $|R_{11}|=0.83$, $|R_{12}|=0.83$, and $|R_{13}|=0.88$ with the PG, FF, and IGVA signals, respectively. In this case, the turbine inlet temperature is selected as a representative example to experimentally demonstrate the proposed methodologies.

4.2 Prediction Methodologies. A four step sequence was followed to analyze the turbine inlet temperature, T_{TT}. First, the steady-state signal was conditioned to obtain a concatenated and filtered signal. Second, the statistical prediction methodology was applied to obtain the signal forecast. Third, the wavelet method was supplied the same signal to predict the system behavior. Finally, a comparison of the two methods was performed. Note that for real time applications, the desired system operating mode must be present before signal filtering and analysis; signal concatenation will not occur.

4.2.1 Signal Conditioning. The turbine inlet temperature profile is shown in Fig. 3(*a*) for a period of $t^*=59{,}000$ min. The signal is somewhat oscillatory due to start ups, shut downs, and different operating loads. For a meaningful analysis of the turbine data, three operating ranges (or modes) were identified for the turbine inlet temperature (200–400°C, 400–60°C, and 600–800°C). These operating ranges are user defined and typically based on turbine operating modes (e.g., light, medium, and heavy loads) per electrical power generating demands. The turbine inlet temperature range of $600<T_{TT}<800$°C was selected since this corresponds to the most common operating mode of maximum turbine load. Specifically, the turbine runs for $t=32{,}200$ min of the total $t^*=59{,}000$ min in the heavy load mode. In Fig. 3(*b*), the concatenated data for the turbine inlet temperature have been displayed. The next task was to normalize the concatenated data using a simple filter, $Y_j^*=Y_j(i+1)-Y_j(i)$, to further reduce fluctuations. The filtered turbine inlet temperature with a mean value of zero, refer to Fig. 3(*c*), shows variations about the actual signal mean, $\bar{y}_j$. In order to investigate the applicability of the proposed strategy, the data have been arbitrary divided into the learning (i.e., $0<t<22{,}200$ min) and the test (i.e., $22{,}100<t<32{,}200$ min) windows, W_L and W_V, respectively. The aim of this experimental demonstration is to calculate the error between the forecasted signal for the period W_V based on analyzing the training data of the segment W_L and the actual observation of the duration W_V. The resulting error is used as the gauging tool for the proposed prediction algorithm. It is useful to mention that the length of each segment should not affect the prediction accuracy if the signal is preprocessed as previously mentioned to eliminate any existing stochastic trend.

4.2.2 Statistical Forecasting. The filtered signal, Y_j^*, was analyzed using the statistical methodology described in Sec. 2 to predict the system behavior. In Fig. 4(*a*), the regression curve for the initial turbine inlet temperature learning data has been graphed versus time with every 100 data point plotted to improve readability. The derived regression curve, $\mathbf{Z}_{ji}$, forecasts the system operation for a period of $t=10{,}000$ min (i.e., $22{,}200<t<32{,}200$ min), as shown in Fig. 4(*b*). When comparing the predicted and actual data in the test window, the forecast error is 11.47%. The system operation forecast for the turbine inlet temperature was mapped back into the operating domain, along with the forecast error

Table 2 Summary of characteristics of the statistical and wavelet methods

No.	Characteristic	Statistical method	Wavelet method
1	Length of learning window	User defined	User defined
2	Forecast error	Low	Least
3	Application suitability	Most convenient for steady-state signals	May be used in presence of intermittencies and transients
4	Number of coefficients	Order dependent	Half the signal length
5	Order	User defined	User defined
6	Signal condition	Stationary, no stochastic trend	Accommodates colored noise

bounds, $\pm\varepsilon$, as shown in Fig. 4(*c*). Note that the forecasted signal displays a nonfluctuating behavior, which predicts the signal mean rather than the specific fluctuations, which may be an advantage in applying adjustable thresholds for remaining useful life calculation.

4.2.3 Wavelet Forecasting. The wavelet prediction algorithm computes the fourth-order wavelet transform of the filtered data, Y_j^*, in the learning window, W_L. This transform yields the low frequency (approximation) and the high frequency (detail) wavelet coefficients. The high frequency content is often the noise associated with the signal, while the low frequency content represents the signal trend that may be used for regression. A least squares fit was performed on the approximation coefficients (refer to Fig. 5(*a*)) with the coefficients forecasted for $t=10{,}000$ min. The signal approximation was reconstructed from the coefficients by taking the inverse wavelet transform. The length of the reconstructed signal approximation was equal to the sum of the desired forecasted signal and the learning window. A comparison between the turbine inlet temperature signal forecast and experimental data for $22{,}000<t<32{,}000$ min is shown in Fig. 5(*b*). The thick line represents the wavelet forecast, which has been superimposed on the experimental data; the forecast error estimation is 9.23%. For a better visual representation, the filtered data and the signal forecast are mapped back into the operating domain along with the error bounds, $\pm\varepsilon$, as shown in Fig. 5(*c*).

4.3 Comparison of Prediction Methods. A comparison of the two prediction techniques, based on the forecast error values, has been presented in Table 1. In addition to the turbine inlet temperature, four other plant signals were forecasted and their respective errors computed. In each of the five cases, the wavelet method produced a lower forecast error and may be ranked as the better prediction strategy. Such a result justifies its application despite the apparent additional calculation effort incurred in this method. Such effort is barely noticeable when available well developed wavelet algorithms are used for the analysis. Figure 6 demonstrates the source of the calculation complexity for the wavelet method compared to the statistical strategy.

Overall, the forecast errors are acceptable for both the methods. To implement the wavelet prediction strategy, the general algorithm is shown in Fig. 7. At the appropriate time, new data may be obtained and the process continues.

5 Summary

Two model-free performance prediction strategies have been presented and applied to simple cycle natural gas turbine in this paper; a summary of the characteristics of the two methodologies is presented in Table 2. A representative set of experimental results was compared and discussed to investigate the performance and the general utility of the proposed health monitoring approaches. The availability of extensive operating data for commercial electrical generating turbines has shown that the estimated forecasts for different turbine signals compare favorably with the actual test data. In general, the wavelet method offers a better prediction of the signals studied. An open research issue is the selection of operating modes to reduce signal fluctuations for improved forecast performance.

Acknowledgment

The research team would like to thank the Department of Energy (DOE Award No. DE-FC26-02NT41431) for its financial support of the research, as well as the Clemson University Facilities Department and the Santee Cooper Electrical Utility (Iva, SC) for their technical assistance.

Nomenclature

$A\chi$ = signal approximation
a = polynomial coefficient
d_e = scaling coefficients
$\mathbf{D}$ = sum of squares of deviations
E = statistical operator for mean
e = scaling coefficient index
i = time index
j = selected output signal number
k = selected input signal number
m = recorded time instances
N = shaft speed (rpm)
n = input signals selected dimensions
F = function frequency (rad/s)
f = final forecast time
g = input signal dimensions
h = output signal dimensions
t = time (minutes)
Δt = sampling rate
t^* = raw data time
U = input signal
U^* = conditioned input signal
u = selected input signal
V = composite data vector
u_0, v_0 = wavelet parameters
W_L = learning window
W_S = sampling window
W_V = validation window
Y = output signal
Y^* = conditioned output signal
y = selected output signal
$\mathbf{Z}$ = regression curve
p = output signals selected dimensions
Q = heat rate
q = regression order index
r = regression order
s = signal component
T_{ex} = exhaust temperature (°C)
ϑ = wavelet function energy
$\Re$ = correlation coefficient
ς = admissibility constant
σ = standard deviation
χ = dilation variable
ψ = mother wavelet
$\hat{\psi}$ = Fourier transform of mother wavelet
η = translation variable
ε = forecast error
ϕ = scaling function
γ = input variable detail coefficients
$\hat{\gamma}$ = output variable detail coefficients
ξ = input variable approx. coefficient
∞ = infinity
κ_d = signal disturbance component
κ_n = signal noise component
$\hat{\xi}$ = output variable approx. coefficient

References

[1] Sekhon, R., Bassily, H., and Wagner, J., 2006, "Real Time Prognostic Strategies With Application to Stationary Gas Turbines," ASME Paper No. IMECE 2006-14068.

[2] Sekhon, R., Bassily, H., Wagner, J., and Gaddis, J., 2006, "Stationary Gas Turbines—A Real Time Dynamic Model With Experimental Validation," *Proceedings of the American Control Conference*, Minneapolis, MN, Jun., pp. 1838–1844, Paper No. WEC13.1.

[3] Lebold, M., McClintic, K., Campbell, R., Byington, C., and Maynard, K., 2000, "Review of Vibration Analysis Methods for Gearbox Diagnostics and Prognostics," *Proceedings of the 54th Meeting of the Society for Machinery Failure Prevention Technology*, Virginia Beach, VA, May, pp. 623–634.

[4] Atlas, L., Bloor, G., Brotherton, T., Howard, L., Jaw, L., Kacprzynski, G., Karsai, G., Mackey, R., Mesick, J., Reuter, R., and Roemer, M., 2001, "An Evolvable Tri-Reasoner IVHM System," *Proceedings of the IEEE Aerospace Conference*, Big Sky, MT, Mar., Vol. 6, pp. 63023–63037.

[5] Brotherton, T., Jahns, G., Jacobs, J., and Wroblewski, D., 2000, "Prognosis of

Faults in Gas Turbine Engines," *Proceedings of the IEEE Aerospace Conference*, Big Sky, MT, Mar. Vol. 6, pp. 163–171.
[6] Wang, P., and Vachtsevanos, G., 2001, "Fault Prognosis Using Dynamic Wavelet Neural Networks," Artif. Intell. Eng. Des. Anal. Manuf., **15**(4), pp. 349–365.
[7] Schwabacher, M., 2005, "A Survey of Data Driven Prognostics," Paper No. AIAA 2005-7002.
[8] Gulen, S., Griffin, P., and Paolucci, S., 2002, "Real Time on Line Performance Diagnostics of Heavy-Duty Industrial Gas Turbines," J. Eng. Gas Turbines Power, **124**(4), pp. 910–921.
[9] Veer, T., Haglerod, K., and Bolland, O., 2004, "Measured Data Correction for Improved Fouling and Degradation Analysis of Offshore Gas Turbines," *Proceedings of the ASME Turbo Expo*, Vienna, Austria, Jun., Vol. 7, pp. 823–830.
[10] Byington, C., Roemer, M., and Galie, T., 2002, "Prognostic Enhancements to Diagnostic Systems for Improved Condition-Based Maintenance," *Proceedings of the IEEE Aerospace Conference*, Big Sky, MT, Mar., Vol. 6, pp. 2815–2824.
[11] Jardim, R., Barata, M., Assis, L., Alavro, J., and Garcao, A., 1996, "Application of Stochastic Modelling to Support Predictive Maintenance for Industrial Environments," *Proceedings of the IEEE International Conference on Systems, Man and Cybernetics*, Beijing, China, Oct., Vol. 1, pp. 117–122.
[12] Greitzer, F., and Ferryman, T., 2003, "Predicting Remaining Life of Mechanical Systems," *Proceedings of the ASNE Intelligent Ship Symposium*, Philadelphia, PA,. Apr.
[13] Barlas, I., Zhang, G., Propes, N., and Vachtsevanos, G., 2003, "Addressing Uncertainty and Confidence in Prognosis," *Proceedings of the ASNE Intelligent Ship Symposium*, Philadelphia, PA, Apr.
[14] Mannapov, R., 1992, "Predicting the Remaining Life of Equipment From Damage Statistics," Journal of Chemical & Petroleum Engineering, **28**(9), pp. 543–546.
[15] Kim, D., and Mead, H., 1999, "Remaining Life Assessment of Refinery Heater Tubes," *Proceedings of the ASME Pressure Vessels and Piping Conference*, Boston, MA, Aug., Vol. 388, pp. 361–366.
[16] Dong, M., and He, D., 2004, "Hidden Semi-Markov Models for Machinery Health Diagnosis and Prognosis," Trans. North Am. Manuf. Res. Inst. SME, **32**, pp. 199–206.
[17] Sulieman, H., McLellan, P., and Bacon, D., 2001, "A Profile-Based Approach to Parametric Sensitivity Analysis of Nonlinear Regression Models," Technometrics, **43**(4), pp. 425–433.
[18] Brockwell, P., and Davis, R., 2002, *Introduction to Time Series and Forecasting*, Springer-Verlag, New York.
[19] McAlpin, R., Tally, P., Bernstein, H., and Holm, R., 2003, "Failure Analysis of Inlet Guide Vanes," J. Eng. Gas Turbines Power, **125**(1), pp. 236–240.
[20] Aboufadel, E., and Schlicker, S., 1999, *Discovering Wavelets*, Wiley Interscience, New York.
[21] Addison, P., 2002, *The Illustrated Wavelet Transform Handbook*, Institute of Physics, Philadelphia, PA.
[22] Sun, Z., Wang, R., Jiang, X., and Xu, M., 2005, "Application of Wavelet Transform to Recursive Prediction of Vibration Signals," J. Harbin Inst. Technol., **12**(5), pp. 483–493.
[23] Feng, C., Yu, Z., and Kusiak, A., 2006, "Selection and Validation of Predictive Regression and Neural Network Models Based on Designed Experiments," IIE Trans., **38**(1), pp. 13–23.
[24] Guo, J., Chen, Q., Hu, W., and Xu, S., 2003, "Nonlinear Generalized Predictive Control Based on Inverse System Using Wavelet Networks," *Proceedings of the International Conference on Wavelet Analysis and Its Applications*, pp. 883–889. China, May, Vol. 2.
[25] Daubechies, I., 1992, *Ten Lectures on Wavelets*, Society for Industrial and Applied Mathematics, Philadelphia, PA.

Data Visualization, Data Reduction and Classifier Fusion for Intelligent Fault Diagnosis in Gas Turbine Engines

William Donat
Kihoon Choi
Woosun An
Satnam Singh
Krishna Pattipati
e-mail: krishna@engr.uconn.edu

University of Connecticut,
Storrs, CT 06268

In this paper, we investigate four key issues associated with data-driven approaches for fault classification using the Pratt and Whitney commercial dual-spool turbofan engine data as a test case. The four issues considered here include the following. (1) Can we characterize, a priori, the difficulty of fault classification via self-organizing maps? (2) Do data reduction techniques improve fault classification performance and enable the implementation of data-driven classification techniques in memory-constrained digital electronic control units (DECUs)? (3) When does adaptive boosting, an incremental fusion method that successively combines moderately inaccurate classifiers into accurate ones, help improve classification performance? (4) How to synthesize classifier fusion architectures to improve the overall diagnostic accuracy? The classifiers studied in this paper are the support vector machine, probabilistic neural network, k-nearest neighbor, principal component analysis, Gaussian mixture models, and a physics-based single fault isolator. As these algorithms operate on large volumes of data and are generally computationally expensive, we reduce the data set using the multiway partial least squares method. This has the added benefits of improved diagnostic accuracy and smaller memory requirements. The performance of the moderately inaccurate classifiers is improved using adaptive boosting. These results are compared to the results of the classifiers alone, as well as different fusion architectures. We show that fusion reduces the variability in diagnostic accuracy, and is most useful when combining moderately inaccurate classifiers. [DOI: 10.1115/1.2838993]

Introduction

Safety-critical systems, such as gas turbine engines, demand real-time fault detection and isolation (FDI), and a decision support system to prescribe corrective actions so that the system can continue to function without jeopardizing the safety of the personnel and equipment involved. Owing to a large number of failure modes, substantial number of operating modes, and possible occurrence of multiple faults simultaneously, FDI in complex safety-critical systems is a formidable challenge.

Engine health-monitoring methods can be classified as being associated with one or more of the following three approaches: model based, knowledge based, or data driven. The model-based FDI has progressed significantly over the past four decades. In this approach, a mathematical model for FDI is developed from the underlying physics and dynamics of the mechanical system. The knowledge-based approach, on the other hand, uses qualitative models (e.g., cause-effect graphs) to develop monitoring methods, and is suited in situations where mathematical models are not readily available. What if a mathematical model (model-based) or cause-effect graph model of system failures and their manifestations (knowledge-based) is not available? The data-driven approach to FDI is an alternative, provided that system monitoring data are available. Due to its simplicity and adaptability, customization of a data-driven approach does not require an in-depth knowledge of the system. In this paper, we will employ support vector machine (SVM), probabilistic neural network (PNN), *k*-nearest neighbor (KNN), principal component analysis (PCA), Gaussian mixture models (GMM), and single fault isolator (SFI) classifiers to investigate four key issues: visual characterization of the degree of difficulty in fault classification, data reduction for improved classification accuracy and real-time implementation, when to use adaptive boosting, and synthesizing fusion architectures.

Improving the performance of an FDI classifier requires an evaluation of its performance. An a posteriori assessment methodology for classifiers (based on training, validation, and test data sets) was presented in Ref. [1]. However, it would be desirable to characterize, a priori, the degree of difficulty in classifying faults. We conduct exploratory data analysis via self-organizing map (SOM) to characterize the classification difficulty. Specifically, we show that a fragmented map is a key indicator of the difficulty of fault classification task.

One of the issues with high-dimensional data sets (caused by multiple modes of system operation, sensor data over time, and large volumes of data) is that not all the measured variables are salient for understanding the underlying phenomena of interest (in our case, nominal and faulty behavior) [2]. Thus, it is of interest to reduce the dimension of the original data to minimize uncorrelated information and memory requirements. Minimization of storage space enables the real-time implementation of data-driven classification techniques in memory-constrained digital electronic control units (DECUs). We show that data reduction techniques improve diagnostic accuracy and enable real-time implementation of data-driven classifiers.

It is generally believed that an ensemble of classifiers improves diagnostic accuracy when compared to individual classifiers. Using adaptive boosting (AdaBoost) and different fusion architectures, we investigate when this assertion is true using the Pratt and

Contributed by the International Gas Turbine Institute (IGTI) of ASME for publication in the JOURNAL OF ENGINEERING FOR GAS TURBINES AND POWER. Manuscript received July 1, 2007; final manuscript received September 5, 2007; published online April 29, 2008. Review conducted by Dilip R. Ballal.

Table 1 Sensors

FEP	Fan exit pressure
N1	Low spool speed
N2	High spool speed
P25	LPC exit pressure
PB	Burner pressure
T25	LPC exit temperature
T3	HPC exit temperature
T49	Exhaust gas temperature
WF	Fuel flow

Whitney engine data as a test case. We show that fusion reduces the variability in diagnostic accuracy, and is most useful when combining moderately inaccurate classifiers.

Description of Engine Data

The data set used to illustrate the methods discussed in this paper was developed from a physics-based engine model of a Pratt and Whitney commercial engine. Samples of each of the 31 modeled faults were created for training and testing the classifiers. Gaussian noise was added in accordance with modeled sensor noise levels. Table 1 enumerates the nine sensors used.

Each snapshot included monitored values from nine sensors taken during quasi-steady-state cruise. Each sample consists of 25 snapshots. The faults presented here are shifts due to abrupt changes in module performance. The 31 modeled faults are shown in Table 2. Additional details on fault types may be found in Ref. [1].

In this paper, we assume that the fault detection task has been completed and we focus on fault isolation only. Detection might be accomplished using the generalized likelihood ratio test or comparable statistical techniques [3]. The effects of gradual deterioration and engine-to-engine performance variation are not considered here and are assumed to be removed before applying these techniques. The experiment is conducted at one operating point during cruise. Cruise data collected at different operating points during implementation (e.g., different altitude, Mach, and power level adjustment (PLA) setting) would have to be normalized prior to processing.

The overall dataflow of this paper is shown in Fig. 1. Assuming that a fault has been detected, raw data are reduced and applied to the classifiers for fault isolation. Various fusion techniques are applied to the output of the classifiers to reach a final decision. A more detailed dataflow diagram is included in the Results section. Although the thrust of this paper is focused on real-time fault isolation, the classification and fusion techniques presented herein could be used for real-time or postflight diagnosis.

Table 2 Fault universe

Fault No.	Fault type	Fault No.	Fault type
1	FAN	17	Seventh SSBld PO
2	LPC	18	Tenth SSBld FO[a]
3	HPC	19	Tenth SSBld PO
4	HPT	20	N1 error
5	LPT	21	N2 error
6	HPC VSV	22	WF error
7	HPT TCC[a]	23	T49 error
8	TCA Valve[a]	24	T25 error
9	FAN DP	25	T3 error
10	FAN Bld	26	P25 error
11	ECS SBld[a]	27	PB error
12	Seventh SBld	28	FEP error
13	Tenth SBld	29	P2 error
14	2.5 Bld FO[a]	30	T2 error
15	2.5 Bld PO	31	P49 error
16	Tenth SSBld FO[a]		

[a]Simulated at 100%.

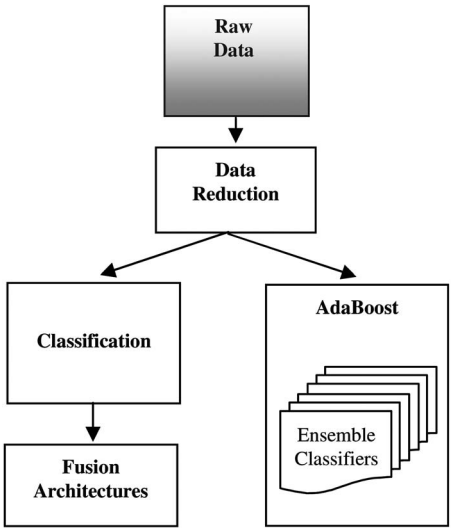

Fig. 1 Overall dataflow diagram

Classifiers

We briefly describe each of the classifiers used in the study. Mathematical details may be found in the cited references.

Support Vector Machine. SVM transforms the data to a higher-dimensional feature space, and finds an optimal hyperplane that maximizes the margin between two classes via quadratic programming [4,5]. There are two distinct advantages of using the SVM for classification [6]. First, the features are often associated with the physical meaning of data making it easy to interpret. The second advantage is that it requires only a small amount of training data. A kernel function, typically a radial basis function, is used for feature extraction. An optimal hyperplane is found in the feature space to separate the two classes. In the multiclass case, a hyperplane separating each pair of faults (classes) is found, and the final classification decision is made based on a majority vote among the binary classifiers.

Probabilistic Neural Network. The PNN is a supervised method to estimate the probability distribution function of each class [4,5]. The likelihood of an input vector being part of a learned category, or class is estimated from these functions. A priori probabilities and misclassification costs can be used to weight the learned patterns to determine the most likely class for a given input vector. If the a priori or relative frequency of the categories is not known, then all the categories can be assumed to be equally likely. In this case, the determination of the category of an input vector is solely based on its closeness to the distribution function of a class. Data reduction methods are essential in real-world applications due to the substantial memory requirements of PNN [6].

***k*-Nearest Neighbor.** A simple nonparametric algorithm, the KNN classifier, is an important benchmark method [7]. This classifier requires two parameters: a distance metric d and a positive integer k. Classification of the testing input vector $\underline{\mathbf{x}}$ is accomplished using the subset of k-feature (training) vectors that are closest to $\underline{\mathbf{x}}$ according to the metric d. The class in majority of the k subset is then assigned to new input vector $\underline{\mathbf{x}}$. Ties can be avoided by choosing k to be an odd number (e.g., 1, 3, 5). This process can be viewed as computing a posteriori class probabilities $P(c_i|\underline{\mathbf{x}})$ as follows:

$$P(c_i|\underline{\mathbf{x}}) = \frac{k_i}{k} p(c_i) \tag{1}$$

where $\underline{k}_i$ vectors belong to class c_i of the total k subset vectors, and $P(c_i)$ is the *prior* probability of class c_i (proportional to the number of training patterns of class c_i). A new input vector $\underline{\mathbf{x}}$ is assigned to the class c_i with the highest posterior probability $P(c_i|\underline{\mathbf{x}})$. The KNN classifier requires the storage of all training patterns; thus, data reduction methods are essential for real-time implementation [6,8].

Principal Component Analysis. By calculating the covariance matrix of the training data and the corresponding eigenvalues and eigenvectors, PCA transforms correlated variables into a smaller number of uncorrelated variables, called principal components. These eigenvalues are then sorted, and the vectors (called scores) with the highest values are selected to represent the data in a reduced space. The number of retained principal components is determined using cross validation [7]. PCA in outer-product form can be expressed as

$$X = \sum_{f=1}^{P} \underline{t}_f \underline{\mathbf{p}}_f^T + \mathbf{E} \tag{2}$$

Here, X is the training data, P is the number of retained principal components, $\mathbf{E}$ is the residual matrix, and $\{\underline{\mathbf{p}}_f\}$ are loading vectors, which are orthonormal and provide the directions of maximum variability. The coordinates of the original data sample in the reduced space are called score vectors ($\underline{\mathbf{t}}_f$) and are developed from the different principal components. A new test pattern is classified by obtaining its predicted scores and residuals. A small residual between the origin of the reduced space and the score vector characterizes a test pattern, which is similar to a specific class in the trained classifier. The distance of test pattern from the origin of the reduced space is computed using the Hotelling statistic [6,9].

Gaussian Mixture Models. GMMs are widely used for unsupervised and supervised classification. These models represent each class c_i as a probability density function (pdf), which is a mixture of K multidimensional Gaussian distributions. Equation (3) shows the pdf of class c_i where $\underline{\mu}_{ij}$ is the mean of distribution j and $\mathbf{\Sigma}_{ij}$ is the corresponding covariance matrix.

$$f_{c_i}(\underline{\mathbf{x}}) = \sum_{j=1}^{K} \lambda_{ij} N(\underline{\mu}_{ij}, \Sigma_{ij}) \tag{3}$$

The mixing parameters $\{\lambda_{ij}\}$ and the density parameters $\{\underline{\mu}_{ij}, \mathbf{\Sigma}_{ij}\}$ are learned from the training data via the expectation-maximization (EM) algorithm [4]. Given the learned pdf for each class, f_{c_i}, classification decisions are made via discriminant functions based on Bayesian decision theory [5].

Physics-Based Single Fault Isolator. The SFI, a model-based classifier, uses a bank of Kalman filters, one for each fault condition, to estimate the size of each fault. These estimates are then ranked using normalized measurement error. This technique can only be used on raw data because it is based on measured physical variables. Consequently, data reduction techniques and AdaBoost methods were not applied to SFI in this paper. In-depth treatment of this technique is presented in Ref. [10].

Self-Organizing Maps

Kohonen's SOM, a popular neural network method, is widely used in a variety of applications, including exploratory data analysis, and as a preprocessor prior to developing a supervised learning technique.

SOM transforms complex, nonlinear relationships between high-dimensional data into topological relationships in a low-dimensional space. Our motivation for employing SOM in FDI is to visually explore the data in a two-dimensional space to gain insights into the difficulty of fault classification task prior to developing a relevant FDI scheme.

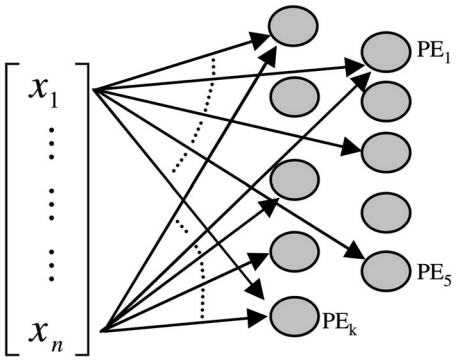

Fig. 2 SOM architecture

A prototypical architecture of SOM is shown in Fig. 2. Here, the n-dimensional input space is reduced, via a nonlinear transformation (shown as processing elements PE_k), by grouping the data into clusters in a lower-dimensional output space (typically, 2 or 3) for visualization [11,12]. The reduced space displays important characteristics of the input space, such that the neighboring points in the input space will be closer in the reduced space as well. As stated succinctly in Ref. [11], SOM may be viewed as an ordered decoder array in which one and only one of the decoders responds to a particular domain of the input signals and that it is the location of the decoder, and not the exact magnitude of its response, that characterizes the input information. The details of SOM are provided in Refs. [11,12] and references therein.

SOM for the engine data sets in Table 3 are shown in Figs. 3 and 4. Each square in the map is an output cluster or neuron while the number shown in each square represents the faults from Table 2, which is in the majority in that cluster. RGB color shading is

Table 3 Data set characteristics

Data set	Data size	Description subjective, magnitude%, No. of samples /fault type (class)
1	2.05 Mbyte	difficult, +(1–3), 80
2	4.31 Mbyte	more difficult, ±(1–3), 80

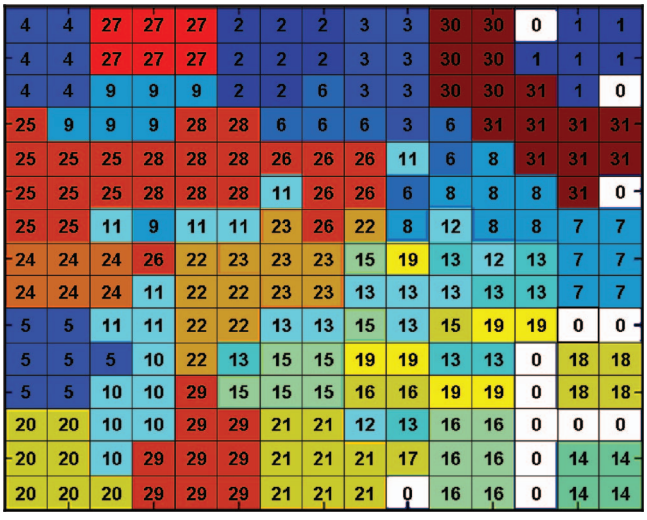

Fig. 3 SOM for Data Set 1

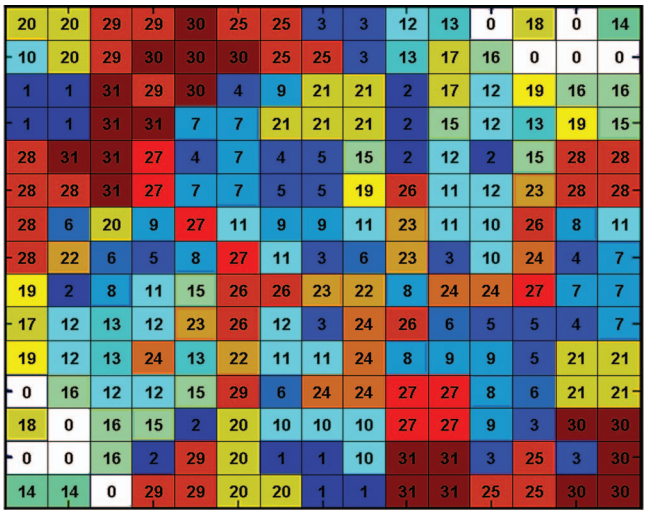

Fig. 4 SOM for Data Set 2

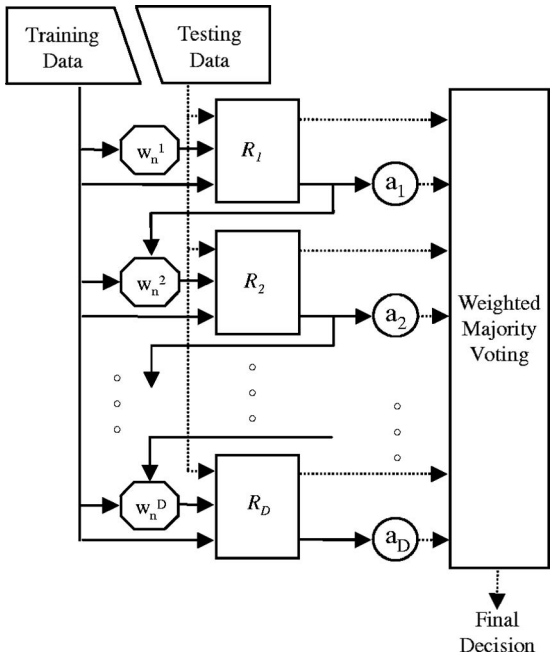

Fig. 5 AdaBoost algorithm

used to illustrate the cluster groupings. Empty clusters are indicated with white shading and are marked with the 0 class. It is evident that Data Set 1 has much better cluster groupings and spatial continuity for each fault when compared to Data Set 2; this is consistent with the subjective assessment of the engine expert (see Table 3). This qualitative analysis is validated when we compare the classification rates of each class. The classification accuracy on raw data was 100% for all classifiers on Data Set 1, while it ranged from 70.3% to 94.52% on Data Set 2. Therefore, we can consider the contiguity of clusters in SOM as an a priori degree of difficulty in classifying a particular data set. This simple example illustrates the power of SOM in qualitatively describing the input signal space.

In the rest of the paper, we will focus on the more difficult to classify Data Set 2 only.

Data Reduction

Large engine health-monitoring data sets present new challenges in data analysis. Traditional statistical methods break down partly because of the increase in the number of observations (measurements), but mostly due to an increase in the number of variables (increase in dimension) associated with each observation [2]. One of the problems with high-dimensional data sets is that not all the measured variables are "important" for understanding the underlying phenomena of interest [2]. Dimension reduction techniques are a good alternative to variable selection in order to overcome the dimensionality problem. Using such techniques, the high-dimensional data are projected onto a lower-dimensional space. There exist a number of linear (e.g., independent component analysis, PCA, factor analysis, wavelets, and partial least squares) and nonlinear (e.g., locally linear embedding, isomap, and multidimensional scaling) data reduction techniques [13–16].

Of the many widely used dimension reduction techniques available, multiway partial least squares (MPLS)-based data reduction technique will be applied in this paper. Partial least squares (PLS) is similar to PCA. In PCA, the scores are calculated to give an optimal summary of $\underline{\mathbf{X}}$, while in PLS, the optimality is relaxed to make scores better predictors of the dependent (response, output) matrix $\mathbf{Y}$ [17]. The PLS algorithm reduces the dimensionality of the input and output spaces to find latent variables which are highly correlated, i.e., those that not only explain the variation in the input X, but their variations that are most predictive of the output Y. Since $\underline{\mathbf{X}}$ is a three-dimensional tensor (data samples $\times$ sensors $\times$ time), we need to perform multiway PLS. The three-dimensional tensor $\underline{\mathbf{X}}$ is decomposed into one set of score vectors (latent variables) $\underline{\mathbf{t}}$ and two weight vectors $\underline{\mathbf{w}}_j$ and $\underline{\mathbf{v}}_k$ in the second and third dimensions, respectively [14,18,19]. The output matrix $\mathbf{Y}$ (fault-type information) is separated into score vectors $\underline{\mathbf{t}}$ and loading vectors $\mathbf{q}$. The input and output matrices $\underline{\mathbf{X}}$ and $\mathbf{Y}$ are given by

$$\underline{\mathbf{X}} = \sum_{f=1}^{P} \underline{\mathbf{t}}_f (\underline{\mathbf{w}}_{jf} \otimes \underline{\mathbf{v}}_{kf}) + \underline{\mathbf{E}}$$

$$\mathbf{Y} = \sum_{f=1}^{P} \underline{\mathbf{t}}_f \mathbf{q}_f^T + U \tag{4}$$

where P is the number of factors or principle components used in the reduced space, j is the number of sensors, the symbol $\otimes$ denotes the Kronecker product, k is time, and U and E are residuals. The values of $\underline{\mathbf{t}}$, $\underline{\mathbf{w}}_j$, $\underline{\mathbf{v}}_k$, and $\mathbf{q}^T$ are found by using a nonlinear iterative partial least squares (NIPALS) algorithm [18,20]. This reduced score matrix will be applied to the classifiers in the following section for fault isolation.

Fusion Techniques

An efficient method to improve the diagnostic accuracy and make it robust is to fuse several classifiers. The fusion techniques are applied to the output labels or the confidence estimates of multiple classifiers, and a final classification decision is made by combining the results of individual classifiers in a statistically rigorous way. This allows diagnostic analysts to use the strengths and weaknesses of each classifier to reduce the overall classification error. In this section, we will discuss AdaBoost and several different fusion architectures.

Adaptive Boosting. AdaBoost creates an ensemble of classifiers, typically 20, called weak learners [5]. Since the data set considered in this paper has multiple classes (31 faults), AdaBoost is implemented and applied to improve individual classifier performance [21]. As depicted in Fig. 5, this algorithm uses a weight for each training pattern w_n^j that is updated at each iteration j to increase the likelihood that the patterns which are more difficult to classify are included in the next training set. At each iteration j, the weights determine which training patterns are used to train the ensemble classifier, R_j. Overall accuracy is improved when the

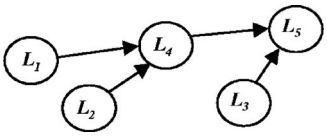

Fig. 6 First-order dependence tree

distribution is controlled via the weights such that the weak learners focus on training patterns, which are hardest to correctly classify and the mislabeled patterns most difficult to differentiate [5]. The final classification decision is made based on a weighted majority rule, where the weights, a_j, are gleaned during training.

Evaluation of Fusion Architectures. We can combine classifiers using a variety of fusion architectures [22–24]. A key issue here is which architectures will enhance the diagnostic accuracy and under what conditions? Considering that classifiers have different accuracies on each class, we develop class-dependent fusion architectures based on the diagnostic accuracies of individual classifiers on the training data for each class.

We consider classifiers arranged in the form of a first order dependence tree for each class. For illustrative purposes, consider Fig. 6, where five classifiers are arranged in the form of a tree. Suppose that the classifiers provide class labels $\{L_j\}_{j=1}^{5}$. Then, the support for class c_i is given by

$$P(\{L_j\}_{j=1}^{5}|c_i) = P(L_5|c_i)P(L_5|L_4,c_i)P(L_5|L_3,c_i) \times P(L_4|L_1,c_i)P(L_4|L_2,c_i) \quad (5)$$

Here, the term $P(L_j|c_i)$ denotes the probability of label L_j given the true class c_i from the confusion matrix of classifier j. The double entries of the form $P(L_k|L_j,c_i)$ represent the output labels of classifiers k and j in the coincidence matrix developed from classifiers k and j on class c_i during training [25,26]. The final decision corresponds to the class with the highest probability in Eq. (5).

Consider a few special cases of the tree architecture shown in Fig. 7. The first architecture, Fig. 7(*a*), combines the decisions of multiple classifiers serially. In this tandem architecture, the classifiers are arranged from the worst, $L_W^{c_i}$, to the best, $L_B^{c_i}$, in terms of training classification accuracy.

The architecture shown in Fig. 7(*b*) is arranged in a parallel configuration with the worst classifier at the fusion center (putting the best classifier at the fusion center gave slightly worse results of 4.73% versus 1.86% misclassifications for this configuration). In this configuration, the same procedure is followed for computing the probability of a class. That is, the conditional probabilities are computed using the coincidence matrices, and a probability

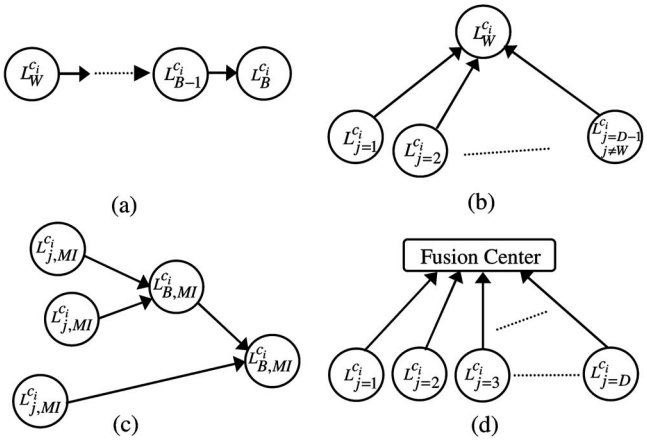

Fig. 7 Classifier fusion architectures

approximation is developed for each class according to Eq. (5).

The question arises: can we arrange the classifiers to maximize diagnostic accuracy? Using mutual information as a surrogate for diagnostic accuracy, we arranged the classifiers as a dependence tree that maximizes the sum of mutual information between all pairs of classifiers [26]. This problem can be solved via a minimum spanning tree algorithm [27].

We calculate the mutual information, $\hat{I}_i(L_f,L_g)$, between classifiers f and g, from the coincidence matrices as follows:

$$\hat{I}_i(L_f,L_g) = \sum_{m=1}^{C}\sum_{n=1}^{C} \log\left(\frac{CI_{f,g}(m,n)E_i}{\sum_{m=1}^{C} CI_{f,g}(m,n) \times \sum_{n=1}^{C} CI_{f,g}(m,n)}\right) \quad (6)$$

where $CI_{f,g}(m,n)$ is the cell (m,n) of the coincidence matrix between classifiers f and g (i.e., how often classifier f gives decision m, while classifier g outputs decision n on the training data), E_i is the number of training elements from ith class, and C is the total number of classes. These mutual information weights for all pairs of classifiers for a given class are negated and are input to a minimum spanning tree (MST) algorithm [27]. This algorithm outputs a tree configuration with the maximum mutual information. Starting with the pair having the most mutual information, $L_{B,\mathrm{MI}}^{c_i}$, we arrange the classifiers, as shown in Fig. 7(*c*).

If the classifiers are arranged in parallel and output labels from all classifiers are fused at once, we will be using the architecture shown in Fig. 7(*d*). Using this configuration, we can compute a score (discriminant function), $g_{c_i}(\underline{\mathbf{x}})$, for each class c_i as follows:

$$g_{c_i}(\underline{\mathbf{x}}) = \log(P(c_i)) + \sum_{j=1}^{D} \log(P(L_j|c_i)) \quad (7)$$

where D is the number of classifiers, $P(c_i)$ is the prior probability of class c_i, and $P(L_j|c_i)$ is the likelihood of class label L_j for a class c_i. This score is calculated for each class, and the class label with the highest score is assigned to the test pattern.

The architecture shown in Fig. 7(*d*) can also be used to combine confidence estimates of an ensemble of classifiers. The probability of class c_i given the test patterns and the training samples can be shown as

$$P(c_i|\underline{\mathbf{x}},Z) = \sum_{j=1}^{D} d_{i,j}(\underline{\mathbf{x}})P(L_j(c_i)|Z) \quad (8)$$

where $d_{i,j}(\underline{\mathbf{x}})$ is the posterior probability of class i from classifier j for the testing pattern $\underline{\mathbf{x}}$. Here, Z is the set of training data and $P(L_j(c_i)|Z)$ are its associated posterior probabilities. The probability or weight of class c_i from L_j given the set of training data Z can be calculated as follows:

$$P(L_j(c_i)|Z) = \frac{P(Z|L_j(c_i))P(L_j(c_i))}{P(Z)} \quad (9)$$

$$= \frac{P(Z|L_j(c_i))P(L_j(c_i))}{\sum_{n=1}^{D} P(Z|L_n(c_i))P(L_n(c_i))} \quad (10)$$

$P(Z|L_j(c_i))$ is calculated via

$$P(Z|L_j(c_i)) = \prod_{l=1}^{N} [d_{i,j}(z_l)]^{t_{i,j}} \quad (11)$$

where N is the number of training samples, z_l is a training sample from class i, and $\mathbf{t}_j$ is $1 \times C$ target vector with a 1 in location i if it belongs to class i. A priori knowledge of the accuracy of classifier j on class i can be expressed as follows:

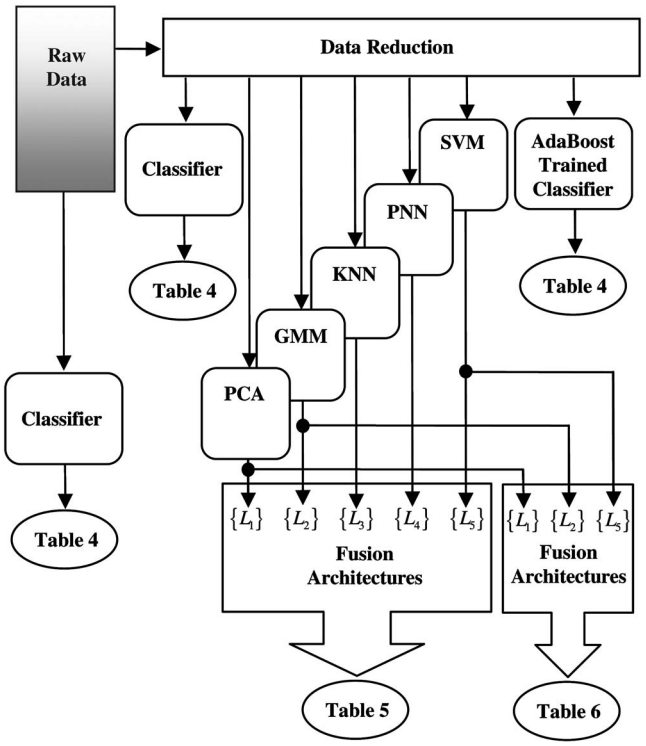

Fig. 8 Computational setup for experiments

$$P(L_j(c_i)) = \frac{a_j(c_i)}{\sum_{q=1}^{D} a_q(c_i)} \tag{12}$$

where $a_j(c_i)$ is the accuracy of classifier j on class i. Finally, the weights $P(L_j(c_i)|Z)$ are normalized to 1. During testing, $P(c_i|\underline{\mathbf{x}},Z)$ is calculated for each class i and the class with the highest probability is chosen as the output.

Results

Experimental results were obtained using the computational setup shown in Fig. 8 on the Data Set 2. Five by two (5×2)-fold cross validation [28] was used to ensure the validity of results in all cases. In 5×2 cross validation, the data are split into two equally sized subsets $\{\Omega_1,\Omega_2\}$. The classifier is trained and tested twice. First, Ω_1 is used to train the classifier and Ω_2 to test the classifier. Then, the roles of the subsets are reversed. This procedure is repeated five times and results of the ten tests are averaged to obtain the final results.

To establish a base line, individual classifiers were evaluated against raw data. The results are shown in Table 4 in terms of misclassification rates.

Data Reduction. As shown in Table 4, the data reduction algorithm yielded a reduction of storage space from 4.31 Mbyte to 118 kbyte on Data Set 2, a nearly 40-fold decrease in memory requirement. The reduction yielded a decrease in the misclassification rate of as much as 22.22% (for PCA). Data reduction also decreased the inaccuracy of the PNN classifier from a misclassification rate of 5.48% to 0.28%, a decrease of 5.2%; a very significant result considering that it is difficult to decrease the inaccuracy of a nearly perfect classifier. Clearly, data transformations can significantly aid in improving the classification accuracy, while substantially reducing the memory requirements. This has been observed in automobile engines as well [6,29].

KNN, the best classifier, yields a misclassification rate of 0.15%, which represents one misclassification over all testing patterns. Across all validation subsets, the errors made by this classifier are due to sensor errors simulated with high noise variance and faults, which have similar signatures. Consequently, even the best classifier was unable to completely eliminate these misclassifications.

AdaBoost. Next, AdaBoost fusion was performed on the reduced data. The results are shown in the fourth column of Table 4. Three of the five classifiers remained unchanged, but two classifiers, SVM and GMM, realized a decrease in misclassification rates of 4.65% and 5.90%, respectively. These results agree with the theory surrounding AdaBoost, viz., AdaBoost will increase the

Table 4 Classification results

	Synthetic raw data Size: 4.31 Mbyte		Reduced data via MPLS Size: 118 kbyte		AdaBoost using MPLS on reduced data Size: 118 kbyte	
Classifier	Misclassification rate ± Std Dev.	Training time (s) Testing time per pattern (s) (Memory (byte))	Misclassification rate ± Std Dev.	Training time (s) Testing time per pattern (s) (Memory (byte))	Misclassification rate ± Std Dev.	Training time (s) Testing time per pattern (s) (Memory (byte))
SVM	21.50 ± 1.32%	72.2 0.0048 (2.4 M)	5.30 ± 0.45%	111.4 0.0076 (264 k)	0.65 ± 0.45%	2554 0.009 (268 k)
PNN	5.48 ± 0.32%	18.1 0.107 (2.36 M)	0.28 ± 0.15%	1.16 0.008 (119 k)	0. 28 ± 0.15%	23.29 0.008 (120 k)
KNN ($k=1$)	6.27 ± 0.36%	35.1 0.029 (2.32 M)	0.15 ± 0.20%	1.30 0.0071 (79 k)	0.15 ± 0.20%	12.4 0.0075 (78 k)
GMM	11.27 ± 2.31%	1.17 0.7 (4.6 k)	10.50 ± 3.48%	0.4 0.0071 (1.2 k)	4.60 ± 1.57%	9.8 0.0077 (1.2 k)
PCA	29.70 ± 1.00%	3.29 0.0019 (601 k)	7.48 ± 1.27%	0.99 0.0074 (69 k)	7.48 ± 1.27%	51.9 0.015 (98 k)
SFI	25.05%[a]					

[a]Standard deviation, training time, and testing time not available for SFI classifier.

Table 5 Fusion results using five classifiers

Fusion architecture using SVM, PNN, KNN, GMM, PCA classifiers on reduced data	Misclassification rate ± Std Dev.	Training time (s) Testing time (s) (Memory (byte))
Fusion Fig. 7(*a*)	1.67 ± 1.00%	211.6,1.14, (1.5 M)
Fusion Fig. 7(*b*)	1.86 ± 0.92%	207.4, 0.918, (1.5 M)
Fusion Fig. 7(*c*)	1.49 ± 0.55%	1583, 1.37, (1.5 M)
Fusion Fig. 7(*d*) Eq. (7)	2.64 ± 0.60%	115.27, 0.142, (571 k)
Fusion Fig. 7(*d*) Eq. (8)	0.15 ± 0.20%	123.5, 0.041, (534 k)

performance of classifiers that have marginal performance, but may have little effect on classifiers that are already performing very well [5]. Since PCA is basically a data transformation method, AdaBoost did not improve its accuracy beyond what was achieved by the earlier data reduction step. Since AdaBoost is a fusion method, this also suggests that fusion may not help when combining nearly perfect classifiers.

Fusion Architectures. Results for the various fusion architectures of Fig. 7 can be found in Tables 5 and 6. Two configurations of these architectures are evaluated. In Table 5, the SVM, PNN, KNN, GMM, and PCA classifiers are fused using the architectures in Fig. 7. Noting that KNN achieves a misclassification rate of 0.15% on the reduced data; the results are within the error of the experiment. Since KNN had almost perfect results, the fusion architectures were unable to yield an increase in classifier performance (the differences are not statistically significant). Once again, it is observed that fusing classifiers that are already performing very well may have little effect. However, fusion has the effect of reducing the variability in diagnostic accuracy, thereby providing consistent diagnostic decisions.

If fusion has marginal effect when classifiers are performing nearly perfectly, what happens if we fuse classifiers that are marginal? In Table 6, results from fusing the decisions of SVM, GMM, and PCA classifiers are shown (the three least accurate classifiers in column 3 of Table 4). The best classifier in this group yielded a misclassification rate of 5.30% before fusion on the reduced data. The fusion architectures yielded decreases in diagnostic inaccuracies ranging from 2.80% to 3.91%, a substantial amount considering that the classifier inaccuracies ranged from 10.50% to 5.30%. The architecture in Fig. 7(*c*), based on maximizing the dependent relationships (mutual information) among classifiers via the MST formalism, yielded the best results. As before, fusion does minimize the variability in diagnostic accuracy, i.e., makes robust decisions.

Implementation Considerations. In addition to misclassification rate, Tables 4–6 display training times, testing times, and the trained network's memory requirements. Training times for the entire training process, measured in seconds, are shown here. Testing times per pattern are shown; this also includes the time for data reduction. The testing times and storage requirements displayed for AdaBoost are averages per ensemble classifier. These values would have to be multiplied by number of classifiers in the ensemble, typically near 20, to calculate overall processing and storage demands for an AdaBoost implementation. Training and testing times were computed using MATLAB® software on a 2 GHz Intel Pentium M processor with 1 Gbyte of RAM. Typically, the times shown could be further reduced by a factor of 10 by implementing the code in the C language. The memory requirements shown in Tables 4–6 represent the memory of the trained network plus any additional information required in the testing algorithm in the form of MATLAB® double precision matrices displayed in bytes. The fusion architectures of Figs. 7(*a*)–7(*c*) have considerable memory requirements, since the architecture requires the storage of confusion and coincidence matrices in addition to the trained networks of all classifiers.

Table 6 Fusion results using three classifiers

Fusion architecture using SVM, GMM, and PCA classifiers on Reduced Data	Misclassification rate ± Std Dev.	Training time (s) Testing time (s) (Memory (bytes))
Fusion Fig. 7(*a*)	2.26 ± 1.89%	126, 0.622, (1.1 M)
Fusion Fig. 7(*b*)	1.86 ± 0.89%	126, 0.522, (1.1 M)
Fusion Fig. 7(*c*)	1.39 ± 0.53%	328, 0.622, (1.1 M)
Fusion Fig. 7(*d*) Eq. (7)	2.50 ± 0.57%	113, 0.062, (357 k)
Fusion Fig. 7(*d*) Eq. (8)	2.16 ± 1.99%	114, 0.025, (336 k)

FDI can be implemented either in the DECU or in a separate module. If the FDI process is implemented within the DECU, memory and processing resources must be considered. If memory in the DECU is constrained, a trade-off between classifier complexity and processor resources must be found. Under a severely memory-constrained DECU, use of the best single classifier may be necessary to minimize the use of processor resources. In Table 4, the KNN classifier operating on reduced data seems to be an obvious choice due to its high accuracy, low testing time, and below average memory requirements. If classifier fusion is needed to reach an acceptable level of classification accuracy, use of the architecture shown in Fig. 7(*d*) is worth considering. This architecture implemented using either Eq. (7) or Eq. (8) offers high accuracy, the least memory, and lowest processing times of the fusion architectures considered.

In addition to processor requirements, operating these algorithms on real-time data presents additional challenges not addressed herein. Preprocessing is required to handle missing or corrupted data and to perform the detection and normalization functions. The operating conditions under which the engine data are collected need to be considered before such an algorithm is considered for deployment.

Conclusion

In this paper, we have illustrated the usefulness of SOMs as a visualization tool for a priori understanding of the nature of input signal space and of the difficulty of the fault classification task. We have shown the power of data transformations to reduce the storage and processing demands, while offering a substantial increase in classifier performance. Data reduction via MPLS has resized the data to less than 3% of its original size, while increasing the diagnostic accuracy by 5.3%. AdaBoost was able to increase the classification rates of those classifiers, which exhibited marginal performance. We have discussed and evaluated several fusion architectures. Again, fusing classifiers that are performing very well had little positive effect. However, we showed that fusing marginal classifiers can increase the diagnostic performance substantially, while reducing their variability.

Our future work will focus on joint optimization of individual classifiers and the fusion architectures, and the fusion of hybrid model-based and data-driven classifiers. In addition, we will explore generalized topography maps [4] to visualize the degree of difficulty of fault classification tasks.

Acknowledgment

This work was supported by Pratt and Whitney via a contract at the University of Connecticut.

Nomenclature

FDI = fault detection and isolation
FO = fully open
GMM = Gaussian mixture model
KNN = *k*-nearest neighbor rule
MPLS = multiway partial least squares

MST = minimum spanning tree
PNN = probabilistic neural network
PO = partially open
SFI = physics-based single fault isolator
SOM = self-organizing map
SVM = support vector machine
AdaBoost = adaptive boosting

References

[1] Butler, S. W., Pattipati, K. R., Volponi, A., Hull, J., Rajamani, R., and Siegel, J., 2006, "An Assessment Methodology for Data Driven and Model-Based Techniques for Engine Health Monitoring," ASME Paper No. GT 2006-91096.

[2] Fodor, I. K., "A Survey of Data Reduction Techniques," available online at: http://www.llnl.gov/casc/sapphire/pubs148494.pdf

[3] Basserville, M., and Nikiforov, I., 1993, *Detection of Abrupt Changes: Theory and Application*, Information and System Science Series, Prentice-Hall, Englewood Cliffs, NJ.

[4] Bishop, C. M., 2006, *Pattern Recognition and Machine Learning*, Springer, New York.

[5] Duda, R. O., Hart, P. E., and Stork, D. G. 2001, *Pattern Classification*, 2nd ed., Wiley, New York.

[6] Choi, K., Luo, J., Pattipati, K. R., Qiao, L., and Chigusa, S., 2006, "Data Reduction Techniques for Intelligent Fault Diagnosis," 2006, *Proceedings of the IEEE Autotestcon*, Anaheim, CA, Sept.

[7] Jackson, J. E., 1991, *A User's Guide to Principal Components*, Wiley, New York.

[8] Shah, J., 2004, "Sequential k-Nearest Neighbor Pattern Recognition for Usable Speech Classification—A Revised Report," Speech Processing Lab, Temple University.

[9] Nomikos, P., 1996, "Detection and Diagnosis of Abnormal Batch Operations Based on Multi-Way Principal Component Analysis," ISA Trans., **35**(3), pp. 259–266.

[10] Volponi, A., Depold, H., Ganguli, R., and Daguang, C., 2000, "The Use of Kalman Filter and Neural Network Methodologies in Gas Turbine Performance Diagnostics: A Comparative Study," ASME Paper No. 2000-GT-547.

[11] Haykin, S., 1999, Neural Networks: A Comprehensive Foundation, 2nd ed., Prentice-Hall, Englewood Cliffs, NJ.

[12] Kohonen, T., Erkki, O., Simula, O., Visa, A., and Kangas, J., 1996, "Engineering Applications of the Self-Organizing Map," Proc. IEEE, **84**(10), pp. 1358–1384.

[13] Hand, D. J., 1981, *Discrimination and Classification*, Wiley, New York.

[14] Mardia, K. V., Kent, J. T., and Bibby, J. M., 1995, *Multivariate Analysis*, Probability and Mathematical Statistics, Academic, New York.

[15] Ripley, B. D., 1996, *Pattern Recognition and Neural Networks*, Cambridge University Press, Cambridge.

[16] Friedman, J., Hastie, T., and Tibshirani, R., 2001, *Elements of Statistical Learning: Prediction, Inference and Data Mining*, Springer, New York.

[17] Wold, S., Kettaneh, N., Friden, H., and Holmberg, A., 1998, "Modeling and Diagnostics of Batch Processes and Analogous Kinetic Experiments," Chemom. Intell. Lab. Syst., **44**(1–2), pp. 331–340.

[18] Wold, S., Geladi, K., Esbensen, K., 1987, "Principle Component Analysis," Chemom. Intell. Lab. Syst., **2**(1–3), pp. 37–52.

[19] Choi, K., Azam, M., Namburu, M., Luo, J., Pattipati, K. R., and Patterson-Hine, A., 2006, "Fault Diagnostics in HVAC Chillers Using Data-Driven Techniques," IEEE Instrum. Meas. Mag., **8**(3), pp. 24–32.

[20] Rasmus, R., 1996, "Multiway Calibration. Multilinear PLS," Geol. J., **10**(1), pp. 47–61.

[21] Eibel, G., and Pfeiffer, K.-P., 2005, "Multi-Class Boosting for Weak Classifiers," J. Mach. Learn. Res., **6**, pp. 189–210.

[22] Tang, Z. B., Pattipati, K. R., and Kleinman, D. L., 1991, "Optimization of Detection Networks: Part I—Tandem Structures," IEEE Trans. Syst. Man Cybern., **21**(5), pp. 1045–1059.

[23] Tang, Z. B., Pattipati, K. R., and Kleinman, D. L., 1992, "A Distributed M-ary Hypothesis Testing Problem With Correlated Observations," IEEE Trans. Autom. Control, **37**(7), pp. 1042–1046.

[24] Pete, A., Pattipati, K. R., and Kleinman, D. L., 1994, "Optimization of Detection Networks With Generalized Event Structures," IEEE Trans. Autom. Control, **39**(8), pp. 1702–1707.

[25] Kuncheva, L. I., 2004, *Combining Pattern Classifiers*, Wiley, New York.

[26] Chou, C. K., and Liu, C. N., 1968, "Approximating Discrete Probability Distributions With Dependence Trees," IEEE Trans. Inf. Theory, **14**(3), pp. 463–467.

[27] Berman, K. A., and Paul, J. L., 1997, *Fundamentals of Sequential and Parallel Algorithms*, PWS, Boston.

[28] Aylpaydin, E., 2004, *Introduction to Machine Learning*, MIT Press, Cambridge.

[29] Choi, K., Singh, S., Kodali, A., Pattipati, K., Shepard, J., Namburu, S., Chigusa, S., Prokhorov, D., and Qiao, L., 2007, "Novel Classifier Fusion Approaches for Fault Diagnosis in Automotive Systems," *IEEE Autotestcon*, Baltimore, MD.

Combustion Chamber Steam Injection for Gas Turbine Performance Improvement During High Ambient Temperature Operations

Abdallah Bouam
Nuclear Research Center of Birine CRNB,
P.O. Box 180,
Aïn-Oussera 17200,
Algeria
e-mail: bouam05_ab3@yahoo.fr

Slimane Aissani
Faculty of Hydrocarbons and Chemistry,
University M'Hamed Bougara Boumerdes,
Street of Independence,
Boumerdes 35000, Algeria
e-mail: slim50dz@yahoo.fr

Rabah Kadi
Nuclear Research Center of Birine CRNB,
P.O. Box 180,
Aïn-Oussera 17200,
Algeria
e-mail: khaled2003@hotmail.com

The gas turbines are generally used for large scale power generation. The basic gas turbine cycle has low thermal efficiency, which decreases in the hard climatic conditions of operation, so the cycles with thermodynamic improvement is found to be necessary. Among several methods shown their success in increasing the performances, the steam injected gas turbine cycle (STIG) consists of introducing a high amount of steam at various points in the cycle. The main purpose of the present work is to improve the principal characteristics of gas turbine used under hard condition of temperature in Algerian Sahara by injecting steam in the combustion chamber. The suggested method has been studied and compared to a simple cycle. Efficiency, however, is held constant when the ambient temperature increases from ISO conditions to 50°C. Computer program has been developed for various gas turbine processes including the effects of ambient temperature, pressure ratio, injection parameters, standard temperature, and combustion chamber temperature with and without steam injection. Data from the performance testing of an industrial gas turbine, computer model, and theoretical study are used to check the validity of the proposed model. The comparison of the predicted results to the test data is in good agreement. Starting from the advantages, we recommend the use of this method in the industry of hydrocarbons. This study can be contributed for experimental tests. [DOI: 10.1115/1.2898834]

Keywords: gas turbine, simple cycles, steam injection, thermal balance, specific power, thermal efficiency

1 Introduction

In the past three decades, industrial gas turbines have gained more importance on the power generation systems, such as nuclear power plant (NPP) and the petroleum power plant. The basic gas turbine cycle has low thermal efficiency which decreases in the hard climatic conditions of operation, so cycle thermodynamic improvements are found to be necessary. Improvements in gas turbines have shown their success in increasing the electrical power output [1–3]. The gas turbine characteristics are highly sensitive to the ambient temperature, which varies considerably between the day and the night, the summer and the winter. The power that it yields, in particular, decreases considerably as the ambient temperature increases. Various additional cycle configurations such as reheating, regeneration, intercooling, and steam injection have been proposed in the literature [4–9]. All of them allow improving the efficiency and specific power of simple cycle gas turbine. A steam injection gas turbine cycle (STIG) becomes an extremely attractive system [10–16]. The most common method to improve the efficiency of simple cycle gas turbine consists of using the heat of exhaust gases to produce steam in a heat recovery steam generator (HRSG).The increase in specific power is a consequence of supplementary mass flow through the combustion chamber. Steam injection has been used in gas turbines to reduce NO_x emissions [17–20]. The amount of steam generated in the HRSG depends on the pinch point of the boiler. Due to this latter and the turbine outlet temperature, the HRSG cannot utilize all the heat required to generate steam.

The present work seeks to yield the principal characteristics of gas turbine used under hard climatic conditions, insensitive with the variation of ambient temperature by injecting suitable quantities of steam in the upstream of combustion chamber. This is done by suggesting a calculation model for steam injected gas turbines. The calculation model has been adapted, validated, and compared to a simple cycle on different industrial machines, without steam injection. Efficiency, however, is held unchanged when the ambient temperature increases from ISO conditions (15°C, 60% relative humidity) to 50°C. Computer program has been developed for a range of pressure ratios and combustion temperature. This is achieved by studying the effect of steam injection on the principal characteristics of gas turbine.

2 Thermodynamic Analysis

2.1 General Description. The gas turbine layout considered in the present study is shown in Fig. 1. It is single-shaft industrial gas turbine. The T-s diagram for this cycle is shown schematically in Fig. 2 [21].

The nonideal cycle is represented on T-s diagram by 1-2-3-4 and it can be characterized by two significant parameters: the pressure ratio and the combustion temperature. Both the compression Process 1-2 and the expansion Process 3-4 show an increase in entropy as compared to the corresponding ideal Processes 1-2′ and 3-4′. Loss of pressure during heat addition (Process 2-3) and

Manuscript received September 12, 2006; final manuscript received January 7, 2008; published online April 23, 2008. Review conducted by Anestis I. Kalfas.

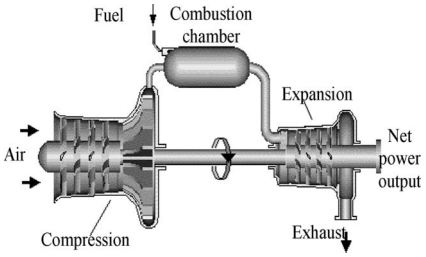

Fig. 1 Illustrative diagram

heat rejection (Process 4-1) are not neglected in this analysis. The compression and expansion processes with pressure loss can be assigned polytropic or isentropic efficiencies.

2.2 Proposed Cycle. The steam injected gas turbine cycle is represented in Fig. 3 by its major components: the gas turbine and the HRSG.

The HRSG contains one economizer, evaporator, and superheater to increase power. Air is driven back downstream from the compressor with a pressure p_2; combustion is carried out in the combustion chamber where fuel is injected in the presence of an additional quantity of the steam. The temperature of exhaust gas water and steam are used as input; the steam mass flow rate is determined. The pressure required to inject this steam into the

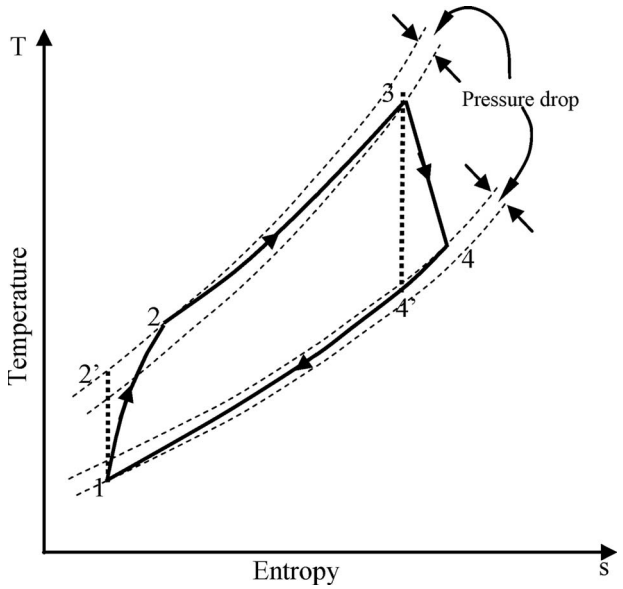

Fig. 2 Thermodynamic cycle T-s of a simple gas turbine

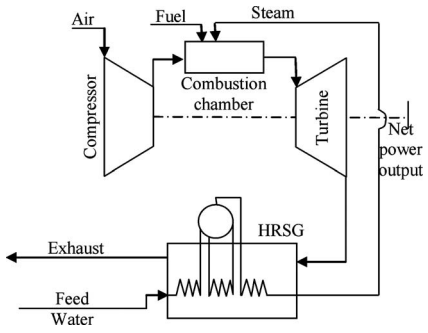

Fig. 3 Scheme of the steam injected plant proposed

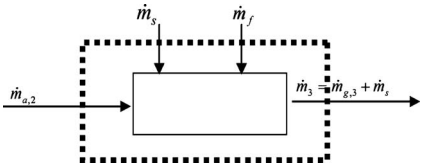

Fig. 4 Control volume of combustion chamber (application of the SFEE)

turbine is relatively low compared to that usually employed in steam turbines. So the HRSG can be a very simple design, which works with one pressure level to increase heat recovery [4].

2.3 Compression Analysis. The compressor is modeled by polytropic compression. The work required to compress the unit mass of air is then represented as

$$w_C = c_{pa,2}T_2 - c_{pa,1}T_1 \tag{1}$$

2.4 Combustion Chamber Analysis. Concerning the combustor, the computer code calculates the thermodynamics properties of the combustion product chemical and thermodynamic equilibrium. The hydrocarbon fuel chemical reaction is determined by the following expression [1]:

$$\mathrm{C}_n\mathrm{H}_m + \lambda\left(\frac{n+m}{4}\right)[\mathrm{O}_2 + 3.76\mathrm{N}_2] + (s)\mathrm{H}_2\mathrm{O} \rightarrow (n)\mathrm{CO}_2 + \left[(\lambda - 1) \times \left(n + \frac{m}{4}\right)\right]\mathrm{O}_2 + \left[3.76\lambda\left(\frac{n+m}{4}\right)\right]\mathrm{N}_2 + (m/2 + s)\mathrm{H}_2\mathrm{O} \tag{2}$$

2.5 Expansion Analysis. The work generated by the turbine per unit mass of air after receiving combustion gas of mass $(1+f)$ can be written as

$$w_T = c_{pg,3}T_3 - c_{pg,4}T_4 \tag{3}$$

3 Performance Analysis of Proposal STIG Type Plant

The analysis discussed in the previous paragraphs concerns simple gas turbine cycle, i.e., without steam injection. Furthermore, the purpose of the following approach is the evaluation of overall parameters of gas turbine changes by injecting the steam produced at the additional HRSG into the upstream of the combustor. The change in the parameters when the steam is injected can be evaluated by applying the steady flow energy equation to the combustion chamber for operation without and with injection [22,23]. A heat balance describing the combustion chamber is shown in Fig. 4.

The steady flow energy equation (SFEE) for the combustion chamber is

$$\dot{m}_a h_{2,a} + \dot{m}_f \mathrm{LCV} + \dot{m}_s h_{s,t_{inj}} = (\dot{m}_a + \dot{m}_f)h_{3,g} + \dot{m}_s h_{s,t_{\mathrm{CC}}} \tag{4}$$

Since the vapor is injected just at the upstream of the combustor, thus the calculating parameters in the part of compression are unchanged.

The flow of the fuel, in the case without injection, is given by

$$\dot{m}_f = \frac{P_{\mathrm{manf}}}{\mathrm{LCV}^* \eta_{\mathrm{manf}}} \tag{5}$$

with

$$f = \frac{\dot{m}_f}{\dot{m}_a}, \quad s = \frac{\dot{m}_s}{\dot{m}_a} \tag{6}$$

However, to maintain the manufactory combustor at constant temperature, with the presence of steam (which the parameters of injection are T_{inj} and p_{inj}), the fuel must be added even more. This new quantity of the fuel is given by

Table 1 Characteristics of the GE MS5002 gas turbine

P_{manf}	18,000 kW	t_{amb}	0/50°C
$\eta_{Th-manf}$	23%	η_{CC}	95%
t_{CC}	900°C	η_G	96%
LCV (GN)	45,119 kJ/kg	η_T	88%
C_f	1.02	η_{mec}	95%
η_C	90%	Δp_G	1.25%
p_{atm}	1.0132 bars	Δp_{CC}	4%
ε	7.38	Δp_{adm}	1%

$$f' = \frac{(h_{3,g} - h_{2,a}) + s(h_{3,s} - h_{2,s})}{\eta^*_{CC}\text{LCV} - h_{3,g}} \tag{7}$$

Thus,

$$s = \frac{(A_1 - C_1)\alpha + (B_1 - C_1)\gamma}{\gamma D_1 - (A_1 - C_1)\beta} \tag{8}$$

with

$$\begin{cases} \alpha = h_{3,g} - h_{2,a} \\ \beta = h_{3,s} - h_{2,s} \\ \gamma = \eta^*_{CC}\text{LCV} - h_{3,g} \end{cases} \quad \text{and} \quad \begin{cases} A_1 = (\eta^*_{th}\text{LCV})/\eta_{mec} \\ B_1 = w_C/\eta_{mec} \\ C_1 = h_{3,g} - h_{4,g} \\ D_1 = h_{3,s} - h_{4,s} \end{cases}$$

As the vapor rate is very small compared to the rate of air, pressure increase in the combustion chamber has been neglected while the steam is injected. The compressor of the engine determines the pressure in the combustion chamber.

The deviation of power output is summarized here for completeness. Power output is expressed as the difference between the energy produced by the turbine and the power absorbed by the compressor. The basic simplified form can be written as

$$P_{Ut} = (\dot{m}_a + \dot{m}_f)(h_{3,g} - h_{4,g}) + \dot{m}_s(h_{s,t_{cc}} - h_{s,t_4}) - \dot{m}_a(h_{a,t_2} - h_{a,t_1}) \tag{9}$$

The overall efficiency can be evaluated as follows:

$$\eta_{th} = \frac{P_{Ut}}{\dot{m}'_f\text{LCV}} \tag{10}$$

The proposal analysis outlined above has been numerically studied using the simulation computer program developed by the authors. The computer program is based on fundamental thermodynamic relations including real gas behavior, thermodynamic properties of steam, and the pressure losses [24–27].

4 Test Data

The validity of the relations presented above and their applicability to estimate the effects of steam injection will be assessed by application of test data from an operating industrial gas turbine. The tests are performed on a single-shaft gas turbine (GE MS5002) [28]. Table 1 shows the characteristic values used in the computation of the cycles. The whole set of data are given at ISO conditions.

5 Results and Interpretations

Calculations of the characteristic parameters of gas turbine components, such as the compressor, combustor, and the turbine, are carried out with the aid of developed computer program. In this section, we will discuss the effect of the major parameters (i.e., ambient temperature, pressure ratio, thermal efficiency, etc.). The values of these parameters can be estimated using basic cycle equations given above and assuming variable values for thermodynamic properties. All the required data were taken from GE MS5002 gas turbine.

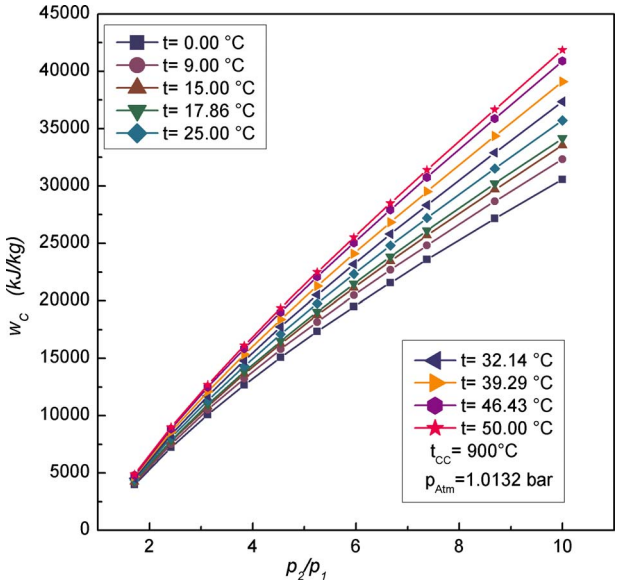

Fig. 5 Specific work of the compressor

In the first case, the STIG cycle performance calculated over wide temperature ranges (0–50°C) and pressure ratio: (1–10) is analyzed at standard ambient conditions. On the other hand, these optimal parameters are stabilized by injecting suitable amount of steam in the upstream of combustion chamber when the ambient temperature becomes higher ISO conditions.

5.1 Simple Gas Turbine Characteristics Analysis Without Steam Injection. For wide values of ambient temperature, the specific work of the compressor and thermal efficiencies can be plotted against pressure ratio. At fixed combustion temperature and ambient pressure, the variations of these parameters are shown, respectively, in Figs. 5 and 6.

It can be derived from Fig. 5 that the specific work increases as the pressure ratio increases for a given ambient temperature. As

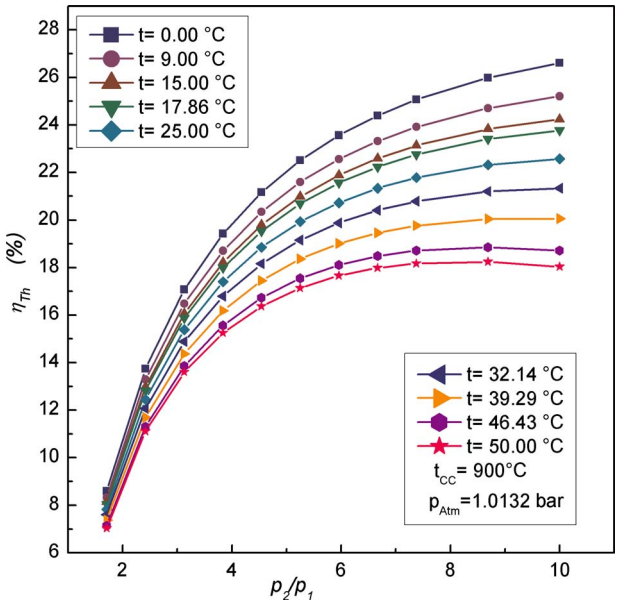

Fig. 6 Thermal efficiency versus pressure ratio at different ambient temperatures

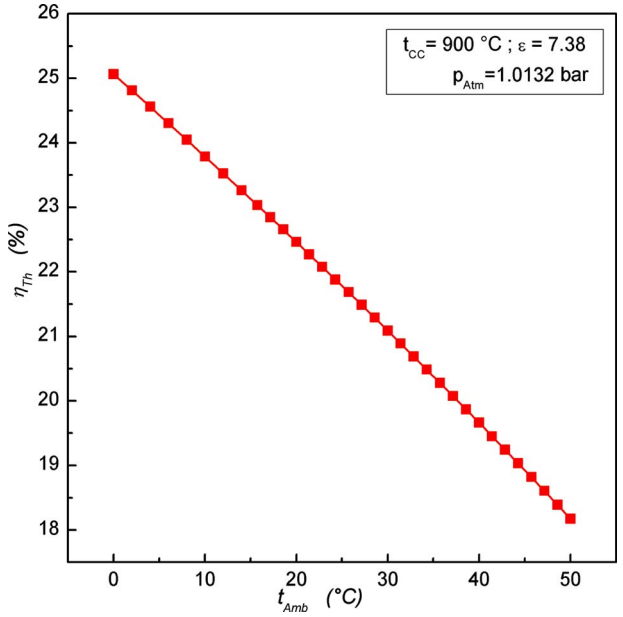

Fig. 7 Thermal efficiency versus ambient temperature at fixed pressure ratio

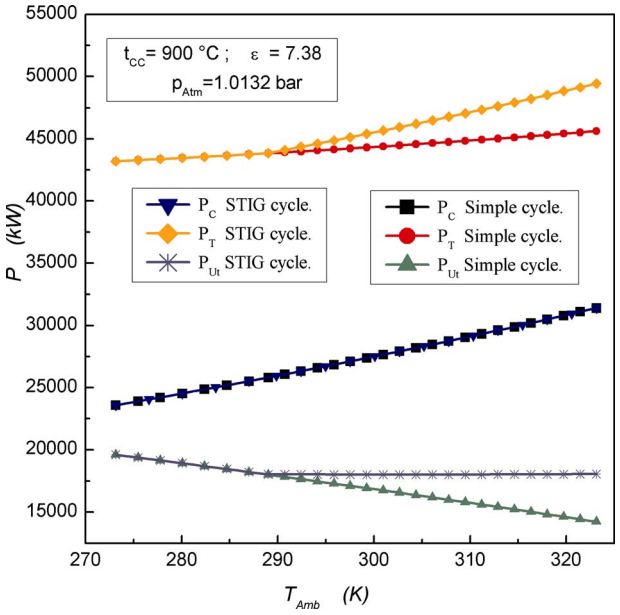

Fig. 8 Powers without and with steam injection

for the effect of ambient temperature, the same variation is obtained. This is the reason of compressing the air at a higher temperature; the compressor needs a more significant work.

In Fig. 6, the efficiency is observed to decrease as the ambient temperature increases at wide range of pressure ratio. Moreover, the pressure ratio corresponding to the maximum efficiency increased with the diminution of the ambient temperature. Due to the metallurgical characteristics of the material, the value of $\varepsilon \approx 7.38$ has been fixed.

Figure 7 illustrates the decrease of efficiency as function of ambient temperature, at fixed combustion temperature, the pressure ratio, and the ambient pressure. It can be seen that, with the increase of the ambient temperature, the compressor work is increased and the net power output is decreased, which affect in decreasing the thermal efficiency.

5.2 Gas Turbine Characteristic Analyses With Steam Injection. Figures 8 and 9 show the comparison between simple cycle gas turbine characteristics and STIG cycle characteristics, at fixed combustion temperature, the pressure ratio, and the ambient pressure.

From Fig. 8, it can be noted that injecting steam increases the turbine power, when the ambient temperature exceeds the ISO conditions.

In contrast, it should be observed that the power absorbed by the compressor has been unchanged with and without steam injection independent of the variation of ambient temperature. With steam injection method, the net power output has been kept stabilized when the ambient temperature reaches T_{ISO}. Same remarks have been observed for the thermal efficiency deviation (Figs. 9 and 10). This is due to the additional vapor mass injected, which thus stabilizes the net power output and so the thermal efficiency.

Figure 11 shows the evolution of thermal efficiency and the steam to air ratio versus ambient temperature, at fixed combustion temperature, value of the pressure ratio, and the ambient pressure. The variation of steam to air ratio is significant as the ambient temperature becomes higher than the ISO temperature (Fig. 12).

Typically, the maximum reduction of efficiency is shown nearly 15 °C. However, steam must be injected with suitable amounts for characteristic improvement purposes. Furthermore, the gas turbine will be insensitive to the variation of ambient temperature.

The comparison of results was established in both cases: for a simple cycle and for STIG cycle during long operating period of the engine. The mass rate of the fluid constituted by combustion gases and the additional steam quantity crossing in the interblading channels of turbine rotor led to increase progressively the power output.

5.3 Influence of the Injection Parameters on the Injected Steam Quantity. The injection pressure and the temperature parameters have been taken in order to analyze their effects on steam quantity injected and on the gas turbine characteristics.

Figures 13–16 show, respectively, the turbine power, the net power output, the steam quantity injected, and efficiencies versus

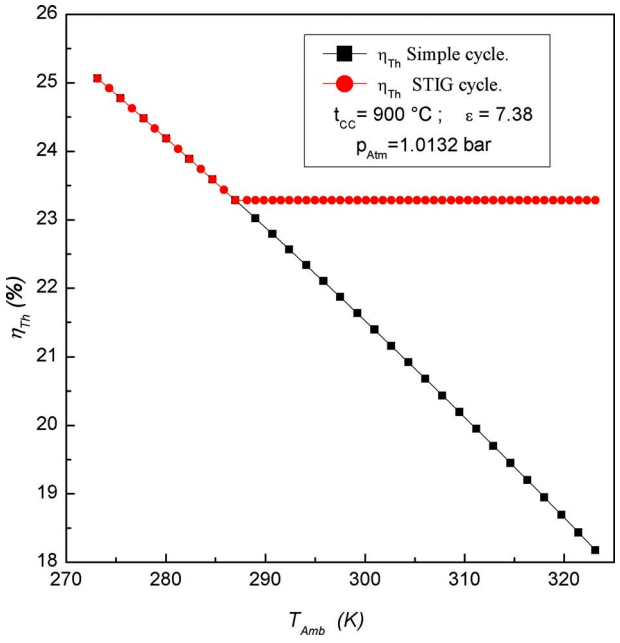

Fig. 9 Efficiency without and with steam injection

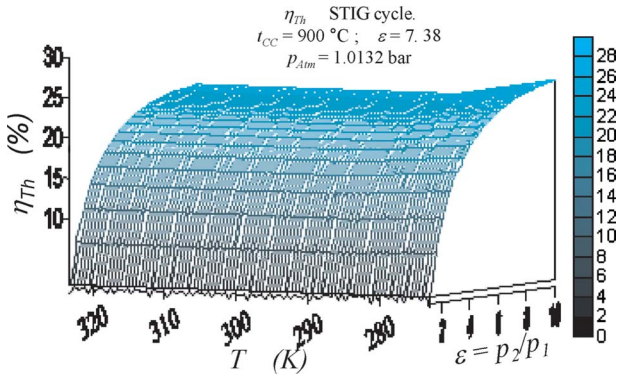

Fig. 10 Total thermal efficiency

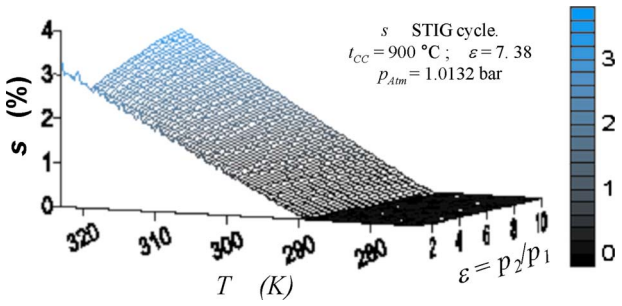

Fig. 12 Steam to air ratio injected

ambient temperature at different values of injection conditions. These evolutions are represented at fixed combustion temperature, value of the pressure ratio, and the ambient pressure.

Figures 13 and 14 show that all curves of characteristics (turbine power and net power) start to change from T_{ISO}. This is the beginning situation of gas turbine performance improvement. The evolution profile represented in these figures are identical to the case of without injection, i.e., $T_{amb} < 288.15$ K.

At the start of steam injection, the amount of steam injection is decreased when the parameter conditions of injection increased (Fig. 15).

Due to the effect of injection parameters on steam injected, it becomes important to hold constant the calorific value of steam in the blade of the turbine. This idea provides a constant efficiency at the output, so our assumption is verified.

In Fig. 16, we note that the variations of thermal efficiencies are independent of the parameters of the injection (efficiencies are identical), because the variation of these parameters influences on the quantity of the fuel to be injected.

The analysis of these figures shows that when we increase the injection steam parameters values we obtained a reduction in the quantity injected of steam.

5.4 Influence of Operating Ambient Temperature (T_{ISO}). It is interesting to visualize the displacement of the point where the injection of the steam water starts, by varying the standard operating temperature (T_{ISO}) of a given step.

The profiles of turbine power, the available steam quantity injected, total thermal efficiencies, and net power output are presented, respectively, in Figs. 17–20.

Starting from T_{ISO} temperature, the power of turbine and steam injected quantity profiles change their course evolution upward when the steam injection starts. These characteristics are analyzed at fixed combustion temperature, values of the injection parameters, and the ambient pressure for different values of standard temperature. The evolution profiles of turbine power, the available steam quantity injected, and total thermal efficiencies have been changed at T_{ISO}, when the steam injected starts.

We note on Fig. 19, when the ambient temperature is inferior to the standard temperature ($T_{amb} < T_{ISO}$), that the gas turbine characteristics decrease by increasing the ambient temperature. This is

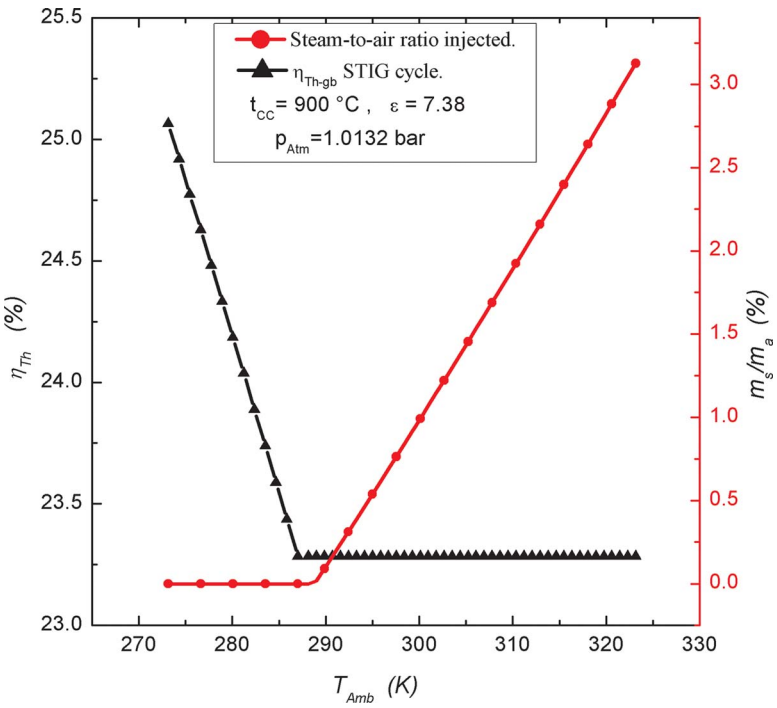

Fig. 11 Efficiency and steam to air ratio injected

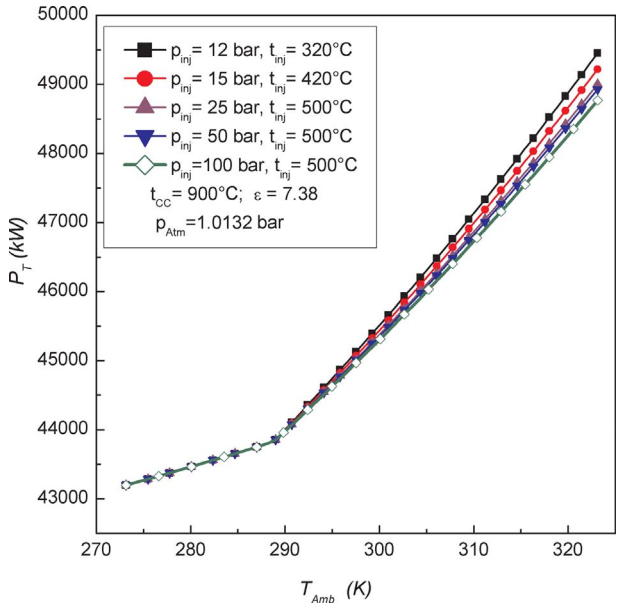

Fig. 13 Turbine power

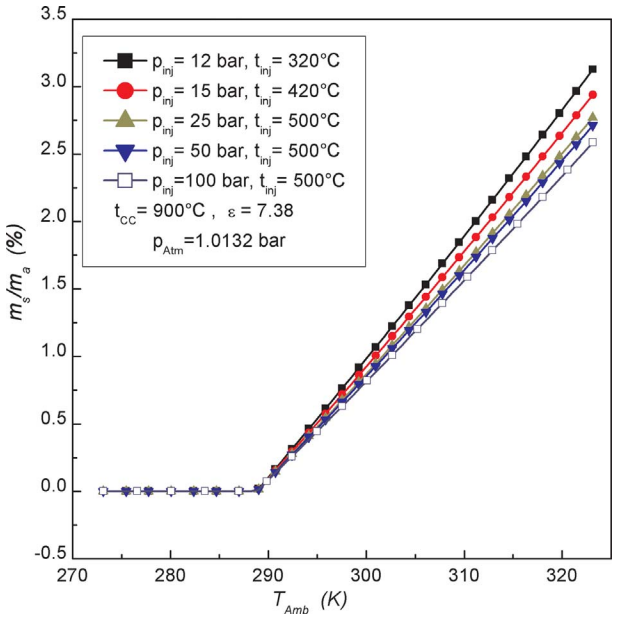

Fig. 15 Steam quantity injected

due to the increasing compressor specific work. When the ambient temperature is higher than the standard temperature ($T_{amb} > T_{ISO}$), the gas turbine efficiencies remain constant with the value, which corresponds to T_{ISO} by the suitable quantity of steam injection in the combustor. We observe the displacement of the beginning point of an injected steam, which corresponds to T_{ISO}.

Figure 20 illustrates the net power output profiles as function of pressure ratio. It is observed that net power output decrease with increasing standard conditions.

5.5 Influence of the Combustion Chamber Temperature. In order to represent the influence of the combustion temperature on the quantity of the steam injected, several values of this applied temperature led to the results of the quantity of steam water and output presented, respectively, on Figs. 21 and 22. It is noted that the injection of the steam water starts from the temperature T_{ISO}, and the injected quantity is inversely proportional to the temperature of combustion; this factor is one of the gas turbine characteristic improvement methods. In this case, there is a combination of two methods; steam injection and the combustion temperature rises. It is also noticed that the output increases when the temperature of combustion increases.

6 Result Validation

The results obtained by the computer model have been verified using data from the performance testing of an industrial gas turbine, which the characteristics are known. Our computer program treats steam injection effects on gas turbine performances that has been adapted. Previous literature studies, modeling the thermodynamic cycles, reveal that best performance is obtained for decreasing NO_x emission, and, therefore, net power output by injecting

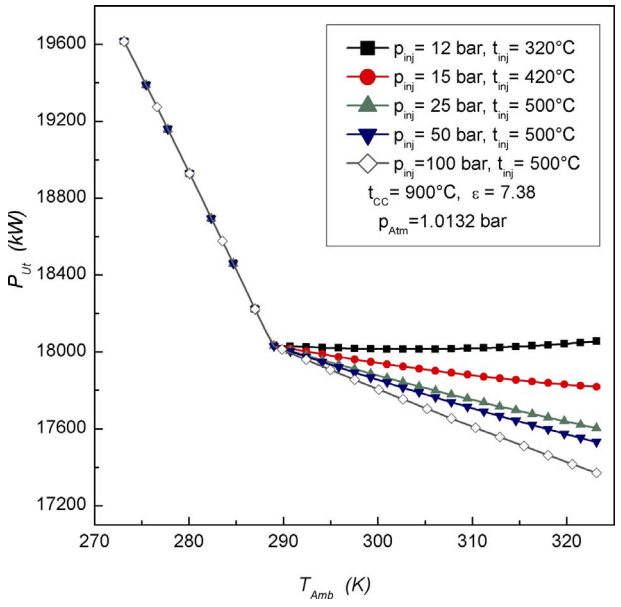

Fig. 14 Net power output

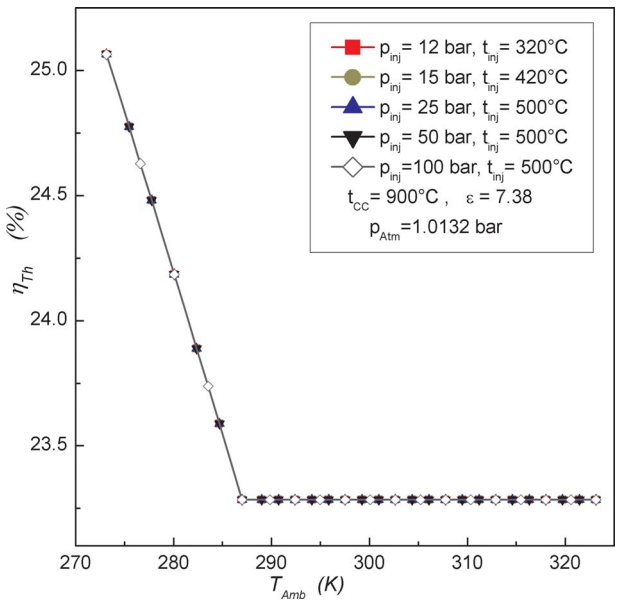

Fig. 16 Efficiencies

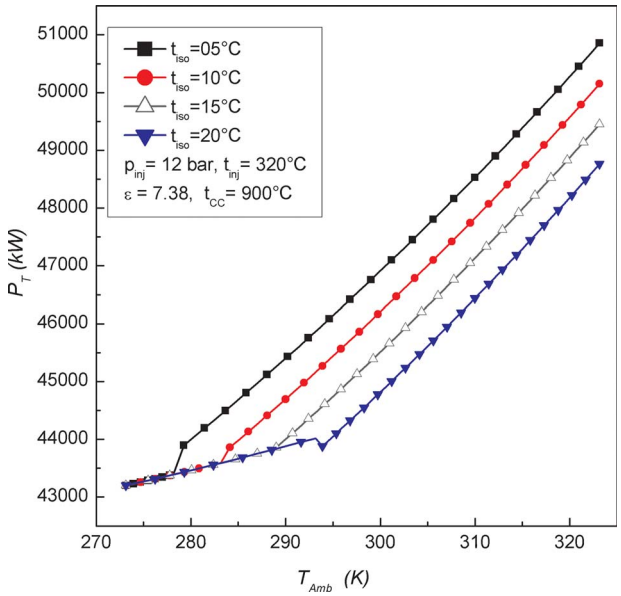

Fig. 17 Power of turbine

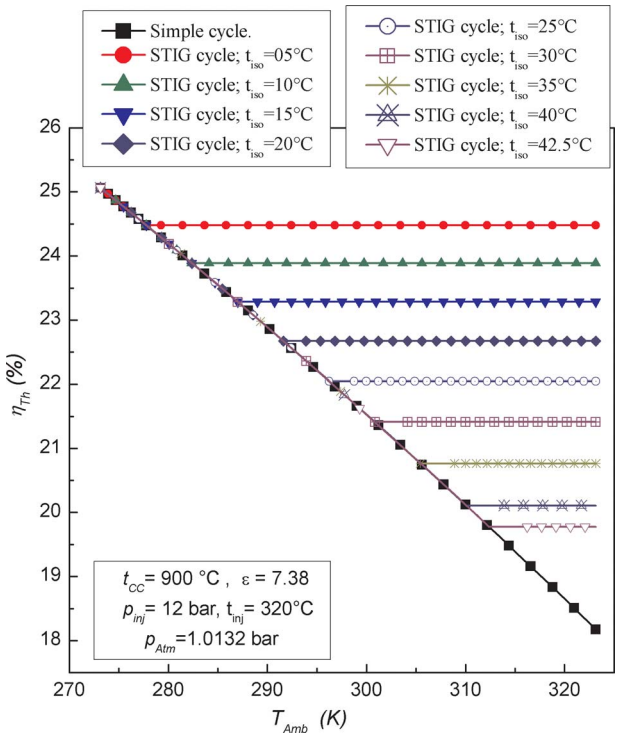

Fig. 19 Efficiencies

steam into combustion chamber [9]. The study presented in this section provides that inlet conditions of compressor are fixed at standard conditions. For a wide range of steam injected quantities, the values obtained were compared to those of the literature [29–31].

6.1 Effects of Steam Injection on the Net Power Output. Figure 23 shows the evolution of the net power output variation as a function of steam to air ratio. Results for operation with injection of steam are shown. The lines represent the prediction using our modified computer code and points prediction of the same conditions.

It is shown that predictions with the proposed model are in very close agreement with data published in the literature. It is interesting to note that for higher steam to air ratio (s), the prediction of the present method is very close to the upper limit (of a range carried out for several gas turbines).

6.2 Effects of Steam Injection on the Efficiency. The effect of steam injection on the gas turbine efficiency is shown in Fig. 24. Typically, the same evolutions are observed as the above figure. We note that our prediction results are in good agreement with those of the literature.

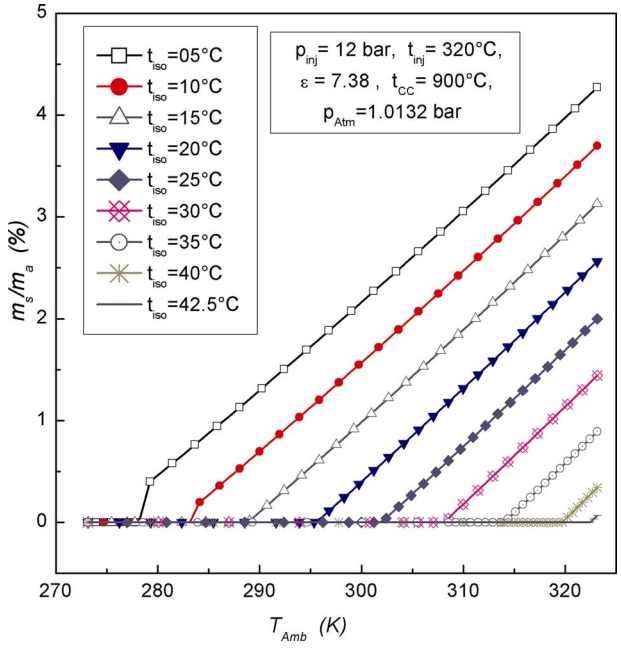

Fig. 18 Steam quantity injected

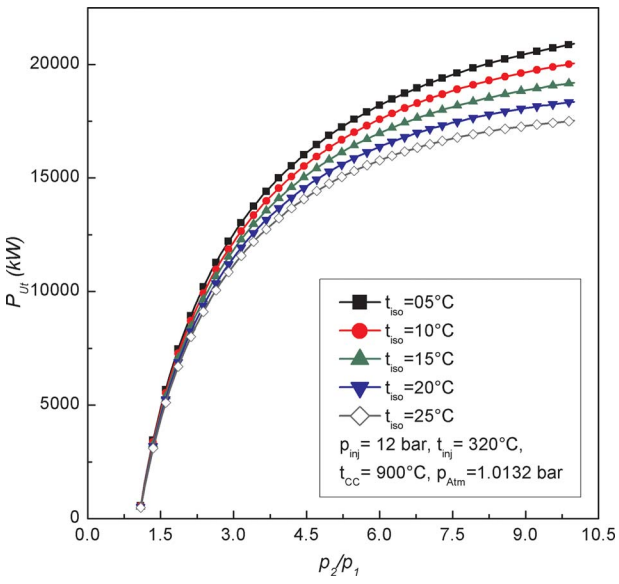

Fig. 20 Net power output

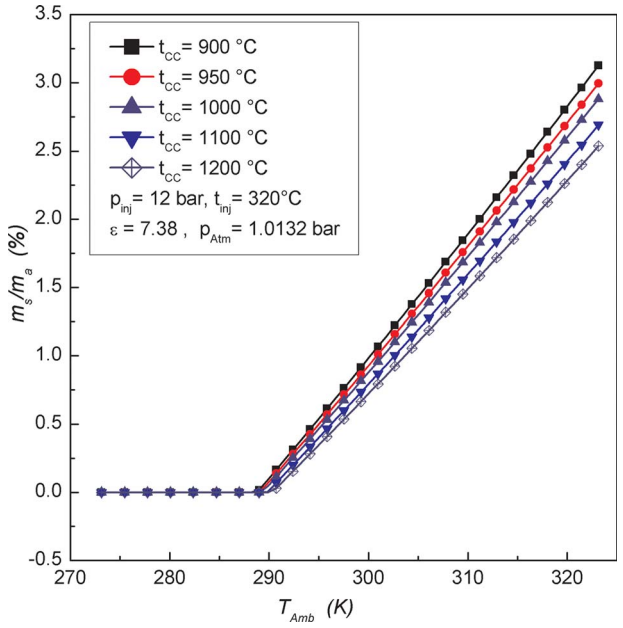

Fig. 21 Steam injected quantity

7 Conclusion and Perspective

The STIG cycle plant plays an important role to improve the gas turbine characteristics. For this purpose, detailed researches were made to study the improvement of real cycle gas turbine with and without steam injection.

Under hard climatic conditions of temperature, the gas turbines of Algerian petroleum plant were used. The ambient temperature that varies considerably during the year can often reach 50°C in summer, reducing 28% of net power output gas turbine.

The objective of the present study is to yield the principal characteristics of gas turbine, used under hard conditions, insensitive to the variation of the ambient temperature by injecting suitable quantities of steam in the upstream of combustion chamber. The suggested method has been studied and compared to a simple cycle. Efficiency, however, is held constant when the ambient temperature increases from ISO conditions to 50°C. Computer program has been developed for various gas turbine processes including the effects of ambient temperature, the pressure ratio, injection parameters of steam, standard temperature, and combustion chamber temperature with and without steam injection. This is achieved by studying the effect of steam injection on the gas turbine characteristics.

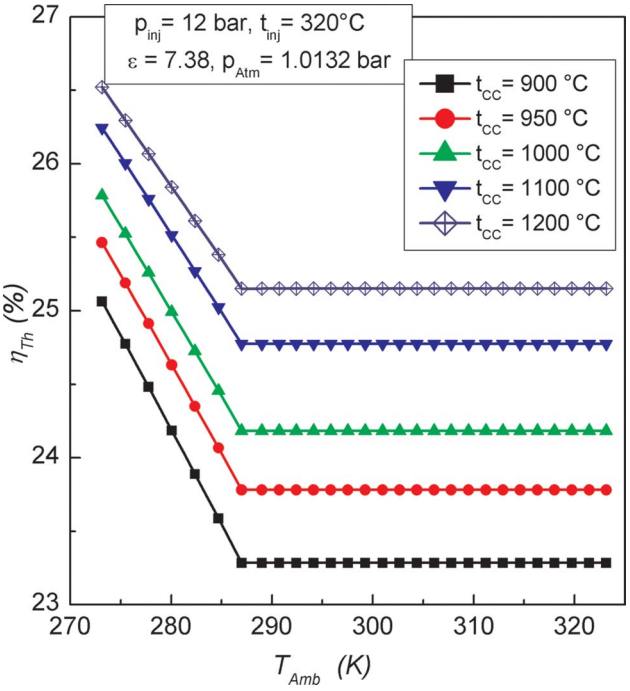

Fig. 22 Efficiencies

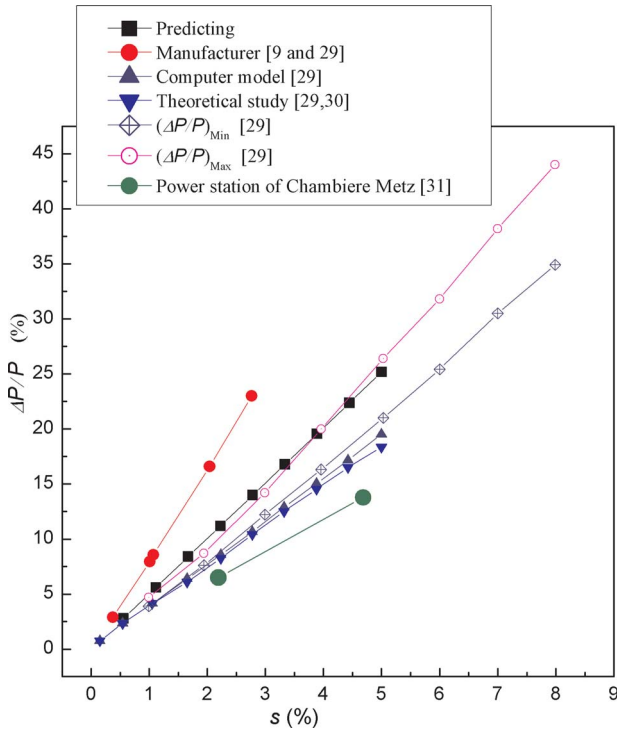

Fig. 23 Net power output deviation

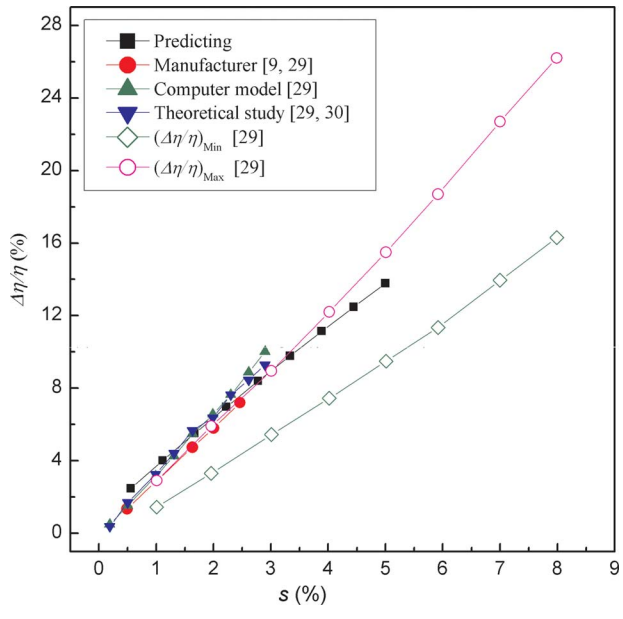

Fig. 24 Thermal efficiency deviation

Data published in the literature from the performance testing are used to verify the validity of the proposed model. Our computer program that treats steam injection effects on gas turbine characteristics has been adapted. It was shown that general trends exist for the current prediction by using published data.

The device installation with a feed water circuit, economizer, and evaporator is proposed. The exhaust is used as an energy source in a HRSG where energy is transferred from the exhaust gases to boiler feed water.

Starting from the advantages, we recommend the use of this method in the industry of hydrocarbons. This study can be contributed for experimental tests.

In perspective, we focused to extend our approach to predict NO_x emissions.

Acknowledgment

We would like to acknowledge Mr. Anis Bousbia Salah (Fabio Moretti, Francesco D'Auria Università di Pisa) for his expertise and generous help in generating this work.

Nomenclature

- C_f = flow coefficient
- c_p, c_v = specific heats at constant pressure and constant volume (J/(kg K))
- $\bar{C}_p$ = average specific heat at constant pressure (J/(kg K))
- f = fuel to air ratio (without steam injection) $f = \dot{m}_f/\dot{m}_a$ (%)
- f' = fuel to air ratio (with steam injection) $f' = \dot{m}_f/\dot{m}_a$ (%)
- GN = natural gas
- h = specific enthalpy (J/kg)
- h_f^o = standard specific enthalpy (J/kg)
- k = polytropic coefficient of the fluid
- LCV = lower calorific value of the fuel (kJ/kg)
- $\dot{m}$ = mass rate of flow (kg/s)
- n_i = fraction of an element in a gas mixture
- p = pressure (total) (bar)
- P = power (W)
- P_C = absorbed power by the compressor (W)
- P_T = power produced by the turbine (W)
- R = specific constant of gas (J/(kg K))
- SFEE = steady flow energy equation
- t = temperature (total) (°C)
- T = temperature (total) (K)
- T_2' = isentropic temperature in the outlet side of the compressor (K)
- T_4' = isentropic temperature on the outlet side of the turbine (K)
- s = steam to air ratio, $s = \dot{m}_s/\dot{m}_a$ (%)
- w = specific work (J/kg)
- γ = isentropic coefficient, $\gamma = c_p/c_v$

Greek

- λ = excess coefficient of air
- Δp = loss of pressure (bar)
- η_C = isentropic efficiency of the compressor (%)
- η_{CC} = combustion efficiency (%)
- η_G = electric generator efficiency (%)
- η_{mec} = mechanical efficiency (%)
- η_T = isentropic output of turbine (%)
- η_{th} = thermal efficiency of the cycle (%)
- ε = pressure ratio, $\varepsilon = p_2/p_1$

Subscripts and Superscripts

- 1, 2, 3, 4 = various points in the thermodynamic cycle of the gas turbine
- a = air
- adm = admission
- amb = ambient
- C = compressor
- CC = combustion chamber
- manf = manufacturer
- f = fuel
- G = electric generator
- g = combustion gases
- inj = parameters of injection
- ISO = standard conditions
- s = steam water
- T = turbine
- th = thermal
- Ut = net power output

References

[1] Horlock, J. H., 2003, *Advanced Gas Turbine Cycles*, Pergamon, Oxford.
[2] Potter, P. J., 1976, *Power Plant Theory and Design*, 2nd ed., Wiley, New York.
[3] El-Wakil, M. M., 1985, *Power Plant Technology*, International Student ed., 1st print, McGraw-Hill Education, Singapore.
[4] Paepe, M. D., and Dick, E., 2000, "Cycle Improvements to Steam Gas Turbines," Int. J. Energy Res., **24**, pp. 1081–1107.
[5] Haselbacher, H., 2005, "Performance of Water/Steam Injected Gas Turbine Power Plants Consisting of Standard Gas Turbines and Turbo Expanders," Int. J. Energy Technology and Policy, **3**(1/2), pp. 12–23.
[6] Traverso, A., and Massardo, A. F., 2002, "Thermo-Economic Analysis of Mixed Gas-Steam Cycles," Appl. Therm. Eng., **22**, pp. 1–21.
[7] Heppenstall, T., 1998, "Advanced Gas Turbine Cycles for Power Generation: A Critical Review," Appl. Therm. Eng., **18**, pp. 837–846.
[8] Milancej, M., 2005, "Advanced Gas Turbine Cycles: Thermodynamic Study on the Concept of Intercooled Compression Process," Diploma thesis, Institut für Thermodynamik und Energie wandlung Technische Universität Wien Vienna.
[9] Cloyd, S. T., and Harris, A. J., 1995, "Gas Turbine Performance—New Application and Test Correction Curves," ASME Paper No. 95-GT-167.
[10] Cheng, D. Y., and Nelson, A. L. C., 2002, "The Chronological Development of the Change Cycle Steam Injected Gas Turbine During the Past 25 years," *Proceedings of ASME Turbo Expo*.
[11] Fraize, W. E., and Kinney, C., 1979, "Effects of Steam Injection on the Performance of Gas-Turbine Power Cycles," ASME J. Eng. Power, **101**, pp. 217–227.
[12] Brown, D. H., and Cohn, A., 1981, "An Evaluation of Steam-Injected Combustion Turbine Systems," ASME J. Eng. Power, **103**, pp. 13–19.
[13] Larson, E. D., and Williams, R. H., 1987, "Steam-Injected Gas-Turbines," ASME J. Eng. Gas Turbines Power, **109**, pp. 55–63.
[14] Macchi, E., Consonni, S., Lozza, G., and Chiesa, P., 1995, "An Assessment of the Thermodynamic Performance of Mixed Gas-Steam Cycles: Part A—Intercooled and Steam-Injected Cycles," ASME J. Eng. Gas Turbines Power, **117**, pp. 489–498.
[15] Rice, I. G., 1995, "Steam-Injected Gas-Turbine Analysis: Steam Rates," ASME J. Eng. Gas Turbines Power, **117**, pp. 347–353.
[16] Nishida, K., Takagi, T., and Kinoshita, S., 2005, "Regenerative Steam-Injection Gas-Turbine Systems," Appl. Energy, **81**, pp. 231–246.
[17] Ohno, Y., Zhao, D., Furuhata, T., Yamashita, H., Arai, N., and Hisazumi, Y., 2000, "Combustion Characteristics and NO_x Formation of a Gas Turbine System With Steam Injection and Two-Stage Combustion," ASME Paper No. IJPGC2000–15046.
[18] Moore, M. J., 1997, "NO_x Emission Control in Gas Turbines for Combined Cycle Gas Turbine Plant," Proc. Inst. Mech. Eng., Part A, **211**, pp. 43–52.
[19] Zhao, D., Ohno, Y., Furuhata, T., Yamashita, H., Arai, N., and Hisazumi, Y., 2001, "Combustion Technology in a Novel Gas Turbine System With Steam Injection and Two-Stage Combustion," J. Chem. Eng. Jpn., **34**(9), pp. 1159–1164.
[20] Daggett, D. L., 2004, "Water Misting and Injection of Commercial Aircraft Engines to Reduce Airport NO_x," National Aeronautics and Space Administration Glenn Research Center NASA.
[21] Cohen, H., Rogers, G. F. C., and Saravanamuttoo, H. L. N., 1996, *Gas Turbine Theory*, 4th ed., Longman, London.
[22] Kling, R., 1980, "Thermodynamique Générale et Applications," Editions Technip Paris.
[23] Sonntag, R. E., Borgnakke, C., and VanWylen, G. J., 1998, *Fundamentals of Thermodynamics*, 5th ed., Wiley, New York.
[24] Keenan, J. H., Chao, J., and Kaye, J., 1980, "Gas Tables Thermodynamic Properties of Air Products of Combustion and Component Gases Compressible Flow Functions," 2nd ed., Wiley, New York.
[25] Goldammer, H. D., 1984, "Computes Thermophysical Properties of Water/Steam," based on rational formulation for the free energy F=U-T*S (Helmholtz-Function) program written and developed by Horet D. Goldammer, B. T. W. B. last Update 30. 04. 1984; Schwaebisch Gmuend, Germany.
[26] International Association for the Properties of Water and Steam, 1997, "Re-

lease on the IAPWS Industrial Formulation 1997 for the Thermodynamic Properties of Water and Steam," Erlangen, Germany.
[27] Jebaraj, S., and Iniyan, S., 2004, "A Review of Energy Models," Renewable Sustainable Energy Rev., **10**, pp. 281–311.
[28] Porchakov, B. P., Aïssani, S., and Mikaelian, E., 1981, "Essais d'une Turbine à Gaz avec Variations de Pertes de Charge Locales à la Sortie," Revue générale de thermique, France No. 231.
[29] Mathioudakis, K., 2002, "Evaluation of Steam and Water Injection Effects on Gas Turbine Operation Using Explicit Analytical Relations," Proc. Inst. Mech. Eng., Part A, **216**, pp. 419–431.
[30] Poullikkas, A., 2005, "An Overview of Current and Future Sustainable Gas Turbine Technologies," Renewable Sustainable Energy Rev., **9**, pp. 409–443.
[31] Boissenin, Y., Moliere, M., and Remy, P., 1994, "Les Atouts de la Turbine à Gaz MS6001 B en Cogénération—Exemple de l'usine d'électricité de Metz," Revue technique Gec Alsthom No. 15.

Performance of a Novel Combined Cooling and Power Gas Turbine With Water Harvesting

J. R. Khan
e-mail: jameel.khan@yahoo.com

W. E. Lear
e-mail: lear@ufl.edu

S. A. Sherif[1]
Fellow ASME
e-mail: sasherif@ufl.edu

Department of Mechanical and Aerospace Engineering,
University of Florida,
232 MAE Building B,
P.O. Box 116300,
Gainesville, FL 32611-6300

John F. Crittenden
Triad Research Corporation,
2825 NW 23rd Drive,
Gainesville, FL 32605
e-mail: jcrittenden@gmail.com

A thermodynamic design-point performance analysis is performed on a novel cooling and power cycle that combines a semiclosed cycle gas turbine called the high-pressure regenerative turbine engine (HPRTE) with a vapor absorption refrigeration system (VARS). Waste heat from the recirculated combustion gas of the HPRTE is used to power the VARS. Water produced as a product of combustion is intentionally condensed and harvested. A part of the VARS cooling is used to chill the gas entering the high-pressure compressor, allowing water condensation and extraction as well as large efficiency gains. The remaining cooling capacity is provided to an external refrigeration load. The cycle is modeled using zero-dimensional steady-state thermodynamics, considering conservative values of polytropic efficiencies, a conservative model for turbine blade cooling, conservative values of pressure drops for the turbomachinery, including heat exchangers, and accurate correlations for the properties of the $LiBr-H_2O$ mixture and the combustion products. The cycle is shown to operate with a thermal efficiency greater than 40% for parameters appropriate to medium sized engines, while producing about 1.5 kg of water per kilogram of fuel (propane) consumed. This thermal efficiency is in addition to the large cooling effect generated in the evaporator of VARS, equivalent to 3–4% increased efficiency. The efficiency would be greater than 51% without turbine cooling bleed. The refrigeration ratio, defined as the ratio of external refrigeration load to the net work output, is found to be 0.38 for the base case. The water extracted is found to be a strong function of the recirculation ratio and low pressure compressor ratio PR_{c1}. Based on these and prior results, which showed that the HPRTE is very compact and has inherently low emissions, it appears that this cycle would be well suited for distributed power and some vehicle applications, especially ones with associated air conditioning loads.
[DOI: 10.1115/1.2830854]

Keywords: high pressure regenerative turbine engine, vapor absorption refrigeration system, water extraction

Introduction

Gas turbines in simple-cycle mode have long been used by utilities for power and heat generation. Industrial facilities use gas turbine units for on-site power generation, usually in combination with process heat production, such as hot water and process steam. In recent years, the performance of industrial gas turbines has been improved due to considerable investment in research and development, in terms of fuel-to-electricity conversion efficiency, plant capacity, availability, and reliability. Also, there has been an increased deployment of gas turbines for power generation to meet the growing demand of power throughout the world. The discovery of additional fuel resources, such as natural gas in various parts of the world, has helped in sustaining this increased deployment of gas turbines. In addition, the significant reduction in capital costs and the introduction of advanced cycles have also been a success factor for the increased deployment of the gas turbines for power generation.

With regard to simple-cycle gas turbine technology, the major driver to enhance the engine performance has been the increase in operational values of temperature and pressure through advancements in materials and cooling methods. The introduction of advanced gas turbines improved the efficiency of the simple-cycle to more than 40%. The combination of the gas turbine cycle (Brayton cycle) with a medium or low temperature bottoming cycle (such as the Rankine cycle), known as the conventional combined cycle, is an effective way to increase the thermal efficiency of the gas turbine cycle. Heavy-duty natural gas-fired gas turbines in combination with heat recovery steam generators and steam turbines represent the state of the art of this approach. Combined cycle plants are already achieving efficiencies well over 58%, with plant capacities in the range between 350 MW and 500 MW.

However, the development pace has decelerated as the most readily available technical advances have been exploited. Thermodynamic cycle developments, such as recuperation, recirculation, intercooling or after cooling, and cycle integration, such as mixed air steam turbines, are among the possible ways to improve the performance of gas turbine-based power plants at reasonable costs. This paper explores the thermodynamic performance of an advanced intercooled/recuperated cycle in which the working fluid is in part composed of recirculated combustion gas, referred to as a semiclosed cycle.

The Sulzer Brothers, Westinghouse, and the US Navy first studied semiclosed gas turbine cycles in depth in the 1940s and 1950s [1]. However, due to operational requirements and program cancellations, those systems were not developed beyond the prototype stage. There is renewed interest in such gas turbine cycles because the improvements in technology and the availability of clean burning fuels may enable advances in efficiency and emission performance, plus some auxiliary system benefits. MacFarlane and Lear [2] reported that water could be extracted from the combustion products of the high-pressure regenerative turbine engine (HPRTE). This water can be used for several applications. They considered the effect of reinjection of water back into the

[1]Corresponding author.

Manuscript received June 25, 2004; final manuscript received October 5, 2007; published online April 28, 2008. Review conducted by Yiguang Li.

system on the efficiency and specific power. Nemec [3] showed that the HPRTE with a Rankine bottoming cycle for ground based power productions could achieve approximately 63% gross thermal efficiency in a moderately large plant utilizing 10% turbine cooling air. Danius [4] and Landon [5] investigated the HPRTE for helicopter and marine applications, respectively, concluding that an increase in range on the order of 20% is feasible. Muley [6] showed that there was a reduction in thermal NO_x of roughly five orders of magnitude in the HPRTE versus typical open-cycle engines due to the dilution of O_2 and the reduced flame temperatures. A study done at Universita degli Studi di Firenze by Facchini et al. [7] showed that a semiclosed cycle engine similar to the HPRTE possessed benefits in terms of exhaust gas treatment (CO_2 sequestration) and peak-load shaving. In a joint study between the University of Florida and Unistry Associates Inc., Lear and Crittenden [8] first showed experimentally the reductions in emissions that occur with the HPRTE. In another joint study between the University of Florida and NASA, Lear and Laganelli [9] demonstrated that the HPRTE produced a constant-efficiency curve at part power and reduced emissions.

Boza et al. [10] modeled the HPRTE cycle combined with a vapor absorption refrigeration system (VARS) using zero-dimensional steady-state thermodynamics. The cycle performance was then studied by producing parametric design curves that showed trends and gave an indication of potential optimized system performance. They considered two cases, a large engine with a nominal power output of 40 MW and a small engine with a nominal power output of 100 kW. Significant improvements were predicted relative to simple-cycle engines in efficiency and specific power. Mostafavi et al. [11] showed that there was enough waste heat available in the exhaust of a twin-spool open-cycle system to precool the inlet to 50°C. There is, however, a lack of literature that describes the performance of such a system. There are apparently no articles in the literature describing a semiclosed absorption refrigeration combined cycle.

For large engines, a percentage of the main air flow, after compression, is bled and used as a cooling flow for the turbine, enabling high turbine inlet temperature. Massardo et al. [12] have estimated this percentage using a blade cooling model for different values of the turbine inlet temperature. They reported that it varied from 8% to 14% as the turbine inlet temperature increased from 900°C to 1400°C. In the past few years, significant efforts have been made to obtain better combustion efficiency due to air preheating without the adverse effect of higher NO_x emissions caused by higher flame temperatures. It was found that strong exhaust gas recirculation combined with air preheating generates relatively low flame temperatures in the combustor. The combustion air is diluted with large amount of recirculated gases, and so the mass fraction of oxygen in the reaction zone is much lower than in the case of undiluted air. As a result, the adiabatic flame temperature is reduced. The combustion regime in such conditions is often referred to as "flameless combustion" or "mild combustion," as discussed in Refs. [13–16]. The characteristics of such combustion phenomena include small temperature fluctuations, no luminosity or sound emission from the flame, and low NO_x emissions. The recuperation and the exhaust gas recirculation in the combined HPRTE/VARS inherently produce the conditions necessary for flameless combustion.

A schematic diagram of the combined HPRTE and VARS model is shown in Fig. 1. Air enters the system at State Point 1 and is compressed by the low-pressure compressor (LPC, labeled C1). It is adiabatically mixed with the recirculated combustion products from the recuperator (RECP) at State Point 2.9. The mixture is then allowed to enter the generator of the VARS before passing on to the heat exchanger MC and the evaporator of the VARS. In the evaporator, the mixture is cooled and the water produced as a product of combustion is extracted. The mixture then enters the high-pressure core where it is compressed in the high-pressure compressor (HPC, labeled C2), heated in the RECP and combustor (CM), and then expanded in the high-pressure turbine (HPT, labeled T1). After leaving the HPT, all of the combustion gases enter the RECP, where they lose heat to the gases entering the CM. At the exit of the RECP, a portion of the gas recirculates to join the compressed air stream, and the remaining air is passed through a low-pressure turbine (LPT, labeled T2) before exiting to the atmosphere. A temperature-entropy (T-S) diagram is shown in Fig. 1(b) for the purpose of explaining the processes in the HPRTE cycle. The T-S diagram is drawn assuming ideal compression, ideal expansion, and no pressure losses in the cycle. The VARS modeled in this study is a typical lithium bromide/water single-stage system, as shown in Fig. 2.

Thermodynamic Analysis

The combined cycle was modeled using zero-dimensional steady-state thermodynamics, as shown in Boza et al. [10]. However, the present model has the following improvements. Boza et al. [10] did not account for liquid water extraction in the evaporator and its effect on the gas composition throughout the cycle. The present work rigorously enforces the species continuity equation for water, which not only yields more accurate calculation of the liquid water yield but also improves the calculation of state variables such as enthalpy. Boza et al. [10] developed a dual CM model to account for the recirculating gases in the inlet air to the CM. In the present model, the combustion software HPFLAME provided in Turns [17] was used for calculating the adiabatic flame temperature at the exit of the CM. Also, the enthalpy of air at different state points was obtained using the coefficients mentioned in Turns [17], which were calculated on the basis of the data provided in the JANAF tables [18]. More accurate correlations given in Kaita [19] have been used in this paper for calculating the properties of $LiBr/H_2O$ mixture.

Although equilibrium chemistry is employed in modeling the CM to calculate stoichiometry, minor species are neglected elsewhere in the cycle in calculating enthalpy. In the case of combustion without the recirculating gases, the equation for typical fuels (see MacFarlane [2]) is as follows:

$$C_XH_Y + (1 + A_e)\left(\frac{Y}{4} + X\right)[O_2 + 3.76N_2] + \alpha H_2O \rightarrow XCO_2 + \left(\frac{Y}{2} + \alpha\right)H_2O + A_e\left(\frac{Y}{4} + X\right)O_2 + 3.76(1 + A_e)\left(\frac{Y}{4} + X\right)N_2 \quad (1)$$

where O_2 is the oxygen molecule, N_2 is the nitrogen molecule, CO_2 is the carbon dioxide molecule, H_2O is the water vapor molecule, C_XH_Y is the fuel, and A_e is the excess air for combustion. Also, in the above equation α refers to the number of moles of water vapor present in the fresh air entering the system and its value is obtained from the humidity ratio of the fresh air entering the system. Continuity is used to determine the mass flow rate and species concentration at each point in the cycle. Recirculation ratio (R) is defined as the ratio of mass flow rate of exhaust gases recirculated to the mass flow rate of fresh air coming into the system. However, in the current study a modified recirculation ratio (R_{mod}) is used for convenience, defined as the mass flow rate of exhaust gases recirculated to the sum of the mass flow rate of fresh air coming into the cycle and the mass flow rate of fuel consumed, less the mass flow rate of water extracted.

$$R_{mod} = \frac{\dot{m}_{10}}{\dot{m}_1 + \dot{m}_{fuel} - \dot{m}_w} \quad (2)$$

In the above equation $\dot{m}_{fuel}$ is defined as the fuel flow rate and $\dot{m}_w$ is the mass flow rate of water extracted. All state points referred to are clearly shown in Fig. 1. The equivalence ratio Φ for the combined cycle is calculated as follows:

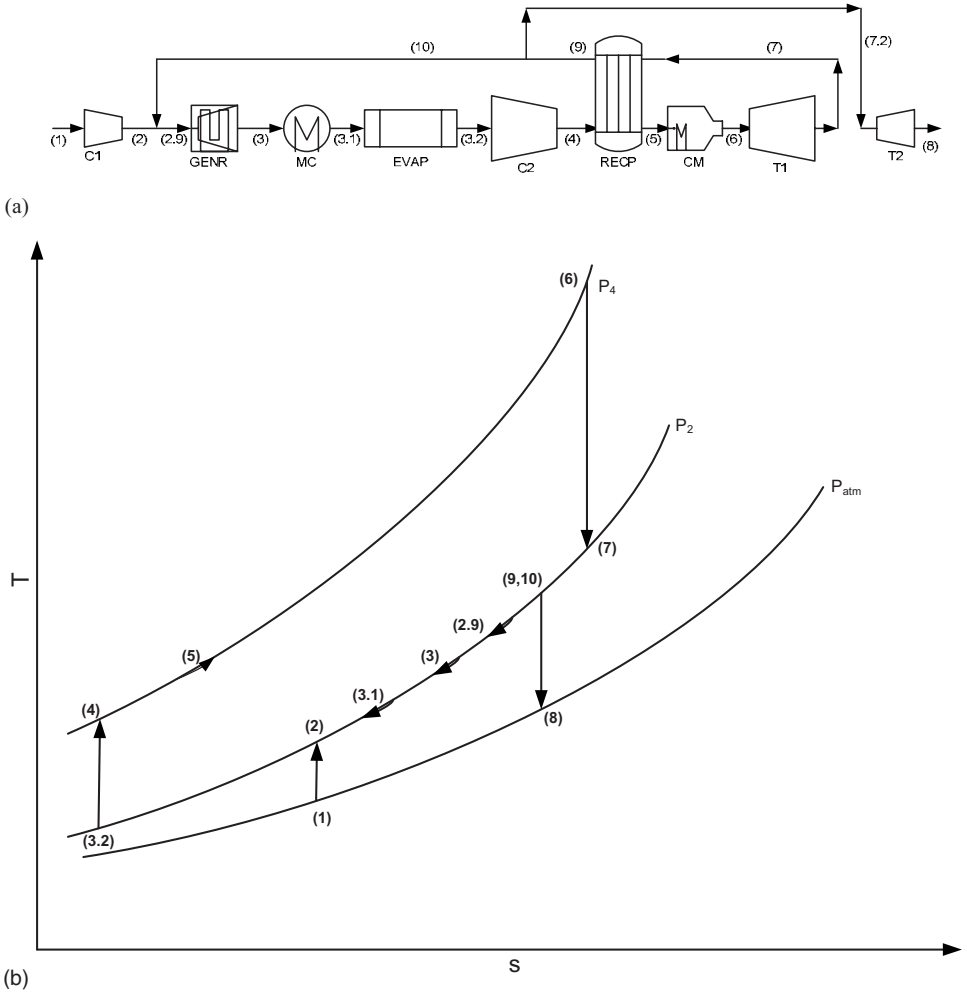

Fig. 1 (*a*) Schematic diagram of the HPRTE cycle. (*b*) *T-S* diagram of the HPRTE cycle with ideal compression, ideal expansion, and no pressure drops.

$$\Phi = \frac{(m_5/m_{\text{fuel}})_{\text{stoic}}}{(m_5/m_{\text{fuel}})_{\text{actual}}} \tag{3}$$

The variable m_5 in the above equation is the mass of air at State Point 5. The value of m_{fuel} for both the actual and stoichiometric conditions is the same and is equal to the mass of 1 mole of fuel. The number of moles of water extracted per mole of fuel burned is given by

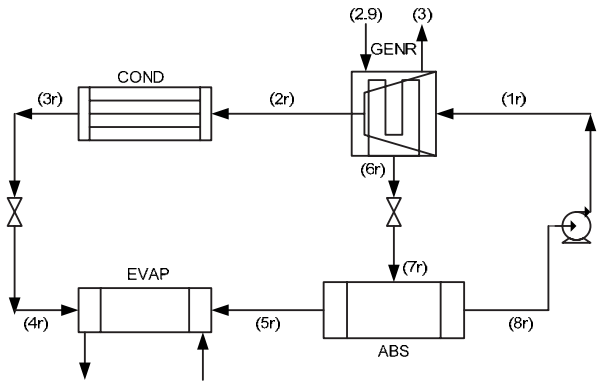

Fig. 2 Schematic diagram of vapor absorption refrigeration system

$$M_R = \frac{n_w}{n_{\text{fuel}}} = \frac{(\dot{m}_w/MW_w)}{(\dot{m}_{\text{fuel}}/MW_{\text{fuel}})} \tag{4}$$

The mass flow rate of water extracted $\dot{m}_w$ can be calculated from the above expression using the values of M_R and $\dot{m}_{\text{fuel}}$. State Point 2.9 is immediately downstream of the mixing junction. The number of moles of individual species present at this state point could be calculated as follows. Initially, the number of moles of individual species on the RHS of Eq. (1) is multiplied with R_{mod} and then M_R moles of water are extracted from the result. Finally, the individual moles of species on the LHS of Eq. (1) are added to the above result to obtain the number of moles of individual species present at State Point 2.9. The compositions of the gas at State Points 3 and 3.1 are the same as at State Point 2.9. The species present at these states can be written as

$$\begin{aligned} N_{2.9,3,3.1} = {} & \left(X + \frac{Y}{4}\right)(1 + A_e + R_{\text{mod}}A_e)\text{O}_2 \\ & + (3.76)(1 + A_e)\left(X + \frac{Y}{4}\right)(1 + R_{\text{mod}})\text{N}_2 \\ & + R_{\text{mod}}X\text{CO}_2 + \left(R_{\text{mod}}\left(\frac{Y}{2} + \alpha - M_R\right) + \alpha\right)\text{H}_2\text{O} \end{aligned} \tag{5}$$

It should be noted that R_{mod} as defined in Eq. (2) is the ratio of mass flow rates, but it is assumed as a molar ratio, when used in the derivation of the above equation, since the mixture molecular

weight is nearly constant when using common liquid fuels. Also, in the above equation the coefficients appearing before the chemical formulas of the species (O_2, N_2, CO_2, and H_2O) represent the number of moles of the species present in the mixture at that state point. Knowing the type and the number of moles of species present at that state point, the weight of the mixture can be easily calculated. It should be noted that some water has already been removed from the control mass, which is reflected in the above equation. After the water extraction in the evaporator, the species present at the State Points 3.2–5 can be written as

$$N_{3.2,4,5} = \left(X + \frac{Y}{4}\right)(1 + A_e + R_{\text{mod}}A_e)O_2 + (3.76)(1 + A_e)\left(X + \frac{Y}{4}\right)(1 + R_{\text{mod}})N_2 + R_{\text{mod}}XCO_2 + \left[R_{\text{mod}}\left(\frac{Y}{2} + \alpha - M_R\right) - M_R + \alpha\right]H_2O \tag{6}$$

The actual value of m_5 in Eq. (3) can be calculated from Eq. (6) where as its stoichiometric value is again obtained from Eq. (6) but by assuming A_e equal to zero. The addition of fuel and the combustion process occurs between State Points 5 and 6. The composition of the gas at the end of the combustion process is obtained as follows. At first, the sum of the number of moles of different components of the gas in Eq. (6), which is the composition of the gas coming into the CM and the number of moles of different components of the gas obtained by simple combustion, which is given on the RHS of Eq. (1), is taken. Then the number of moles of different components of air consumed in combustion, which is given on the LHS of Eq. (1), is subtracted from the sum of the number of moles obtained earlier. The final composition at State Point 6, which will be same at State Points 7 and 9, is given as

$$N_{6,7,9} = (1 + R_{\text{mod}})\left\{XCO_2 + A_e\left(X + \frac{Y}{4}\right)O_2 + 3.76(1 + A_e)\left(X + \frac{Y}{4}\right)N_2\right\} + \left[R_{\text{mod}}\left(\alpha + \frac{Y}{2} - M_R\right) - M_R + \frac{Y}{2} + \alpha\right]H_2O \tag{7}$$

Using the definition of the recirculation ratio, the composition at State Points 8 and 10 can be written as

$$N_8 = XCO_2 + A_e\left(X + \frac{Y}{4}\right)O_2 + 3.76(1 + A_e)\left(X + \frac{Y}{4}\right)N_2 + \left[\alpha + \frac{Y}{2} - M_R\right]H_2O \tag{8}$$

$$N_{10} = R_{\text{mod}}XCO_2 + R_{\text{mod}}A_e\left(X + \frac{Y}{4}\right)O_2 + R_{\text{mod}}(3.76)(1 + A_e) \times \left(X + \frac{Y}{4}\right)N_2 + R_{\text{mod}}\left[\alpha + \frac{Y}{2} - M_R\right]H_2O \tag{9}$$

It is assumed that the air coming out of the evaporator is saturated and the ratio of the saturated pressure of water vapor to the total pressure can be related to the mole ratio of the substances for the working fluid and can be written as (see MacFarlane [2])

$$\Pi_{\text{sat}} = \frac{P_{3.2,\text{sat}}}{P_{3.2}} = \frac{n_w}{n_{\text{total}}} \tag{10}$$

The value of M_R can be easily calculated from the above equation and can be written as

$$M_R = \frac{\left(\frac{\Pi_{\text{sat}}}{1 - \Pi_{\text{sat}}}\right)R_{\text{big}} - \left\{R_{\text{mod}}\left(\frac{Y}{2} + \alpha\right) + \alpha\right\}}{-1 - R_{\text{mod}}} \tag{11}$$

$$R_{\text{big}} = R_{\text{mod}}X + (1 + A_e + R_{\text{mod}}A_e)\left(\frac{Y}{4} + X\right) + 3.76(1 + R_{\text{mod}})(1 + A_e)\left(\frac{Y}{4} + X\right)$$

The ratio of mass flow rate of water extracted to the mass flow rate of fuel consumed is given by

$$\frac{\dot{m}_w}{\dot{m}_{\text{fuel}}} = \left(\frac{18.02}{12.011X + 1.0079Y}\right)M_R \tag{12}$$

From the above equation, the mass flow rate of water extracted in the evaporator to the mass flow rate of fresh air at the inlet can be easily calculated and is given by the following equation:

$$R_W = \frac{\dot{m}_w}{\dot{m}_1} \tag{13}$$

The performance of the system is expressed in terms of the water extraction parameter R_W, the thermal efficiency η_{th}, and refrigeration ratio β. The thermal efficiency is defined as the net work output of the cycle divided by the net heat input based on the lower heating value (LHV) of the fuel propane (C_3H_8). It should be noted that the code is written to consider different fuels, such as methane, ethane, acetylene etc.,

$$\eta_{\text{th}} = \frac{\dot{W}_{\text{net}}}{\dot{Q}_{\text{LHV}}} \tag{14}$$

The refrigeration ratio is defined as the ratio of external refrigeration load to the net work output of the cycle

$$\beta = \frac{\dot{Q}_{\text{ref}}}{\dot{W}_{\text{net}}} \tag{15}$$

It should be noted that external refrigeration represents the refrigeration effect available in the evaporator of the VARS after it takes the sensible and the latent heat load of the air mixture of the HPRTE: The sensible heat load is due to the cooling of the air mixture and latent heat load is due to the water extraction in the evaporator.

Solution Method

A computer code was written in FORTRAN to simulate the performance of the combined cycle. The code includes several subroutines that calculate the properties of the combustion products, such as enthalpy, entropy, specific heat, density, given temperature, and composition of the gas. For energetic calculations, dissociation was neglected. The error introduced was estimated by comparing to equilibrium chemistry results from the HPFLAME program, and essentially identical results were obtained at the CM exit. Since that would be the location of maximum dissociation, ignoring minor species was deemed justified. The value of temperature at each state point is either given as input or calculated using the value of enthalpy at that state point. The pressure at each state point is calculated using the values of pressure drops (in the case of turbines and heat exchangers) and pressure rise (in the case of compressors). The code is capable of calculating engine performance (net work output, water extraction flow rate, and thermal efficiency) as a function of the input parameters (turbine inlet temperature, RECP inlet temperature, generator temperature, evaporator exit temperature, LPC ratio, recirculation ratio, turbomachinery efficiencies, heat exchanger effectiveness, equivalence ratio, and pressure drops).

In the FORTRAN program, initially a value of R_{mod} is assumed to

start the code. The chemical compositions of the gas at all the state points of the cycle are then calculated knowing the values of R_{mod} and the specified value of Φ. The code then calculates all the unknown parameters (enthalpy, entropy, specific heat, density, temperature, pressure, and the adiabatic flame temperature at the exit of CM) if any, at all the state points of the cycle. During the subsequent iterations, the assumed value of R_{mod} is varied, to closely match the calculated value of the adiabatic flame temperature at the exit of the CM, with the specified value of turbine inlet temperature. The code terminates when the difference between these two temperatures is very small or zero. The $LiBr/H_2O$ VARS is modeled using the equations given by Goswami et al. [18]. The following simplifying assumptions are made in writing the VARS code in addition to those made earlier for the combined cycle:

1. The refrigerant and absorbent phases are in equilibrium.
2. With the exception of pressure reduction across the expansion devices, pressure reductions in the lines and heat exchangers are neglected.
3. Pressures at the evaporator and condenser are equal to the vapor pressure of the refrigerant, i.e., water.
4. The pump is isentropic, valves are adiabatic, and there are no jacket heat losses.

The values of the generator, absorber, and the evaporator temperatures are similar to those given by Goswami et al. [20]. The COP of the VARS system obtained from the sample calculation is around 0.78, which is comparable to the values given for a single effect $LiBr/H_2O$ VARS used in a combined heat and power (CHP) system by Mone et al. [21]. It should be noted that the actual COP of a real system would be lower than 0.78. However, the simple model assumed for VARS will not affect the thermal efficiency of the combined cycle because the temperature of the gas entering the HPC is fixed. However, if a more advanced VARS is assumed for the combined cycle, then the refrigeration ratio will increase.

The cycle input and calculated parameter values (from the computer code) are given in Table 1. The input parameters are underlined to differentiate them from the calculated parameters. The ambient temperature in Table 1 was determined based on a hot day in which air conditioning would typically is required. The LPC pressure ratio PR_{C1} was based on prior studies [2], yielding maximum thermal efficiency and reasonable water extraction. The temperature of the gaseous mixture entering the HPC C2 is fixed and is equal to 10°C, which is reasonable, considering that the evaporator temperature is conservatively fixed at 5°C. The turbomachinery polytropic efficiencies were based on state-of-the-art values as reported by Mattingly [22] and Carcasci and Facchini [23]. The pressure drops in the RECP and the CM are similar to the values reported by Fiaschi et al. [24]. The equivalence ratio Φ was set to 0.9 based on previous studies with the HPRTE, as given in Boza et al. [10]. It was assumed to be equal to 0.9, because it was hypothesized that at least 10% excess air was necessary to ensure complete combustion [2]. The gas entering the CM is air diluted with recirculated combustion products, which lowers the adiabatic flame temperature toward the specified turbine inlet temperature. Choosing the maximum practical value of recirculation ratio maximizes the water extraction and excess refrigeration.

The effectiveness of the RECP is assumed to be 0.85 and the RECP inlet temperature (on the hot side) is limited to 800°C. These are conservative values based on existing commercial equipment [25]. Turbine blade cooling is considered for higher turbine inlet temperatures, and the model for turbine blade cooling used is similar to that given by Massardo et al. [12]. This model gives a relation between the turbine inlet temperature and the percentage of main compressor flow used for turbine blade cooling. In the proposed HPRTE/VARS combined cycle, the cool air required for turbine blade cooling is bled from the main airflow after the HPC C2 at State Point 4 in Fig. 1.

Table 1 Input and calculated parameters of the combined HPRTE/VARS cycle

Input or calculated parameters	Values
Turbine inlet temperature, T_6 °C	1400
Recuperator inlet temperature, T_7 °C	800
Ambient temperature, °C, ambient pressure, P_1 atm	30, 1
Low-pressure compressor ratio (PR_{C1})	2
Turbomachinery polytropic efficiencies	90%
Combustor equivalence ratio, Φ	0.9
Effectiveness of the recuperator (RECP), ε_R	0.85
Effectiveness of the heat exchanger (MC), ε_{MC}	0.85
Relative humidity of inlet air, ϕ_r	0.9
Pressure drop in the combustor, $\Delta P/P$	0.05
Pressure drop in the heat exchanger MC, $\Delta P/P$	0.03
Pressure drop in the generator, $\Delta P/P$	0.03
Pressure drop in the evaporator, $\Delta P/P$	0.03
Pressure drop in the recuperator (turbine (T1) exit side), $\Delta P/P$	0.06
Pressure drop in the recuperator (compressor (C2) exit side), $\Delta P/P$	0.02
Ratio of mass flow rate of water extracted to mass flow rate of fuel used, R_F	1.51
Ratio of mass flow rates at State Point 10 to State Point 1	2.37
Ratio of mass flow rates at State Point 3.2 to State Point 1	3.29
Ratio of mass flow rates at State Point 6 to State Point 1	2.88
Modified recirculation ratio (R_{mod})	2.44
Temperature at State Point 5, °C	724.2
High pressure compressor ratio, PR_{C2}	9.02
Turbine blade cooling flow rate/mass flow rate at State Point 4	0.14
Temperature at State Point 3, °C	110
Temperature at State Point 3.1, °C	29.25
Temperature at State Point 3.2, °C	10
Temperature in the condenser of the VARS, °C	45
Temperature in the absorber of the VARS, °C	35
Temperature in the generator of the VARS, °C	100
Temperature in the evaporator of the VARS, °C	5
COP of the VARS	0.78
Pressure ratios across turbine T1	7.2
Thermal efficiency η_{th}	40.4%
Refrigeration ratio β and $Q_{evap,VARS}/W_{net}$	0.38, 0.65
Q_{genr}/Q_{cond}, Q_{genr}/Q_{abs} of the VARS	1.19, 0.82

It should be noted that the inlet temperature to compressor C2 is lower because of the presence of evaporator of VARS, as shown in Fig. 1(*a*). This will result in lower exit temperature from C2 for the same pressure ratio, when compared with other cycles having no inlet air cooling. As a result, the temperature of the cooling flow in the proposed HPRTE/VARS combined cycle is much lower, compared with other cycles. Therefore, lower cooling flow rates than assumed in this paper will be sufficient for turbine blade cooling, which will result in higher thermal efficiency for the base case.

Results and Discussion

The computer code described above was used for the parametric analysis of the cycle. The effect of variation of the important cycle parameters, such as the turbine inlet temperature, RECP inlet temperature, and the LPC ratio, on the overall cycle performance was studied. The values of all other parameters were kept as constant and were equal to their values given in Table 1 during this study. The result of this study is given below and is explained by various plots. Any variations in the values of any of the cycle parameters from their respective values in Table 1 are clearly mentioned in the plots.

Effect of Turbine Inlet Temperature T_6. Figures 3(*a*) and 3(*b*) show the effect of turbine inlet temperature T_6 on the thermal

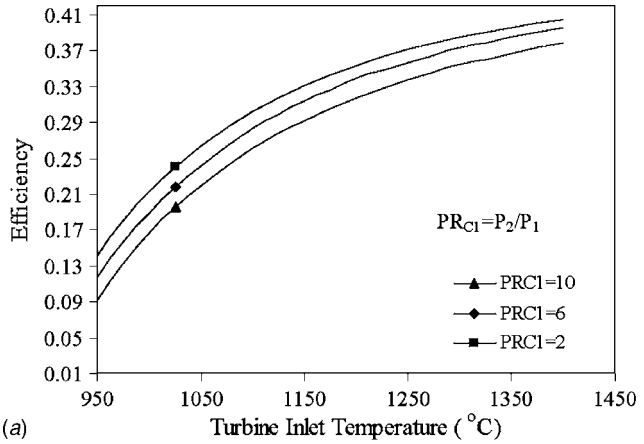

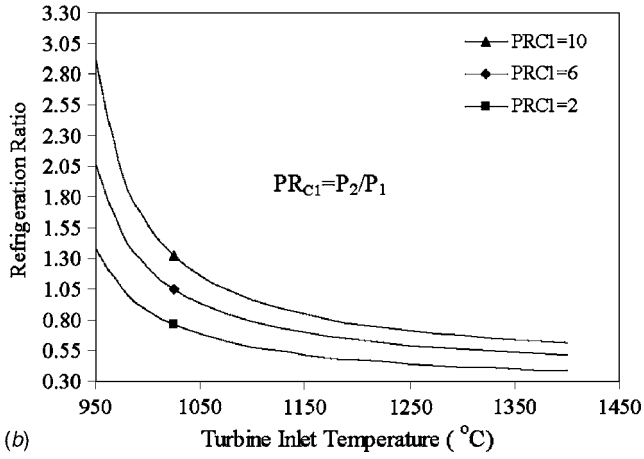

Fig. 3 (*a*) Thermal efficiency η_{th} versus turbine inlet temperature for different values of the LPC ratio (PR_{C1}). (*b*) Refrigeration ratio β versus turbine inlet temperature for different values of the LPC ratio (PR_{C1}).

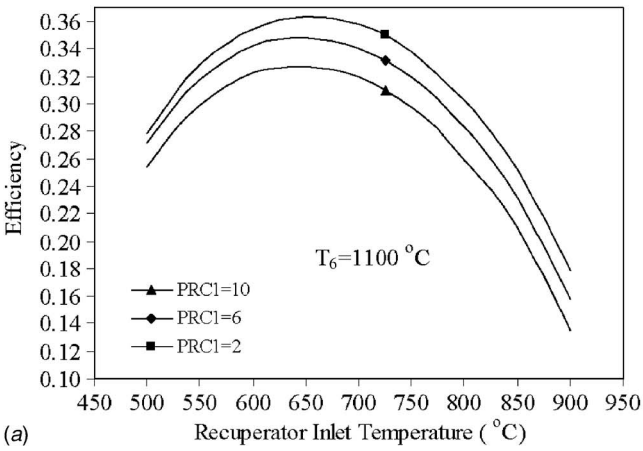

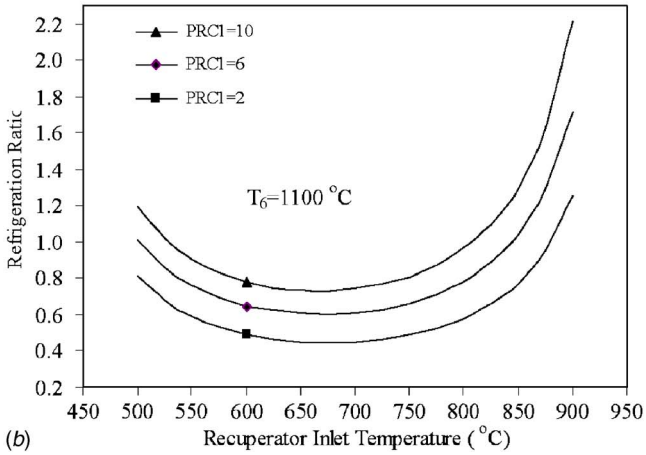

Fig. 4 (*a*) Thermal efficiency η_{th} versus RECP inlet temperature for different values of the LPC ratio (PR_{C1}). (*b*) Refrigeration ratio β versus RECP inlet temperature for different values of the LPC ratio (PR_{C1}).

efficiency η_{th} and the refrigeration ratio β, respectively, at a constant LPC ratio PR_{C1}. The turbine exit temperature is fixed in drawing these plots and, as T_6 is increased, the pressure ratios across the HPT and the HPC increase. The net work output from the system increases, resulting in higher values of η_{th} for higher values of T_6. The figure shows that at any fixed value of turbine inlet temperature, the thermal efficiency decreases with increasing values of PR_{C1}. It is noted that as the value of PR_{C1} is increased from 2 to 10, the values of both the work input into the compressor C1 and the work output from the LPT T2 increase. However, the increase in work input into the compressor C1 is greater compared with the increase in the work output from the turbine T2. As a result, the net work output from the combined cycle is reduced. Figure 3(*b*) shows that β decreases with the increasing values of T_6 at a constant value of PRC1. It is observed that as T_6 increases the net work output from the system and the amount of refrigeration produced in the evaporator increase. However, the rate of increase of the net work output is more than that of Q_{ref}. The overall effect is the decrease in the values of β at higher values of T_6.

Effect of Recuperator Inlet Temperature T_7. Figures 4(*a*) and 4(*b*) show the effect of RECP hot-side inlet temperature T_7 on η_{th} and the refrigeration ratio β, respectively. The figure shows that, for a fixed value of T_6, η_{th} increases with T_7 before reaching a maximum point, and then its value starts decreasing. Increasing T_7 has two converse effects on the system. Higher values of T_7 result in reduced pressure ratios across the HPC C2 (and turbine T1), shown in Fig. 5. The lower pressure ratios across the compressor will result in lower work of compression. However, lower pressure ratio across the turbine will result in lower work output. These two competing factors affect the net work output in such a way that before the maximum efficiency point the work reduction in the compressor is more than the decrease in work output from

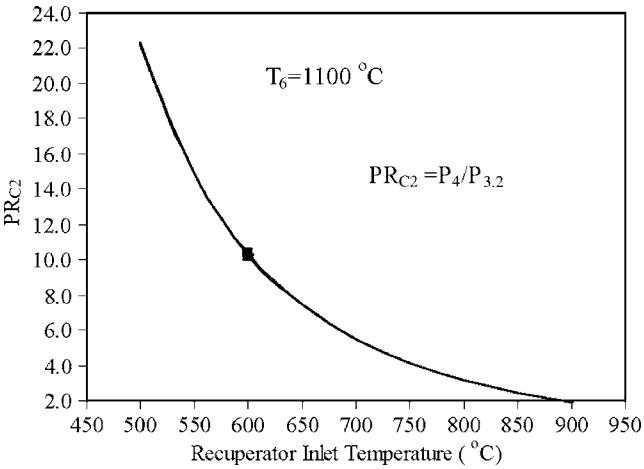

Fig. 5 HPC ratio (PR_{C2}) versus the RECP inlet temperature for different values of the LPC ratio (PR_{C1})

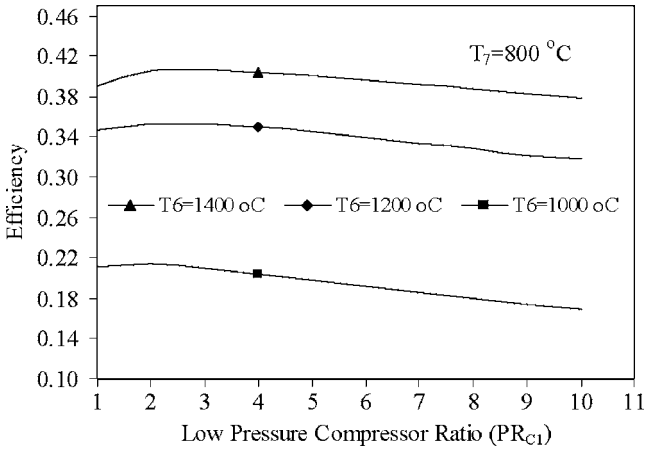

Fig. 6 Variation of thermal efficiency versus LPC ratio (PR_{C1}) for different values of the turbine inlet temperature (T_6)

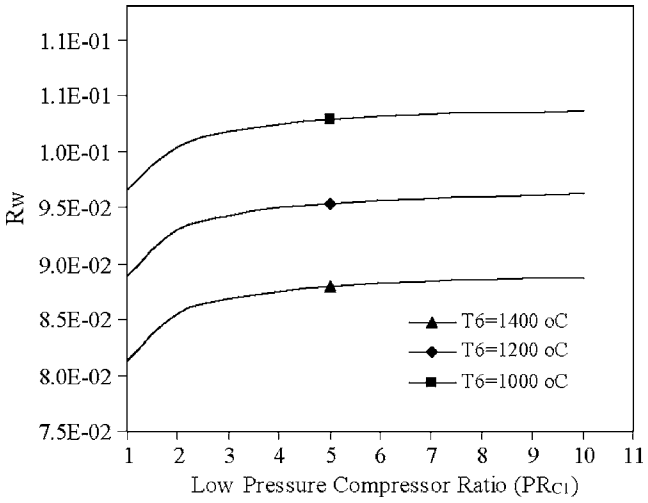

Fig. 7 Water extraction parameter R_W versus LPC ratio (PR_{C1}) for different values of the turbine inlet temperature (T_6)

the turbine, hence the increase in the net work output. However, after the maximum efficiency point the work reduction in the compressor is less than the reduction in the work output from the turbine, resulting in reduced values of net work output. Comparison of Figs. 4(*a*) and 4(*b*) shows that β has an inverse relationship with η_{th}, implying that inefficient operation of the combined cycle will have a higher value of β.

It should be noted that the value of recirculation ratio R_{mod} decreases with increasing values of T_6, holding the values of Φ and all other input parameters constant. However, its value increases with increasing values of T_7, again keeping the values of Φ and all other input parameters constant. In the case of increasing values of T_6, there is an inverse relationship between R_{mod} and the η_{th} as can be concluded from Fig. 3(*a*). However, in the case of increasing values of T_7, there is both direct and inverse relationships between R_{mod} and η_{th}, as can be concluded from Fig. 4(*a*). The pressure ratio across the compressor C2 increases as the difference between T_6 and T_7 increases. The above findings show that the value of R_{mod} and therefore the value of η_{th} is a strong function of the pressure ratio across C2, which also determines the expansion ratio across the turbine T1.

Figure 4(*a*) may be used for determining the influence of the RECP. The figure shows that for a specified value of T_6, the value of η_{th} is maximum for an optimal value of T_7. Moreover, this optimal value is independent of the LPC ratio PR_{C1}. It should be noted that the value of PR_{C1} determines the pressure in the RECP at its hot side (State Point 9), as shown in Fig. 1(*a*). The optimal value of T_7 should be the highest designed temperature for the RECP, selected for the combined HPRTE/VARS cycle.

Effect of Low-Pressure Compressor Ratio (PR_{C1}). Figure 6 shows the effect of the LPC ratio PR_{C1} on the values of η_{th}. The plots are obtained for three different values of T_6. Figure 6 shows that, as PR_{C1} increases, η_{th} increases, reaches a broad maximum, and then decreases. The figure shows that for all the three temperatures T_6, considered η_{th} is found to be highest at around PR_{C1} equal to 2. However, if the values of PR_{C1} is increased to 4, there is no appreciable drop in the efficiency of the combined cycle. Under such conditions, the system becomes more compact, which is an added advantage of the combined HPRTE/VARS cycle over other power and refrigeration cycles. Figure 7 shows the variation of R_W with PR_{C1}. The plots are drawn for different values of T_6. The figure shows that at a fixed value of T_6, the value of R_W increases rapidly when the value of PR_{C1} is increased from 1 to 2 and the increase in its value is less significant when PR_{C1} is increased from 3 to 10.

The heat rejection from the combined HPRTE/VARS cycle takes place, in addition to the hot exhaust, through three heat exchangers: the condenser and absorber of the VARS and the heat exchanger MC of the HPRTE. The total amount of heat to be rejected from all the three heat exchangers is calculated to be about 70.7% of the fuel heat input to the cycle, for the base case shown in Table 1. It should be noted that the source of heat to be rejected includes both the fuel combustion as well as the external refrigeration load. The total heat rejected from the condenser and the absorber of the VARS is calculated to be 60% of the fuel heat input and heat to be rejected from the heat exchanger MC is calculated to be 10.7% of the total heat input. The heat exchanger MC could be designed and selected by using the values of ε_{MC} and ΔP, given in Table 1. It is important to point out that the model adopted is independent of the method of cooling. The availability of water should result in higher heat exchanger effectiveness. Thus, using an air-cooled MC will make the numbers presented in this paper a bit on the conservative side.

The advantages of the combined HPRTE/VARS cycle over advanced conventional cycles such as the intercooled (IC)-RECP configuration are shown in Table 2. The two cycles are exactly the same in configuration except that the IC/RECP cycle does not have the recirculation loop and the VARS. As shown in Table 2, all the input variables to the two codes were kept the same to obtain an accurate comparison. Two different configurations of the IC/RECP cycle were investigated. In the first configuration labeled as cf_1 in the table, the fresh air compression process was intercooled. In the second configuration labeled as cf_2 in the table, the compressor was not intercooled, yielding a purely recuperated cycle. The results clearly show the advantages of HPRTE/VARS cycle over either IC/RECP cycle when cooling is a desired cycle output. The value of η_{th} for the HPRTE/VARS cycle is lower by 2.2 percentage points compared to the IC/RECP cf_1 configuration, whereas η_{th} of the HPRTE/VARS cycle is higher by 1.4 percentage points over the IC/RECP cycle in the cf_2 configuration. However, the value of combined efficiency η_{comb} is higher for HPRTE/VARS cycle compared with both IC/RECP cycles. The value of η_{comb} is the same as η_{th} for the IC/RECP cycles because there is no refrigeration output in these cycles. The η_{comb} is defined as the ratio of sum of the net work output and the refrigeration output to the net heat input to the cycle. The refrigeration output is the ratio of external refrigeration load to the value of a practical COP of a vapor compression refrigeration system, which in this case is conservatively taken as 3.2. The specific power of HPRTE/VARS cycle is 204% higher than that of the IC/RECP with cf_1 configuration. The specific power of HPRTE/VARS cycle is 231% higher than that of the IC/RECP cycle with cf_2 configuration. This means

Table 2 Comparison of HPRTE/VARS cycle with IC/RECP cycle

Input of calculated parameters	HPRTE/VARS	IC/RECP cf_1	IC/RECP cf_2
Turbine inlet temperature, T_6 °C	1400	1400	1400
Recuperator inlet temperature, T_7 °C	800	800	800
Ambient temperature, °C, ambient pressure, P_1 atm	30, 1	30, 1	30, 1
Pressure across LPC (C1), PR_{C1}	2	2	1
Turbomachinery polytropic efficiencies	90%	90%	90%
Combustor equivalence ratio, Φ	0.9	0.31	0.31
Effectiveness of the recuperator (RECP), ε_R	0.85	0.85	0.85
Effectiveness of the heat exchanger (MC), ε_{MC}	0.85	0.85	0.85
Temperature of chilled water used for cooling, $T_{cw,i}$ °C	30	30	30
Relative humidity of inlet air, ϕ_r	0.9	NA	NA
Pressure drop in the combustor, $\Delta P/P$	0.05	0.05	0.05
Pressure drop in the heat exchanger MC, $\Delta P/P$	0.03	0.03	0.03
Pressure drop in the generator, $\Delta P/P$	0.03	NA	NA
Pressure drop in the evaporator, $\Delta P/P$	0.03	NA	NA
Pressure drop in the recuperator (turbine (T1) exit side), $\Delta P/P$	0.06	0.06	0.06
Pressure drop in the recuperator (compressor (C2) exit side),$\Delta P/P$	0.02	0.02	0.02
Ratio of mass flow rates at State Point 10 to State Point 1	2.37	NA	NA
Ratio of mass flow rates at State Point 3.2 to State Point 1	3.29	1.0	1.0
Ratio of mass flow rates at State Point 6 to State Point 1	2.88	0.87	0.87
Ratio of mass flow rates at State Point 7.2 to State Point 1	1.0	1.0	1.0
Temperature at state point 5, °C	724.2	710.8	724.5
Pressure ratio across HPC (C2), PR_{C2}	9.02	3.79	8.04
Turbine blade cooling flow rate/mass flow rate at State Point32	0.14	0.14	0.14
Temperature at state point 3.2, °C	10	28.35	17.25
Pressure ratios across HPT (T1), PR_{T1}	7.2	6.40	6.83
Pressure ratios across LPT (T2), PR_{T2}	2	1	1
Ratio of water extracted to mass flow rate of fuel consumed, R_F	1.51	0	0
Refrigeration ratio, β	0.34	0	0
Specific power (W_{net}/m_1), kW/(kg/s)	1057.5	348.3	319.7
Thermal efficiency η_{th}	40.4%	42.6%	39.9%
Combined efficiency, $\eta_{comb}=(W_{net}+(Q_{ref}/COP))/Q_{LHV}$	44.80%	42.6%	39.9%

that the HPRTE/VARS cycle ingests less than half the air of the comparison cycles for the same power output. The value of Φ is lower for both IC/RECP cycles, implying leaner combustion, compared with the HPRTE/VARS cycle, which is consistent with the specific power results.

The efficiency values obtained from the proposed combined HPRTE/VARS cycle are in the range of 25–40.4% for higher values of T_6, depending parametrically on the design. It should be noted that the HPRTE/VARS cycle is an emerging technology and has not yet been optimized for specific applications. However, its efficiency values may be compared with other gas turbine cycles using some form of inlet air cooling. Wang and Chiou [26] studied the steam injection STIG and inlet air cooling technologies IAC for improving the power output and power generation efficiency of a simple gas turbine GENSET. The steam needed in the STIG and IAC features is generated from the energy recovered from the system's own exhaust gases. They reported an efficiency of 35% for a turbine inlet temperature of 1264 K. Under similar operating conditions, the efficiency obtained for the combined HPRTE/VARS cycle is equal to 37%.

As mentioned earlier, there are three important products of the combined HPRTE/VARS cycle: power, refrigeration, and water extraction, in addition to available waste heat. There is the potential for injecting the extracted water back into the cycle after the compressor C2 to increase the efficiency and/or power. However, according to the recent study by Khan et al. [27], there is no appreciable increase in the value of η_{th} of the combined cycle by the injection of the extracted water back into the cycle.

A stepwise developmental program is under way at the Energy and Gas Dynamic Systems Laboratory at the University of Florida to construct and demonstrate the workings of the combined HPRTE/VARS cycle. Additionally, a significant effort is under way to develop and validate computer models for the combined HPRTE/VARS cycle. One of the earliest developmental steps was to construct, experimentally investigate, and model the operations of a modified HPRTE cycle. In this modified HPRTE cycle as reported in Khan et al. [28], two water cooled heat exchangers were used in the place of the VARS. The computer code for the complete HPRTE/VARS cycle reported in this paper was modified to simulate the performance of the modified HPRTE cycle. In the later stage of the development of the HPRTE/VARS cycle as reported in Khan et al. [29], an ammonia-water (NH_3/H_2O) vapor absorption refrigeration unit was integrated with the HPRTE cycle. The experimental results from both the experiments were compared with the model results. The difference between the two results was found to be within acceptable limits, given the assumptions made in the model. These experiments, plus benchmarking with several proprietary codes used by gas turbine engine manufacturers, provided reasonable validation of the cycle code used in the present work.

Conclusions

A zero-dimensional steady-state model was used for the thermodynamic design-point performance analysis of a novel cooling and power cycle that combines the HPRTE semiclosed cycle gas turbine with a VARS. The following is the summary of the major findings:

- The value of thermal efficiency of the combined HPRTE/VARS cycle is shown to be greater than 40% for the base case, which represents a medium sized engine with conservative values of design parameters.
- A combined efficiency parameter was developed, including as output the power necessary to produce the same amount of refrigeration as the combined cycle. The HPRTE/VARS

was shown to have more than 2% combined efficiency advantage over an IC/R engine with identical component performance parameters.
- The amount of cooling capacity produced and the quantity of water extracted in the evaporator of VARS has been found to be directly proportional to the recirculation ratio and the LPC ratio. The ratio of the cooling capacity to the net work output was found to be greater than 0.65 for the base case. A part of the cooling capacity is designed to be taken up by an external refrigeration load. The ratio of this cooling capacity to the net work output of the combined cycle defined as refrigeration ratio was found to be greater than 0.38 for the base case. The quantity of water extracted increases significantly when the pressure ratio is increased from 1 to 2. However, the increase is less significant if the pressure ratio is further increased. The quantity of water extracted is calculated to be greater than 1.5 kg, per kilogram of fuel consumed, for the base case.

The design parameters of the combined cycle can be selected according to the requirements/demands of the power plants/consumers to obtain an optimal combination of efficiency, refrigeration capacity, and water extraction. If the combined cycle is designed for maximum efficiency by choosing higher values of turbine inlet temperature then it would not have maximum cooling capacity and water extraction in the evaporator. However, if the combined cycle is designed for maximum cooling capacity and water extraction by choosing higher values of LPC ratios and recirculation ratios then the efficiency would be lower than the maximum. The design parameters of the combined cycle for the base case, in the present study, were chosen for maximum thermal efficiency and reasonable water extraction and they are turbine inlet temperature equal to 1400°C, the RECP inlet temperature equal to 800°C, LPC ratio equal to 2, and all other input parameters are exactly equal to those given in Table 1. The turbine blade cooling flow required for the given turbine inlet temperature is calculated from the blade cooling model and is found to be 14% of the main core flow. The value of maximum efficiency obtained will be greater than 40% and approximately 1.5 kg of water per kilogram of fuel consumed would be extracted from the combined cycle. In addition, it will have a refrigeration ratio greater than 0.38.

We would like to emphasize that the turbine blade cooling model assumed in this study is conservative. The temperature of the cooling flow in the proposed HPRTE/VARS combined cycle is much lower, compared with simple cycles. Therefore, much lower cooling flow rates than those assumed in this paper will be sufficient for turbine blade cooling, which will result in higher thermal efficiency. In the extreme case, if steam blade cooling or external cooling air for turbine blades is assumed, reducing the cooling air bleed flow to zero, then the efficiency would be greater than 51% in addition to the cooling capacity produced in the evaporator.

In addition to the advantages/characteristics of the combined cycle shown in this paper, it has several other projected advantages:

(1) Very small change in power and efficiency as ambient temperature increases (due to the constant HPC inlet temperature).
(2) More compactness than competing nonadiabatic technology, due to high overall pressure ratio and close system integration. This also implies very low usage of hot section superalloys, thereby reducing cost.
(3) Inherent extremely low emissions of NO_x, CO, and soot, even on liquid hydrocarbon fuels. NO_x levels will be dictated primarily by fuel-bound nitrogen levels, not by the thermal (Zeldovich) chemical mechanism as discussed in Ref. [17], which is usually dominant. The demonstrator engine, discussed by Khan et al. [30], reduced CO by two orders of magnitude compared to the base line commercial engine. In addition, the particulate emissions were found to be below the opacity detection limits.

Considering all the issues/points mentioned above, it can be concluded that the combined HPRTE/VARS cycle seems to be a promising candidate for distributed power generation with the potential for efficient, clean production of power, water, and refrigeration.

Acknowledgment

The authors acknowledge the support provided by the U.S. Egypt Joint Board on Scientific and Technological Cooperation. Support from the Department of Mechanical and Aerospace Engineering at the University of Florida is also gratefully acknowledged.

Nomenclature

ABS = absorber
C1 = low-pressure compressor
C2 = high-pressure compressor
COP = coefficient of performance
COND = condenser
E = sum of different parameters (see Eq. (11))
EVAP = evaporator
GENR = generator
LHS = left-hand side
$\dot{m}$ = mass flow rate
m = mass of the mixture
MC = heat exchanger
MW = molecular weight
M_R = ratio of number moles of water extracted to number of moles of fuel burned [Eq. (10)]
n = number of moles
NA = not applicable
N = sum of the number of moles of several species present at a given state
P = pressure
PR_{C1} = low-pressure compressor pressure ratio
PR_{C2} = high-pressure compressor pressure ratio
PR_{T1} = high-pressure turbine expansion ratio
R = recirculation ratio
RHS = right-hand side
R_F = ratio of mass flow rate of water extracted to mass flow rate of fuel used
R_{mod} = modified recirculation ratio
R_W = ratio of mass flow rate of water extracted to mass flow rate of fresh air (Eq. (13))
S = entropy
T = temperature
TR = ton of refrigeration
T1 = high-pressure turbine
T2 = low-pressure turbine
α = number of moles of water vapor in the air entering the system at State 1
β = refrigeration ratio (Eq. (15))
ΔP = pressure drop
Φ = combustor equivalence ratio
η_{th} = thermal efficiency (Eq. (14))
Π = ratio of water vapor saturation pressure to total pressure at evaporator exit [Eq. (11)]

Subscripts

abs = absorber of the VARS
cf_1, cf_2 = IC/RECP configurations
comb = combined
cond = condenser of the VARS
fuel = fuel (propane)
net = net work done

ref = refrigeration
sat = saturated
stoic = stoichiometric
w = water

References

[1] Gasparovic, N., 1965, "The Advantage of Semi-Closed Cycle Gas Turbines for Naval Ship Propulsion," Nav. Eng. J., **77**, pp. 275–333.
[2] MacFarlane, R. S., and Lear, W. E., 1997, "System Impact of H2O Production and Injection on a Novel Semi-Closed Cycle Gas Turbine," Paper No. AIAA-97-0374.
[3] Nemec, T. S., 1995, "Thermodynamic Design Point Study of a Semi-Closed Recuperated Intercooled Gas Turbine Combined With a Rankine Bottoming Cycle," M.S. thesis, University of Florida, Gainesville.
[4] Danias, G. E., 1997, "Design and Off Design Point Study of Two Regenerative Feedback Gas Turbine Engines for Helicopter Applications," M.S. thesis, University of Florida, Gainesville.
[5] Landon, J. C., 1996, "Design and Off Design Point Study of Two Regenerative Feedback Gas Turbine Engines for Marine Applications," M.S. thesis, University of Florida, Gainesville.
[6] Muley, N. S., and Lear, W. E., 2003, "Effect of Exhaust Gas Recirculation (EGR) on Thermal NO_x Formation Rate," Paper No. AIAA-2003-0503.
[7] Facchini, B., Fiaschi, and D., Manfrida, G., 1997, "SCGT/CC: An Innovative Cycle With Advanced Environmental and Peakload Shaving Features," Energy Convers. Manage., **38**(15–17), pp. 1647–1653.
[8] Lear, W. E., and Crittenden, J. F., 1995, "Exploratory Design of a Depleted Oxygen Gas Turbine Combustor," Final Report for the Phase I SBIR Contract No. NAS3-27380.
[9] Lear, W. E., and Laganelli, A. L., 1999, "High Pressure Regenerative Turbine Engine: 21st Century Propulsion," Final Test Report for Contract No. NAS3-27396.
[10] Boza, J. J., Lear, W. E., and Sherif, S. A., 2003, "Performance of a Novel Semi-Closed Gas Turbine Refrigeration Combined Cycle," ASME Paper No. 2003-GT-38576.
[11] Mostafavi, M., Alaktiwi, A., and Agnewc, B., 1998, "Thermodynamic Analysis of Combined Open-Cycle-Twin-Shaft Gas Turbine (Brayton Cycle) and Exhaust Gas Operated Absorption Refrigeration Unit," Appl. Therm. Eng., **18**, pp. 847–856.
[12] Massardo, F., Cazzola, W., and Lagorio, G., 2004, "Widget-Temp: A Novel Web-Based Approach for the Thermoeconomic Analysis and Optimization of Conventional and Innovative Cycles," ASME Paper No. 2004-GT-54115.
[13] Wünning, J. A., and Wünning, J. G., 1997, "Flameless Oxidation to Reduce Thermal NO_x-Formation," Prog. Energy Combust. Sci., **23**, pp. 81–94.
[14] Coelho, P. J., 2001, "Numerical Simulation of a Mild Combustion Burner," Combust. Flame, **124**(3), pp. 503–518.
[15] Plessing, T., Peters, N., and Wünning, J. G., 1988, "Laseroptical Investigation of Highly Preheated Combustion With Strong Exhaust Gas Recirculation," *27th Symposium (International) on Combustion*, The Combustion Institute, Pittsburgh, PA, pp. 3197–3204.
[16] Cavaliere, A., de Joannon, M., and Ragucci, R., 1999, "Mild Combustion of High Temperature Reactants," International Symposium on High Temperature Air Combustion and Gasification, Kaohsiung, Taiwan, Jan. 20–22, Paper B4.
[17] Turns, S. R., 1996, *An Introduction to Combustion-"HPFLAME" Combustion Equilibrium Code*, McGraw-Hill, New York.
[18] Stull, D. R., and Prophet, H., 1971, *JANAF Thermochemical Tables*, 2nd ed., National Bureau of Standards, Washington, DC, NSRDS-NBS, 37.
[19] Kaita, Y., 2001, "Thermodynamic Properties of Lithium Bromide-Water Solutions at High Temperatures," Int. J. Refrig., **24**, pp. 374–390.
[20] Goswami, D. Y., Kreith, F., and Kreider, J. F., 1999, *Principles of Solar Engineering*, 2nd ed., Taylor & Francis, Philadelphia.
[21] Mone, C. D., Chau, D. S., and Phelan, P. E., 2001, "Economic Feasibility of Combined Heat and Power and Absorption Refrigeration With Commercially Available Gas Turbines," Energy Convers. Manage., **42**, pp. 1559–1573.
[22] Mattingly, J. D., 1996, *Elements of Gas Turbine Propulsion*, McGraw-Hill, New York.
[23] Carcasci, C., and Facchini, B., 2000, "Comparison between two Gas Turbine Solutions to Increase Combined Power Plant Efficiency," Energy Convers. Manage., **41**, pp. 757–773.
[24] Fiaschi, D., Lombardi, L., and Tapinassi, L., 2004, "The Recuperative Auto Thermal Reforming and Recuperative Reforming Gas Turbine Power Cycles With CO_2 Removal—Part II: The Recuperative Reforming Cycle," ASME J. Eng. Gas Turbines Power, **126**, pp. 62–68.
[25] http://www.proepowersystems.com/proe90.htm
[26] Wang, F. J., and Chiou, J. S., 2004, "Integration of Steam Injection and Inlet Air Cooling for a Gas Turbine Generation System," Energy Convers. Manage., **45**, pp. 15–26.
[27] Khan, J. R., Lear, W. E., Sherif, S. A., Crittenden, J. F., Meitner, P. L., and Howell, B. H., 2006, "A Novel Pressurized CHP System With Water Extraction," Paper No. AIAA-2006-4180.
[28] Khan, J. R., Lear, W. E., Sherif, S. A., Crittenden, J. F., and Howell, E. B., 2006, "Water Extraction and Performance of a Pressurized CHP System," Paper No. AIAA-2006-1499.
[29] Khan, J. R., Lear, W. E., Sherif, S. A., Crittenden, J. F., Meitner, P. L., and Howell, B. H., 2006, "Testing and Modeling of a Semi-Closed Gas Turbine Cycle Integrated With a Vapor Absorption Refrigeration System," Paper No. IMECE-2006-15403.
[30] Khan, J. R., Lear, W. E., Sherif, S. A., and Crittenden, J. F., 2005, "Demonstration of a Novel Combined Cooling and Power Gas Turbine With Water Harvesting," Paper No. AIAA 2005-571.

Multidimensional Load Estimation Algorithms That Enable Performance Analysis of Industrial Gas Turbines Without A Priori Information

Takuya Yoshida
Power and Industrial Systems R&D Laboratory,
Hitachi Ltd.,
3-1-1 Saiwaicho,
Hitachi, Ibaraki 317-8511, Japan
e-mail: takuya.yoshida.ru@hitachi.com

Masaaki Bannai
Urban Planning and Development Systems,
Hitachi Ltd.,
14-1 Sotokanda 4-chome,
Chiyoda-ku, Tokyo 101-8010, Japan
e-mail: masaaki.bannai.xu@hitachi.com

Minoru Yoshida
e-mail: minoru.yoshida.gs@hitachi-hes.com

Hiroyuki Yamada
e-mail: hiroyuki.yamada.ah@hitachi-hes.com

Masaki Ishikawa
e-mail: masaki.ishikawa.vw@hitachi-hes.com

Energy Solution Engineering Division,
Hitachi Engineering & Services Co., Ltd.,
15-1 Higashiohnumacho 1-chome,
Hitachi, Ibaraki 316-0023, Japan

Performance analysis and diagnosis for gas turbines usually assume the use of detailed design specifications or similar kinds of information for building and configuring engine models. This allows the nonlinearity of gas turbine performance characteristics to be taken into account. However, this approach tends to make it difficult for users of industrial gas turbines to analyze performance because (1) detailed design specifications are not necessarily supplied to the users, and (2) even if they were available, use of these kinds of information may often lead to complex procedures for model building and for making adjustments and configurations that all require high expertise. The purpose of this paper was to propose a direct modeling approach based only on operating data and not requiring a priori information like manufacturer-supplied specifications while preserving sufficient accuracy. The core element of this approach was the automatic identification and selection of base load operating data from various operating conditions. A set of load estimation algorithms was proposed. They were applied to 31,000 h of operating data for two types of engines, which involved actual failure occurrences, and subsequent performance modeling and analysis were carried out. The following results were obtained. (1) The relative performance trends obtained revealed the quantitative extent of degradation during operation and of recovery by repair or engine change. (2) The performance trends gave a good account of actual failures. (3) The accuracy of the performance modeling measured by the 99th percentile of error was on the order of 1%. The proposed direct modeling approach offers sufficient accuracy to quantify the gradual degradation of performance and its recovery by maintenance. The performance trends obtained are useful for further fault diagnosis. [DOI: 10.1115/1.2900727]

Keywords: performance degradation, performance analysis, diagnosis, industrial gas turbine, base load, fault detection

Introduction

As demands for reduced operational and maintenance costs grow, performance analysis and diagnosis have been increasing in importance. Particularly in industrial use, since owners or operators are not primarily motivated by power generation itself, they are unlikely to put high priority on investments in complicated measurement and diagnostic systems. Therefore, emphasis should be placed on easiness in use and cost effectiveness of the diagnostic systems.

After an early report on gas path analysis (GPA) by Urban [1], methods of performance analysis and diagnosis for gas turbines have been greatly developed [2]. Diakunchak [3] discussed the causes of performance degradation and predicted typical rates of performance degradation for industrial gas turbines under the assumptions of desirable operating conditions and proper maintenance scenarios. Lakshminarasimha et al. [4] simulated performance degradation focusing on compressor fouling and erosion, and reported that the results were consistent with observations. There have also been reports [5,6] presenting actual applications of performance analysis to online monitoring. Recently, some studies [7–9] have been shifting focus from gas turbine components to combined cycle plants.

However, these methods usually assume the use of detailed design specifications such as componentwise performance maps, efficiencies, heat/mass balances, and control set points. This makes it difficult for industrial engine users to analyze performance for several reasons.

(1) Detailed design specifications are usually not supplied to the users [4].
(2) Even if these specifications were available, or could partly be estimated by techniques like that of Ref. [4], use of detailed a priori information is apt to lead to complex procedures for model building and for making adjustments and configurations that all require high expertise.
(3) If engines already in service are to be analyzed, there are probably changes in performance characteristics from the initial conditions due to degradation from long operating hours or due to several occurrences of maintenance events such as overhauls or part repairs. This may affect the accuracy of performance analysis and succeeding diagnosis. To deal with this, frequent model adjustments and configurations may be necessary after every major maintenance task, requiring further expertise as well as human and capital resources.

Therefore, a simpler and easier method without requiring a priori information on specifications is needed. However, to develop

Manuscript received March 21, 2007; final manuscript received January 16, 2008; published online April 28, 2008. Review conducted by Pericles Pilidis.

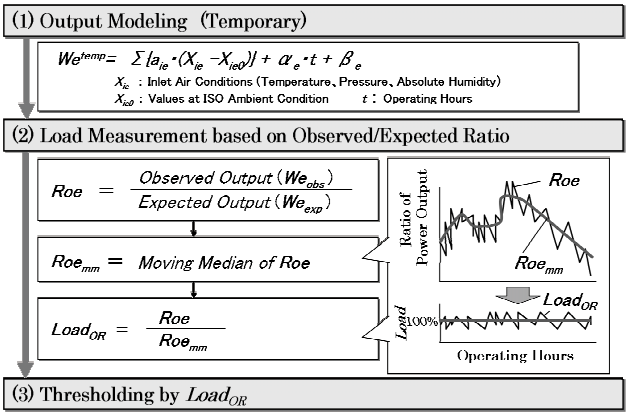

Fig. 1 Procedure of base load data selection by output ratio algorithm

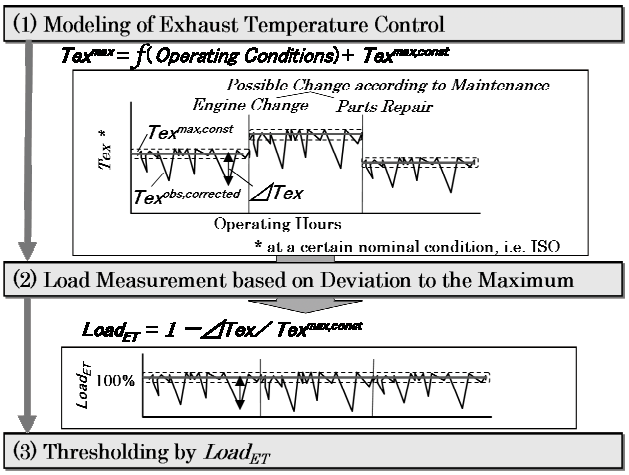

Fig. 2 Procedure of base load data selection by exhaust temperature algorithm

such a simple method, we encounter the problem of nonlinearity of gas turbine performance that may affect accuracy if improperly handled. A study by Kamboukos and Mathioudakis [10] showed that linear modeling provides as accurate an estimation as a nonlinear one for parameters like inlet air flow rate, but produces inaccuracy for parameters like turbine inlet temperature. A question arises here as to how to analyze performance in a simple manner while preserving enough accuracy. Little attention seems to have been given to this question.

The purpose of this paper is to present a direct modeling approach that does not require a priori information such as manufacturer-supplied specifications while preserving sufficient accuracy. We paid attention to the fact that for economical reasons, most industrial gas turbines are predominantly operated at base load, i.e., maximum power output according to varying inlet air conditions. This led us to assume that if base load data could be correctly separated from the whole operating range, performance characteristics of these turbines might be modeled with enough accuracy by linear equations. Under this assumption, we developed a set of load estimation algorithms for automatic identification and selection of base load data. The algorithms were designed to be computed based only on operating data.

In this paper, we describe the proposed algorithms for base load data selection together with subsequent performance modeling, and we present results of their application to operating engines. Engines having had actual fault occurrences were chosen for analysis. We also describe the accuracy and applicability of the proposed approach and recommend which algorithm to use for base load data selection from a practical viewpoint.

Algorithms for Selection of Base Load Operating Data

Here, we describe four algorithms we have developed to select data at the base load operating point: the former two represent different standpoints of load measurement; the latter two integrate the former two.

Output Ratio Algorithm. This algorithm measures the load using the ratio of the observed power output to the expected maximum. It is outlined in Fig. 1 and consists of the following steps.

In the first step, engine power output is temporarily modeled as a function of inlet air conditions and operating hours as shown in Eq. (1), where the upper right symbol $*$ stands for the deviation from the ISO ambient condition and t_p is a constant to normalize operating hours. The coefficients a_{1e}, α_{2e}, α_{3e}, α_e, and constant β_e are determined by least-squares regression using actual operating data. The regression at this stage is quite rough, because the equation does not include fuel input as a parameter to reflect varying load levels in operating data. However, this defect is corrected in the next step.

In the second step, the above equation is used to calculate the expected output. Then, the ratio of the observed output to the expected output is obtained (Eq. (2)). This output ratio is further divided by its moving median (Eq. (3)). Alternately, instead of the moving median (i.e., the 50th percentile), the moving average at a certain percentile can be used so that the moving average may follow the center of fluctuation.

Finally, the operating data that fall within the range of $100 \pm \tau_{OR}$ percent in load_{OR} are selected as base load data.

$$W_e^{\text{temp}} = a_{1e}(T_{ci} - 15) + a_{2e}(P_{ci} - 1013.25) + a_{3e}(AH - 0.0063) + \alpha_e(t/t_p) + \beta_e = (a_{1e}T_{ci}^{*} + a_{2e}P_{ci}^{*} + a_{3e}AH^{*}) + \alpha_e(t/t_p) + \beta_e \quad (1)$$

$$R_{oe} = \frac{We_{obs}}{We_{exp}} \quad (2)$$

$$\text{load}_{OR} = \frac{R_{oe}}{R_{oe_{mm}}} \quad (3)$$

One point in Eq. (1) is that fuel input is not included. The intention here is to represent the expected maximum level, which may primarily depend on ambient conditions but not on fuel input. This means that the ratio of Eq. (2) basically represents the load level.

Another point is the division of this observed/expected output ratio by its moving median in Eq. (3). This is to correct for long term drift of the observed/expected output ratio due to the rough regression of Eq. (1) as mentioned above. In other words, this allows us to trace a base load operating line even if there may be probable occurrences of performance changes due to degradation or fault.

Exhaust Temperature Algorithm. Figure 2 illustrates the concept of this algorithm. The deviation of turbine exhaust temperature to its upper limit is employed to measure load. Gas turbines generally have certain upper limits of exhaust temperature to protect gas path components. The exhaust temperature algorithm assumes that this upper limit is equivalent to the operating point of the base load.

It primarily follows that the exhaust temperature deviation of the observed value to the upper limit is used, as shown in Eq. (4). However, the upper limit of the exhaust temperature varies according to operating conditions. This relationship is necessary to

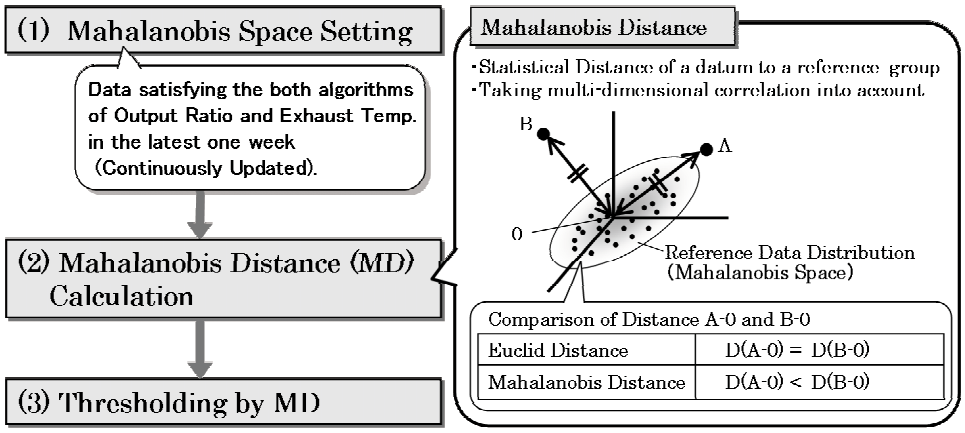

Fig. 3 Procedure of base load data selection by MT algorithm

calculate Eq. (4). Equation (5) gives a simple approximation for this. The upper limit of the exhaust temperature is expressed as a function of inlet air temperature and steam injection flow rate. If fitting of this equation is successfully performed, the last term on the right hand side, which is a constant, can be interpreted as an indicator of a preset maximum load level that is independent of varying operating conditions. Using this constant, we can normalize the load in the context of the exhaust temperature, as shown in Eq. (6). The operating data that fall within the range of $100 \pm \tau_{ET}$ percent in load_{ET} are selected as base load data.

$$\Delta T_{ex} = T_{ex}^{\max} - T_{ex}^{obs} \tag{4}$$

$$T_{ex}^{\max} = (a_{ex1} T_{ci}^{*} + a_{ex2} G_s^{*}) + T_{ex}^{\max,const} \tag{5}$$

$$\begin{aligned} \text{load}_{ET} &= 1 - \Delta T_{ex}/T_{ex}^{\max,cosnt} \\ &= (T_{ex}^{obs} - a_{ex1} T_{ci}^{*} - a_{ex2} G_s^{*})/(T_{ex}^{\max} - a_{ex1} T_{ci}^{*} - a_{ex2} G_s^{*}) \end{aligned} \tag{6}$$

Another point in Eq. (5) is that the fuel flow rate is excluded as a parameter. This is because the upper limit of the exhaust temperature is basically determined by gas path protection requirements and also because the variation of the upper limit is mainly due to inlet air conditions; these are both independent of fuel flow rate.

Overlap Algorithm. This algorithm simply selects the overlap between the results of the previous two algorithms. The operating data that are within both thresholds by output ratio and exhaust temperature algorithms are selected.

Mahalanobis–Taguchi Algorithm. The Mahalanobis–Taguchi algorithm (abbreviated to MT algorithm hereafter), proposed by Taguchi was originally a technique for fault detection or pattern recognition [11]. As illustrated in Fig. 3, it uses the multidimensional statistical distance called Mahalanobis distance (MD) between an observed datum and a group of reference data to measure the degree of anomaly. The group of reference data is called the Mahalanobis space. The MD, in contrast to ordinary Euclidean distance (ED), scales the distance according to a distribution density taking into account the correlations among the dimensions: the MD for a datum in a densely distributed area is scaled close to the ED; the MD for a datum in a sparsely distributed area is enlarged.

In the present study, we employ the two types of loads measured by the output ratio algorithm (Eq. (3)) and exhaust temperature algorithm (Eq. (6)) to form a two-dimensional space. The procedure for this consists of the following steps, as outlined in Fig. 3.

In the first step, the members of the Mahalanobis space are selected from the operating data of the last one week. The data selected by both the output ratio and exhaust temperature algorithms are adopted as members of the Mahalanobis space; this space is updated every hour using the latest one-week data. Then, the values of the Mahalanobis space members are normalized as in Eq. (7) so that they have the average of 0 and the standard deviation of 1 for each dimension (i.e., load_{OR} and load_{ET}).

$$U_{jk} = \frac{x_{jk} - \bar{x}_j}{\sigma_j} \tag{7}$$

In the second step, the MD between the observation and the Mahalanobis space is calculated using Eq. (8).

$$\text{MD} = \sqrt{\frac{1}{n}\mathbf{u}^t \mathbf{R}^{-1} \mathbf{u}} = \sqrt{\frac{1}{n}\sum_{j=1}^{n}\sum_{l=1}^{n}(u_j r^{jl} u_l)} \tag{8}$$

Here, n stands for the number of dimensions (in this case 2), $\mathbf{u}$ is the vector of the normalized observation, $\mathbf{R}^{-1}$ is the inverse of the correlation matrix for the Mahalanobis space, u_j is the jth element of the normalized observation, and r^{jl} is the (j,l)th element of the inverse of the correlation matrix. The division by n on the right hand side is another normalization to let the MD have an average of 1 for the referenced Mahalanobis space.

Finally, the operating data with MD between 0 and threshold τ_{MT} are selected as base load data.

The purpose of this algorithm is not merely to incorporate viewpoints of the output ratio and exhaust temperature algorithms but also to take into account the correlation between the loads measured by these different algorithms so that priority is given to the data close to the center of the two-dimensional distribution.

Another point in the present application is the constant update of the Mahalanobis space. This allows the selection of base load data which can trace almost any pattern of trend regardless of the causes such as degradation, faults, or drift in performance characteristics.

Performance Modeling

Using the selected base load data, performance indicators are basically formulated as a function of inlet air conditions and operating hours. For a combustor with steam injection, the flow rate of the steam is additionally taken into account. In this paper, power output and fuel flow rate are presented for examples of the indicators (Eqs. (9)–(12)). Also, thermal efficiency is evaluated using these two indicators as described later.

Table 1 Engines studied

Engine	A	B
Type name	SGT100 (formerly Typhoon)	
Manufacturer	Siemens (formerly Alstom)	
Rated power (kW)	4880	5000
Fuel	Heavy oil	Synthesis gas
Combustor type	Steam injection	Dry low emission
Option	—	Inlet air cooling
Operating hours[a]	Approx. 20,000	Approx. 11,000
Number of major maintenance[a]	5	2
Number of engine change[a]	2	0
History before the data period	Multiple core engine changes followed by 1900 h of operation	New

[a]During the data period.

$$W_e = (a_{1e}T_{\mathrm{ci}}^{*} + a_{2e}P_{\mathrm{ci}}^{*} + a_{3e}\mathrm{AH}^{*}) + (b_eG_s^{*}) + \alpha_e(t/t_p) + \beta_e \tag{9}$$

$$F = (a_{1F}T_{\mathrm{ci}}^{*} + a_{2F}P_{\mathrm{ci}}^{*} + a_{3F}\mathrm{AH}^{*}) + (b_FG_s^{*}) + \alpha_F(t/t_p) + \beta_F \tag{10}$$

$$G_s^{*} = G_s - G_{s_N} \tag{11}$$

$$G_{s_N} = (a_{1s}T_{\mathrm{ci}}^{*} + a_{2s}P_{\mathrm{ci}}^{*} + a_{3s}\mathrm{AH}^{*}) + \beta_s \tag{12}$$

Coefficients a_{ie} $(i=1-3)$, b_e, α_e, a_{iF} $(i=1-3)$, b_F, α_F, a_{is} $(i=1-3)$ and constants β_e, β_F, β_s are determined by least-squares regression using the base load data selected by one of the algorithms described in the previous section. The base load data are selected from a certain period for modeling. This modeling period has conditions that (1) it is not interrupted by major maintenance, and (2) its length is about 5–8 months. Condition (1) is to avoid inaccurate modeling due to a change in performance characteristics due to a major repair or overhaul. Condition (2) is drawn from conflicting requirements for (i) a longer period to cover expected operating range of inlet air conditions and (ii) a shorter period to limit inaccuracy because of the linear degradation assumption introduced in Eqs. (9) and (10).

Using the coefficients and constants determined in the above regression, we correct the observed power output and fuel flow rate to the equivalent values at the ISO ambient condition (Eqs. (13)–(16)). Here, the coefficients α_e and α_F concerning degradation in Eqs. (9) and (10) are not used since the purpose now is to correct only operating conditions. This makes performance analysis applicable for a period longer than the modeling period, apart from the above mentioned linear degradation assumptions in Eqs. (9) and (10). Using the power output and fuel flow rate corrected in this manner, we also evaluate thermal efficiency as in Eq. (17).

$$W_{e_N} = W_{e_{\mathrm{obs}}} - f_{\mathrm{cr}_e}(T_{\mathrm{ci}}, P_{\mathrm{ci}}, \mathrm{AH}, G_s) \tag{13}$$

$$f_{\mathrm{cr}_e}(T_{\mathrm{ci}}, P_{\mathrm{ci}}, \mathrm{AH}, G_s) = (a_{1e}T_{\mathrm{ci}}^{*} + a_{2e}P_{\mathrm{ci}}^{*} + a_{3e}\mathrm{AH}^{*}) + b_eG_s^{*} \tag{14}$$

$$F_N = F_{\mathrm{obs}} - f_{\mathrm{cr}_F}(T_{\mathrm{ci}}, P_{\mathrm{ci}}, \mathrm{AH}, G_s) \tag{15}$$

$$f_{\mathrm{cr}_F}(T_{\mathrm{ci}}, P_{\mathrm{ci}}, \mathrm{AH}, G_s) = (a_{1F}T_{\mathrm{ci}}^{*} + a_{2F}P_{\mathrm{ci}}^{*} + a_{3F}\mathrm{AH}^{*}) + b_FG_s^{*} \tag{16}$$

$$\eta_{e_N} = W_{e_N}/(F_N \times \mathrm{LHV}) \tag{17}$$

Application to Operating Data

Engines Studied. The proposed algorithms of base load data selection and subsequent performance modeling were applied to two engines in the field, as shown in Table 1. The engines with different combustor and fuel options as well as different actual failure occurrences were chosen to examine if the performance changes due to operation and maintenance events could be quantified by our approach. Engine A fueled by heavy oil and equipped with steam injecting combustor was chosen because it had experienced frequent major maintenance work such as overhauls and blade changes during the data period and it was in a relatively aged state. Using this engine, we compared the proposed base load selection algorithms in detail. Engine B fueled by gas and equipped with dry low emission combustor and inlet air cooling was adopted to verify algorithm applicability to a different combustor type.

Evaluation Metrics. The proposed algorithms of base load data selection were compared in terms of selection ratio and accuracy. An algorithm allowing as many data selections as possible while maintaining high accuracy is preferable. This is particularly important in such cases as daily start-stop operation where fewer data for modeling are available compared to continual operation. The selection ratio was defined as the ratio of the number of the data selected as base load to the number of all operating data excluding those belonging to occasional stops. Accuracy was measured by the 99th percentile of error. The error was calculated as the deviation of the predicted power output from the measurement during the modeling period. The reason the 99th percentile was employed instead of the maximum is that the latter is too sensitive and unstable for comparison of accuracy.

Performance Tracking Results. Figure 4 shows the results of the performance analysis based on the base load data selection algorithm of MT. The trends obtained by other selection algorithms were close to those in this figure with relative deviation within 0.3%. Historical events concerning major maintenance are listed in Table 2.

The results clearly showed the degradation tendency during the course of operation and the recovery that occurred for major maintenance tasks. The following items were noted regarding power output.

(i) The performance recoveries by the two occurrences of engine changes ((2) and (5) in the figure) were both greater than those by other maintenance events. This was consistent with generally known facts and supported the accuracy of the analysis.
(ii) The performance drop was especially rapid during several hundred hours before the thermocouple change at

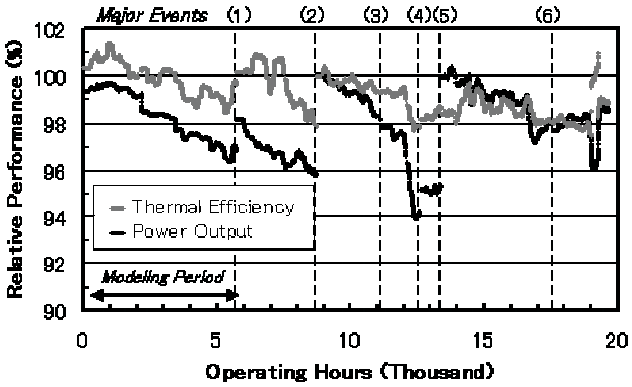

Fig. 4 Relative performance evaluated for Engine A (base load data selection by MT algorithm)

12,500 h ((4) in the figure) following the two unscheduled maintenance times. This suggested that a rapid performance drop like this could be interpreted as a symptom of certain kinds of anomalies.

(iii) There were other sudden performance drops at approximately 17,000 h and 19,000 h. Between these two, deformation of the shroud was found by inspection (at (6) in the figure). These two points suggested the occurrences of physical changes associated with this deformation.

The next point we noted was the difference between the percentage of degradation of power output and thermal efficiency and its cause. Figure 4 suggested that the degradation of power output consisted not only of that of thermal efficiency but also of decreased fuel flow rate. As formulated in Appendix A, the relationship among the percentages of degradation for power output, thermal efficiency, and fuel flow rate can be expressed as in Eq. (18), where δ stands for a sufficiently small number compared to the other terms. This means that the difference between the percentage of degradation of power output and thermal efficiency is practically identical to the decrease in fuel flow rate.

$$W_{eP_{\mathrm{dgr}}} - \eta_{eP_{\mathrm{dgr}}} = F_{P_{\mathrm{dgr}}} - \delta \tag{18}$$

Table 2 Maintenance history of Engine A

No.	Operating hours	Description of maintenance	Notes
(1)	5700	Blade change	
(2)	8700	Engine change	Unscheduled
(3)	11,000	Fuel flow valve change	Unscheduled
(4)	12,500	Thermocouple change	Unscheduled
(5)	13,500	Engine change	
(6)	17,600	Inspection only	Shroud deformation found

The cause of this decreased fuel flow rate can be explained as a result of component efficiency degradation and its effect on the exhaust temperature control. The decreased component efficiency, either in compressor efficiency or in turbine efficiency, raises the turbine exhaust temperature. The turbine exhaust temperature, as explained earlier, has a certain upper limit as a function of operating conditions, and is kept close to this limit when operated at base load. This control of the turbine exhaust temperature is performed by adjusting the fuel flow rate. Therefore, when the engine component performance decreases, the turbine exhaust temperature control lowers the fuel input so that the exhaust temperature remains below the upper limit. In other words, the difference between the percentage of degradation of the power output and the thermal efficiency, which practically equals the percentage of degradation of the fuel flow rate, is the secondary effect of component efficiency degradation mediated by the exhaust temperature control.

The last point we noted was that the fluctuation of the trend of thermal efficiency was larger than that of the power output. This was due to the variation of the lower heating value and density of fuel particularly because heavy oil was used. Since the lower heating value and density of the oil were not measured online, they were treated as constant in the analysis. However, their relative variations obtained from offline measurements were considerably higher than the measurement error of the power output.

Selection of Base Load Data. Figure 5 shows the comparison of selection ratio and accuracy among the algorithms of base load data selection. Here, the threshold for each algorithm was determined so that the 99th percentile of error would fall within roughly the same range. (1) For the output ratio and exhaust temperature algorithms, thresholds were set so that the selection ratios were within 60–70% range. (2) For the overlap algorithm, the same thresholds as output ratio and exhaust temperature algorithms were used. (3) The MT algorithm had three thresholds in this paper. The first two for the selection of the Mahalanobis space were the same as in the overlap algorithm; the last one for the selection of base load data was set to 3. The last threshold was presumably intended to select the data within the range of up to three times the average distance to the center of the referenced Mahalanobis space.

The results showed the difference in selection ratio by the algorithms of base load data selection, while the accuracies shown by errors were almost the same except for the output ratio algorithm. The MT algorithm had the highest selection ratio. Its selection ratio was not only 20% higher than the overlap algorithm, which was simply a combination of the output ratio and exhaust temperature algorithms, but also higher than the ratios given by its basis, the output ratio and exhaust temperature algorithms.

The reason for this difference in selection ratio can be explained by plotting the area selected by each algorithm, as shown in Fig. 6. In this figure, the area selected by (1) the output ratio algorithm is between the two vertical bold lines representing the range of $(100 \pm 2)\%$ in $\mathrm{load}_{\mathrm{OR}}$, (2) the exhaust temperature algo-

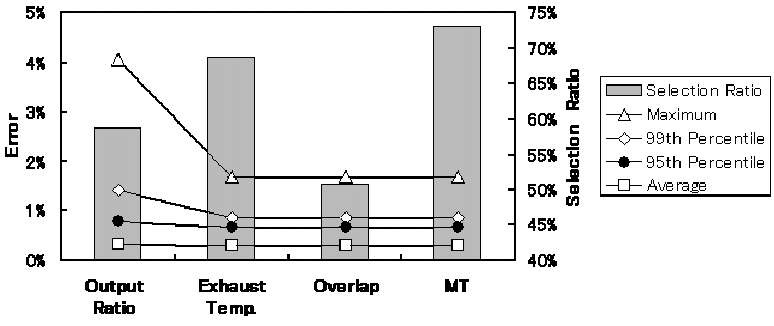

Fig. 5 Comparison of error and selection ratio according to algorithms of base load data selection (Engine A)

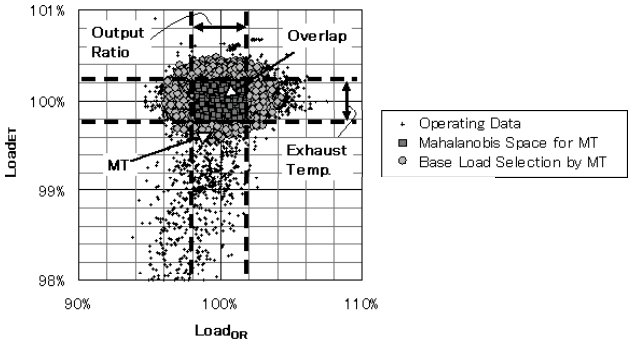

Fig. 6 Identified base load data range according to algorithms of selection (Engine A)

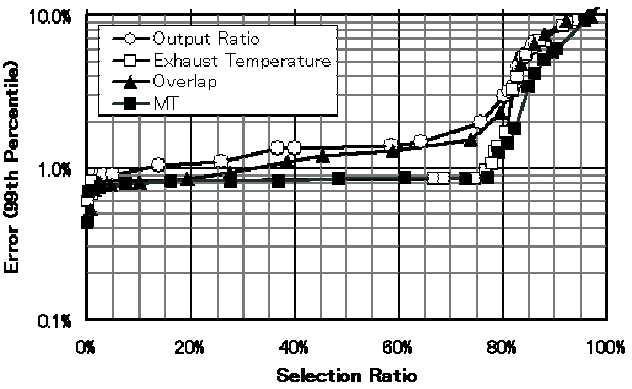

Fig. 7 Trade-off between error and selection ratio according to algorithms of base load data selection

rithm is between the two horizontal bold lines representing the range of approximately $(100 \pm 0.2)\%$ in load_{ET}, (3) the overlap algorithm is the rectangular area where the areas by the output ratio and exhaust temperature algorithms overlap, and (4) the MT algorithm is the elliptic area expanded outward from the area by the overlap method.

This figure illustrates how base load data are selected in the MT algorithm. The area of selection has its base at the center of the distribution and expands its outer edge according to the distribution density. In this way, the correlation between the two dimensions of load_{OR} and load_{ET} is taken into account. This mechanism enables the MT algorithm to select more data than the other algorithms while keeping accuracy.

Threshold Sensitivity. There is a trade-off between accuracy and selection ratio when performing selection of base load data. Inappropriate selection may affect accuracy. We investigated sensitivities of accuracy and selection ratio to setting of the threshold.

Thresholds here were normalized for comparison among the algorithms of selection. For output ratio and exhaust temperature algorithms, loads obtained in Eqs. (3) and (6) were scaled to have the average of 0 and the standard deviation of 1 as in Eqs. (19) and (20). These normalized thresholds were applied to the overlap algorithm in a manner that the two thresholds were simultaneously varied to the same degree. For the MT algorithm, the first two thresholds for the selection of the Mahalanobis space as determined in the previous section were kept unchanged; the last threshold of the MD for the selection of base load data was varied. The MD did not need to be normalized here since it had already been scaled to have the average of 1, as mentioned in Eq. (8). To be precise, these scalings for the algorithms of selection do not have the same basis because the former three and the last one do not have the same average and standard deviation. However, as their values are close enough to be on the same order, they may provide a base to compare the sensitivities and allowable margins associated with the thresholds.

$$\text{NL}_{OR} = \frac{\text{load}_{OR} - \mu_{\text{load}_{OR}}}{\sigma_{\text{load}_{OR}}} \tag{19}$$

$$\text{NL}_{ET} = \frac{\text{load}_{ET} - \mu_{\text{load}_{ET}}}{\sigma_{\text{load}_{ET}}} \tag{20}$$

Figure 7 shows the trade-off between accuracy and selection ratio parametrized by threshold. In general, the 99th percentile of error was about 1% for selection ratio under approximately 80%, and sharply increased to 7% or more for selection ratios above 80%. Among the algorithms of the base load selection, the MT algorithm stably showed the smallest error over the whole range of selection ratios.

Figure 8 presents the variation of selection ratio and accuracy by threshold. A desirable threshold would be in an area offering both high selection ratio and high accuracy. Such an area appeared to be around 70% or more in selection ratio and below the order of 1% in the 99th percentile error. This was equivalent to the normalized threshold of some 0.4–0.5 for the output ratio algorithm, exhaust temperature algorithm, and overlap algorithm, and approximately 3–20 for the MT algorithm. Compared to the quite narrow range for the others, the MT algorithm had a by far broader acceptable threshold margin in which accuracy was kept, and it was consequently less affected by the threshold. This was owed to the scaling by MD where the inverse of the correlation matrix was multiplied as in Eq. (8), thus extending the distance for the sparsely distributed area. In this way, the MT algorithm allowed easy threshold setting with stably kept accuracy.

Applicability to Different Combustor Type. Figure 9 shows the performance tracking results for Engine B with dry low emission combustor and inlet air cooling. Here, the results based on the base load selection by the MT algorithm are shown for an example. The results by all selection algorithms are in Appendix B. Historical events concerning major maintenance along the time series are listed in Table 3.

Although there was a little difference according to the algorithms of the base load data selection as noted in Appendix B, the results revealed the same performance changes of (1) a continual

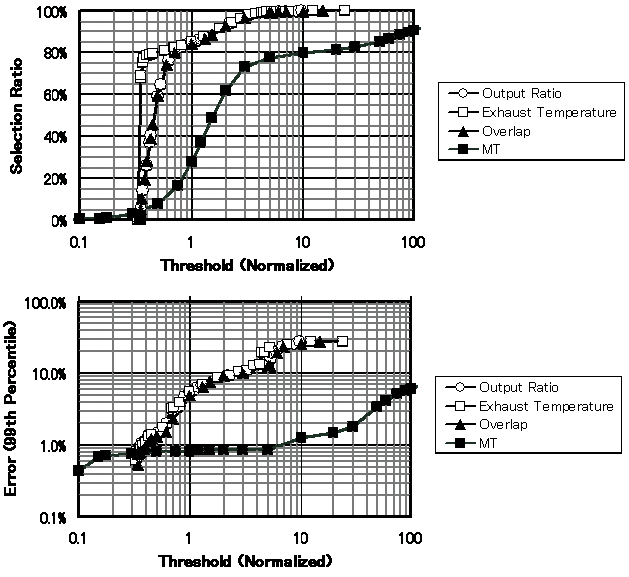

Fig. 8 Sensitivity of selection ratio and error to threshold

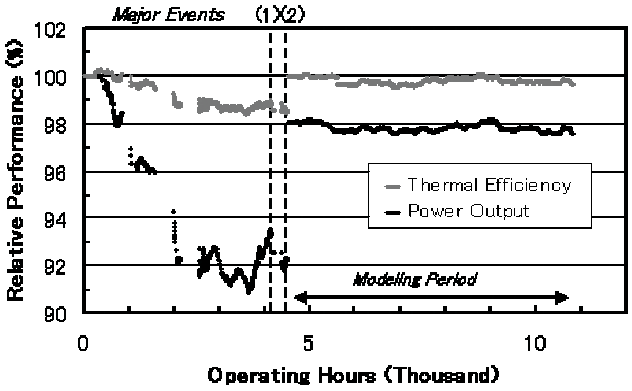

Fig. 9 Relative performance evaluated for Engine B (base load selection by MT algorithm)

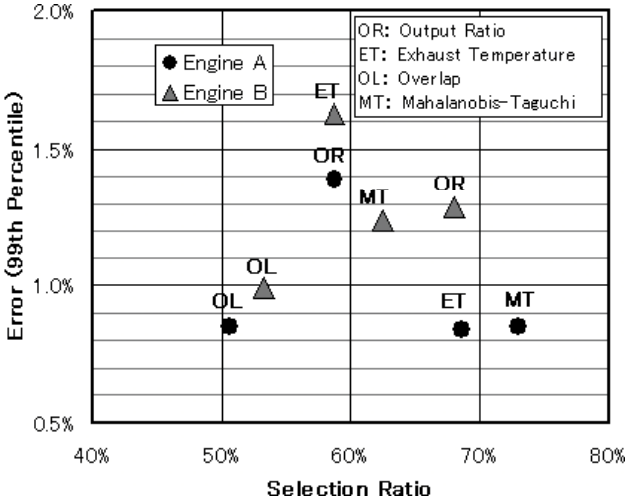

Fig. 10 Accuracy and selection ratio for the engines studied

drop to approximately 92% for power output and 98% for thermal efficiency during the initial 4100 hours, (2) recovery at 4500 h by the compressor repair, (3) little degradation thereafter, and (4) significant difference in the extent of degradation between the power output and the thermal efficiency particularly in the initial 4100 h.

Point (4) suggested that the degradation of the power output in the initial 4100 h was primarily due to the decrease in fuel flow rate. The reasons were as follows. (1) As mentioned earlier using Eq. (18), the difference in extent of degradation between the power output and the thermal efficiency was practically identical to the decrease in fuel flow rate. (2) The drop of the thermal efficiency in this period was quite small compared to that of the power output.

This led to the question: What caused this decrease in fuel flow rate? Such a large decrease in fuel flow rate may not be caused by typical mechanical faults like blade failures, because this type of trouble might involve a serious drop in component performance that would directly lead to a significant drop in thermal efficiency. However, as discussed earlier, a decrease in fuel flow rate was a result of component performance drop mediated by the exhaust temperature control.

We thought that the component performance drop in this case was not caused by some mechanical trouble that directly affected the component efficiency, but by the shift of the operating point from the original one to one far off the design point. This would be caused by parts outside the power train but not by inner driving parts of the engine. The actual cause of the compressor fault in this case was one of the guide vane tension rods breaking. The performance tracking results with the above interpretation gave a good account of what was happening before and after this failure.

These results showed that the proposed approach based on the selection of base load data was also applicable to dry low emission combustors as well as engines equipped with inlet air cooling.

Accuracy and Selection Ratio for the Two Engines. Figure 10 compares selection ratio and accuracy obtained for the different algorithms of base load data selection for the two engines. Comparing the basic algorithms of output ratio and exhaust temperature algorithms, in the sense that both the overlap algorithm and MT algorithm are based on them, we saw that the exhaust temperature algorithm had better accuracy and selection ratio for Engine A, but the output ratio algorithm was better in the same sense for Engine B. When compared to these two algorithms, the MT algorithm had a higher selection ratio while keeping accuracy for Engine A and it had a higher accuracy despite a smaller selection ratio compared to the output ratio algorithm for Engine B.

These results indicated that which of the basic algorithms of output ratio and exhaust temperature algorithms is superior was site dependent. The results also showed that regardless of relative superiority between these two algorithms, the MT algorithm practically gave equal or slightly better accuracy than these did, keeping roughly the same order of selection ratio as the output ratio and exhaust temperature algorithms.

Table 3 Maintenance history of Engine B

No.	Operating hours	Description of maintenance	Notes
(1)	4100	Temporary repair of compressor inlet guide vane failure	Unscheduled
(2)	4500	Permanent repair of the above failure	

Rates of Degradation According to Fuel Types. The rates of performance degradation for the two engines were calculated from periods without occurrence of failure. These results are compared to literature predictions [3] in Table 4. Here, the literature predictions were measured from the degradation curves in Ref. [3]. In the present study, the rate of degradation by heavy oil was approximately six times as fast as that by synthesis gas. This was in good agreement with the number of approximately 5 for the literature prediction. Although the extent of degradation rates differed between the present study and the literature that could be attributed to the difference of preconditions, the present study showed the actual rate of degradation under the condition compressor cleaning was not performed except at occasions of major overhaul; the prediction by the literature represented the nonrecoverable portion of degradation under the assumption of proper frequent cleaning.

Discussion

As described in the previous section on the application to the two engines (Figs. 4 and 9), we found that the proposed algorithms of the base load data selection in combination with subsequent linear modeling (1) were capable of quantifying the extent of degradation during the course of operation and the extent of recovery by making repairs or changing engines; (2) gave a good account of actual fault cases, including revealing steep performance drops before unexpected failures; and (3) achieved accuracy of the 99th percentile error on the order of 1% (Fig. 10). To confirm these effects of the base load data selection, we had attempted to obtain similar results only by linear modeling. However, despite adding parameters such as fuel flow rate to Eqs. (9) and (10), we were unsuccessful. These results showed the vital

Table 4 Comparative rates of degradation between fuel types (power output)

Fuel type	Degradation rate per 5000 h of operation: Present study	Degradation rate per 5000 h of operation: Literature (Ref. [3])	Notes
Heavy oil	2.2%	1.4%	Initial 5700 h for the present study (Engine A). As 1900 h of the preceding operation had occurred before this, literature data were taken from the period of 1900–7600 h.
Synthesis gas	0.4%	0.3%	Period of 4500–11,000 h for the present study (Engine B). Literature data are for natural gas.

role of the proposed algorithms of the base load data selection as a pretreatment for linear performance modeling. The removal of part load data by the proposed algorithms eased the initially stated problem of nonlinearity. The results also suggested further potential of this approach for early fault detection with existing measurements.

Among the proposed algorithms of the base load data selection, the MT algorithm is recommendable for several advantages. These are primarily owed to the nature of this algorithm to integrate multiple points of view for measuring load. First, it offers stably kept accuracy that is less affected by the threshold (Fig. 8). Second, there is a high case-independency offering results close to the results of the optimal modeling regardless of which of the two basic algorithms, i.e., output ratio algorithm or exhaust temperature algorithm, is superior to the other (Fig. 10).

A third advantage of the MT algorithm is its extendibility. The basic algorithms of load measurement presented in this paper have been limited to those based on the power output and to those based on the exhaust temperature. However, there may be other alternatives. The following are some candidates that would offer broader contexts for load estimation: (1) pressure ratio as a function of inlet air temperature and fuel input, and (2) fuel input as a function of inlet air temperature and pressure ratio. If proved effective, they can be employed as additional dimensions for the MT algorithm. In this way, the proposed direct modeling approach would be developed further.

Finally, the following are our recommendations. Although these techniques have not been employed in this paper, they would help obtain stable results in some cases.

(1) There might be cases where the engine has an upper limit of the power output due to generator capacity or due to contractual reasons concerning rating. In such cases, dividing the performance model (Eqs. (9)–(12)) into separate inlet air temperature ranges is recommended. Such a point of division can be identified as an inflection point of the power output to inlet air temperature relationship.
(2) Adding constraints in performing the least-squares regression like Eqs. (9) and (10) is also advisable. Approximate maximum and minimum bounds of coefficients for inlet air temperature, pressure, or absolute humidity can be obtained by plotting the relationships between an objective performance indicator and each of these parameters.

Conclusions

This paper proposed a direct modeling approach for performance analysis of industrial gas turbines that can be performed without a priori information like manufacturer-supplied specifications.

The core element of this approach is the selection of base load data. A set of load estimation algorithms was proposed; the algorithms were based on (1) power output ratio of expected to observed, (2) exhaust temperature deviation to the expected maximum, (3) overlap of the results of the former two, and (4) multidimensional integration of the former two applying the MT algorithm.

The proposed base load data selection algorithms, together with the subsequent performance modeling as a linear function of ambient conditions, were applied to a total of 31,000 h of operating data of two engines, which had experienced actual failure occurrences. The following results were obtained.

(1) The performance tracking results quantified the extent of degradation during the course of operation and of recovery by making repairs or engine changes.
(2) The quantified rates of performance degradation, for comparison between engines using heavy oil and synthesis gas, were consistent with predictions using the literature.
(3) The accuracy of the performance modeling measured by the 99th percentile of error was on the order of 1%.
(4) Among the proposed algorithms of base load data selection, the multidimensional integration of the power output ratio and exhaust temperature deviation by the MT algorithm showed the most stable and accurate results.
(5) The performance tracking results also gave a good account of actual failures, revealing steep performance drops prior to occurrences of unscheduled maintenance.

From these results, we concluded the following.

(1) The proposed base load data selection algorithms allow performance analysis by linear modeling without requiring a priori information; only operating data are needed.
(2) The performance tracking by the proposed approach is sufficiently accurate to quantify the gradual degradation of performance or its recovery by maintenance. It also provides a base for the further purpose of fault diagnosis.

Nomenclature

AH = absolute humidity
a = regression coefficient
b = regression coefficient
F = fuel flow rate
f_{cr} = function for correction
G_s = steam injection flow rate
LHV = lower heating value
MD = Mahalanobis distance
NL = normalized load
n = number of dimensions
P_{ci} = inlet air pressure
$\mathbf{R}^{-1}$ = inverse of the correlation matrix for Mahalanobis space
R_{oe} = ratio of observed output to expected output
T_{ci} = inlet air temperature
T_{ex} = turbine exhaust temperature
t = operating hours (Eqs. (1), (9), and (10))

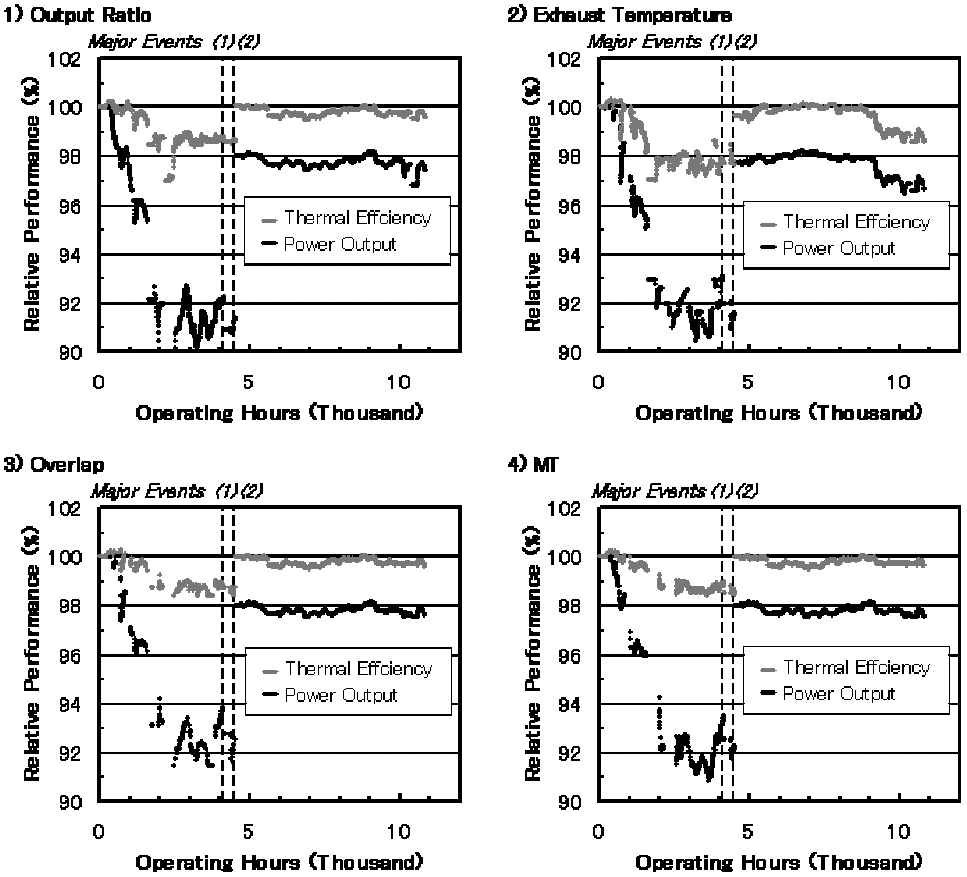

Fig. 11 Relative performance evaluated for Engine B according to algorithms of base load data selection

$\mathbf{u}$ = vector of the observation normalized
W_e = power output
α = regression coefficient for degradation rate during modeling period
β = constant by regression
δ = small number compared to other terms in equation
η_e = thermal efficiency
μ = mean value
σ = standard deviation
τ = threshold

Subscripts and Superscripts

const = constant
ET = exhaust temperature method
e = power output
ex = exhaust temperature
exp = expected
F = fuel flow rate
MT = Mahalanobis–Taguchi algorithm
max = maximum (upper limit)
mm = moving median
N = ISO ambient condition
OR = output ratio algorithm
obs = observed
P_{dgr} = percentage of degradation
s = steam injection
t = transpose of vector (Eq. (8))
temp = temporary formulation
r^{jl} = (j,l)th element of the inverse of correlation matrix
$*$ = deviation from the value at the ISO ambient condition

Appendix A

The percentage of degradation for power output, fuel flow rate, and thermal efficiency can be defined as follows, where the subscripts 1 and 2 stand for before and after degradation.

$$W_{eP_{\mathrm{dgr}}} = 1 - W_{e_2}/W_{e_1} \tag{A1}$$

$$F_{P_{\mathrm{dgr}}} = 1 - F_2/F_1 \tag{A2}$$

$$\eta_{eP_{\mathrm{dgr}}} = 1 - \eta_{e_2}/\eta_{e_1} \tag{A3}$$

$$\eta_{e_i} = W_{e_i}/(F_i \times \mathrm{LHV}) \quad (i = 1,2) \tag{A4}$$

From these equations, we obtain

$$W_{eP_{\mathrm{dgr}}} = F_{P_{\mathrm{dgr}}} + \eta_{eP_{\mathrm{dgr}}} - F_{P_{\mathrm{dgr}}}\eta_{eP_{\mathrm{dgr}}} \tag{A5}$$

Since the third term on the right hand side is sufficiently lower than the others, we can rewrite this equation as

$$W_{eP_{\mathrm{dgr}}} - \eta_{eP_{\mathrm{dgr}}} = F_{P_{\mathrm{dgr}}} - \delta \tag{A6}$$

Appendix B

Figure 11 shows the performance tracking results for Engine B based on each algorithm of base load data selection. Historical events according to operating hours are listed in Table 3. The performance trends for the periods after 4500 h, in particular, after 9000 h by exhaust temperature algorithm were a little different

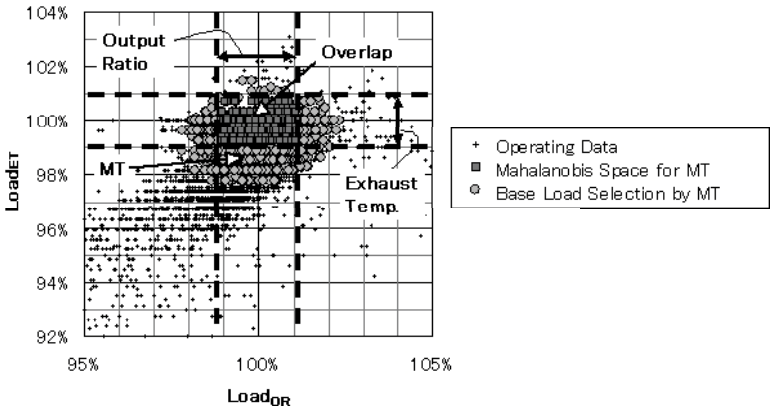

Fig. 12 Identified base load data range according to algorithms of selection (Engine B)

from the others, although the deviations were below 1%. These differences appeared to be caused by the outliers scattered around 103–105% in $load_{OR}$ in the selected area by the exhaust temperature algorithm, as shown in Fig. 12. This was supported by the fact that when these outliers were excluded as in the overlap algorithm, the performance trends became similar to those of the output ratio algorithm.

The existence of these outliers would be explained as follows. The exhaust temperature algorithm is based on the assumption that the maximum exhaust temperature is the equivalent of the maximum load under varying inlet air conditions. However, this may not necessarily hold true for every situation because (1) whether this assumption is true depends to some extent on the design of the exhaust temperature control, and (2) there is a deviation of the actual measurement of the exhaust temperature from the theoretical value due to the spatial distribution of temperature and located points of measurement, and this deviation may vary according to inlet air conditions affecting the load measurement of Eq. (6) by this algorithm.

References

[1] Urban, L. A., 1975, "Parameter Selection for Multiple Fault Diagnostics of Gas Turbine Engines," ASME J. Eng. Power, **74-GT-62**, pp. 225–230.
[2] Li, Y. G., 2002, "Performance-Analysis-Based Gas Turbine Diagnostics: A Review," Proc. Inst. Mech. Eng., Part A, **216**(5), pp. 363–377.
[3] Diakunchak, I. S., 1992, "Performance Deterioration in Industrial Gas Turbines," ASME J. Eng. Gas Turbines Power, **114**(2), pp. 161–168.
[4] Lakshminarasimha, A. N., Boyce, M. P., and Meher-Homji, C. B., 1994, "Modeling and Analysis of Gas Turbine Performance Deterioration," ASME J. Eng. Gas Turbines Power, **116**(1), pp. 46–52.
[5] Gulen, S. C., Griffin, P. R., and Paolucci, S., 2000, "Real-Time On-Line Performance Diagnostics of Heavy-Duty Industrial Gas Turbines," ASME Paper No. 2000-GT-312.
[6] Gustafsson, J. O., 2006, "Condition and Performance Monitoring of Turbo Machinery by Thermodynamic Modeling," *Joint Baltic-Nordic Acoustics Meeting 2006*, Gothenburg, Sweden, Nov. 8–10.
[7] Zwebek, A., and Pilidis, P., 2003, "Degradation Effects on Combined Cycle Power Plant Performance—Part I: Gas Turbine Cycle Component Degradation Effects," ASME J. Eng. Gas Turbines Power, **125**(3), pp. 651–657.
[8] Zwebek, A., and Pilidis, P., 2003, "Degradation Effects on Combined Cycle Power Plant Performance—Part II: Steam Turbine Cycle Component Degradation Effects," ASME J. Eng. Gas Turbines Power, **125**(3), pp. 658–663.
[9] Zwebek, A., and Pilidis, P., 2004, "Degradation Effects on Combined Cycle Power Plant Performance—Part III: Gas and Steam Turbine Component Degradation Effects," ASME J. Eng. Gas Turbines Power, **126**(2), pp. 306–315.
[10] Kamboukos, Ph., and Mathioudakis, K., 2005, "Comparison of Linear and Nonlinear Gas Turbine Performance Diagnostics," ASME J. Eng. Gas Turbines Power, **127**(1), pp. 49–56.
[11] Taguchi, G., and Jugulum, R., 2002, *The Mahalanobis-Taguchi Strategy: A Pattern Technology System*, Wiley, New York.

Technology Options for Gas Turbine Power Generation With Reduced CO_2 Emission

Timothy Griffin[1]

Dominikus Bücker

ALSTOM Power Technology Center,
CH-5405 Baden-Daettwil, Switzerland

Allen Pfeffer
Alstom Power Plant Laboratories,
Windsor, CT 06095

ALSTOM Power R&D laboratories run various programs aimed at finding options that reduce or avoid CO_2 emissions through the following: (a) high efficiency power generation equipment to utilize fossil fuels with the lowest possible emissions, and (b) technologies to remove and sequester CO_2 created in power plants in an environmentally and economically favorable manner. In this paper, an overview of ongoing CO_2 mitigation activities for gas turbine power generation is addressed. Energy efficiency improvements for both new and existing fossil fuel power plants are briefly reviewed. Customer requirements for future power plants with reduced CO_2 emissions are discussed. Novel power generation cycles with exhaust gas recirculation for enhanced CO_2 removal are introduced and evaluated. Conclusions are drawn regarding their efficiency, energy consumption, and technical feasibility. [DOI: 10.1115/1.2898717]

Introduction

ALSTOM is a company that has been a leader in supplying equipment for the production of energy since its founding in Belfort, France in 1879. For this reason, the company takes a long-range view of the energy business and anticipates future directions in product development. We are aware of the present scientific concerns regarding greenhouse gas emissions and the role of fossil fuel use for power generation.

CO_2 emissions are produced from the utilization of fossil fuels in various sectors. The Power Sector (public electricity and heat production) represents both the largest emitting sector, and the fastest growing one. It accounted for 40% of global human generated CO_2 emissions in 2002, and CO_2 emissions from this sector are expected to grow from 9417 Mtons to 16,771 Mtons by 2030 (see Fig. 1).

Since fossil fuel-fired power plants exist at fixedlocations, they are easier to regulate than other major sources of CO_2. Should CO_2 reductions be deemed necessary, it is likely that the electricity and heat generation sector would be required to make significant contributions. Such actions will have a profound impact on the use of fossil fuels and the entire power generation business.

A variety of technical options are being evaluated, which could reduce such emissions. These include improved energy efficiency, fuel switching, renewable energy sources, and nuclear power. Alternatively, greenhouse gases, in particular, the CO_2 emitted from fossil fuel use, may be captured and stored. Such capture and sequestration technologies are required to achieve long-term stabilization of the CO_2 concentrations in the atmosphere necessary to avoid the potential consequences of global warming.

Sequestration of CO_2 entails the storage or utilization of CO_2 in such a way that it is kept out of the atmosphere. While a long-range strategy for decreasing dependence on fossil fuels is theoretically attractive, short-term major disruptions in our energy infrastructure have major economic consequences. Carbon capture and sequestration may be an effective transitional strategy.

Despite its environmental importance, there is currently little market motivation for investment in CO_2 sequestration technologies, due to the absence of a CO_2 tax for power plants. (Most projections for sequestration of CO_2 generated by combustion of coal do not envision substantial capture until after 2015 [2].) Uncertainties in the long-term forecasting of fuel prices (coal versus natural gas) also present challenges in determining the focus of research efforts. A market opportunity that exists today for CO_2 capture from power plants is enhanced oil recovery [3]. Injecting CO_2 into oil wells can significantly increase their yield and recent analyses have indicated a relatively high value for CO_2, linked to oil prices, which is close to the current costs for CO_2 removal from fossil fuel-fired power plants. This market is small compared to the total amount of carbon emitted, but is expected to be the proving ground for the capture and sequestration technologies eventually deployed. Enhanced oil recovery thus represents an important opportunity for market introduction of CO_2 removal technologies.

In discussion with various stakeholders, the company has summarized the most important customer requirements for CO_2 removal technologies for gas turbines. This information is summarized in Table 1, in which the importance of various parameters is estimated for both the enhanced oil recovery and for CO_2 sequestration markets.

Table 1 can be used to benchmark various technological options for CO_2 removal. While both markets have similarities in their customer requirements (high process efficiency and low CO_2 removal costs), there are some important differences. The enhanced oil recovery markets exist already and thus need solutions with a short time to market and the possibility to perform a demonstration quickly. Injecting CO_2 into an oil well slowly displaces and extracts oil over time; thus, there are fewer requirements placed on the operational flexibility and reliability of the CO_2 removal process. Also, the purity of CO_2 for enhanced oil recovery is higher than what would be required if the CO_2 is stored in places where it cannot get out.

Options for Reducing Energy Related CO_2 Emissions

The company has begun the evaluation and development of CO_2 removal technologies in power plants. If these options can be found to be technically and economically feasible, they could play a substantial role in limiting greenhouse gas emissions and allow for the continued use of established fossil fuel infrastructure in an environmentally acceptable manner. Our gas turbine related programs include enhanced capture of CO_2 (ENCAP) (EU Project No. SES6-CT-2004-502666), where the main focus is placed on adapting combustion technology to burn hydrogen rich fuels with low NO_x emissions and evaluating novel cycles, AZEP [4] where

[1]Present address: University of Applied Sciences, Northwestern Switzerland, CH-5210 Windisch, Switzerland.

Contributed by the International Gas Turbine Institute (IGTI) of ASME for publication in the JOURNAL OF ENGINEERING FOR GAS TURBINES AND POWER. Manuscript received September 1, 2005; final manuscript received October 3, 2007; published online April 24, 2008. Review conducted by Dilip R. Ballal.

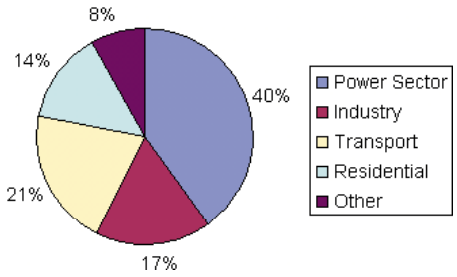

Fig. 1 2002 total CO_2 emissions from fossil fuel combustion by sector (values taken from Ref. [1])

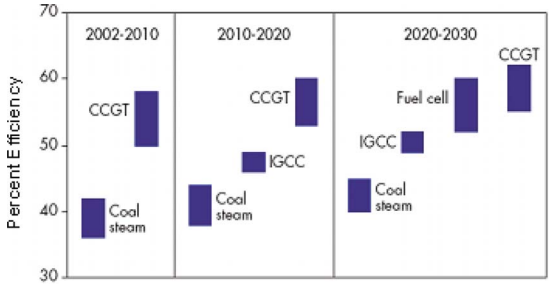

Fig. 3 Evolution of efficiency in various power generation technologies. Past and future (from Ref. [1]).

we are working on the integration of oxygen transport membranes into gas turbine combustors, and Gaszep [5] where we are studying CO_2 capture in an oxygen-fired gas turbine.

Improved Efficiency and Fuel Switching. In 2002, over 6000 Mtons of CO_2 were emitted by coal-fired power plants. In contrast, less than 2000 Mtons CO_2 were produced by natural-gas-fired plants and roughly 1000 Mtons were emitted by oil-fired plants [1].

There are large variations in CO_2 emissions per kW h of electricity generated due to differences in generation efficiency, fuel selection, and plant age. Figure 2 summarizes information for a variety of coal and natural gas based power generation technologies. Simply switching from conventional coal power generation to a modern natural gas-fired gas turbine combined cycle power plant can reduce the emitted CO_2 per kW h by almost a factor of 3.

Additionally, improvements in power plant electrical efficiency will also reduce the emitted CO_2. Latest designs in combined cycle heavy gas turbines can achieve efficiencies of nearly 60% (based on lower heating value), with a high degree of operational flexibility. Hence, there is a potential today for up to 30% reduction in CO_2 emissions by raising overall efficiency from the 40% level to the 60% level. Further efforts are being made to continually increase efficiency and reduce power plant emissions in this way. Figure 3 summarizes the current efficiencies achieved in power generation and predictions regarding evolutionary improvements in the future.

Currently about 20% of the world's generating capacity is over 30 years old. Much of this capacity is in the form of older, low efficiency coal based power plants. In the coming decade, much of this plant capacity will have to be replaced. To the extent that these replacement power plants will be gas fired, there will be a net reduction of CO_2 emissions in many of the countries with developed economies. However, recent increases in the price of natural gas in some areas have highlighted the importance of considering all economic aspects of this problem. Of course, as fuel prices increase, the driver for efficiency is stronger. Thus, for economical and environmental reasons, the development of high efficiency and highly reliable GTCC power systems remains a key.

Although substantial reductions in emissions of CO_2 could be achieved by increases in efficiency of energy conversion and utilization, these reductions alone may not be sufficient to achieve atmospheric CO_2 stabilization. This is mainly due to the projections that electricity demand will increase worldwide by over 2% per year for the next decades and this large increase will more than offset conservation and efficiency increases. Noncarbon or renewable sources are not foreseen to be sufficient to handle this need, and large decreases in carbon emissions per kW h are required.

Table 1 Customer requirements for CO_2 removal technologies (Scale: 1 (least important) to 5 (most important))

	Enhanced oil recovery	CO_2 sequestration
Low efficiency penalty	4	4
Operation flexibility	2	4
Low CO_2 avoidance cost	5	5
Reliability and availability	3	4
Time to market	5	2
Retrofittable to current GTs	1	4
Maximum removal rate of CO_2	3	5
Fuel flexibility	3	3
Suitability for demo scale	5	2

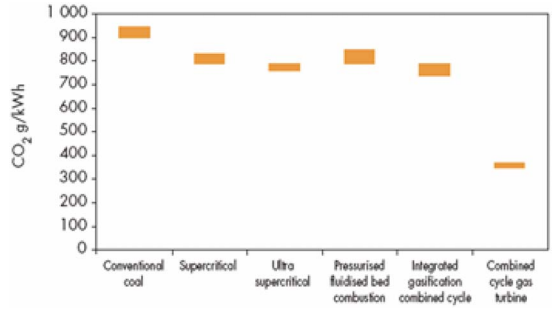

Fig. 2 CO_2 emission rates from various fossil fuel technologies. The emissions shown in this chart are based on a range of efficiencies (from Ref. [1]).

Carbon Capture Technologies

The company has thus also directed effort towards the capture and sequestration of CO_2 in the exhaust of fossil fuel-fired power plants (typically in CO_2 concentrations of 3–15% by volume). We are actively evaluating the three main possibilities for CO_2 capture:

- precombustion methods (fuel decarbonization)
- combustion in O_2/CO_2 atmospheres (oxyfuel firing)
- postcombustion capture, possibly including recycle of exhaust gas to enhance the removal efficiency

For the purpose of this paper, we will concentrate on methods for producing a concentrated stream of CO_2 from a gas turbine and trust that the technology to handle the CO_2 downstream will be developed in projects such as CASTOR (EU Project, "CO_2—from Capture to Storage").

Fuel Decarbonization. Prior to combustion, several methods can be adopted to extract H_2 from hydrocarbon fuels. These processes result in the production of "syngas," which can be further treated to yield CO_2 and H_2; the former is recovered while the latter is subsequently combusted. Different methods of hydrogen production exist, i.e., steam reforming, gasification, and partial

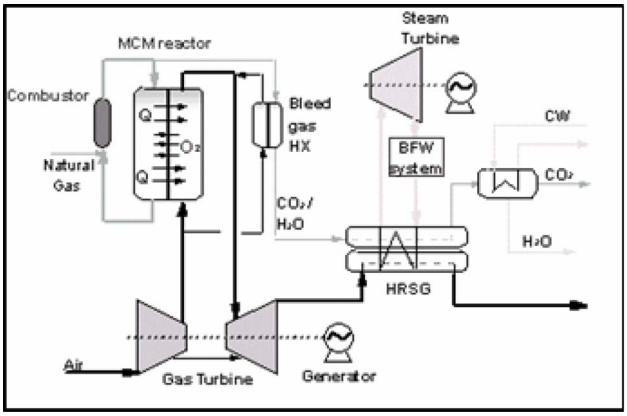

Fig. 4 Zero emission gas turbine-based power generation concept (including an integrated membrane for production of oxygen)

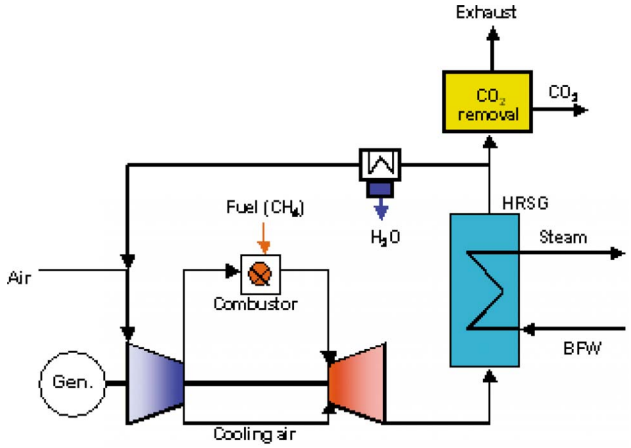

Fig. 5 Exhaust gas CO_2 removal in a gas turbine with exhaust gas recirculation

oxidation. The CO_2 has to be removed from the resulting hydrogen gas mixture by a CO_2 removal process, such as amine scrubbing. Thus, both a syngas manufacturing plant and a CO_2 removal and transport infrastructure are required for fuel decarbonization, significantly adding to the total plant capital cost. Furthermore, the utilization of hydrogen rich synthesis gas requires modifications to currently available gas turbines. One of the key issues is the optimization of the combustion technology to deliver economically and environmentally advantageous systems. Recent cost estimates for integrated gasification systems with CO_2 capture have been reported [6].

Oxyfuel Firing. The combustion in O_2/recycled flue gas includes different power generation cycles using pure or highly enriched oxygen as the oxidant instead of air [7–9]. The exhaust gas consists mainly of H_2O and CO_2; the H_2O can be separated easily by condensation. In all of these cycles, the working fluid of the main power turbine is changed from an air-based gas containing mainly N_2 to fluid containing mixtures of carbon dioxide and steam. To achieve the high efficiencies quoted in the literature, these power turbines must be operated at the high temperatures of today's air-based gas turbines. Unfortunately, a significant R&D and field validation effort would be required to realize such a novel gas turbine.

Additionally, when using conventional cryogenic processes for air separation, a substantial energy penalty is incurred due to the large power requirements of producing pure oxygen. This usually results in a total loss of electrical efficiency of up to 10% points. Substantial improvements are envisioned for the application of future air separation membrane technology to produce the oxygen required for the combustion process. However, such improvements cannot be envisioned for at least a decade.

Oxygen Membrane Concepts for Zero Emissions. The AZEP concept, as shown in Fig. 4, has the potential to offer low CO_2 avoidance costs without significant efficiency penalty [10(a),10(b)]. Within the AZEP concept, the combustor in an ordinary gas turbine is replaced by the mixed conducting membrane (MCM) reactor, which includes a combustor, an air separation membrane (MCM), and a high temperature heat exchanger (for reactor details, see Ref. [4]). In the membrane section, 20–30% of the oxygen in the air stream is transported through the MCM and serves as oxidant within the AZEP combustor.

Unlike oxyfuel cycles, within the AZEP concept the gas turbine and its auxiliary systems can be based on slightly modified standard, air-based equipment. This approach limits the need for the development of an entirely new cycle—and its associated new equipment—substantially reducing technical and commercial risks.

The biggest challenge in commercializing the AZEP process is developing the required air separation membranes. Despite large investment in such membrane systems, there is still at least ten years of development required before they can be applied commercially for large, heavy-duty gas turbines. Material thermal stability issues within the membrane reactor also limit the turbine inlet temperature and, thus, the overall process performance. Higher efficiencies can be achieved with auxiliary firing within a sequential combustor; this, however, leads to CO_2 emissions from the process.

Postcombustion Capture of CO_2. In a conventional tail-end capture process, CO_2 is captured after the flue gas has expanded in the gas turbine expander, i.e., the operating pressure of the CO_2 separation unit is 1 atm. The major drawback of this is that the CO_2 partial pressure is very low due to the low CO_2 concentrations in gas turbine flue gases (typically 3–4 vol % with a natural gas fuel) and hence large and expensive equipment is needed to capture the CO_2. The CO_2 concentration at the stack, and hence its partial pressure, can be raised by recycling part of the flue gases to the gas turbine compressor (see, for instance, U.S. Patent No. 5,832,712, Rønning et al., 1998), but it still remains quite low (~6–10 vol %). Such a process is shown schematically in Fig. 5.

Several different methods to remove CO_2 from a gas stream exist, including absorption and adsorption techniques. These CO_2 capture processes have significant energy requirements, which reduce the power generation plant's efficiency by approximately 10% points. Using CO_2 separation methods based on chemical absorption, physical absorption or adsorption, it is possible to recover 85–95% of CO_2 in the fuel. CO_2 can also be captured by utilizing solid chemicals that react with the gas in solid form [11]. These chemicals can be removed from the gas stream more easily and with less energy intensity than traditional solution scrubbing techniques. The solids can be regenerated producing a relatively pure CO_2 stream for utilization or sequestration.

The carbon dioxide capture project (CCP) has evaluated a number of processes for exhaust gas capture of CO_2 in a combined cycle gas turbine plant with exhaust gas recycle [12]. This work has indicated a large potential for improving such processes (increasing efficiency and lowering the CO_2 avoidance costs) by integrating the CO_2 absorption plant into the GT heat recovery steam generator. Avoidance costs lower than \$30/ton CO_2 were reported, with only a 5% point loss of efficiency. Of course, the performance of such processes is largely dependent upon the amount of exhaust gas that can be recycled without compromising

Table 2 Postcompression CO_2 capture: Effect of carbon dioxide removal rate

Case	O_2 supply	CO_2 removed in separation unit (%)	Total CO_2 removed (%)	CO_2 molar fcn entering separation unit
1	Air	80	61	0.04
2		20	26	0.08
3	Enriched air	80	93	0.05
4		20	53	0.14

combustion stability.

The following assumptions have been made.

Postcompression Capture of CO_2 in Gas Turbines. A new variation, applicable for gas turbine cycles with flue gas recycle, is to relocate the CO_2 separation process to a location after the compressor or to an intercooling stage. By doing so, the partial pressure of carbon dioxide is significantly raised, which improves the driving force for separation, and the volume of the gas to be treated is vastly decreased. These two factors will reduce the size of the CO_2 separation equipment along with its energy flows and, therefore, decrease the cost per avoided ton of carbon dioxide emitted. Furthermore, heat sources such as intercooling can be used to drive the separation process. This type of process is so-called "postcompression capture."

A disadvantage of postcompression CO_2 separation is that large heat exchangers are needed to cool down and reheat the working fluid if a cold CO_2 separation process is utilized, for instance, amine scrubbing, or a low temperature CO_2 membrane. For good power plant performance, it is critical to retain the compressor outlet temperature and thus keep fuel consumption low. If CO_2 removal can be integrated with an intercooled compressor, then this disadvantage could be mitigated.

Examining postcompression capture closer, the design purpose is to raise the partial pressure of carbon dioxide in the separation unit. Table 2 summarizes an examination of the impact of CO_2 removal degree within the separation unit on the molar fraction of CO_2 within the separation unit. Calculations were performed for a generic large-scale gas turbine with natural gas firing. The cycle schematic is shown in Fig. 6.

- The recycle ratio at the outlet of the heat recovery steam generator is chosen in all cases to yield an air excess ratio (lambda) of 1.2 in the combustor.
- For the "enriched air" cycles, compressed oxygen is supplied directly to the combustor. A mass flow ratio of 0.63 between fresh air and oxygen supply has been chosen.

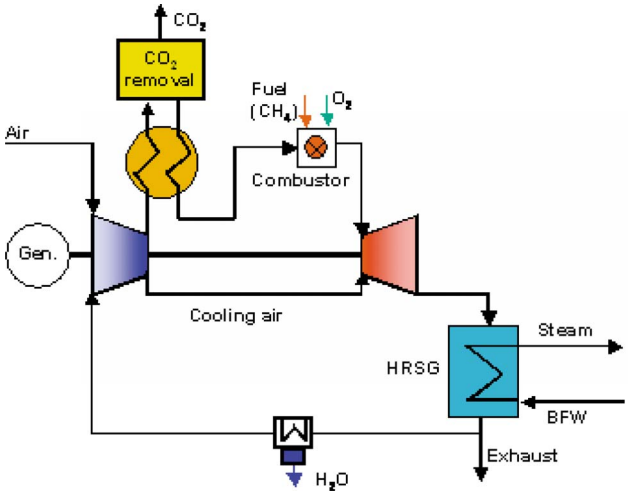

Fig. 6 "Postcompression" CO_2 capture

If most of the carbon dioxide in the compressed working fluid is removed (80% or above), then low carbon dioxide concentrations will be found in the exhaust gas, the recycle to the compressor, and consequently, in the carbon dioxide capture unit, as indicated in Cases 1 and 3. (The inlet air may be enriched with oxygen (Cases 3 and 4), allowing a higher flue gas recycle ratio and higher CO_2 concentrations in the separation unit.) While this high-separation strategy will decrease the amount of carbon dioxide leaving the cycle in the exhaust, the concentration of carbon dioxide in the cycle is not allowed to build up. In summary, if most of the carbon dioxide is removed after the compressor, only moderate carbon dioxide partial pressures will be found during separation and the design purpose is compromised. This type of configuration is described by a patent filed with the French National Institute of Industrial Property (INFI), application number FR 0108000, and is described by Cases 1 and 3 in Table 2 for an air-blown and an oxygen-enriched air-blown cycle, respectively.

If only a minor part of the carbon dioxide is removed in a postcompression CO_2 capture process, it is possible to significantly increase the partial pressure of CO_2 in the separation unit, especially in combination with oxygen-enriched air. Table 2, Case 4 illustrates this effect, whereby an overall carbon dioxide capture of 53% is possible when separating only 20% of the carbon dioxide in the working fluid in conjunction with an oxygen enriched-air feed. This is possible as carbon dioxide is allowed to build up in the cycle through a higher carbon dioxide concentration in the flue gas. In order to minimize the release of carbon dioxide to the atmosphere, the combustion gases may be enriched with oxygen, which allows a higher flue gas recycle ratio and decreases the flow rate to the stack. An example of this can be seen comparing Cases 2 and 4 in Table 1. By separating only a part of the carbon dioxide from the working fluid, equipment capital savings may be made through decreasing the separation demand on the equipment and by increasing the driving forces. The optimal removal efficiency will be determined economically in a trade-off between the cost of releasing more carbon dioxide to the atmosphere (assuming a CO_2 tax or loss in value associated with less CO_2 production for enhanced oil recovery) and the operational and capital savings associated with a more favorable separation process.

The GT26 architecture offers a very flexible system, which is well suited to the realization of "postcompression" CO_2 capture. The concept of postcompression CO_2 removal could be adapted to this engine, as indicated in Fig. 7. In contrast to the previous case of an intercooled engine, here only a part of the compressed medium is cooled.

In particular, the following features of the GT26 are relevant

- Roughly 25% of the total incoming air is removed from the compressor, cooled, and reinjected into the cycle as cooling

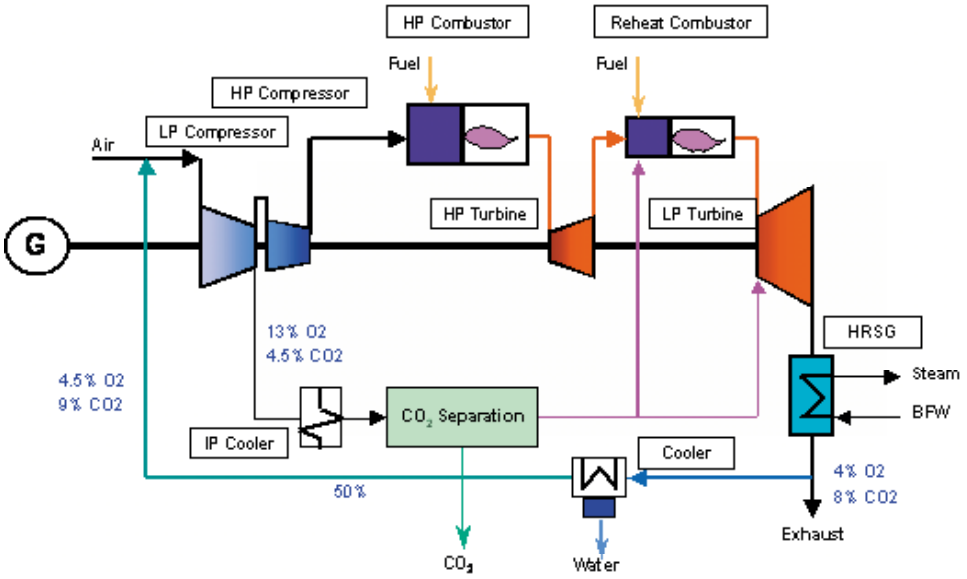

Fig. 7 "Postcompression" CO_2 capture as applied to the GT26 cycle

air for the secondary (SEV) combustion chamber and for the first stage low-pressure turbine (LPT). For this reason, its auxiliary systems can be more easily modified to handle postcompression CO_2 capture than those of competing engines.

- The sequential combustion of the GT26 allows much greater flexibility in handling the challenges of low-excess oxygen, zero emissions combustion. (1) Staged concepts can be used allowing a sensible management of the fuel-air equivalence ratio. (2) The high inlet temperatures of the SEV combustor are suited to handle the challenges of self-igniting a highly diluted mixture of fuel steam and carbon dioxide at low oxygen excess concentrations.
- The high level of operational flexibility of the GT26 would allow an easy start-up and shutdown of the CO_2 removal process and allow CO_2 mitigation at part load conditions.

These last two features of the GT26 also make it well suited for application in exhaust gas CO_2 removal concepts with exhaust gas recirculation.

Postcompression Capture for the GT26. An investigation has been started to assess different options for postcompression CO_2 removal from the GT26. The main goal is to identify solutions that enable a partial removal of CO_2 from the process at low additional investment cost and with a low penalty on the thermodynamic cycle efficiency. Another major goal is to assess options for retrofittable solutions, i.e., the possibility to add postcompression CO_2 removal to an existing GT26 in the field.

A retrofittable solution will have to meet the following requirements.

- Only streams that are removed from and reinjected to the gas turbine in conventional operation may be treated in the CO_2 separation unit. (In the GT26, these are the intermediate-pressure and high-pressure cooling flows.)
- No major changes to the turbomachinery should be necessary. In particular, the arrangement of the turbomachinery shall not be changed by the process modifications.

While these restrictions constrain the CO_2 removal rate of the total cycle to values below ~30%, they offer the potential for retrofit CO_2 capture at minimum additional cost. Higher total cycle CO_2 removal rates can be achieved if the following is observed.

(a) Fresh air and recycled flue gas are compressed separately in different compressors. This increases the concentration and thus the mass flow of CO_2 at the inlet of the separation unit and decreases the flow of CO_2 that flows through the engine without being treated.

(b) A higher mass flow is recycled and led to the separation unit than what is needed for cooling purposes. The surplus flow is reinjected to the gas turbine at the inlet of the HP compressor, or at the inlet to the first or sequential combustion chambers, respectively. The potential CO_2 removal rate of this option is restraint by the maximum flue gas recycle rate, which in turn is restricted by the demand of oxygen for combustion (stoichiometric case).

Figure 8 shows the potential for CO_2 removal of the retrofittable solutions and the more advanced options (a) and (b) as discussed above.

While the more advanced options clearly offer a higher potential for CO_2 removal, they are associated with higher efficiency penalties and higher additional investment costs. The retrofittable solution on the other hand only requires moderate changes to the conventional GT26 cycle and minimizes efficiency losses. Therefore, the retrofittable solution is expected to have an attractive economic potential. Targets for the cost per ton avoided CO_2 emission as a function of the cycle's CO_2 removal rate are shown in Fig. 9.

Evaluation of CO_2 Removal Technologies

In this section, the ability of the presented CO_2 removal technologies to address the customer requirements is discussed.

By applying exhaust gas recycle to postcombustion CO_2 capture, the performance can be greatly improved due to the increase in CO_2 concentration. The potential reported for process efficiency and cost of CO_2 removal is attractive [11]. About 85–95% of the CO_2 can be captured but the economic optimum may be at a much lower capture rate. Exhaust gas capture can be retrofitted to existing gas turbines, and various removal technologies (for example, amine scrubbing) are already available, giving a short time to market and the potential for field demonstrations. The

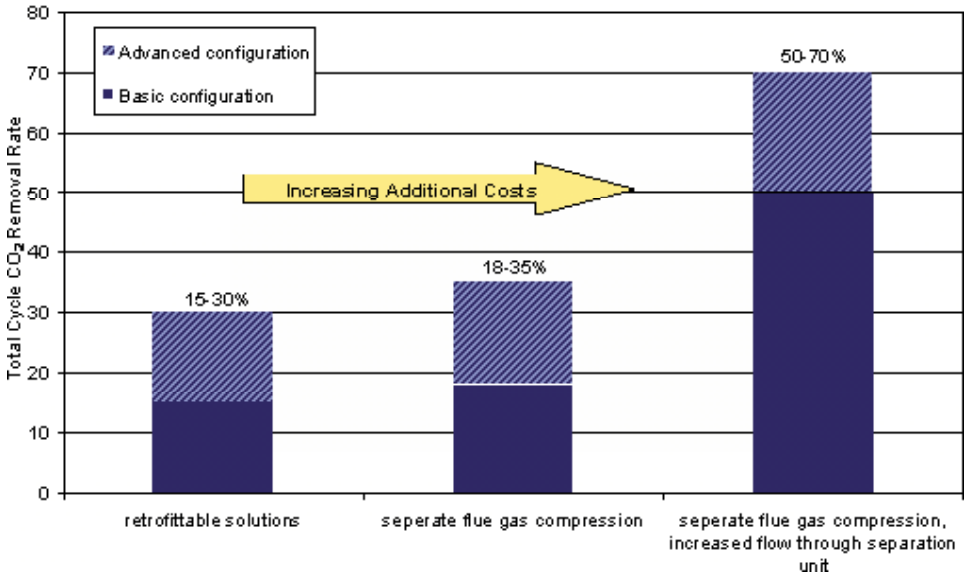

Fig. 8 Expected CO_2 removal rates for postcompression capture options applied to the GT26

technology is also applicable to the wide range of fuels typically employed in gas turbines. Additionally, the application of exhaust gas CO_2 removal should not considerably affect the operational reliability of the plant, since it should be possible to bypass the CO_2 removal unit, if necessary, due to process upsets.

Postcompression CO_2 capture, in which CO_2 is removed from a part of the overall compressor flow at elevated pressures, has the potential to remove CO_2 at lowest possible per unit cost, especially if the CO_2 removal device can be integrated into existing hardware (coolers for GT26 or intercoolers). However, this option has a limited overall amount of CO_2 that can be removed. This may restrict the market application of the technology. Additionally, the concept is most suited to physical CO_2 separation methods, such as membranes, giving it potentially a long time to market introduction. This option would be markedly improved by ongoing developments in CO_2 membrane technology, aimed at membrane use at higher process temperatures. In principle, this technology can be retrofitted into existing gas turbines with postcompression air extraction, or intercoolers.

The AZEP process offers potentially the best overall cycle performance, provided that its ceramic membrane reactor can be operated at temperatures approaching today's gas turbine combustors [4]. If the temperature of the ceramic components is limited, either the performance will suffer or postmembrane auxiliary firing will produce CO_2 emissions. The AZEP process is completely dependent upon the operational reliability of the ceramic components, which has not yet been validated, and this represents its greatest potential weakness. Market introduction in large scale GTs will not be possible until field validation of high temperature, ceramic, air separation membranes is completed. Ceramic air separation membranes are also highly sensitive to any impurities present in fuels, thus limiting the fuel flexibility of the process.

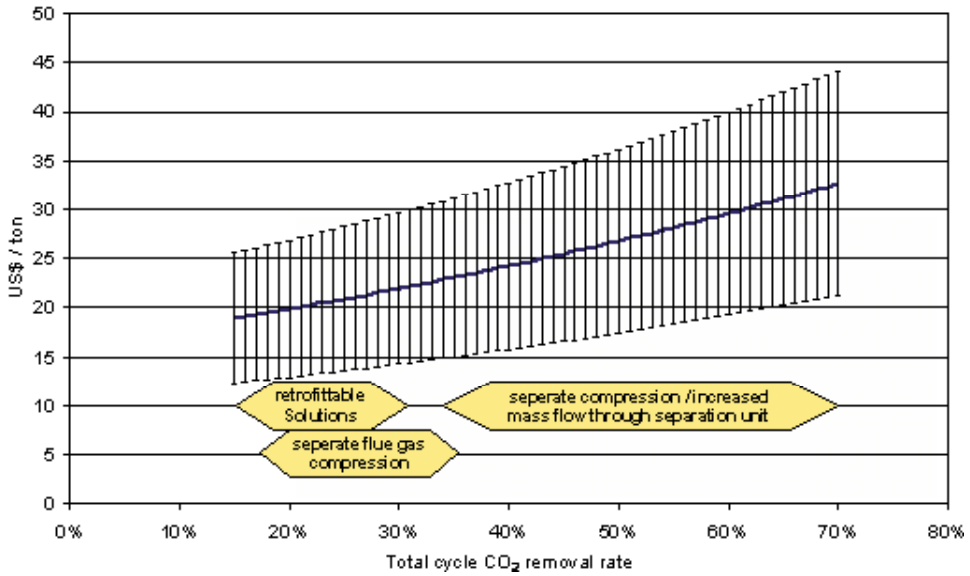

Fig. 9 Expected costs per ton avoided CO_2 emission for postcompression capture options applied to the GT26. (These costs include liquefaction and compression of CO_2 to 100 bars, but exclude costs for its transport and storage.)

Table 3 Evaluation of different CO_2 mitigation techniques to gas turbines. References 6, 10(a), 10(b), and 11 used in the evaluation.

	Post comb. capture with exhaust gas recycle	Post compression CO_2 removal	Fuel decarbonization	AZEP
Low efficiency penalty	0	+	−	+
Operational flexibility	0	−	−	−
Low CO_2 avoidance cost	+	+	−	+
Reliability and availability	+	0	−	−−
Time to market	+	0	+	−
Retrofittable to current GTs	+	+	−	−−
Maximum removal rate of CO_2	+	−	++	+
Fuel flexibility	0	0	+	−−
Suitability for demo scale	+	−	0	+
Overall ranking	1	2	3	4

Finally, due to the size of the AZEP membrane reactors and the necessary GT design modifications, this technology cannot be considered retrofittable.

Fuel decarbonization is an attractive option for a number of reasons. Nearly all the CO_2 can be removed from synthesis gas under high pressure, enabling much smaller volume flows and the use of high-pressure adsorption technology as an alternative to monoethanolamine (MEA) scrubbing. The necessary equipment is smaller and less expensive than the scrubbers required for tail-end capture. However, additional reactors are required to generate the synthesis gas by a combination of steam reforming and/or partial oxidation and water-shift reaction. The technology for fuel decarbonization is more or less already commercially available, and thus there is a short time to market. Over all, the energy penalty for fuel decarbonization is on the order of 10% points (absolute). The availability and reliability of gasification processes, while improving, is still a major issue. Equipment redundancy (e.g., spare gasifiers) may address this, but adds considerably to the already high capital costs. The CO_2-capture rate is comparable to the one achieved by MEA scrubbing. NO_x levels in the exhaust gas will be higher than for natural gas-fired turbines using comparable combustion technology due to the difficulty of burning hydrogen.

Table 3 summarizes the ability of the discussed methods to satisfy customer requirements for CO_2 removal taking the comments above for its analysis. The apparent winner technology from this comparison is postcombustion CO_2 removal with exhaust gas recycle. It must be stated, however, that the assessment of this option is based mainly on an external evaluation performed by the CCP. Additionally, we have considered the potential to employ the sequential combustion technology of the GT26 to this cycle. As mentioned above, sequential combustion potentially offers higher combustion stability at low oxygen excess concentrations, and thus would allow greater recycle ratios. Although this cycle has not received any "++" scores, it appears to have no major weaknesses, and its retrofittability and short time to market (i.e., low risk) are great advantages.

Even though fuel decarbonization may not be the first choice under environmental and economic aspects, it is a very attractive "least-effort/least-risk solution" from the point of view of a gas turbine supplier. Gas turbines working with synthesis gas are state of the art; the potentially critical components of the process are located upstream of the gas turbine, which are delivered by third parties. This technology also has an advantage due to its fuel flexibility; coal, residual oil, or even natural gas may be used. Security of fuel supply and the associated stable fuel price may drive the medium term development of fuel decarbonization.

Conclusions

There is no single, all-encompassing, technological option for greenhouse gas mitigation; rather, there will be a variety of actions that will be needed. Gas turbines, as a proven technology and with a fast growing fraction of the generating capacity market, will significantly contribute to the reduction of greenhouse gas emissions per unit of energy produced.

In this paper, we have discussed various technological options for CO_2 mitigation in gas turbines. In particular, the development of concepts involving exhaust gas recirculation appears attractive in satisfying customer requirements for CO_2 removal. Technological options, in parallel with more integrated emission management solutions (emission monitoring and reporting, and emission trading), shall provide the industry a cost-effective way to comply with the challenges posed by climate change and the global environment.

References

[1] World Energy Outlook, 2004, IEA—International Energy Agency, Paris, France.

[2] Gielen, D., 2003, "The Future Role of CO_2 Capture and Storage Results of the IEA-ETP Model," IEA/EET Working Paper.

[3] Hustad, C.-W., Austell, J. M., and Coleman, D. L., 2004, "Fiscal Mechanisms to Promote CO_2 for Enhanced Oil Recovery in the North Sea: Understanding the CO_2 Value Chain," Seventh International Conference on Greenhouse Gas Control Technologies, Vancouver, Canada, September 5–9, Paper No. 224.

[4] Griffin, T., Sundkvist, S. G., Aasen, K., and Bruun, T., 2003, "AZEP: Advanced Zero Emissions Power Plant," ASME Paper No. GT-2003-38426.

[5] DTI OST/FORSIGHT LINK Programme—Natural Gas Fired Zero Emissions Powerplant (GAS-ZEP), Project Reference No. D01; Wall, R. A., 2004, "Gas Powered Zero Emissions Powerplant," Bled Conference CAME GT Second International Conference on Industrial Gas Turbine Technologies, April 29–30.

[6] Holt, N., Booras, G., and Todd, D., 2003, "Summary of Recent IGCC Studies of CO_2 Capture for Sequestration," 2003 Gasification Technology Conference, San Francisco, CA, October 12; www.gasification.org/Docs/2003Papers/31Holft.pdf

[7] Sanz, W., Jericha, H., Moser, M., and Heitmeir, F., 2004, "Thermodynamic and Economic Investigation of an Improved Graz Cycle Power Plant for CO_2 Capture," ASME Paper No. GT2004-53722.

[8] Smith, J. R., Surles, T., Marais, B., Brandt, H., and Viteri, F., 2000, "Power Production with Zero Atmospheric Emissions for the 21st Century," Fifth International Conference on Greenhouse Gas Control Technologies, Cairns, Australia, August 13–16.

[9] Mathieu, P., 1998, "Presentation of an Innovative Zero Emission Cycle for Mitigation of the Global Climate Change," Int. J. Thermodyn., **1**, pp. 21–31.

[10] (a) Eklund, H., Sundkvist, S. G., Wilhelmsen, K., Aasen, K., and Griffin, T., 2003, "Development of a Membrane-Based CO_2 Emission-Free Gas Turbine System," *Proceedings of the Seventh International Conference on Technologies and Combustion for a Clean Environment*, Lisbon, July; (b) Bücker, D., Holmberg, D., and Griffin, T., 2004, "Techno-economic Evaluation of a Power Plant Using Mixed Conducting Membranes," *CCP Technical Summary Volume*, in press.

[11] Contarini, S., Barbini, M., Del Piero, G., Gambarotta, G., Mazzamurro, G., Riocci, M., and Zappelli, P., 2002, "Solid Sorbents for the Reversible Capture of Carbon Dioxide," 6th IEA Greenhouse Gas Technology Conference, Kyoto, 2002.

[12] Chinn, D., Eimer, D., and Hurst, P., 2004, "Post Combustion: Best Integrated Technology (BIT)," Third Annual DOE/NETL Conference, Alexandria, VA, May.

Unsteady Heat Transfer Measurements from Transonic Turbine Blades at Engine Representative Conditions in a Transient Facility

W. D. Allan
Department of Mechanical Engineering,
Royal Military College of Canada,
Kingston, ON, K7K 7B4, Canada
e-mail: billy.allan@rmc.ca

R. Ainsworth

S. Thorpe

University of Oxford,
Oxford OX1 2JD, United Kingdom

The unsteady heat transfer measurements about a transonic turbine blade at engine representative Mach and Reynolds numbers are presented. High density, fast-response thin film gauges are employed at the midheight streamline. A description of the novel development of gold gauges together with a brief overview of their calibration and signal processing is presented. Detailed time and phase-averaged measurements have been obtained, providing insight into the role of upstream nozzle guide vane (NGV) wakes and shock features. These heat transfer results compliment recent fast-response aerodynamic results on this and similar transonic profiles, which highlight the dominance of the upstream vane-rotor interaction over convected wake segments, particularly in light of unsteady turbine blade loading. From a heat transfer standpoint, however, while the periodic shock events contributed to abrupt, localized heat transfer enhancements, the influence of NGV wake segments on the boundary layer could not be discounted when duration of unsteadiness was considered. [DOI: 10.1115/1.2898836]

Keywords: turbomachinery, heat transfer, turbine, internal aerodynamics

Introduction

Modern gas turbine engines have undergone tremendous advances in performance and efficiency in recent years. This has come about through developments in control systems, advanced materials, and complex internal aerodynamic designs, made possible through advances in design and manufacturing techniques. In a comprehensive review of turbomachinery research, Dunn [1] articulated that the focus on driving turbine inlet temperatures as close to stoichiometric values would not let up. Improvements can also be realized through careful consideration of the losses on the gas turbine system through drawing work from the system itself for such auxiliary tasks as secondary power generation, aircraft cabin conditioning, or cooling of the engine components. Minimization of bleed requirements has a direct positive effect on the overall performance of the gas turbine and, consequently, on its overall efficiency. This has led researchers over the years to focus on the high temperature components to explore their specific operating environments and the challenges that they pose to the gas turbine designer. Understanding primary and secondary flows in modern engines is not sufficient, neither is the characterization of an average operating environment. The transient and unsteady flow phenomena contribute greatly to the hostile conditions under which a transonic turbine operates. Much remains to be done to validate the computational fluid dynamics (CFD) codes, which are widely used in complex designs of the day. Prediction of blade stresses, deflections, operating environment, and ultimate blade life is dependent on a detailed understanding of the aerothermal environment in which turbine blades operate.

Developments in turbine research at the University of Oxford have been widely reported beginning with steady two-dimensional transonic experiments that saw the development of heat transfer measurement techniques. A novel transient facility was introduced to the research community in 1977. The isentropic light piston tunnel (ILPT) enabled the third dimension along with the introduction of high frequency experimental measurements to be made in the rotor's frame of reference. This led to complementary studies on pressure and heat transfer on a modern transonic turbine under engine representative conditions. The unique use of surface-mounted, unsteady pressure instrumentation, developed for that aspect of the experiments, generated much interest and led to many successful applications by researchers. While the unsteady pressure observations were reported in the literature, unsteady heat transfer results have yet to be released to the research community. Thus, the objective of this paper is to present some highlights of the unsteady heat transfer observations taken from the midheight streamline of the transonic rotor blades using thin film gauges especially developed for this application.

Related Research

The use of surface-mounted heat transfer gauges to make high frequency aerodynamic measurements was described by Schultz and Jones [2]. They demonstrated that an electrical analog would precisely model the transfer of heat between a semi-infinite surface and a convective fluid. The technique was applied to the transient cascades mounted in the ILPT, and was very effective for the short duration for which a significant gas-to-wall temperature difference was present. A 0.62 scale rotor was installed necessitating a modification in approach due to the need for metal substrates. However, it was shown that three-dimensional structures behaved as essentially semi-infinite 2D structures for the duration of the experiments [3].

Historically, heat transfer measurement techniques were used in cascades to measure the effects of passage of upstream wakes first discussed by Meyer [4] and modeled using rotating bars over the cascades reported by Doorly and Oldfield [5,6] and Doorly et al.

Contributed by the International Gas Turbine Institute for publication in the JOURNAL OF ENGINEERING for GAS TURBINES AND POWER. Manuscript received December 4, 2006; final manuscript received November 29, 2007; published online April 23, 2008. Review conducted by Je-Chin Han.

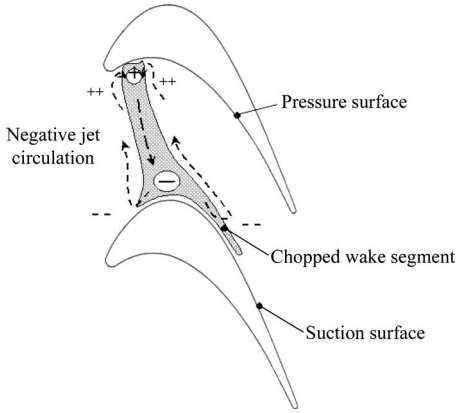

Fig. 1 The negative jet effect of a wake segment in a rotor passage

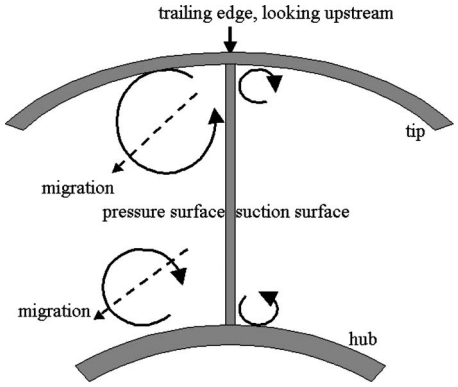

Fig. 3 The horseshoe (passage) vortex

[7]. Amongst their results was the significant observation that heat transfer was enhanced up to 500% by the presence of the wakes and their influence on the boundary layer. The impact of the wakes was observed to propagate a negative jet effect reported by Hodson [8], measured using hot wire anemometers on a range of turbine configurations. Figure 1 shows a schematic of the negative jet effect.

Mayle and Dullenkopf [9,10] first reported that turbulent spots were generated by the presence of the wake segment. This resulted in enhanced heat transfer from the high temperature gas to the blade surface, a phenomenon that prominently figures in this paper. The transonic nature of the flow resulted in the obvious presence and implication of shock waves both from the upstream stators and their reflections from adjacent rotor blades.

A number of experiments were reported from the Oxford facility by Johnson et al. [11,12] and summarized by Jones [13] among others. A rotating bar mechanism was employed upstream of a cascade to explore the combined effects of wakes and shocks. Another secondary flow of interest is the horseshoe vortex generated at the leading edge of a rotor blade, as the end wall boundary layers roll up with the arrival of the rotor. Figure 2 shows a sketch of the proposed development of the horseshoe vortex. The legs of this vortex sweep downstream and become the passage vortices reported and observed, respectively, by Herzig et al. [14] and Langston [15]. Figure 3 is a sketch of the migration of the legs of the horseshoe vortex (the passage vortices), looking upstream from the trailing edge.

The migration of the counter-rotating passage vortex components has been reported by Graziani et al. [16] and observed using laser Doppler velocimetry in stator rows by Herbert and Tiederman [17], then explored further by Sieverding [18]. While passage vortices are considered to be present in the rotor, they are equally considered to be encountered downstream of stator passages by the rotor leading edges. The periodic cutting of these vortices was proposed by Binder [19,20] to result in bursts of turbulence caused either by the sudden collapse and filling of the vortex segments or by their brief propagation and deformation in the local pressure field of the rotor passage. Figure 4 shows the streamwise trailing edge vortices generated by stator passage vortices.

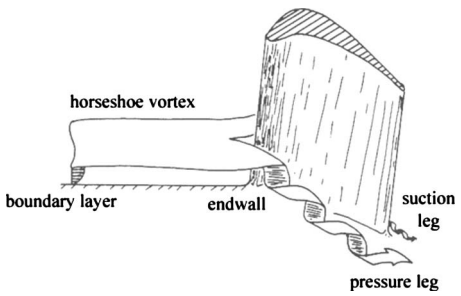

Fig. 2 Formation of passage vortex around a stator

The rotating frame of reference presented many challenges to researchers, but commendable studies were published by Guennette et al. [21] where the full-scale transonic turbine in the MIT facility produced mean heat transfer results from the rotating frame. An advantage of that facility was the matching of exhaust gas ratio of specific heats using argon and Freon-12, and a higher gas-to-wall temperature ratio than the Oxford rig. Dunn [22,23] included the instrumentation description and some phase and time-resolved heat transfer results from the full-scale Teledyne 702 turbine at Calspan. That research noted the enhanced heat transfer coincident with periodic boundary layer transition caused by the passage of upstream wake segments. Complete mean heat transfer results for a number of streamlines on the blades from a General Electric HP turbine, with some comparison to 3D CFD predictions, were presented by Haldeman and Dunn [24]. Although they did not find significant agreement between the predictions and the experiments, the paper provided a very comprehensive data set for such a turbine stage. Their approach will be used for a future presentation of the data for the profile tested in this paper and will be compared it with off-mid-height streamlines.

The flow physics of vane-rotor interaction has been considered in several recent papers related to high-speed turbine test facilities. For example, the work of Dunn et al. [25] both experimentally and numerically investigated the changes in interaction as the vane-blade spacing is increased. This work measured both the blade surface static pressure and heat transfer at midspan of a transonic turbine. The data allowed a detailed assessment of the phase relationship between pressure and heat flux at particular points on the blade surface, and identified the influence of the vane generated unsteadiness as well as the influence of the rotor passage shock. It was found that at some locations, the pressure and heat transfer were largely in phase, while at others, the phase relationship was more complicated. This suggests the complex combination of shock and wake effects on the unsteady heat transfer. Similar effects have been observed by Didier et al. [26] who also investigated the blade surface heat transfer and static pressure on a transonic experimental turbine. In this case, most of the unsteadiness in the heat transfer was considered to be caused by the vane trailing edge shock. By employing the same short duration test facility, Denos et al. [27] investigated the unsteady turbine aerodynamics, and compared the extensive data to CFD predictions of the unsteady aerodynamics of the complete turbine stage. This combination of experiment and simulation particularly proved enlightening in regard to the physical structure of the vane

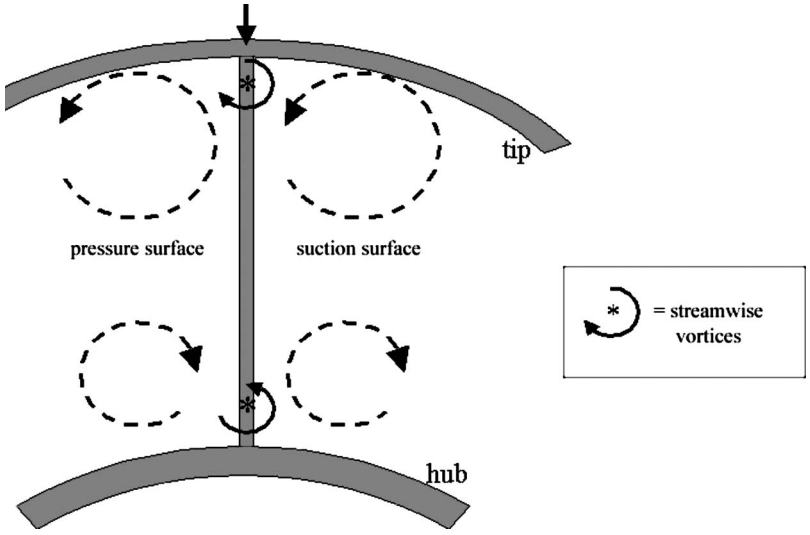

Fig. 4 The stator trailing vortices

trailing edge shock and wake flow, and how these are manipulated by the rotor blade potential field and shock reflections. The sweeping nature of the vane trailing edge shock wave, first impinging on the rotor blade crown and then moving forward along the suction surface, was demonstrated, and the formation of an effective throat/divergent section between vane trailing edge and rotor leading edge discussed. This view of the unsteady vane-rotor interaction is further explored by Miller et al. [28] relating to experimental and computational work on the Oxford transonic turbine. By employing midheight fast-response pressure sensors, these workers were able to demonstrate the strengthening of the vane trailing edge shock, and modulation of the vane exit Mach number according to the relative positions of vane and blade. This paper employed the same experimental facility as Miller et al. [28] and presents time-resolved heat transfer data for the midheight position on the rotor blades.

The behavior of the shock generated by the upstream nozzle guide vanes was of considerable interest to research teams, including Wesner et al. [29]. They used interferometry and a unique flow facility to visualize shock passage over a turbine cascade. They showed the effects of the shock in enhancing heat transfer along the forward suction surface and the early pressure surface. Once those shocks reflected, their influence was observed to a lesser degree on the downstream suction surface. Despite tremendous advances in recent years, much remains to be explored regarding unsteady phenomena in axial turbines. A comprehensive overview of the state of the art was undertaken by Dunn [1]. It concludes that numerous gaps in the research need attention, including turbulence intensity determination, exploration of fully cooled turbine stages, exploration into the migration of hot streaks from the combustion section, and significantly, increased efforts to validate and develop CFD techniques for gas turbine engines.

Facility

It was shown by Schultz et al. [30] that the temperature differences encountered by turbine components could be scaled down in experiments. Nondimensionalized heat transfer rates could then be established, thereby adequately modeling engine conditions. The ILPT provided a transient flow of test air that, having been isentropically heated through sudden compression by the light piston, flowed over the testing surfaces. In this application, the test section was annular, housing a set of 36 nozzle guide vanes leading to a 0.62 scale model rotor of RT27A (midheight) profile blades [3]. That profile was the subject of many studies including Horton et al. [31] and Doorly and Oldfield [6,7]. The first heat transfer measurements were reported by Hilditch and Ainsworth [32].

Figure 5 shows a schematic of the facility, which will not be described in detail in this paper. During a typical run, the test section was evacuated, while the ILPT upstream tube was preset to a pressure that, when coordinated with gate-valve opening, would provide the desired temperature difference between the rotor blade surfaces and the test gas. The desired temperature ratio of 1.3 was obtained at the design rpm of 8343 rpm, which occurred as the rotor accelerated between the evacuated run up speeds of 7000 rpm and approximately 9000 rpm. Note that this temperature ratio was further reduced when the rotating reference frame was taken into account. Data were obtained at high frequencies for approximately 200 ms as the rotor passed through its design speed. The validity of this approach was established by Ainsworth et al. [3], Ainsworth et al. [33], Sheard and Ainsworth [34], and Hilditch and Ainsworth [32]. Table 1 shows the design point provided by Rolls-Royce plc, for their RT27A profile.

Instrumentation

Unique heat transfer instrumentation was developed for this work. In order to install high spatial resolution instrumentation, hand-painted platinum thin film gauges were deemed too large. Thus, a conductor, which had more sensitive thermoelectric properties, was sought. Gold was found to have suitable attributes, but did not share the durability of platinum thin film gauges. Gold (KA6 paint) was painted onto the rotor blades, which had been previously coated with 3/C vitreous enamel, as described by Hilditch and Ainsworth [32]. A photoetching technique was devel-

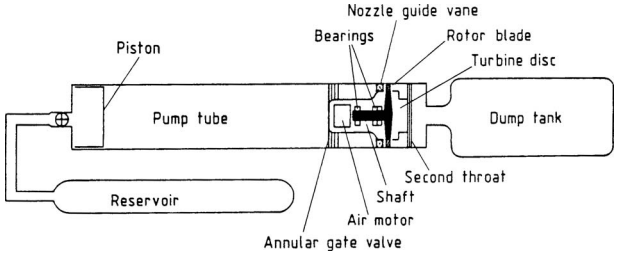

Fig. 5 ILPT schematic

Table 1 ILPT rotor test conditions (design point); Ref.: Hilditch [35]

Parameter	Symbol	Note	Design point value
Rotor speed	rpm		8343
Specific speed	$N/\sqrt{T_0}$	—	436 rpm/$K^{1/2}$
Mass flow number	$\frac{\dot{m}\sqrt{T_0}}{P_0}$	—	7.04×10^{-4} ms/$K^{1/2}$
Reynolds number	Re	Based on NGV exit conditions and axial chord at midheight	2.7×10^{6}
NGV exit Mach number	M_{exit}	Isentropic, midheight	0.946
Rotor relative exit Mach number	M_r	Isentropic, midheight	0.959
NGV axial chord	c_{NGV}	—	0.0312

oped using the pattern shown in Fig. 6. The process was first presented by Allan [36] and involved painting a layer of pure gold onto the enamel substrate of the test specimen rotor blades. The blades were then immersed into a liquid photoresistive coating (AZ111 made by Hoescht, UK). It was very important to draw the blades out of the liquid at a steady rate in order to ensure even deposition. Meanwhile, the gauge pattern (Fig. 6) was photographically reduced to the desired size, and identical patterns were distributed along desired streamlines on a mask, which was subsequently slid over the rotor blade to be instrumented.

Steadily rotating the test blades under the 400 W 386 nm ultraviolet light, the coated blades were evenly exposed. Any photoresistive coating, which had not been previously masked, was also exposed. A diluted developer for the photoresistive coating (AZ303 Hoescht UK) was used to lift the exposed AZ111 coating. The gold left unprotected by the unexposed photoresistive layer was then etched off using a mixture of potassium iodide and iodine. Great care was necessary to prevent that solution from undercutting the tiny serpentine gauges, the width of which was nominally 40 μm, but varied somewhat from gauge to gauge. The final resistance for the photoetched thin film gauges at ambient temperatures was targeted to be between 30 Ω and 70 Ω.

Figure 7 is a photograph taken through a microscope of a completed thin film gauge. Gauges were successfully placed at all but the regions of highest curvature where hand-painted platinum thin film gauges were mounted. The serpentine area was approximately 0.9 mm$\times$1 mm. Typical variations in the width of the etched gold gauge can be seen in this figure. Figure 8 shows the completed blade for the 50% span streamline. The gauges were calibrated using the procedures described by Hilditch and Ainsworth [32].

Laser calibration was undertaken to successfully determine both the thermal product and the thickness to conductivity ratio of the new thin film gauges. A de-ionized water bath provided a means to calibrate the thermal coefficient of resistance of the thin film gauges. The calibration resulted in unique values for the temperature coefficient of resistance (α), the ratio of enamel thickness (a/k), and the thermal product ($\sqrt{(\rho c k_1)}$) of the enamel sublayer, all critical for the data processing to recover transient heat transfer from voltage measurements. The gauges were mounted on a substrate, which could only be considered to be semi-infinite for a short duration. Therefore, the thickness of the enamel substrate (a), specifically its relationship to the thermal conductivity of the enamel, and finally the thermal capacitance of the enamel at the gauge location were essential in determining the frequency response of the thin film gauges. High frequency response of the gauges was not deteriorated by variations in substrate thickness and properties. The lower ranges of frequency were affected, however, but not within the time frames of the transient tests used in this series of experiments. The disadvantage of the gold gauges was their reduced durability when compared to platinum gauges. The tiny, thin fine gold circuits that were the thin film gauges could be broken with careless handling, or after impact with de-

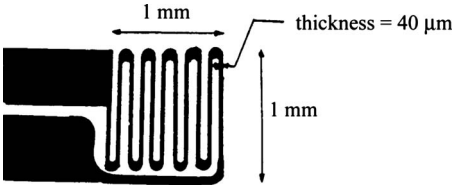

Fig. 6 Mask for photoetched thin film gauges

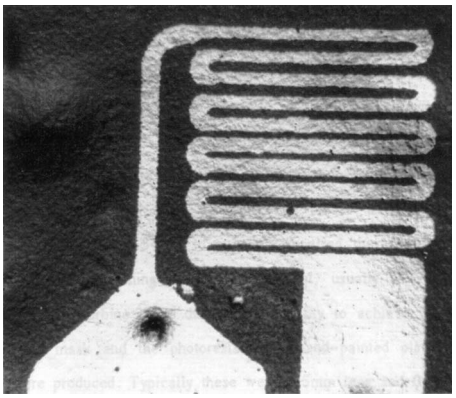

Fig. 7 Microscope photograph of a photoetched thin film gauge

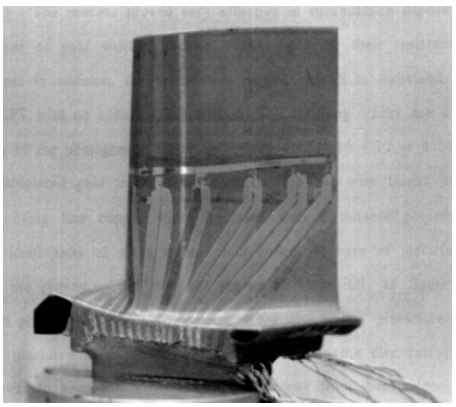

Fig. 8 Midspan thin film gauges

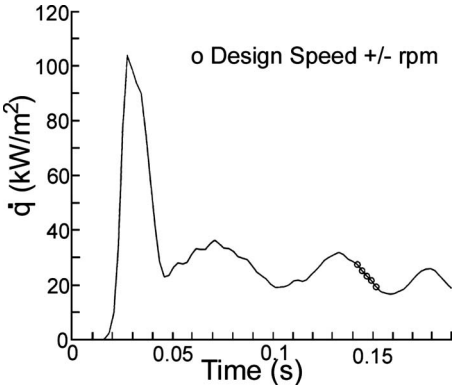

Fig. 9 Data points averaged for mean heat transfer value

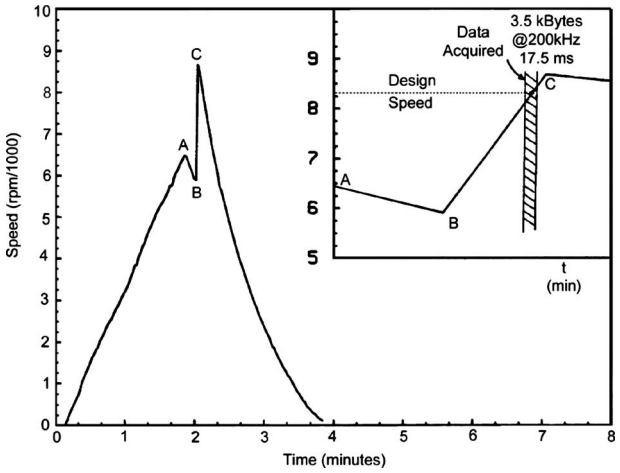

Fig. 10 Typical rotor speed versus time plot

bris. Retaining the gauges intact for 20 or more runs was easily possible, however, and they could be repaired using the gold paint under a powerful microscope. After repairs, calibration was checked and regularly found to be unchanged, since the calibrations pertained to the substrate. The frequency response of the gold gauges was similar to that of the hand-painted platinum gauges. They were beneficial in increasing the spatial resolution, except in regions of high curvature such as the leading edge, where the thin line of a platinum gauge, when aligned spanwise, was superior.

Data Acquisition

It was shown by Hilditch and Ainsworth [32] that the frequency response of thin film gauges on a semi-infinite substrate greatly varied. As described by Schultz and Jones [2], electrical analogs were very effective at modeling the heat transfer in semi-infinite substrates but the challenges faced by the rotating frame were twofold. First, the substrate had two layers and second, the available instrumentation space in the rotating frame did not allow for full analogs. To address the latter, frequency-dependent amplifiers were used to provide appropriate gains for the bandwidth of interest. These were mounted on circuit boards in the rotating shaft of the rotor. These in-shaft electronics are described in detail by Ainsworth et al. [3]. In addition to frequency-dependent gain shaping, the in-shaft electronics provided multiplexing capability allowing eight thin film gauges to be selected from the stationary frame for any given transient experiment. Sixteen postslip ring AMP-05 high frequency differential amplifiers were built to amplify the thin film gauge signals before they were transmitted through the high electronic-noise environment of the laboratory. Low frequency data acquisition was separately carried out, and high frequency (200 kHz) ac-coupled thin film gauge signals were stored on transient recorders. Voltage measurements were digitized, processed in the frequency domain using methods described in detail by Hilditch and Ainsworth [32], and finally restored to the time domain, resulting in the mean and high frequency, high resolution heat transfer measurements recorded in this paper.

Steady Heat Transfer Results

Mean heat transfer results were obtained at 435 Hz for the duration of the transient ILPT run. The rotor passed through design point at 8343 rpm where mean observations of interest were isolated. Figure 9 shows a typical result for a pressure surface midpoint thin film gauge ($x/S=47.7$). The visible oscillations (± 8000 W/m^2) were due to the cyclical application of test gas caused by piston oscillations (dynamic response of the finite mass of the "light" piston as its rapid forward motion, while compressing the test gas, was slowed, and then suddenly restored as the annular gate valve was blown open). The five circular points shown between the time of 0.14 s and 0.15 s indicate the region where the rotor speed was within 100 rpm of the design point.

Figure 10 shows the rotor speed versus time. The steep spike near the 2 min point indicates the transient run of the tunnel. One can see in the inset graph the data acquisition zone. Thus, the oscillations in tunnel conditions did not greatly affect the actual test conditions. All measurements were taken at that moment, which approximately represented two revolutions of the rotor. Mean data were recorded at design rpm where the temperature ratio of 1.3 was met, later to be scaled to match engine representative conditions.

Heat transfer rates measured for the midheight streamline are shown in Fig. 11. Nondimensionally, they are shown in Fig. 12. Data uncertainty was determined to be ± 10.5 including errors introduced by thin film gauge calibration, data acquisition, and processing. Results were verified by repeated testing at the same test conditions.

These results are shown with the commissioning data obtained by Hilditch [35] and presented by Hilditch and Ainsworth [32]. For five of seven points presented in that work, excellent agreement can be seen in the results presented. The outlying points on the pressure surface ($x/S=0.6$) and on the suction surface ($x/S=0.1$) were from a single run reported in the Hilditch data, which they were unable to replicate. The midheight results were scaled to compare with cascade data obtained by a number of researchers including Doorly and Oldfield [5]. This was necessary to account for differences in gas-to-wall temperature ratios between the two experiments, complicated due to the need to consider the rotor frame of reference. The cascade tests had a gas-to-wall ratio of 1.5. This can be compared to that observed in the rotor testing, shown for a typical run in Fig. 13. The cascade tests were conducted at two different freestream turbulence levels: 0.2%Tu with wakes generated by bar passing and at 4%Tu with no wakes. The rotor rig had between 1% and 2% turbulence levels prior to the flow meeting the nozzle guide vanes. The rotor results, scaled to the heat transfer parameters of the rotor midheight profile, are shown in Fig. 14. The three curves presented in this figure represent two sets of cascade results on the same profile as the midheight of the rotor that is the subject of this paper. Of greater significance was the simulation of wake passage over the cascade using the wakes of cylindrical bars rotating upstream (the dotted line in Fig. 14).

The scaled cascade heat transfer rates provided good predictions of the three-dimensional situation on the early pressure surface. Considering the pressure surface trailing edge first (left to right in Fig. 14), one notices the generally higher heat transfer results most likely due to the impingement of nozzle guide vane

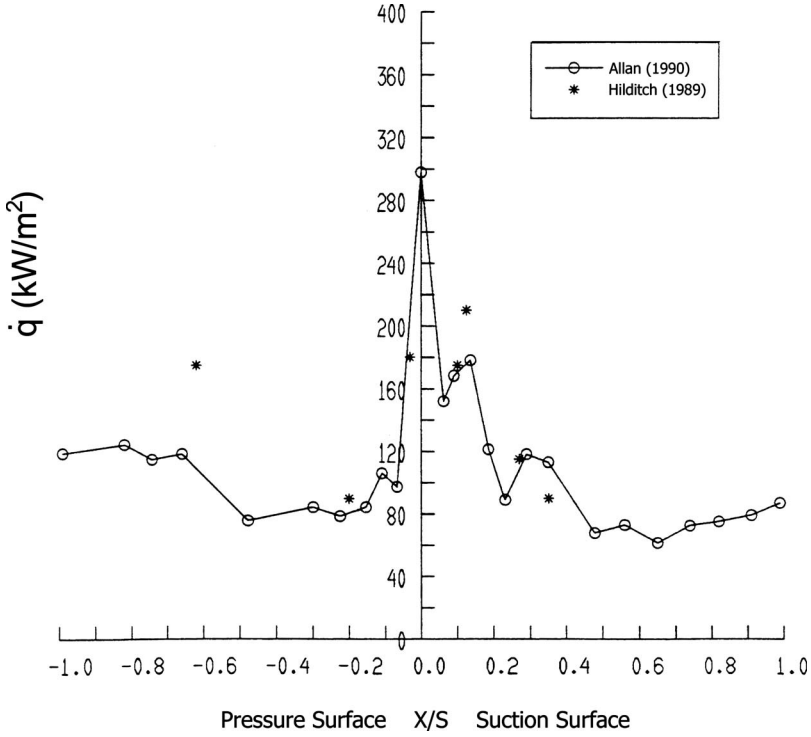

Fig. 11 Rotor mean heat transfer rate: midheight streamline

trailing edge shocks reflected from the early suction surface of the adjacent blade. The extremely high heat transfer rates on the leading edge were expected due to the regular wake passage, coupled with the sweeping of the leading edge by nozzle trailing edge shocks. This phenomenon is responsible for the high mean heat transfer results between x/S of 0 and 0.1 on the suction surface. The close corroboration between the cascade with wakes results between x/S of 0.1 and 0.3 indicates the importance of the wakes in that region. The relatively low and constant heat transfer rates observed on the later suction surface were not expected. It had been anticipated that three-dimensional effects would present the physical processes necessary for elevated heat transfer rates on the order of those seen on the later pressure surface. Furthermore, the migration of flow phenomena from the midpressure surface to the suction surface was anticipated, as described earlier in this paper. Nevertheless, the slightly elevated values toward the trailing edge may be evidence of the negative jet effect acting upon the boundary layer, and through the resulting turbulent spots, introducing the influence of higher temperature midpassage gases.

Unsteady Heat Transfer Results

Unsteady measurements were taken for just over two revolutions of the rotor, over approximately 80 wake events from the 36 upstream nozzle guide vanes. For analysis purposes, a 2.5 ms time

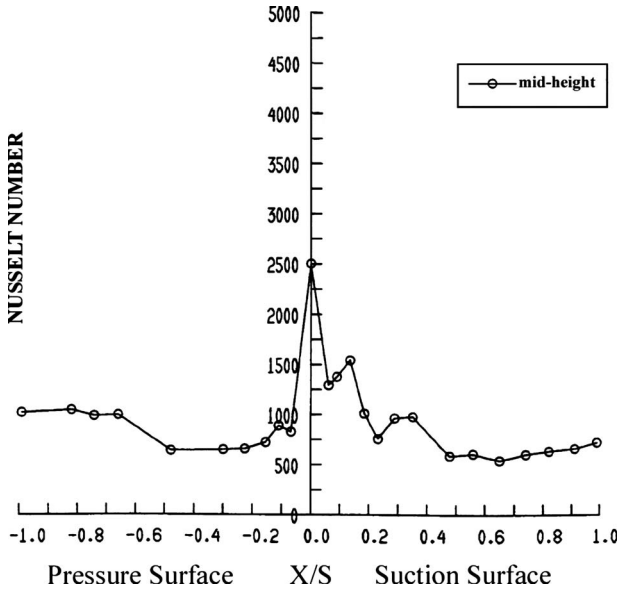

Fig. 12 Rotor midheight Nusselt number

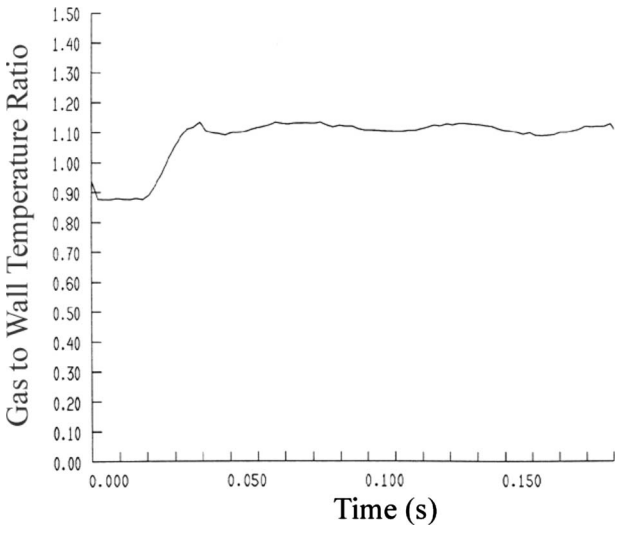

Fig. 13 Typical rotor relative gas-to-wall temperature ratio

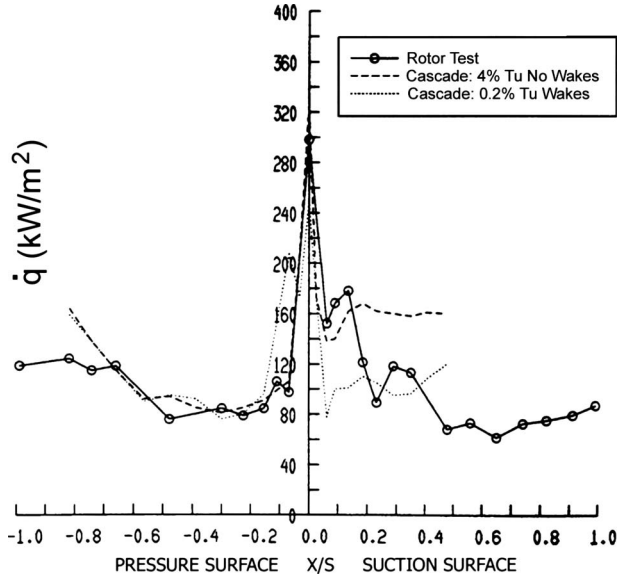

Fig. 14 Rotor midheight mean heat transfer rate: comparison to 2D cascade/wake simulation results

slice of these data was selected, usually 12 vane passages. Due to the number of channels on the slip ring, eight channels could be read simultaneously; therefore, individual wake segments could not always be tracked along a blade. In addition, to raise the concentration of thin film gauges, particularly at the midheight location, instrumentation was distributed over several blades. This was not always the case, and many observations were made of simultaneous heat transfer measurements on a single blade. Figure 15 presents typical traces for the same test from two adjacent gauges spaced streamwise by approximately 10% chord. The vertical grid represents the upstream nozzle guide vane passage frequency, but not necessarily the trailing edge location. This figure is intended not to explore the features, but to demonstrate the great variation that can be encountered from wake to wake, and the evolution of flow features as they are swept downstream. These gauges serve best to illustrate the data reduction methods and are not found on the midheight streamline. One must also remember that the effects of wakes and shocks may be very different in terms of propagation speed and even direction at any point on the blades. Comparison of pressure data with this heat transfer data for this profile has not yet been completed in a comprehensive fashion. It would be very enlightening and must be

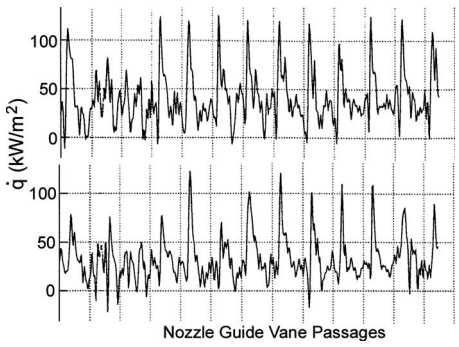

Fig. 15 Demonstration of streamwise differences in unsteady heat-transfer-processed results

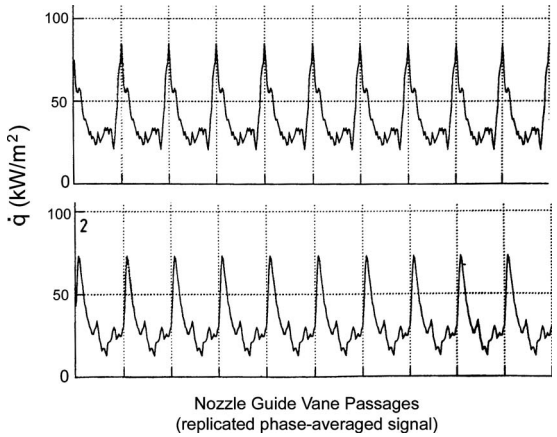

Fig. 16 Demonstration of streamwise differences in unsteady heat-transfer-repeated phase-averaged results

completed to fully characterize the phenomena apparent in the unsteady heat transfer results. Without discussing the features of the measurements, the unique nature of each transient event is clearly apparent, as is the similarity in the two traces.

To support analysis of the unsteady results, two methods were used to help isolate flow features, which could be distinguished from any wake event, regardless of the unique signatures of upstream blades, and local flow about individual rotor blades, and through individual passages. A 36-line encoder signal provided a means to phase average unsteady heat transfer measurements. This processing served to normalize the wake passage events, eliminating any minor mean changes. Second, 40-step discretization in time was done to obtain a filtering mechanism, which isolated flow characteristics were common to all guide vane passages. Identical phase-averaged signals were presented in artificial sequence to allow similar comparison, so flow features could be easily distinguishable due to the passage-to-passage averaging.

To demonstrate the effects of this processing on the data, phase-averaged results of the same two gauges presented in Fig. 15 are shown in Fig. 16. Of significance is the dramatic reduction in the magnitude of both peaks and valleys. One must be careful to use the phase-averaged results for comparison of major features that are consistent from passage to passage, but not for extremes in heat transfer experienced by individual blades. It is apparent from Fig. 17 that unsteady maxima and minima are far in excess of phase-averaged extremes. Negative heat transfer was a phenomenon observed by Schultz and Jones [2].

To provide an indication of the suitability of the transient facility being used for steady-state results, a comparison of the two revolutions typically occurred during the data acquisition sequence on any given run in the ILPT. The incidence angle varied by no more than 0.5 deg between the two runs. Figure 17 is an example of the revolution-to-revolution variations from the same thin film gauge. The same traces are presented in their phase-averaged form in Fig. 18 but note that the upper trace is purposefully offset up on the graph for clarity in comparisons. Therefore, the vertical scale for Revolution 2 is meaningless in Fig. 18. There were inevitable differences from run to run due to the conditions when the annular gate valve of the ILPT was triggered open. The phase-averaged routine was useful when it came to assessing signals from runt to run. Figure 19 shows the similarity of signals processed from the same gauge from two different runs. Finally, a measure of "unsteadiness" was obtained by taking the average of the absolute values in their discrete form, of fluctuations about the local mean of the phase-averaged trace. Figure 20 presents the phase-averaged results from two gauges, the processing for which

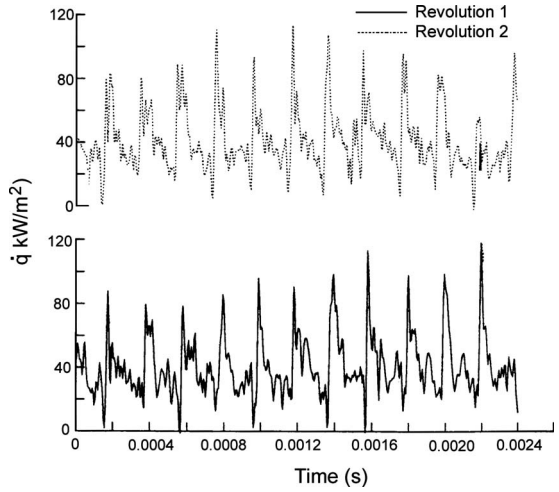

Fig. 17 Rotor revolution-to-revolution variations in unsteady heat transfer

resulted in unsteadiness levels of 2750 W/m^2 and 5080 W/m^2. This provided a means of quantifying the apparent unsteadiness variations between the two signals.

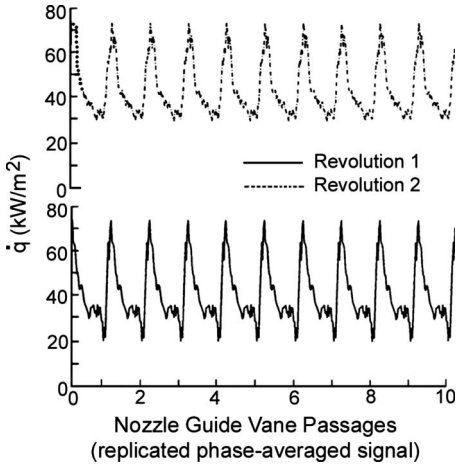

Fig. 18 Rotor revolution-to-revolution variations in phase-averaged unsteady heat transfer rate

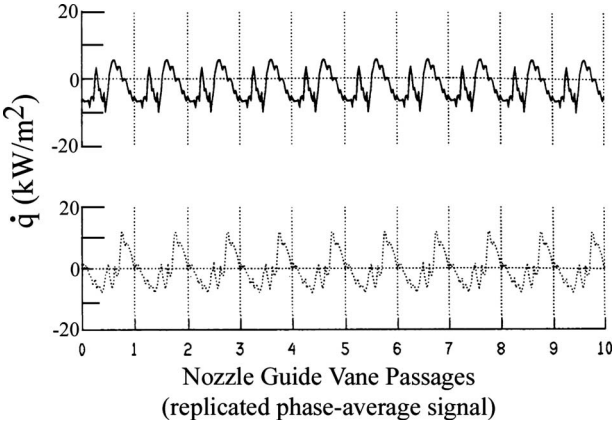

Fig. 19 Phase averaging: reliability between runs

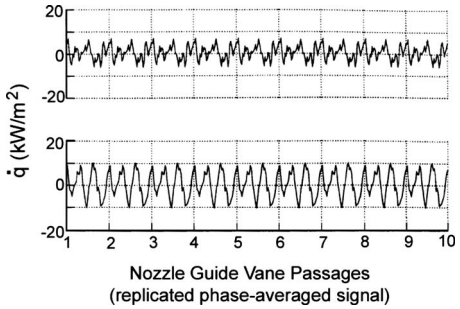

Fig. 20 "Unsteadiness level" variations

Twenty-six thin film gauges distributed about the midheight streamline contributed to the unsteady heat transfer measurements presented in the following figures. Phase-averaged results have been presented in apparent sequences of three consecutive upstream vane passings.

Figure 21 displays the suction surface, while Fig. 22 shows the pressure surface results. Note that the scales vary from graph to graph while x/S for each specific plot noted thereon.

Discussion

The figures presented will be discussed with particular emphasis on secondary flow evidence along the midheight streamline. Considering Fig. 21, of particular note are the large fluctuations evident on the early suction surface, which diminish in magnitude until they are relatively insignificant by $x/S=0.351$. These are suggested to be the effects of the passage nozzle guide value (NGV) wakes introducing elevated turbulence levels over this surface. The observations of a double peak early on the suction surface of cascades by Doorly and Oldfield [5,6] were also observed on this rotor, apparent at $x/S=0.232$ and forward. The effect was observed in early suction surface gauges at $x/S=0.168$, 0.136, 0.091, and the peaks were apparently coincident at $x/S=0.068$. Note that the spacing between the peaks varies due to the upstream motion of the shock and the downstream motion of the wake segment. This apparently indicates the presence of a shock wave emanating from the trailing edge of the NGV, moving forward on the suction surface while the wake segment moves downstream. This phenomenon will be studied later in this paper when unsteady heat transfer results (not phase averaged) will be presented. The heat transfer aft of the crown of the turbine blade on the suction surface is relatively steady consistent with the findings of Doorly and Oldfield [5] cascade results, indicating the presence of a turbulent boundary layer. Some slight modulation at wake passing frequency is evident at $x/S=0.351$ and $x/S=0.479$. This can be explained by the effects of wake passing on the state of boundary layer; slightly higher turbulent fluctuation levels were present in the turbulent boundary layer when wakes from upstream components were present in the flow.

In the later suction surface region, fluctuations are clearly evident, again characterized by sharp spikes, both positive and negative in heat transfer rate. This can be attributed to the presence of reflected trailing edge shocks from the adjacent rotor blade being modulated across this area of the suction surface at wake passing frequency; however, this theory can only be confirmed by cross correlations. Nevertheless, the unsteadiness observed in this later suction surface midheight region did not significantly affect the mean heat transfer levels. This was due in part to the strength of the shocks being diminished once they were reflected. As indicated in the preceding section, the measurements, once scaled to the cascade/wake simulation experimental conditions [5,6], were lower than the cascade results by $x/S=0.4$ on the suction surface. Although no comparisons were possible with a wake passing

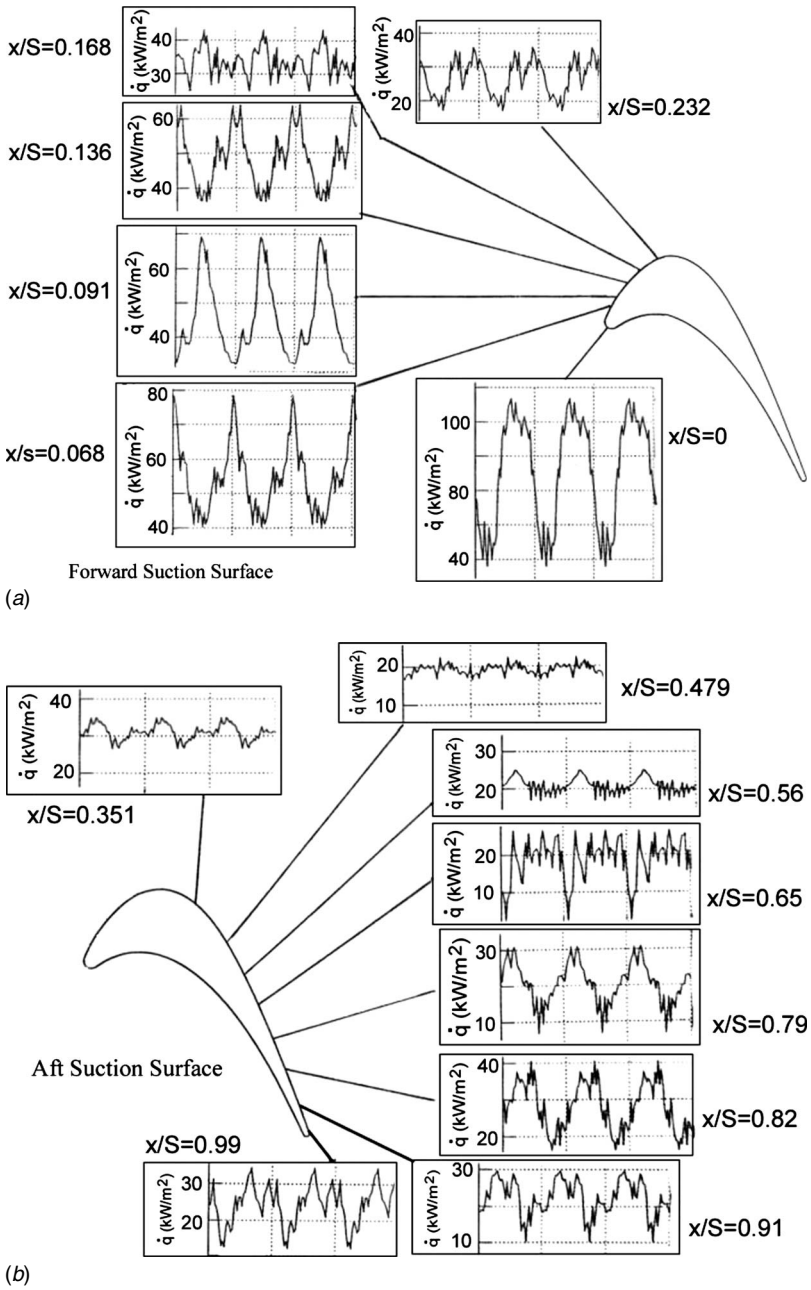

Fig. 21 Rotor midheight phase-averaged unsteady heat transfer

simulation, heat transfer rate results for the same cascade at 4% inlet freestream turbulence and design conditions tended to gradually rise as the trailing edge was approached, as observed by Nicholson et al. [37] (Figs. 14 and 21).

The unsteady heat transfer measurements for the pressure surface of the midheight streamline are presented in phase-averaged form in Fig. 22. The leading edge data point is slightly located toward the pressure surface side of the apparent geometric stagnation point as explained earlier. The nature of that unsteady signal slightly varied only from the leading edge data point presented in Fig. 21 in that the levels were comparable and the distinct double peak was observed in the phase-averaged results for that streamline's suction and pressure surfaces. This leading edge measurement was taken from a thin film gauge on one blade, whereas the results shown in Fig. 21 were from gauges on two other blades. The double peak in the heat transfer rate was likely due to a shock followed by the passage of a wake event, as observed by Doorly and Oldfield [5] and Hontou et al. [31]. Another possibility for the second peak in heat transfer is the presence of a vortical bubble caused when the incident shock becomes normal to the surface of the leading edge.

The level of unsteadiness on the pressure surface was insignificant with the exception of the measurement taken at $x/S=0.659$ where a distinct double fluctuation was observed at wake passing frequency. This is consistent but to a lesser degree at the two later pressure surface data points: $x/S=0.819$ and $x/S=0.99$. This could also be due to weak reflected shocks from the forward suction surface of the adjacent rotor blade: The shock activity was studied by Doorly and Oldfield [5] for the RT27A profile, and studied in detail by Miller et al. [28] and Denos et al. [27]. Some Schlieren flow visualization was used in the cascade study (Doorly and Oldfield [5]), and a sample of this is presented in Fig. 23 of this work. In that figure, the shock from the bar wake gen-

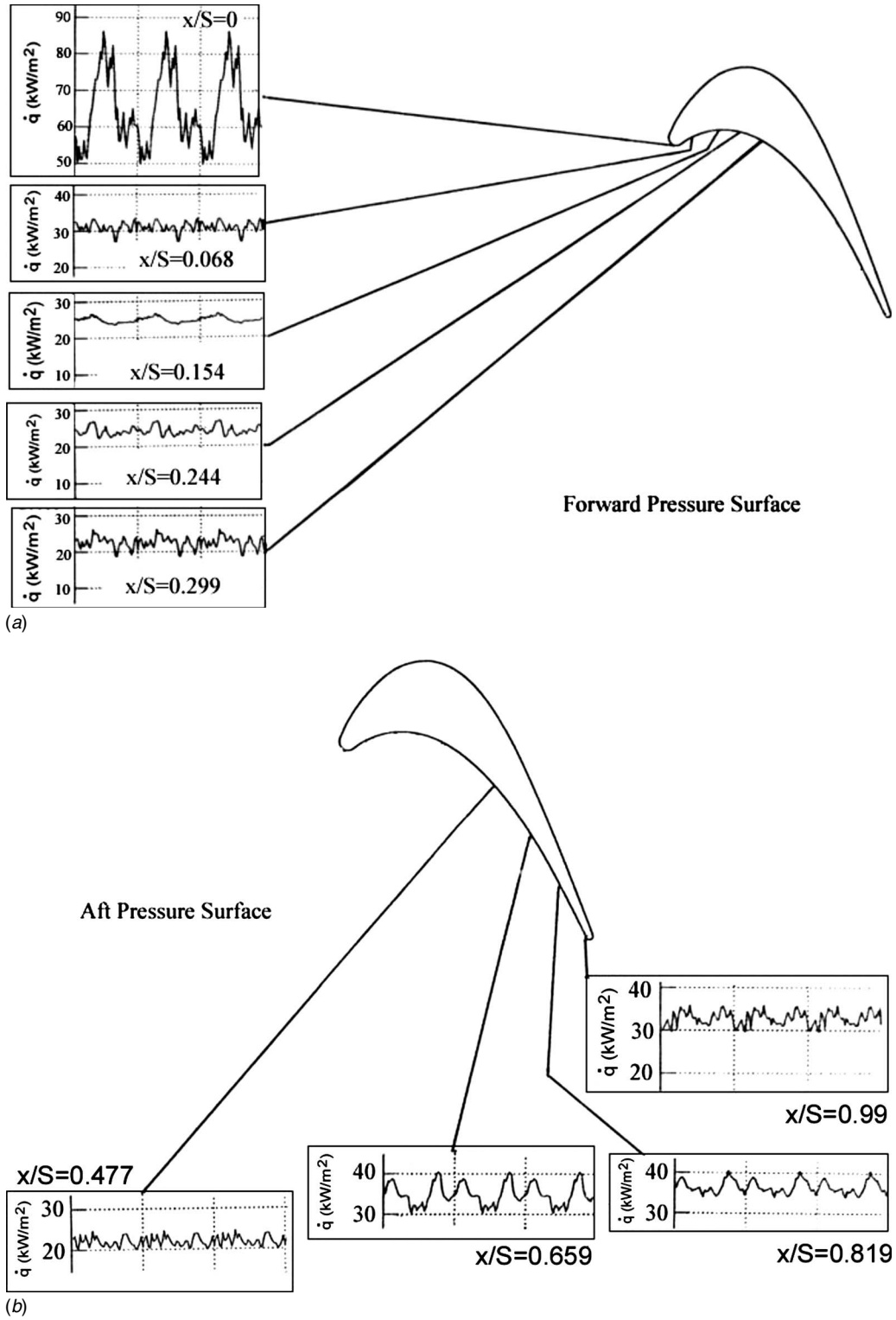

Fig. 22 Rotor midheight phase-averaged unsteady heat transfer pressure surface

erator can be seen reflecting off the forward suction surface of a rotor blade and contacting the pressure surface of the adjacent blade in the late midchord regions.

Transition would be complete near the crown of the suction surface, and low levels of unsteadiness indicate that the turbulent boundary layer is relatively unaffected by any unsteady events moveing at NGV passing frequency. It can be concluded that the increased heat transfer unsteadiness levels observed at the trailing edge of the suction surface are due to reflected shock waves from the adjacent rotor blade trailing edge. These have been observed in cascade studies to be modulated at wake passing frequency along this late suction surface region.

The unsteadiness levels observed on the pressure surface are in agreement with previous studies as mentioned earlier, with only slight increases in unsteady heat transfer levels near $x/S=0.659$ where reflected shocks apparently impinge on the boundary layer.

During one particular run, five midheight suction surface thin

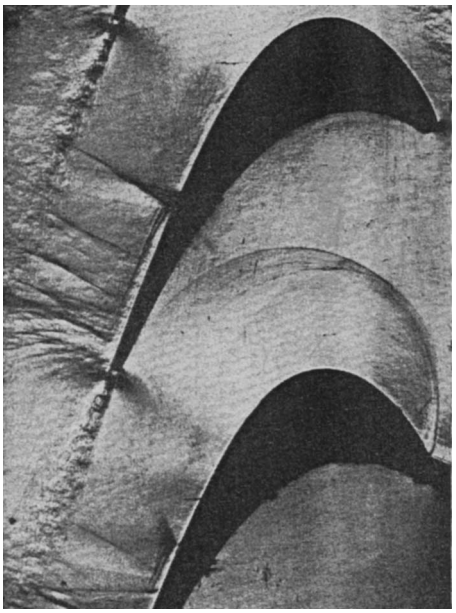

Fig. 23 Rotor passage Schlieren flow visualization of shock activity (Doorly and Oldfield [5])

film gauges were monitored simultaneously; a portion of the unsteady heat transfer results from Gauges 3, 5, 6, 7, and 8 on are shown in Fig. 24. Note the change in the vertical scale from graph to graph.

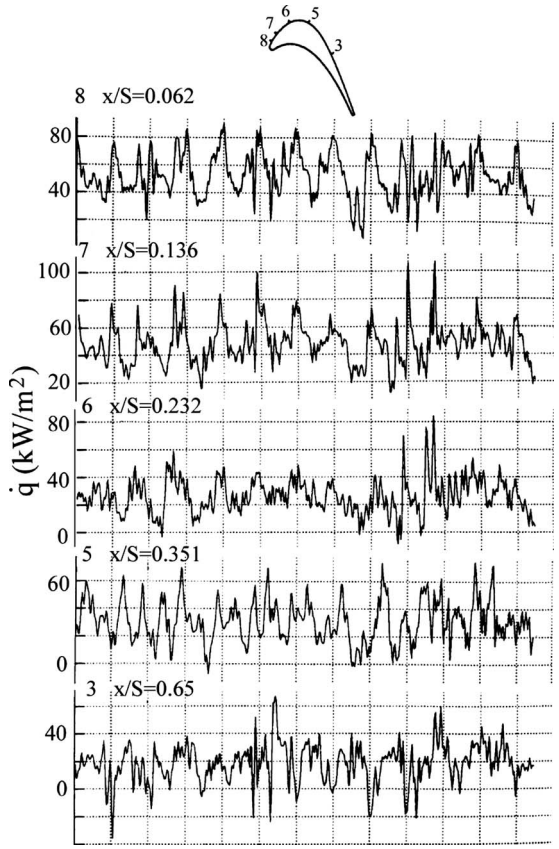

Fig. 24 Unsteady heat transfer measurements: run 6551 midheight Gauges 3–8

It is evident that the structure of this unsteady heat transfer is very complicated in the forward suction surface. Although a double peak caused by a wake/shock event is not clear or consistent at $x/S=0.65$, there is little doubt of its presence upstream, on the upper four graphs. The spacing diminishes as expected, but passage-to-passage variations are not inconsiderable. Negative heat transfer is present during some shock events, certainly at $x/S=0.232$, 0.351, and 0.65. The value of using a phase-averaged technique to analyze these data becomes apparent. It is expected that the wake events contact Gauges 8 ($x/S=0.062$) and 7 ($x/S=0.136$) almost simultaneously, then propagate past Gauges 6 ($x/S=0.0232$) and 5 ($x/S=0.351$). Gauge 3 ($x/S=0.650$), on the other hand, is found well after transition and likely shows the impacts of shock waves from the adjacent rotor blade trailing edge on the boundary layer.

Conclusions

High spatial resolution mean and unsteady heat transfer rate measurements were taken on the midheight streamline on the blades of the Oxford rotor. The rotor was mounted in the working section of the ILPT and operated at engine representative conditions in this transient facility. Gold thin film gauges were developed, making use of a photoetching technique to provide high density instrumentation; consequently, low flow intrusion, low surface area, and low resistance leads have been necessary to conduct thin film gauge signals to the blade root area.

All thin film gauges were simultaneously connected through use of the multiplexing capability of the in-shaft electronics; this equipment was also necessary to preferentially amplify the thin film gauge signals before transmitting them through the slip ring to the stationary frame of reference. This ensured that the high frequency components of the signals were not lost in the discretization process, as the signals were stored on transient recorders.

The midheight thin film gauge heat transfer results were scaled for run conditions to compare to the data obtained by Doorly and Oldfield [4,5] in their cascade/wake simulation experiments carried out on the same blade profile. Remarkably, good comparisons were made on the early pressure surface and suction surface, and the points of transition were similar, on both surfaces, to those measured in the cascade experiments. Despite the fact that the rotor accelerated through its design speed, and flow incidence is only instantaneously on the geometric stagnation point, the leading edge heat transfer rate measurements compared well to those from the two-dimensional work.

The rotor blades operating at engine representative conditions present a very complicated unsteady heat transfer environment, and measurements were phase averaged to enhance those flow effects, which occur at the NGV (wake passing frequency). These have been presented for thin film gauges on the midheight streamline, and some of the unsteady and secondary flow effects observed by other researchers, whose work has been briefly reviewed, have been proposed as likely causes for some observations in this study. Levels of unsteadiness taken from the phase-averaged unsteady heat transfer measurements have been presented. These were beneficial in visualizing the areas on the streamline, which are most affected by flow unsteadiness occurring at wake passing frequency.

The understanding of the results presented in this paper would be enhanced by cross correlation of the unsteady heat transfer measurements to determine the nature and movement of unsteady events as they affect the heat transfer rates of different thin film gauges on the same streamlines. Comprehensive comparaison with published unsteady pressure data for this profile must also be conducted. In addition, the unsteady two-dimensional and time mean three-dimensional flow measurements taken in recent years at Oxford for this blade profile should be analyzed in concert with the results presented in this work. The use of experimental results

such as these to validates CFD predictions for the better understanding and more accurate prediction of the heat loads involved in operational gas turbines.

Acknowledgment

The support of Rolls-Royce plc and the UK Department of Trade and Industry is gratefully acknowledged.

References

[1] Dunn, M. G., 2001, "Convective Heat Transfer and Aerodynamics in Axial Flow Turbines," ASME J. Turbomach., **123**(4), pp. 637–686.
[2] Schultz, D. L., and Jones, T. V., 1973, "Heat Transfer Measurements in Short-Duration Hypersonic Facilities," AGARDograph No.165.
[3] Ainsworth, R. W., Schultz, D. I., Davies, M. R. D., Forth, C. J. P., Hilditch, M. A., Oldfield, M. L. G., and Sheard, A. G., 1988, "A Transient Flow Facility for the Study of Thermofluid Dynamics Under Engine Representative Conditions," ASME Paper No. 88-GT-144.
[4] Meyer, R. N., 1957, "The Effect of Wakes on the Transient Pressure and Velocity Distributions in Turbomachines," ASME Paper No. 57-A-83.
[5] Doorly, D. J., and Oldfield, M. L. G., 1985, "Simulation of Wake Passing in a Stationary Turbine Rotor Cascade," J. Propul. Power, **1**(4), pp. 316–318.
[6] Doorly, D. J., and Oldfield, M. L. G., 1985, "Simulation of the Effects of Shock Wave Passing on a Turbine Rotor Blade," ASME J. Eng. Gas Turbines Power, **107**, pp. 998–1006.
[7] Doorly, D. J., Oldfield, M. L. G., and Schrivener, C. T. J., 1985, "Wake-Passing in a Turbine Rotor Cascade," Report No. AGARD CP-390.
[8] Hodson, H. P., 1984, "Boundary Layer and Loss Measurements on the Rotor of an Axial Flow Turbine," ASME J. Eng. Gas Turbines Power, **106**, pp. 391–399.
[9] Mayle, R. E., and Dullenkopf, K., 1989, "A Theory for Wake-Induced Transition," ASME Paper No. 89-GT-57.
[10] Mayle, R. E., and Dullenkopf, K., 1990, "More on the Turbulent Strip Theory for Wake-Induced Transition," ASME Paper No. 90-GT-137.
[11] Johnson, A. B., Rigby, M. J., Oldfield, M. L. G., Ainsworth, R. W., and Oliver, M. J., 1988, "Surface Heat Transfer Fluctuations on a Turbine Rotor Blade Due to Upstream Shock Wave Passing," ASME Paper No. 88-GT-172.
[12] Johnson, A. B., Oldfield, M. L. G., Rigby, M. J., and Giles, M. B., 1990, "Nozzle Guide Vane Shock Wave Propagation and Bifurcation in a Transonic Turbine Rotor," ASME Paper No. 90-GT-310.
[13] Jones, T. V., 1988, "Gas Turbine Studies at Oxford 1969–1987," ASME Paper No. 88-GT-112. Jones, T. V., Schultz, D. L., and Hendley, A. D., 1973, "On the Flow in an Isentropic Light Piston Tunnel," ARC, Reports and Memoranda No. 3731.
[14] Herzig, H. Z., Hansen, A. G., and Costello, G. R., 1953, "A Visualization Study of Secondary Flows in Cascades," NACA Report No. 1163.
[15] Langston, L. S., 1980, "Crossflows in a Turbine Cascade Passage," ASME Paper No. 80-GT-5.
[16] Graziani, R. A., Blair, M. F., Taylor, J. R., and Mayle, R. E., 1980, "An Experimental Study of Endwall and Airfoil Surface Heat Transfer in a Large Scale Turbine Blade Cascade," ASME J. Eng. Power, **102**, pp. 257–267.
[17] Hebert, G. J., and Tiederman, W. G., 1989, "Comparison of Steady and Unsteady Secondary Flows in a Turbine Stator Cascade," ASME Paper No. 89-GT-79.
[18] Sieverding, C. H., 1985, "Recent Progress in the Understanding of Basic Aspects of Secondary Flows in Turbine Blade Passages," ASME J. Eng. Gas Turbines Power, **107**, pp. 248–257.
[19] Binder, A., 1985, "Turbulence Production Due to Secondary Vortex Cutting in a Turbine Rotor," ASME Paper No. 85-GT-193.
[20] Binder, A., Forster, W., Mach, K., and Rogge, H., 1986, "Unsteady Flow Interaction Caused the Stator Secondary Vortices in a Turbine Rotor," ASME Paper No. 86-GT-302.
[21] Guenette, G. R., Epstein, A. R., Giles, M. B., Haimes, R., and Norton, R. J. G., 1989, "Fully Scaled Transonic Turbine Rotor Heat Transfer Measurements," ASME J. Turbomach., **111**, pp. 1–7.
[22] Dunn, M. G., 1986, "Heat Flux Measurements for the Rotor of a Full-Stage Turbine: Part 1: Time Averaged Results," ASME Paper No. 86-GT-77.
[23] Dunn, M. G., 1989, "Phase and Time-Resolved Measurements of Unsteady Heat Transfer and Pressure in a Full-Stage Rotating Turbine," ASME Paper No. 89-GT-135.
[24] Haldeman, C. W., and Dunn, M. G., 2003, "Heat Transfer Measurements and Predictions for the Vane and Blade of a Rotating High-Pressure Turbine Stage," ASME Paper No. GT2003-38726.
[25] Dunn, M. G., Haldemann, R. S., Abhari, R. S., and McMillan, M. L., 2000, "Influence of Vane/Blade Spacing on the Heat Flux for a Transonic Turbine," ASME J. Turbomach., **122**(4), pp. 684–691.
[26] Didier, F., Denos, R., and Arts, T., 2002, "Unsteady Rotor Heat Transfer in a Transonic Turbine Stage," ASME J. Turbomach., **124**(4), pp. 614–622.
[27] Denos, R., Arts, T., Paniagua, G., Michelassi, V., and Martelli, F., 2001, "Investigation of the Unsteady Rotor Aerodynamics in a Transonic Turbine Stage," ASME J. Turbomach., **123**(1), pp. 81–89.
[28] Miller, R. J., Moss, R. W., Ainsworth, R. W., and Harvey, N. W., 2003, "Wake, Shock and Potential Field Interactions in a 1.5 Stage Turbine: Part I: Vane-Rotor and Rotor Vane Interaction," ASME J. Turbomach., **125**(1), pp. 33–39.
[29] Wesner, A., Schetz, J. A., and Grabowski, H., 1999, "Interferometric Study of Unsteady Passing Shock Flow in a Turbine Cascade," J. Propul. Power, **15**(4), pp. 489–496.
[30] Schultz, D. L., Jones, T. V., Oldfield, M. L. G., and Daniels, L. C., 1977, "A New Transient Cascade Facility for the Measurement of Heat Transfer Rates," Report No. AGARD CP-229.
[31] Horton, F. G., Schultz, D. L., and Forest, A. E., 1985, "Heat Transfer Measurements With Film Cooling on a Turbine Blade Profile in Cascade," ASME Paper No. 85-GT-117.
[32] Hilditch, M. A., and Ainsworth, R. W., 1990, "Unsteady Heat Transfer Measurements on a Rotating Gas Turbine Blade," ASME Paper No. 90-GT-175.
[33] Ainsworth, R. W., Allen, J. L., Davies, M. R. D., Doorly, J. E., Forth, C. J. P., Hilditch, M. A., Oldfield, M. L. G., and Sheard, A. G., 1989, "Developments in Instrumentation and Processing for Transient Heat Transfer Measurement in a Full Stage Model Turbine," ASME J. Turbomach., **111**, pp. 20–27.
[34] Sheard, A. G., and Ainsworth, R. W., 1990, "The Aerodynamic and Mechanical Performance of a High Pressure Turbine Stage in a Transient Wind Tunnel," ASME Paper No. 90-GT-353.
[35] Hilditch, M. A., 1989, "Unsteady Heat Transfer Measurements in a Rotating Gas Turbine Stage," Ph.D. thesis, Oxford University, Oxford.
[36] Allan, W. D. E., 1990, "Heat Transfer and Instrumentation Studies on Rotating Turbine Blades in a Transient Facility," Ph.D. thesis, University of Oxford, Oxford.
[37] Nicholson, J. H., Forest, A. E., Oldfield, M. L. G., and Schultz, D. L., 1984, "Heat Transfer Optimized Turbine Rotor Blades—An Experimental Study Using Transient Techniques," ASME J. Eng. Gas Turbines Power, **106**, pp. 173–182.

Effect of Misalignment on the Characteristics of Journal Bearings

A. M. Ahmed
Department of Mechanical Power Engineering,
Cairo University,
Giza 12316, Egypt
e-mail: amahmed@eng.cu.edu.eg

A. El-Shafei
Department of Mechanical Design
and Production,
Cairo University,
Giza 12316, Egypt
e-mail: elshafei@ritec-eg.com

Due to the renewed interest in the effect of misalignment on the dynamic characteristics of journal bearings, this paper presents a study of the effect of misalignment on the dynamic characteristics of journal bearings. A 2D finite difference program is developed and used for this study. The results show that there are a total of 16 stiffness and 16 damping coefficients considering horizontal and vertical displacements and rotations. The variation of these coefficients with journal tilting (i.e., angular misalignment) is illustrated. It is shown that misalignment can have a significant effect on the bearings' dynamic characteristics. [DOI: 10.1115/1.2800347]

Introduction

The effect of misalignment on the journal bearing dynamic characteristics has attracted very little attention [1] from researchers in the field, even though significant work on journal bearings and their characteristics are reported in the literature. However, in recent work by one of the authors and his colleagues [2], it became evident experimentally that misalignment, in particular, angular misalignment, has significant effects on the stability of journal bearings.

In this work [2], a set of experiments was conducted on a test rig to experimentally determine the onset of instability. For the test rig under consideration, on plain journal bearings, the theoretical and experimental onset of instability was at 3150 rpm. However, upon the introduction of angular misalignment in the coupling, the test rig did not exhibit any instability up to the maximum test rig speed of 7000 rpm. This is significant, in particular, on its effects on operating journal bearings.

The results documented in Ref. [2] motivated the authors to investigate the effect of misalignment, particularly, angular misalignment, on the stability characteristics of journal bearings. The first step was to investigate the effect of misalignment on the stiffness and damping coefficients of journal bearings. As far as the authors could determine, very little work has gone into studying the effects of angular misalignment on journal bearings. Yu and Adams [1] studied coefficient characteristics without calculating the coefficients. San Andres [3] provided a study of shaft misalignment on force coefficients of annular pressure seals.

In order to study the effect of misalignment on plain journal bearings, the authors developed a 2D finite difference program based on the work of Someya [4]. The program has standard features including Reynolds cavitation boundary conditions. The program was tested and benchmarked against Someya for accuracy. The program was then used to investigate the effect of misalignment on the stiffness and damping coefficients of plain journal bearings. A parametric study is performed to show the effects of varying misalignment angles in the horizontal and vertical planes on the values of the stiffness and damping coefficients. The results show that there are significant changes in the values of these coefficients.

Contributed by the International Gas Turbine Institute of ASME for publication in the JOURNAL OF ENGINEERING FOR GAS TURBINES AND POWER. Manuscript received May 21, 2007; final manuscript received June 17, 2007; published online April 9, 2008. Review conducted by Dilip R. Ballal. Paper presented at the ASME Turbo Expo 2006: Land, Sea and Air (GT2006), 2006, Barcelona, Spain, May 8–11, 2006.

Mathematical Model

Reynolds Equation. The starting point of calculating the bearing stiffness and damping coefficients is the solution of the dimensionless, laminar, steady state, and isoviscous Reynolds equation, which can be written as

$$\frac{\partial}{\partial\theta}\left(H^3\frac{\partial\Lambda}{\partial\theta}\right)+\frac{\partial}{\partial\zeta}\left(H^3\frac{\partial\Lambda}{\partial\zeta}\right)=6\frac{\partial H}{\partial\theta}+12(\varepsilon\dot{\phi}\sin\theta+\dot{\varepsilon}\cos\theta) \quad (1)$$

In Eq. (1), θ is the circumferential direction, ζ is the dimensionless axial direction ($\zeta=z/r$, where z is the axial direction coordinate and r is the bearing radius), ε is the eccentricity ratio, φ is the attitude angle, $(\dot{\varepsilon},\dot{\phi})$ are time derivatives of ε and φ with respect to dimensionless time ($\tau=\omega t$), ω is the angular velocity, Λ is the dimensionless pressure calculated from

$$\Lambda=\frac{p}{\mu\omega}\left(\frac{C}{r}\right)^2 \quad (2)$$

p is the dimensional pressure, μ is the dynamic viscosity, C is the radial clearance, and H is the dimensionless film thickness calculated from [3]

$$H=1+\varepsilon\cos(\theta-\phi)+\bar{z}\phi_y\cos\theta-\bar{z}\phi_x\sin\theta \quad (3)$$

for misaligned bearings. In Eq. (3), $\bar{z}=(z-z_0)/C$ is the dimensionless z coordinate, $z_0=L/2$, and (φ_x and φ_y) are the misalignment angles, as shown in Fig. 1.

Numerical Method. Reynolds equation (1) is solved numerically using the finite difference method (FDM). However, doing this directly leads to numerical error propagation due to high local pressure in the minimum film thickness position. To overcome this difficulty, we apply the following transformation (Someya [4]).

$$\bar{\Lambda}=H^{3/2}\Lambda \quad (4)$$

Reynolds equation in terms of the new pressure variable $\bar{\Lambda}$ is given by

$$\frac{\partial^2\bar{\Lambda}}{\partial\theta^2}+\frac{\partial^2\bar{\Lambda}}{\partial\zeta^2}+C_1\bar{\Lambda}=C_2 \quad (5)$$

where

$$C_1=\frac{-3}{4}\left\{\left(\frac{1}{H}\frac{\partial H}{\partial\theta}\right)^2+\frac{2}{H}\frac{\partial^2 H}{\partial\theta^2}\right\} \quad (6a)$$

and

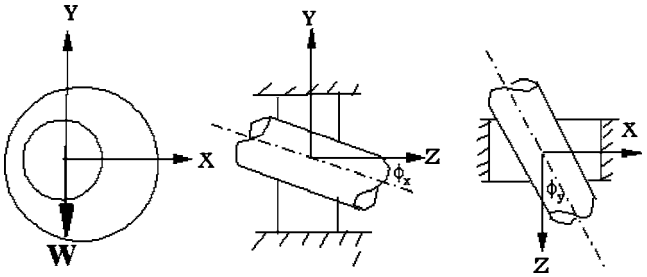

Fig. 1 Misaligned journal bearing configuration

$$C_2 = 6H^{-3/2}\left(\frac{\partial H}{\partial \theta} + 2(\varepsilon\dot{\phi}\sin\theta + \dot{\varepsilon}\cos\theta)\right) \tag{6b}$$

In order to solve Eq. (5) using FDM, the bearing is unwrapped and is uniformly discretized in the θ and ζ directions using grid sizes N and M in each direction, respectively. Let i and j be the grid point subscripts such that $1 \leqslant i \leqslant M$ and $1 \leqslant j \leqslant N$, then the partial derivatives of the dimensionless pressure at any point, ij, are discretized using finite increments $\Delta\theta$ and $\Delta\zeta$ as follows:

$$\frac{\partial \bar{\Lambda}_{ij}}{\partial \theta} = \frac{1}{2\Delta\theta}(\bar{\Lambda}_{i+1,j} - \bar{\Lambda}_{i-1,j})$$

$$\frac{\partial \bar{\Lambda}_{ij}}{\partial \zeta} = \frac{1}{2\Delta\zeta}(\bar{\Lambda}_{i,j+1} - \bar{\Lambda}_{i,j-1})$$

$$\frac{\partial^2 \bar{\Lambda}_{ij}}{\partial \theta^2} = \frac{1}{\Delta\theta^2}(\bar{\Lambda}_{i+1,j} - 2\bar{\Lambda}_{i,j} + \bar{\Lambda}_{i-1,j})$$

$$\frac{\partial^2 \bar{\Lambda}_{ij}}{\partial \zeta^2} = \frac{1}{\Delta\zeta^2}(\bar{\Lambda}_{i,j+1} - 2\bar{\Lambda}_{i,j} + \bar{\Lambda}_{i,j-1}) \tag{7}$$

Substituting these derivatives in Eq. (5), we get

$$AE_{ij}\bar{\Lambda}_{i+1,j} + AW_{ij}\bar{\Lambda}_{i-1,j} + AN_{ij}\bar{\Lambda}_{i,j+1} + AS_{ij}\bar{\Lambda}_{i,j-1} + AP_{ij}\bar{\Lambda}_{i,j} = C_{2ij} \tag{8}$$

where

$$AE_{ij} = \frac{1}{\Delta\theta^2}$$

$$AW_{ij} = \frac{1}{\Delta\theta^2}$$

$$AN_{ij} = \frac{1}{\Delta\zeta^2}$$

$$AS_{ij} = \frac{1}{\Delta\zeta^2}$$

$$AP_{ij} = C_{1ij} - AE_{ij} - AW_{ij} - AN_{ij} - AS_{ij} \tag{9}$$

The system of Eq. (8) is solved using Stone's strongly implicit procedure (SIP). Since the solver is iterative, solution is stopped when the residual error becomes less than 10^{-5}.

Boundary Conditions. In order to solve Eq. (8) numerically, boundary conditions must be specified. In the calculations, the pressure is set to atmospheric values at the point of maximum film thickness, i.e., $\theta=0$, and at the bearing edges. Moreover, during the solution of the Reynolds equation, negative pressure values are generated due to cavitation. In order to determine the cavitation boundary, the classical Reynolds boundary conditions are imposed as follows:

$$\bar{\Lambda} = 0 \quad \text{at } \theta = 0$$

$$\bar{\Lambda} = 0 \quad \frac{\partial \bar{\Lambda}}{\partial \theta} = 0 \quad \text{at } \theta = \theta^*$$

$$\bar{\Lambda} = 0 \quad \text{at } \zeta = 0, \zeta^* \tag{10}$$

In Eq. (10), ζ^* is the dimensionless bearing width ($\zeta^* = L/r$). By using these boundary conditions, the pressure is positive in the range ($0 < \theta < \theta^*$) and zero in the range ($\theta^* < \theta < 2\pi$).

Bearing Load and Attitude Angle. The bearing load-carrying capacity is defined as the reaction force of the lubricating film. Therefore, it can be obtained by integrating the film pressure calculated from the solution of Reynolds equation. The dimensionless film reaction force $\bar{F}$ and its components with respect to the eccentricity direction and its perpendicular direction, $\bar{F}_\varepsilon, \bar{F}_\phi$, are given by the following equations:

$$\bar{F}_\varepsilon = \frac{1}{4(L/D)}\int_A \int \Lambda \cos\theta d\theta d\zeta$$

$$\bar{F}_\phi = \frac{1}{4(L/D)}\int_A \int \Lambda \sin\theta d\theta d\zeta$$

$$\bar{F} = \sqrt{\bar{F}_\varepsilon^2 + \bar{F}_\phi^2} \tag{11}$$

where A is the bearing surface area.

In the static equilibrium state, $\bar{F}$ must be equal to the bearing load. $\bar{F}$ is called the dimensionless bearing load-carrying capacity at the static equilibrium position. The Sommerfeld number (S) is calculated from

$$S = \frac{1}{2\pi\bar{F}} \tag{12}$$

The static equilibrium position is determined by repeating the calculations using different attitude angles, until a certain angle is reached where the bearing load is along the same line of action of the applied load. If the x coordinate is along the line of action as the applied load and the y coordinate normal to it, then $\bar{F}_x$ and $\bar{F}_y$ are as follows:

$$\bar{F}_x = \bar{F}_\varepsilon \cos\phi - \bar{F}_\phi \sin\phi$$

$$\bar{F}_y = \bar{F}_\varepsilon \sin\phi + \bar{F}_\phi \cos\phi \tag{13}$$

Thus, at equilibrium,

$$W = \bar{F}_x$$

$$\bar{F}_y = 0 \tag{14}$$

where W is the applied load. In the computations, φ is initially set to 10 deg then $\bar{F}_y$ is calculated. If calculated $\bar{F}_y$ is greater than zero, then equilibrium is not reached and φ is incremented by 10 deg. If calculated $\bar{F}_y$ is less than zero, an interpolation for the value φ at which $\bar{F}_y=0$ is done. Calculations are repeated until the error in the attitude angle is less than 10^{-5}.

Stiffness and Damping Coefficients. The dimensionless force stiffness and damping coefficients due to displacements are calculated from [5]

$$\bar{K}_{xx} = -\frac{\partial \bar{F}_\varepsilon}{\partial \varepsilon}\cos^2\phi - \frac{\partial \bar{F}_\phi}{\varepsilon \partial \phi}\sin^2\phi + \left(\frac{\partial \bar{F}_\phi}{\partial \varepsilon} + \frac{\partial \bar{F}_\varepsilon}{\varepsilon \partial \phi}\right)\frac{\sin 2\varphi}{2} - \frac{\bar{F}_y}{\varepsilon}\sin\phi \tag{15a}$$

$$\bar{K}_{xy} = -\frac{\partial \bar{F}_\varepsilon}{\varepsilon \partial \phi}\cos^2\phi + \frac{\partial \bar{F}_\phi}{\partial \varepsilon}\sin^2\phi + \left(\frac{\partial \bar{F}_\phi}{\varepsilon \partial \phi} - \frac{\partial \bar{F}_\varepsilon}{\partial \varepsilon}\right)\frac{\sin 2\varphi}{2} + \frac{\bar{F}_y}{\varepsilon}\cos\phi$$

$$\bar{K}_{yx} = -\frac{\partial \bar{F}_\phi}{\partial \varepsilon}\cos^2\phi + \frac{\partial \bar{F}_\varepsilon}{\varepsilon \partial \phi}\sin^2\phi + \left(\frac{\partial \bar{F}_\phi}{\varepsilon \partial \phi} - \frac{\partial \bar{F}_\varepsilon}{\partial \varepsilon}\right)\frac{\sin 2\varphi}{2} + \frac{\bar{F}_x}{\varepsilon}\sin\phi$$

$$\bar{K}_{yy} = -\frac{\partial \bar{F}_\phi}{\varepsilon \partial \phi}\cos^2\phi - \frac{\partial \bar{F}_\varepsilon}{\partial \varepsilon}\sin^2\phi - \left(\frac{\partial \bar{F}_\varepsilon}{\varepsilon \partial \phi} + \frac{\partial \bar{F}_\phi}{\partial \varepsilon}\right)\frac{\sin 2\varphi}{2} - \frac{\bar{F}_x}{\varepsilon}\cos\phi$$

$$\bar{C}_{xx} = -\frac{\partial \bar{F}_\varepsilon}{\partial \dot{\varepsilon}}\cos^2\phi + \frac{\partial \bar{F}_\phi}{\partial \dot{\varepsilon}}\frac{\sin 2\varphi}{2} - \frac{2\bar{F}_x}{\varepsilon}\sin\phi$$

$$\bar{C}_{xy} = \frac{\partial \bar{F}_\phi}{\partial \dot{\varepsilon}}\sin^2\phi - \frac{\partial \bar{F}_\varepsilon}{\partial \dot{\varepsilon}}\frac{\sin 2\varphi}{2} + \frac{2\bar{F}_x}{\varepsilon}\cos\phi$$

$$\bar{C}_{yx} = -\frac{\partial \bar{F}_\phi}{\partial \dot{\varepsilon}}\cos^2\phi - \frac{\partial \bar{F}_\varepsilon}{\partial \dot{\varepsilon}}\frac{\sin 2\varphi}{2} - \frac{2\bar{F}_y}{\varepsilon}\sin\phi$$

$$\bar{C}_{yy} = -\frac{\partial \bar{F}_\varepsilon}{\partial \dot{\varepsilon}}\sin^2\phi - \frac{\partial \bar{F}_\phi}{\partial \dot{\varepsilon}}\frac{\sin 2\varphi}{2} + \frac{2\bar{F}_y}{\varepsilon}\cos\phi \tag{15b}$$

For the misaligned case, additional stiffness and damping coefficients arise due to the creation of forces and moments due to the rotations caused by the angular misalignment. Therefore, the force stiffness and damping coefficients due to rotations are calculated from

$$\bar{K}_{X\phi_x} = -\frac{\partial \bar{F}_\varepsilon}{\partial \phi_x}\cos^2\phi - \frac{\partial \bar{F}_\phi}{\partial \phi_y}\sin^2\phi + \left(\frac{\partial \bar{F}_\phi}{\partial \phi_x} + \frac{\partial \bar{F}_\varepsilon}{\partial \phi_y}\right)\frac{\sin 2\varphi}{2} \tag{16a}$$

$$\bar{K}_{X\phi_y} = -\frac{\partial \bar{F}_\varepsilon}{\partial \phi_y}\cos^2\phi + \frac{\partial \bar{F}_\phi}{\partial \phi_x}\sin^2\phi + \left(\frac{\partial \bar{F}_\phi}{\partial \phi_y} - \frac{\partial \bar{F}_\varepsilon}{\partial \phi_x}\right)\frac{\sin 2\phi}{2}$$

$$\bar{K}_{Y\phi_x} = -\frac{\partial \bar{F}_\phi}{\partial \phi_x}\cos^2\phi + \frac{\partial \bar{F}_\varepsilon}{\partial \phi_y}\sin^2\phi + \left(\frac{\partial \bar{F}_\phi}{\partial \phi_y} - \frac{\partial \bar{F}_\varepsilon}{\partial \phi_x}\right)\frac{\sin 2\phi}{2}$$

$$\bar{K}_{Y\phi_y} = -\frac{\partial \bar{F}_\phi}{\partial \phi_y}\cos^2\phi - \frac{\partial \bar{F}_\varepsilon}{\partial \phi_x}\sin^2\phi - \left(\frac{\partial \bar{F}_\varepsilon}{\partial \phi_y} + \frac{\partial \bar{F}_\phi}{\partial \phi_x}\right)\frac{\sin 2\phi}{2}$$

$$\bar{C}_{X\phi_x} = -\frac{\partial \bar{F}_\varepsilon}{\partial \dot{\phi}_x}\cos^2\phi - \frac{\partial \bar{F}_\phi}{\partial \dot{\phi}_y}\sin^2\phi + \left(\frac{\partial F_\phi}{\partial \dot{\phi}_y} + \frac{\partial F_\varepsilon}{\partial \dot{\phi}_x}\right)\frac{\sin 2\phi}{2}$$

$$\bar{C}_{X\phi_y} = \frac{\partial \bar{F}_\phi}{\partial \dot{\phi}_x}\sin^2\phi - \frac{\partial \bar{F}_\varepsilon}{\partial \dot{\phi}_y}\cos^2\phi + \left(\frac{\partial F_\phi}{\partial \dot{\phi}_y} - \frac{\partial F_\varepsilon}{\partial \dot{\phi}_x}\right)\frac{\sin 2\phi}{2}$$

$$\bar{C}_{Y\phi_x} = -\frac{\partial \bar{F}_\phi}{\partial \dot{\phi}_x}\cos^2\phi + \frac{\partial \bar{F}_\varepsilon}{\partial \dot{\phi}_y}\sin^2\phi + \left(\frac{\partial F_\phi}{\partial \dot{\phi}_y} - \frac{\partial F_\varepsilon}{\partial \dot{\phi}_x}\right)\frac{\sin 2\phi}{2}$$

$$\bar{C}_{Y\phi_y} = -\frac{\partial \bar{F}_\varepsilon}{\partial \dot{\phi}_x}\sin^2\phi - \frac{\partial \bar{F}_\phi}{\partial \dot{\phi}_y}\cos^2\phi - \left(\frac{\partial F_\phi}{\partial \dot{\phi}_x} + \frac{\partial F_\varepsilon}{\partial \dot{\phi}_y}\right)\frac{\sin 2\phi}{2} \tag{16b}$$

The moment stiffness and damping coefficients due to displacements are calculated from

$$\bar{K}_{\phi_x X} = -\frac{\partial \bar{M}_\varepsilon}{\partial \phi_x}\cos^2\phi - \frac{\partial \bar{M}_\phi}{\partial \phi_y}\sin^2\phi + \left(\frac{\partial \bar{M}_\phi}{\partial \phi_x} + \frac{\partial \bar{M}_\varepsilon}{\partial \phi_y}\right)\frac{\sin 2\varphi}{2} \tag{17a}$$

$$\bar{K}_{\phi_x Y} = -\frac{\partial \bar{M}_\varepsilon}{\partial \phi_y}\cos^2\phi + \frac{\partial \bar{M}_\phi}{\partial \phi_x}\sin^2\phi + \left(\frac{\partial \bar{M}_\phi}{\partial \phi_y} - \frac{\partial \bar{M}_\varepsilon}{\partial \phi_x}\right)\frac{\sin 2\phi}{2}$$

$$\bar{K}_{\phi_y X} = -\frac{\partial \bar{M}_\phi}{\partial \phi_x}\cos^2\phi + \frac{\partial \bar{M}_\varepsilon}{\partial \phi_y}\sin^2\phi + \left(\frac{\partial \bar{M}_\phi}{\partial \phi_y} - \frac{\partial \bar{M}_\varepsilon}{\partial \phi_x}\right)\frac{\sin 2\phi}{2}$$

$$\bar{K}_{\phi_y Y} = -\frac{\partial \bar{M}_\phi}{\partial \phi_y}\cos^2\phi - \frac{\partial \bar{M}_\varepsilon}{\partial \phi_x}\sin^2\phi - \left(\frac{\partial \bar{M}_\varepsilon}{\partial \phi_y} + \frac{\partial \bar{M}_\phi}{\partial \phi_x}\right)\frac{\sin 2\phi}{2}$$

$$\bar{C}_{\phi_x X} = -\frac{\partial \bar{M}_\varepsilon}{\partial \dot{\phi}_x}\cos^2\phi - \frac{\partial \bar{M}_\phi}{\partial \dot{\phi}_y}\sin^2\phi + \left(\frac{\partial \bar{M}_\phi}{\partial \dot{\phi}_x} + \frac{\partial \bar{M}_\varepsilon}{\partial \dot{\phi}_y}\right)\frac{\sin 2\phi}{2}$$

$$\bar{C}_{\phi_x Y} = \frac{\partial \bar{M}_\phi}{\partial \dot{\phi}_x}\sin^2\phi - \frac{\partial \bar{M}_\varepsilon}{\partial \dot{\phi}_y}\cos^2\phi + \left(\frac{\partial \bar{M}_\phi}{\partial \dot{\phi}_y} - \frac{\partial \bar{M}_\varepsilon}{\partial \dot{\phi}_x}\right)\frac{\sin 2\phi}{2}$$

$$\bar{C}_{\phi_y Y} = -\frac{\partial \bar{M}_\varepsilon}{\partial \dot{\phi}_x}\sin^2\phi - \frac{\partial \bar{M}_\phi}{\partial \dot{\phi}_y}\cos^2\phi - \left(\frac{\partial \bar{M}_\phi}{\partial \dot{\phi}_x} + \frac{\partial \bar{M}_\varepsilon}{\partial \dot{\phi}_y}\right)\frac{\sin 2\phi}{2}$$

$$\bar{C}_{\phi_y X} = -\frac{\partial \bar{M}_\phi}{\partial \dot{\phi}_x}\cos^2\phi + \frac{\partial \bar{M}_\varepsilon}{\partial \dot{\phi}_y}\sin^2\phi + \left(\frac{\partial \bar{M}_\phi}{\partial \dot{\phi}_y} - \frac{\partial \bar{M}_\varepsilon}{\partial \dot{\phi}_x}\right)\frac{\sin 2\phi}{2} \tag{17b}$$

Similarly, the moment stiffness and damping coefficients due to rotations are calculated from

$$\bar{K}_{\phi_x\phi_x} = -\frac{\partial \bar{M}_\varepsilon}{\partial \varepsilon}\cos^2\phi - \frac{\partial \bar{M}_\phi}{\varepsilon \partial \phi}\sin^2\phi + \left(\frac{\partial \bar{M}_\phi}{\partial \varepsilon} + \frac{\partial \bar{M}_\varepsilon}{\varepsilon \partial \phi}\right)\frac{\sin 2\varphi}{2} - \frac{\bar{M}_y}{\varepsilon}\sin\phi \tag{18a}$$

$$\bar{K}_{\phi_x\phi_y} = -\frac{\partial \bar{M}_\varepsilon}{\varepsilon \partial \phi}\cos^2\phi + \frac{\partial \bar{M}_\phi}{\partial \varepsilon}\sin^2\phi + \left(\frac{\partial \bar{M}_\phi}{\varepsilon \partial \phi} - \frac{\partial \bar{M}_\varepsilon}{\partial \varepsilon}\right)\frac{\sin 2\phi}{2} + \frac{\bar{M}_y}{\varepsilon}\cos\phi$$

$$\bar{K}_{\phi_y\phi_x} = -\frac{\partial \bar{M}_\phi}{\partial \varepsilon}\cos^2\phi + \frac{\partial \bar{M}_\varepsilon}{\varepsilon \partial \phi}\sin^2\phi + \left(\frac{\partial \bar{M}_\phi}{\partial \varepsilon} - \frac{\partial \bar{M}_\varepsilon}{\varepsilon \partial \phi}\right)\frac{\sin 2\phi}{2} + \frac{\bar{M}_x}{\varepsilon}\sin\phi$$

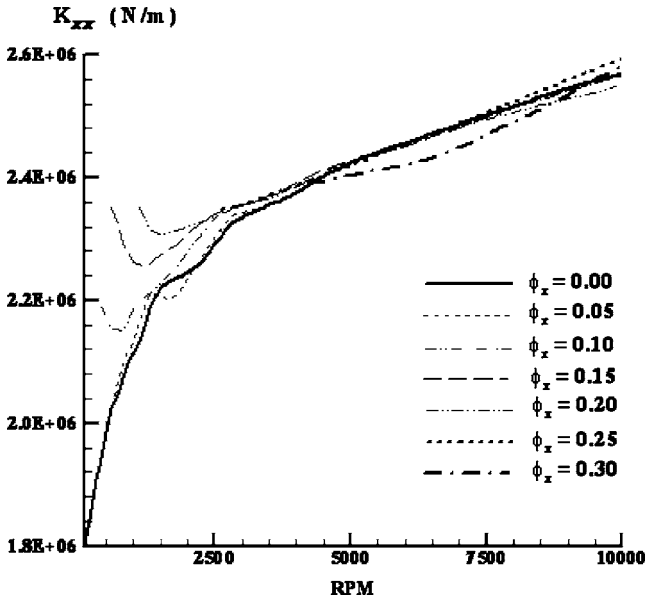

Fig. 2 Effect of varying ϕ_x on K_{xx}, W=137 N

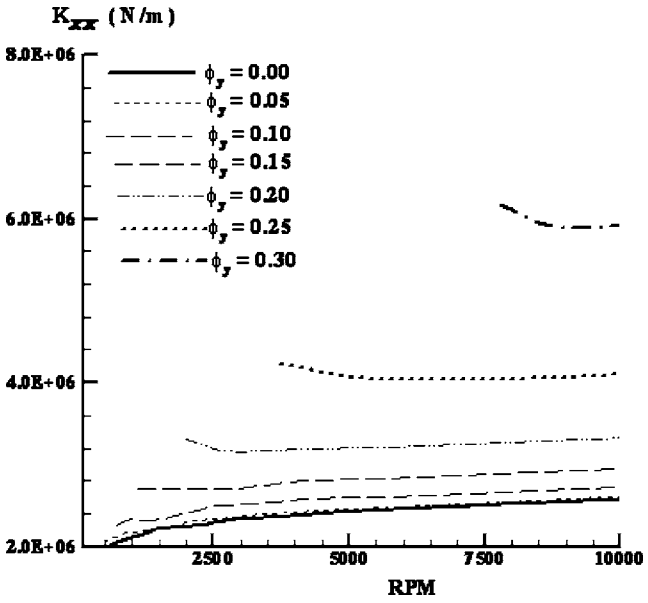

Fig. 4 Effect of varying ϕ_y on K_{xx}

$$\bar{K}_{\phi_y\phi_y} = -\frac{\partial \bar{M}_\phi}{\varepsilon \partial \phi}\cos^2\phi - \frac{\partial \bar{M}_\varepsilon}{\partial \varepsilon}\sin^2\phi - \left(\frac{\partial \bar{M}_\varepsilon}{\varepsilon \partial \phi} + \frac{\partial \bar{M}_\phi}{\partial \varepsilon}\right)\frac{\sin 2\phi}{2} - \frac{\bar{M}_x}{\varepsilon}\cos\phi$$

$$\bar{C}_{\phi_x\phi_x} = -\frac{\partial \bar{M}_\varepsilon}{\partial \dot{\varepsilon}}\cos^2\phi - \frac{\partial \bar{M}_\phi}{\varepsilon \partial \dot{\phi}}\sin^2\phi + \left(\frac{\partial \bar{M}_\phi}{\partial \dot{\varepsilon}} + \frac{\partial \bar{M}_\varepsilon}{\varepsilon \partial \dot{\phi}}\right)\frac{\sin 2\phi}{2}$$

$$\bar{C}_{\phi_x\phi_y} = \frac{\partial \bar{M}_\phi}{\partial \dot{\varepsilon}}\sin^2\phi - \frac{\partial \bar{M}_\varepsilon}{\varepsilon \partial \dot{\phi}}\cos^2\phi + \left(\frac{\partial \bar{M}_\phi}{\varepsilon \partial \dot{\phi}} - \frac{\partial \bar{M}_\varepsilon}{\partial \dot{\varepsilon}}\right)\frac{\sin 2\phi}{2}$$

$$\bar{C}_{\phi_y\phi_x} = -\frac{\partial \bar{M}_\phi}{\partial \dot{\varepsilon}}\cos^2\phi + \frac{\partial \bar{M}_\varepsilon}{\varepsilon \partial \dot{\phi}}\sin^2\phi + \left(\frac{\partial \bar{M}_\phi}{\varepsilon \partial \dot{\phi}} - \frac{\partial \bar{M}_\varepsilon}{\partial \dot{\varepsilon}}\right)\frac{\sin 2\phi}{2}$$

$$\bar{C}_{\phi_y\phi_y} = -\frac{\partial \bar{M}_\varepsilon}{\partial \dot{\varepsilon}}\sin^2\phi - \frac{\partial \bar{M}_\phi}{\varepsilon \partial \dot{\phi}}\cos^2\phi - \left(\frac{\partial \bar{M}_\phi}{\partial \dot{\varepsilon}} + \frac{\partial \bar{M}_\varepsilon}{\varepsilon \partial \dot{\phi}}\right)\frac{\sin 2\phi}{2} \quad (18b)$$

In Eq. (18*a*), the moment components are calculated from

$$\bar{M}_x = \bar{M}_\varepsilon \cos\phi - \bar{M}_\phi \sin\phi$$

$$\bar{M}_y = \bar{M}_\varepsilon \sin\phi + \bar{M}_\phi \cos\phi \quad (19)$$

where

$$\bar{M}_\varepsilon = \frac{-1}{4(L/D)}\int_A \int \Lambda Z \sin\theta \, d\theta \, d\zeta$$

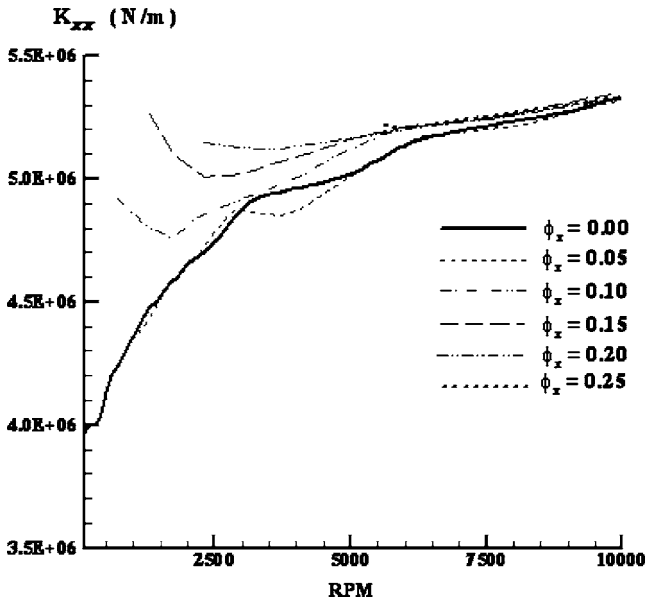

Fig. 3 Effect of varying ϕ_x on K_{xx}, W=304 N

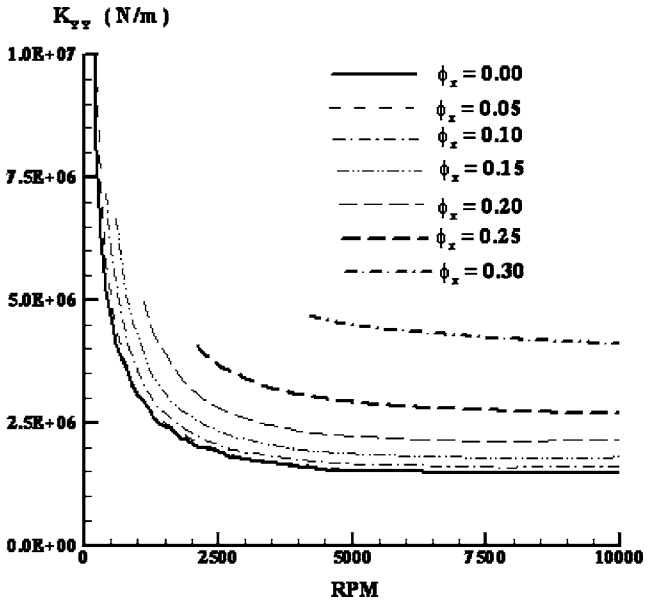

Fig. 5 Effect of varying ϕ_x on K_{yy}

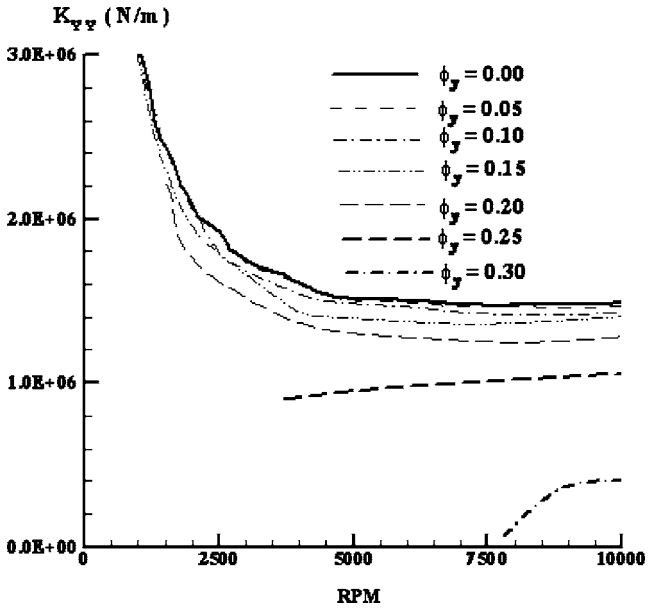

Fig. 6 Effect of varying ϕ_y on K_{yy}

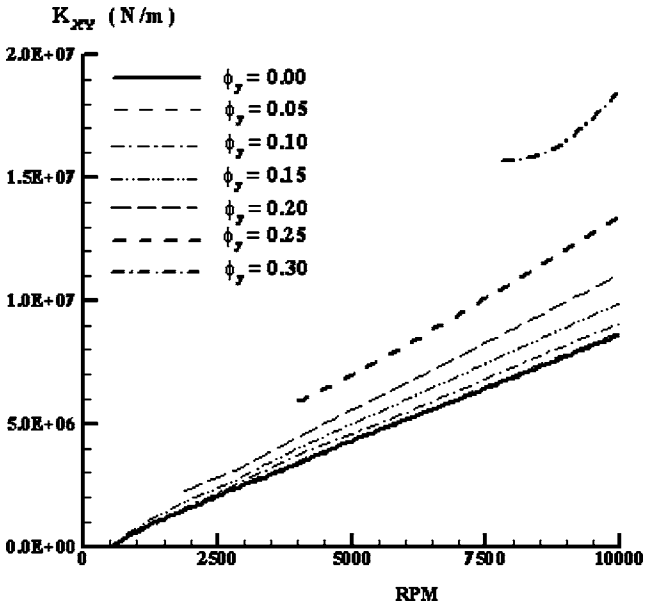

Fig. 8 Effect of varying ϕ_y on K_{xy}

$$M_\phi = \frac{1}{4(L/D)} \int_A \int \Lambda Z \cos\theta d\theta d\zeta \tag{20}$$

It should be noted that the nondimensional coefficients $\bar{K}_{xy}$, $\bar{K}_{yx}$, etc., and $\bar{C}_{xy}$, $\bar{C}_{yx}$, etc. are related to their dimensional counterparts k_{xy}, k_{yx}, etc., and c_{xy}, c_{yx}, etc. through

$$\bar{K}_{xy} = \frac{C}{LD\mu N(R/C)^2} k_{xy} \quad \text{etc.}$$

and

$$\bar{C}_{xy} = \frac{C\omega}{LD\mu N(R/C)^2} c_{xy} \quad \text{etc.} \tag{21}$$

However, since the following nondimensionalization

$$K_{xy} = \frac{C}{W} k_{xy} \quad \text{etc.}$$

and

$$C_{xy} = \frac{C\omega}{W} c_{xy} \quad \text{etc.} \tag{22}$$

is used, then the values from Eqs. (15)–(18) are multiplied by the Sommerfeld number to obtain K and C.

To determine the stiffness and damping coefficients in Eqs. (15)–(18), the partial derivatives of the force and moment components should be determined. In the computations, these coefficients were calculated in two different ways. The first method is to calculate these numerical coefficients by deriving equations for the pressure derivatives from Reynolds equations, which are then integrated to obtain the force and moment derivatives. The second method is to evaluate these derivatives numerically. However, in

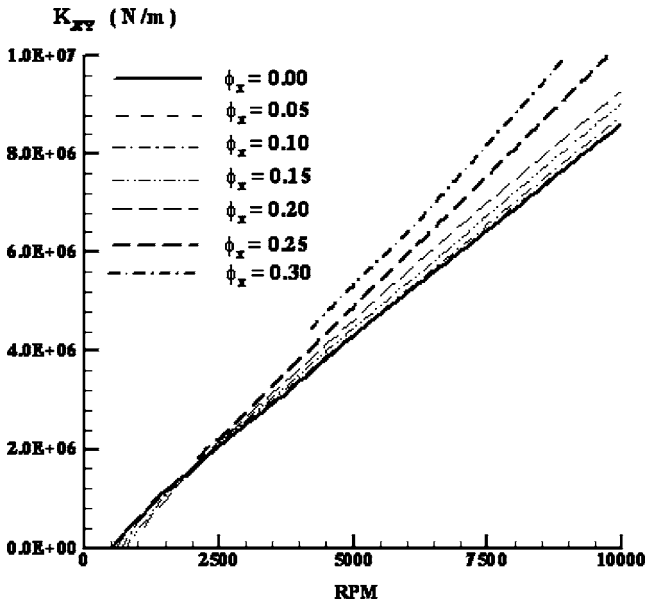

Fig. 7 Effect of varying ϕ_x on K_{xy}

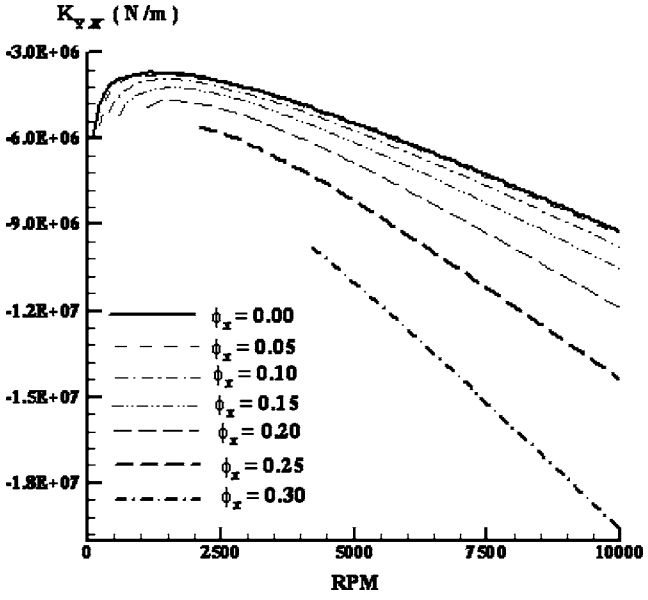

Fig. 9 Effect of varying ϕ_x on K_{yx}

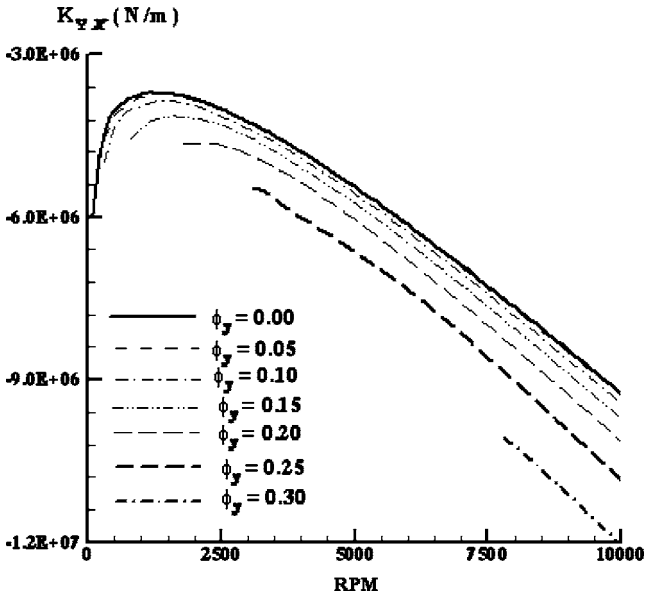

Fig. 10 Effect of varying ϕ_y on K_{yx}

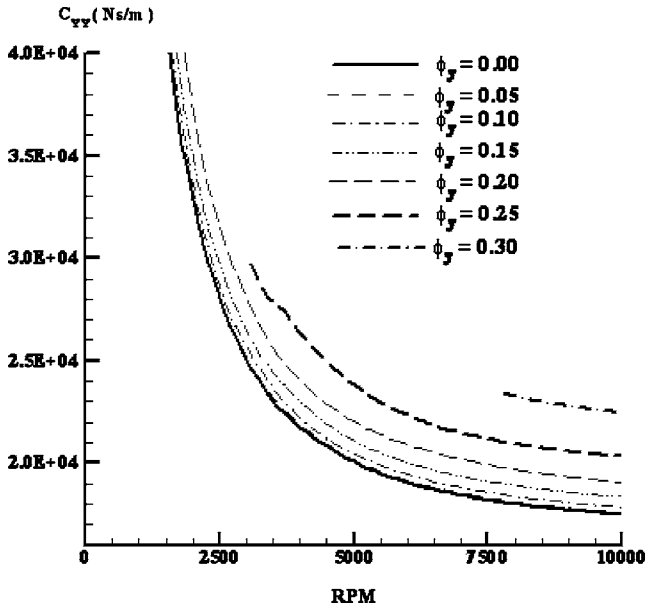

Fig. 12 Effect of varying ϕ_y on C_{yy}

the second method, the derivatives are sensitive to the sizes of perturbations. The method introduced by Adams [6], to evaluate the size of the perturbations, is adopted in the computations. Both methods gave similar values for the derivatives.

Results

In order to determine the order of magnitude of the stiffness and damping coefficients under misalignment conditions, a parametric study is performed. The values of ϕ_x and ϕ_y were varied independently from 0.0 deg to 0.3 deg in steps of 0.05. The calculations are performed for a journal bearing of 0.09 m diameter, 0.045 m length, and a radial clearance of 135 μm, with a dynamic oil viscosity of 6.9 Pa s. The bearing loads used were 137 N and 304 N. These loads are just representative quantities, and the conclusions are independent of these specific values.

Figures 2 and 3 show the effect of varying ϕ_x on K_{xx} for the cases with bearing loads of 137 and 304, respectively. The figures show that the variation in K_{xx} is similar in both cases. The main difference between the two figures is in the increase in the magnitude of K_{xx} as the load increases. Also, there is no curve for the case of ϕ_x=0.3 in Fig. 3, because contact takes place as the load increases. This is normal, since increasing the load increases the bearing eccentricity. This in turn increases the chance of bearing contact, as the misalignment increases. Since the load magnitude did not affect the trends of the results, all the figures shown here with the exception of Fig. 3 are for the case with W=137 N. However, similar results were obtained at higher loads.

Figure 4 shows the effect of varying ϕ_y on K_{xx}. The figure shows a monotonic increase in K_{xx} as ϕ_y increases. The size of this change is larger than that noticed in Fig. 2 for the effect of varying ϕ_x for the same case. The reason for this different behavior is because increasing ϕ_x loads the bearing in the y direction, while increasing ϕ_y loads the bearing in the x direction. This is also seen in Fig. 5 and 6, which show the effects of varying ϕ_x

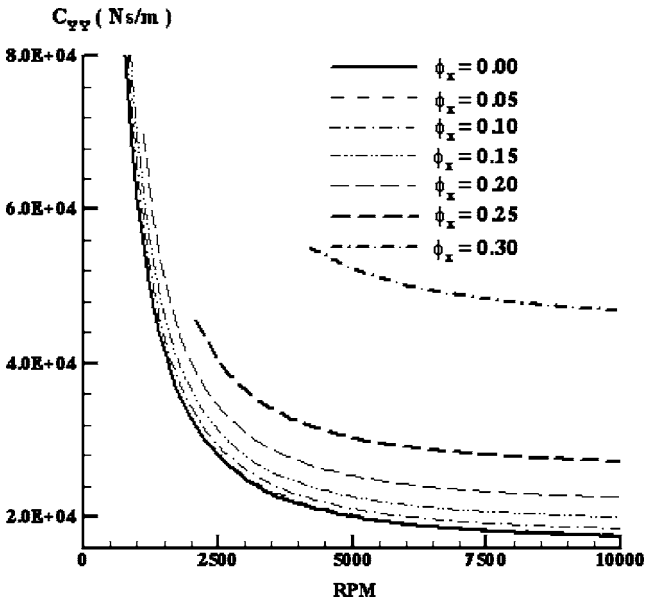

Fig. 11 Effect of varying ϕ_x on C_{yy}

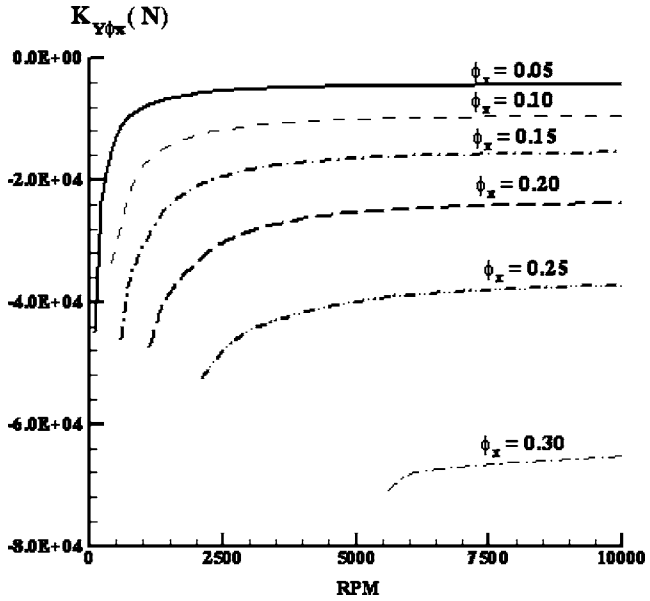

Fig. 13 Effect of varying ϕ_x on $K_{Y\phi_x}$

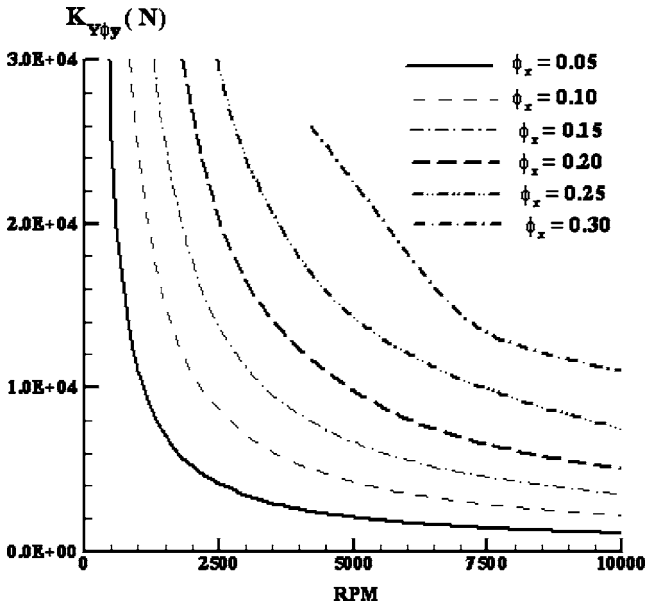

Fig. 14 Effect of varying ϕ_x on $K_{Y\phi_y}$

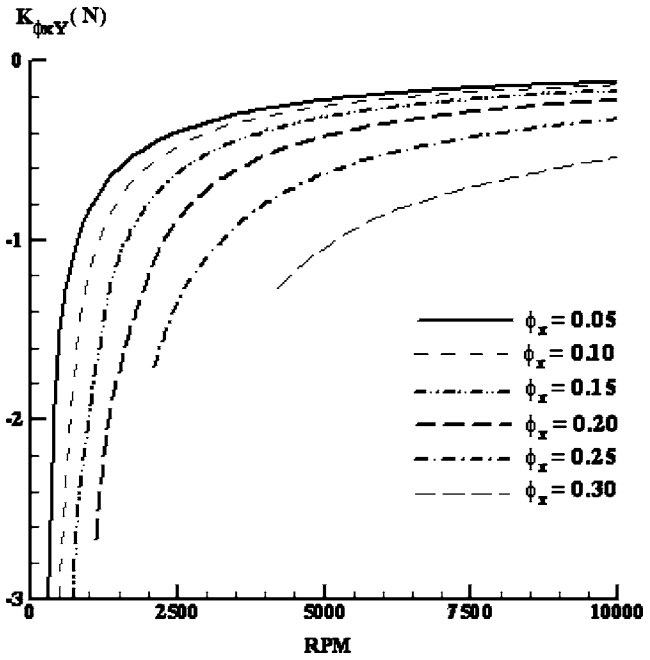

Fig. 16 Effect of varying ϕ_x on $K_{\phi_{xY}}$

and ϕ_y on the values of K_{yy}. The figures show that increasing ϕ_x caused a corresponding increase in K_{yy}, while increasing ϕ_y caused a corresponding decrease in K_{yy}.

Figures 7 and 8 show the effect of varying ϕ_x and ϕ_y on K_{xy}, respectively. The figures show that ϕ_y has a more pronounced effect on K_{xy} than ϕ_x. The opposite trend is observed in Fig. 9 and 10, where increasing ϕ_x causes a greater change in K_{yx} than that caused by ϕ_y. Again, the reason for this behavior is because increasing ϕ_x increases the bearing loading in the y direction, while increasing ϕ_y increases the bearing loading in the x direction.

The effect of varying ϕ_x and ϕ_y on C_{yy} is shown in Fig. 11 and 12, which show that increasing both ϕ_x and ϕ_y increases C_{yy}. However, the increase in ϕ_x caused larger increases in C_{yy} than that of ϕ_y. This is again due to the same reason, i.e., θ_x causes more bearing loading in the y direction, while ϕ_y causes more bearing loading in the x direction. This behavior occurs also for C_{xx} (not shown), which exhibits similar behavior with the variation of ϕ_x and ϕ_y. The changes in C_{xy}, C_{yx} were negligible and are not shown here for brevity.

Figures 13 and 14 show the effect of varying ϕ_x on $K_{Y\Phi x}$ and $K_{Y\Phi y}$, respectively. The figures show that increasing ϕ_x increases $K_{Y\Phi x}$ and $K_{Y\Phi y}$. The effect of varying ϕ_x on $K_{X\phi y}$ (not shown) is similar to that of $K_{Y\Phi x}$. The changes in $K_{x\Phi x}$ due to varying ϕ_x were negligible and thus was not shown here. The effect of varying ϕ_y on $K_{x\Phi y}$, $K_{y\Phi y}$, $K_{x\Phi x}$, and $K_{x\Phi x}$ was similar to that of ϕ_x and was not shown here for brevity. Note that these stiffness coefficients arise only due to misalignment and are not present in the aligned case.

Figure 15 shows the effect of varying ϕ_x on $C_{Y\Phi y}$. The figure

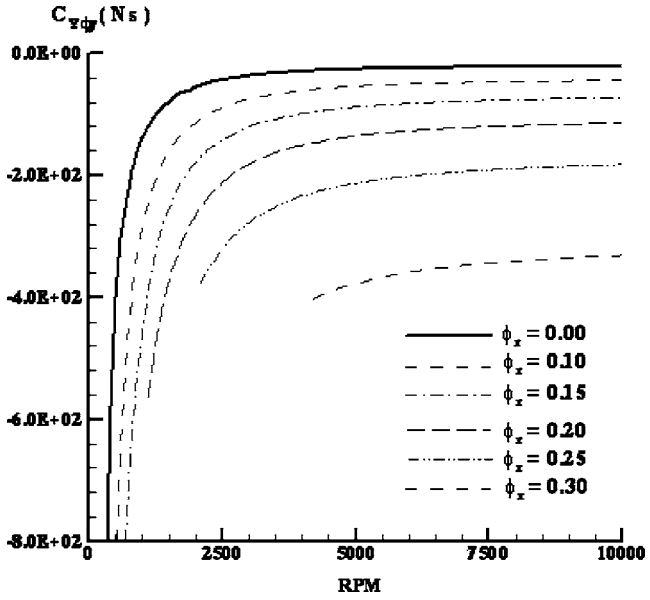

Fig. 15 Effect of varying ϕ_x on $C_{Y\phi_y}$

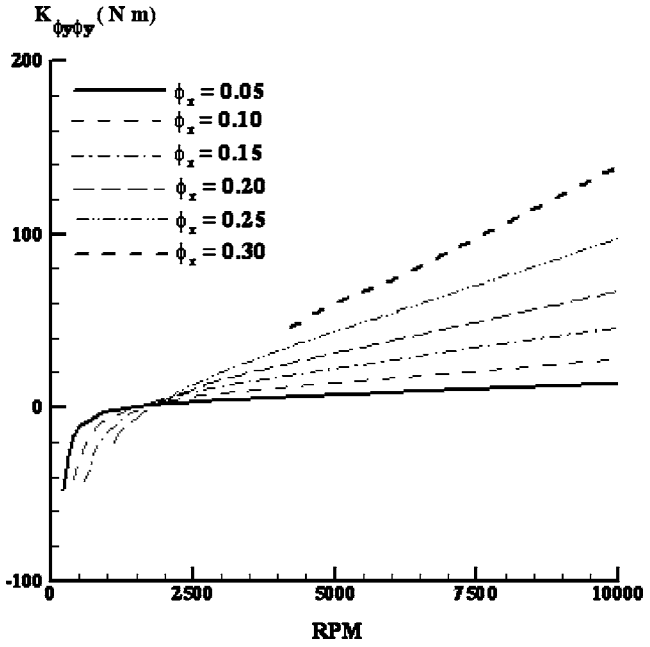

Fig. 17 Effect of varying ϕ_x on $K_{\phi_y\phi_y}$

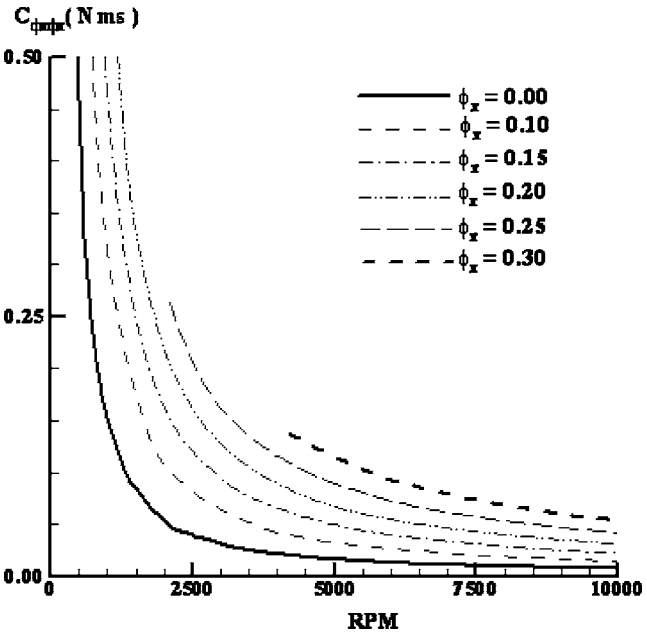

Fig. 18 Effect of varying ϕ_x on $C_{\phi_x\phi_x}$

shows an increase in $C_{Y\Phi_y}$ as ϕ_x increases. The effect of varying ϕ_x on $C_{X\Phi_y}$, $C_{Y\Phi_x}$, and $C_{Y\Phi_y}$ showed similar behavior and again is not shown here for brevity. The effect of varying ϕ_y on the same coefficients showed similar behavior and also is not shown here.

The effect of varying ϕ_x and ϕ_y on the values of the moment stiffness coefficients due to displacements, $K_{\Phi xX}$, $K_{\Phi xY}$, $K_{\Phi yX}$, and $K_{\Phi yY}$, showed similar behavior to the trends stated earlier. However, the values of these moment coefficients were small as is exemplified in Fig. 16 for the values of $K_{\Phi xY}$. Again, increasing ϕ_x increases $K_{\Phi xY}$. The effect of varying ϕ_x and ϕ_y on the moment damping coefficients due to displacements, $C_{\Phi xX}$, $C_{\Phi xY}$, $C_{\Phi yX}$, and $C_{\Phi yY}$, showed similar behavior and thus is not shown here.

The effect of varying ϕ_x and ϕ_y on the values of the moment stiffness and damping coefficients due to rotations, $K_{\Phi x\Phi x}$, $K_{\Phi x\Phi y}$, $K_{\Phi y\Phi x}$, $K_{\Phi y\Phi y}$, $C_{\Phi x\Phi x}$, $C_{\Phi x\Phi y}$, $C_{\Phi y\Phi x}$, and $C_{\Phi y\Phi y}$, showed similar behavior to their counterpart due to displacement explained earlier. Here, we only show the effect of varying ϕ_x on $K_{\Phi y\Phi y}$ and $C_{\Phi x\Phi y}$ in Figs. 17 and 18, respectively.

Conclusions

The results show the effect of shaft misalignment on the values of force and moment stiffness and damping coefficients. It was shown that shaft misalignment has a significant effect on all the coefficients. This effect increased as the magnitude of misalignment increased. It was also shown that the moment coefficients were much smaller than force coefficients. However, the magnitudes of the force coefficients due to rotations were comparable to the original force coefficients due to displacements. Thus, when designing rotors that could run with misalignment, considerations of the changes in stiffness and damping coefficients should be taken into consideration.

It is planned to further study this problem for alternate bearing designs and considering variation of viscosity with temperature. The application of these coefficients to rotordynamic models is also planned.

References

[1] Yu, H., and Adams, M. L., 1989, "The Linear Model for Rotor-Dynamic Properties of Journal Bearings and Seals With Combined Radial and Misalignment Motions," J. Sound Vib., **131**(3), pp. 367–378.
[2] El-Shafei, A., Tawfick, S. H., Raafat, M. S., and Aziz, G. M., 2007 "Some Experiments on Oil Whirl and Oil Whip," ASME J. Eng. Gas Turbines Power, **129**(1), pp. 144–153.
[3] San Andres, L., 1993, "Effect of Shaft Misalignment on the Dynamic Force Response of Annular Pressure Seals," Tribol. Trans., **36**(2), pp. 173–182.
[4] Someya, T., 1989, *Journal-Bearing Databook*, Springer-Verlag, Berlin.
[5] Szeri, A. Z., 1998, *Fluid Film Lubrication, Theory and Design*, Cambridge University Press, Cambridge.
[6] Adams, M. L., 2001, *Rotating Machinery Vibration*, Dekker, New York.

Model Calibration of Anisotropic Rotordynamic Systems With Speed-Dependent Parameters

A. A. Younan

A. El-Shafei

Department of Mechanical Design and Production,
Faculty of Engineering, Cairo University,
Giza 12316, Egypt

In this paper, a method for calibrating rotordynamic models of speed-dependent systems with anisotropic support is presented. The method is based on the comparison between the calculated eigenvalues and those extracted from the measured synchronous frequency response functions. An eigensensitivity analysis is conducted to calculate the sensitivity of the computed eigenvalues to the selected elements to be updated. This method is suitable for field application since it requires simple coastdown tests. The method is illustrated on a test rig with fluid film bearings and is shown to be effective in the calibration of rotordynamic models at the speeds of the modes excited within the operating speed range. [DOI: 10.1115/1.2770485]

Introduction

Rotordynamic models are widely used in the field. These models, based on either finite element methods [1,2] or transfer matrices [3], are able to offer an estimate of the dynamic behavior of machines. This behavior is illustrated by the calculation of the natural frequencies and associated mode shapes, the study of the system dynamic stability, and the prediction of the forced response due to various exciting forces.

The costs of creating these dynamic models are high, but without any validation of the output results, much of the time and effort exerted may be wasted. Furthermore, based on a calibrated dynamic behavior, the field engineer will reach better solutions for vibration problems and will take wiser decisions for maintenance procedures. As an example, the feasibility of rotor balancing without trial weights [4] is strongly dependent on the knowledge of the orbital mode shape extracted from the dynamic model of the rotor. In fact, the success of selecting the suitable balancing weights and planes is dependent on the model's accurate representation of the actual behavior of the rotor. It is clear that a calibrated dynamic model is a basic necessity rather than a luxury in the rotordynamics field [5].

Thus, the modeling effort should not only focus on the dimensions, support parameters, and system properties input to the models but should also consider the output results and their correlation with the behavior of the real system. Furthermore, some difficulties confronted during the input phase of the modeling could be solved in the calibration phase. These difficulties are caused by the inadequate capabilities in modeling damping effects, in particular, and many basic elements effects, such as fluid film bearings, seals, and fluid-structure interaction. In addition, some elements, such as rolling element bearings, have stiffness properties that are load dependent. In the field, these problems are circumvented by ad hoc methods of tweaking model parameters to fit or satisfy coastdown data. However, too much rides on the use of calibrated dynamic models to be left to ad hoc procedures.

In this paper, a structured calibration procedure is illustrated to update finite element models in the field. Currently, the best way to calibrate a rotordynamic model is to conduct a modal test [6] to correlate the modal parameters of the model to the ones of the actual system. However, conducting a complete modal test is not practical in field applications since it is expensive, time consuming, and requires magnetic exciters that are not often available.

In addition, for speed-dependent systems, the excitation of the rotor at a given rotation speed with different frequencies will excite the system eigenvalues corresponding to the system characteristics at this specific speed. These eigenvalues are not the actual critical speeds excited during the coastdown since the system parameters and the eigenvalues change with the speed. Therefore, the peaks of coastdown [7] (synchronous frequency response functions (SFRFs)) are the most representative for the actual critical speeds for this type of system.

The presented methodology is based on conducting simple coastdowns. By using the modal testing theories, the system's modal parameters, within the required speed range, are extracted [8]. The system model is constructed using the complex representation of the response in order to identify the directivity of the modes. A sensitivity analysis is conducted in order to study the sensitivity of the eigenvalues to the changes in the selected elements of the system stiffness and damping matrices. These elements represent both the conservative and nonconservative forces, which affect the natural frequencies and damping ratios, respectively. Lastly, the inverse eigensensitivity method [6,9] is conducted at each critical speed separately to update the selected sensitive elements to reach the extracted complex eigenvalues with an accepted deviation in the norm between the calculated and measured mode shapes.

Future work will be continued to include mode shape updating in a global optimization procedure. This calibration procedure is simple; however, it is believed that such a technique is useful for calibrating a speed-dependent system with anisotropic support in the field. This proposed technique was conducted on a rotor system supported on speed-dependent anisotropic bearings, and the results are illustrated.

Computerized Model

Using the finite element method, the rotordynamic system can be modeled with a finite number of degrees of freedom (DOFs) (N), within a limited frequency range [10],

$$\mathbf{M}_r\ddot{\mathbf{q}}_r + \mathbf{C}_r\dot{\mathbf{q}}_r + \mathbf{K}_r\mathbf{q}_r = \mathbf{F}_r \tag{1}$$

where $\mathbf{M}_r$ is the $N \times N$ global mass matrix, $\mathbf{C}_r$ represents the $N \times N$ speed-dependent global damping matrix, and $\mathbf{K}_r$ is the $N \times N$ speed-dependent global stiffness matrix of the system. Note that the damping matrix contains both the damping and gyroscopic terms. The vector $\mathbf{q}_r$ represents the nodal displacement, which consists of four DOFs for each node (X, Y, θ_X, and θ_Y), two

Contributed by the International Gas Turbine Institute of ASME for publication in the JOURNAL OF ENGINEERING FOR GAS TURBINES AND POWER. Manuscript received July 14, 2005; final manuscript received May 11, 2007; published online April 24, 2008. Review conducted by Matthew O. T. Cole. Paper presented at the ASME Turbo Expo 2005: Land, Sea and Air (GT2005), Reno, NV, June 6–9, 2005. Paper No. GT2005-68887.

translational and two rotational degrees in the horizontal and vertical planes, respectively. The vector $\mathbf{F}_r$ represents the excitation force on the system.

This representation of rotordynamic systems in a real representation has a disadvantage in its inability to identify the directivity of the modes. Hence, it is convenient to introduce the complex representation [11] (see Appendix). The complex representation is able to represent the orbital response of the rotor in polar coordinates, and it is able to give a clear distinction of the directivity of modes, e.g., forward and backward whirling [12]. The complex representation has the form

$$\mathbf{M}\ddot{\mathbf{q}} + \mathbf{C}\dot{\mathbf{q}} + \mathbf{K}\mathbf{q} = \mathbf{F} \tag{2}$$

where $\mathbf{M}$ is the complex global mass matrix, $\mathbf{C}$ is the speed-dependent complex global damping matrix, and $\mathbf{K}$ is the speed-dependent complex global stiffness matrix of the system [13]. The vector $\mathbf{q}$ represents the complex nodal displacement, which consists of DOFs for each node ($X+iY$, $X-iY$, $\theta_X+i\theta_Y$, and $\theta_X-i\theta_Y$), two complex translational and two complex rotational degrees. The vector $\mathbf{F}$ represents the complex excitation force.

In order to calculate the modal parameters of the system, the system is transformed to a first order system (state space representation), where

$$\begin{bmatrix} \mathbf{0} & \mathbf{M} \\ \mathbf{M} & \mathbf{C} \end{bmatrix}\begin{bmatrix} \ddot{\mathbf{q}} \\ \dot{\mathbf{q}} \end{bmatrix} + \begin{bmatrix} -\mathbf{M} & \mathbf{0} \\ \mathbf{0} & \mathbf{K} \end{bmatrix}\begin{bmatrix} \dot{\mathbf{q}} \\ \mathbf{q} \end{bmatrix} = \begin{bmatrix} \mathbf{0} \\ \mathbf{F} \end{bmatrix} \tag{3}$$

or

$$\mathbf{A}\dot{\mathbf{w}} + \mathbf{B}\mathbf{w} = \mathbf{Q}$$

Due to the presence of the gyroscopic effect as well as the hydrodynamic effect of the bearing, the above system has nonsymmetric matrices (non-self-adjoint system) [8]. In order to solve this eigenvalue problem, both right and left eigenvectors should be calculated. The right eigenvectors and the complex natural frequencies can be obtained from the homogenous part of the first order equation,

$$(\lambda_j \cdot \mathbf{A} + \mathbf{B})\mathbf{r}_j = \mathbf{0} \quad j = 1, \ldots, 2N \tag{4}$$

where $\mathbf{r}_j$ is the jth right eigenvector and λ_j is its complex eigenvalue.

The left eigenvectors, which represent the excitability of each mode from different DOFs [11] and its complex natural frequencies, can be obtained in the same manner from the first order equation,

$$\mathbf{l}_j^T(\lambda_j \cdot \mathbf{A} + \mathbf{B}) = \mathbf{0}^T \quad j = 1, \ldots, 2N \tag{5}$$

where $\mathbf{l}_j$ is the jth left eigenvector and λ_j is its complex eigenvalue.

The right and left eigenvectors may be orthonormalized so as to satisfy the following equations:

$$\mathbf{L}^T \cdot \mathbf{A} \cdot \mathbf{R} = \mathbf{I} \tag{6}$$

$$\mathbf{L}^T \cdot \mathbf{B} \cdot \mathbf{R} = \mathbf{D} \tag{7}$$

Updating Procedure and Sensitivity Analysis

The objective of the updating procedure is to guide the computed model using the experimental eigenvalues in order to reach similar calculated ones. This updating will focus on modifying the conservative elements in the stiffness matrix ($\mathbf{K}_{xx}, \mathbf{K}_{yy}$) and in the damping matrix ($\mathbf{C}_{xy}, \mathbf{C}_{yx}$). These elements have a direct effect on the calculation of the natural frequency. In addition, the analysis will include the nonconservative elements in the stiffness matrix ($\mathbf{K}_{xy}, \mathbf{K}_{yx}$) and in the damping matrix ($\mathbf{C}_{xx}, \mathbf{C}_{yy}$). These elements affect the damping in the rotordynamic systems, which has a direct effect on the calculation of the damping ratio.

The conventional updating was divided into two successive procedures [6]. First, iterations were carried out to update the system to meet the measured natural frequency by calculating the sensitivity matrix of the stiffness matrix to the imaginary part of the eigenvalues. Then, the second iterations were focused on updating the damping ratios by calculating the sensitivity of the damping matrix to the real part of the eigenvalues. However, the complex representation will have the advantage of blending those two procedures in a single one for updating the total complex eigenvalues.

In other words, a sensitivity analysis of the four complex elements of the stiffness matrix (Appendix) is conducted to calculate their effects on the calculation of the eigenvalues. The real parts of these elements represent the conservative forces, which affect mainly the imaginary parts of the eigenvalues (mainly the natural frequencies). The imaginary parts of these elements represent the nonconservative forces, which affect mainly the real parts of the eigenvalues (mainly the damping ratios).

In addition, this analysis will also include the effect of the four complex elements of the damping matrix (Appendix). The real parts of these elements represent the nonconservative forces, which affect mainly the real parts of the eigenvalues (mainly the damping ratios). The imaginary parts of these elements represent the conservative forces, which affect mainly the imaginary parts of the eigenvalues (mainly the natural frequencies).

The selected updated locations are the bearing and support locations, which are believed to be the sensitive elements in the rotordynamic systems and which affect directly the calculation of the eigenvalues of the system. In addition, the disk locations are also modified in order to account for their aerodynamic effect on the damping and their fixation effect on the stiffness.

It is important to note that the system parameters are speed dependent. Therefore, the correction parameters ($\boldsymbol{\delta}$) are also speed dependent, which urges the updating procedure to calibrate each speed separately. In the complex presentation, since the elements are complex conjugate, the number of the correction parameters is halved (two damping and two stiffness parameters)

$$\mathbf{A} = \mathbf{A}_o + \mathbf{A}'(\boldsymbol{\delta}) \tag{8}$$

$$\mathbf{B} = \mathbf{B}_o + \mathbf{B}'(\boldsymbol{\delta}) \tag{9}$$

where $\mathbf{A}_o$ and $\mathbf{B}_o$ are the original matrices calculated without any updating at the designated speed, and they remain constant during the iterations. These two matrices represent the identity of the original system. $\mathbf{A}'(\boldsymbol{\delta})$ and $\mathbf{B}'(\boldsymbol{\delta})$ are zero matrices, except at the selected locations to be updated where a correction parameter $\boldsymbol{\delta}_h$ is added. These correction parameters will be altered during iteration through the sensitivity matrix as well as the difference between the calculated and the measured eigenvalues.

The target of the updating process is to minimize this difference, which is illustrated in the following equation:

$$\boldsymbol{\lambda}_d(\boldsymbol{\delta}) = \boldsymbol{\lambda}_m - \boldsymbol{\lambda}_c(\boldsymbol{\delta}) \tag{10}$$

Retaining first order terms,

$$\boldsymbol{\lambda}_c(\boldsymbol{\delta}_o + \Delta\boldsymbol{\delta}) = \boldsymbol{\lambda}_c(\boldsymbol{\delta}_o) + \mathbf{S} \cdot \Delta\boldsymbol{\delta} \tag{11}$$

$\mathbf{S}$ is the complex sensitivity matrix of calculated eigenvalues to the variation in the updated elements. $\boldsymbol{\delta}_o$ represents the vector of the original values of the correction parameters,

$$\boldsymbol{\lambda}_d(\boldsymbol{\delta}) = \boldsymbol{\lambda}_m - (\boldsymbol{\lambda}_c(\boldsymbol{\delta}_o) + \mathbf{S} \cdot \Delta\boldsymbol{\delta}) \tag{12}$$

$$\boldsymbol{\lambda}_d(\boldsymbol{\delta}) = \Delta\boldsymbol{\lambda}_m - \mathbf{S} \cdot \Delta\boldsymbol{\delta} \tag{13}$$

where $\Delta\boldsymbol{\lambda}_m = \boldsymbol{\lambda}_m - \boldsymbol{\lambda}_c(\boldsymbol{\delta}_o)$.

Using the inverse eigensensitivity method, the objective function is chosen to minimize the difference $\Delta\boldsymbol{\lambda}_m$; hence, the updating parameter is calculated from the following equation:

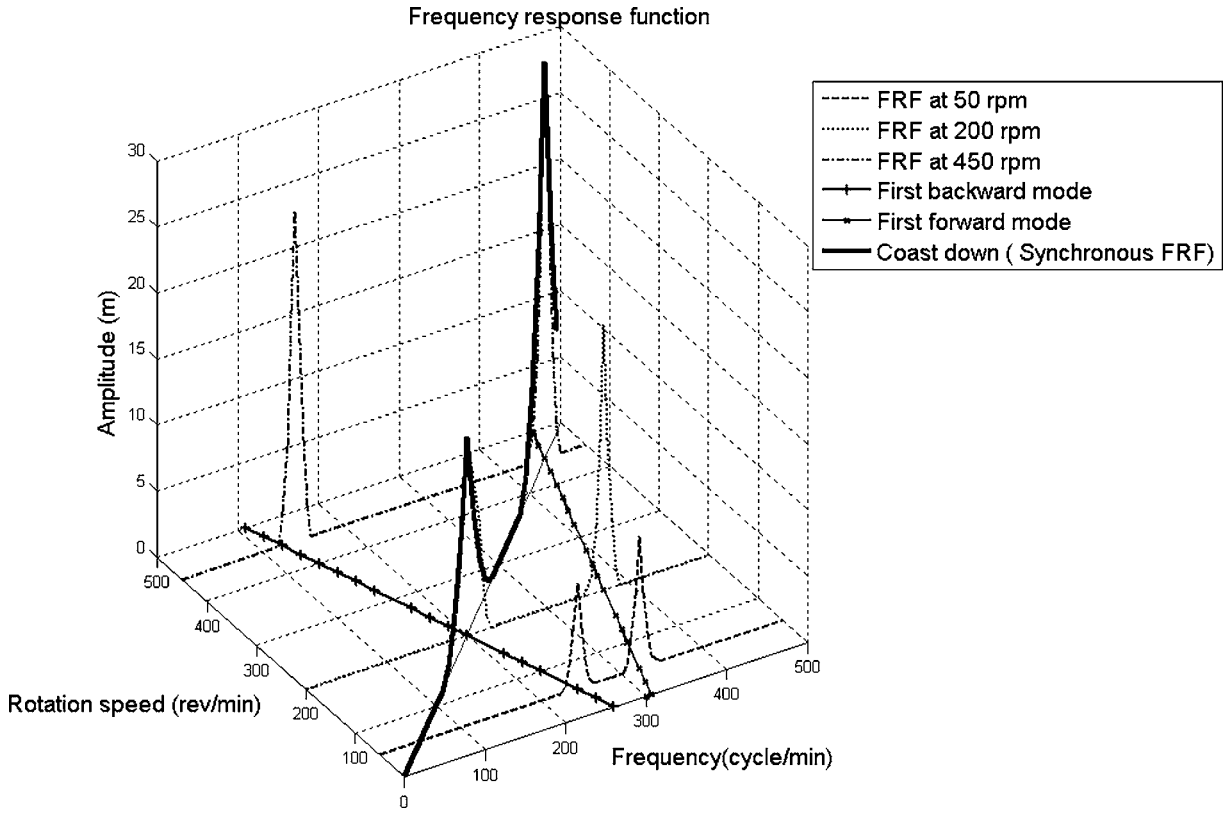

Fig. 1 Combined waterfall and Campbell diagram of the hypothetical system

$$\Delta\boldsymbol{\lambda}_m = \mathbf{S} \cdot \Delta\boldsymbol{\delta} \tag{14}$$

In order to calculate the sensitivity, the eigenvalue problem in Eq. (4) will be differentiated with respect to the parameters $\boldsymbol{\delta}$. For the hth parameter, the sensitivity is given by

$$\frac{\partial}{\partial \delta_h}[(\lambda_j \cdot \mathbf{A} + \mathbf{B})\mathbf{R}_j] = \mathbf{0} \tag{15}$$

where $h = 1, \ldots, 4 \times$ number of updated locations $j = 1, \ldots, 2N$,

$$\left(\frac{\partial \lambda_j}{\partial \delta_h} \cdot \mathbf{A} + \lambda_j \cdot \frac{\partial \mathbf{A}}{\partial \delta_h} + \frac{\partial \mathbf{B}}{\partial \delta_h}\right) \cdot \mathbf{R}_j + (\lambda_j \cdot \mathbf{A} + \mathbf{B})\frac{\partial \mathbf{R}_j}{\partial \delta_h} = \mathbf{0} \tag{16}$$

Using the orthogonality property of the eigenvectors, Eq. (16) will be premultiplyed by the jth left eigenvector

$$\mathbf{L}_j^T\left(\frac{\partial \lambda_j}{\partial \delta_h} \cdot \mathbf{A} + \lambda_j \cdot \frac{\partial \mathbf{A}}{\partial \delta_h} + \frac{\partial \mathbf{B}}{\partial \delta_h}\right) \cdot \mathbf{R}_j + \mathbf{L}_j^T(\lambda_j \cdot \mathbf{A} + \mathbf{B})\frac{\partial \mathbf{R}_j}{\partial \delta_h} = \mathbf{0} \tag{17}$$

Substituting Eqs. (4) and (5) into Eq. (16), the sensitivity of the jth eigenvalue to the hth updating location is given by

$$\mathbf{S}(j,h) = \frac{\partial \lambda_j}{\partial \delta_h} = -\lambda_j \cdot \mathbf{L}_j^T \cdot \frac{\partial \mathbf{A}}{\partial \delta_h} \cdot \mathbf{R}_j - \mathbf{L}_j^T \cdot \frac{\partial \mathbf{B}}{\partial \delta_h} \cdot \mathbf{R}_j \tag{18}$$

In order to calculate the correction parameters in Eq. (14), the pseudoinverse of the complex sensitivity matrix is calculated. It is important to note that the sensitivity matrix $\mathbf{S}$ can be used in selecting the updating locations. Wherever the sensitivity matrix has large elements would be a prime candidate location for the updating since any deviation in the parameters at that location would result in a large change in the eigenvalues. Thus, an examination of the sensitivity matrix confirmed the physical selection of the bearings and disk locations as appropriate updating locations.

Calibration Procedure

First, a finite element model of the studied system is constructed using the rotor dimensions, material properties, and support parameters. The eigenvalues and the associated eigenvectors are calculated using the original system matrices. Second, a coastdown test is conducted on the rotor in order to extract the natural frequencies and damping ratios of the system within the concerned operating speed range. These extracted eigenparameters will be the target of the model calibration procedure. At each measuring point, the vibration is measured in the horizontal as well as in the vertical direction in order to have full orbital information at each measured location.

At this point, it is important to clarify that the FRF measured during a coastdown test is actually a unique form of the FRF for speed-dependent systems. It is actually the FRF measured along the synchronous line, as shown in Fig. 1, where a waterfall diagram for several FRFs is superimposed over a Campbell diagram for an anisotropic rotordynamic system. The peaks of the usual FRF at a given speed are the natural frequencies at this speed. However, the peaks of the synchronous FRF are actually the critical speeds obtained by exciting the rotor by an unbalance force during a coastdown. Due to the anisotropic nature of the support, each mode exhibits both forward and backward components. The directivity of the mode is determined from the largest magnitude of these two. The response to the unbalance force, with its forward nature, will be dominated by forward modes [12].

It should be clear that the excited modes during a coastdown are system characteristics. Therefore, the natural frequencies and damping characteristics of these modes can be identified accurately, irrespective of the synchronous excitation of the system. Since these are system characteristics, it is expected that the amplification factor (and thus the damping characteristics) are similar

whether the excitation is synchronous or otherwise. This explains the practice of obtaining damping properties from the Bode and Nyquist plots in the field.

For the hypothetical system shown in Fig. 1, we excite, and thus can only identify, a limited number of all the natural frequencies. However, this limited number of natural frequencies are deemed to be the most important since they correspond to the critical speeds. It is also assumed that the damping properties of each of these critical speeds calculated from the coastdown would be the most representative of the system damping because the system properties are determined by the eigenvalues, irrespective of the excitation mechanism. In the rotordynamic design of rotating machinery, the critical speeds are the most important eigenvalues to be considered since they can be excited during run-up and coastdown, and are usually the most important modes in predicting the system behavior. Therefore, from a practical point of view, updating the eigenvalues corresponding to the critical speeds, although not complete, is sufficient to obtain a useful calibrated model.

The presented calibration procedure is limited only to the eigenvalues and not to the eigenvectors. However, the residue representing the modal contribution does not change much. This will be clear when comparing the figures of the original and updated mode shapes. The conclusion is that updating the eigenvalue alone does not worsen the prediction of the eigenvectors. The procedure for a simultaneous updating of the eigenvalues and eigenvectors requires many more measurement points, which may not be available for field applications. The work has been extended by the authors to update the eigenvalues and eigenvectors, and it is quite successful. The technique for a simultaneous updating is reserved for laboratory use, while the technique presented in this paper is more suitable for field application.

For each critical speed of the measured coastdown, the complex sensitivity matrix of the eigenvalues with respect to the updated locations is calculated from Eq. (18) using the eigenvectors of the original system. Then, the correction parameters ($\Delta\delta_h$) are calculated from Eq. (14) using the difference between the measured and calculated complex eigenvalues. After adding the correction parameters, the modal parameters are recalculated from Eqs. (4) and (5) using the updated matrices **A** and **B**. Then, the difference is computed between the experimental data and the updated modal parameters. The iteration continues until the specified acceptable error is obtained. The flow chart shown in Fig. 2 illustrates the procedure of the proposed technique for calibrating the natural frequencies of the rotordynamic models.

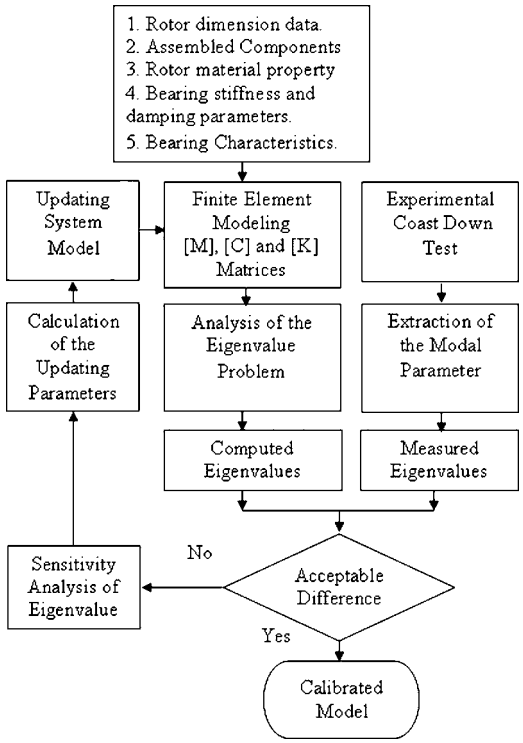

Fig. 2 Calibration procedure flow chart

Test Rig Description

The updating procedure was implemented on a test rig with 1 in. diameter rotor and 1.2 m length [14]. The rotor is a chrome-coated stainless steel, with 7800 kg/m^3 density and 210 GPa modulus of elasticity. Four disks are fixed on the shaft, one central disk and three overhung disks, as shown in Fig. 3. Each disk has a 170 mm outer diameter, a 15 mm thickness, and a 2.6 kg mass.

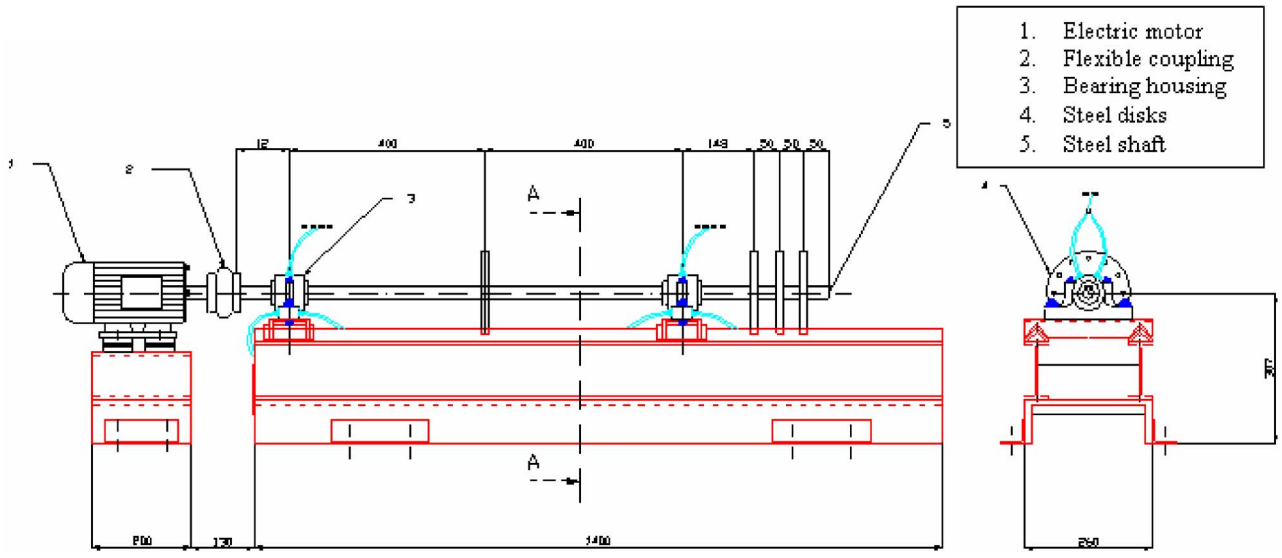

Fig. 3 Experimental test rig used to verify the procedure

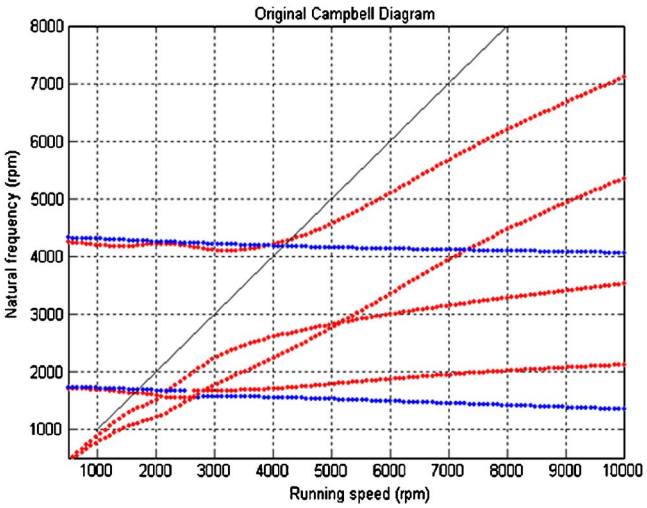

Fig. 4 Original calculated Campbell diagram

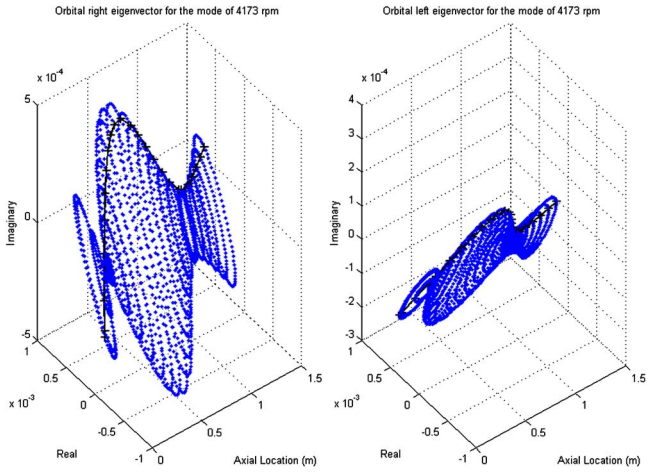

Fig. 6 Second calculated orbital right and left eigenvectors

Twelve 8 mm diameter holes are drilled in each disk on a 140 mm diameter circle in order to allow for balancing mass fixation.

This rotor configuration was selected in an overhung shape in order to cross two critical speeds in a relatively low speed range and to allow for a large modal activity at the bearings. The shaft is driven by a three phase electric motor of 2.2 kW power through a Fenaflex flexible coupling. Speed was controlled using a FUJI electric frequency inverter (FVR-E11, 2.2 kW). The rotor is supported on two plain journal bearings. The bearing material is SAE 64 phosphor bronze, which is considered as a typical copper alloy cast bearing material. The bearings have 62 mm outer diameter, 25.4 mm inner diameter, 35 μm diametral clearance, and 15 mm effective length; thus, $\mathbf{L}/\mathbf{D}$ is equal to 0.6.

Measurement System

The measurement of the vibration signal at each point was carried out by two proximity probes, 90 deg apart, in the horizontal as well as in the vertical position.

The proximity probes are Bently Nevada, series 7200, and 5 mm in diameter. A Schenck photoelectric probe, model P84, is used to measure the rotational speed of the shaft. The photoelectric probe monitors a reflective tape fixed on the shaft and acts as a phase reference. Signals from the proximity probes and the photoelectric probe are simultaneously fed to a Bently Nevada digital vector filter (DVF-3) and a 20 MHz analog oscilloscope, BK Precision Model 2522A. The DVF-3 is a two channel tracking filter.

At each point, the x and y probes and the phase reference were fed to the DVF-3. The oscilloscope was used to view orbital data. The computer used was a Pentium IV, 2.4 GHz with 256 Mbytes random access memory (RAM) and 40 Gbytes hard disk. It is equipped with a National Instruments GPIB card Model PCMCIA complying with the IEEE 488.2 standards. The card was used to interface with the DVF-3. The data were analyzed and displayed using LABVIEW 6 in order to monitor the coastdown and to store it.

It should be pointed out that in the field, although it is possible to measure vibration within the interior of the operating machinery using proximity probes; however, these probes are not abundant in the field. That is why we selected to update only the eigenvalues because measurement of the eigenvector requires measurement from many probes, but this is not available in the field.

Finite Element Modeling

Using the rotor dimensions, material property, and bearing parameter, a finite element model of this test rig was constructed using 25 key points, 24 rotor elements, 5 disk elements, and 2 speed-dependent journal bearings. The total number of DOFs was 100 (four DOFs for each key point). The gyroscopic effect was taken into consideration. The global mass, damping, and stiffness matrices were computed, and then the eigenvalue problem was solved in order to calculate the modal parameters.

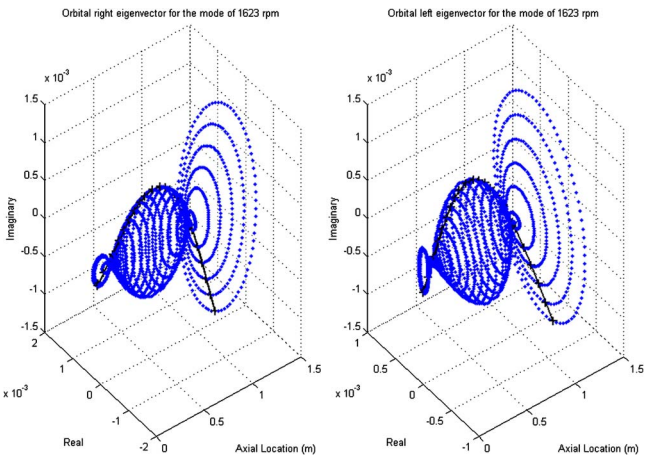

Fig. 5 First calculated orbital right and left eigenvectors

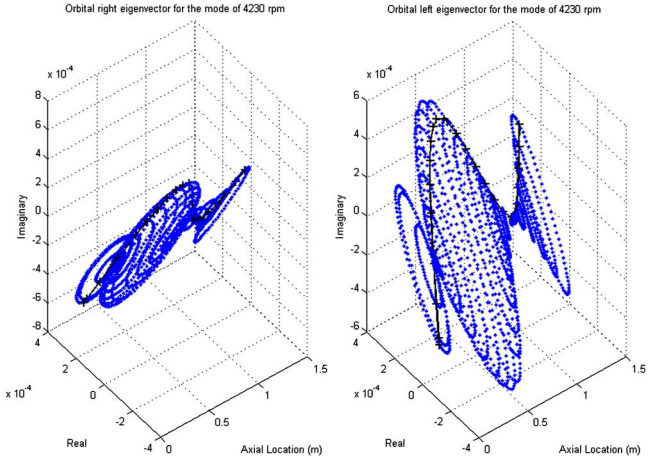

Fig. 7 Third calculated orbital right and left eigenvectors

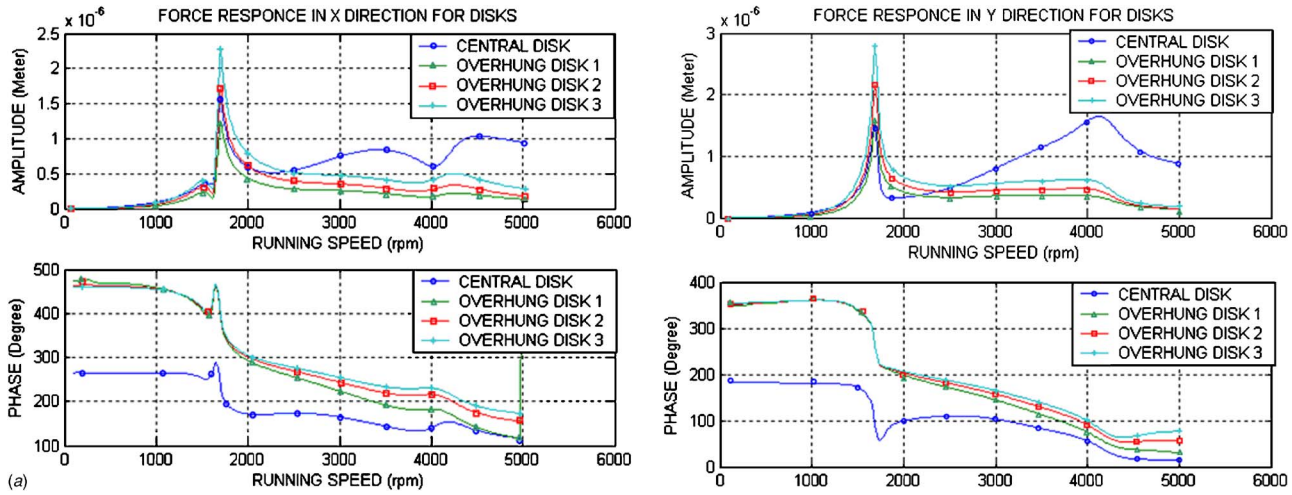

Fig. 8 (*a*) Horizontal calculated unbalance response. (*b*) Vertical calculated unbalance response.

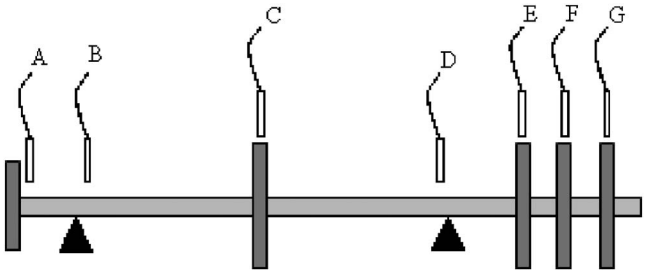

Fig. 9 Schematic diagram of the measured points

The calculated critical speeds are shown in Fig. 4 at different speeds in the Campbell diagram format. From an inspection of the Campbell diagram, the first mode has bearing parameters of an isotropic nature; this is clear from the eigenvalues at the zero speed. For the second mode, the bearing parameters are anisotropic. In the isotropic mode, the forward component of the major backward mode is zero; therefore, no excitation was found by the unbalance forced response. From the 45 deg line, which represents the synchronous excitation line, the calculated critical speeds were at 1623 rpm and 4278 rpm from the intersection with the major forward modes and at 4173 rpm from the intersection with the minor forward mode. The mode shapes are illustrated in

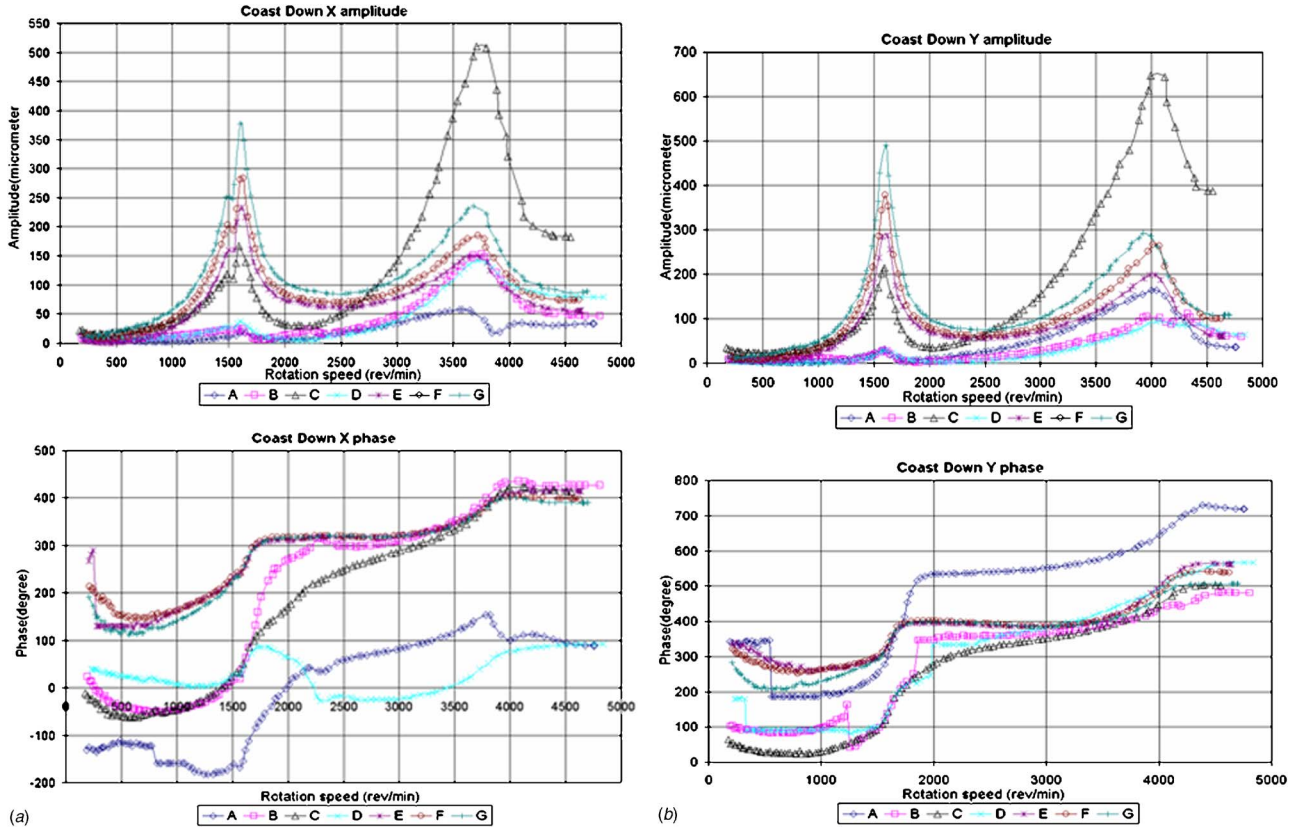

Fig. 10 (*a*) Horizontal coastdown (synchronous FRF). (*b*) Vertical coastdown (synchronous FRF).

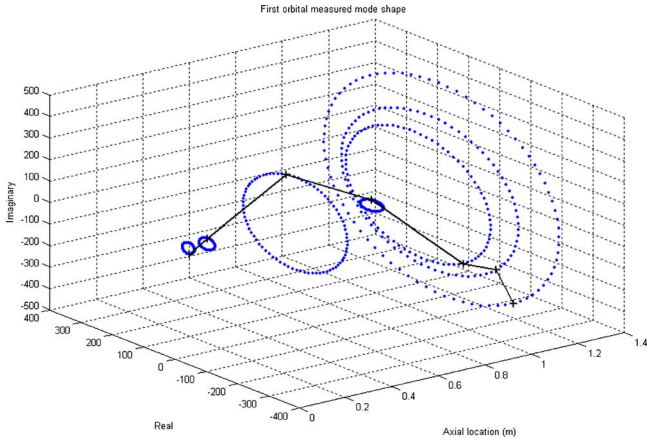

Fig. 11 First orbital mode shape (1593 cycles/min)

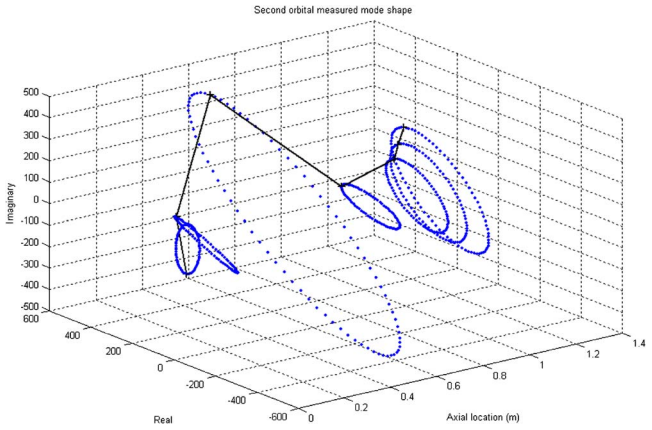

Fig. 12 Second orbital mode shape (3614 cycles/min)

Figs. 5–7. Each mode is presented in the horizontal and vertical planes, which could be combined in order to have complete orbital information. Also, the computed unbalance response in the horizontal and vertical planes is shown in Fig. 8.

Experimental Data

In order to acquire the actual parameters of the system, coastdown tests were conducted. In the tests, the rotor was divided to a number of measured points. The measured points are indicated in Fig. 9: point A is near the coupling, points B and D are at each bearing, and points C, E, F, and G are located at each disk. At each point, the vibration was measured in the horizontal direction (x) and in the vertical direction (y) in order to have the complex orbital vibration. The SFRFs are presented in Fig. 10.

It should be pointed out that the coastdown tests were conducted while the motor is shut off. The rotor was coasting down under its own inertia and, thus, any torque effects were eliminated. The modal parameters were extracted from the experimental data using modal testing theories [8]. The circle fit method was used to identify the eigenvalues using an in-house developed algorithm [14]. Although one measurement point along the rotor was sufficient to obtain the eigenvalues, the results from several horizontal and vertical planes were measured and identified. The extracted eigenvalues are thus the averaged values for several measurements. The three extracted eigenvalues in a complex representation were $(-143.91+1593i)$ cycles/min, $(-548.3+3614i)$ cycles/min, and $(-530.3+4045i)$ cycles/min. These eigenvalues correspond to the damped system behavior. The corresponding undamped natural frequencies for the first three forward modes are 1599.5 cycles/min, 3655.38 cycles/min, and 4079.59 cycles/min, respectively, and the corresponding damping ratios are 0.08997, 0.1500, and 0.1300, respectively. The experimental mode shapes were calculated from the FRFs at each measuring point. These mode shapes are illustrated in Figs. 11–13.

After calculating the difference between the calculated eigenvalues of the model and those extracted from the experimental data, the updating process is conducted for each speed separately in order to update the elements of the complex stiffness matrix of the two bearings as well as the elements of the complex damping matrix of the bearings. After the iteration, the updated damping ratio and the natural frequency results are as illustrated in Tables 1 and 2, respectively.

From the tables, the updating procedure reached the measured values in a limited number of iterations. Thus, the calibration procedure has updated the system matrices at the three critical speeds obtained from the synchronous FRF.

It is interesting to understand the corrections for the damping and stiffness matrices at each of the locations. It should be noted that the order in the computed stiffness matrices was 10^9 N/m and that in the damping was 10^4 N s/m. The changes required to calibrate the model were less than 1% for the stiffness and 20% for the damping, which indicate that the update was successful to retain the basic physical model without a significant alteration of the initial values. Tables 3 and 4 illustrate the orders of the correction stiffness and damping parameters at selected locations on the rotor. As illustrated throughout the paper, complex numbers were used; hence, the complex stiffness and damping should be converted to the real representation in order to have their "physical meaning" as in the usual representation (see Appendix).

An inspection of the tables indicates that the largest corrections occurred at the drive end (DE) bearing at the third critical speed for both stiffness and damping parameters. This means that to calibrate the modal properties at the third critical speed, the stiffness and damping at the DE bearing were the elements that required the largest updating effort; i.e., the DE bearing was modeled inadequately in the original model.

Also, Tables 3 and 4 clearly illustrate that matching the eigenproperties at each of the critical speeds requires a different updating, and thus each critical speed will have different stiffness and damping updating parameters. This means that the updating is valid only for each of the critical speeds, independently, and cannot be extrapolated to different speeds. This is to be expected since the rotor and the bearings have speed-dependent properties, and thus it would not be prudent to expect that the same calibration parameters can be applied at all speeds.

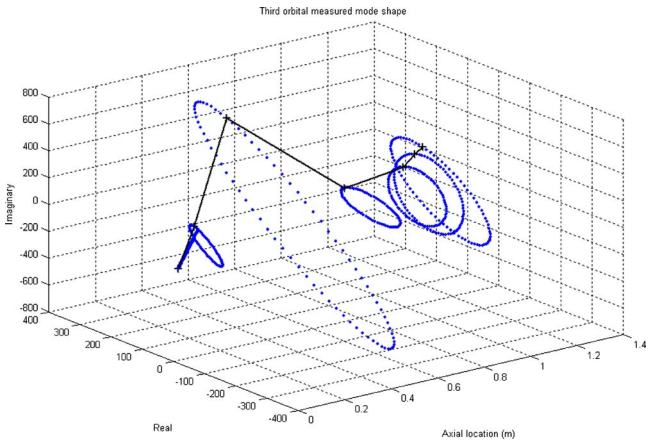

Fig. 13 Third orbital mode shape (4045 cycles/min)

Table 1 Result of the damping ratio updating

Measured	0.08997		0.1500		0.1300	
Iteration	First zeta	% error	Second zeta	% error	Third zeta	% error
1	0.11999	33.360	0.3720	148.016	0.0688	−47.078
5	0.09571	6.381	0.2409	60.605	0.0956	−26.456
10	0.09055	0.643	0.1646	9.703	0.1097	−15.618
15	0.09002	0.052	0.1530	1.983	0.1184	−8.890
20	0.08997	−0.002	0.1508	0.548	0.1236	−4.926
25	0.08997	0.001	0.1503	0.169	0.1274	−2.004
30	0.08997	0.001	0.1501	0.052	0.1297	−0.197
35	0.08997	0.000	0.1500	0.016	0.1300	−0.003
40	0.08997	0.000	0.1500	0.004	0.1300	0.008

Table 2 Results of the natural frequency updating

Measured	1599.50	Cycles/min	3655.38	Cycles/min	4079.59	Cycles/min
Iteration	First ω_n	% error	Second ω_n	% error	Third ω_n	% error
1	1640.77	2.580	4443.77	21.568	4188.79	2.6765
5	1613.59	0.881	3944.97	7.922	4090.07	0.2568
10	1604.47	0.311	3739.09	2.290	4076.55	−0.0746
15	1601.32	0.114	3683.73	0.776	4076.54	−0.0750
20	1600.17	0.042	3664.44	0.248	4079.89	0.0072
25	1599.69	0.012	3658.23	0.078	4083.50	0.0957
30	1599.59	0.006	3656.29	0.025	4080.52	0.0226
35	1599.50	0.000	3655.68	0.008	4079.88	0.0070
40	1599.50	0.000	3655.48	0.003	4079.70	0.0025

To clearly illustrate this point, consider Figs. 14 and 15. In each of these figures a Campbell diagram is plotted. In Fig. 14, the updating correction parameters, as calculated at the first critical speed, are added as constant values to the stiffness and damping elements, and the Campbell diagram is computed and plotted in Fig. 14. Similarly, Fig. 15 is the Campbell diagram as computed by adding constant updating parameters obtained at the second critical speed. Clearly the Campbell diagrams in Figs. 14 and 15 are incorrect (compare to Fig. 4). Thus, it can be concluded that the updating presented in this paper is a local updating at particular critical speeds. If a global updating of the model is required, then a method based on calibrating Campbell diagrams should be devised.

Finally, the eigenvectors of the updated system were also calculated and compared with the measured and original ones, as shown in Fig. 16, which illustrates that there was only a small

Table 3 Orders of magnitude of correction parameters of stiffness matrices at selected updating locations (N/m)

Location	At first critical speed	At second critical speed	At third critical speed
	Re+i Img	Re+i Img	Re+i Img
Coupling	$O(10^5+i10^5)$	$O(10^4+i10^4)$	$O(10^5+i10^5)$
DE breaking	$O(10^5+i10^5)$	$O(10^5+i10^5)$	$O(10^6+i10^7)$
Central disk	$O(10^5+i10^4)$	$O(10^4+i10^4)$	$O(10^5+i10^5)$
NDE bearing	$O(10^5+i10^5)$	$O(10^5+i10^5)$	$O(10^5+i10^5)$
Overhung disk	$O(10^4+i10^4)$	$O(10^4+i10^4)$	$O(10^5+i10^5)$

Table 4 Orders of magnitude of correction parameters of damping matrices at selected updating locations (N s/m)

Location	At first critical speed	At second critical speed	At third critical speed
	Re+i Img	Re+i Img	Re+i Img
Coupling	$O(10^3+i10^2)$	$O(10^2+i10^2)$	$O(10^3+i10^3)$
DE bearing	$O(10^3+i10^3)$	$O(10^3+i10^2)$	$O(10^4+i10^3)$
Central disk	$O(10^2+i10^2)$	$O(10^2+i10^1)$	$O(10^2+i10^2)$
NDE bearing	$O(10^3+i10^3)$	$O(10^2+i10^3)$	$O(10^2+i10^2)$
Overhung disk	$O(10^1+i10^1)$	$O(10^2+i10^2)$	$O(10^2+i10^2)$

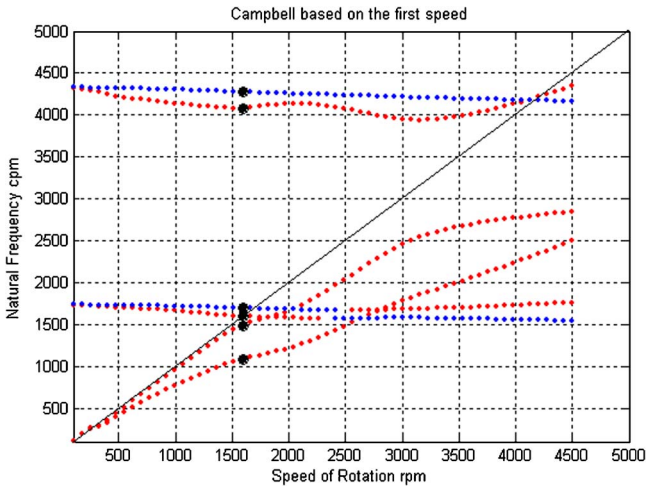

Fig. 14 Updated Campbell diagram based on the correction parameters of the first critical speed

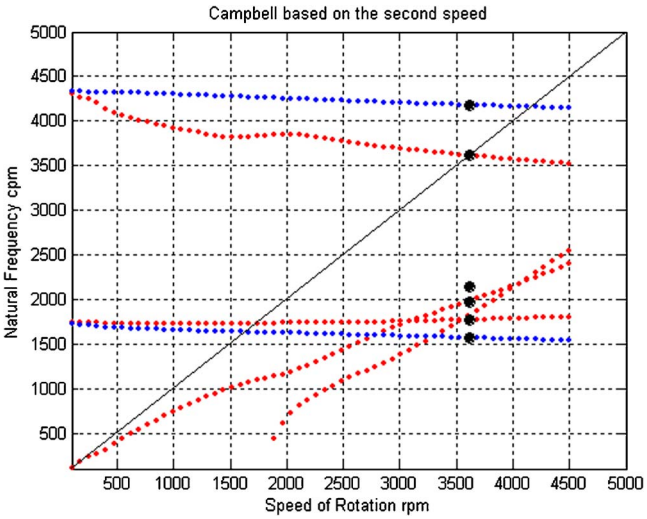

Fig. 15 Updated Campbell diagram based on the correction parameters of the second critical speed

deviation in the eigenvector. Thus, it can be concluded that in many applications it may be sufficient to update only the eigenvalues, and the eigenvectors will not always have to be accurately calibrated. This would be a blessing in field applications since there would be limited access to the many measurement points required to identify the eigenvectors.

Conclusions

In this paper, a calibration procedure was presented to update the model of a speed-dependent system with anisotropic support. The technique implements the eigensensitivity method to reduce the difference between the extracted and calculated modal parameters. The modal parameters were extracted from coastdown tests, which are simple tests for the field application. The complex representation of the system response allowed the updating of the stiffness and damping matrix simultaneously. The results obtained show that the updated damping ratios and natural frequencies have reached the target measured ones.

Appendix

The general real representation for a two DOF system is

$$\underbrace{\begin{bmatrix} m_{xx} & m_{xy} \\ m_{yx} & m_{yy} \end{bmatrix}}_{\mathbf{M}_r} \underbrace{\begin{bmatrix} \ddot{x} \\ \ddot{y} \end{bmatrix}}_{\ddot{\mathbf{q}}_r} + \underbrace{\begin{bmatrix} c_{xx} & c_{xy} \\ c_{yx} & c_{yy} \end{bmatrix}}_{\mathbf{C}_r} \underbrace{\begin{bmatrix} \dot{x} \\ \dot{y} \end{bmatrix}}_{\dot{\mathbf{q}}_r} + \underbrace{\begin{bmatrix} k_{xx} & k_{xy} \\ k_{yx} & k_{yy} \end{bmatrix}}_{\mathbf{K}_r} \underbrace{\begin{bmatrix} x \\ y \end{bmatrix}}_{\mathbf{q}_r} = \underbrace{\begin{bmatrix} f_x \\ f_y \end{bmatrix}}_{f_r}$$

The transformation from real to complex DOFs can be expressed as

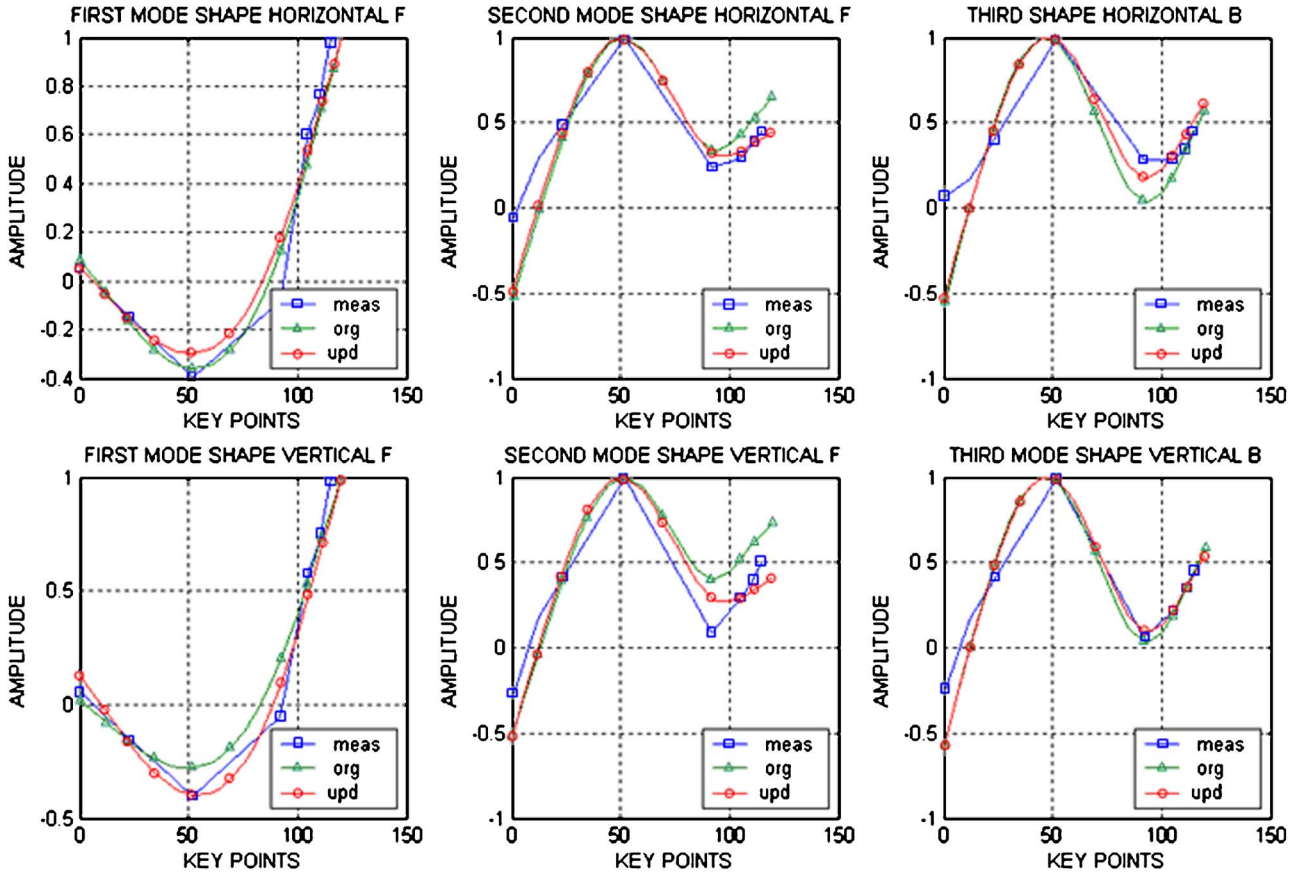

Fig. 16 The comparison between the measured, original, and updated mode shapes

$$z = x + iy \quad \bar{z} = x - iy$$

$$\begin{bmatrix} x \\ y \end{bmatrix} = \frac{1}{2}\begin{bmatrix} 1 & 1 \\ -i & i \end{bmatrix}\begin{bmatrix} z \\ \bar{z} \end{bmatrix} \quad \mathbf{q}_r = T\mathbf{q}$$

$$T^{-1}\mathbf{M}_r T\ddot{\mathbf{q}} + T^{-1}\mathbf{C}_r T\dot{\mathbf{q}} + T^{-1}\mathbf{K}_r T\mathbf{q} = T^{-1}\mathbf{F}_r$$

$$\mathbf{M} = \begin{bmatrix} (m_{xx} + m_{yy}) - i(m_{xy} - m_{yx}) & (m_{xx} - m_{yy}) + i(m_{xy} + m_{yx}) \\ (m_{xx} - m_{yy}) - i(m_{xy} + m_{yx}) & (m_{xx} + m_{yy}) + i(m_{xy} - m_{yx}) \end{bmatrix}$$

$$\mathbf{C} = \begin{bmatrix} (c_{xx} + c_{yy}) - i(c_{xy} - c_{yx}) & (c_{xx} - c_{yy}) + i(c_{xy} + c_{yx}) \\ (c_{xx} - c_{yy}) - i(c_{xy} + c_{yx}) & (c_{xx} + c_{yy}) + i(c_{xy} - c_{yx}) \end{bmatrix}$$

$$\mathbf{K} = \begin{bmatrix} (k_{xx} + k_{yy}) - i(k_{xy} - k_{yx}) & (k_{xx} - k_{yy}) + i(k_{xy} + k_{yx}) \\ (k_{xx} - k_{yy}) - i(k_{xy} + k_{yx}) & (k_{xx} + k_{yy}) + i(k_{xy} - k_{yx}) \end{bmatrix}$$

$$\mathbf{F} = \begin{bmatrix} f_x + if_y \\ f_x - if_y \end{bmatrix}$$

$$\mathbf{M}\ddot{\mathbf{q}} + \mathbf{C}\dot{\mathbf{q}} + \mathbf{K}\mathbf{q} = \mathbf{F}$$

Nomenclature

- $\mathbf{A}$ = augmented complex mass matrix
- $\mathbf{B}$ = augmented complex stiffness matrix
- $\mathbf{A}'$ = augmented updating mass matrix
- $\mathbf{B}'$ = augmented updating stiffness matrix
- $\mathbf{C}_r$ = real global damping matrix
- $\mathbf{C}$ = complex global damping matrix
- $\mathbf{D}$ = eigenvalue diagonal matrix
- $\mathbf{F}_r$ = real excitation force vector
- $\mathbf{F}$ = complex excitation force vector
- i = imaginary number ($i^2 = -1$)
- I = identity matrix
- $\mathbf{K}_r$ = real global stiffness matrix
- $\mathbf{K}$ = complex global stiffness matrix
- $\mathbf{l}$ = unormalized left eigenvectors
- $\mathbf{L}$ = normalized left eigenvectors
- $\mathbf{M}_r$ = real global mass matrix
- $\mathbf{M}$ = complex global mass matrix
- N = number of DOFs
- $\mathbf{q}_r$ = real nodal DOF vector
- $\mathbf{q}$ = complex nodal DOF vector
- $\mathbf{Q}$ = augmented excitation force vector
- $\mathbf{r}$ = unormalized right eigenvectors
- $\mathbf{R}$ = normalized right eigenvectors
- $\mathbf{S}$ = complex sensitivity matrix
- X = horizontal nodal displacement
- Y = vertical nodal displacement
- $\mathbf{w}$ = augmented nodal DOF vector
- $\boldsymbol{\delta}$ = correction parameter vector
- $\boldsymbol{\lambda}_d$ = error between measured and calculated eigenvalues
- θ_X = horizontal nodal rotation
- θ_Y = vertical nodal rotation
- $\boldsymbol{\lambda}$ = complex eigenvalue

Subsript

- o = original value
- r = real matrix
- j,h = jth/hth component
- m = measured variable
- c = calculated variable
- d = difference

References

[1] Nelson, H. D., and McVaugh, J. M., 1976, "The Dynamics of Rotor Bearing Systems Using Finite Elements," ASME J. Eng. Ind., **98**, pp. 593–600.

[2] El-Shafei, A., Bayoumi, H. N., and Mansour, A. M. A, 1998, "Nonlinear Rotor Dynamic Analysis Using Finite Elements and Equivalent Linearization," *Fifth IFToMM International Conference on Rotor Dynamics*, Darmstadt, Germany, pp. 175–187.

[3] Lund, J. W., 1975, "Stability and Damped Critical Speeds of a Flexible Rotor in Fluid-Film Bearings," ASME J. Eng. Ind., **96**(4), pp. 1325–1332.

[4] El-Shafei, A., El-Kabbany, A. S., and Younan, A. A., 2004, "Rotor Balancing Without Trial Weight," ASME J. Eng. Gas Turbines Power, **126**(3), pp. 445–683.

[5] Eshleman, R. L., and Guy, K., 1990, "Validation of Rotor-Dynamics Models Using Dynamic Testing," *Proceedings of the Third IFToMM International Conference on Rotordynamics*, Lyon, France, pp. 27–31.

[6] Irretier, H., and Lindemann, S., 2002, "Improvement of Damping Parameters of Flexible Rotors by Experimental Modal Analysis and Model Updating," *Proceedings of the Sixth IFToMM International Conference on Rotordynamics*, Sydney, Australia, pp. 388–395.

[7] Smart, M. G., Friswell, M. I., and Lees, A. W., 2000, "Estimating Turbogenerator Foundation Parameters: Model Selection and Regularization," Proc. R. Soc. London, Ser. A, **456**, pp. 1583–1607.

[8] Ewins, D. J., 2000, *Modal Testing: Theory, Practice and Application*, 2nd ed., Research Studies Press Ltd., Baldock, Hertfordshire, England.

[9] Mottershead, J. E., and Friswell, M. I., 1993, "Model Updating in Structural Dynamics: A Survey," J. Sound Vib., **167**(2), pp. 347–375.

[10] Bayoumi, H. N, 1995, "Development of a Finite Element Program for Nonlinear Rotordynamics Analysis Using Equivalent Linearization," M.Sc. thesis, Faculty of Engineering, Cairo University.

[11] Lee, C. W., 1993, *Vibration Analysis of Rotors*, Kluwer, Dordrecht.

[12] Kessler, C., and Kim, J., 2002, "Vibration Analysis of Rotor Utilizing Implicit Directional Information of Complex Variable Descriptions," ASME J. Vibr. Acoust., **124**, pp. 340–349.

[13] Gutierrez-Wing, E. S., and Ewins, D. J., 2002, "Characterization of Rotating Machinery Dynamics Within Limited Frequency Intervals Using Modal Analysis," *Proceedings of the Sixth IFToMM International Conference on Rotordynamics*, Sydney, Australia, pp. 486–495.

[14] Younan, A. A., 2004, "Calibration of Rotor Dynamic Models," M.Sc. thesis, Faculty of Engineering, Cairo University.

Experimental and Numerical Investigation of Rotating Bladed Disk Forced Response Using Underplatform Friction Dampers

Ibrahim A. Sever
Rolls-Royce plc,
P.O. Box 31,
Derby DE24 8BJ UK
e-mail: ibrahim.sever@rolls-royce.com

Evgeny P. Petrov
e-mail: y.petrov@imperial.ac.uk

David J. Ewins
e-mail: d.ewins@imperial.ac.uk

Department of Mechanical Engineering,
Imperial College London,
London SW7 2AZ, UK

In this paper, we present a methodology and results from an experimental investigation of forced vibration response for a bladed disk with fitted underplatform "cottage-roof" friction dampers, together with the corresponding numerical predictions. A carefully designed and constructed rotating test rig is used to make precise measurements, which involve only the phenomena of interest. For this purpose, the measurement rig is operated under vacuum to eliminate aerodynamic effects on the rotating blisk and noncontact excitation and measurement techniques are employed so as not to modify the bladed disk dynamics. The experimental data measured are used for validation of multiharmonic balance-based prediction tools developed at the Imperial College. Predictions are carried out both with and without taking inherent mechanical mistuning into account, which is identified from measured data. Measured and predicted response curves are compared with each other and the degree of correlation is discussed. [DOI: 10.1115/1.2903845]

Introduction

Increased demand for higher performance of gas turbine engines makes the safer option of leaving all resonances out of the operating range almost impossible. As a result, bladed disks may be subjected to unacceptably high vibration amplitudes for considerable time, thus threatening their structural integrity. Energy dissipation devices are commonly used in such cases to bring high levels of vibration down to acceptable limits. This is often achieved by using so-called underplatform friction dampers where the vibration energy in the blades is dissipated by rubbing of the mating damper and bladed disk surfaces.

The problem of controlling and predicting the vibration amplitudes of bladed disks has been a primary concern for many years. There have been a number of experimental studies aimed at understanding of characteristics of friction damping as well as its effects on system response. An experimental evaluation of effectiveness of different damping mechanisms on a rotating bladed disk was given by Jaiswal and Bhave [1]. Here, two groups of 7 blades, each covering 90 deg sectors of the bladed disk circumference were considered. Several configurations of damping pins, lacing wires, and damping wire were investigated, where the latter is found to be the most effective. However, the way blades were arranged and fixed to the bladed disk did not allow the effect of coupling between blades on the damping characteristics of overall bladed disk to be observed. This is highlighted in a paper presented by Hollkamp and Gordon [2,3], where they carried out an experimental work to identify damping in jet engine blades. They showed that the common test practice of damping only a few of blades in a bladed disk and keeping the remaining ones undamped in identification of damping values was valid only if the damped blades' response was localized. Berruti et al. [4] designed a test rig to investigate friction damping effects on a stator low pressure stage blade segments, where the friction damping was introduced through contact of neighboring surfaces. They also studied behavior of an asymmetric underplatform damper [5] in a two-blade setup. D'Ambrosio et al. investigated forced response of shrouded bladed disks [6] by first considering a simple cantilever beam and then by assembling a number of these beams, linked by simple shrouds, around a disk. Koh and Griffin used a blades/damper test setup to analyze the dynamic behavior of spherical friction dampers [7]. They concluded that strain concentrations in contact region caused significant reductions in effective stiffness of dampers compared with damper bulk stiffness from finite element (FE) analysis. Sextro [8] published a paper, in which he presented a contact model for shrouded blades with friction contact and experimentally demonstrated its effectiveness. A blade with two non-Hertzian contact surfaces was used in experiments and normal contact force was simulated by dead weights. Additional studies concerning two-blade-and-a-damper arrangement are reported in Refs. [9,10]. In the former, Sanliturk et al. sought to validate predictions of vibration response of underplatform dampers for turbine blades using a test setup comprising two turbine blades and a damper in between. In the latter, Stanbridge et al. aimed at identification of damping characteristics at high temperatures up to 1000°C using noncontacting measurements via a laser Doppler velocimeter (LDV). A similar study is given by Filippi et al. in Ref. [11].

Most of the experimental studies deal with the problem of friction damping in turbomachinery on simple test setups such as those comprising two blades and a damper in between, at rest. Performing experiments with underplatform dampers at rest requires introducing a special system to simulate action of centrifugal forces that are inherent in realistic blade disks. Adequate simulation of action of centrifugal forces is usually difficult to achieve and, moreover, such systems can change the dynamic properties of a structure measured. To the best authors' knowledge, there have been no experimental studies of bladed disks with dampers in rotating conditions. In this study, we present a methodology and results from an experimental investigation using a rotating test rig where a specially designed integral bladed disk (blisk) is fitted with a full set of underplatform friction dampers and operated under rotation with an aim to provide necessary reference data for validation of corresponding numerical nonlinear models developed by the Imperial College [12–15].

Contributed by the International Gas Turbine Institute (IGTI) of ASME for publication in the JOURNAL OF ENGINEERING FOR GAS TURBINES AND POWER. Manuscript received July 30, 2007; final manuscript received July 30, 2007; published online April 29, 2008. Review conducted by Dilip R. Ballal.

Experimental Setup

Experimental investigations, especially aimed at validation of numerical predictions of forced response for a bladed disk with fitted friction dampers, would be extremely difficult if they were attempted to be made on a real gas turbine engine. This is because, in the engine, there are many factors which affect the bladed disk vibration response and yet remain unknown and not included in the mathematical model. In most cases, there is not enough room in a real engine to incorporate an adequate measurement system to acquire all the necessary data required for analysis.

Therefore, these measurements should be made on a carefully constructed experimental setup, which exhibits only the phenomena under investigation. The number of unknown factors should be minimized, and parameters of the setup should allow identification to enable numerical modeling. The following sections give details of such experimental setup for achieving the objectives of study at hand. More details on the test setup can found in Ref. [21].

Test Piece. Main considerations in the design of test piece were to capture the representative dynamic characteristics of a real bladed disk and at the same time to reduce complexity by introducing necessary simplifications. To this end, the bladed disk was designed as an integral piece (i.e., a blisk) to eliminate contact interfaces in blade root joints, a common feature of bladed disks, and therefore friction damping in these joints and uncertainties in their modeling. Special effort was made during the design of the test piece to have natural frequencies of the first flap (1F) family of modes sufficiently well separated, so that the tuned modes could be clearly identified in measurements, and that these modes could be excited by steady-state engine order (EO) forcing at speeds which would be achievable under laboratory conditions (less than 4000 rpm). Platforms were introduced at 1/3 of blade height to provide a means of incorporating interblade, underplatform friction dampers. The damper sockets in these platforms were designed to allow dampers of various types to be accommodated. Blades were staggered, so that 1F vibration mode shapes have roughly similar components both in the plane of the disk (to give reasonably relative underplatform damper motion) and out of plane (to give sufficient blade disk modal coupling). A picture of the machined test piece and a FE model of a single bladed sector are shown in Fig. 1.

Test Rig. The rig designed for the investigation presented here was operated in vacuum to eliminate aerodynamic effects. The blisk was mounted on a rotating shaft as overhang and accommodated in a cylindrical casing. The shaft was kept fairly short to avoid critical speeds within the operation range. A separate disk was also introduced to enable attachment of balancing masses in case needed. The rig was driven by an electric motor, which provided a rotational speed range of 0–4000 rpm. A tacho signal was acquired via an optical sensor by observing a high-reflectivity mirror mounted on the drive shaft to measure the actual rotor speed. This signal was also used as a trigger signal for vibration measurements. The drive shaft was coupled to the motor by a drive belt. Comparison of speed values from the motor encoder and the tacho signal revealed differences of up to 0.1%, confirming absence of significant slippage in the belt drive. Vibration response data were acquired via a data acquisition PC. Through a code written in MATLAB, the rotational speed, magnet position, and the blade to be measured could all be controlled, and vibration data, force, and tacho signals could be acquired and saved for a range of rotational speeds automatically, without any intervention from the user. Pictures of the rig and the measurement system are given in Fig. 2.

Measurement System. Making successful response measurements on rotating machinery is always a challenge. In real gas turbine engines, this is often done via strain gauges or at times

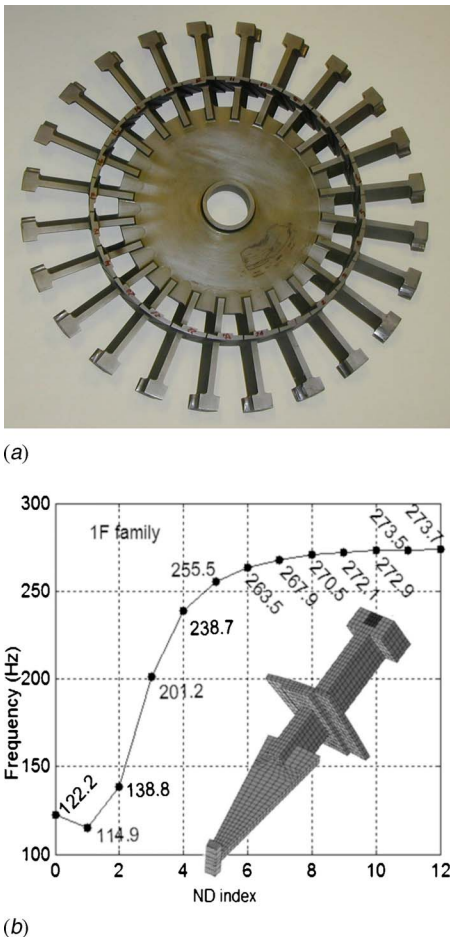

Fig. 1 Manufactured blisk (*a*) and its cyclic-sector FE model used to calculate the 1F family natural frequencies (*b*)

using tip timing technology. These techniques, although effective, are very demanding in terms of amount of work required for instrumentation and/or data acquisition and processing. Because of this, in these tests, a LDV is used, which has advantages of ease of use and being nonintrusive and, therefore, does not affect the dynamic properties of the structure being measured.

Generally, this is done by using the deflection mirrors in the LDV head and by synchronizing the signals driving these mirrors with the rotational speed of the rig. However, as the rotation speed is increased, due to inertia of the mirrors and the motors driving them, the laser beam gets delayed by a certain amount. This results in a phase shift with respect to the input signal, and this shift becomes significant as speed increases. In order to overcome this spurious phase shift, a system of vibration response measurement using a LDV, which is independent of rotational speed, was designed. This so-called "self-tracking" technique is based on the idea proposed by Lomenzo et al. in Ref. [16] but it is modified considerably, by introducing a 45 deg conical mirror and a 45 deg center mirror fixed to the rotor axis. A schematic description of the self-tracking measurement system is given in Fig. 2(*b*). These mirrors allow the laser beam to be directed to a blade tip at a right angle without moving the LDV head. Moreover, a 45 deg center mirror rotating with the blisk (see Fig. 2(*b*)) is mounted on a special mechanism, which provides a means of selecting the blade to measure on a rotating blisk. Each operation of this mechanism moves the center mirror, and thus the laser beam, from one blade to the next, enabling all blades to be measured without stopping the rig. More details on the measurement system can be found in Ref. [17]. In addition, circular continuous scanning LDV

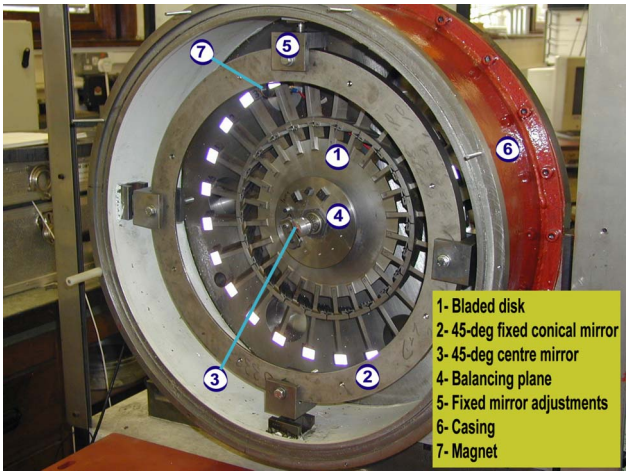

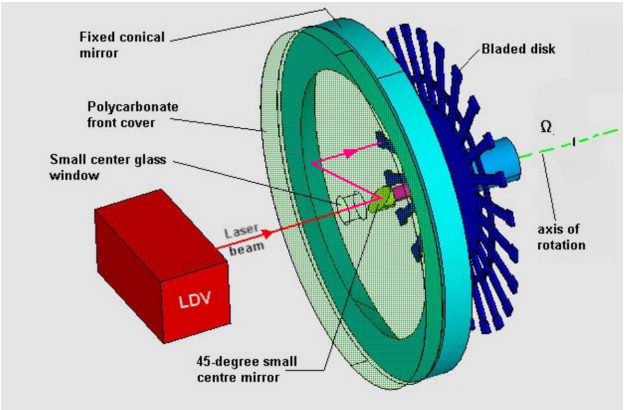

Fig. 2 Test rig and measurement system

(CSLDV) method developed in Ref. [18] was used to measure circumferential operating deflection shapes (ODSs) on stationary and rotating blisks.

Excitation. Most of the vibration-related problems in bladed disks in real gas turbine engines are caused by aerodynamic forces, which introduce excitation at multiples of engine rotation speed, so-called EOs. An excitation system for the test rig, therefore, is required to produce EO type excitation and by noncontacting means. This can be done in a number of ways such as (i) by holding the test piece and the exciters (electromagnets or speakers) stationary and by phasing exciters accordingly [19,20], or, (ii) by again holding the test piece stationary but to mount the exciter(s) on a rotating fixture. However, since simulating realistic operation conditions of friction dampers require the rotation of the test piece itself, both solutions are inapplicable in the present investigation. In our rig, the excitation was simulated, in its simplest form, by employing a permanent magnet fixed to the rig. The rotation of test piece provides time varying forcing and, moreover, inclusion of the centrifugal effects enables friction dampers to operate.

The provision was also made to incorporate up to six magnets, equally distributed around the blisk. The magnitude of steady force could be adjusted via a stepper motor, which controlled the magnet-blade gap. Although the use of electromagnets would allow the frequency of excitation to be varied independently of the rotational speed, the force produced via these magnets was so small that they could not be used.

As a result of the adopted excitation scheme, in normal operation conditions, the bladed disks are being excited by phased pulses generated by the magnet, each time a blade rotates past it. The excitation force fluctuates from near zero when the magnet is between blades, to a maximum when the magnet is centered on a blade tip; hence, the variable excitation load has many harmonic components.

Moreover, in the present case, the magnet can only attract the blades; therefore, all the force values are positive and the excitation load has also a constant component. The amplitudes of the multiharmonic components of excitation force together with its constant component were calculated by performing Fourier analysis of the force variation over one full rotation cycle. Each such component excites traveling wave forced response excitation and the amplitude of the nth harmonic of the magnet force therefore gives the amplitude of the nth EO excitation.

The excitation force variation was measured by a force transducer, which was attached to a mass block and mounted on the rig frame. The proximity of the magnet to blade was controlled via a stepper motor to vary the excitation force amplitude.

Underplatform Friction Dampers

One of the most important choices in the planning of tests with friction dampers is to determine the speed range, in which the dampers will operate successfully. A damper has a certain mass value and the centrifugal load exerted on it increases with increasing speed. Usually, at a certain point, this centrifugal load becomes so high that it prevents dampers from slip and hence from energy dissipation. Dampers in such a state are said to be locked up. In this situation, the neighboring blades are interconnected through dampers, which lead to substantial stiffness increases in the assembly, thus resulting in the natural frequencies being raised. Often, the shifts in natural frequencies are considerably higher so that exciting the "new" resonances may not be possible within the speed range of the test setup.

In order to reduce the possibility of such a situation, it is essential that certain parameters such as damper mass, excitation forces, operating speed range, etc., are chosen accordingly. It was decided to use cottage-roof (CR) dampers in the experiments since they were commonly used in real engines and relatively cheap to manufacture. A rather simple approach was adopted to calculate a rough estimate for the damper mass, which would allow dampers to slip. The idea was to work out the relationship between the blade tip response amplitudes and the forces applied to the dampers. Therefore, assuming a blade tip amplitude response, the mass of a damper, which could ensure damper slip, could be calculated from forces applied to a damper. The dampers were considered in their stuck position (i.e., no relative motion between the dampers and blades), so that the system behaved linearly. To this end, a 0.5 mm blade tip amplitude was assumed and the amplitude of the applied harmonic force was adjusted so that the assumed response amplitude could be obtained. The dampers were represented by their equivalent stiffnesses, obtained from FE analysis. As the relation between blade tip amplitude and the force in the stiffness elements (representing the dampers) was of interest, a simple model, such as the one shown in Fig. 3(a), could be used. The resultant forces in the springs representing the dampers were then fed into the free body diagram of Fig. 3(b) and the forces on the damper faces were balanced.

Assuming a friction coefficient of 0.3 and a roof angle of 150 deg, the mass of the CR damper allowing slip was calculated as a function of rotational speed, Ω, and was identified as 4.5 g at the maximum rig speed of 4000 rpm. This meant that they would work for even smaller response amplitudes at lower rotational speeds. The simplifying assumptions necessitated further measures to be taken to ensure the success of the test campaign. For this purpose, it was decided to have another set of dampers made from a lighter material in case the original ones, which were to me made from steel, proved too heavy to be effective. This second set was made from titanium, which reduced the damper mass to 2.2 g.

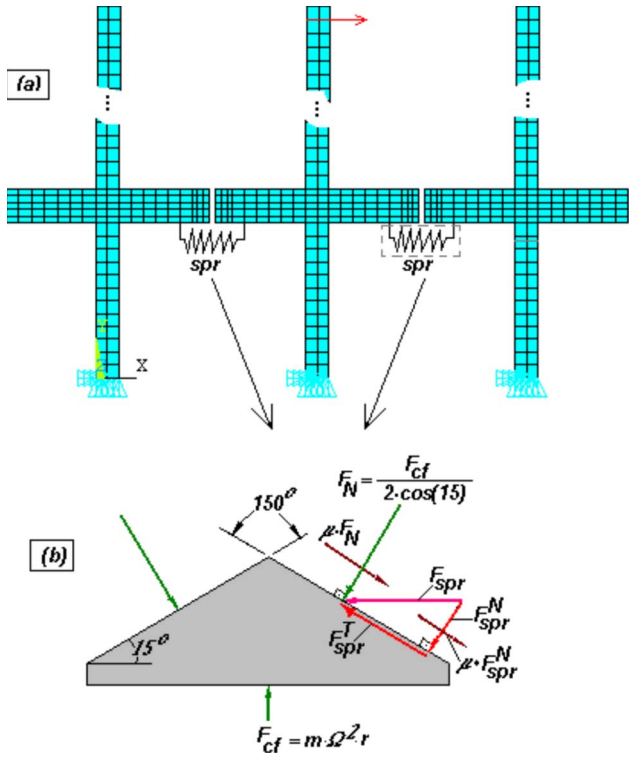

Fig. 3 (*a*) **Simple FE model used in the damper design;** (*b*) **free body diagram of a damper**

Identification of Blisk Characteristics

When predictions of a particular model are to be compared with those of the real component they simulate, it is important that the model is validated to make sure that it is a good representation of the actual specimen. For this purpose, the natural frequencies and mode shapes or more precisely ODSs of the blisk were measured.

At the beginning, a noticeable amount of frequency split in double modes of the 1F family were measured together with highly irregular mode shapes, which indicated a significant level of mistuning in the blisk. In an attempt to obtain a tuned reference blisk, a tuning process was undertaken. This was achieved by removing metal from tip of each blade so that all the first family of natural frequencies were as near identical as possible. Only the first blade-alone natural frequency was tuned, and, during the tuning process, blades of the blisk were isolated so that their natural frequencies could be measured individually, uninfluenced by the other blades on the blisk.

ODS for 1F modes were remeasured after tuning using circular scanning LDV so that the tuned state of the blisk could be assessed. Measured ODSs were found to be regular deflection shapes for mode shapes with number of nodal diameters (NDs) up to ND=7, as would be expected from a tuned blisk. However, they were distorted for higher ND numbers, eventually becoming highly localized for 9–12 ND modes. In fact, this was not entirely surprising since there are many ways in which the first blade-alone frequencies can be tuned. However, not all of them can yield the desired assembly modes. For a successful tuning process, one may need to target a number of blade-alone frequencies rather than the fundamental one alone.

Measurements on Rotating Blisk

Undamped Rotating Blisk Analysis. Here, the undamped analysis refers to the case of no additional damping other than material damping. It was important to validate predictions of the linear model prior to introduction of complexity through nonlinear friction elements. This required mistuned response predictions to be conducted. The tool used in these predictions, program code MISTRES, (see Ref. [15]), was validated in Ref. [22]. Therefore, likely deviations of forced response from measurements would, in effect, indicate inaccuracies in mistuning identification or in its representation.

All the blades in the blisk were measured for a speed range around 9 EO-9 ND resonance as this mode was significantly mistuned and multitude of resonances were observed in the frequency range studied. This, it was believed, would provide enough data to gauge the degree of correlation between measurements and numerical simulation. For example, the results of measurements for two of blisk blades are compared with the predicted ones in Fig. 4. Given the fact that a small frequency range was considered and that inherent mistuning was not identified accurately, the general behavior of the response curves is well predicted. Deviations in the locations of resonances were generally around 0.3%. Frequency splits shown in predicted curves could not be captured in measurements for some of the modes. This is mainly because of the insufficient sweep rate and frequency resolution achieved in measurements. The excitation frequency in measurements was controlled by rotational speed and the motor controller used did not allow finer speed resolution to be used. Also, due to this reason and very lightly damped nature of the blisk, the resonance peak amplitudes could not be measured accurately. In addition to frequency response curves, some ODSs under rotation were also measured for various EO resonances and compared with the pre-

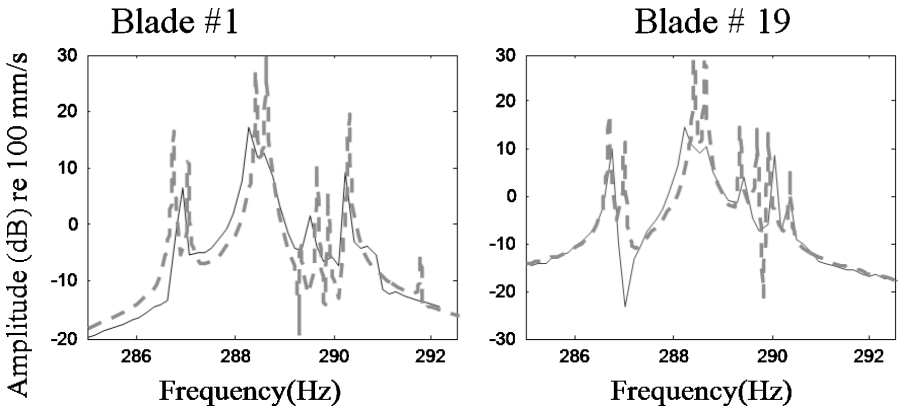

Fig. 4 Comparison of two blade responses to nine EO excitation. —Measured; - - predicted.

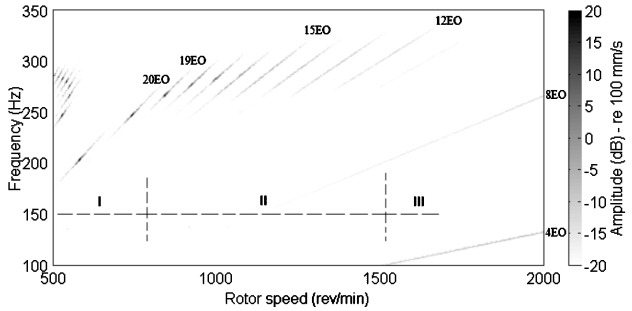

Fig. 5 Blisk response with fitted Ti CR damper

dictions. Reasonable correlation was obtained for lower ND modes, which were regular modes with all blades responding with similar amplitudes, and, therefore, vibrated in the form of traveling waves. Higher ND modes, on the other hand, exhibited vibrations in the form of standing waves as they were significantly localized due to inherent mistuning.

Damped Rotating Blisk Measurements. The friction dampers are intended to reduce resonant vibration by energy dissipation via the friction forces occurring at the contact surfaces of the blisk and dampers, as the latter are pressed to blade platform by centrifugal forces and there is partial or full slipping motion at the damper contact interfaces. In the case of low excitation and, accordingly, low response amplitudes, the dampers will lock up and will not operate, i.e., will not slip and dissipate energy. Since, in such a situation, there is no relative motion between the dampers and the blisk, the individual blades will be permanently coupled through the dampers, and such stiffening of the system leads to substantial increase in the natural frequencies while producing little if any damping. Realistic reduction of resonance amplitudes via friction damping is achieved when vibration amplitude level allowing dampers to slip is exceeded. This threshold amplitude level depends on the ratio of the excitation forces to the static load applied to damper surfaces, on the mode shape considered and on the level of the centrifugal forces. The latter are proportional to the damper mass and the square of the rotational speed. The effectiveness of the damper in reducing the response amplitude levels can decrease with increase of the vibration levels when those are very high, since at higher amplitudes, the energy dissipation does not rise proportionally to the blisk's vibration energy. The effectiveness of the dampers therefore depends, amongst the factors which can be varied and adjusted in experiments, on the rotational speed of the rotor, the damper mass, and the strength of the exciting force. The latter two can be chosen to make the dampers work in the speed range of interest. However, the forcing magnitude cannot be increased in very wide ranges due to the danger of producing a fatigue failure in the test blisk.

Overall forced vibration response of blisk was mapped via measurements taken on a blade in 0–2000 rpm speed range.

As mentioned before, two sets of dampers were manufactured: one from steel and one from titanium. Despite all the attempts made at increasing the excitation force, it was not possible to excite resonances in the analyzed rotation speed range when dampers made of steel were fitted in the blisk. They proved to be too heavy and locked up for the most of speed range. Excitation of the blisk with the titanium dampers produced resonance peaks and, therefore, all the effort was directed to experimental investigation of titanium dampers. The results of measurements of blisk response with these dampers are shown in the interference or z-mod diagram given in Fig. 5. Examining the plot in detail, three groups of modes may be distinguished: (i) those excited by 20 EOs and above, in which the damper forces are too small to produce significant damping, (ii) those excited by 12–19 EOs, which appear to be "spread," signifying that there is significant damping, and (iii) those excited by 11 EOs and below, which have apparently disappeared from the picture because the dampers have "locked up," shifting the natural frequencies out of the measured range. Strong EO lines in the z-mod picture at 4 and 8 EOs are probably due to misalignment in the LDV measurement laser beam, rather than to true vibration.

Attention was directed, primarily, at a rotation speed range of 800–1050 rpm, which covered the range in which the dampers make transition between the operational modes described above. This range contained resonances excited by 17, 18, 19, and 20 EOs, which excite, due to spatial aliasing, modes with 7, 6, 5, and 4 NDs, respectively. Additionally, the modes excited in this range were mostly tuned, so that the inherent mistuning in the blisk would have a minimal effect. Undamped measurements and predictions (with and without mistuning) corresponding to 19 and 17 EOs are compared in Fig. 6. A very good correlation was obtained. Some resonances were missed in measurements because of insufficient frequency resolution that could be achieved in experiments, which, as mentioned before, does not allow measurements of some very sharp secondary resonance peaks in the mistuned blisk with low damping.

Damped Individual Blade Measurements. At the beginning of tests, forced response for a selected blade was monitored over a period of time to ensure that the dampers had bedded in and that the measurements were repeatable. Following repeatability tests, all blade responses were measured in 800–1050 rpm speed range. Measured forced response curves demonstrated reasonable consistency in terms of overall shape and frequency corresponding to maximum amplitude, as seen in Fig. 7(a). However, there was a significant variation in the level of maximum amplitude of each blade. Measurements of blade amplitudes were made sequentially from the first blade to the last blade in the blisk. The rig running

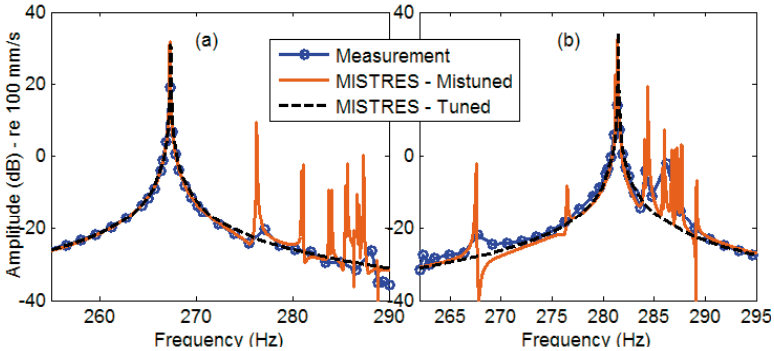

Fig. 6 Undamped response of Blade 1 to (*a*) 19 EO and (*b*) 17 EO excitations

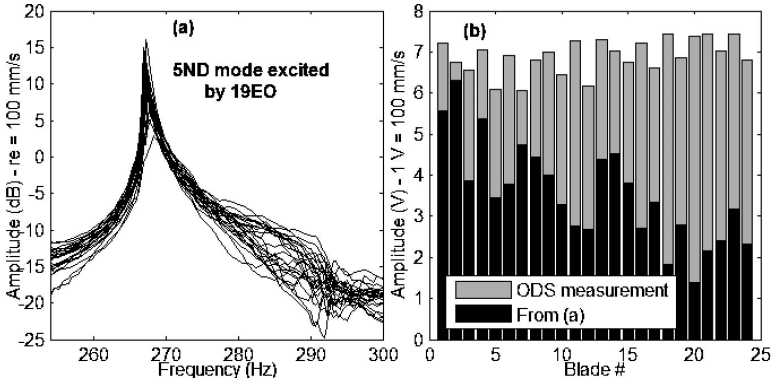

Fig. 7 (*a*) Response of all Blades and (*b*) maximum amplitude variation to 19 EO excitations

time increases with the number of a blade measured and, therefore, damper contact surfaces were subjected to different times of rubbing and were not exactly identical for all blades. As a result, these resonance response levels showed a general trend of decreasing with increasing blade number and were considerably lower than those obtained through ODS measurements at the beginning of the measurement session, Fig. 7(*b*).

Some of the blades were remeasured after the given set of blade measurements was completed and large variations in amplitudes from run to run were observed. To locate the source of such variations, the response of Blade 1 at the 19 EO/5 ND resonance was recorded over 20 min of continuous rig running and the recorded response is given in Fig. 8, top inset.

Despite generally steady-state behavior with almost constant amplitude, the vibration response exhibits several jumps occurring at random intervals. Further investigation showed that the conditions at the damper-insert interface were changing with the time of running the rig. Close inspection of dampers and blade inserts, after shutting down the rig, revealed presence of significant amount of fretting debris over some parts of the damper contact surfaces. Some of the dampers were jammed on one side and thus were unable to operate, possibly because of fretting debris, which had accumulated between the contacting surfaces of inserts and dampers. This situation worsened with the increase of rig operation time, resulting in big discrepancies between blade response curves. A photograph of some of the dampers after shutting down is given in Fig. 8. Inspection of used and unused damper contact surfaces under the microscope revealed no significant visual differences in surface conditions. During the operation of the rig, the contact of dampers and blade inserts accommodating them was taking asperities off at their contact interfaces. This so-called "bedding-in" period continued until smooth insert surfaces were obtained, at the cost of the presented variability in response measurements.

In an attempt to improve the consistency of the response amplitudes, the dampers were taken out and both steel insert and damper surfaces were cleaned thoroughly. However, the amplitudes again varied with the rig running time. This process had to

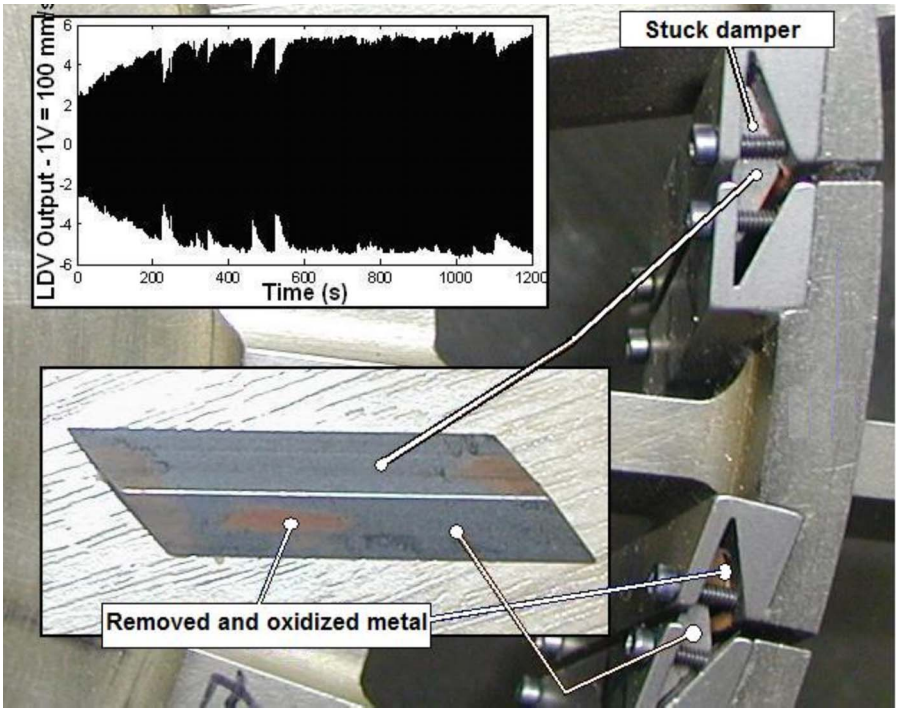

Fig. 8 Blade 1 tip response–19 EO/5 ND resonance (inset top) and damper surface after shutting down (inset bottom)

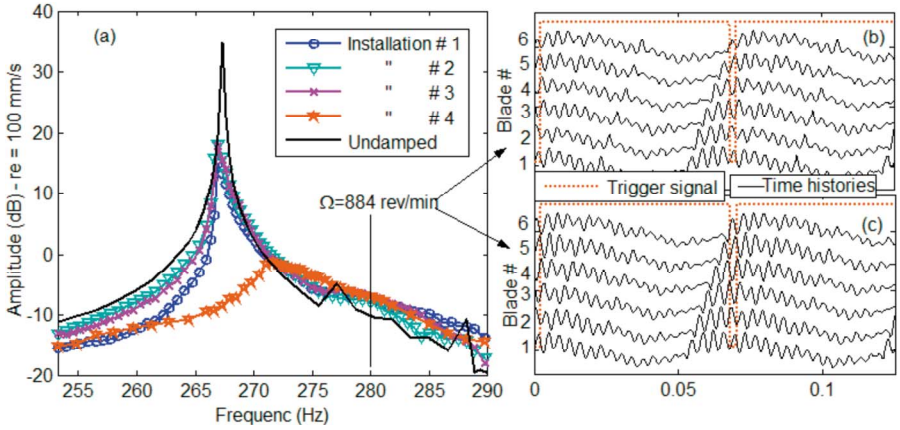

Fig. 9 (*a*) **Response of Blade 1 to 19 EO excitations for all installations, and time histories at 884 rpm for** (*b*) **Installation 1 and** (*c*) **Installation 4**

be repeated three times, resulting in four different installations of dampers in the blisk. Each time, care was taken to put the individual dampers back in those slots where they were removed from. Measurements reported for the first installation were repeated for each new installation of dampers. For the last installation during measurements, the speed range of interest was limited to an even shorter time interval in an attempt to finalize measurements quickly, to ensure that the same or, at least, similar conditions were attained for all blade measurements. The results of the last installation, unlike the first three, showed consistent results throughout the entire measurement session. However, the response curves were significantly different from those of the first three installations, both in terms of resonance amplitudes and shape of the forced response curve. Forced response of Blade 1 around 19 EO/5 ND resonance frequency is given in Fig. 9 for all installations, together with the undamped response curve for the same blade. Despite consistency observed from the first three installations, the fourth one presents a substantial shift in the resonance frequency with much reduced amplitudes. Since the excitation force was kept the same in all installations, the deviation can be attributed to a substantial change in the friction coefficient value. Dampers were further away from stuck condition in the first three installations, as evident from high amplitudes. As a result of damper slipping, no additional stiffness was brought into the system and the natural frequencies were very close to that of the undamped case. However, in the case of the last installation, the dampers were closer to the stuck condition, and as a result they increased the stiffness of the system as well as the damping, which not only reduced the resonance peak amplitude but also shifted the resonance frequency to a higher value.

Short samples of time histories of the first six blades are also given in Figs 9(*b*) and 9(*c*), and these were measured after the first and last installations of the dampers, respectively.

The low frequency oscillations are due to laser beam-rotation axis misalignment. The fact that each following blade received the impulse of the excitation force at a slightly later time than the preceding one is manifested by the given time histories, which exhibit larger blade displacements almost exactly at times corresponding to magnet passing. Although the blisk as a whole was excited at all times, the damping was high enough to significantly reduce blade vibration amplitudes over one blisk rotation before the arrival of the next impulse from the magnet. In some cases, these vibrations were completely damped out before the time of next passing of the magnet. However, the first three installations displayed no significant decay of the vibration amplitudes in the close proximity of the shown resonance peak.

Variation of Response With Amplitude of Excitation Force. The main goal in this set of measurements was to measure the response of selected blades for different excitation levels. The latter were controlled by variation of values of the magnet-blade gaps. Figure 10(*a*) shows the variation of the peak-to-peak amplitude of the force signal with rotational speed for four different magnet-blade distances. The corresponding response curves are

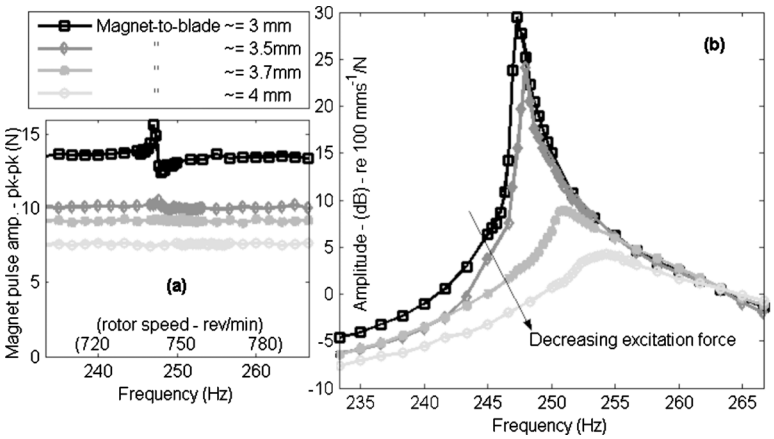

Fig. 10 (*a*) **Variation of force signal amplitude with rotational speed, and** (*b*) **response of Blade 1 to 20 EO excitations at various blade-magnet gaps**

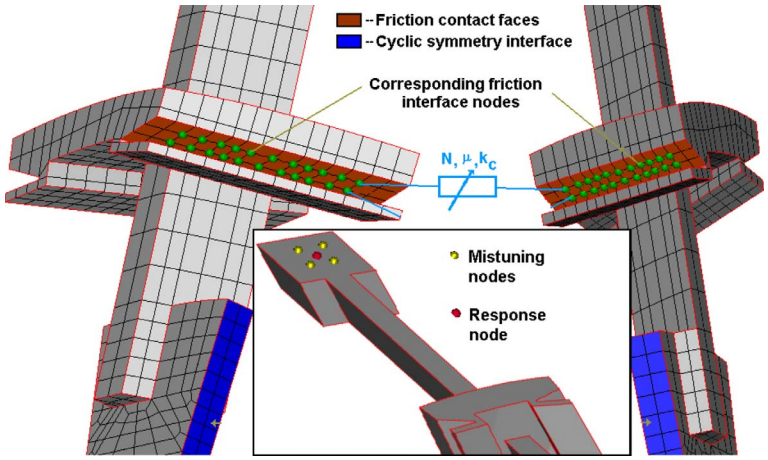

Fig. 11 Modeling of friction dampers and introduction of mistuning (inset)

given in Fig. 10(*b*). The black curve in Fig. 10(*a*) reveals significant force magnitude modulation around the resonance. This is because around a resonance blade vibrations cause a change in the gap between the magnet and the blades. As the clearance was increased, this effect became negligible. It is clearly seen from Fig. 10(*b*) that the damping and the resonance frequency increase with a decrease in the excitation force, as the dampers moved closer to the "stuck" condition.

Correlation of Predictions With Measurements

Prediction Tool. For numerical analysis of the blisk with dampers, new, non-Coulomb friction models developed for modeling of friction contact interaction take into account effects of variable normal loads on friction forces and on time instants of slip-stick transitions [12,13]. Unilateral contact interaction is allowed for including cases of temporary and partial separations of contact surfaces. Multiharmonic balance method is used for formulation of equations of motion in frequency domain. Nonlinear equation of steady-state forced response is calculated using Newton–Raphson method in conjunction with solution continuation techniques. Expressions for nonlinear contact interaction forces and tangent stiffness matrices of contact interfaces are derived analytically, which provides very fast and numerically accurate calculation of forced response even for strongly nonlinear contact interactions, which occur in bladed disks with underplatform dampers. The effectiveness of the friction contact interactions and special accurate condensation techniques allow using large-scale finite element models for bladed disks.

Mode detailed description of the models and methods can be found in Refs. [12–14]. These theoretical developments were implemented in a program code force response suite (FORSE) developed at the Imperial College, which is used here for numerical predictions of the nonlinear forced response of a blisk with CR dampers.

Modeling of Friction Dampers. Figure 11 shows the way the friction dampers are modeled. The forced response analyses for the whole blisk were performed using a cyclic sector of the blisk. A FE model of one sector used in the calculation contains 21,555 degrees of freedom. Nodes of finite element mesh of adjacent blades were connected by friction interface elements (see Ref. [13]), as shown in the figure. The structural damping due to dissipation in material of the blisk was low: $\eta=7.5E-5$. The interaction of all sectors is accounted for by applying cyclic conditions at boundaries where adjacent sectors are connected; i.e., at the sector planes cutting the disk (shown in Fig. 11 in blue). In order to include the elasticity of the damper body, an estimate of the contact stiffness of the friction contact elements was determined from damper FE model. This stiffness was determined from solution of elastic deformation problem for the FE damper model subjected to a uniform load on one CR damper contact face while fixing the other contact face. The damper stiffness coefficients were calculated by application of this load along normal and along tangential directions to the damper contact surface in turn and then by establishing a relationship between average displacement over the loaded face and the applied load.

Forced Response Predictions. The inset of Fig. 11 shows nodes where forced response is calculated. The nodes where mistuning identified in earlier sections was introduced are also displayed here.

Validation of the damped vibration response predictions was carried out by using a subset of the experimental results as presented in the previous section. Owing to the variability observed in measured response characteristics between different installations, the predicted results were compared with all installations whenever the corresponding experimental data were available. It was observed that the first three installations exhibited similar dynamic behavior, which was different from that of the last installation. There were no verified data about friction coefficient of the contact interface and in order to help us explain this variation, the predictions were made for different contact parameter values.

Numerical analyses showed that the damped blisk response was insensitive to contact stiffness variations and sensitive to normal load and the coefficient of friction. Since the normal load was known accurately from centrifugal load acting on dampers of known masses and location, the observed variation between the different installations was likely to be caused by variation in the friction coefficient. The predictions were carried out first for a friction coefficient, μ, of 0.45. This value was measured in an earlier study for the titanium alloy used and was expected to yield close predictions for the results of the first three installations. The preliminary predictions showed that varying the coefficient of friction from 0.45 to 0.6 allowed the variability observed in the vibration response measured to be covered. Therefore, predictions were performed for both values of friction coefficient and measurement results obtained from all installations were included in comparison plots.

Main effort in measurements was directed to 19 EO/5 ND resonance though 17, 18, and, in some cases, 20 EO excitations were also considered. The 19 EO responses of Blade 1 for all four installations is compared to the corresponding predictions ($\mu=0.45$) in Fig. 12. The predictions were performed for two cases: (i) monoharmonic excitation, when excitation only by 19 EOs is applied, and (ii) multiharmonic excitation, when simultaneous excitation by 17, 18, 19, 20, and 21 harmonics was considered. The

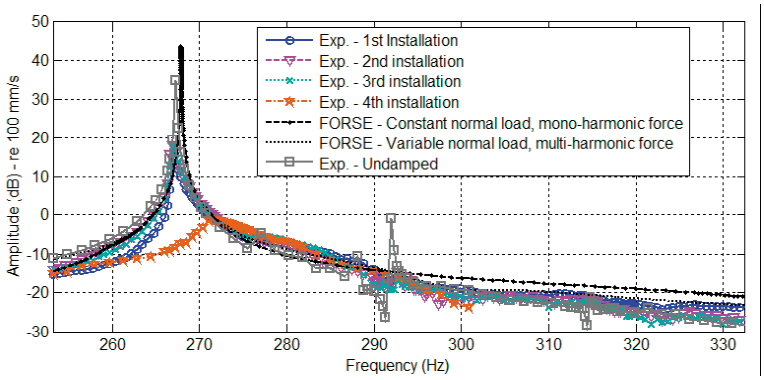

Fig. 12 Comparison of measured and computed damped response in Blade 1: 19 EOs, μ=0.45

results of both analyses are shown in the figure. In the case of multiharmonic force, 5 harmonics (17–21) were considered. Additionally, although the normal load was taken as constant in the monoharmonic force case, its variation with rotational speed was taken into consideration for the multi-harmonic case.

It is seen from Fig. 12 that the predictions correlate much better with the first three installations than the last one. The apparent natural frequency of the damped system obtained from the first three installations and the predictions was almost the same as that of the undamped system. (Note that the undamped curve given in the figure was obtained by amplitude scaling of the original curve, which was measured in the presence of a much smaller input force.) As the vibration amplitudes were sufficiently large, the dampers slid on the blade insert faces freely, and, therefore, their contribution to the system stiffness was minimal. The consideration of variable normal load and of, especially, multiharmonic vibrations produced better predictions, particularly at positions away from the main resonance. The solid black curve in Fig. 12 follows the measurements reasonably, both qualitatively and quantitatively. The predictions given in the plots were performed in the presence and absence of mistuning. No significant difference was observed between the tuned and mistuned cases. This is not surprising as the mode excited in this case (5 NDs) was found to be a regular ND mode, unaffected by small inherent mistuning in the blisk left after the blisk tuning.

Despite the mentioned similarities between the measurements of the first three installations and the predictions given in Fig. 12, the resonance amplitudes predicted were much higher. Close inspection of measured time data revealed that the signals were truncated as they have exceeded data acquisition board's limits and that they were higher than recorded levels. Moreover, the resonance peaks were very sharp that even the finest allowable steep steps (i.e., achievable frequency resolution) in measurements could not capture resonance peaks accurately. Nonetheless, the predictions showed that compared with the undamped case, a 70% reduction in the resonance peak amplitude was achieved by the dampers.

Response curves measured for 17 EO and 18 EO excitations were also correlated with predictions, as shown in Fig. 13. The speed range used for the fourth installation was smaller as it was intended to cover the 19 EO/5 ND resonance only. Although not available for the entire frequency range of other curves, the extracted response of 18 EO excitations for this last installation was given as an indication of the departure in its behavior from the other installations. Only the predictions with variable normal load and multiharmonic force are shown. Despite the unavailability of the complete response curve, the behavior of the last installation is, again, considerably different from the others. As for the 17 EO excitation responses, a different trend was observed between the predictions and the measurements of first three installations. Here, the dampers were predicted to be working more effectively; thanks to the higher normal load. In fact, the increase in the normal load (i.e., due to increasing rotation speed) was around 10%, which demonstrated that the performance of the dampers was very sensitive to the normal load. Measurement data from the last installation were not available and therefore are not given. For all other installations, the response curves obtained for Blade 1 were similar and somehow dissimilar to the predicted one. Particularly near the resonance peak, the amplitudes as well as the apparent natural frequency were observed to be different. Recalling the variability encountered in the measurements of the first installation, the response of the minimum responding blade (Blade 18) is also given in Fig. 13(*b*) to indicate the range of variation. The measured amplitude response of this blade agreed better with the predicted one.

The predictions were repeated by using a friction coefficient of 0.6. This case was expected to simulate the last installation, although the exact actual value of the friction coefficient was not available. The vibration response data for the 17 EO/7 ND resonance were not available for the last installation and only the 18 and 19 EO excitation responses were compared. The comparisons obtained are given in Fig. 14.

The predictions obtained in this case were clearly better correlated with the measurements of the last installation, as expected. It is seen from the figure that the increase in the coefficient of friction from 0.45 to 0.6 resulted in a significant reduction in response amplitudes, covering the range of amplitude variation observed at various stages of the measurements. This finding strengthens the explanation that the mentioned response variation between the first three installations and the last was due to variation of coefficient of friction. Despite the incompleteness of the data, Fig. 14(*a*) shows very good agreement between the measurements of the last installation and the predictions. Although the amplitudes are not predicted as accurately in Fig. 14(*b*), a reasonable qualitative agreement is evident. However, in Figs. 14(*a*) and 14(*b*), resonance frequency is apparently a little underpredicted. Since the predictions for the undamped blisk for this resonance frequency were demonstrated to be closer, the discrepancy here is probably due to the modeling of the underplatform dampers or discrepancy between actual friction coefficient value and used in the numerical simulations.

At this stage, it is worth mentioning that although the predictions are given for two extreme values of friction coefficient, the actual values of this parameter in reality were probably changing even within the same measurement session. By giving predictions for different values of coefficient of friction, it was aimed to show that provided that the correct values of this parameter were available at corresponding stages of the measurements, reasonable predictions could be obtained. The evidence presented in this section demonstrated that the prediction tool was capable of providing

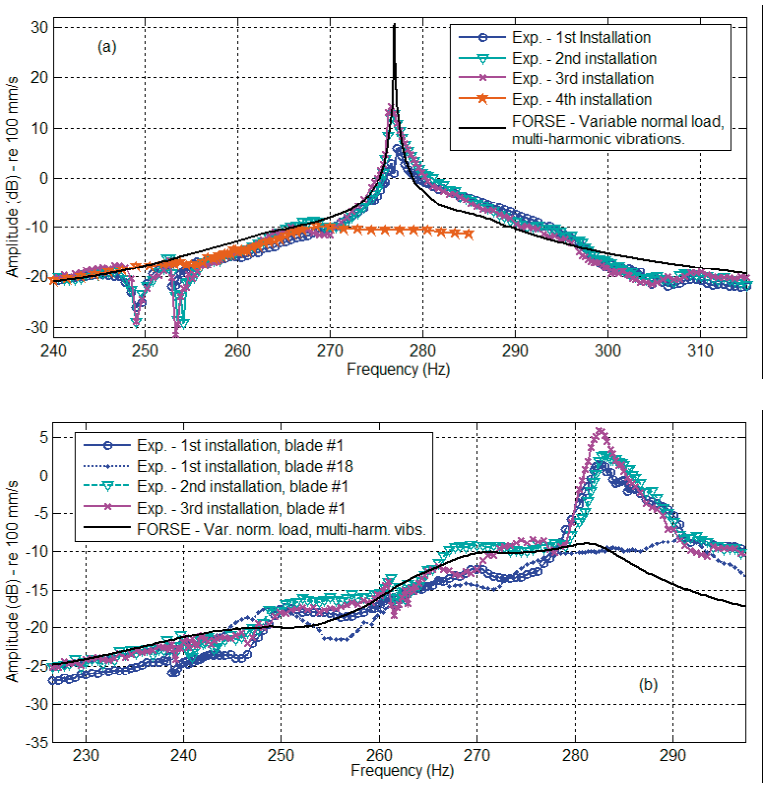

Fig. 13 Measured and computed damped response in Blade 1: (*a*) for 18 EO and (*b*) for 17 EO excitations (μ=0.45)

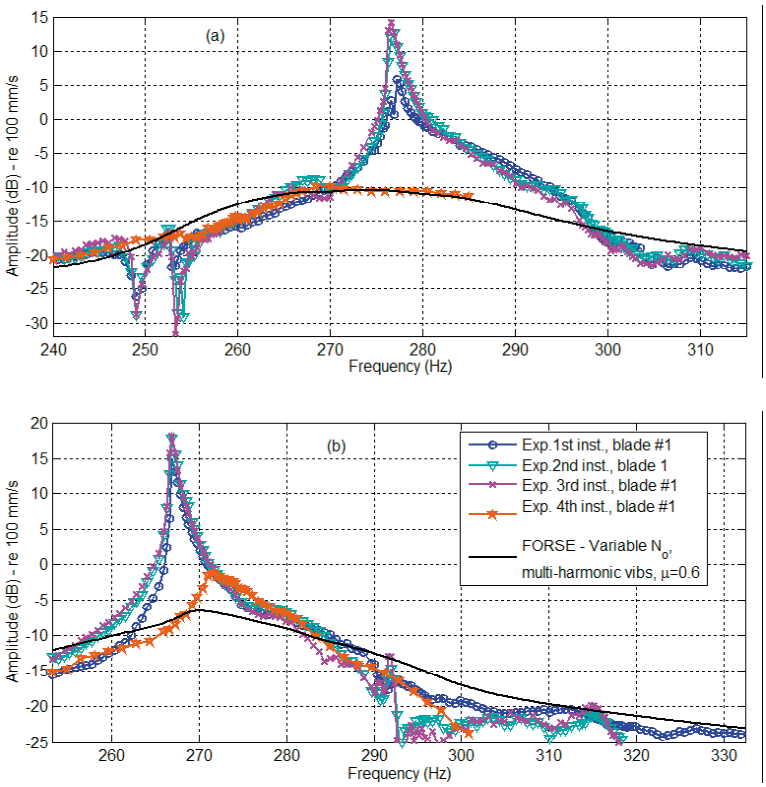

Fig. 14 Measured and computed damped response in Blade 1: (*a*) for 18 EO and (*b*) for 19 EO excitations (μ=0.6)

reliable estimates for a blisk integrated with underplatform friction dampers once the correct input parameters were supplied.

Concluding Remarks

A forced response investigation has been performed of an integral bladed disk with fitted underplatform friction dampers in rotating conditions for correlation with corresponding predictions. To the best of the authors' knowledge, an experimental investigation of a rotating bladed disk fitted with a full set of friction dampers under realistic operating conditions is reported here for the first time.

A carefully designed and constructed rotating test rig is described and a methodology is presented for acquisition of reliable experimental data collected through nonintrusive measurement and excitation methods.

The modeling of a blisk with underplatform friction dampers was achieved by considering a single sector and by making use of cyclic symmetry. Predictions were carried out by a multiharmonic forced response solver. Performed preliminary sensitivity analysis showed that the contact stiffness was found to have less impact compared with the friction coefficient which, together with the normal load, was demonstrated to have played a greater role in forced response. Since the normal load was accurately known, the friction coefficient was varied to account for the variability observed during the measurements.

Given the complicated nature of measurement data, obtained correlation between measurements and predictions showed that numerical tool captured response characteristics under such realistic conditions reasonably well, provided that the variability in input data was accounted for.

Acknowledgment

The authors gratefully acknowledge the support of the European Union for this work within ADTurB II Project No. G4RD-CT2000-00189. We are also grateful to all the project partners for their support.

References

[1] Jaiswal, B. L., and Bhave, S. K., 1994, "Experimental Evaluation of Damping in a Bladed Disk Model," J. Sound Vib., **177**(1), pp. 111–120.
[2] Hollkamp, J. J., and Gordon, R. W., 2001, "Modal Test Experience With a Jet Engine Fan Model," J. Sound Vib., **248**(1), pp. 151–165.
[3] Hollkamp, J. J., and Gordon, R. W., 1998, "An Experimental Investigation of Non-Uniform Damping in Bladed Disks," Paper No. IAA-98–3747.
[4] Berruti, T., Goglio, L., Filippi, S., and Gola, M. M., 2000, "A Test Rig for Frictionally Damped Bladed Segments," *Proceedings of ASME Turbo Expo*, Munich, Germany.
[5] Berruti, T., Gola, M. M., Zucca, S., and De Poli, G. P., 2005, "Underplatform Damper Performance With Turbine Blades," *Proceedings of NATO AVT-121 Symposium on Evaluation, Control and Prevention of High Cycle Fatigue in Gas Turbine Engines*, Granada, Spain, Oct. 3–7.
[6] D'Ambrosio, F., Chatelet, E., Ravoux, J., and Jacquet-Richardet, G., 2004, "Forced Response of Shrouded Bladed Disc Assemblies: A Jointed Experimental Numerical Approach," *Proceedings of ASME Turbo Expo*, Vienna, Austria, Jun. 14–17.
[7] Koh, K.-H., and Griffin, J. H., 2006, "Dynamic Behavior of Spherical Friction Dampers and Its Implication to Damper Contact Stiffness," *Proceedings of ASME Turbo Expo*, Barcelona, Spain, May 8–11.
[8] Sextro, W., 2000, "The Calculation of the Forced Response of Shrouded Blades With Friction Contacts and Its Experimental Verification," *Proceedings of ASME TurboExpo*, Munich, Germany.
[9] Sanliturk, K. Y., Ewins, D. J., and Stanbridge, A. B., 2001, "Underplatform Dampers for Turbine Blades: Theoretical Modeling, Analysis and Comparison With Experimental Data," ASME J. Eng. Gas Turbines Power, **123**, pp. 919–929.
[10] Stanbridge, A. B., Sanliturk, K. Y., and Ewins, D. J., 1999, "Measurement and Analysis of High-Temperature Friction Damper Properties, " Fourth US International Turbine Engine High Cycle Fatigue (HCF) Conference.
[11] Filippi, S., Rodrigues, E. B., and Gola, M. M., 2006, "Experimental Characterization of Contact Hysteresis at High Temperatures," *Proceedings of ASME Turbo Expo*, Barcelona, Spain, May 8–11.
[12] Petrov, E. P., and Ewins, D. J., 2004, "Generic Friction Models for Time-Domain Vibration Analysis of Bladed Discs," ASME J. Turbomach., **126**, pp. 184–192.
[13] Petrov, E., and Ewins, D. J., 2003, "Analytical Formulation of Friction Interface Elements for Analysis of Nonlinear Multiharmonic Vibrations of Bladed Disks," J. Turbomach., **125**, pp. 364–371.
[14] Petrov, E. P., 2004, "A Method for Use of Cyclic Symmetry Properties in Analysis of Nonlinear Multiharmonic Vibrations of Bladed Discs," ASME J. Turbomach., **126**, pp. 175–183.
[15] Petrov, E. P., Sanliturk, K. Y., and Ewins, D. J., 2002, "A New Method for Dynamic Analysis of Mistuned Bladed Discs Based on Exact Relationship Between Tuned and Mistuned Systems," Trans. ASME: J. Eng. Gas Turbines Power, **122**, pp. 586–597.
[16] Lomenzo, R. A., Barker, A. J., and Wicks, A. L., 1999, "Laser Vibrometry System for Rotating Bladed Disks," *Proceedings of the 18th IMAC*, pp. 277–282.
[17] Sever, I. A., Stanbridge, A. B., and Ewins, D. J., 2006, "Turbomacinery Blade Measurements With Tracking LDV Under Rotation," Seventh AIVELA Conference, Ancona, Italy.
[18] Stanbridge, A. B., Marterelli, M., and Ewins, D. J., 1999, "Modal Testing Using a Scanning Laser Doppler Vibrometer," Mech. Syst. Signal Process., **13**(2), pp. 255–270.
[19] Kruse, M. J., and Pierre, C., 1997, "An Experimental Investigation of Vibration Localization in Bladed Disks, Part I: Free Response," *Proceedings of the 42nd ASME Gas Turbine and Aeroengine Congress*, Orlando, FL.
[20] Jones, K., and Cross, C., 2002, "A Traveling Wave Excitation System for Bladed Disks," AIAA paper No. 2002-1531.
[21] Sever, I. A., 2004, "Experimental Validation of Turbomachinery Blade Vibration Predictions," Ph.D. thesis, Imperial College London, England.
[22] Sever, I. A., Stanbridge, A. B., and Ewins, D. J., 2006, "Experimental Validation of Mistuned Bladed Disk Vibration Predictions," Seventh IFToMM Rotor Dynamics Conference, Vienna, Austria, Sept. 25–28.

The Impact of Real Gas Properties on Predictions of Static and Rotordynamic Properties of the Annular Gas Seals for Injection Compressors

Yoon-Shik Shin
Graduate Research Assistant
Purdue University

Dara W. Childs
Leland T. Jordan Professor

Department of Mechanical Engineering,
Turbomachinery Laboratory,
Texas A&M University,
College Station, TX 77843
e-mail: dchilds@tamu.edu

Predictions are presented for an annular gas seal that is representative of the division-wall seal of a back-to-back compressor or the balance-piston seal of an in-line compressor. A two-control-volume bulk-flow model is used including the axial and circumferential momentum equations and the continuity equations. The basic model uses a constant-temperature prediction (ISOT) and an ideal gas law as an equation of state. Two variations are used: adding the energy equation with an ideal gas law (IDEAL), and adding the energy equation with real gas properties (REAL). The energy equations assume adiabatic flow. The ISOT model has been used for prior calculations. Concerning predictions of static characteristics, the calculated mass leakage rates were, respectively, 9.46 kg/s, 9.55 kg/s, and 7.87 kg/s for ISOT, IDEAL, and REAL. For rotordynamic coefficients, predicted effective stiffness coefficients are comparable for the models at low excitation frequencies. At running speed, REAL predictions are roughly 40% lower than ISOT, which could result in lower predicted critical speeds. Predicted effective damping coefficients are also generally comparable. REAL and IDEAL predictions for the crossover frequency are approximately 20% lower than ISOT. REAL predictions for effective damping are modestly lower in the frequency range of 40–50% of running speed where higher damping values are desired. [DOI: 10.1115/1.2904891]

Introduction

Injection compressors are being applied at progressively higher discharge pressures on the order of 1000 bars or higher. The division-wall (back-to-back designs) or balance-piston (straight-through design) seals of these machines have a major impact on their vibration characteristics. Increasingly, these seals use a stator with a hole-pattern (HP) roughness and a smooth rotor design versus a labyrinth. Published analysis procedures for HP seals are based on bulk-flow models with constant temperature that use an ideal gas law for the properties. Test results have regularly shown significant temperature changes in seals tested in air with 70 bar supply pressure [1,2]. Nonetheless, a constant-temperature model has given good results for leakage and rotordynamic coefficients. The applicability of the ideal gas law for very high pressures is the central issue addressed in this work. The model used here includes the energy equation for temperature calculation and a National Institute of Standards (NIST) code to account for real gas properties. Comparisons are made between predictions for these newer models and the constant-temperature model.

Analysis

Governing Equation. Nelson's models [3,4] for a smooth annular gas seal are the starting point for development. Nelson used a one-control-volume, bulk-flow model consisting of an axial momentum equation, a circumferential momentum equation, the continuity equation, and an ideal gas equation for property definition. Ha and Childs [5] proposed the two-control-volume model illustrated in Figs. 1 and 2. Control volume *A* is the basis for Nelson's models, and Control volume *B* accounts for the gas contained in the holes. Transient radial flow is possible between the two control volumes and is represented by the velocity component *V* in Fig. 2. The governing equations are provided below.

(a) Continuity equation for Control Volume A

$$\frac{\partial}{\partial t}(\rho H) + \frac{1}{R}\frac{\partial}{\partial \theta}(\rho U H) + \frac{\partial}{\partial Z}(\rho W H) + \rho V = 0 \tag{1}$$

(b) Continuity equation for Control Volume B

$$\rho V = \gamma_c H_d \frac{\partial \rho}{\partial t} \tag{2}$$

(c) Axial momentum equation

$$-H\frac{\partial P}{\partial Z} = \tau_{sz} + \tau_{rz} + \rho W V + \frac{\partial(\rho H W)}{\partial t} + \frac{\partial(\rho H W U)}{R\partial\theta} + \frac{\partial(\rho H W^2)}{\partial Z} \tag{3}$$

(d) Circumferential momentum equation

$$-\frac{H}{R}\frac{\partial P}{\partial \theta} = \tau_{s\theta} + \tau_{r\theta} + \rho U V + \frac{\partial(\rho H U)}{\partial t} + \frac{\partial(\rho H U^2)}{R\partial\theta} + \frac{\partial(\rho H W U)}{\partial Z} \tag{4}$$

(c) Energy equation

Contributed by the International Gas Turbine Institute (IGTI) of ASME for publication in the JOURNAL OF ENGINEERING FOR GAS TURBINES AND POWER. Manuscript received October 3, 2007; final manuscript received October 4, 2007; published online April 29, 2008. Review conducted by Dilip R. Ballal.

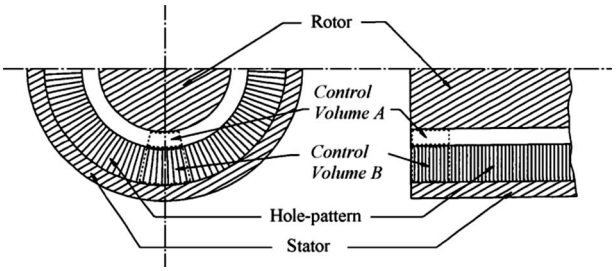

Fig. 1 Geometry of HP seal [6]

$$0 = \rho H \frac{De}{Dt} + \rho \gamma_c H_d \frac{\partial e}{\partial t} + \frac{\partial}{\partial Z}(PWH) + \frac{1}{R}\frac{\partial}{\partial \theta}(PUH) + R\omega\tau_{r\theta} \tag{5}$$

where

$$\frac{D}{Dt} = \frac{\partial}{\partial t} + \frac{U}{R}\frac{\partial}{\partial \theta} + W\frac{\partial}{\partial Z} \tag{6}$$

$$e = \hat{u} + \frac{U^2}{2} + \frac{W^2}{2} \tag{7}$$

$$\hat{u} = C_v T = \frac{1}{Z_c(\gamma - 1)}\frac{P}{\rho} \tag{8}$$

V, the transient radial velocity from *Control Volume A* to *Control Volume B*, can be eliminated by substituting V from Eq. (2) into Eqs. (1), (3), and (4). Following the analyses of Nelson [3,4], the energy balance is modeled as adiabatic flow; therefore, no heat flow term appears in the energy equation. The internal energy $\hat{u}$ of Eq. (8) has an ideal gas equation of state. Kleynhans and Childs [6] first produced results for this two-control-volume model showing strongly frequency-dependent stiffness and damping coefficients; however, they used a constant-temperature model. Real gas properties replace the ideal gas equation in the next section.

The wall shear stresses are defined using Hirs' [7] bulk-flow model for lubrication. The viscosity is defined as

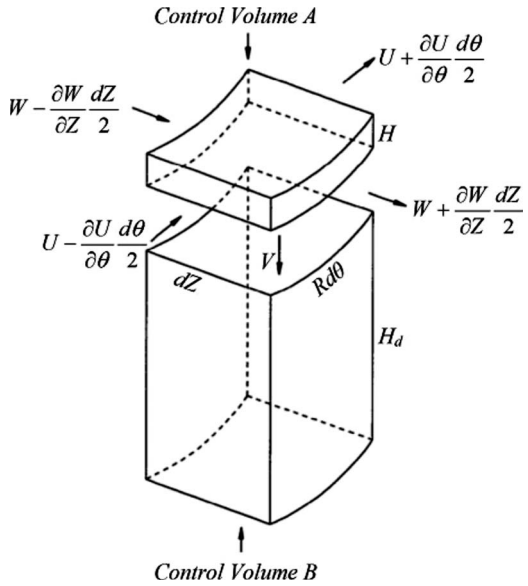

Fig. 2 Flow in and flow out of the control volumes [6]

$$\frac{\mu}{\mu_R} = \left(\frac{T}{T_R}\right)^{\kappa} \tag{9}$$

where κ is a fluid-specific constant. For air, $\kappa = 0.7$.

The sudden contraction with loss at the inlet is modeled as

$$P_R - P(0) = \frac{1 + \xi}{2}\rho(0)W^2(0) \tag{10}$$

and an ideal gas isentropic relationship is used between just before and just after the inlet.

$$\frac{P(0)}{P_R} = \left(\frac{\rho(0)}{\rho_R}\right)^{\gamma} \tag{11}$$

Exit recovery is modeled as

$$P_S - P(1) = \frac{1 - \xi_e}{2}\rho(1)W^2(1) \tag{12}$$

Linearization. The first-order governing equations are obtained via the following perturbed variables:

$$H = H_0 + \varepsilon H_1 \tag{13}$$

$$W = W_0 + \varepsilon W_1 \tag{14}$$

$$P = P_0 + \varepsilon P_1 \tag{15}$$

$$U = U_0 + \varepsilon U_1 \tag{16}$$

$$\rho = \rho_0 + \varepsilon \rho_1 \tag{17}$$

$$\hat{u} = \hat{u}_0 + \varepsilon \hat{u}_1 \tag{18}$$

The first-order pressure is integrated to get perturbation reaction force components. The general reaction-force/motion transfer model is

$$-\begin{Bmatrix} \mathbf{F}_X(j\Omega) \\ \mathbf{F}_Y(j\Omega) \end{Bmatrix} = \begin{bmatrix} \mathbf{D}(j\Omega) & \mathbf{E}(j\Omega) \\ -\mathbf{E}(j\Omega) & \mathbf{D}(j\Omega) \end{bmatrix}\begin{Bmatrix} X(j\Omega) \\ Y(j\Omega) \end{Bmatrix} \tag{19}$$

where Ω is the rotor precession frequency, $\boldsymbol{F}_X(j\Omega)$ and $\boldsymbol{F}_Y(j\Omega)$ are reaction-force vector components, and $X(j\Omega)$ and $Y(j\Omega)$ are the components of the relative displacement vector between stator and rotor. In terms of frequency-dependent rotordynamic coefficients, the model is

$$-\begin{Bmatrix} \mathbf{F}_X \\ \mathbf{F}_Y \end{Bmatrix} = \begin{bmatrix} K(\Omega) & k(\Omega) \\ -k(\Omega) & K(\Omega) \end{bmatrix}\begin{Bmatrix} X \\ Y \end{Bmatrix} + \begin{bmatrix} C(\Omega) & c(\Omega) \\ -c(\Omega) & C(\Omega) \end{bmatrix}\begin{Bmatrix} \dot{X} \\ \dot{Y} \end{Bmatrix} \tag{20}$$

Therefore,

$$\mathbf{D}(j\Omega) = K(\Omega) + jC(\Omega) \tag{21}$$

$$\mathbf{E}(j\Omega) = k(\Omega) + jc(\Omega) \tag{22}$$

The frequency-dependent effective stiffness and effective damping coefficients are defined as

$$K_{\text{eff}}(\Omega) = K(\Omega) + c(\Omega)\Omega \tag{23}$$

$$C_{\text{eff}}(\Omega) = C(\Omega) - \frac{k(\Omega)}{\Omega} \tag{24}$$

Comparisons of Model Predictions to Test Results for Leakage Rates Using Air as the Test Fluid. Figure 3 provides comparisons for measured and calculated mass leakage rates at 20,000 rpm for a smooth-stator/honeycomb (HC) stator seal [2] with nominally zero preswirl. The seal had an inner diameter of ~114.7 mm, a radial clearance of 0.203 mm, and a length/diameter ratio of 0.75. The HC cell widths were 0.794 mm. Supply pressures and temperatures are provided in Table 1. All mod-

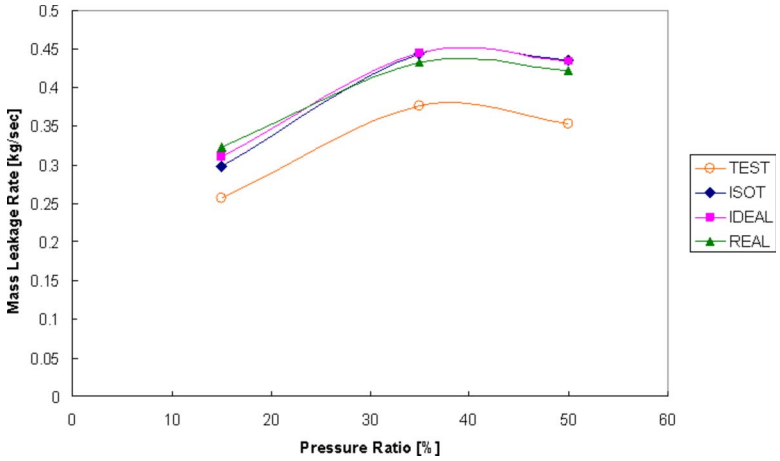

Fig. 3 Calculated versus measured mass leakage results for a HC-stator seal, sealing air

els overpredict the measured leakage rate by about the same amount. They also predict choked flow for the 15% pressure ratio.

NIST SUPERTRAPP. For real gas properties, a commercial code by Huber [8] (NIST SUPERTRAPP) is used. The code returns real gas properties as functions of any two of the following variables: pressure, temperature, or density.

For example, the internal energy $\hat{u}$ of Eq. (8) and temperature dependent viscosity, μ, are directly obtained actively from the NIST SUPERTRAPP code during the iteration process. Partial derivatives of any property can also be obtained with the code by implementing a small increment of variable.

Operating Conditions for Example Prediction. Example predictions are compared for a methane gas compressor seal with the real gas model (REAL) and the ideal gas model (IDEAL). REAL uses real gas properties from NIST SUPERTRAPP, while IDEAL gets gas properties from the ideal gas equation of state. Comparisons are done with high-pressure application of 1034.2 bars (15,000 psi) to 620.5 bars (9000 psi). The running condition and geometry for this application are

- P_R=1034.2 bars
- P_S=620.5 bars
- T_R=400°C
- ω=10,000 rpm
- D=250 mm
- L=150 mm
- C_r=0.3 mm
- H_d=2 mm
- γ_c=0.684
- $\mu=2.0\times10^{-5}$ Pa s
- Preswirl ratio=0
- Molecular weight=16.043
- γ=1.299
- m_s=−0.1101
- n_s=0.0785
- m_r=−0.217
- n_r=0.0586

Table 1 Test conditions

Pressure ratio (%)	Supply temperature (K)	Inlet pressure (MPa)	Exit pressure (MPa)
15	289.9	4.888	0.703
35	292.8	7.033	2.410
50	290.1	7.074	3.089

Predicted Static Results. The calculated mass leakage rates were, respectively, 9.46 kg/s, 9.55 kg/s, and 7.87 kg/s for ISOT, IDEAL, and REAL. Although not illustrated, the calculated static pressure distribution is very similar for all three models. Similarly, the circumferential-velocity distribution is almost identical for all

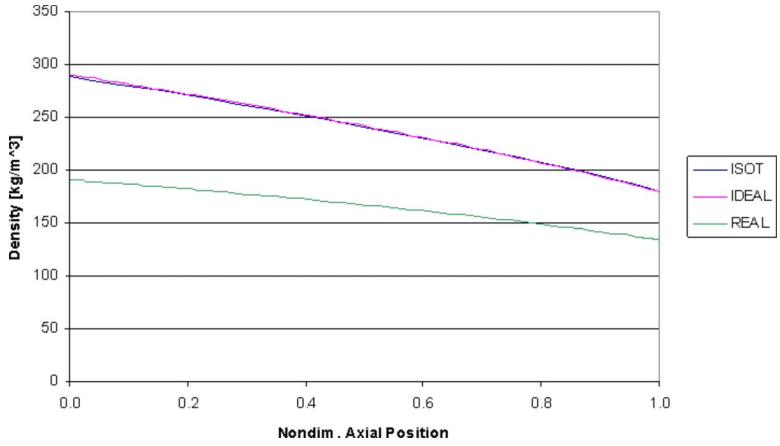

Fig. 4 Density distribution versus axial position

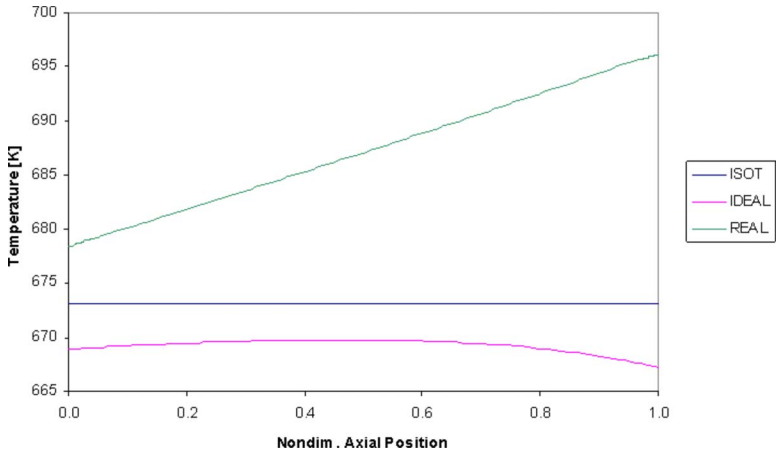

Fig. 5 Temperature distribution versus axial position

three models.

Figure 4 illustrates the density distribution, showing almost identical results for IDEAL and ISOT, but significantly reduced values for REAL. Figure 5 shows the temperature distribution along the seal axis, with pronounced differences in predictions for the three models. The differences between the models for density and temperature arise due to the sudden contraction model of Eqs. (10) and (11). The inlet temperature for all three models was identical at 673.15 K. The temperatures immediately inside the seal are obtained from these relations for the separate models.

Figure 6 presents the predicted speed of sound for the three models, showing that the real gas model predicts a substantially higher value. Hence, the ISOT and IDEAL models would predict choked flow at notably lower differential pressures than the real gas model.

Predicted Rotordynamic Coefficients. For compressors, the issues of interest in comparing predictions from the three models concern rotordynamic stability and the locations of critical speeds. A high-pressure HP seal can have predicted direct stiffnesses on the same order of magnitude as the bearings with a significant impact on critical speed locations. The effective stiffness defined in Eq. (23) provides the best measure of the seal's impact on critical speed locations. For the present seal, $c(f)$ provides a negligible contribution to $K_{\text{eff}}(f)$. Figure 7 illustrates predicted $K_{\text{eff}}(f)$ values, showing comparable magnitudes for the three models at low precession frequencies. At synchronous frequencies, ISOT has the highest predicted stiffness, followed in order by the REAL and IDEAL models. The roughly 40% predicted reduction in K_{eff} at synchronous speed with REAL versus ISOT could produce an appreciable reduction in the compressor's predicted critical speeds. The first critical speed of a back-to-back compressor is particularly sensitive to the stiffness developed by the division-wall seal.

As defined in Eq. (24), C_{eff} combines the stabilizing influence of the direct damping coefficient C and the destabilizing influence of the cross-coupled coefficient k. Figure 8 illustrates predicted $k(f)$ values, showing the IDEAL values slightly higher than the REAL values. However, ISOT predictions are significantly higher, particularly at low frequencies.

Figure 9 illustrates predicted $C(f)$ values, showing comparable IDEAL and ISOT values at low frequencies, both moderately higher than the REAL values. At synchronous frequencies, IDEAL and REAL values are comparable, both modestly lower than ISOT.

Predicted values for C_{eff} are provided for the three models in Fig. 10. The frequency at which C_{eff} changes from negative to positive is called the crossover frequency. The crossover frequency should be as low as possible and certainly below the first critical speed. The predicted crossover frequency roughly coincides for the REAL and IDEAL models, and is modestly lower than ISOT predictions. Most compressors have a running speed on the order of 2–2.5 times the first natural frequency. A HP seal is designed to provide peak effective damping at low frequencies near the first critical speed. From this perspective, the IDEAL model has the best predicted effective damping characteristics with a peak near $f=0.4$. To the extent that the REAL model is

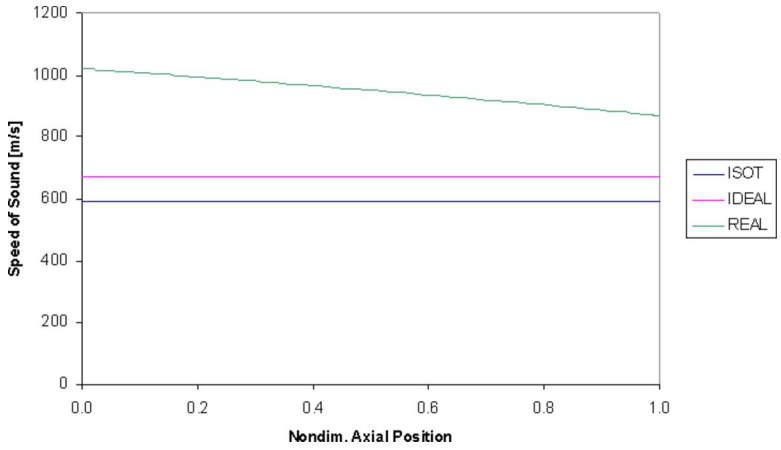

Fig. 6 Speed of sound for the three models

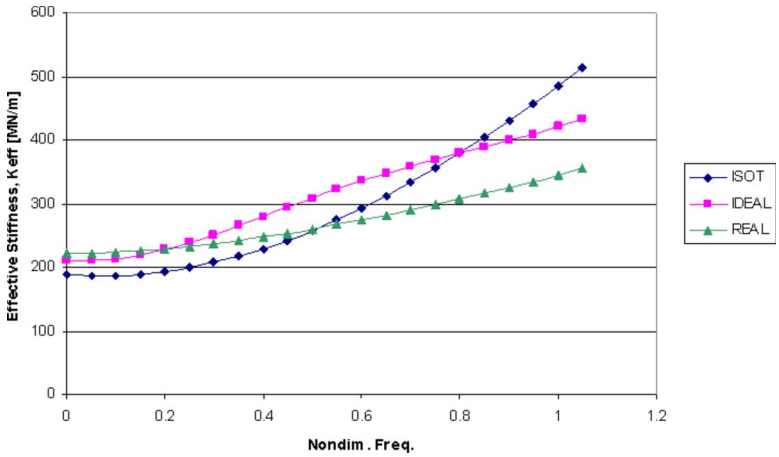

Fig. 7 Effective stiffness $K_{eff}(f)$ versus nondimensional frequency f

assumed to provide the most accurate results, lower values for C_{eff} are predicted for nondimensional frequencies near 0.4.

Summary, Conclusions, and Discussion

Extending the two-control-volume model of Ref. [5] to include the energy equation with either ideal gas properties or real gas properties makes the following changes in static properties.

(a) The ISOT prediction for leakage at 9.46 kg/s increases to 9.55 kg/s for IDEAL and decreases to 7.87 kg/s for REAL.

(b) Predicted pressure distribution and the development of circumferential-velocity versus axial position within the seal coincide for all models.

(c) The predicted density variation versus axial position co-

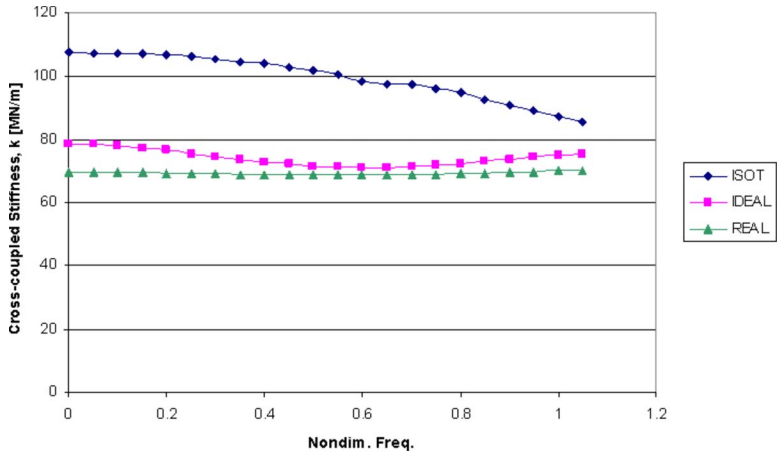

Fig. 8 Cross-coupled stiffness $k(f)$ versus nondimensional frequency f

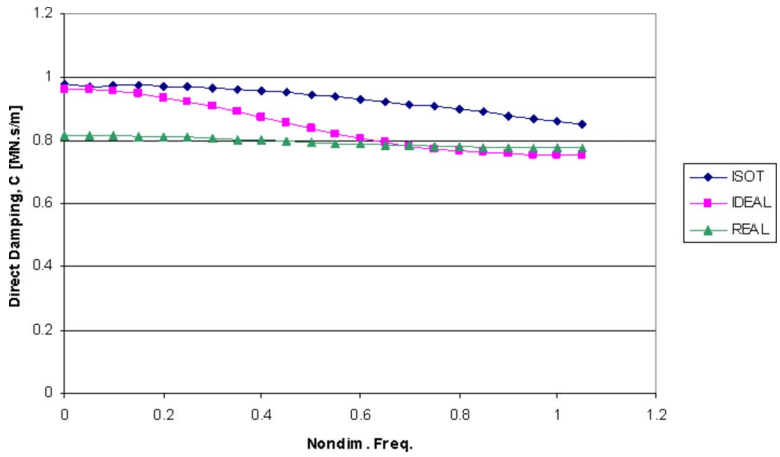

Fig. 9 Direct damping $C(f)$ versus nondimensional frequency f

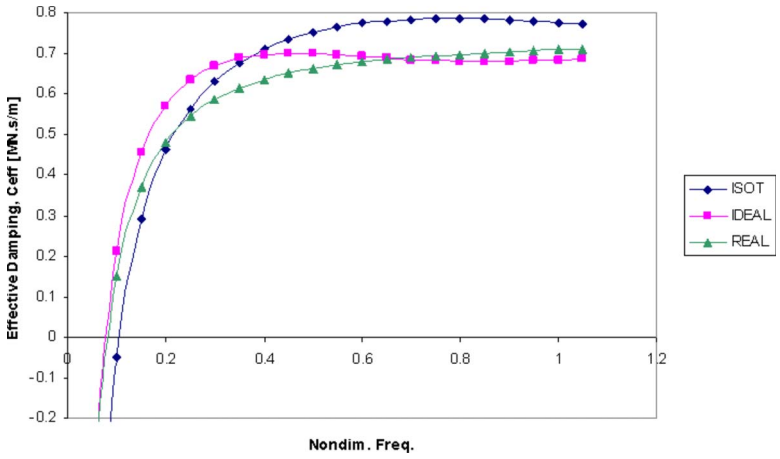

Fig. 10 Effective damping C_{eff} (f) versus nondimensional frequency f

incides for ISOT and IDEAL models; however, predicted densities are consistently lower for REAL. The predicted temperatures are lower from the IDEAL model with a small drop toward the exit versus a steady increase for the REAL model. The differences between the models for density and temperature at the inlet arise due to the sudden contraction model of Eqs. (10) and (11).

(d) The ISOT and IDEAL models predict substantially lower acoustic velocity than REAL. Hence, they will predict choked flow at an erroneously low-pressure differential.

The following changes are predicted for the rotordynamic coefficients.

(a) Predicted effective stiffness coefficients are comparable for all models. However, REAL predictions are roughly 40% lower than ISOT predictions for synchronous effective stiffness.

(b) Predicted effective damping coefficients are comparable for the three models. However, REAL and IDEAL models are more optimistic in predicting roughly a 20% lower crossover frequency. The REAL model predicts modestly lower peak damping in a frequency range expected for a compressor critical speed.

These predictions do not make an overwhelming case in favor of switching from the constant temperature model, ISOT. Possibly at still higher supply pressures or with different gas mixtures, a different outcome would be produced. These results suggest that predictions from a constant-temperature model should provide reasonable estimates for the contributions of annular HP seals in a rotordynamic model. However, if numbers from this type of model result in marginal stability margins, a real gas model is advisable.

Nomenclature

C, c = direct and cross-coupled damping coefficient (FT/L)
C_{eff} = effective damping coefficient (FT/L)
C_r = seal radial clearance (L)
C_v = specific heat at constant volume ($L^2/(T^2\Theta)$)
D = seal diameter (L)
$\boldsymbol{D}$ = direct force impedance due to displacement (F/L)
e = internal energy (L^2/T^2)
$\boldsymbol{E}$ = cross-coupled force impedance due to displacement (F/L)
f = nondimensional frequency
f_s, f_r = friction factor of stator and rotor
$\boldsymbol{F}_X, \boldsymbol{F}_Y$ = components of seal reaction force (F)
H = local clearance (L)
H_d = hole depth (L)
j = $\sqrt{-1}$
K, k = direct and cross-coupled stiffness coefficient (F/L)
K_{eff} = effective stiffness coefficient (F/L)
L = seal length (L)
n = blasius friction factor coefficient
m = blasius friction factor exponent
P = pressure (F/L^2)
R = seal radius (L)
T = temperature (Θ)
t = time (T)
U = circumferential bulk fluid velocity (L/T)
$\hat{u}$ = internal energy (L^2/T^2)
V = radial bulk fluid velocity (L/T)
W = axial bulk fluid velocity (L/T)
X, Y = relative displacement between stator and rotor (L)
Z = axial coordinate (L)
Z_c = compressibility factor
γ = specific heat ratio
γ_c = ratio of hole-pattern area to total stator surface area
ε = perturbation eccentricity ratio
θ = angle coordinate
κ = viscosity power law exponent
μ = fluid viscosity (FT/L^2)
ξ = entrance loss factor
ξ_e = exit recovery factor
ρ = fluid density (M/L^3)
τ = shear stress (F/L^2)
Ω = rotor precessional frequency ($1/T$)
ω = rotor rotational frequency ($1/T$)

Subscripts

in, ex = inlet and exit, respectively
R, S = denotes reservoir and sump, respectively
r, s = denotes rotor and stator, respectively
z, θ = axial and circumferential, respectively
0, 1 = zeroth-order and first-order perturbations in the dependent variables, respectively

Abbreviations

ISOT = constant-temperature model
IDEAL = model including the energy equation with an ideal gas model
REAL = model including the energy equation with real properties

Appendix: Perturbation Analysis

(1) Nondimensionalized parameters

$$w=\frac{W}{R\omega},\quad p=\frac{P}{P_R},\quad u=\frac{U}{R\omega},\quad \tilde{\rho}=\frac{\rho}{\rho_R},\quad h=\frac{H}{C_r},$$

$$h_d=\frac{H_d}{C_r},\quad c_r=\frac{C_r}{R},\quad l=\frac{L}{R},\quad z=\frac{Z}{L},\quad \tau=t\omega,$$

$$p_S=\frac{P_S}{P_R},\quad \tilde{\hat{u}}=\frac{\hat{u}}{\hat{u}_R} \tag{A1}$$

(2) Zeroth-order equations

Continuity:

$$0=\tilde{\rho}_0 w_0\frac{\partial h_0}{\partial z}+w_0 h_0\frac{\partial\tilde{\rho}_0}{\partial z}+\tilde{\rho}_0 h_0\frac{\partial w_0}{\partial z} \tag{A2}$$

Axial momentum:

$$-\frac{P_c}{l\tilde{\rho}_0}\frac{\partial p_0}{\partial z}=\frac{w_0}{2c_r h_0}(u_{s0}f_{s0}+u_{r0}f_{r0})+\frac{w_0}{l}\frac{\partial w_0}{\partial z} \tag{A3}$$

Circumferential momentum:

$$0=\frac{1}{2c_r h_0}(u_0u_{s0}f_{s0}+(u_0-1)u_{r0}f_{r0})+\frac{w_0}{l}\frac{\partial u_0}{\partial z} \tag{A4}$$

Energy-real gas:

$$0=\frac{\hat{u}_c\tilde{\rho}_0 w_0}{l}\frac{\partial\tilde{\hat{u}}_0}{\partial p_0}\frac{\partial p_0}{\partial z}+\left(\hat{u}_c\tilde{\rho}_0\frac{\partial\tilde{\hat{u}}_0}{\partial\tilde{\rho}_0}-\frac{p_0}{\tilde{\rho}_0}\right)\frac{w_0}{l}\frac{\partial\tilde{\rho}_0}{\partial z}-\frac{\tilde{\rho}_0}{2P_c c_r h_0}(u_{s0}{}^3f_{s0}+u_{r0}{}^3f_{r0}) \tag{A5}$$

Energy-ideal gas:

$$0=\frac{w_0}{lZ_c(\gamma-1)}\frac{\partial p_0}{\partial z}-\left(\frac{1}{Z_c(\gamma-1)}+1\right)\frac{p_0 w_0}{l\tilde{\rho}_0}\frac{\partial\tilde{\rho}_0}{\partial z}-\frac{\tilde{\rho}_0}{2P_c c_r h_0}(u_{s0}{}^3f_{s0}+u_{r0}{}^3f_{r0}) \tag{A6}$$

where

$$u_{s0}=\sqrt{u_0{}^2+w_0{}^2} \tag{A7}$$

$$u_{r0}=\sqrt{(u_0-1)^2+w_0{}^2} \tag{A8}$$

$$f_{s0}=n_s(g\tilde{\rho}_0 h_0 u_{s0})^{m_s} \tag{A9}$$

$$f_{r0}=n_r(g\tilde{\rho}_0 h_0 u_{r0})^{m_r} \tag{A10}$$

$$g=\frac{2\rho_R\bar{C}_r R\omega}{\mu} \tag{A11}$$

(3) First-order equations

Continuity:

$$0=\tilde{\rho}_0\frac{\partial h_1}{\partial\tau}+(h_0+\gamma_c h_d)\frac{\partial\tilde{\rho}_1}{\partial\tau}+\tilde{\rho}_0 u_0\frac{\partial h_1}{\partial\theta}+\tilde{\rho}_0 h_0\frac{\partial u_1}{\partial\theta}+u_0 h_0\frac{\partial\tilde{\rho}_1}{\partial\theta}+\frac{1}{l}\left[\frac{\partial(\tilde{\rho}_0 w_0 h_1)}{\partial z}+\frac{\partial(\tilde{\rho}_0 w_1 h_0)}{\partial z}+\frac{\partial(\tilde{\rho}_1 w_0 h_0)}{\partial z}\right] \tag{A12}$$

Axial momentum:

$$-\frac{P_c}{l\tilde{\rho}_0}\left(\frac{\partial p_1}{\partial z}-\frac{\tilde{\rho}_1}{\tilde{\rho}_0}\frac{\partial p_0}{\partial z}\right)=\frac{1}{2c_r h_0}\left[w_0u_{s0}\left(f_{s1}-\frac{h_1}{h_0}f_{s0}\right)+(w_1u_{s0}+w_0u_{s1})f_{s0}\right]+\frac{1}{2c_r h_0}\left[w_0u_{r0}\left(f_{r1}-\frac{h_1}{h_0}f_{r0}\right)+(w_1u_{r0}+w_0u_{r1})f_{r0}\right]+\frac{\partial w_1}{\partial\tau}+u_0\frac{\partial w_1}{\partial\theta}+\frac{1}{l}\left(w_0\frac{\partial w_1}{\partial z}+w_1\frac{\partial w_0}{\partial z}\right) \tag{A13}$$

Circumferential momentum:

$$-\frac{P_c}{\tilde{\rho}_0}\frac{\partial p_1}{\partial\theta}=\frac{1}{2c_r h_0}\left[u_0u_{s0}\left(f_{s1}-\frac{h_1}{h_0}f_{s0}\right)+(u_1u_{s0}+u_0u_{s1})f_{s0}\right]+\frac{1}{2c_r h_0}\left[(u_0-1)u_{r0}\left(f_{r1}-\frac{h_1}{h_0}f_{r0}\right)+(u_1u_{r0}+(u_0-1)u_{r1})f_{r0}\right]+\frac{\partial u_1}{\partial\tau}+u_0\frac{\partial u_1}{\partial\theta}+\frac{1}{l}\left(w_0\frac{\partial u_1}{\partial z}+w_1\frac{\partial u_0}{\partial z}\right) \tag{A14}$$

Energy-real gas:

$$\frac{p_0}{h_0}\frac{\partial h_1}{\partial\tau}=\hat{u}_c\tilde{\rho}_0\frac{\partial\tilde{\hat{u}}_0}{\partial p_0}\left[\frac{\partial p_1}{\partial\tau}+u_0\frac{\partial p_1}{\partial\theta}+\frac{1}{l}\left(w_0\frac{\partial p_1}{\partial z}+w_1\frac{\partial p_0}{\partial z}+\frac{\tilde{\rho}_1}{\tilde{\rho}_0}w_0\frac{\partial p_0}{\partial z}\right)\right]+\hat{u}_c\tilde{\rho}_0\frac{\partial\tilde{\hat{u}}_0}{\partial\tilde{\rho}_0}\left[\frac{\partial\tilde{\rho}_1}{\partial\tau}+u_0\frac{\partial\tilde{\rho}_1}{\partial\theta}+\frac{1}{l}\left(w_0\frac{\partial\tilde{\rho}_1}{\partial z}+w_1\frac{\partial\tilde{\rho}_0}{\partial z}+\frac{\tilde{\rho}_1}{\tilde{\rho}_0}w_0\frac{\partial\tilde{\rho}_0}{\partial z}\right)\right]-\frac{p_0}{\tilde{\rho}_0}\left[\frac{\partial\tilde{\rho}_1}{\partial\tau}+u_0\frac{\partial\tilde{\rho}_1}{\partial\theta}+\frac{1}{l}\left(w_0\frac{\partial\tilde{\rho}_1}{\partial z}+w_1\frac{\partial\tilde{\rho}_0}{\partial z}+\frac{p_1}{p_0}w_0\frac{\partial\tilde{\rho}_0}{\partial z}-\frac{\tilde{\rho}_1}{\tilde{\rho}_0}w_0\frac{\partial\tilde{\rho}_0}{\partial z}\right)\right]+\frac{\gamma_c h_d}{h_0}\left[\hat{u}_c\tilde{\rho}_0\frac{\partial\tilde{\hat{u}}_0}{\partial p_0}\frac{\partial p_1}{\partial\tau}+\left(\hat{u}_c\tilde{\rho}_0\frac{\partial\tilde{\hat{u}}_0}{\partial\tilde{\rho}_0}-\frac{p_0}{\tilde{\rho}_0}\right)\frac{\partial\tilde{\rho}_1}{\partial\tau}+\frac{\tilde{\rho}_0}{P_c}\left(u_0\frac{\partial u_1}{\partial\tau}+w_0\frac{\partial w_1}{\partial\tau}\right)\right]-\frac{\tilde{\rho}_0}{2P_c c_r h_0}\left[u_{s0}{}^2(u_{s0}f_{s1}+3u_{s1}f_{s0})+\left(\frac{\tilde{\rho}_1}{\tilde{\rho}_0}-\frac{h_1}{h_0}\right)u_{s0}{}^3f_{s0}\right]-\frac{\tilde{\rho}_0}{2P_c c_r h_0}\left[u_{r0}{}^2(u_{r0}f_{r1}+3u_{r1}f_{r0})+\left(\frac{\tilde{\rho}_1}{\tilde{\rho}_0}-\frac{h_1}{h_0}\right)u_{r0}{}^3f_{r0}\right] \tag{A15}$$

Energy-ideal gas:

$$\frac{p_0}{h_0}\frac{\partial h_1}{\partial \tau} = \frac{1}{Z_c(\gamma-1)}\left[\frac{\partial p_1}{\partial \tau} + u_0\frac{\partial p_1}{\partial \theta} + \frac{1}{l}\left(w_0\frac{\partial p_1}{\partial z} + w_1\frac{\partial p_0}{\partial z}\right)\right] - \left(\frac{1}{Z_c(\gamma-1)}+1\right)\frac{p_0}{\tilde{\rho}_0}\left[\frac{\partial \tilde{\rho}_1}{\partial \tau} + u_0\frac{\partial \tilde{\rho}_1}{\partial \theta} + \frac{1}{l}\left(w_0\frac{\partial \tilde{\rho}_1}{\partial z} + w_1\frac{\partial \tilde{\rho}_0}{\partial z} + \frac{p_1}{p_0}w_0\frac{\partial \tilde{\rho}_0}{\partial z}\right.\right.$$
$$\left.\left. - \frac{\tilde{\rho}_1}{\tilde{\rho}_0}w_0\frac{\partial \tilde{\rho}_0}{\partial z}\right)\right] + \frac{\gamma_c h_d}{h_0}\left[\frac{1}{Z_c(\gamma-1)}\frac{\partial p_1}{\partial \tau} - \left(\frac{1}{Z_c(\gamma-1)}+1\right)\frac{p_0}{\tilde{\rho}_0}\frac{\partial \tilde{\rho}_1}{\partial \tau} + \frac{\tilde{\rho}_0}{P_c}\left(u_0\frac{\partial u_1}{\partial \tau} + w_0\frac{\partial w_1}{\partial \tau}\right)\right] - \frac{\tilde{\rho}_0}{2P_c c_r h_0}\left[{u_{s0}}^2(u_{s0}f_{s1} + 3u_{s1}f_{s0})\right.$$
$$\left. + \left(\frac{\tilde{\rho}_1}{\tilde{\rho}_0} - \frac{h_1}{h_0}\right){u_{s0}}^3 f_{s0}\right] - \frac{\tilde{\rho}_0}{2P_c c_r h_0}\left[{u_{r0}}^2(u_{r0}f_{r1} + 3u_{r1}f_{r0}) + \left(\frac{\tilde{\rho}_1}{\tilde{\rho}_0} - \frac{h_1}{h_0}\right){u_{r0}}^3 f_{r0}\right] \tag{A16}$$

where

$$u_{s1} = \frac{u_0 u_1 + w_0 w_1}{u_{s0}} \tag{A17}$$

$$u_{r1} = \frac{(u_0 - 1)u_1 + w_0 w_1}{u_{r0}} \tag{A18}$$

$$f_{s1} = m_s f_{s0}\left(\frac{\tilde{\rho}_1}{\tilde{\rho}_0} + \frac{h_1}{h_0} + \frac{u_{s1}}{u_{s0}}\right) \tag{A19}$$

$$f_{r1} = m_r f_{r0}\left(\frac{\tilde{\rho}_1}{\tilde{\rho}_0} + \frac{h_1}{h_0} + \frac{u_{r1}}{u_{r0}}\right) \tag{A20}$$

References

[1] Childs, D., and Wade, J., 2004, "Rotordynamic-Coefficient and Leakage Characteristics for Hole-Pattern-Stator Annular Gas Seals—Measurements Versus Predictions," ASME J. Tribol., **126**, 326–333.

[2] Sprowl, B., and Childs, D., 2004, "A Study of the Effects of Inlet Preswirl on the Dynamic Coefficients of a Straight-Bore Honeycomb Gas Damper Seal," ASME J. Eng. Gas Turbines Power, **129**(1), pp. 220–229.

[3] Nelson, C. C., 1984, "Analysis for Leakage and Rotordynamic Coefficients of Surface-Roughened Tapered Annular Gas Seals," ASME J. Eng. Gas Turbines Power, **106**, 927–934.

[4] Nelson, C. C., 1985, "Rotordynamic Coefficients for Compressible Flow in Tapered Annular Seals," ASME J. Tribol., **107**, 318–325.

[5] Ha, T.-W., and Childs, D., 1994, "Annular Honeycomb-Stator Turbulent Gas Seal Analysis Using a New Friction-Factor Model Based on Flat Plate Tests," ASME J. Tribol., **116**, 352–360.

[6] Kleynhans, G., and Childs, D., 1997, "The Acoustic Influence of Cell Depth on the Rotordynamic Characteristics of Smooth-Rotor/Honeycomb-Stator Annular Gas Seals," ASME J. Eng. Gas Turbines Power, **119**, 949–957.

[7] Hirs, G., 1973, "A Bulk-Flow Theory for Turbulence in Lubricating Films," ASME J. Lubr. Technol., **95**, 137–146.

[8] Huber, M. L., 2003, NIST Thermophysical Properties of Hydrocarbon Mixtures Database (SUPERTRAPP), Version 3.1, U. S. Department of Commerce, National Institute of Standards and Technology, Standard Reference Data Program, Gaithersburg, MD.

Squeeze Film Damper With a Mechanical End Seal: Experimental Force Coefficients Derived From Circular Centered Orbits

Luis San Andrés
Mast-Childs Professor
Fellow ASME

Adolfo Delgado
Research Assistant

Mechanical Engineering Department,
Texas A&M University,
College Station, TX 77843

The paper presents parameter identification measurements conducted on a squeeze film damper (SFD) featuring a nonrotating mechanical seal that effectively eliminates lubricant side leakage. The SFD-seal arrangement generates dissipative forces due to viscous and dry-friction effects from the lubricant film and surfaces in contact, respectively. The test damper reproduces an aircraft application that must contain the lubricant for extended periods of time. The test damper journal is 2.54 cm in length and 12.7 cm in diameter, with a nominal clearance of 0.127 mm. The damper feed end opens to a plenum filled with lubricant, and at its discharge grooved section, four orifice ports evacuate the lubricant. In earlier publications, single frequency force excitation tests were conducted, without and with lubricant in the squeeze film land, to determine the seal dry-friction force and viscous damping force coefficients. Presently, further measurements are conducted to identify the test system and SFD force coefficients using two sets of flow restrictor orifice sizes (2.8 mm and 1.1 mm in diameter). The flow restrictors regulate the discharge flow area and thus control the oil flow through the squeeze film. The experiments also include measurements of dynamic pressures at the squeeze film land and at the discharge groove. The magnitude of dynamic pressure in the squeeze film land is nearly identical for both sets of flow restrictors, and for small orbit radii, dynamic pressures in the discharge groove have peak values similar to those in the squeeze film land. The identified parameters include the test system damping and the individual contributions from the squeeze film, dry friction in the mechanical seal and structure remnant damping. The identified system damping coefficients are frequency and motion amplitude dependent due to the dry-friction interaction at the mechanical seal interface. Squeeze film force coefficients, damping and added mass, are in agreement with simple predictive formulas for an uncavitated lubricant condition and are similar for both flow restrictor sizes. The SFD-mechanical seal arrangement effectively prevents air ingestion and entrapment and generates predicable force coefficients for the range of frequencies tested.
[DOI: 10.1115/1.2800345]

Introduction

Squeeze film dampers (SFDs) are widely employed to reduce rotor vibration or to suppress instabilities in rotating machinery equipment. Main applications of SFD include aircraft jet engines and process gas compressors. The technology of SFDs has continuously evolved over the past 40 plus years, with numerous researchers contributing to the analysis and experimental verification of dampers applied into high performance turbomachinery. Della Pietra and Adiletta [1,2] presented a monumental review of the state of the art of SFDs, highlighting most of the research work, analytical and experimental, conducted until 2002.

Tiwari et al. [3] presented a comprehensive review of the different types of procedures, time, and frequency domain to identify force coefficients in fluid film bearings, seals, and SFDs. The paper includes experimental methodologies, physical modeling, and parameter extraction algorithms. References [4–6] detail more recent work in parameter identification and characterization of SFDs. In particular, Kim and Lee [4] tested a grooved SFD with a novel sealing arrangement comprised of a two-stage liquid seal.

Despite the research advanced and field SFD applications, lubricant dynamic vapor or gas cavitation and the phenomenon of pervasive air entrapment are issues of permanent interest. Occurrence of air ingestion and entrapment is closely related to the SFD end sealing type, lubricant feed arrangement, and the kinematics of journal motion (amplitude and frequency). Air ingestion leads to a dramatic reduction of SFD damping capability [7]. Until recently, the loss in damping was deemed favorable when occurring at high frequencies, i.e., operation above a rotor-bearing system's natural frequency, to avoid the damper transmitting excessive forces to the casing. However, this desirable performance characteristic proved difficult to predict and worse to control. Presently, high performance turbomachinery operates at ever increasing rotational speeds while traversing one or more natural frequencies. Accurate (predictable) squeeze film damping coefficients must be attained to meet stringent vibration standards and to ensure the stability of a rotor-bearing system. For these applications, sealed SFDs prove to be less prone to air ingestion/entrapment, thus maintaining their damping ability at high operating frequencies.

References [8,9] introduce a SFD tightly sealed by contact forces between a whirling journal and its support bearing. Figures

Contributed by the International Gas Turbine Institute of ASME for publication in the JOURNAL OF ENGINEERING FOR GAS TURBINES AND POWER. Manuscript received May 10, 2007; final manuscript received June 6, 2007; published online April 29, 2008. Review conducted by Dilip R. Ballal. Paper presented at the ASME Turbo Expo 2007: Land, Sea and Air (GT2006), Montreal, Quebec, Canada, May 14–17, 2007.

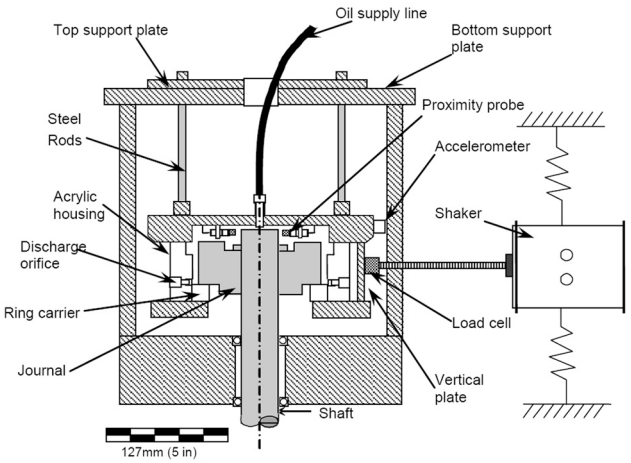

Fig. 1 Test rig for dynamic force measurements and flow visualization in a sealed and SFD

1 and 2 depict the test rig and damper, respectively. The damper, fed with lubricant at the top plenum, integrates a (nonrotating) mechanical seal at the film discharge section. The exit section includes a deep groove and four orifice outlet ports for the discharge of the lubricant. This damper, for use in unmanned aircraft engines, eliminates side lubricant leakage and air ingestion, while containing the lubricant in the film lands for extended periods of time. In the noted prior art, experiments to identify the SFD-seal force coefficients are conducted with dynamic loads inducing journal motions along straight path and circular centered orbits (CCOs). Note that the contact seal introduces a dry-friction force, which depends on the assembly preload of the wave spring as well as the condition of the contacting surfaces. Thus, the SFD-mechanical seal device is a nonlinear mechanical element. Careful experimentation is required to isolate the equivalent viscous damping coefficients arising from the squeeze film and the contact seal independently.

In the test procedure, the test rig structural stiffness and mass, without the mechanical seal in contact and with no lubricant flow, are first obtained. Next, dynamic load test experiments, with the mechanical seal in place and without any lubricant (dry condition), permit the determination of the dry-friction force and its equivalent viscous damping action. The seal damping coefficient is (roughly) inversely proportional to the excitation frequency and the amplitude of motion. Lastly, with lubricant flowing through the SFD, measurements of bearing displacements due to periodic

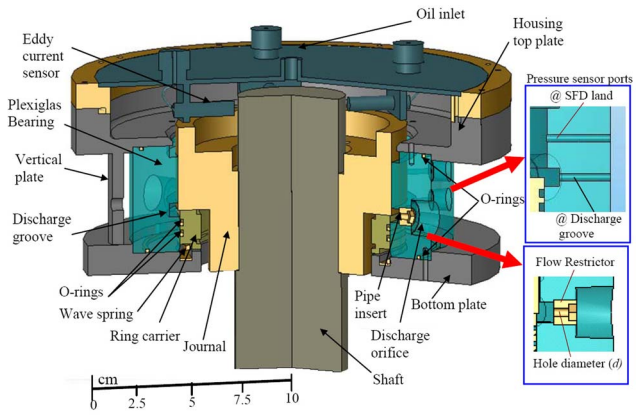

Fig. 2 Cut view of SFD with mechanical seal and details of outlet flow restrictor and pressure sensor locations

single frequency loads render transfer functions for the estimation of the test system force coefficients (wet condition). Subtraction of the seal dry-friction action from the system force coefficient reveals the squeeze film damping coefficient alone. The tests also identify the lubricant fluid inertia coefficient, which reduces significantly the natural frequency of the test apparatus. Comparisons of the experimentally derived SFD damping and inertia coefficients agree well with predictions based on the short length damper model.

This paper continues the experimental work in Refs. [8,9] and assesses the dynamic forced performance of the test damper for flow conditions determined by two sets of outlet restrictors with hole diameters equal to 2.8 mm and 1.1 mm, respectively. In addition, measurements of dynamic pressures at the squeeze film and groove are conducted to evaluate the effectiveness of the mechanical seal in preventing air ingestion. References [8,9] provide a relevant literature review, fully detailing the test rig characteristics, parameter identification procedure, and uncertainty analysis. Brief descriptions of the test SFD rig, parameter identification procedure, and experimental results follow.

Test Rig Description

Figure 1 depicts a schematic view of the general test rig assembly, including the SFD test section, instrumentation, and two orthogonally placed shakers. The composite SFD housing hangs from a top frame with four steel rods, giving a structural stiffness to the test bearing section. The top portion of the rig incorporates a sliding mechanism comprising of two flat plates and which allows centering and off-centering of the bearing with respect to its journal.

Figure 2 shows a cut view of the SFD with mechanical seal and other main components. The SFD consists of an acrylic bearing sandwiched by two thick steel plates, fastened together with vertical steel plates. A vertical rigid shaft, supported by three precision ball bearings, holds the steel journal. The journal is 127 mm (5 in.) in diameter and 76.2 mm (3 in.) in length. The natural frequency of the shaft and journal equals 400 Hz [10], well above the operating frequency of the test rig.

The damper film land length (L) is 25.4 mm (1 in.) and the film radial clearance (c) is $127\ \mu\text{m} \pm 6\ \mu\text{m}$ at room temperature (23 °C). The mechanical seal interface is formed by a metallic ring holder in the bearing housing and the journal bottom surface (see Fig. 1). A wave spring, pushing the ring holder against the journal, applies a contact force between the matting surfaces. At one end of the squeeze film land, the bearing incorporates a discharge groove, 4.25 mm deep and 7.62 mm in length.

The instrumentation includes thermocouples and static pressure gauges at the inlet and outlet sections of the test rig; two load cells and four eddy current sensors for the measurement of applied dynamic forces and bearing displacements; and two flush-mounted strain gauge absolute pressure sensors, one in the squeeze film lands at its mid axial plane ($1/2L$) and the other in the discharge groove.

ISO VG 2 lubricant is pressure fed into the damper at its top section. The lubricant flows through the squeeze film land, fills the discharge groove, and exits the bearing through four outlet ports (see the details in Fig. 2). The current tests include two sets of flow restrictors; one with 2.8 mm diameter holes and the other with 1.1 mm diameter holes. The discharge holes control the lubricant through flow rate. Smaller holes restrict the flow, and thus the static pressure in the deep groove increases, a desirable condition to prevent the entrainment of air into the squeeze film land. Most tests hereby reported are conducted with a low supply pressure, approximately ~0.31 bar (4.5 psi (gauge)), as in the actual aircraft. At the test temperature of 23 °C, the lubricant viscosity (η) and density (ρ) are 3.1 cP and 800 kg/m^3, respectively.

Note that the lubricant temperature in the aircraft SFD application is higher. However, the lubricant used in the experiments is

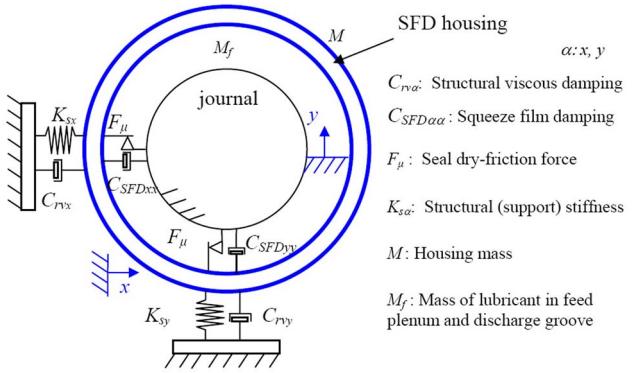

Fig. 3 Schematic view of physical model representation for SFD and mechanical seal

quite light (ISO VG 2), which reproduces accurately the specifications of a MIL lubricant at high temperatures, typically 150°C.

Structural Stiffness and Mass of Test Section

Figure 3 depicts a schematic view of the mechanical model for the SFD and end seal system. The test damper mass (M) is supported by elastic rods with lateral stiffnesses $(K_s)_{x,y}$ and (small) damping coefficients $(C_{rv})_{x,y}$. The seal frictional force (F_μ) and SFD forces connect the test housing to the nonspinning journal. The test system structural parameters, stiffness and mass, are obtained from impact load tests exerted on the bearing, with the mechanical seal disengaged (i.e., not in contact) and without any lubricant, i.e., a *dry condition*. Table 1 lists the identified test bearing support stiffnesses $(K_s)_{x,y}$, equivalent mass (M), and viscous damping $(C_{rv})_{x,y}$ coefficients. The structure damping C_{rv}, hereby named as remnant, is less than 1% of the overall damping of the lubricated test system, as shown later. Presently, in comparison with measurements reported in Ref. [8], the frame structure holding the test damper and support rods was stiffened to increase its natural frequency from 50 Hz to 150 Hz, well beyond the range of frequencies (20–70 Hz) for excitation of the test SFD.

Test System Parameter Identification Procedure

Upon assembly, the wave spring pushes the ring into contact with the bottom surface of the damper journal, and a dry-friction force (F_μ) arises. Once filled with lubricant, the SFD becomes active. Two shakers impose single frequency loads (F_x, F_y) along directions (x) and (y), respectively. The equations of motion for the test system are

Table 1 SFD test section identified parameters (no lubricant) (uncertainty of parameter listed in parentheses)

Parameter		x	y
Stiffness	K_s (kN/m)	853 (±34)	885 (±35)
Mass[a]	M (kg)	9.7 (±0.5)	
Remnant damping	C_{rv} (N s/m)	65	58
Damping ratio	ζ	0.01	0.01
Natural frequency	f_n (Hz)	48 ± 1	49 ± 1

[a]Includes seal components: ring and wave spring.

$$(M+M_f)\begin{Bmatrix}\ddot{x}\\ \ddot{y}\end{Bmatrix}+\begin{Bmatrix}C_{rv_x}\dot{x}\\ C_{rv_y}\dot{y}\end{Bmatrix}+\begin{Bmatrix}K_{sx}x\\ K_{sy}y\end{Bmatrix}=\begin{Bmatrix}F_x\\ F_y\end{Bmatrix}-\begin{Bmatrix}F_x\\ F_y\end{Bmatrix}_{\text{seal}}-\begin{Bmatrix}F_x\\ F_y\end{Bmatrix}_{\text{SFD}} \quad (1)$$

where $M_f=0.62$ kg is the lubricant mass enclosed in the plenum above the fluid film lands and in the discharge groove at the damper bottom. The reaction force from the mechanical seal is modeled as

$$\begin{Bmatrix}F_x\\ F_y\end{Bmatrix}_{\text{seal}}=F_\mu\frac{1}{|\mathbf{V}|}\begin{Bmatrix}\dot{x}\\ \dot{y}\end{Bmatrix}\approx\begin{Bmatrix}C_{\text{seal}_x}\dot{x}\\ C_{\text{seal}_y}\dot{y}\end{Bmatrix} \quad (2)$$

where $\mathbf{V}=(\dot{x},\dot{y})^T$ is the velocity vector. $C_{\text{seal}_\alpha}=(F_\mu/\omega|\alpha|)_{\alpha=x,y}$ represents the equivalent viscous damping action of the mechanical seal. Note that this coefficient is nonlinear, depending on the excitation frequency and amplitude of motion.

The SFD reaction forces follow a linearized description in terms of damping and inertia force coefficients, i.e.,

$$\begin{Bmatrix}F_x\\ F_y\end{Bmatrix}_{\text{SFD}}=\begin{bmatrix}C_{\text{SFD}_{xx}} & C_{\text{SFD}_{xy}}\\ C_{\text{SFD}_{yx}} & C_{\text{SFD}_{yy}}\end{bmatrix}\begin{Bmatrix}\dot{x}\\ \dot{y}\end{Bmatrix}+\begin{bmatrix}C_{\text{SFD}_{xx}} & C_{\text{SFD}_{xy}}\\ C_{\text{SFD}_{yx}} & C_{\text{SFD}_{yy}}\end{bmatrix}\begin{Bmatrix}\ddot{x}\\ \ddot{y}\end{Bmatrix} \quad (3)$$

Periodic loads with frequency (ω), i.e., $F_x(t)=\bar{F}_x e^{i\omega t}, F_y(t)=\bar{F}_y e^{i\omega t}$, produce system motions with identical frequency,[1] i.e., $x(t)=\bar{x}e^{i\omega t}, y(t)=\bar{y}e^{i\omega t}$, where $\bar{x}=x_R+ix_I, \bar{y}=y_R+iy_I$ are the complex amplitudes of motion. In particular, for excitations inducing circular orbits, the amplitudes of motion along x and y are identical but 90° out of phase, $\bar{y}=-i\bar{x}$. In the frequency domain, Eq. (1), including the force versus motion definitions stated in Eqs. (2) and (3), reduces to

$$(K_{s_x}-\omega^2 M_{s-xx}+\omega C_{s-xy})+i(\omega C_{s-xx}+\omega^2 M_{s-xy})=\left(\frac{\bar{F}_x}{\bar{x}}\right)$$

$$(K_{s_y}-\omega^2 M_{s-yy}+\omega C_{s-yx})+i(\omega C_{s-yy}+\omega^2 M_{s-yx})=\left(\frac{\bar{F}_y}{\bar{y}}\right) \quad (4)$$

where

$$C_{s-xx}=C_{\text{SFD}_{xx}}+C_{\text{seal}}+C_{rv_x} \quad M_{s-xx}=M_{\text{SFD}_{xx}}+M_f+M$$

$$C_{s-yy}=C_{\text{SFD}_{yy}}+C_{\text{seal}}+C_{rv_y} \quad M_{s-yy}=M_{\text{SFD}_{yy}}+M_f+M$$

$$C_{s-yx}=C_{\text{SFD}_{yx}} \quad C_{s-xy}=C_{\text{SFD}_{xy}} \quad M_{s-yx}=M_{\text{SFD}_{yx}} \quad M_{s-xy}=M_{\text{SFD}_{xy}} \quad (5)$$

are the *test system* inertia and damping force coefficients. In Eq. (4), $(\bar{F}_x/\bar{x})$ and $(\bar{F}_y/\bar{y})$ denote the measured mechanical impedances in the frequency domain. As detailed in Ref. [9], SFD cross-coupled damping and inertia effects are negligible since the lubricant in the squeeze film does not cavitate or show signs of air ingestion. Dynamic film pressure measurements, presented later, further confirm the original assumption. In the absence of cross-coupled effects, the parameter identification procedure is much simpler.

Equivalent Viscous Damping Coefficient for Mechanical Seal. Prior to identifying the test system force coefficients, experiments are conducted without any lubricant in the test section to determine the mechanical seal equivalent viscous damping coefficient (C_{seal}). Figure 4 depicts C_{seal} dropping rapidly as the exci-

[1]This condition requires sufficiently large loads to prevent stick-slip effects at the mechanical seal contact area.

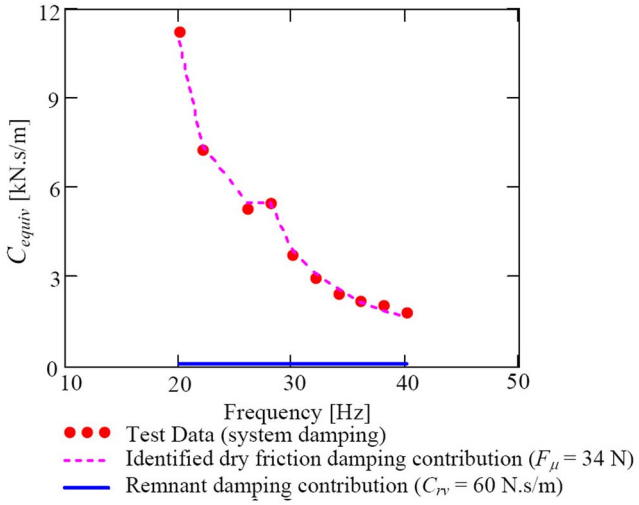

Fig. 4 Equivalent viscous damping (dry friction+remnant) versus excitation frequency (dry SFD, end seal in place)

tation frequency increases, as expected. The remnant structural damping C_{rv} is a minute fraction of the dissipation action offered by the mechanical seal. The seal viscous damping corresponds to a dry-friction force F_μ=34 N [9]. The contact normal force is 90 N ($\pm$10 N) for an estimated friction coefficient ($\mu \sim 0.37$) [11].

Damping and Inertia Coefficients of Test System and Squeeze Film Damper. With lubricant flowing through the damper lands, two single frequency (20–70 Hz) dynamic loads generate CCOs with amplitudes of motion increasing from 12 μm to 50 μm. The largest orbital amplitude amounts to ~40% of the damper radial clearance. The oil inlet pressure is 31 kPa (4.5 psi (gauge)) and the static pressure in the discharge groove equals 8.6 kPa (1.25 psi (gauge)) to 15.5 kPa (2.25 psi (gauge)) for restrictors with hole diameters equal to 2.8 mm and 1.1 mm, respectively. Figure 5 depicts typical measurements of loads and ensuing circular orbit motions for excitation at 70 Hz.

Figure 6 depicts the real part of the mechanical impedances $(\bar{F}_x/\bar{x}), (\bar{F}_y/\bar{y})$, also known as dynamic stiffnesses, and the curves modeling $(K_{s-\alpha\alpha} - \omega^2 M_{s-\alpha\alpha,\alpha=x,y})$ that render the test system inertia coefficients for the largest amplitude of motion (50 μm). Notice the substantial drop in test system natural frequency, from 48 Hz to ~34 Hz, due to the large fluid inertia in the squeeze film land in conjunction with the discharge groove.[2] Table 2 presents the structural parameters and the identified SFD inertia coefficients for both sets of flow restrictors. The high correlation coefficient (R^2), no less than 0.99, denotes that the test data are best represented by the physical model advanced. Predicted SFD inertia coefficients are within ~16% of the test identified inertia coefficients. Furthermore, the identified squeeze film inertia coefficients are similar (within 8%) to those obtained from unidirectional load tests in Ref. [8], i.e., $M_{\mathrm{SFD}xx}$=9.4 kg and $M_{\mathrm{SFD}yy}$ =8.1 kg. The flow restrictor size does not affect the magnitude of the fluid inertia coefficient.

The system damping coefficients are obtained from the imaginary part of the mechanical impedances. From Eqs. (4),

[2]Dynamic pressures in the discharge groove are not insignificant and contribute to the generation of an enhanced film inertia force coefficient. Figures 9 and 10 show measured pressures in the groove and film that evidence this effect.

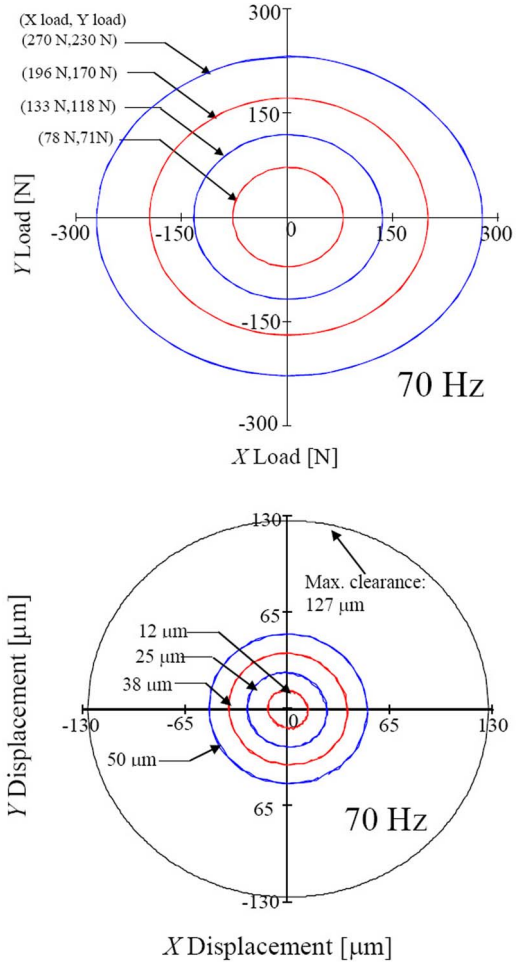

Fig. 5 Recorded load and ensuing displacement orbits for four amplitude load levels. Clearance circle noted (70 Hz, lubricated SFD, CCO, 2.8 mm diameter flow restrictor).

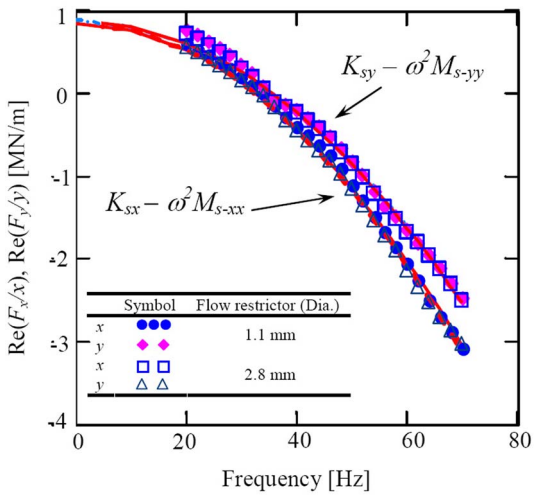

Fig. 6 Test system dynamic stiffness versus frequency. CCOs of amplitude *D*: 50 μm (K_{sx}=853 kN/m, K_{sy}=885 kN/m; 2.8 mm and 1.1 mm flow restrictors). Solid lines represent analytical curve fits.

Table 2 Test system and SFD inertia force coefficients identified from CCO tests (amplitude of motion: 50 μm; frequency range: 20–70 Hz)

Flow restrictor size	2.8 mm		1.1 mm	
Parameter	*xx*	*yy*	*xx*	*yy*
System mass (M_s) (kg)	20.2	17.5	20.5	17.6
Squeeze film inertia (M_{SFD}) (kg)	9.9	7.2	10.2	7.3
R^2 (goodness of curve fit for physical model)	0.99	0.99	0.99	0.99
Predicted SFD inertia, $M_{SFD}=\rho\pi R(2L)^3/210c$ (kg)		8.4		

K_{sx}=853 kN/m, K_{sy}=885 kN/m, M_f=0.62 kg, M=9.7 kg, ρ=800 kg/m^3, $\eta=2.8\times10^{-3}$ Pa s
$M_{SFDxx}=M_{s-xx}-M-M_f$; $M_{SFDyy}=M_{s-yy}-M-M_f$

$$C_{s-xx}=\mathrm{Im}\left(\frac{\bar{F}_x}{\bar{x}}\right)\frac{1}{\omega}\quad C_{s-yy}=\mathrm{Im}\left(\frac{\bar{F}_y}{\bar{y}}\right)\frac{1}{\omega} \tag{6}$$

Squeeze film damping coefficients at each excitation frequency follow from

$$C_{\mathrm{SFD}_{xx}}=C_{s-xx}-\frac{F_\mu}{|\bar{x}|\omega}-C_{rv_x}$$

$$C_{\mathrm{SFD}_{yy}}=C_{s-yy}-\frac{F_\mu}{|\bar{y}|\omega}-C_{rv_y} \tag{7}$$

For comparison to the identified parameters, the direct damping coefficient for a short length open end SFD describing CCOs is [12]

$$(C_{\mathrm{SFD}_{xx}}=C_{\mathrm{SFD}_{yy}})_{\mathrm{theory}}=\frac{\pi\eta R}{(1-[e/c]^2)^{3/2}}\left(\frac{L}{c}\right)^3 \tag{8}$$

applicable to a full film condition. Above, e is the orbit radius and η is the lubricant viscosity. At the test temperature, the measured clearance (c) equals 0.125 mm.

Figure 7 depicts the test system damping coefficients (C_{s-yy}) versus excitation frequency for increasing amplitudes of circular orbits (12 μm, 25 μm, 38 μm, 50 μm) and for flow restrictors with 2.8 mm and 1.1 mm hole diameters. The system damping coefficients, which include the SFD and dry friction from the mechanical seal, show a similar trend as those obtained in Ref. [8,9]; i.e., the system damping decays steadily with excitation frequency. Furthermore, for the smallest amplitude (12 μm), the coefficient is significantly larger than those identified from larger motion amplitudes. This evidences the large influence of dry friction arising from the mechanical seal. Importantly enough, the

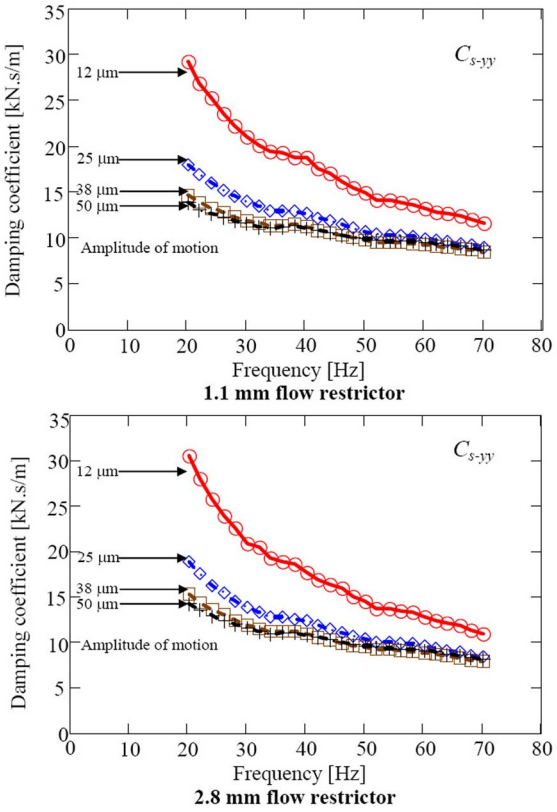

Fig. 7 Identified test system damping coefficients (C_{s-yy}) versus excitation frequency for increasing orbit amplitudes. (CCOs, lubricated SFD)

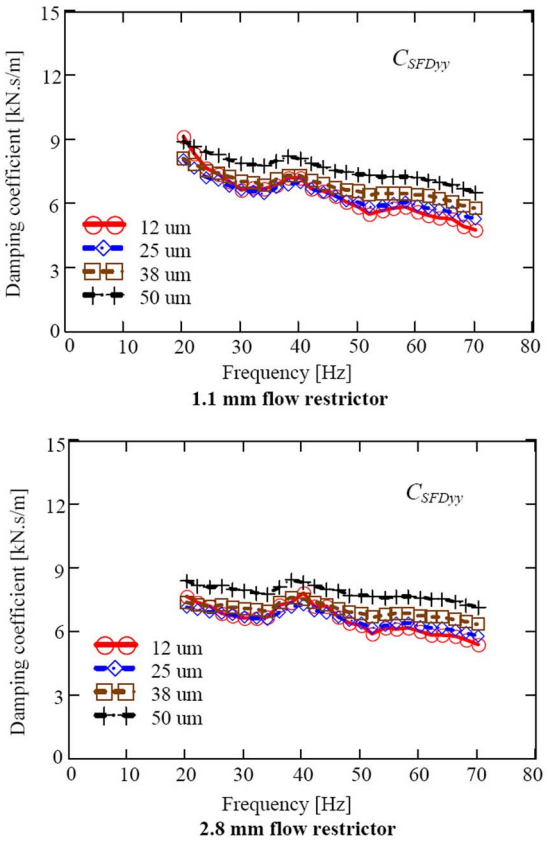

Fig. 8 Squeeze film damping coefficients (C_{SFDyy}) versus excitation frequency for increasing orbit amplitudes (CCOs, lubricated SFD)

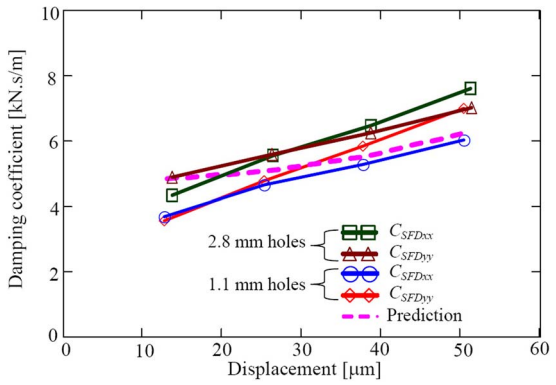

Fig. 9 Squeeze film damping coefficients (C_{SFDxx}, C_{SFDyy}) versus orbit amplitude (CCOs; flow restrictors: 1.1 mm and 2.8 mm in diameter)

dependency of the damping coefficient upon the amplitude of motion is less predominant as the excitation frequency increases, as is common in systems with dry friction, i.e., $C_{seal}=F_\mu/|\dot{\bar{x}}|\omega$.

Figure 8 displays the SFD coefficients (C_{SFDyy}) extracted from the test system damping (see Eq. (7) for both sets of flow restrictors). The squeeze film damping coefficients show a weak dependency on frequency, which further confirms the significant contribution of the dry-friction interaction to the system overall damping coefficient. Notice that both sets of flow restrictor render similar squeeze film damping coefficients.

Figure 9 shows the squeeze film damping coefficients (C_{SFDxx}, C_{SFDyy}) and predictions from Eq. (8) versus amplitude of motion (orbit radius) for the two flow restrictor sizes. The squeeze film viscous damping coefficients, as opposed to the system damping coefficients, increase steadily with the amplitude of motion. For motion orbit amplitudes larger than 25 μm, the experimentally derived C_{SFDxx} and C_{SFDyy}, from the tests with 2.8 mm holes, overestimate by 18% and 10% the predicted damping coefficient, respectively. For the 1.1 mm flow restrictors, the identified SFD parameters are within 10% of the predicted magnitude.

The test results show that the SFDs with 2.8 mm and 1.1 mm diameter flow restrictors render very similar damping coefficients (within 6% in Y and 14% in X) for the largest orbit amplitudes (50 μm) (R^2=0.99). For the smallest motion amplitudes, <25 μm, the test damping coefficients show a larger discrepancy, up to 25%. At these small amplitudes, for the physical model advanced in Eq. (7), the correlation coefficient R^2 equals 0.97, with the mechanical seal most likely influencing the accuracy of the estimated viscous damping parameter.

For the test conditions noted, the discharge orifices restrict the lubricant throughflow and raise the static pressure in the exit groove. The orifices do not distort (enhance or degrade) the dynamic film pressures and reaction forces in the SFD land. This assertion is only valid for conditions when there is no lubricant cavitation or air ingestion and entrapment, as intended in the present application.

The sources of uncertainty of the identified force coefficients include instrument errors in the measurement of force and displacements and the analytical correlations (curve fits) for the physical modeling of the mechanical impedances. A full Kline–McClintock [13] uncertainty analysis shows that the squeeze film damping coefficient uncertainty is ~9% for the largest test amplitude. All dynamic load measurements were repeated to verify duplicability, and the results are consistent with the reported uncertainty.

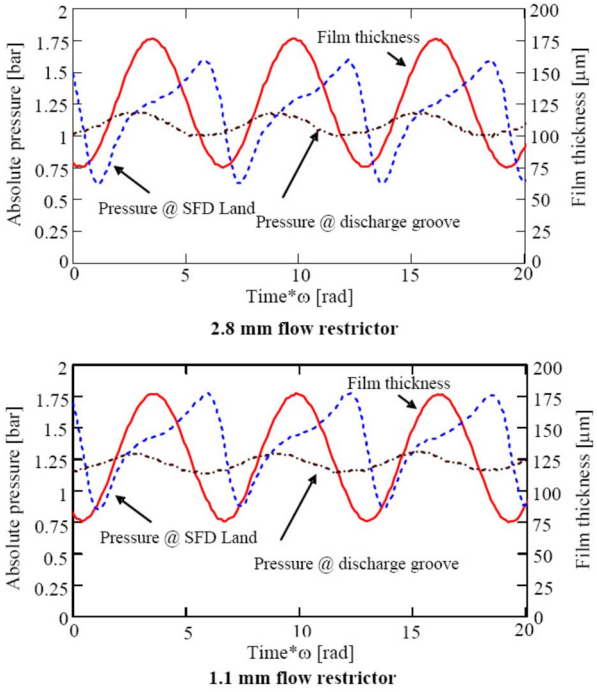

Fig. 10 Dynamic pressure measurements at SFD land and discharge groove and film thickness. Frequency of 70 Hz, 50 μm orbit amplitude, supply pressure=0.31 bar.

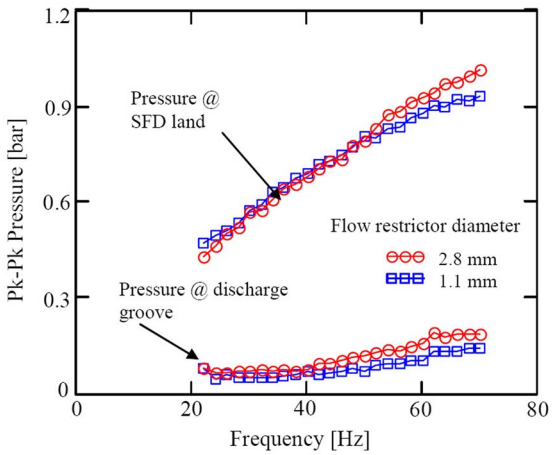

Fig. 11 Peak-peak dynamic pressures in SFD land and discharge groove. Tests at 0.31 bar supply pressure and largest (50 μm) orbit amplitude. 2.8 mm and 1.1 mm diameter flow restrictors.

Dynamic Pressures at Squeeze Film Land and Discharge Groove

The test rig includes ports for installation of pressure sensors and measurements at the mid axial plane of the squeeze film length and at the discharge groove (see details in Fig. 2). The sensors are of the strain-gauge type recording absolute pressure. The measurements are of importance to determine the magnitude of dynamic pressures generated due to the squeeze film motion

and to ascertain the occurrence of oil cavitation (vapor or gas) or air ingestion, particularly at the discharge groove next to the sealed surfaces in contact.

Figure 10 depicts recorded dynamic pressures versus (dimensionless) time for forced excitation at 70 Hz resulting in orbits of 50 μm in amplitude. The top and bottom graphs correspond to measurements with orifice ports of diameter equal to 2.8 mm and 1.1 mm, respectively. Both graphs, displaying three full periods of whirl motion, include an amplified depiction of the film thickness recorded at the location of pressure measurements. Note that as the local film thickness decreases, the pressure in the squeeze film land increases, and vice versa. On the other hand, the dynamic pressure in the groove has a clear phase shift and denotes mainly a fluid inertia effect [14]. The measurements corroborate the generation of dynamic pressures in the deep discharge groove. Importantly enough, the pressure signals show no sign of lubricant cavitation or air ingestion, thus evidencing the effectiveness of the mechanical seal.

Figure 11 shows that the peak-peak difference of dynamic pressure at the squeeze film are quite similar[3] for the two size orifice port sets and increase steadily with excitation frequency. The pressures at the deep groove are a fraction of those at the squeeze film, though large enough to contribute to the fluid inertia coefficient of the SFD.

Note from Fig. 9, for example, that the mean or static value of the recorded pressures is largest for the SFD with the smallest diameter (1.1 mm) discharge holes. The discharge orifices control the flow through the SFD; however, the exit ports do not affect significantly the generation of dynamic film pressures and the ensuing SFD reaction forces (damping and inertia coefficients). Delgado and San Andrés [15] detailed the characterization of the flow through the squeeze film land and through the orifice ports as a function of the film geometry and restrictor flow area. Details of the measurements and analysis are omitted for brevity.

Conclusions

This paper extends prior experimental work [8,9] to identify the damping and inertia force coefficients of a unique SFD configuration that incorporates a mechanical seal. The damper type, although used in certain unmanned aircraft engines, has not been adequately characterized as per its dynamic force performance.

The structural parameters of the test system are first identified via static load tests on the "dry" system without the seal. With the seal in place, single frequency loads generating CCOs on the dry (no lubricant) test system serve to identify the dry-friction force at the seal contact surface. An equivalent viscous damping coefficient represents the dissipative action of dry friction in the mechanical seal. This equivalent damping coefficient is nonlinear, inversely proportional to the amplitude and frequency of motion.

Single frequency (20–70 Hz) dynamic load excitations inducing circular centered motions are exerted on the test system with lubricant flowing through the SFD. Experiments are conducted for two sets of discharge flow restrictors (2.8 mm and 1.1 mm in diameter). The orifice outlet ports control the lubricant throughflow and determine the static pressure in a discharge groove. The test system damping and inertia force coefficients are identified from frequency domain mechanical impedances (load/displacement). The system damping coefficients, combining the effects of dry friction at the seal interface and the viscous action at the squeeze film land, are functions of the excitation frequency and amplitude of motion.

Squeeze film damping and inertia force coefficients are extracted from the system coefficients. Predicted squeeze film damping coefficients, based on the short length bearing model without lubricant cavitation, agree well (within 18%) with the experimental results. The predicted fluid inertia coefficient lies within 16% of the test identified coefficient.

The experiments demonstrate that for both sets of flow restrictors, the mechanical end seal effectively prevents air ingestion and entrapment into the squeeze film land for the frequencies and amplitudes of motion tested. Furthermore, the coefficients obtained for both restrictor hole sizes are similar, as expected. Measurements of dynamic pressures show an absence of air ingestion into the squeeze film, while at the deep discharge groove significant dynamic pressures aid to an amplification of fluid inertia forces. Future work will include measurements at larger excitation loads and at higher frequencies, and tests with closed discharge ports (i.e., no lubricant throughflow).

Acknowledgment

The continued support from the TAMU Turbomachinery Research Consortium is gratefully acknowledged.

Nomenclature

c = squeeze film radial clearance (m)
C_{rv} = structure remnant damping coefficient (N s/m)
C_{seal} = equivalent viscous damping of mechanical seal (N s/m)
$C_{s-\alpha\alpha}$ = identified test system damping coefficients (N s/m) $\alpha=x,y$
$C_{\text{SFD}\alpha\alpha}$ = identified squeeze film damping coefficients (N s/m) $\alpha=x,y$
d = orifice diameter in flow restrictor (m)
e = amplitude or radius of CCO (m)
F_x, F_y = $\bar{F}_x e^{i\omega t}$, $\bar{F}_y e^{i\omega t}$ periodic forces applied to test bearing (N), $\bar{F}_x = F_{x_R} + iF_{x_I}$, $\bar{F}_y = F_{y_R} + iF_{y_I}$
F_μ = dry-friction force from contact in mechanical seal (N)
f_n = test system natural frequency (Hz)
i = $\sqrt{-1}$, imaginary unit
K_{sx}, K_{sy} = structural (support) stiffnesses (N/m)
L, R = length and radius of SFD land (m)
M = equivalent mass of bearing housing (kg)
M_f = mass of lubricant in feed plenum and end groove (kg)
$M_{\text{SFD}\alpha\alpha}$ = squeeze film inertia coefficients (kg), $\alpha=x,y$
$M_{s-\alpha\alpha}$ = identified system inertia coefficients (kg), $\alpha=x,y$
x, y = $\bar{x}e^{i\omega t}, \bar{y}e^{i\omega t}$, bearing periodic motions (m), $\bar{x}=x_R+ix_I, \bar{y}=y_R+iy_I$
μ = dry-friction coefficient from mechanical contact seal
ρ, η = lubricant density (kg/m^3) and viscosity (Pa s)
ω = excitation frequency (rad/s)
ζ = $C/[2(K_s M)^{1/2}]$, viscous damping ratio

References

[1] Della Pietra, L., and Adiletta, G., 2002, "The Squeeze Film Damper Over Four Decades of Investigations. Part I: Characteristics and Operating Features," Shock Vib. Dig., **34**(1), pp. 3–26.
[2] Della Pietra, L., and Adiletta, G.,2002, "The Squeeze Film Damper Over Four Decades of Investigations. Part II: Rotordynamic Analyses With Rigid and Flexible Rotors," Shock Vib. Dig., **34**(2), pp. 97–126.
[3] Tiwari, R., Lees, A. W., and Friswell, M. I., 2004, "Identification of Dynamic Bearing Parameters: A Review," Shock Vib. Dig., **36**(2), pp 99–124.
[4] Kim, K., and Lee, C., 2005, "Dynamic Characteristics of Sealed Squeeze Film Damper With a Central Feeding Groove," ASME J. Tribol., **127**(1), pp. 103–111.
[5] Defaye, C., Arghir, M., Carpentier, P., Bonneau, O., Debailleux, C., and Imbourg, F., 2005, "Experimental Investigation of the Design Parameters and of the Working Conditions on the Global Characteristics of a Squeeze Film Damper," *Proceedings of the World Tribology Congress III*, Washington D.C., Paper No. WTC2005-64270, pp. 287–288.

[3]The dynamic portions of the pressure signals are nearly identical, thus generating damping and inertia force coefficients of very similar magnitudes.

[6] Adiletta, G., and Della Pietra, L., 2006, "Experimental Study of a Squeeze Film Damper With Eccentric Circular Orbits," ASME J. Tribol., **128**(2), pp 365–377.
[7] Diaz, S., and San Andrés, L., 2001, "Air Entrainment Versus Lubricant Vaporization in Squeeze Film Dampers: An Experimental Assessment of Their Fundamental Differences," ASME J. Eng. Gas Turbines Power, **123**, pp. 871–877.
[8] San Andrés, L., and Delgado, A., 2007, "Identification of Force Coefficients in a Squeeze Film Damper With a Mechanical Seal—Part I: Unidirectional Load Tests," ASME J. Eng. Gas Turbines Power, **129**(3), pp. 858–864.
[9] San Andrés, L., and Delgado, A., 2007, "Identification of Force Coefficients in a Squeeze Film Damper With a Mechanical Seal-Centered Circular Orbit Tests," ASME J. Tribol., **129**(3), pp. 660–668.
[10] San Andrés, L., and De Santiago, O., 2004, "Forced Response of a Squeeze Film Damper and Identification of Force Coefficients From Large Orbital Motions," ASME J. Tribol., **126**(2), pp. 292–300.
[11] Delgado, A., 2005, "Identification of Force Coefficients in a Squeeze Film Damper With a Mechanical Seal," MS thesis, Texas A&M University, College Station, TX.
[12] Vance, J. M., 1988, *Rotordynamics of Turbomachinery*, Wiley, New York, Chapt. 6.
[13] Coleman, H. W., and Steele, G. W., 1988, *Experimentation and Uncertainty Analysis for Engineers*, Wiley, New York, Chap. 1–4.
[14] Arauz, G., and San Andrés, L., 1994, "Effect of a Circumferential Feeding Groove on the Force Response of a Short Squeeze Film Damper," ASME J. Tribol., **116**(2), pp. 369–377.
[15] Delgado, A., and San Andrés, L., 2006, "Identification of Force Coefficients in a Squeeze Film Damper With a Mechanical Seal," Texas A&M University, TRC Report No. TRC-SFD-1-06.

Flexure Pivot Tilting Pad Hybrid Gas Bearings: Operation With Worn Clearances and Two Load-Pad Configurations

Luis San Andrés
Mast-Childs Professor
Fellow ASME
e-mail: lsanandres@mengr.tamu.edu

Keun Ryu
Research Assistant
e-mail: keun@tamu.edu

Mechanical Engineering Department,
Texas A&M University,
College Station, TX 77843-3123

*Gas film bearings enable the successful deployment of high-speed microturbomachinery. Foil bearings are in use; however, cost and lack of calibrated predictive tools prevent their widespread application. Other types of bearing configurations, simpler to manufacture and fully engineered, are favored by commercial turbomachinery manufacturers. Externally pressurized tilting pad bearings offer a sound solution for stable rotor support. This paper reports measurements of the rotordynamic response of a rigid rotor, 0.825 kg and 28.6 mm in diameter, supported on flexure pivot tilting pad hybrid gas bearings. The tests are performed for various imbalances, increasing supply pressures, and under load-on-pad (LOP) and load-between-pad (LBP) configurations. Presently, the initial condition of the test bearings shows sustained wear and dissimilar pad clearances after extensive testing reported earlier, (Zhu, X., and San Andrés, L., 2007, "Rotordynamic Performance of Flexure Pivot Hydrostatic Gas Bearings for Oil-Free Turbomachinery," ASME J. Eng. Gas Turbines Power, **129**, pp. 1020–1027). In the current measurements, there are no noticeable differences in rotor responses for both LOP and LBP configurations due to the light-weight rotor, i.e., small static load acting on each bearing. External pressurization into the bearings increases their direct stiffnesses and reduces their damping, while raising the system critical speeds with a notable reduction in modal damping ratios. The rotor supported on the worn bearings shows an ~10% drop in first critical speeds and roughly similar modal damping than when tested with pristine bearings. Pressurization into the bearings leads to large times for rotor deceleration, thus demonstrating the little viscous drag typical of gas bearings. Rotor deceleration tests with manually controlled supply pressures eliminate the passage through critical speeds, thus paving a path for rotordynamic performance without large amplitude motions over extended regions of shaft speed. The rotordynamic analysis shows critical speeds and peak amplitudes of motion agreeing very well with the measurements. The synchronous rotor responses for increasing imbalances demonstrate the test system linearity. Superior stability and predictable performance of pressurized flexure pivot gas bearings can further their implementation in high performance oil-free microturbomachinery. More importantly, the measurements show the reliable performance of the worn bearings even when operating with enlarged and uneven clearances.* [DOI: 10.1115/1.2800346]

Introduction

Gas bearings are widely used as support elements in high-speed compact rotating machinery due to their distinct advantages when compared to mineral oil lubricated bearings. Gas bearings eliminate complex oil lubrication and sealing systems, and reduce friction, heat generation, and power losses. These advantages have led to commercial applications in MTM (output power below 200 kW) with distinctive advantages including low part count number, light weight, reduced energy costs, and extreme temperature operation [1].

Gas bearings, however, have a very limited load-carrying capacity since the gas viscosity is quite small [2]. This limitation also results in very low damping coefficients, not large enough to dissipate effectively vibrational energy and to reduce amplitudes of motion while traversing critical speeds, for example. At low surface speeds, while at rotor start-up or shutdown, gas bearings are not able to generate large enough hydrodynamic pressures supporting applied (static or dynamic) loads; thus, intermittent or sustained operation with contact of the rotor within its bearings is unavoidable. This operating condition increases dramatically the friction and drag, while accelerating the wear (and damage) of the surfaces in contact [3]. Gas hydrostatic bearings, integrating an external pressurization source, avoid the issues of contact and wear during start up and shut down [4]. While the rotor rests on its bearings (not spinning), the external pressure lifts the rotor, thus eliminating the likeliness of contact while the machine starts up. Within the framework of MTM applications, the pressurized gas (air typically) could be readily available in small canisters. In operation of a turbocharger, for example, gas bleed-off from the compressor can readily replenish the pressurized gas spent during start-up. Micro gas turbines are already implementing this bearing concept [5].

Tilting pad bearings are widely applied in high performance TM because of their proven stability characteristics since they do not generate cross-coupled stiffnesses for certain static load orientations [6]. Flexure pivot tilting pad bearings were introduced to provide many of the advantageous rotordynamic characteristics of tilting pad bearings with a single-piece mechanical component fabricated with the electric discharge machining (EDM) process [7]. This bearing type also eliminates pivot wear and contact

Contributed by the International Gas Turbine Institute of ASME for publication in the JOURNAL OF ENGINEERING FOR GAS TURBINES AND POWER. Manuscript received May 10, 2007; final manuscript received June 6, 2007; published online April 29, 2008. Review conducted by Dilip R. Ballal. Paper presented at the ASME Turbo Expo 2007: Land, Sea and Air (GT2007), Montreal, Quebec, Canada, May 14–17, 2007.

stresses, pad flutter, and minimizes manufacturing and assembly tolerances' stack-up. Armentrout et al. [8] calculate flexure pivot tilting pad bearing stiffness and damping coefficients as a function of pad flexure rotational stiffness, and also present a rotordynamic analysis for a high-speed turbocompressor implementing these bearings. De Choudhury et al. [9] report imbalance responses of a two stage compressor rotor supported on flexure pivot tilting pad bearings. The selected bearings show lower temperature operation and less drag power losses when compared to identical size five-pad tilting pad journal bearings. Chen et al. [10] demonstrate that the vibration of a compressor rotor decreases with flexible pivot tilting pad bearings as compared to conventional tilting pad bearings for an unusual operation under surge conditions. Kepple et al. [11] describe field applications of TM rotors becoming stable when implementing flexure pivot tilting pad bearings; the opposite effect being observed with spherical pivot tilting pad bearings.

For use in oil-free TM, Zhu and San Andrés [12] demonstrate the stable performance of a high-speed rotor supported on hybrid (hydrostatic and hydrodynamic) flexure pivot tilting pad bearings. With external pressurization, the rotor-bearing system is stable to the top speed, 100 krpm, of the drive motor. Zhu and San Andrés [13] also perform similar experiments with a rotor supported on Rayleigh-step gas bearings. Severe instabilities arise at nearly fixed whirl frequencies (system natural frequency). The test Rayleigh-step gas bearings exhibit a much reduced stable operation range, up to ~20 krpm.

Gas foil bearings used in commercial MTM offer high temperature operation with tolerance to large rotor motions (rubbing and misalignment) and a load capacity exceeding that of rigid surface gas bearings. Kim and San Andrés [14] present an efficient computational tool for prediction of the static and dynamic force performance of foil bearings. San Andrés et al. [15] measure the rotordynamic performance of a test rotor supported on foil bearings and find severe subsynchronous whirl amplitude motions forced by increasing mass imbalances. The design tools and experimental results complement the development of oil-free TM with high efficiency. References [14] and [15] include extensive literature reviews on the state of art in gas foil bearings.

The current research continues earlier work [12] and presents further rotordynamic measurements of a test rotor supported on worn flexure pivot tilting pad gas hydrostatic bearings. The tests are conducted with the bearings under load-on-pad (LOP) and load-between-pad (LBP) configurations. Rotor speed coast-down tests to calibrated imbalance masses are performed for increasing feed gas pressures. Predictions from computational programs for gas bearing performance and rotordynamic response show excellent agreement with the experimental results.

Experimental Facility

Figure 1 shows the schematic cross sectional view of the gas bearing test rig with a steel main body integrating a brushless ac motor armature (maximum speed of 99 krpm). The test rotor is supported on two flexure pivot hydrostatic bearings, denoted as left and right, respectively. This rotor, 0.825 kg in mass, is a steel shaft, 15 mm in diameter and 190 mm in length, onto which two cylindrical sleeves are press fit. The rotor has a diameter of 28.55 mm. The rotor at the bearing locations is hard-chrome coated (thickness 0.010 ± 0.001 in.). On each rotor end face, eight holes, 1 mm in diameter, are spaced equally for insertion of small imbalance masses. Pins with a spring loaded elastomer head hold the rotor axially. Alignment bolts position the test bearings, shown in Fig. 2, within their housings. Piezoelectric load cells are installed between each bolt and bearing outer surface. Side caps and o-rings push on the bearing sides to form a feed groove for external pressurization into the bearings. Pairs of eddy current sensors, orthogonally positioned and facing the rotor ends, measure the rotor motions along the *X*-(vertical) and *Y*-(horizontal) planes. An infrared tachometer serves as a keyphasor signal for data acquisition.

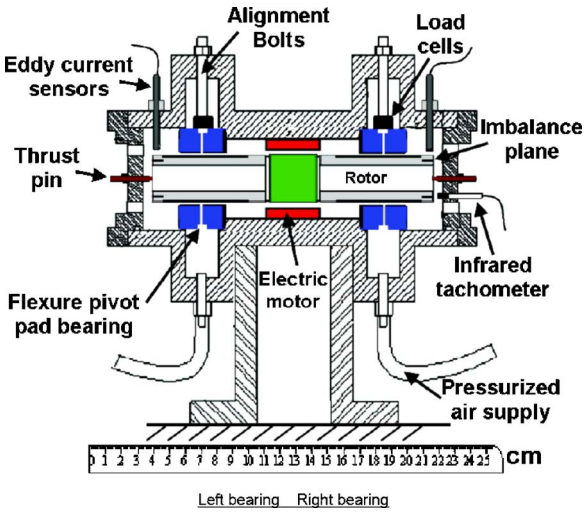

Fig. 1 Schematic cross sectional view of test rig

Figure 2 depicts a test flexure pivot tilting pad hydrostatic bearing. Each bearing, made of bronze, has four arcuate 72 deg pads connected to the housing through a thin structural web. Four radial holes, 0.62 mm in diameter, are machined directly through the flexural webs and served to pressurize each pad. A coating of Permalon® (10 ± 1 μm thick) was applied onto the pads surfaces to reduce friction upon rotor start-up and shutdown. The surface of each pad was finished with 600 grit ultrafine grade sandpaper. Table 1 lists the dimensions of the test rotor and its bearings.

Prior extensive testing with the bearings [12] left the pads' surfaces with a number of scratches and uneven wear. The present condition of the bearings, even after application of the coating and hand polishing, shows quite dissimilar clearances along the circumference and axial length of each pad. The original bearing nominal clearance and dimensionless pad preload, as reported in Ref. [12], are 40 ± 4.5 μm and 40%, respectively. The current bearing clearances are estimated by subtracting the rotor diameter from the bearing diameter. The pad curvature is generally established prior to initial machining, and the pad clearance equals to the difference between the machined pad bore diameter and the rotor diameter. Presently, the estimated radial clearances vary from 20–60 μm for the left bearing and 20–40 μm for the right bearing, as depicted in Fig. 3 [16]. The uncertainties of the estimated clearances are approximately ± 5 μm (with 95% confidence) at each measurement position. The left bearing has a much larger clearance variation than the right bearing. The differences in clearances from the nominal (design) magnitudes will have a profound impact on the static and dynamic performance characteristics of the rotor-bearing system since one bearing will show larger direct stiffnesses than the other, thus affecting the location of critical speeds and imbalance response of the rotor.

The baseplate supporting the test rig can be rotated by hand and fixed at a desired angular location. This feature allows for tests to be conducted with the rotor weight acting along a pad (LOP) when the baseplate is horizontal, or load in between two pads (LBP) when the baseplate is at 45 deg. Note that LOP and LBP conditions are most common in practice.

Experimental Procedure and Results

Rotor coast-down speeds tests are conducted for various imbalance conditions and feed supply pressures equal to 2.36 bars, 3.72 bars, and 5.08 bars (absolute) [20 psig, 40 psig, and 60 psig]. The feed pressures cover the range of delivery for typical single-stage centrifugal compressors used in micro gas turbines and automotive turbochargers, for example, see Ref. [17].

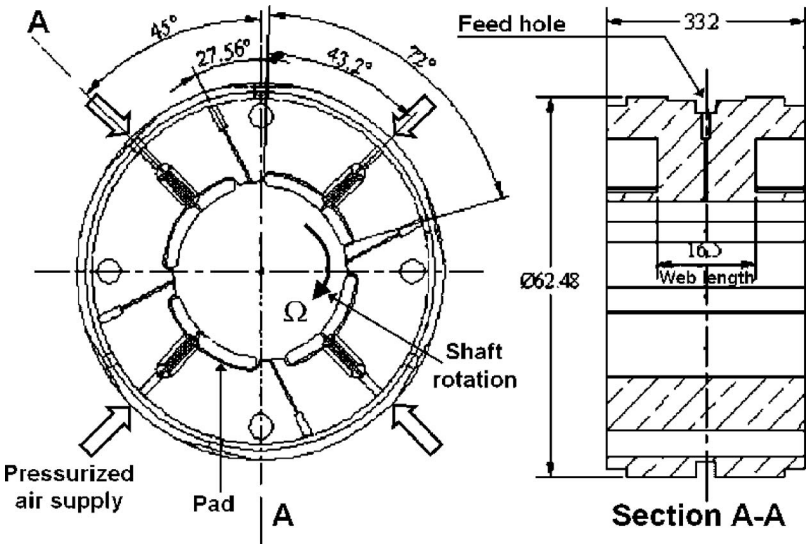

Fig. 2 Dimensions of flexure pivot tilting pad hydrostatic bearing (units: mm)

It is important to note that within the typical test speed range (<50 krpm), the test rotor can be regarded as a rigid body. Table 2 summarizes the imbalance mass and location for the two types of imbalance tests. In test $U(A_1) \sim U(A_3)$, the imbalance masses are positioned at the same angular location at each rotor end, whereas in test $U(B_1) \sim U(B_3)$, the imbalance masses on each end are 180 deg out of phase.

The API permissible residual imbalance ($4W/N$) is 0.261 g mm. The added masses (m_i) render larger imbalance conditions (0.36 g mm, 0.41 g mm, and 0.48 g mm). At 20 krpm and for the largest added mass (0.04 g), the imbalance force ($2m_iR'\Omega^2$) equals 4.21 N, i.e., 52% rotor weight, exceeding the admissible API specification, i.e., "the maximum admissible unbalance force on any bearing at the maximum continuous speed shall not exceed 10% of the static loading of that bearing." Note that satisfying API constraints in small machinery rotating at high speeds is not always practical.

To prevent damage of the bearings and rotor during speed start-up to a high speed, the supply pressure is maintained at 2.36 bar absolute while the rotor passes through its critical speed(s). This precaution is also in place when the procedure calls for coast-down experiments without external pressurization. Once operating well above the critical speed, the feed pressure lines are closed and the rotor runs up to 50,000 rpm. During this operation condition, the bearings work purely in the hydrodynamic film regime.

Table 1 Main parameters of test rig and flexure pivot bearings

Parameter	Value	Unit
Rotor mass, M	0.825	kg
Rotor diameter, D_j	28.55 ± 0.001	mm
Bearing axial length, L	33.2	mm
Pads number and arc length	4 (72 deg)	
Pad pivot offset	60%	
Nominal preload	0.3	
Pad mass, m_p	10.85	g
Pad mass moment of inertia, I_p	0.253	g mm^2
Web rotational stiffness, $K_{\delta\delta}$	20	N m/rad
Number of feed orifices	4	
Feed orifice diameter	0.62	mm

Baseline Rotor Response. Figure 4(*a*) depicts the recorded

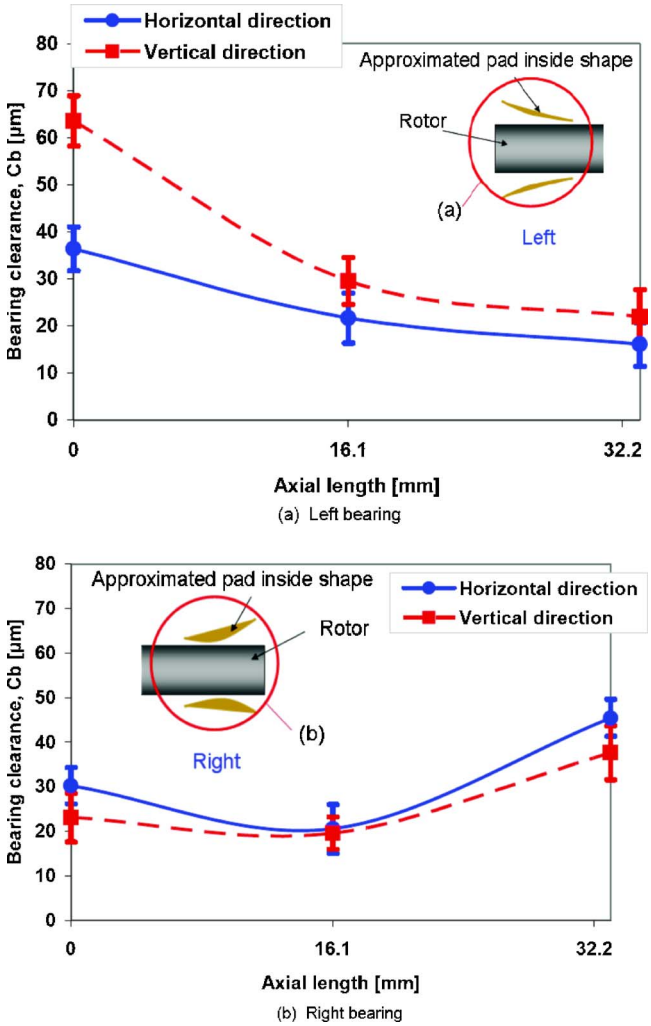

Fig. 3 Estimated radial clearances and axial shape of pads in test bearings

Table 2 Imbalance mass magnitudes and locations (uncertainty in mass is ±0.002 g and displacement (u) ±0.029 μm)

Imbalance name	Mass m_i (g)	Displacement u (μm)	Location
$U(A_1)$	0.030	0.44	In phase 0 deg
$U(A_2)$	0.034	0.49	
$U(A_3)$	0.040	0.58	
$U(B_1)$	0.030	0.44	Out of phase 180 deg
$U(B_2)$	0.034	0.49	
$U(B_3)$	0.040	0.58	

synchronous amplitudes (0-peak) of rotor motion obtained at 5.08 bar absolute feed pressure for the LOP condition with slow roll compensation at 4000 rpm. This response is termed as baseline since it does not include any added imbalance masses. The graph shows the amplitudes recorded on the outer sides of the left and right bearings, and along the horizontal and vertical directions for each bearing. The response for each bearing shows a distinctive single peak at a particular rotor speed. The speeds at which the amplitude peaks along the left vertical (LV), left horizontal (LH), right vertical (RV), and right horizontal (RH) directions are 16,700 rpm, 13,700 rpm, 20,400 rpm, and 20,000 rpm, respectively. The multitude of peaks reveals the different dynamic force characteristics from each bearing and also evidences a compli-

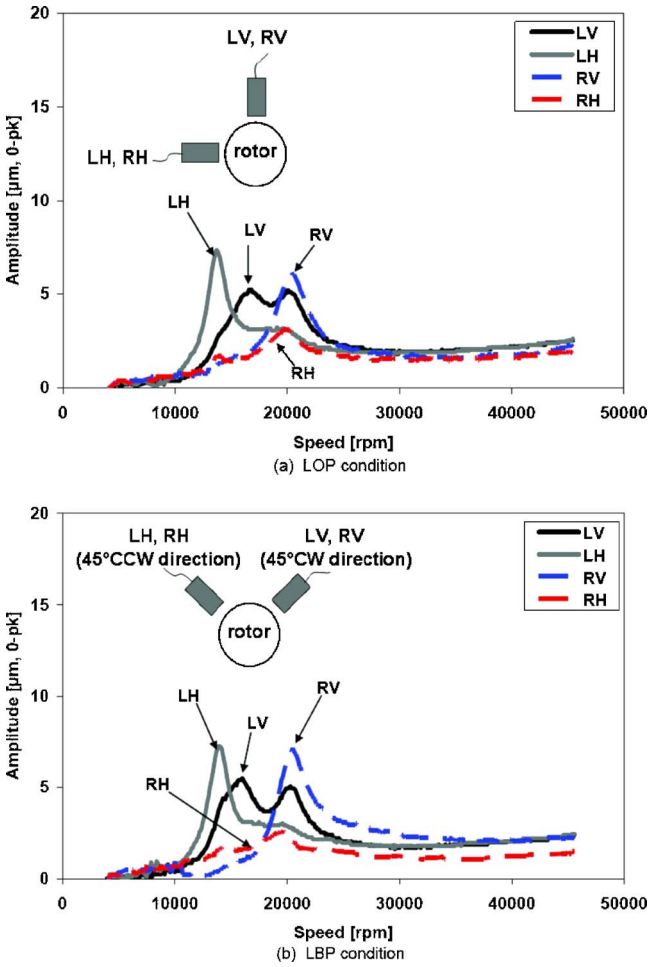

Fig. 4 Amplitudes of rotor synchronous response versus speed. Baseline imbalance. 5.08 bar feed pressure. Test setup for static experiments. Side view.

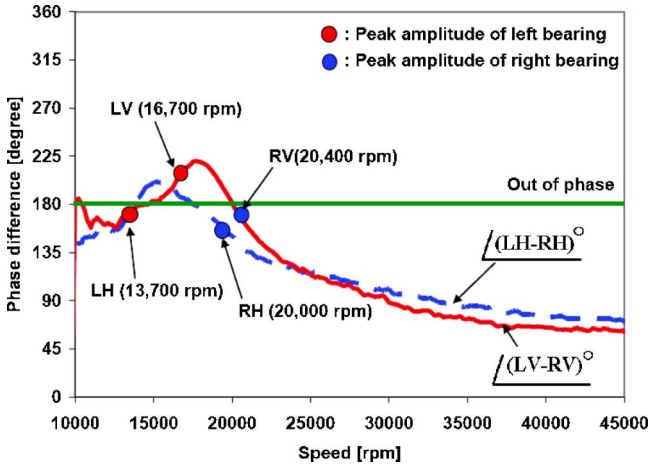

Fig. 5 Phase difference (left/right) of recorded imbalance responses versus speed. Baseline imbalance, LOP configuration, 5.08 bar feed pressure.

cated remnant imbalance distribution. Recall that the clearance on the left bearing (LB) is larger than that of the right bearing (RB), and hence the LB support stiffness must be lower than that of the RB, which explains the lower speed at which the rotor amplitude peaks. Furthermore, also recall that the clearances along the vertical and horizontal directions are different for each worn bearing.

The rotor is *rigid* within the speed range; thus, the shape of the synchronous responses can be readily determined by subtracting the phase angles of the measured displacements at the left and right sides of the rotor. Operation with near 0 deg phase difference indicates a cylindrical mode, while a phase difference of 180 deg denotes a conical mode. Figure 5 depicts a phase difference of ~180 deg while traversing the speeds with largest amplitudes, and then decreasing steadily toward 45 deg at the top speed, 45 krpm. Figure 6 displays the ratio of amplitudes recorded at the left and right ends of the rotor along the vertical and horizontal planes, respectively. This ratio aids to determine the relative size of the end displacements, and along with the phase angle information, it conveys the rotor mode shape, conical or cylindrical, as shown in the graphical insets in Fig. 6. Note that a conical mode is prevalent while traversing the critical speeds of the rotor-bearing system. At the lowest critical speed, 13.7 krpm, the rotor motions are largest along the horizontal plane at the left bearing.

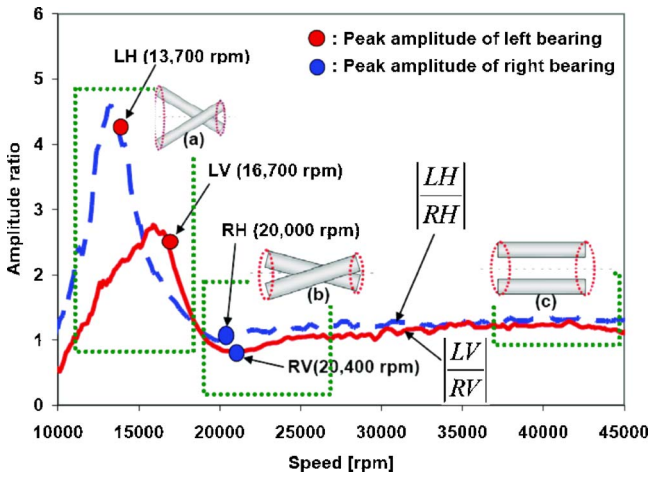

Fig. 6 Amplitude ratio (left/right) of recorded imbalance responses versus speed. Baseline imbalance, LOP configuration, 5.08 bar feed pressure.

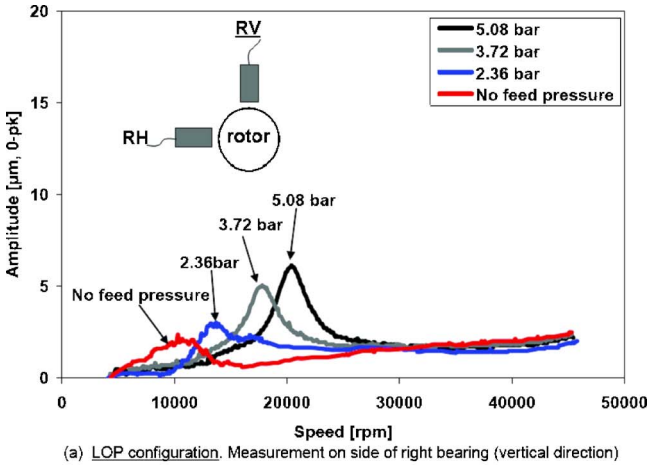

(a) LOP configuration. Measurement on side of right bearing (vertical direction)

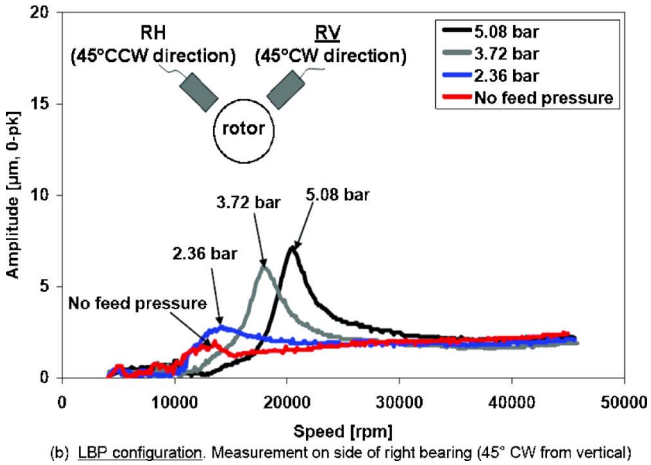

(b) LBP configuration. Measurement on side of right bearing (45° CW from vertical)

Fig. 7 Effect of increasing supply pressure on test rotor synchronous response. Baseline imbalance.

At the critical speed of 20 krpm, the node in the conical mode moves from the right side of the rotor toward the rotor center, and both amplitudes of motion are nearly identical. At higher speeds, say, 45 krpm, the phase difference and amplitude ratio (~1) denote operation closely resembling a cylindrical mode.

For the LBP configuration, Fig. 4(*b*) depicts the recorded synchronous amplitudes (0-peak) of rotor motion obtained at 5.08 bar absolute feed pressure. The graph shows the amplitudes recorded on the outer sides of the left and right bearings, and note that the (LV, RV) and (LH, RH) displacement sensors are located 45°CW and 45°CCW from the vertical plane, respectively. As with the LOP condition, the response for each bearing shows a distinctive single peak at a particular rotor speed. The speeds at which the amplitude peaks along the LV, LH, RV, and RH directions are 16,000 rpm, 14,000 rpm, 20,500 rpm and 19,700 rpm, respectively. These speeds are nearly identical to the LOP measured results and demonstrate that the rotor (light) weight acting on LOP or LBP has little effect on the dynamic forced performance of the test bearings. Note that the rotor responses with external pressurization (feed pressure >2 bars) for the LOP and LBP conditions are stable without any subsynchronous vibration, thus demonstrating the test bearings have insignificant cross-coupled stiffness.

Figures 7(*a*) and 7(*b*) depict the amplitudes (0-peak) of rotor synchronous motion for increasing feed pressures. The test results correspond to the baseline imbalance condition and the LOP and LBP configurations, respectively. The graphs show rotor responses for supply pressure into the bearings equal to 5.08 bars, 3.72 bars, and 2.36 bars (absolute) and no external pressurization. There is little difference in response amplitude for the two load configurations. As the supply pressure increases, the gas bearing direct stiffnesses increase, thus the rotor-bearing system critical speed also increases. However, the system damping ratio decreases; hence, larger peak amplitudes of motion are evident as the supply pressure increases. Reference [12] also reports similar observations. The shaft (critical) speeds at which the rotor motion peaks correspond to the second conical mode with largest amplitudes on the left end of the rotor, see Fig. 6. Note that the critical speed without external pressurization is ~10 krpm, while for the largest feed pressure (5 bars), the critical speed is ~22 krpm. The 10+ krpm difference offers an opportunity to operate the system with controlled external pressurization to avoid entirely the passage through a critical speed, as shown later.

For the test system operating with pristine bearings (LOP), Ref. [12] records conical mode critical speeds at 10.8 krpm, 13.2 krpm, and 15.0 krpm and damping ratios ~0.111, 0.080, and 0.080, for supply pressures of 2.36 bars, 3.72 bars, and 5.08 bars, respectively. The critical speeds of the current rotor-worn bearing system are 9.8 krpm, 12.2 krpm, and 13.7 krpm for similar feed pressures, with corresponding damping ratios equal to 0.133, 0.117, and 0.055. The current first critical speeds are ~10% lower than those in Ref. [12] while the damping ratios are just slightly higher. The drop in critical speed and slight increase in modal damping are due to the enlarger bearing clearances, 20–60 μm [16], as compared to ~40 μm for the original bearings [12].

Coast-Down Rotor Speed and Type of Drag. Figures 8(*a*) and 8(*b*) depict the rotor coast-down speed curves versus time for increasing gas feed pressures and for the LOP and LBP configurations, respectively. The time for the rotor to coast down is quite large, over 2 min, as long as the gas bearings are pressurized. That is, external pressurization ensures a low drag friction operation over the entire speed range. For the highest supply pressures, 3.72 bars and 5.08 bars, there are little differences in the recorded speeds for the LOP and LBP configurations. The rotor coast-down curves show a decaying exponential shape, typical of a rotational system with viscous drag. Note that for feed pressure of 2.36 bars, the rotor-bearing with LOP bearings decelerates faster than for the LBP configuration. Most notably, however, is the rapid rotor deceleration when the gas bearings are not pressurized, in particular, for the LBP configuration. For speeds below 15 krpm, the rotor versus time relationship is linear, typical of dry friction (rubbing condition).

Rotor Responses With Added Imbalance Masses. Table 2 lists the conditions for each test with increasing mass imbalances, in or out of phase locations. For imbalance condition $U(B_2)$, u =0.49 μm, Fig. 9 depicts the recorded synchronous (0-peak) amplitudes of rotor motion obtained at a 5.08 bar absolute feed pressure for the LOP configuration with slow roll compensation at 4000 rpm. The graph shows the amplitudes recorded on the outer board of the left and right bearings, and along the horizontal and vertical directions for each bearing. As with the baseline measurements, the response for each bearing shows a distinctive single peak at a particular rotor speed. The speeds at which the amplitude peaks along the LV, LH, RV, and RH directions are 16,900 rpm, 13,800 rpm, 21,200 rpm, and 22,900 rpm, respectively. The largest amplitude of motion is 16.5 μm (RV), approaching the minimum estimated bearing radial clearance (~20 μm).

Control of Supply Pressure to Eliminate Passage Through a Critical Speed. The imbalance responses acquired for increasing supply pressures suggest the prospect of operating the rotor without actually exciting a critical speed, i.e., without large amplitudes of motion. To this end, experiments are conducted where, as the rotor speed decelerates from its top speed of 45 krpm, the supply pressure is steadily increased from 1.7 bars to 5 bars over a narrow coast-down speed range (15–10 krpm), as shown in Fig. 10. Figure 11 depicts the synchronous amplitude (0-peak) of rotor

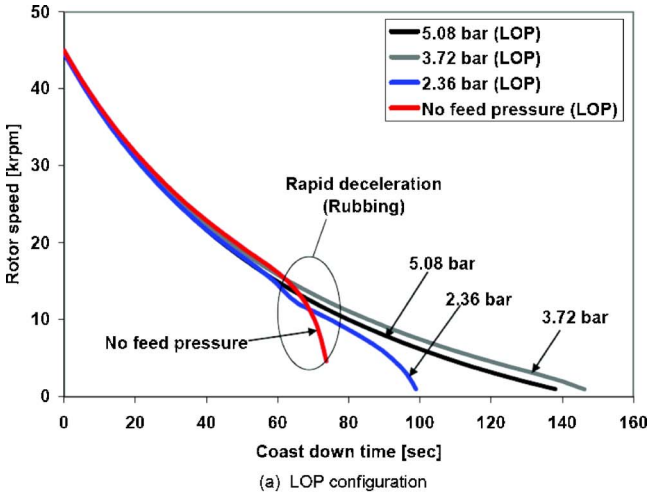

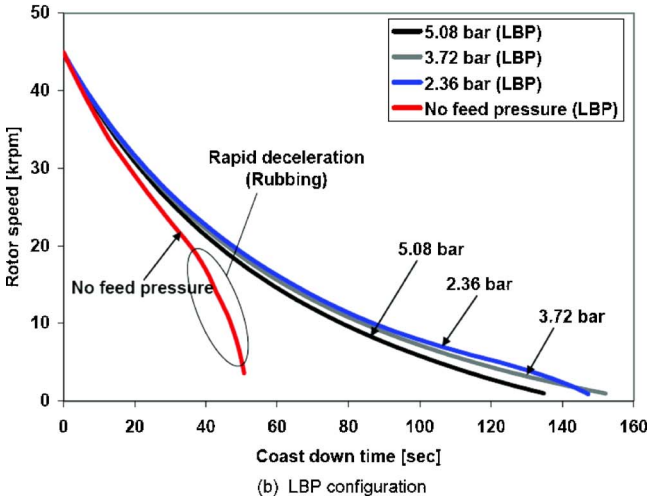

Fig. 8 Effect of supply pressure on time extent for coast-down rotor response. Baseline imbalance.

motion versus shaft speed with controlled supply pressure into the bearings. The broken lines show the responses, also depicted in Fig. 7(*a*), for supply pressures kept constant over the entire speed range. The measurements demonstrate the elimination of the

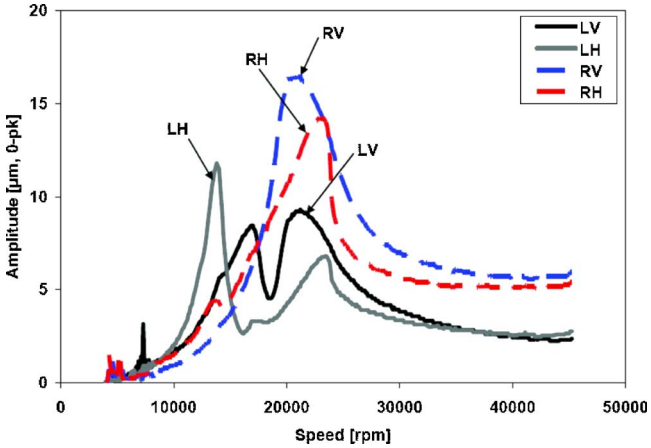

Fig. 9 Amplitudes of rotor synchronous response versus speed. Imbalance displacement $U(B_2)$: 0.49 μm (out of phase), LOP configuration, 5.08 bar feed pressure.

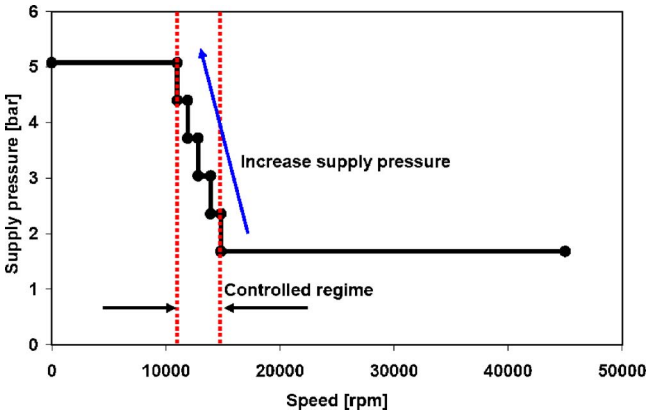

Fig. 10 Manual changes in supply pressure as rotor speed coasted down

speed region where the amplitudes peak, i.e., no excitation of a critical speed. Note the remarkable reduction on amplitude of motion in the speed range from 20 krpm to 12 krpm.

The measurements evidence the benefits of a controlled operation of the rotor-bearing system. In practice, external pressurization is only needed at low rotor speeds to ensure rotor lift-off as well as to increase the system critical speed. At high speeds, external pressurization can be brought to a minimum, without affecting the dynamic response of the system. Note that the rotor response measurements were conducted under quasistatic conditions. The results presented do not actually represent a true coast-down speed response. The change from high to low feed pressure versus rotor speed must be automated with due attendance to the time needed to eliminate a critical speed while the rotor accelerates or decelerates.

Prediction of Rotordynamic Response and Comparison to Test Results

A computational analysis program given in Ref. [18] predicts the static and the dynamic forced response of fixed or tilting pad gas bearings (hydrostatic, hydrodynamic, or both). Table 1 presents the bearing dimensions and Table 3 below details the representative radial clearances and preload for the test bearings. The

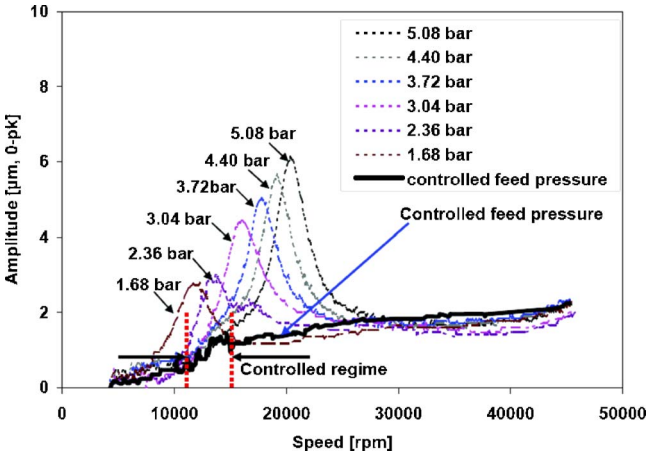

Fig. 11 Amplitudes of rotor synchronous response versus speed for controlled feed pressures. LOP configuration, baseline imbalance. Measurements at right bearing side, vertical direction (RV).

Table 3 Representative clearances and preload for prediction of force coefficients for worn test bearings

Bearing	Radial clearance $C=R_p-R_j$ (μm)	Pad preload (0.30) (μm)
Right	38.0	11.4
Left	44.5	13.3

magnitudes noted are representative only since the clearances for both worn bearings vary along the axial and circumferential directions.

Mass flow rate measurements into each bearing are conducted with calibrated turbine flow meters, uncertainty of 0.001 g/s. Figure 12 depicts the predicted and measured mass flow rate for increasing feed pressures. The mass flow rate into the left bearing is larger than that of the right bearing because of its larger clearance. The predictions agree well with the measurements, thus lending credence to the inherent orifice flow model in the analysis. Note that a reduced flow rate denotes also a reduction in the gas film pressure acting on the bearing at the orifice location. This reduction in pressure will cause (in general) a drop in bearing direct stiffnesses.

Appendix includes the predicted (synchronous speed) rotordynamic force coefficients for the gas bearings (left and right) for two supply pressures, and LOP and LBP configurations. Figure 13 shows the 24 finite element structural model of the composite test rotor. The predicted first and second free-free natural frequencies are 1.95 kHz and 6.13 kHz, in good agreement with measured values of 1.92 kHz and 6.12 kHz (uncertainty in measurements: $\pm$16 Hz). Predicted free-free mode shapes also agree very well with the measurements, see Ref. [16]. The test data thus validate the rotor structural model. Furthermore, the measurements of free-free mode shapes show the rotor can be regarded as rigid over the speed range of tests ($<$50 krpm).

Damped Natural Frequencies and Damping Ratios. The eigenvalue analysis of the rotor-bearing system renders the natural frequencies and modal damping ratios, depicted in Figs. 14 and 15, respectively. The critical speeds are 16.2 krpm and 20.1 krpm, and correspond with conical rigid body modes. The predicted conical modes reproduce closely the recorded mode shapes, as depicted in the graphical insets on Fig. 6. The appearance of the two conical modes is a direct consequence of the difference in force coefficients for the left and right bearings. Note that critical

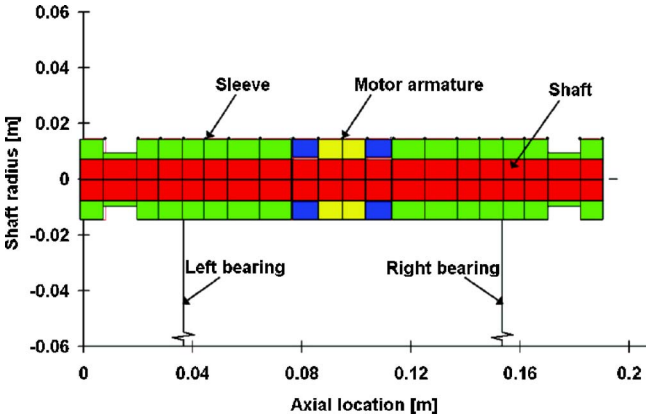

Fig. 13 Structural model of test rotor

speeds and damping ratios are identical for the LOP and LBP configurations, since the bearing force coefficients for both configurations are nearly identical, except for pure hydrodynamic operation. The static load acting on each bearing is rather small, and hence the rotor operates at a nearly centered condition, in particular, at high speeds.

Comparison Between Predictions and Measured Imbalance Responses. Figure 16 depicts the measured and predicted amplitudes (0-peak) of synchronous response at the left bearing (verti-

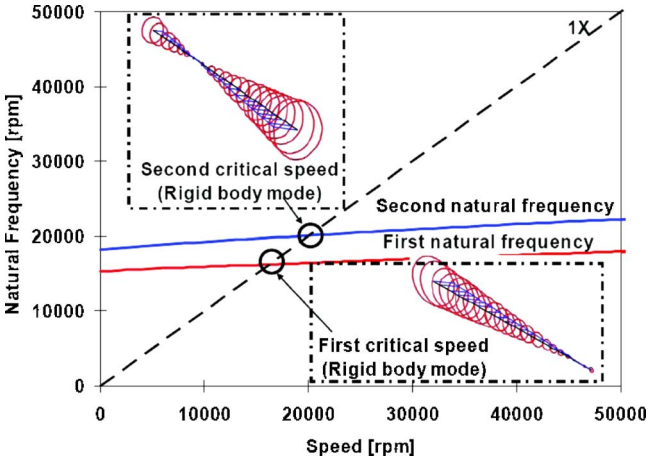

Fig. 14 Damped natural frequency map of test rotor-bearing system. 5.08 bar feed pressure. LOP configuration.

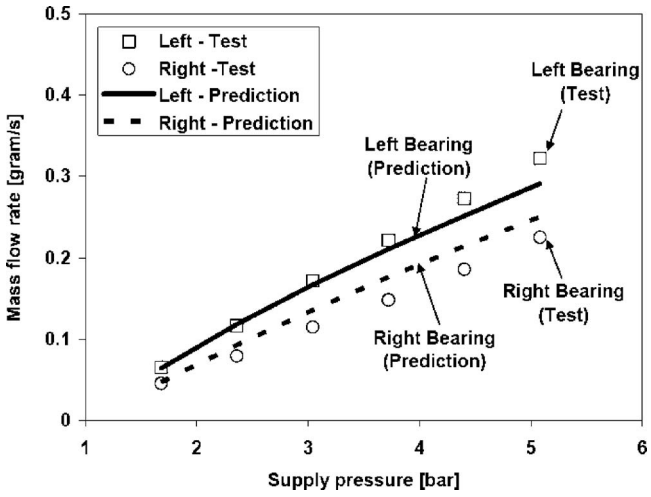

Fig. 12 Measured and predicted mass flow rates versus supply pressure for test bearings. LOP configuration.

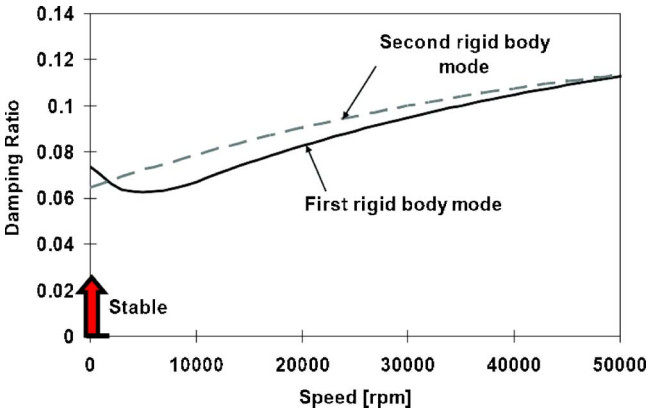

Fig. 15 Predicted damping ratios for rotor-bearing system versus rotor speed. 5.08 bar feed pressure. LOP configuration.

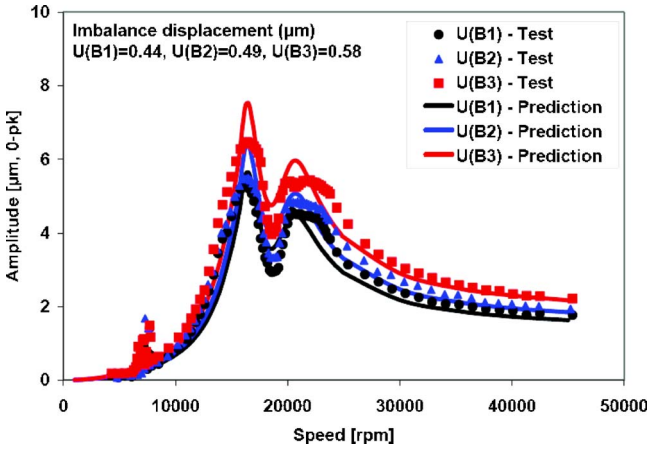

Fig. 16 Predicted and measured imbalance response for three mass imbalance conditions. Tests at 5.08 bar feed pressure. LOP configuration. Displacements at left bearing, vertical direction (LV). Baseline response subtracted.

cal direction) for the out of phase imbalance conditions, $U(B_{1,2,3})$. The baseline condition is subtracted from the measured imbalance response to estimate the response due to the imbalance mass added. Note that this consideration is only valid in linear systems. The predictions show a remarkable agreement in the location of the critical speeds and the peak amplitudes of motion.

The linearity of the test rotor-bearing system response is verified by normalizing the amplitudes of motion, as shown in Fig. 17. The graph depicts the responses obtained for imbalance masses $U(B_{x=2,3})$ multiplied by the ratio of added masses $U(B_{x=2,3})/U(B_1)$. The three measured results show nearly identical curves, thus denoting the rotor response amplitude of motion is proportional to the mass imbalance. Note that the rotor-gas bearing linearity in response is most unusual considering the large amplitudes of motion recorded (40% of bearing clearance), in particular, for the largest imbalance $U(B_3)$.

Conclusions

Experiments on a test rotor, 0.825 kg and 28.6 mm diameter, supported on flexure pivot tilting pad hybrid gas bearings are performed for various mass imbalances, increasing feed gas pressures, and under LOP and LBP configurations. From prior testing [12], the gas bearings show sustained wear with uneven pad shapes and dissimilar clearances along the axial and circumferential directions. The changes in clearances affect the static and dynamic force performance characteristics of the rotor-bearing system. In coast-down rotor responses with initial speed at 50 krpm, the rotor traverses critical speeds corresponding to rigid body modes, conical and cylindrical conical. There are no noticeable differences in rotor response for the LOP and LBP configurations due to the light-weight rotor; i.e., low static load acting on each bearing. External pressurization into the bearings increases their direct stiffnesses and reduces their damping, while raising the system critical speed and lessening the viscous damping ratio. Extended times, over 2 min, for rotor coast downs with the bearings pressurized demonstrate the little drag typical of gas bearings. Manual rotor deceleration tests with changes in external pressurization are conducted to eliminate passage through a critical speed where the rotor motion peaks. This important demonstration paves a way to operate oil-free turbomachinery with controlled external pressurization at high speeds and avoiding the excitation of system critical speeds.

A computational program for modeling of flexure pivot tilting pad hybrid gas bearings predicts the rotordynamic coefficients of the test bearings. A finite element structural model for the test rotor shows free-free mode elastic modes and natural frequencies matching well the measurements. The model links synchronous bearing force coefficients to predict the imbalance response of the test rotor-bearing system. Predicted mass flow rates are in good agreement with measurements. With external pressurization (pressure supply >2 bars), predicted bearing force coefficients are nearly identical for both LOP and LBP configurations within the test speed range (<50 krpm) since the static load acting on each bearing is rather low. Force coefficients for the condition without external pressure (hydrodynamic case) differ considerably from those with external pressurization and between the LOP and LBP configurations. Predicted critical speeds and peak amplitudes of synchronous rotor motion agree well with the measurements. The synchronous rotor response for increasing imbalance masses verifies the test rotor-bearing system's linearity for in phase and out of phase imbalance conditions.

The measurements demonstrate the superior stability and dynamic forced performance of the test flexure pivot tilting pad bearings over other bearing configurations experimented with earlier, namely, three-lobe bearings [4] and Rayleigh-step bearings [13], and further validate the computational model. The experimental results further show the reliable performance of the gas bearings even when operating with worn pad surfaces, i.e., enlarged and uneven clearances. The test results thus enable the engineered design and implementation of this type of gas bearing into high performance micro-turbomachinery.

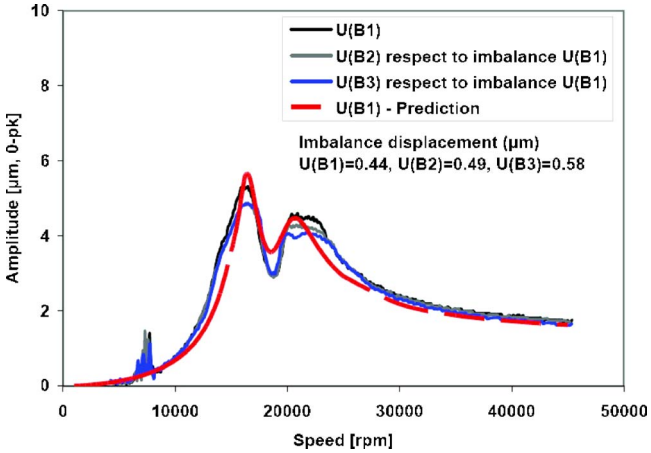

Fig. 17 Predicted and measured normalized imbalance responses. Tests at 5.08 bar feed pressure. LOP configuration. Displacements at left bearing, vertical direction (LV). Baseline response subtracted.

Acknowledgment

The continued support of the TAMU Turbomachinery Research Consortium is gratefully acknowledged.

Nomenclature

C = bearing radial clearance (m)
$C_{i,j}$ = bearing damping coefficients; $i,j=X,Y$ (N s/m)
D_j = rotor diameter (m)
e = journal eccentricity (m)
I_p = pad mass moment of inertia (kg m^2)
K_i = bearing stiffness coefficients, $i,j=X,Y$ (N/m)
$K_{\delta\delta}$ = flexure web rotational stiffness (N m/rad)
L = bearing axial length (mm)
m_i = calibrated imbalance mass (g)
m_p = pad mass (kg)
M = rotor mass (kg)
N = rotor speed (rev/min)
R_p = pad radius (m)

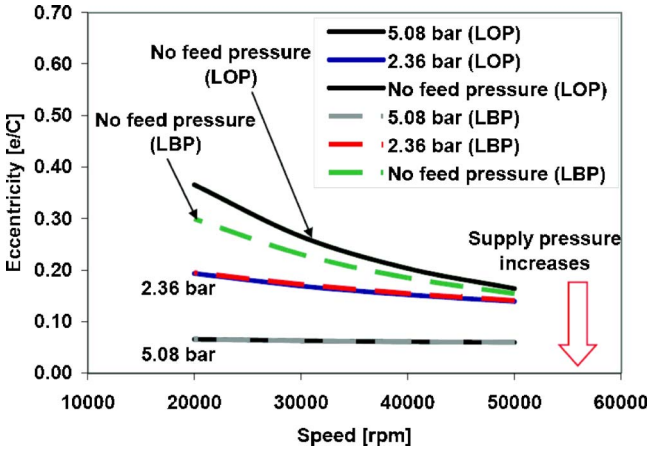

Fig. 18 Predicted static journal eccentricity (e/C) for increasing feed pressures. Right bearing, LOP and LBP configurations.

R_j = rotor radius (m)
R' = radial location of imbalance mass (m)
u = mass imbalance displacement (m), $u=m_iR'/(m_i+M)$
W = rotor weight (1b)
X, Y = inertial coordinate system
Ω = rotor speed (rad/s)

Appendix: Predicted Bearing Stiffness and Damping Force Coefficients

Figures 18 and 19 depict the predicted LOP and LBP journal eccentricities and attitude angles of the right bearing versus rotor speed for increasing feed pressures. The applied static load on each bearing is 4.04 N, i.e., half the rotor weight. Note that the maximum dimensionless eccentricity is 0.70 for the pure hydrodynamic condition and lowest shaft speed, 10 krpm. Hydrostatic pressurization leads to smaller journal eccentricities, nearly independent of rotor speed; importantly enough, without significant differentiation between the LOP and LBP configurations. The attitude angle is largest for the no feed pressure condition, though

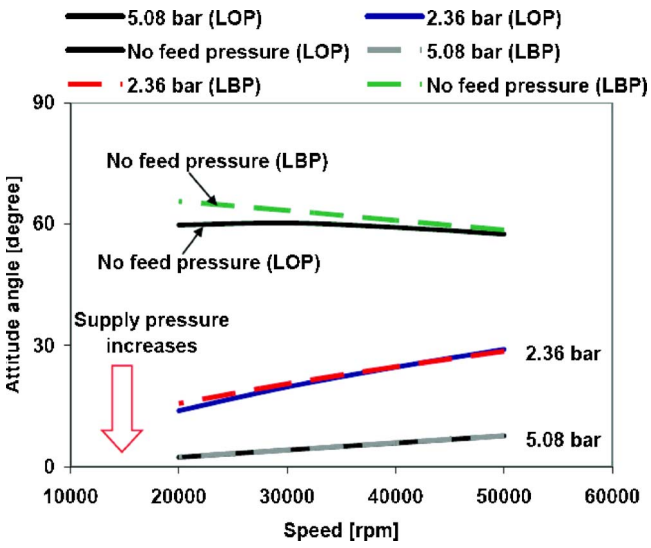

Fig. 19 Predicted attitude angle for increasing feed pressures. Right bearing, LOP and LBP configurations.

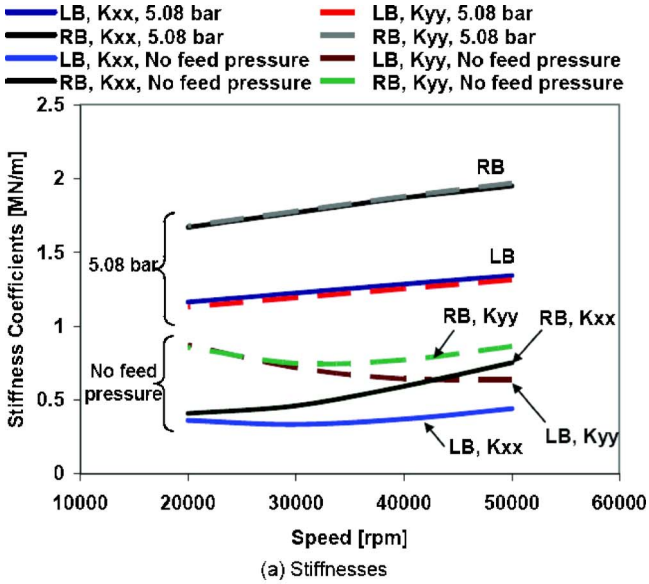

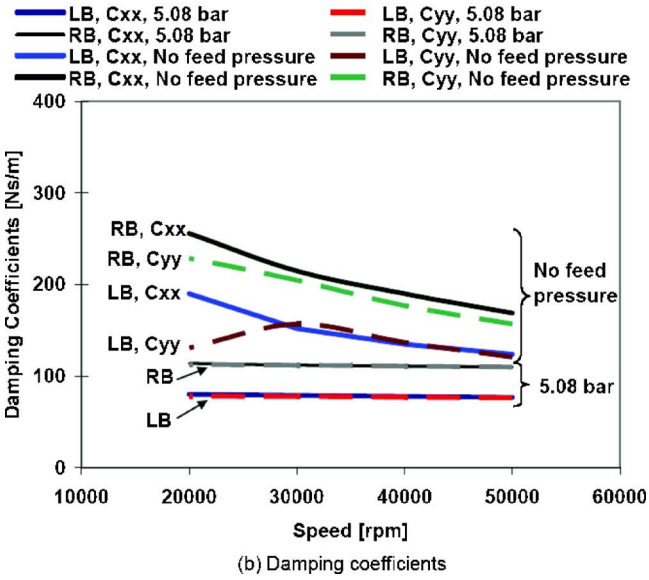

Fig. 20 Predicted synchronous direct bearing force coefficients versus speed. LB and RB. LOP configuration. 5.08 bars (absolute) and no feed pressure.

nearly invariant with shaft speed. The bearings without pressurization perform more like a rigid pad bearing rather than true tilting pad bearings.

Figures 20(a) and 20(b) show the direct stiffness and damping coefficients for the LOP configuration and for two supply pressure conditions. A higher supply pressure renders larger direct stiffnesses. The LB, having larger clearance, shows smaller direct force coefficients than the RB. Note that the force coefficients along the static load direction (X) are similar to those along (Y), i.e., $K_{XX}=K_{YY}$, for the conditions with external feed pressure (5.08 bars). However, $K_{YY}>K_{XX}$ for the hydrodynamic case, i.e., without feed pressure. As the supply pressure increases, the direct damping coefficients decrease.

For supply pressures equal to 5.08 bars, 3.72 bars, and 2.36 bars, the force coefficients for the LOP and LBP configurations are nearly identical within the test speed range (<50 krpm). On the other hand, the no feed pressure condition renders appreciably different stiffness and damping coefficients for both LOP and LBP configurations. Figures 21(a) and 21(b)

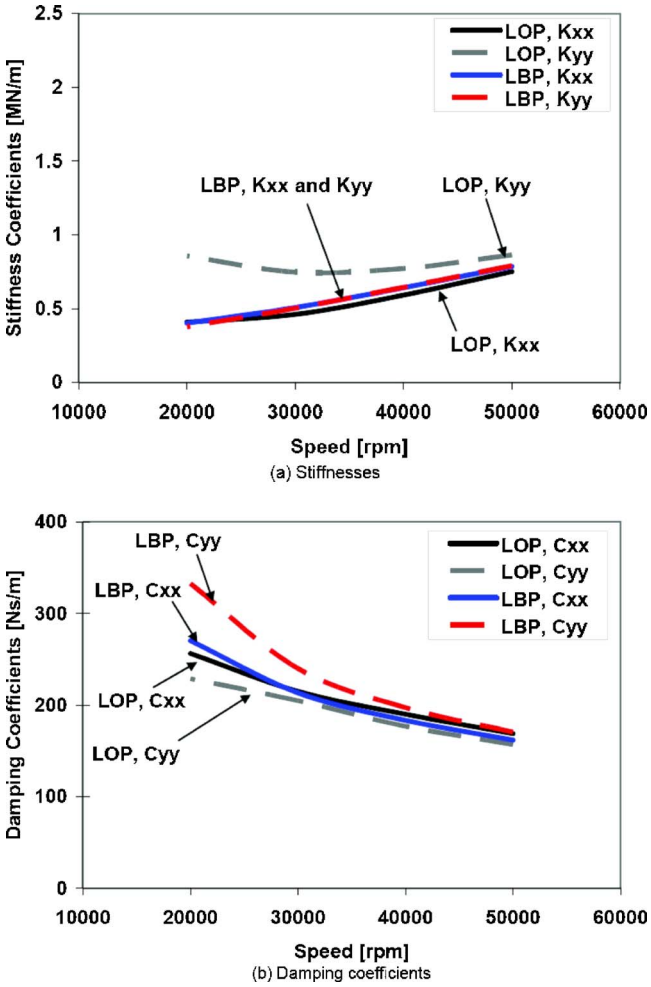

Fig. 21 Comparison of direct bearing force coefficients for LOP and LBP configurations. Right bearing without feed pressure. Synchronous speed coefficients.

compare the direct stiffness and damping coefficients for both LOP and LBP configurations. Significant differences are apparent at the lower rotor speeds where the static journal eccentricities are largest. Note that the LBP K_{XX} and K_{YY} are almost the same denoting stiffness symmetry. The direct stiffness for the LBP configuration is close to the loading direction's stiffness (K_{XX}) of the LOP case. The LBP configuration also offers a little larger damping than the LOP configuration.

References

[1] Ohkubo, Y., 2005, "Outlook on Gas Turbine," R&D Rev Toyota CRDL, **41**, pp. 1–11.

[2] Hamrock, B. J., 1994, *Fundamentals of Fluid Film Lubrication*, McGraw-Hill, New York.

[3] Powell, J. W., 1970, "A Review of Progress in Gas Lubrication," Rev. Phys. Tech., **1**, pp. 96–129.

[4] Wilde, D. A., and San Andrés, L., 2006, "Experimental Response of Simple Gas Hybrid Bearings for Oil-Free Turbomachinery," ASME J. Eng. Gas Turbines Power, **128**, pp. 626–633.

[5] Tanaka, S., Isomura, K., Togo, S., and Esashi, M., 2004, "Turbo Test Rig With Hydroinertia Air Bearings for a Palmtop Gas Turbine," J. Micromech. Microeng., **14**, pp. 1449–1454.

[6] Childs, D., 1993, *Turbomachinery Rotordynamics: Phenomena, Modeling, and Analysis*, Wiley, New York.

[7] Zeidan, F., 1992, "Developments in Fluid Film Bearing Technology," Turbomach. Int., **9**, pp. 24–31.

[8] Armentrout, R. W., and Paquette, D. J., 1993, "Rotordynamic Characteristics of Flexure-Pivot Tilting-Pad Journal Bearings," STLE Tribol. Trans., **36**, pp. 443–451.

[9] Choudhury, P. D., Raumond, H. M., and Paquette, D. J., 1992, "A Flexible Pad Bearing Systems for a High Speed Centrifugal Compressor," *Proceedings of the 21st Turbomachinery Symposium*, Houston, TX, pp. 57–64.

[10] Chen, W. J., Zeidan, F. Y., and Jain, D., 1994, "Design, Analysis, and Testing of High Performance Bearings in a High Speed Integrally Geared Compressor," *Proceedings of the 23rd Turbomachinery Symposium*, Houston, TX, pp. 24–31.

[11] Kepple, K. E., Agahi, R., Ershagih, B., and Zeidan, F. Y., 1998, "Experience in the Use of Flexure Pivot Tilt Pad Bearings in Boiler Feedwater Pumps," *Proceedings of the 15th International Pump Users Symposium*, Houston, TX, pp. 77–83.

[12] Zhu, X., and San Andrés, L., 2007, "Rotordynamic Performance of Flexure Pivot Hydrostatic Gas Bearings for Oil-Free Turbomachinery," ASME J. Eng. Gas Turbines Power, **129**, pp. 1020–1027.

[13] Zhu, X., and San Andrés, L., 2005, "Experimental Response of a Rotor Supported on Rayleigh Step Gas Bearings," ASME Paper No. GT 2005–68296.

[14] Kim, T. H., and San Andrés, L., 2005, "Heavily Loaded Gas Foil Bearings: AModel Anchored to Test Data," ASME Paper No. GT 2005–68486; ASME J. Eng. Gas Turbines Power, to be published.

[15] San Andrés, L., Rubio, D., and Kim, T. H., 2007, "Rotordynamic Performance of a Rotor Supported on Bump Type Foil Gas Bearings: Experiments and Predictions," ASME J. Eng. Gas Turbines Power, **129**, 850–857.

[16] San Andrés, L., and Ryu, K., 2006, "Test Results for Load-On-Pad and Load-Between-Pad Hybrid Flexure Pivot Tilting Pad Gas Bearings," Turbomachinery Laboratory Research Report No. TL-B&C-1–06.

[17] Lymberopoulos, N., 2004, "Microturbines and Their Application in Bio-Energy," European Commission DG-TREN Contract Report No. NNE5-PTA-2002–003/1.

[18] San Andrés, L., 2006, "Hybrid Flexure Pivot-Tilting Pad Gas Bearings: Analysis and Experimental Validation," ASME J. Tribol., **128**, pp. 551–558.

Probabilistic Engine Performance Scatter and Deterioration Modeling

Stefan Spieler
e-mail: stefan.spieler@ila.uni-stuttgart.de

Stephan Staudacher

Institute of Aircraft Propulsion Systems,
Stuttgart University,
Pfaffenwaldring 6,
70569 Stuttgart, Germany

Roland Fiola

Peter Sahm

Matthias Weißschuh

Rolls-Royce Deutschland Ltd & Co KG,
Eschenweg 11,
15827 Blankenfelde-Mahlow, Germany

The change of performance parameters over time due to engine deterioration and production scatter plays an important role to ensure safe and economical engine operation. A tool has been developed which is able to model production scatter and engine deterioration on the basis of elementary changes of numerous construction features. In order to consider the characteristics of an engine fleet as well as random environmental influences, a probabilistic approach using Monte Carlo simulation (MCS) was chosen. To quantify the impact of feature deviations on performance relevant metrics, nonlinear sensitivity functions are used to obtain scalars and offsets on turbomachinery maps, which reflect module behavior during operation. Probability density functions (PDFs) of user-defined performance parameters of an engine fleet are then calculated by performing a MCS in a performance synthesis program. For the validation of the developed methodology pass-off test data, endurance engine test data, as well as data from engine maintenance, incoming tests have been used. For this purpose, measured engine fleet performance data have been corrected by statistically eliminating the influence of measuring errors. The validation process showed the model's ability to predict more than 90% of the measured performance variance. Furthermore, predicted performance trends correspond well to performance data from engines in operation. Two model enhancements are presented, the first of which is intended for maintenance cost prediction. It is able to generate PDFs of failure times for different features. The second enhancement correlates feature change and operating conditions and thus connects airline operation and maintenance costs. Subsequently, it is shown that the model developed is a powerful tool to assist in aircraft engine design and production processes, thanks to its ability to identify and quantitatively assess main drivers for performance variance and trends. [DOI: 10.1115/1.2800351]

Keywords: performance deterioration, production scatter, probabilistic modeling, Monte Carlo Simulation

Introduction

The change of performance parameters over time due to engine deterioration and production scatter plays an important role to ensure safe and economical engine operation. Therefore, each engine is tested after production and monitored during operation to ensure that selected performance parameters are within given limits. Since essential design parameters are fixed at an early product development stage, the development of a tool which is able to model performance variance as well as trends of engine performance parameters at this stage is of crucial importance.

Since both production scatter and feature changes due to deterioration mean a change in elementary construction features from their nominal value, the development of a feature-based method suggests itself. For the development of the model, it was assumed that performance variance is primarily a result of production scatter as well as assembly variance and measuring errors, whereas performance trends result from the abrupt and random or continuous change of single features within the engine.

Feature-Based Performance Modeling

Engine performance synthesis calculation is the core of the feature-based model. Modern performance programs use a number of metrics and maps to describe characteristics both of engine modules and of environmental or operational conditions. Hence, for the modeling of engine production scatter and deterioration, these metrics and maps are used. The modeling is basically done in three steps. First, engine feature changes over time are quantified (e.g., high pressure compressor (HPC) blade surface roughness over time), then, the impact of feature changes on performance metrics and maps is calculated (e.g., HPC efficiency) to finally simulate the impact on global performance parameters (e.g., specific fuel consumption (SFC). In the following, the feature-based modeling method is described.

Impact of Single Feature Changes on Module Performance Parameters

Characteristics of engine modules are based on a number of features of the components it consists of. In order to quantify the features' impact on module parameters, detailed physical and thermodynamic analyses and calculations are required. Therefore, detailed knowledge of engine design and behavior as well as close collaboration with the engine manufacturer's design engineers is required.

The impact of single features on module performance parameters can basically be modeled by using sensitivity parameters (so-called exchange rates) [1]. Sensitivity parameters generally describe a linear connection between two metrics at a defined operating point. In this case, exchange rates describe the correlation between the deviation of a feature from its nominal value and its impact on certain performance parameters. Since linearization

Contributed by the International Gas Turbine Institute of ASME for publication in the JOURNAL OF ENGINEERING FOR GAS TURBINES AND POWER. Manuscript received May 24, 2007; final manuscript received May 29, 2007; published online April 29, 2008. Review conducted by Dilip R. Ballal. Paper presented at the ASME Turbo Expo 2007: Land, Sea and Air (GT2007), Montreal, Quebec, Canada, May 14–17, 2007.

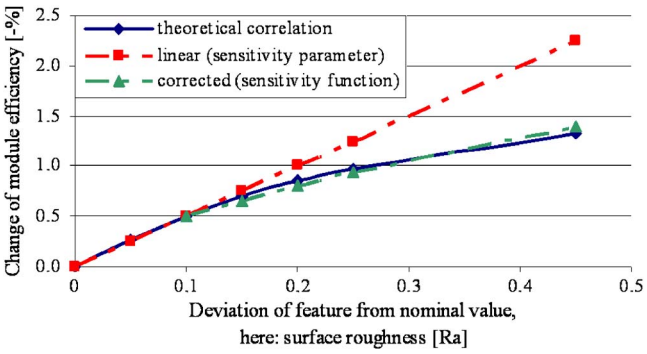

Fig. 1 Exemplary illustration of method of sensitivity parameter correction, impact of surface roughness increase on HPC efficiency (data removed due to confidentiality)

is usually an approximation, a modeling error is made, which increases with growing deviation from the reference point. Thus, the use of sensitivity parameters is only valid within a certain interval.

With expected increasing deviation from a reference point, detailed physical modeling becomes more essential. Production scatter is expected to lead to relatively small deviations from a nominal value, whereas deterioration of certain features during engine operation is expected to lead to significant deviations. Therefore, nonlinear sensitivity functions were introduced and used in the model on hand. Hereby, the constant sensitivity parameters are corrected by a nonlinear correction term. The latter reflects the physical connection between the performance parameter to be modeled and the deviation of a feature from its nominal value. To ensure application for different features with different physical correlations, the relative distance is introduced as the basis for the following correction term:

$$d_{\text{rel}} = \frac{x - x_{\text{nom}}}{x_S - x_{\text{nom}}} \tag{1}$$

It is the quotient of the deviation of a feature from its nominal value and the interval used for calculating the sensitivity parameter. The increasing deviation and error from a linear connection can be approximated by using power functions with one additional parameter. The correction terms are calculated from

$$C = \left(\frac{x - x_{\text{nom}}}{x_S - x_{\text{nom}}} \right)^{\alpha} \tag{2}$$

where α is determined such that a best possible approximation to real correlations is achieved. For less sensitive features, α was estimated by component experts. For the most sensitive features, sound theoretical correlations have been determined. In the following, the method is exemplified with compressor efficiency and its correlation with compressor blade surface roughness (see Fig. 1). In Ref. [2], polytropic efficiency at hydraulic smooth conditions is given as a function of Reynolds number of the first compressor stage.

With increasing Reynolds number, the curve flattens. After achieving the so-called critical Reynolds number which is determined by surface roughness (see Ref. [3]), efficiency no longer depends on Reynolds number—now there are hydrodynamically rough conditions. This way a functional correlation between HPC efficiency and surface roughness can be established.

In Fig. 1, three graphs are shown. A linear correlation based on a sensitivity parameter, a theoretical correlation based on the correlation explained above, and a corrected correlation using Eq. (2). The example presented shows that the introduced correction term significantly reduces calculation errors compared to a linearized calculation. In other words, given an allowed calculation error, calculations with sensitivity parameters can be extended to a significantly larger interval.

Impact of Multiple Feature Changes on Module Performance Parameters. In reality, it has to be supposed that multiple features influence multiple module performance parameters. Assuming linear independency between relevant features, changes of module performance parameters resulting from deviations of different features can simply be summed up. With Eq. (3), the term "sensitivity parameter matrix" is introduced. It mathematically connects multiple performance parameters ΔMod_m with multiple features ΔF_n by using exchange rates:

$$\begin{pmatrix} \Delta\text{Mod}_1 \\ \vdots \\ \Delta\text{Mod}_m \end{pmatrix} = \begin{pmatrix} ex_{\text{Mod}_1,F_1} & \cdots & ex_{\text{Mod}_1,F_n} \\ \vdots & \ddots & \vdots \\ ex_{\text{Mod}_m,F_1} & \cdots & ex_{\text{Mod}_m,F_n} \end{pmatrix} \cdot \begin{pmatrix} \Delta F_1 \\ \vdots \\ \Delta F_n \end{pmatrix} \tag{3}$$

Considering the correction term introduced with Eq. (2), the sensitivity parameter matrix (3) is enhanced to

$$\mathbf{S} = \begin{pmatrix} ex_{\text{Mod}_1,F_1} \cdot C(\Delta F_1) & \cdots & ex_{\text{Mod}_1,F_n} \cdot C(\Delta F_n) \\ \vdots & \ddots & \vdots \\ ex_{\text{Mod}_m,F_1} \cdot C(\Delta F_1) & \cdots & ex_{\text{Mod}_m,F_n} \cdot C(\Delta F_n) \end{pmatrix} \tag{4}$$

Considering that the correction term C generally is a function of multiple features, C becomes

$$C = C(\Delta F_1, \ldots, \Delta F_n) \tag{5}$$

and the sensitivity parameter matrix thus describes an n-dimensional area. In literature, this area is often referred to as response surface model (RSM) or higher-order regression model [4][1].

For the model on hand, it was concluded that a regression model with correction terms according to Eq. (4) will be feasible. The model was applied and adapted to the RR BR700-710 engine. It considers 105 features and calculates their influence on 25 global module and engine performance parameters. Therefore, sensitivity parameters for each feature considered have been calculated [5].

Calculation of Global Engine Performance Parameters. In principle, global engine performance parameters could also be calculated using sensitivity parameters (e.g., $+x\%$ HPC efficiency results in $-y\%$ SFC). However, according to Ref. [6], rematching effects due to a number of cumulated influences can lead to significant calculation errors in engine performance modeling. This was confirmed by analyzing the correlation of turbine exit temperature and HPC efficiency, first calculated using sensitivity parameters, and then calculated using engine performance synthesis software.[2]

Hence, the performance synthesis software SAEPP was used for modeling the BR710 engine. Component maps and a multitude of metrics were provided by the engine manufacturer and the performance synthesis model validated against the engine manufacturer's model.

Engine Fleet Simulation. An engine fleet is simulated by performing a Monte Carlo Simulation (MCS). Hereby, one single calculation simulates one engine out of the fleet by generating random values out of probability density functions (PDFs) (so-called sampling) for each of the 105 features used for modeling. For each randomly generated set of values, 25 module perfor-

[1]Response surface models can be derived by monitoring specific changes (so-called experiments) of input variables. Often used experimental designs are Box–Behnken, Central Composite, or three-level full factorial designs, which differ in approximation quality and number of experiments [4].

[2]Thereby, the square of Pearson's correlation coefficient R^2 was determined to only 0.945 with a deviance of HPC efficiency of 2.5%.

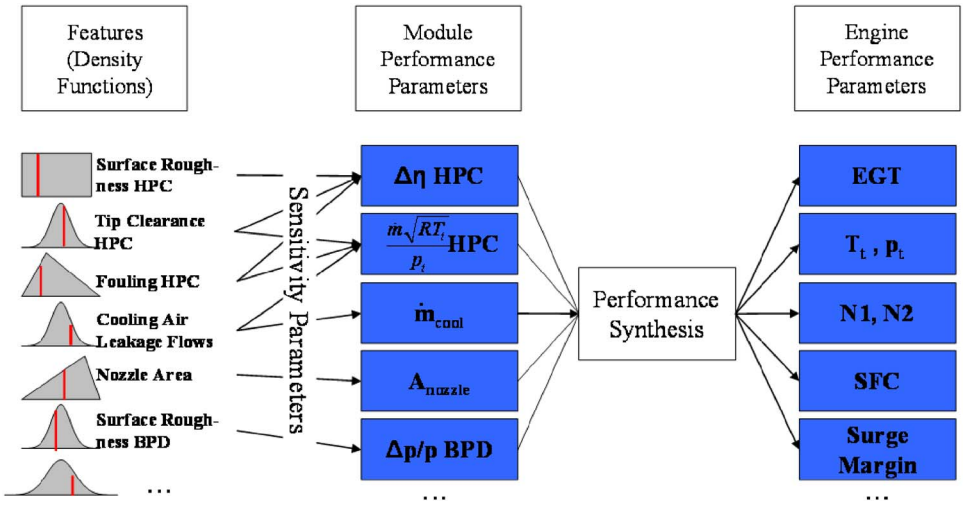

Fig. 2 Schematic illustration of the modeling method

mance parameters are deterministically calculated according to Eq. (4). These in turn are input parameters for the synthesis calculation software SAEPP, which works as a nonlinear black box generating global performance parameters.

By n-fold repetition of these steps, an engine fleet of the size of n randomly produced, assembled, and operated engines is simulated. With a sufficiently high number of repetitions, PDFs (or rather their statistical metrics such as mean, standard deviation, etc.) converge to their true value.

By this means, the impact of production scatter as well as deterioration trend and scatter of a multitude of features on global engine performance parameters is simulated (see Fig. 2).

Engine Production Scatter Modeling

In Fig. 2, a schematic overview of the modeling method is given. It becomes apparent that a statistical description of the features' conditions provides the basis for this methodology.

It is assumed that production scatter and engine deterioration are the main causes for engine performance change and scatter over time. There is a specific database quantifying the condition of the features after production and during operation. Statistical process control (SPC) data are used for simulating the features' condition straight after production or—if not available—their probable condition scatter is derived from comparable features. Here, the commonly used (and therefore available) process capability index Cp allows for realistic assumptions [7]. The index Cp links given tolerance limits (upper specification limit (USL) and lower specification limit (LSL) of a production feature to its real production scatter. For its calculation, it is assumed that production scatter can be described by Gaussian distributions and its characteristic metric standard deviation σ. Cp is calculated as given in Eq. (6) [7].

$$\mathrm{Cp} = \frac{\mathrm{USL} - \mathrm{LSL}}{6\sigma} \tag{6}$$

Cp thus provides a metric evaluating the capability of a manufacturing process to produce a certain feature. For example, a Cp value of 1 means that 99.7% ($\pm 3\sigma$) of the features produced are within the given tolerance limits. Since Cp is a nondimensional metric, it can be used to describe almost any process scatter [8]. Due to its widespread use in production, Cp data are available and the metric Cp is used as direct input parameter in the model on hand. For the application of process capability indices in low batch size industries, such as engine manufacturing, see Ref. [9].

Derivation of Set Mean Scatter on the Basis of Single Feature Scatter. For performance modeling, it is assumed that the mean value of all features of one kind, i.e., features which are nominally the same, installed in an engine represents the performance impact. Hence, for performance scatter modeling, the scatter of the mean value of an assembled feature set—in contrast to single feature scatter—is used to calculate the performance synthesis. Basically, there are two methods to consider set scatter, empirical MCS and analytical calculation. In both cases, the number of components of one kind becomes a relevant number.

In the case of Gaussian distribution for feature scatter, there is a mathematical-statistical connection between single feature and set scatter. Set scatter σ_{set} depends on single feature scatter σ_{part} and the number of parts installed according to Ref. [10]:

$$\sigma_{\mathrm{set}} = \frac{\sigma_{\mathrm{part}}}{\sqrt{n}} \tag{7}$$

Considering Eq. (6), it follows that

$$\mathrm{Cp}_{\mathrm{set}} = \mathrm{Cp}_{\mathrm{part}}\sqrt{n} \tag{8}$$

Basically, set mean scatter is smaller than single feature scatter. Thus, it can be concluded that the higher the number of parts of one kind installed is, the lower the performance scatter is (i.e., negative correlation).

In the case of (empiric) distributions, which cannot be approximated by Gaussian distributions or when considering certain design impacts, an analytical handling is not possible or too complex. Then, MCS is used to approximate any distributions.

Both methods are only valid for randomly generated sets drawn from a basic population. However, in reality, it has to be assumed that single feature characteristics in one set correlate positively, i.e., real sets show more homogeneous characteristics than randomly generated sets. Reasons for that might be batch production[3] or set assembly. This implies higher set scatters than theoretically derived according to Eq. (7).

For this reason, a correlation correction factor according to

[3]Term from production logistics: Components are produced simultaneously or promptly successively. This generally results in more homogeneous characteristics than when produced in single part production.

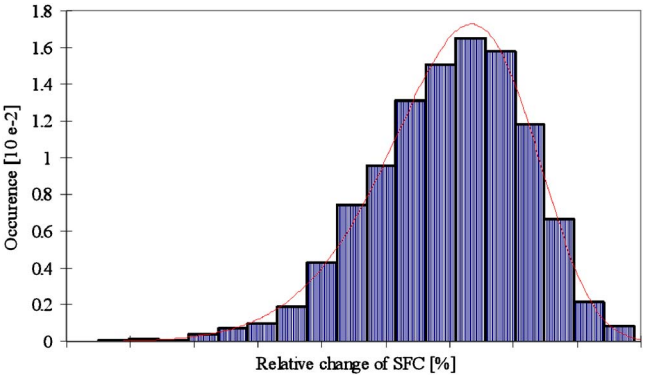

Fig. 3 PDF of relative SFC change due to fan tip clearance scatter (data removed due to confidentiality)

$$C_{\text{set}} = 1 - \frac{\text{Cp}_{\text{set}} - \text{Cp}_{\text{part}}}{\text{Cp}_{\text{part}}\sqrt{n-1}} \tag{9}$$

is introduced. C_{set} can take values between 0 and 1 and can be calculated after analyzing real generated sets with regard to their correlation. This way, the assumption of higher than theoretically calculated set scatters was confirmed.

Example: Fan Tip Clearance. The method shall be exemplified by analyzing the impact of the feature fan tip clearance on fan and engine performance.

The fan tip clearance of a new engine is influenced by a number of different features, such as casing diameter, liner thickness, blade root accuracy, disk diameter, disk groove accuracy, rotor eccentricity, and much more. Consideration of all influencing features is associated with a lot of effort. However, by analyzing construction details of fan tip clearance, it becomes obvious that the complexity of this problem can be reduced significantly: The fan was designed in such a way that blade tip rubbing is intended to achieve a minimum possible tip clearance. Thus, minimum average fan tip clearance can be determined by the difference of the longest blade (it causes the blade rub and removes liner material) and the average of all other blades in the set. Depending on engine power settings, fan tip clearance will be higher than the fan tip clearance calculated. However, for performance scatter modeling purposes, only differences of the average tip clearances in the engine fleet are relevant.

In order to model the impact of tip clearance, a Cp value for fan blade length was determined. With the assumption that blades lying outside the given tolerance scope/bandwidth are refused by quality inspections, a Gaussian distribution with truncated ends at upper and lower limits was generated to simulate different blade lengths. The fan of the Rolls-Royce BR710 engine consists of 22 blades. By using MCS, a multitude of randomly generated fan blade sets were generated and analyzed with regard to longest blade in set and average length of all other blades. This way, a cumulative distribution function (CDF) for the average fan tip clearance of engines after their first run is achieved.

By using sensitivity functions on a fan capacity scalar as well as efficiency delta and subsequent performance synthesis calculation, the impact of fan tip clearance on, for example, SFC has been calculated (see Fig. 3).

Engine Deterioration Modeling

The model described so far can simulate the impact of production scatter of a multitude of features on engine performance. It makes sense to enhance this feature-based methodology to engine deterioration, since deterioration itself results from deviations of certain features from their condition as new.

Phenomenological Description of Engine Deterioration Mechanisms. Several authors give excellent overviews of engine deterioration mechanisms. Their findings are summarized below.

Fouling means the adherence of particles on the surface of gas stream components, supported by the presence of water or oil films. The resulting coating usually increases surface roughness and changes blade profiles to a certain degree [11]. Fouling depends on environmental conditions (e.g., air particle concentration and size) as well as operating schemes (e.g., operating time at low altitudes), and primarily affects compressor components. In parts, fouling can be removed by engine washing [12].

Hot corrosion aims at material losses of gas path components due to chemical reactions with certain gas constituents (e.g., salts, mineral acids). Scales can flake off and cause damage. High temperature corrosion on the other hand characterizes the chemical reaction of metallic atoms of gas path components with oxygen from the surrounding gas. Due to corrosion-resistant materials, these chemical reactions mainly occur in high temperature areas, such as burner and turbine [13].

Physical deterioration mechanisms such as abrasion, erosion, and damage significantly cause engine deterioration. Abrasion refers to loss of material due to frictional forces, e.g., between rotor and casing liner. Typically, abrasion leads to increased tip or sealing clearances, usually depending on flight number rather than flight time.

Erosion means the abrasive removal of material due to hard particle. Typically, particles larger than $2-10$ μm tend not to follow the gas stream but impinge on component surfaces due to inertial forces [14]. While this mainly causes a changed profile form, surface roughness, and tip clearances in the low pressure compressor area, the HPC area is mainly confronted with changed blade tips, loss of liner, and changes in surface roughness. Furthermore, leading edges blunt due to impinging particles, trailing edges tend to thin [12].

Damage can be classified in foreign object damage (FOD) and domestic object damage (DOD). FOD results from objects entering the engine with the air and impinging on mainly low pressure compressor (LPC) components. DOD results from internal objects, e.g., shed parts or ice. In contrast to (continuous) erosion, damage tends to be a one-time event, causing dents, cracks, or even the breakup of parts [13].

Change of Features Over Time. Similar to production scatter modeling, a feature-based engine deterioration methodology was developed to model the change of performance parameters over time. However, there is a major difference of production scatter modeling and deterioration modeling: While the difference of the average features of an engine fleet and the features' nominal value is usually zero when regarding production scatter, this difference can increase significantly when regarding deterioration modeling—i.e., in addition to a changing scatter, features show a certain trend over time due to the deterioration mechanisms mentioned above. Thus, for modeling purposes, a mathematical-statistical description of scatter and trend over time for all relevant features has to be generated—as a description of their condition at any point in time—in order to describe their condition at any point in time.

Different starting points have been identified when it comes to generating such data. First of all, there are numerous maintenance records of engines in operation and development engines with detailed component analysis data for numerous features. Furthermore, there are various component test data, e.g., used for engine certification. Analyzing these records with regard to their development over time, a trend plot including a relative frequency of occurrence can be generated. Together with component experts, these sources of information have been consolidated to generate trend and scatter plots over time for each feature. Two examples of such plots are presented in Fig. 4, whereby the scatter noticeable at $t=0$ (new engine) represents production scatter.

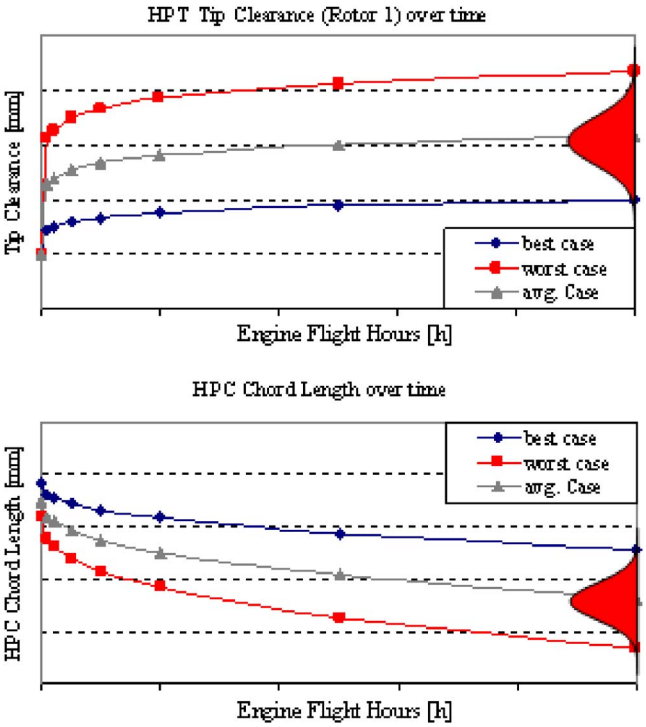

Fig. 4 Exemplary trend and scatter plots over time for HPT tip clearance (upper chart) and HPC chord length (lower chart) (data removed due to confidentiality)

The dotted lines in Fig. 4 represent the average feature condition of the engine fleet over time, whereas the other two lines represent the "worst" and "best" feature conditions in the sense of three sigma.

Performance Modeling. The impact of engine deterioration on performance is modeled in the same way as production scatter modeling by using the feature-based method explained above. In this context, separate performance MCSs have been conducted for multiple user-defined points of time. This way, CDFs for global engine performance parameters were generated for each point of time. These were approximated by regression analysis, e.g., for the average or ± 3 sigma engine (see Fig. 6). As a result of multiple performance MCSs at different points in time, three-dimensional CDFs for each global engine performance parameter are generated.

Model Validation by Means of Engine Performance Test Data

In order to carry out a model validation, corresponding performance data of new (for production scatter) and operated (for deterioration) engines are required. Usually, performance data are generated at engine performance tests. Since each engine is subject to a performance delivery test after production and assembly, there is a sufficiently large database to validate the model's performance scatter predictions of new engines. For the validation of engine deterioration predictions, though, the available database is much smaller and does not allow for an adequate validation of performance trend and scatter over time. However, a comparison of model results with available data and according model evaluation is possible.

Preparation of Performance Delivery Test Data. Performance delivery tests are conducted with every engine after production assembly to assure safe operation. Performance data are converted to a standard operation point, evaluated to identify, among others, possible faults or unusual trends and documented.

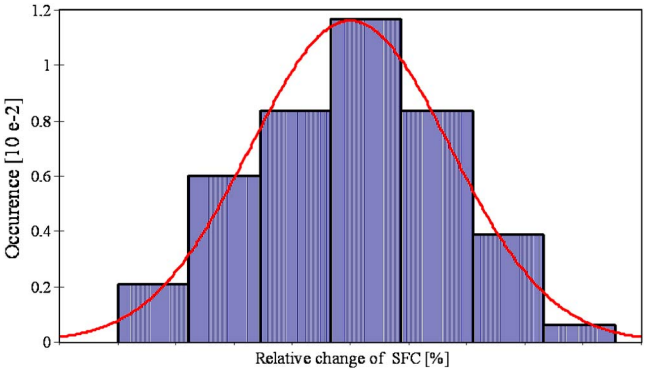

Fig. 5 Standardized empiric PDF of SFC scatter according to delivery test data with approximated Gaussian PDF (data removed due to confidentiality)

Based on this documentation, performance scatter data of certain performance parameters are available. Assuming the database to be correct and complete, it can be used for model validation.

In a first step, empiric CDFs of different performance parameters were generated using database values. Then, all values were divided by their mean value. This way, a standardized and dimensionless empiric CDF has been achieved. To allow for a mathematical description and handling, several steady and unimodal CDFs were approximated to the empiric CDF and tested for their fit.

Tests for Gaussian distribution[4] showed that for most performance parameters, Gaussian distributions can be assumed (see empiric and Gaussian distribution function in Fig. 5).

Consideration of Measuring Errors During Performance Tests. One has to be aware that, in principle, measured test data include measuring errors. For further data analysis, measuring errors have to be taken into account.

For single performance measurements, quantification of measuring errors after an engine test is impossible. However, measuring errors can be accounted for in a statistical way for a sufficiently large number of measurements. According to Ref. [10], in practice, most measurement errors are Gaussian distributed and thus can be described by their standard deviation. The latter can be obtained by uncertainty analyses[5] of measuring probes in combination with information about their number and coupling in the engine.

Using Gauss' law of error propagation [10], the true performance parameter scatter can be calculated by statistically eliminating Gaussian distributed measuring errors:

$$\sigma_{\text{true}} = \sqrt{\sigma_{\text{measured}}^2 - \sigma_{\text{error}}^2} \tag{10}$$

By this means, measuring errors for all relevant performance parameters were determined and the true performance scatter calculated according to Eq. (10).

In addition to errors of measuring probes for measuring performance data (or required parameters for calculating them), measuring errors also influence the operating point of an engine during performance tests. The intended operating point can only be set up with the accuracy of corresponding measuring probes. This results in an other than intended operating point associated with a corresponding change in performance. Furthermore, measured data used for converting performance data to the standard operating point are only possible with the accuracy of the measured environmental data. These measurement errors are considered in the

[4]Such as Anderson–Darling or chisquare [10].

[5]Hereby, different sources of uncertainty (such as calibration uncertainty, drift, hysteresis, etc.) as well as their interaction in the probe are analyzed to derive a distribution function (usually Gaussian) for their measuring error [10].

Table 1 Modeling ratios of selected performance parameters

Performance parameter	Modeling ratio
SFC	92.3%
HPC exit pressure	91.4%
LP shaft speed	95.3%

performance synthesis software. Thereby, controller or target values (e.g., target thrust) and environmental parameters (e.g., air humidity, temperature, and pressure) are randomly varied in accordance with the measuring error of the probes used.

Assessment of Performance Scatter Modeling Quality. The derived true scatter of performance parameters marks a target that a performance scatter model should achieve. The degree to which a model is able to explain this true scatter can be seen as a metric for the assessment of modeling quality. Hence, the quality metric modeling ratio R_m is introduced. It is defined by the modeled performance parameter variance divided by the true performance parameter variance according to

$$R_m = \frac{\sigma_{\text{model}}^2}{\sigma_{\text{true}}^2} \tag{11}$$

With R_m=0.9, the model would be able to explain 90% of the performance scatter observed during delivery tests. On the other hand, this would mean that there are certain influences that are not yet included in the model or that the influences considered have been underestimated.

In Table 1, modeling ratios of different performance parameters are presented. Modeling ratios of more than 90% are supposed to indicate an excellent modeling of performance parameter scatter.

Assessment of Performance Trend Modeling Quality. In addition to the variance of performance parameters, the trend of performance parameters over time is crucial for deterioration modeling. Model results are therefore given in three-dimensional distribution functions, the validation of which requires a sufficiently large database. As mentioned before, the available database of operated engine performance data is small and does not allow for this.

However, a comparison of the model's results of the average (median) engine with available engine performance data was suitable. With available performance test data, a regression analysis (here, power regression) was conducted with a best fitting curve in the form of Eq. (12).

$$y = a + bt^C \tag{12}$$

This line (see Fig. 6, red/gray line) can then be compared to the model's average engine (see Fig. 5, solid line). As can be seen in

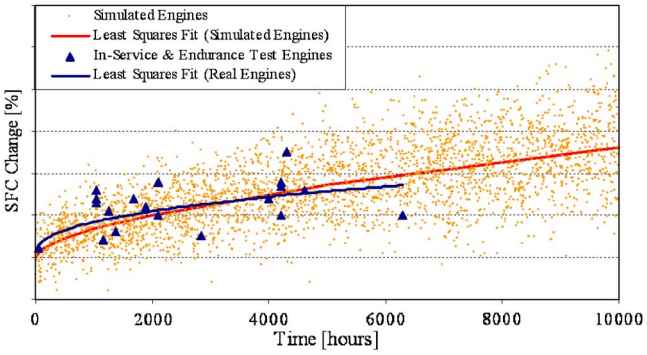

Fig. 6 Comparison of model results with Real engine test data for the parameter SFC including production scatter PDF at *T*=0 (data removed due to confidentiality)

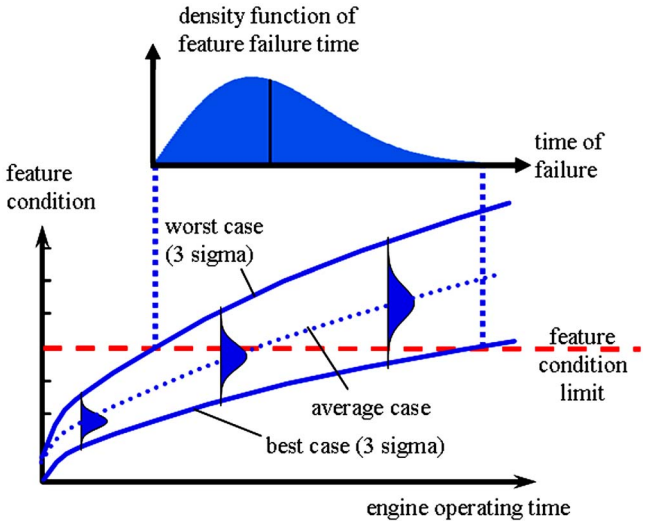

Fig. 7 Methodology to generate the PDF of failure times out of the trend and scatter plot

Fig. 6 with the blue/dark line being positioned above the red/gray line beyond 3500 h, model average deterioration prediction is higher than actual engine data shown. One reason for that might be the consideration of endurance test engines for regression analysis. These engines were operated on test beds only. It is assumed that test bed operation with filtered air and missing g forces leads to a lower deterioration rate for these engines than engines operated on aircrafts. Another reason for a too high deterioration prediction is believed to be caused by maintenance actions, which are not yet regarded in the model on hand. Indeed, the engines used for regression analysis have not been overhauled yet; however, line maintenance actions (e.g., fan blade change, core wash), in fact, influence engine performance.

All engines considered for regression analysis are lying within the predicted ±3 sigma performance scatter range. Due to the small database, no significant results can be expected with further analyses, which therefore are set aside. However, based on the analysis above, it can be said that model predictions show great correlation with real engine fleet performance deterioration.

Model Enhancement I: Time to Failure Modeling for Maintenance Cost Prediction

Maintenance Feature Condition Limits. Feature conditions continuously change over time. This change is modeled by three-dimensional distribution functions, as illustrated in Fig. 4. For certain features, there are limits for their condition, e.g., due to specifications of the maintenance manual. Starting at some point in time, an increasing number of engines will exceed this limit.

For further analyses, a methodology described in Ref. [15] is used: By statistically analyzing these failures, a PDF of failure times $f(t)$ is generated (see Fig. 7). Mathematical integration leads to the CDF $f(t)$. The latter gives the percentage of failed features over time, i.e., accumulation of features which exceed the given limit.

Statistical analyses of real component failure times show that failure behavior can be approximated by Weibull distribution functions in many cases. The PDF $f(t)$ of a Weibull distribution is given by Eq. (13).

$$f(t) = \left(\frac{\eta}{\tau}\right)\left(\frac{t - t_0}{\tau}\right)^{\eta - 1} e^{-((t - t_0)/\tau)^{\eta}} \tag{13}$$

For this reason, Weibull distributions are approximated to the given PDFs of failure times. Hereby, the variables τ (characteristic

life), η (slope) as well as t_0 (time shift) are adjusted for best fit by using chi-square goodness of fit tests. If it was not possible to achieve a sufficient p value, other common distribution functions for deterioration and failure modeling were tested for their fit (such as lognormal, normal, etc.).

Having generated statistical distribution functions for various maintenance relevant features, these serve as input functions for available statistical maintenance cost programs, such as presented in Ref. [16]. For a detailed description of the maintenance cost methodology developed by the author, see Ref. [17].

Model Enhancement II: Operating Dependent Feature Condition Modeling

Multiple Regression Models for Feature Description. Previously, feature condition was modeled on an empirical basis, for example, by analyzing maintenance data and deriving CDFs over time for each feature. This statistical description method does not allow for a connection of operating schemes (e.g., environmental parameters such as air particle concentration or temperature as well as hour to cycle ratio) and engine deterioration rate. For this reason, a model enhancement in the form of a module of deterministic feature condition modeling has been developed. Each feature condition is mathematically modeled over time with independent variables being a number of operating schemes. By performing a MCS, i.e., randomly changing operating schemes within user-defined limits, deterioration of a certain engine fleet is modeled.

According to Ref. [15], due to the complexity of deterioration mechanisms, a high number of influencing factors, unknown interactions, and missing material parameters, a closed deterministic mathematical modeling of deterioration mechanisms is not possible yet. For this reason, a half-empirical model has been developed, where the average engine with average feature condition, calculated by the methodology explained in the previous chapters, is defined to be exposed to average standard operating schemes. Furthermore, the dependencies of feature conditions from single operating parameters are mathematically modeled based on publicly available deterioration research data. This way, a higher-order regression model with average deterioration as center point is generated.

Example: High Pressure Compression Blade Erosion. One of the most important deterioration mechanisms for aircraft engines is erosion. There are a number of publications focusing on titanium alloy erosion and analyzing the dependency of the erosion rate from different factors. For this analysis, the following factors have been identified to be the most relevant regarding blade erosion: dust concentration, particle size, and ambient air temperature. Speed and angle of impact as important factors regarding erosion were ignored for this analysis since they are assumed to be independent from engine fleet operation environment.

Dust concentration and thus ingested particle mass significantly decrease with altitude (see Ref. [18]); therefore, the time flying in lowest altitudes as well as taxiing and start can be seen as key drivers for erosion. For this reason, HPC blade erosion is modeled dependent on flight cycles rather than flight hours. Ambient temperature influences engine gas temperature and thus blade material temperature. Early analyses of titanium wear due to particle erosion with consideration of material temperature were conducted and published in Ref. [19]. Correlations of erosion rate and material temperature as well as dust concentration are presented. An empirical correlation between material temperature and erosion rate has been derived for titanium alloys:

$$E = 1.3784e^{-0.0008(T_{\text{amb}}-273.15)} \tag{14}$$

Average HPC blade erosion rate at standard operating conditions was defined to equal the standard erosion rate E_0. Deviances from these standard operating conditions are incorporated by single correction terms, representing correlations between erosion rates and operating conditions.

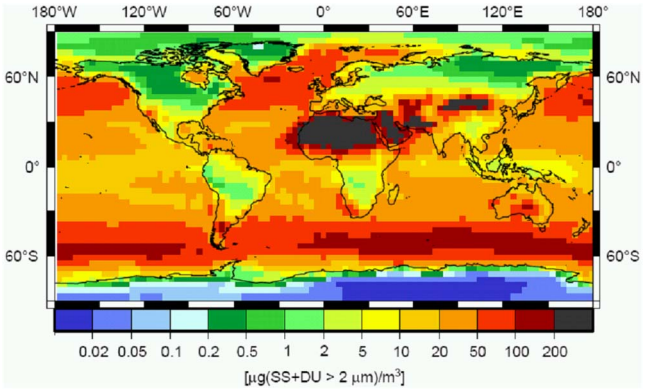

Fig. 8 Example of environmental data input, here: global sea salt and dust concentration of particles larger than 2 μm [18]

The correction term $C\ (T_{\text{amb}})$, for example, considers the relative impact of ambient temperature based on the results of Ref. [19]. It is the ratio of the erosion rate at standard temperature and the erosion rate at regarded ambient temperature:

$$C(T_{\text{amb}}) = \frac{1.3784e^{-0.0008(T_{\text{amb}}-273.15)}}{1.3784e^{-0.0008(T_0-273.15)}} = e^{0.0008(T_0-T_{\text{amb}})} \tag{15}$$

Generic correction terms for dust particle concentration and dust particle size are presented in Refs. [19,20] as follows:

$$C(c_{\text{dust}}) = \frac{-0.7962\ln(c)+8.333}{-0.7962\ln(c_0)+8.333} = \frac{\ln(c)+8.333}{\ln(c_0)+8.333} \tag{16}$$

$$C(D_{\text{dust}}) = \frac{\ln(D)+0.0002}{\ln(D_0)+0.0002} \tag{17}$$

Using such correlations for the correction terms as well as environmental data of user-defined global regions (see Fig. 8), the relative erosion rate E/E_0 is calculated according to

$$\frac{E}{E_0} = C(T_{\text{amb}})C(c_{\text{dust}})C(D_{\text{dust}}) \tag{18}$$

By multiplying the relative erosion rate with dust concentration, material removal relative to standard conditions and thus relative feature change is derived.

Applying such correlations to numerous features resulted in a model enhancement, which is able to correlate engine performance deterioration with airline operation. Due to scarcely available data, further research is required in this area.

Model Application and Results

Engine Scatter Analysis. A sensitivity analysis has been conducted to identify the most influential features with regard to performance scatter and deterioration. Model results are presented in Pareto charts by means of the parameter SFC.

The maximum impact of single features on SFC scatter of new engines is illustrated in Fig. 9. It is apparent that few features cause most of the SFC scatter. For the calculation of the percentage line, Eq. (17) has been used,

$$P_{\text{cum},n} = \frac{\sum_{i=1}^{n}\sigma_i^2}{\sigma_{\text{model}}^2} = \sum_{i=1}^{n} P_n \tag{19}$$

The cumulative percentage is the sum of the variance caused by the n most influential features. The percentage line in Fig. 9 indicates that 12 (of 105) features cause more than 90% of the SFC scatter modeled, i.e., $P_{\text{cum},12} > 0.9$. Since the percentage of total

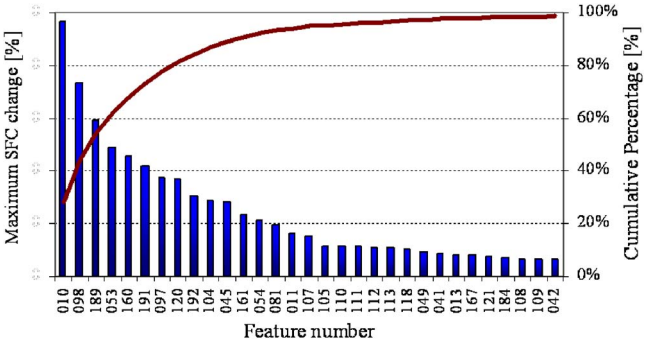

Fig. 9 Pareto bar chart and cumulative percentage line of the features with the most significant impact on New Engine SFC scatter (data removed due to confidentiality)

variance for the 25th feature is lower than 0.2%, i.e., $P_n < 0,2\%$, the methodology can be considered as very robust. Since SFC scatter is dominated by few features, consideration of further minor features will insignificantly influence SFC scatter.

Engine Trend Analysis. In a further sensitivity analysis, the most influential features regarding performance trends have been identified. As shown in the Pareto chart in Fig. 10, numerous features cause an increase in SFC. Most features are different from the features causing SFC scatter.

The cumulative percentage line of Fig. 10 indicates that the performance trend is based on a much broader number of features than performance scatter. 90% of SFC increase is caused by 20 features. The 25th feature increases SFC by 0.62%.

Conclusions

Production scatter and engine deterioration directly affect engine performance. A tool has been developed which is able to model this impact on the basis of the condition of elementary design elements, so-called features. Thus, a direct correlation of feature changes and engine performance has been established.

The model is able to quantify the impact of single manufacturing operations, design elements, and deterioration mechanisms on engine performance. Model results show great congruence with real engine performance test data for the RR BR710 engine with respect to engine performance scatter and performance deterioration. However, adaptability of the methodology to other engines has yet to be demonstrated.

The modeling quality regarding performance scatter significantly depends on two factors. First of all, on production scatter data, i.e., SPC data from quality assurance. In particular, this holds true for the most sensitive features, since 90% of performance scatter is caused by 12 of the 105 features modeled. Secondly, production scatter modeling requires detailed uncertainty analyses of the measuring probes used for performance tests since measuring errors account for—depending on the performance regarded parameter—up to approximately 60% of the performance scatter measured on engine test beds. Modeling quality regarding deterioration (trend) modeling depends on the ability to quantify feature conditions over time. Accurate maintenance records proved to be a reliable database for this purpose. However, for some features, thorough estimations of component experts are required.

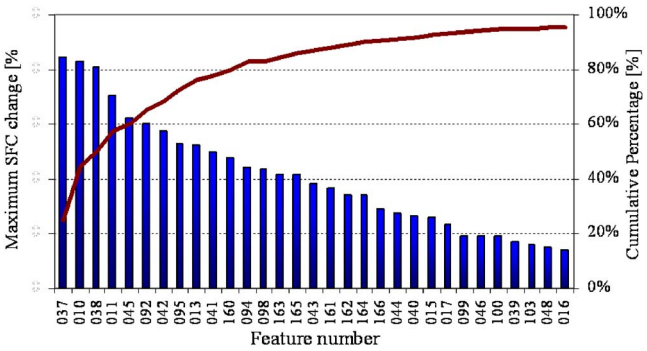

Fig. 10 Pareto bar chart and cumulative percentage line of the features with the most significant impact on SFC trend (here, after 10,000 h) (data removed due to confidentiality)

The model on hand offers manifold applications for engine manufacturers and operators. Some shall be outlined in the following.

The possibility to perform sensitivity analyses allows for an identification of the most sensitive features—regarding performance scatter and trend. As an example, this provides a basis for the selection of features to be statistically monitored during production or features, whose production tolerance range should be checked or reduced. Furthermore, the impact of new design features or technologies on engine performance scatter and deterioration can be predicted.

Due to a simulation methodology close to reality, two significant model enhancements have been achieved. With a mathematical description of feature condition dependent on engine operating schemes, a correlation of airline operation and engine deterioration has been realized. Moreover, CDFs for feature failure times can be derived as data input for statistical maintenance cost software.

Acknowledgment

The model was developed in the OPTIFER research project, which was conducted in the framework of the German National Aeronautical R&T programme (Contract No. 20T0306B). The authors are thankful to many Rolls-Royce colleagues for their helpful support during the course of this study. This interdisciplinary model could not have been achieved without that.

Nomenclature

Latin Symbols

c = dust concentration (g/m^3)
$\dot{m}$ = mass flow rate (kg/s)
n = shaft revolutions; parts count (s^{-1})
t = time (s)
x = feature condition (divers)
C = correction term or factor
CDF = (cumulative) distribution function
Cp = a process capability index
D = dust particle size (μm)
E = erosion rate (mg/g)
EGT = exit gas temperature (K)
HPC = high pressure compressor
HPT = high pressure turbine
LSL = lower specification limit
MCS = Monte Carlo simulation
P_n = percentage of the nth features
PDF = (probability) density function
R_m = modeling ratio
RSM = response surface model
S = sensitivity parameter
SAEPP = sophisticated aeroengine performance program
SFC = specific fuel consumption (kg/s N)
SPC = statistical process control
T = temperature (K)
USL = upper specification limit

Greek Symbols

η = efficiency; slope (Weibull)
μ = mean value (divers)
τ = characteristic life (Weibull) (s)

Subscripts

- $1,2,\ldots,n$ = consecutive numbers
- amb = ambient
- cum = cumulative
- F = feature
- mod = module performance parameter
- nom = nominal
- rel = relative

References

[1] Spieler, S., Staudacher, S., Fiola, R., and Sahm, P., 2006, "Merkmalsbasierte Modellierung von Produktionsschwankungen bei Flugzeugtriebwerken," *Proceedings of DGLR*, Braunschweig, Germany.

[2] Wassell, A. B., 1968, "Reynolds Number Effects in Axial Compressors," ASME J. Eng. Power, to be published.

[3] Schlichting, H., and Gersten, K., 2000, *Boundary Layer Theory*, 8th ed., Springer, Berlin.

[4] Craney, T. A., 2003, "Probabilistic Engineering Design," Reliability Review, The R&M Engineering Journal, **23**(2), pp. 1–6.

[5] Norton, I., 2002, "BR700-710 C4-11 Basic Design Data for GV-SP," Rolls-Royce Deutschland Technical Report No. E-TR476/02 ISS03.

[6] Fiola, R., 1993, "Berechnung des Instationären Betriebsverhaltens von Gasturbinen Unter Besonderer Berücksichtigung von Sekundäreffekten," Ph.D. thesis, Technical University Munich, Germany.

[7] Chrysler Corporation, Ford Motor Company, General Motors Corporation, 2005, *Statistical Process Control (SPC) Reference Manual*, 2nd ed., Detroit.

[8] Franke, B., Spieler, S., Staudacher, S., and Gebser, D., 2005, "Factory and Process Simulation in Aero-Engine Component Manufacturing," ASME Paper No. GT2005-68309, Reno, NV.

[9] Sembacuttiarachy, S., 2004, "Anwendbarkeit von Prozessfähigkeitskennwerten bei Kleinen Serien," Diploma thesis, Stuttgart University, Germany.

[10] Bronstein, I. N., Semendjajew, K. A., Musiol, G., and Mühlig, H., 2000, *Taschenbuch der Mathematik*, 5th ed., Harri Deutsch, Frankfurt, Germany.

[11] Kurz, R., and Brun, K., 2001, "Degradation in Gas Turbine Systems," ASME J. Eng. Gas Turbines Power, **123**, pp. 70–77.

[12] Tarabrin, A. P., Bodrov, A. L., Schurovsky, V. A., and Stalder, J. P., 1996, "An Analysis of Axial Compressor Fouling and a Cleaning Method of Their Blading," ASME Paper No. GT1996-363.

[13] Rossmann, A., 2000, *Die Sicherheit von Flugtriebwerken*, 1st ed., Turbo Consult, Karlsfeld, Germany.

[14] Zaita, A. V., Buley, G., and Karlsons, G., 1998, "Performance Deterioration Modeling in Aircraft Gas Turbine Engines," ASME J. Eng. Gas Turbines Power, **120**, pp. 344–349.

[15] Eichler, Ch., 1990, *Instandhaltungstechnik*, 5th ed., Technik GmbH, Berlin, Germany.

[16] Burkett, M. A., 2006, "DM-Trade—A Rolls-Royce Tool to Model the Impact of Design Changes and Maintenance Strategies on Lifetime Reliability and Maintenance Cost," ASME Paper No. GT2006-90023, Barcelona, Spain.

[17] Spieler, S., Staudacher, S., Kappmeyer, G., and Lou, W., 2006, "Reparaturverfahren und ihre Bedeutung für die Bewertung von Blisks über den Lebenszyklus von Flugtriebwerken," *Proceedings of DGLR*, Braunschweig, Germany.

[18] Lauer, A., Hendricks, J., Ackermann, I., Schell, B., Hass, H., and Metzger, S., 2005, "Simulating Aerosol Microphysics with the ECHAM/MADE GCM Part I: Model Description and Comparison With Observations," Atmos. Chem. Phys., **5**, pp. 3251–3276.

[19] Sage, W., and Tilly, G. P., 1970, "The Interaction of Particle and Material Behavior in Erosion Processes," Wear, **16**, pp. 447–465.

[20] Espenschade, P. W., and Wood, C. D., 1965, "Mechanisms of dust erosion," SAE Trans., **73**, pp. 515–523.

An Experimental Study of Spark Anemometry for In-Cylinder Velocity Measurements

D. P. Gardiner

G. Wang

M. F. Bardon

M. LaViolette

W. D. Allan
e-mail: billy.allan@rmc.ca

Department of Mechanical Engineering,
Royal Military College of Canada,
Kingston, ON K7K 7B4, Canada

It has been demonstrated by previous researchers that an approximate value of the bulk flow velocity through the spark plug gap of a running spark ignition engine may be deduced from the voltage and current wave forms of the spark. The technique has become known as spark anemometry and offers a robust means of velocity sensing for engine combustion chambers and other high temperature environments. This paper describes an experimental study aimed at improving performance of spark anemometry as an engine research tool. Bench tests were conducted using flow provided by a calibrated nozzle apparatus discharging to atmospheric pressure. While earlier studies had relied upon assumptions about the shape of the stretching spark channel to relate the spark voltage to the flow velocity, the actual spark channel shape was documented using high-speed video in the present study. A programmable ignition system was used to generate well-controlled constant current discharges. The spark anemometry apparatus was then tested in a light duty automotive engine. Results from the image analysis of the spark channel shape undertaken in the present study have shown that the spark kernel moves at a velocity of less than that of the freestream gas velocity. A lower velocity threshold exists below, which there is no response from the spark. It is possible to obtain a consistent, nearly linear relationship between the first derivative of the sustaining voltage of a constant current spark and the freestream velocity if the velocity falls within certain limits. The engine tests revealed a great deal of cycle-to-cycle variation in the in-cylinder velocity measurements. Instances where the spark restrikes occur during the cycle must also be recognized in order to avoid false velocity indications.
[DOI: 10.1115/1.2898835]

Keywords: instrumentation, diagnostics, spark ignition engine, velocity, anemometry, sparks

Introduction

History of Spark Anemometry. The use of electrical discharges to measure the flow velocity of gases was attempted as early as 1934, when Lindvall reported experiments involving a 'glow discharge anemometer' [1]. Almost 50 years later, Meinel and co-workers reported a detailed theoretical analysis of the effects of flow fields on the properties of glow and arc discharges and developed a technique intended to measure flow parameters in a firing engine using the existing spark plug and ignition system [2,3]. Maly et al. referred to this as voltage rise anemometry (VRA).

Kim and Anderson [4] later reported measurements of the bulk gas velocity at the spark plug gap of a firing engine using a modified version of the technique of Maly et al. Kim and Anderson used the term spark anemometry and this term has also been adopted by the present authors. The technique of Kim and Anderson was later adapted by Pashley et al. who reported measurements in a pressurized flow rig and a firing engine [5].

Potential Applications. Kim and Anderson [4] proposed that information obtained from spark anemometry could be used to identify variations in flow between cylinders in production multicylinder engines. Variable valve timing systems and variable inlet systems using port control valves can change the flow characteristics of the engine as a function of operating conditions. Spark anemometry could be used to monitor the behavior of such systems during development tests.

Spark anemometry offers a relatively simple means of obtaining approximate velocity data from production engines. The information would not be sufficient to make an assessment of how one should improve the design of a combustion chamber, but could be used to assess the effectiveness of changes in the design after they are made.

Principles of Anemometry. Spark anemometry is based upon the relationship between the flow field velocity and the instantaneous length of a spark discharge channel. A simplified example of this is depicted in Fig. 1. Previous studies [2–5] state that the plasma has no inertial contribution. Plasma formed across the discharge gap or another electrode arrangement (d_g) of a spark plug will be convected by the local flow it encounters. Thus, the derivative of the displacement of this plasma with respect to time ($\mathrm{d}x/\mathrm{d}t$) will equal the local velocity, u.

Since the plasma channel must remain attached to the cathode and anode (the negative and positive electrodes), *channel legs* form between the electrodes and the spark *head* that has left the gap due to the flow. As shown in Fig. 1, the two *legs* lengthen at the same rate as the *head* is convected away from the electrodes; hence, the rate of change of the total length of the plasma channel will be twice the rate of change of the distance between the spark *head* and the electrodes. This results, for an idealized case, in a rectangular or *U*-shaped channel whose total length changes as a function of the convection velocity of the spark head.

Another aspect of spark anemometry is the relationship between the length of the plasma channel and the voltage drop that

Contributed by the Internal Combustion Division of ASME for publication in the JOURNAL OF ENGINEERING FOR GAS TURBINES AND POWER. Manuscript received December 1, 2006; final manuscript received January 23, 2008; published online April 23, 2008. Review conducted by Margaret Wooldridge.

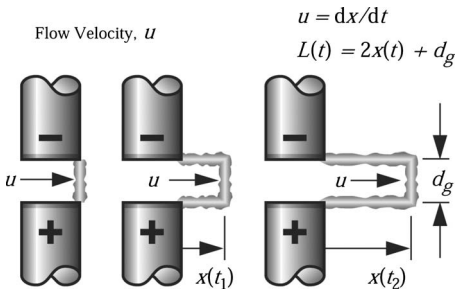

Fig. 1 Simplified relationship between velocity and spark length

can be measured across the spark gap. Under otherwise identical conditions, there will be a linear relationship between the voltage drop across the channel and its length, i.e., the effective resistance of the channel increases with length. Thus, the derivative of the spark voltage with respect to time (dV/dt) can be used to determine the rate of change of the length of the spark, hence, the flow velocity without the need for optical access.

In practice, there are numerous factors, which impede the ability to achieve viable spark anemometer measurements based upon these simple relationships between spark length and flow velocity and spark voltage and spark length. These include the following.

Local flow field conditions. The flows in engine combustion chambers are three dimensional and thus cannot be characterized completely by spark anemometry techniques. However, many engines have by design a dominant in-cylinder charge motion such as swirl or tumble. In these cases, the spark plug gap is exposed to an oncoming bulk flow from a known direction. Although the convection field in the vicinity of the spark plug gap will have three-dimensional features, there will be a dominant two-dimensional flow that can be measured by the spark anemometer. Nevertheless, it is likely that the three-dimensional features present in engines will affect the bulk flow measurements, so the use of calibration techniques with laminar flow (as done in the present study) has limitations.

The flow field conditions encountered by the spark differ from the freestream conditions upstream of the *probe*. The spark anemometer is inherently intrusive particularly in cases where conventional spark plugs are used as *sensors*. Kim and Anderson [4] subjected a spark plug to laminar freestream conditions, and measured actual velocity and turbulence intensity in and near the spark gap using hot wire anemometry (HWA). They found that the average velocity in the gap was considerably lower than the freestream velocity, and that turbulence developed downstream of the gap. Kim and Anderson based the bench calibration of their sensor on the actual gap velocity as measured by HWA rather than the freestream velocity.

If a spark anemometer is used in some types of engine research, the gap velocity would be the more desirable measurement because of its influence on the early growth of the flame kernel [4]. In other cases, where a general purpose anemometer is required to measure swirl tumble or squish velocities, the sensor can be calibrated relative to the freestream velocity. This was done by Meinel and co-workers et al. [2,3], and a reasonably linear relationship between the predicted and freestream velocities was demonstrated.

Spark shape. The relationship between the total spark length and the location of the spark *head* (the leading edge of the plasma converted by the flow) may be more complex than that predicted by a simple rectangular or *U*-shaped geometry.

In practice, the shape of the spark differs considerably from the simple geometry depicted in Fig. 1. This fact was recognized by previous researchers [2–5], and can lead to measurement errors when a model employing assumptions about geometry is used to predict the velocity. The actual spark shape will be dictated by factors such as the geometry of the electrodes, the spark gap dimensions, and the resulting distortion of the flow field downstream of the gap. Furthermore, the shape of the spark can vary substantially from discharge to discharge under constant freestream flow conditions.

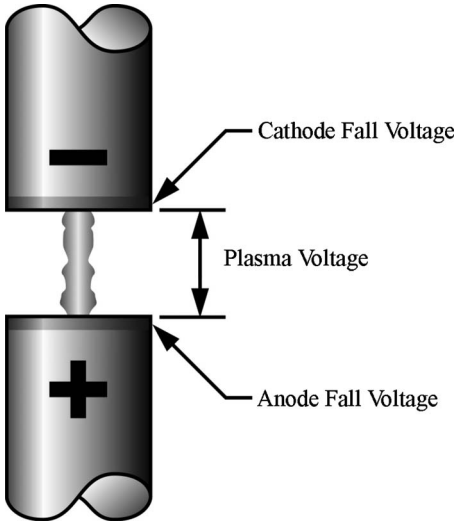

Fig. 2 Components of measured spark voltage

Spark voltage measurements. The spark voltage measurements used for spark anemometry are typically done with a high voltage probe at the spark plug connector. The raw voltage measurements from the probe contain information about the instantaneous length of the spark, but the voltage levels are also affected by other factors. The following section identifies these factors and discusses means of overcoming their influence on the spark voltage signal.

(a) *Cathode and anode fall voltages*. In addition to the voltage drop across the plasma channel of the actual spark, the measured voltages include the voltage drops called *fall voltages* at the surfaces of the electrodes, as depicted in Fig. 2. The anode fall voltage is usually constant, typically at $\approx$25 V. The cathode fall voltage can vary by several hundred volts depending upon whether the discharge is in the arc mode where thermionic emission of electrons occurs or glow mode where cold cathode electron emission by ion bombardment mechanism occurs. Detailed explanations of the arc and glow modes of the spark can be found in Refs. [4–6]. If the discharge mode of the cathode does not change during the period of the spark used for the spark anemometry measurements, the sum of the electrode fall voltages will be constant, and will not obscure the rate of change in the plasma channel voltage.

A problem has been observed by researchers [2–5] because the conventional ignition systems typically used for spark anemometry produce a decaying current wave form. The spark current may initially be high enough to produce an arc mode discharge, and a transition to a glow mode discharge occurs once the current falls to a level that is insufficient to maintain an arc. Kim and Anderson used an assumed arc-to-glow transition threshold of 40 mA in their spark anemometer model [4]. However, the actual threshold can vary considerably from spark to spark. Teets and Sell [7] showed that the discharge may even transition back and forth between arc and glow several times within the same spark. Thus, it would be desirable to provide spark current conditions such that the

discharge was either well above or well below the arc-to-glow threshold during the measuring period so that arc-to-glow transitions are entirely avoided.

(b) *Voltage drop from resistor spark plugs*. Spark plugs commonly contain internal resistors for the suppression of the radio frequency interference. If the voltage is sensed at the spark plug terminal, a voltage proportional to the spark current will be produced across the resistor. Of course, nonresistor spark plugs or plugs with low resistance inductive noise suppression can be used to reduce or eliminate this effect, but the superior noise suppression properties of the resistor spark plugs offer significant benefits for the signal-to-noise ratio of the spark anemometer. With a conventional decaying current spark wave form, this voltage error varies in proportion to the current during the measurement period.

Kim and Anderson [4] accounted for this error by measuring the instantaneous spark current and calculating the instantaneous voltage drop based upon a static measurement of the spark plug resistance.

(c) *Effect of spark current on plasma channel voltage*. The voltage drop across the plasma channel of a given length is inversely proportional to I^n, where I is the spark current. The exponent is different for arc and glow modes (0.75 and 0.32, respectively, according to Ref. [4]), so the situation becomes more complicated if arc-to-glow transitions occur during the measurement period. Maly and Meinel [2] reported that satisfactory results could be obtained using a conventional inductive ignition system with linearly decreasing current characteristics. This was possible if the measurement period was small, e.g., 50 μs, so that little change in current occurred and was timed to occur at the desired current level. However, such a short measuring period would result in a velocity measurement window that is too short to reveal fluctuations in velocity during the spark duration. Furthermore, as shown by Pashley et al. [5], the spark current/time characteristics of inductive ignition systems are affected by flow through the gap. Thus, the instantaneous current level at a given time in the discharge may not be predictable.

Kim and Anderson [4] were able to lengthen the period available for the velocity measurement by measuring the instantaneous spark current along with the spark voltage so that the current as well as arc and glow effects could be included in the calculation of the plasma channel voltage.

(d) *Effects of gas properties on plasma channel voltage*. The plasma channel voltage of a given channel length is proportional to P^n, where P is the pressure of the gas. This must be considered when comparing high pressure experimental measurements with calibrations carried out at atmospheric pressure. Kim and Anderson used a pressure exponent for air of 0.51. For engine experiments, a correction can be applied based upon cylinder pressure measurements. According to Maly et al. [3], the temperature of the gas has a negligible effect due to the much higher core temperature of the plasma column (1000 K according to Ref. [6]). Maly et al. [3] noted that there was a small effect ($<1.5\%$) between unburned reactants and combustion products in a methane-air flame.

Fansler et al. [8] reported that the spark voltage traces of individual cycles varied in response to changes in gas composition as well as velocity in tests using a stratified charge engine where liquid fuel was injected directly into the cylinder. Thus, the signal interpretation would become more complicated in cases like this where substantial fluctuations in the local fuel/air ratio were present. With modern premixed charge engines having good fuel/air mixing, this should be less of a problem.

Potential Improvements to Spark Anemometry

As previously discussed, a number of the problems associated with obtaining a signal proportional to the spark length from a voltage measurement are related to changes in spark current during the measurement period. The use of an ignition system capable of maintaining a constant spark current at an optimum level would eliminate the need for a number of corrections, and permit the rate of change of the length of the spark to be monitored directly based upon the derivative of the spark voltage. This would offer the possibility for real-time monitoring of the instantaneous gas velocity, as the need for postprocessing and manual analysis of the spark voltage wave forms (in Refs. [2–5]) could be avoided.

In addition, it was believed that the problems associated with the relationship between spark length and the gas velocity that the anemometer was intended to measure could be better addressed if the actual spark geometry could be visualized. This led to the present study, which combined a constant current spark anemometry technique with high-speed video analysis of spark plasma in flows.

Experimental Details

Bench Tests. Bench tests were conducted using two different flow apparatuses. Initial tests, which included high-speed video recordings of the spark shape, were carried out using a simple calibrated nozzle apparatus with a 12 mm outlet diameter. This was later replaced with larger, more sophisticated apparatus with a 63.5 mm outlet diameter. Because it provided a relatively large area of uniform velocity, the larger apparatus was much less sensitive to the position of the spark plug in the flow stream, and produced more consistent results. Unfortunately, it was not possible to repeat the spark video recordings with this apparatus due to a problem with the video camera.

The spark plug used as the *anemometer probe* was a conventional automotive resistor plug with 1.0 mm diameter platinum pins on the center and ground electrodes. When compared with plain inconel electrodes, the platinum pin design was found to provide a more consistent discharge location from spark to spark. The spark plug was fired using a Nexum Inc. programmable ignition system. This ignition system enables the user to select spark current and duration independently, and is capable of producing constant current sparks as well as decaying current sparks and multispark wave forms. It has previously been used to study the effects of spark characteristics on engine combustion [7]. The spark current is measured from the voltage drop across a shunt resistor in series with the secondary winding of the ignition coil. The spark voltage and current signals were recorded using the on-board wave form digitizer of the ignition system, at a sample rate of 11 MHz. The first derivative of the voltage wave forms was determined numerically during postprocessing.

Images of the spark were recorded using a Redlake Model PCI 8000S high-speed video camera. The maximum framing rate of 8000 frames/s (allowing a framing interval of 125 μs) was used. The images were then examined to determine the displacement and length of the visible plasma using INSPECTOR™ image analysis software.

Engine Tests. Limited engine testing was carried out using the same spark plug design and ignition system as with the bench tests. However, in this case the voltage wave form was differentiated in real time. This was achieved by clipping the original signal from a Tektronix 6015 1000:1 probe to remove the high voltage levels associated with the spark ionization voltage. The signal was filtered with a low-pass eighth order Bessel filter with a 5 kHz cut-off frequency. Finally, it was differentiated with an analog circuit.

The test engine was a GM four cylinder 2.2 liter light truck engine with a pushrod actuated valve train and two valves per cylinder. It was equipped with an aftermarket control system to permit operator adjustments to the fuel injection and ignition timing values. The engine was fueled with gasoline using the stan-

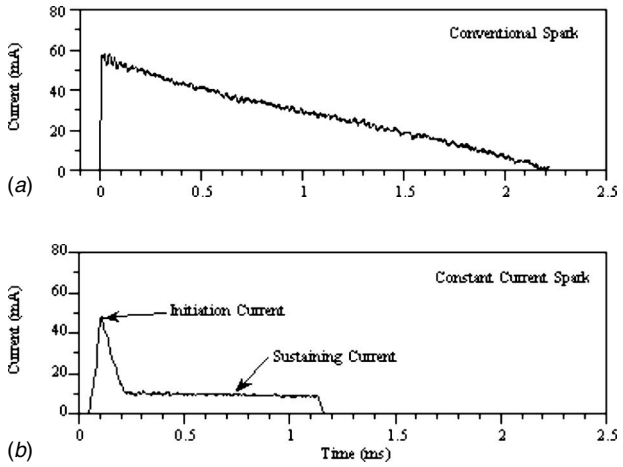

Fig. 3 Comparison of conventional decaying current spark and constant current spark

dard port fuel injection, and the air/fuel ratio was maintained under stoichiometric closed loop control using the standard exhaust gas oxygen sensor.

The programmable ignition system replaced the standard inductive ignition system on one cylinder, which was also equipped with a Kistler 6121 piezoelectric cylinder pressure transducer. The programmable spark was triggered from the inductive ignition control system. The voltage and current wave forms were recorded at 2.5 MHz on a digital storage oscilloscope. The engine was loaded using a water brake dynamometer, and the tests were conducted at 1800 rpm, 3 bar brake mean effective pressure, with no exhaust gas recirculation, and minimum spark advance for best torque (spark advance of 30 deg before top dead center). Since the engine was operated at a constant rpm and load, changes in operating conditions were not used to obtain different in-cylinder velocities. The different velocities discussed in the remainder of this paper were due to cycle-to-cycle variation.

Results and Discussion

Bench Tests. Figure 3 shows examples of the current wave forms of a conventional inductive ignition system spark and the programmable spark source used in the present study. The current level of the conventional spark decays during the spark duration. The constant current spark is initiated with a brief pulse of elevated current with a peak value similar to that of the conventional spark to ensure reliable ionization and ignition. It is sustained afterwards at a lower current level with a decay rate of less than 1 mA/ms. The peak initiation current and the level and duration of the sustaining current were adjustable.

For much of the experimental data presented in this paper, the peak initiation current was about 50 mA, and the sustaining current was 10 mA. This was the lowest sustaining current level that could be stabilized in the engine with the existing apparatus. The low sustaining current level was well below the arc-to-glow threshold (typically 40 mA), which ensured that a glow discharge always existed during the measurement period.

Figure 4 shows examples of video records of 10 mA constant current sparks at different freestream velocities. In each case, the length of the initial spark (seen in the top frames) was equal to the electrode gap spacing of 1 mm. The greater rate of *stretching* of the spark at 9.4 m/s versus 5 m/s can be clearly seen. In both of the cases, the shape of the developed spark approximates a *U*-channel, but contains significant irregularities. At 15.3 m/s, the spark assumed a more pointed appearance; a restrike is recorded in the fifth frame. The restriking phenomenon has been discussed by previous researchers [2,5], and occurs when the voltage needed

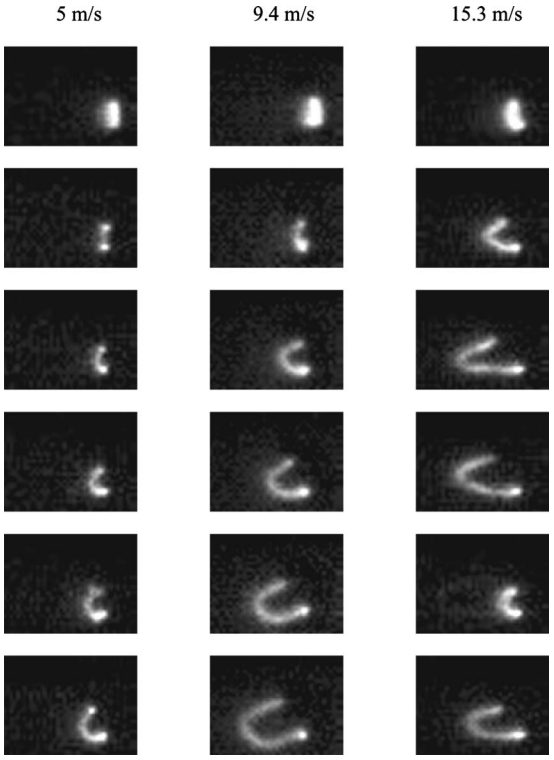

Fig. 4 Examples of 10 mA constant current sparks at different velocities (8000 frames/s and 125 μs framing interval)

to sustain the elongated spark exceeds the voltage required to reionize the gas across a shorter distance at or near the electrode gap. Under these conditions, the original spark *blows out*, a new, shorter spark is formed, and the stretching process begins again. At higher velocity, multiple restrikes can occur during a single spark event.

Examples of the voltage wave forms from 10 mA constant current sparks at different freestream velocities are shown in Fig. 5. The spark plug actually fired with negative polarity high voltage typical of most automotive systems but the wave forms have been inverted for clarity. It can be seen that the voltage dropped abruptly at the beginning of the wave form when the spark gap ionizes and *breakdown* occurs. Following a transitional period during which the spark current drops from the 50 mA initiation to the 10 mA sustaining value, the wave form assumes a steady

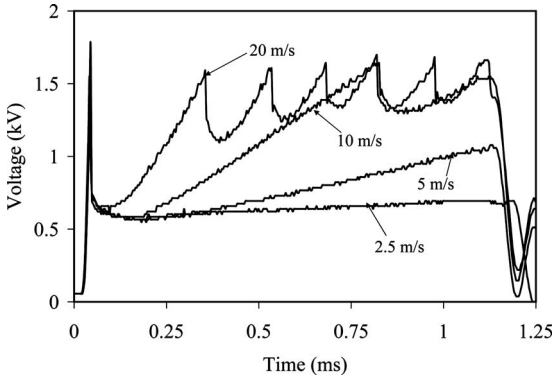

Fig. 5 Effect of velocity on voltage wave forms of 10 mA constant current sparks

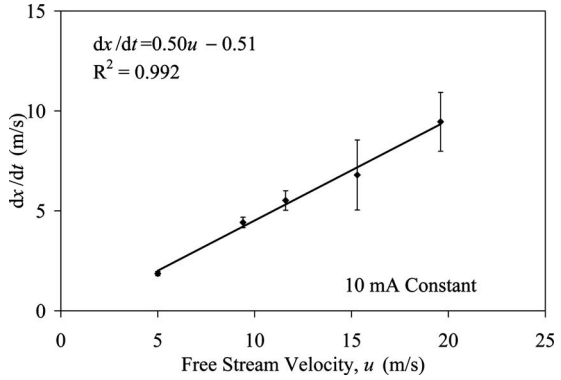

Fig. 6 Relationship between velocity of spark head and freestream velocity

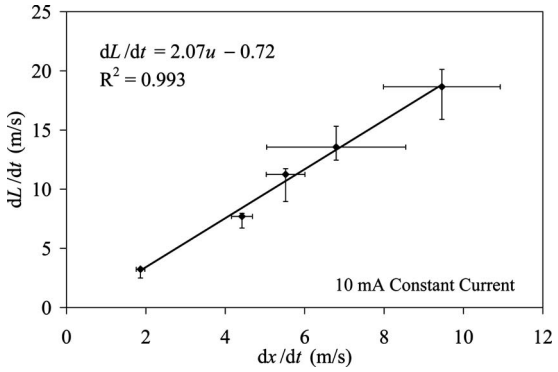

Fig. 8 Relationship between first derivative of spark length and velocity of spark head

slope for a given velocity.

At higher velocities (10 m/s and 20 m/s in Fig. 7), the waveform developed the sawtooth pattern previously described by Kim and Anderson [4]. The abrupt voltage drops of the sawtooth pattern indicate restriking of the spark. The fact that the minimum voltage values immediately following each restrike are well above the initial sustaining voltage observed immediately after the initial breakdown indicates that the new discharge was not initiated at the point of minimum separation between the electrodes (the plug gap). Rather, it followed a longer path somewhere between the plug gap and the stretched spark that blew out.

Evidence of this can be seen in Fig. 4 at 15.3 m/s, where the restrike in Frame 5 was downstream of the plug gap. This may be due to the presence of ionized species in the gas part way downstream of the gap, which despite the longer breakdown path reduced the breakdown voltage requirement to less than that directly across the gap.

The restrike events destroyed the relationship between the slope of the spark voltage and the flow velocity, so spark anemometry measurements must be carried out prior to the first restrike. In the remainder of this paper, any average first derivative values for the spark voltage are the mean values for the interval between the establishment of a stable constant current value and the first occurrence of any restriking.

Figure 6 shows the relationship between the velocity of the downstream edge of the spark head and the freestream velocity upstream of the spark plug. The data were based on manual analysis of consecutive video frames similar to those shown in Fig. 4. The error bars each show plus/minus one standard deviation from five processed spark events.

These results show a spark head velocity of about half the freestream velocity. The actual flow field velocity in the vicinity of the spark gap was not measured (as Kim and Anderson did using HWA [4]), so it cannot be confirmed that this discrepancy was due to a reduction in the velocity relative to the freestream velocity or due to the intrusive nature of the spark plug. However, Kim and Anderson reported that their apparatus produced a spark gap velocity considerably lower than the freestream velocity, so it is likely that a similar situation existed in the present study.

As shown in Fig. 7, the rate of change of the total spark length obtained through video image analysis showed a strong correlation with the freestream velocity. This occurred despite the fact that the spark shape was often rather irregular as similar to the cases in Fig. 4. It is possible that significant elongation of the spark occurred in the third dimension due to three-dimensional

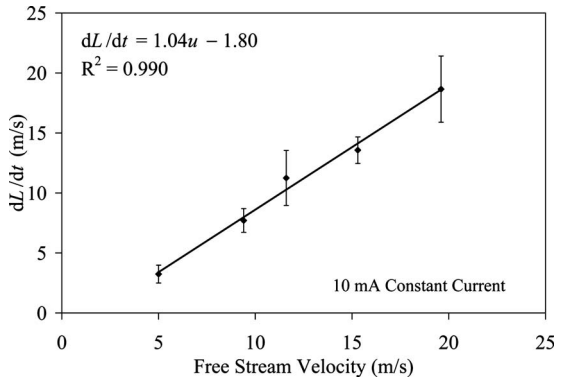

Fig. 7 Relationship between first derivative of spark length and freestream velocity

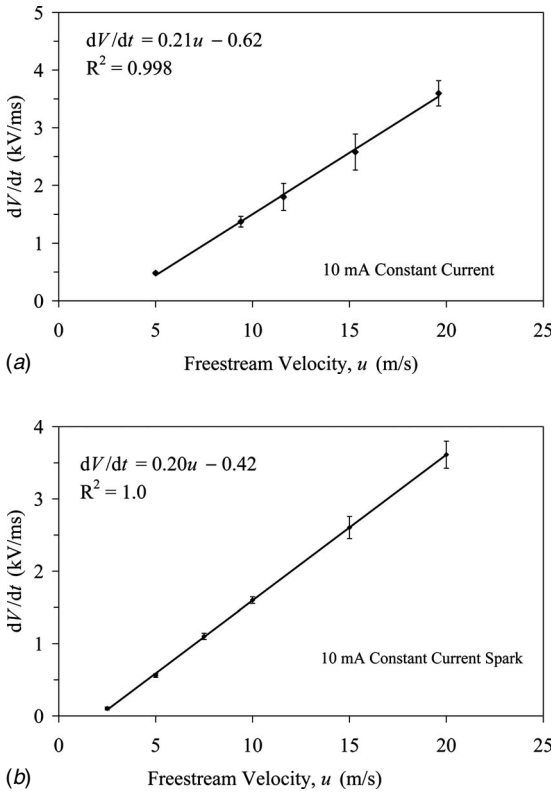

Fig. 9 (*a*) Relationship between first derivative of spark voltage and freestream velocity. (*b*) Relationship between first derivative of spark voltage and freestream velocity using 63.5 mm flow nozzle.

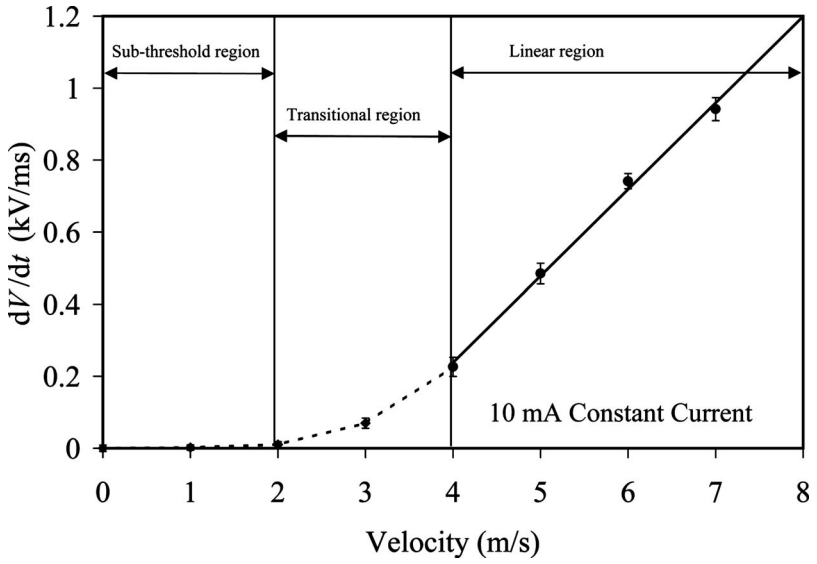

Fig. 10 First derivative of spark voltage (d*V*/d*t*) at low velocities (10 mA constant current spark)

(3D) features in the flow. This portion of the elongation would not be captured by the two-dimensional (2D) video images, but would be reflected in the spark voltage signal. In the model of Kim and Anderson [4], a rectangular spark shape was assumed (Fig. 1), which led to the approximation that the spark would lengthen at a rate twice that of the spark head velocity or

$$dL/dt = 2dx/dt$$

In Fig. 8, this approximation was surprisingly close to the actual relationship. The slope of dL/dt versus dx/dt was nearly 2.

The relationship between the first derivative of the spark voltage and the freestream velocity is shown in Fig. 9(*a*). As discussed earlier, measurement of the spark voltage serves as a nonoptical means of measuring the rate of change of the spark length. In comparing Figs. 7 and 9(*a*), it can be seen that the voltage-based measurements actually showed less scatter and better linearity than the image-based measurements. This was due to the

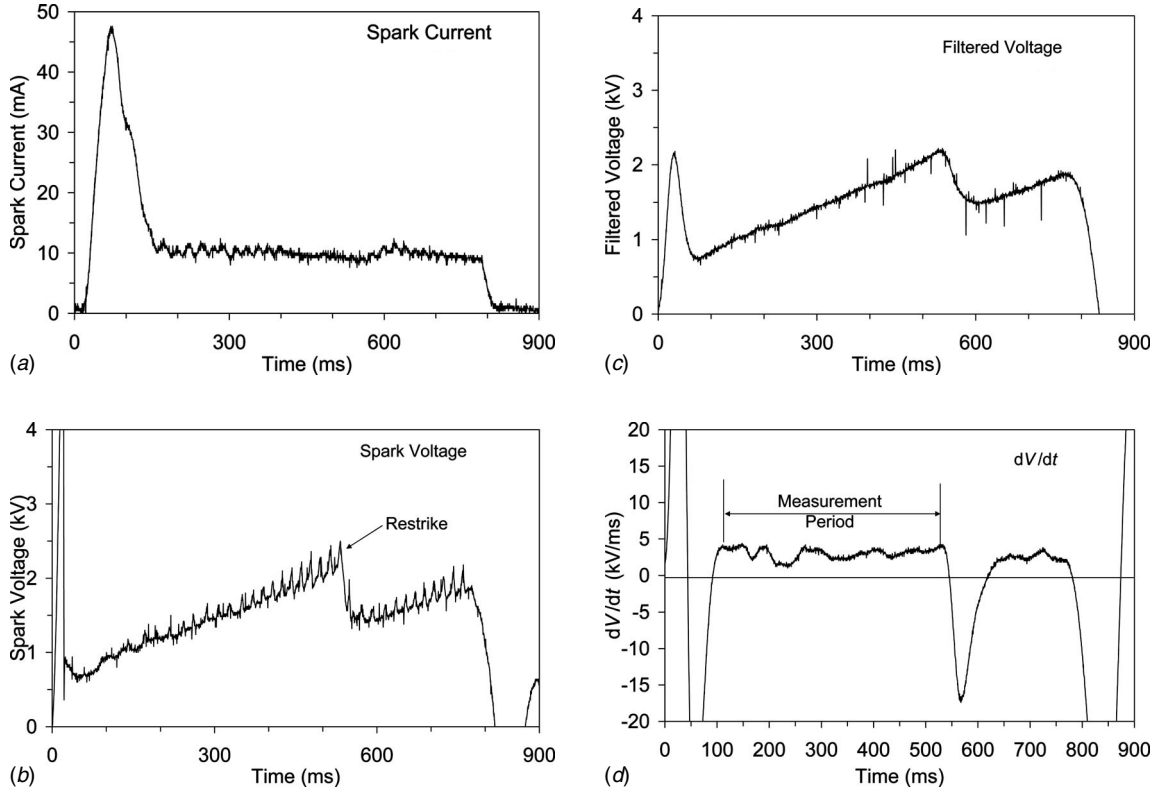

Fig. 11 Wave forms from in-cylinder velocity measurements

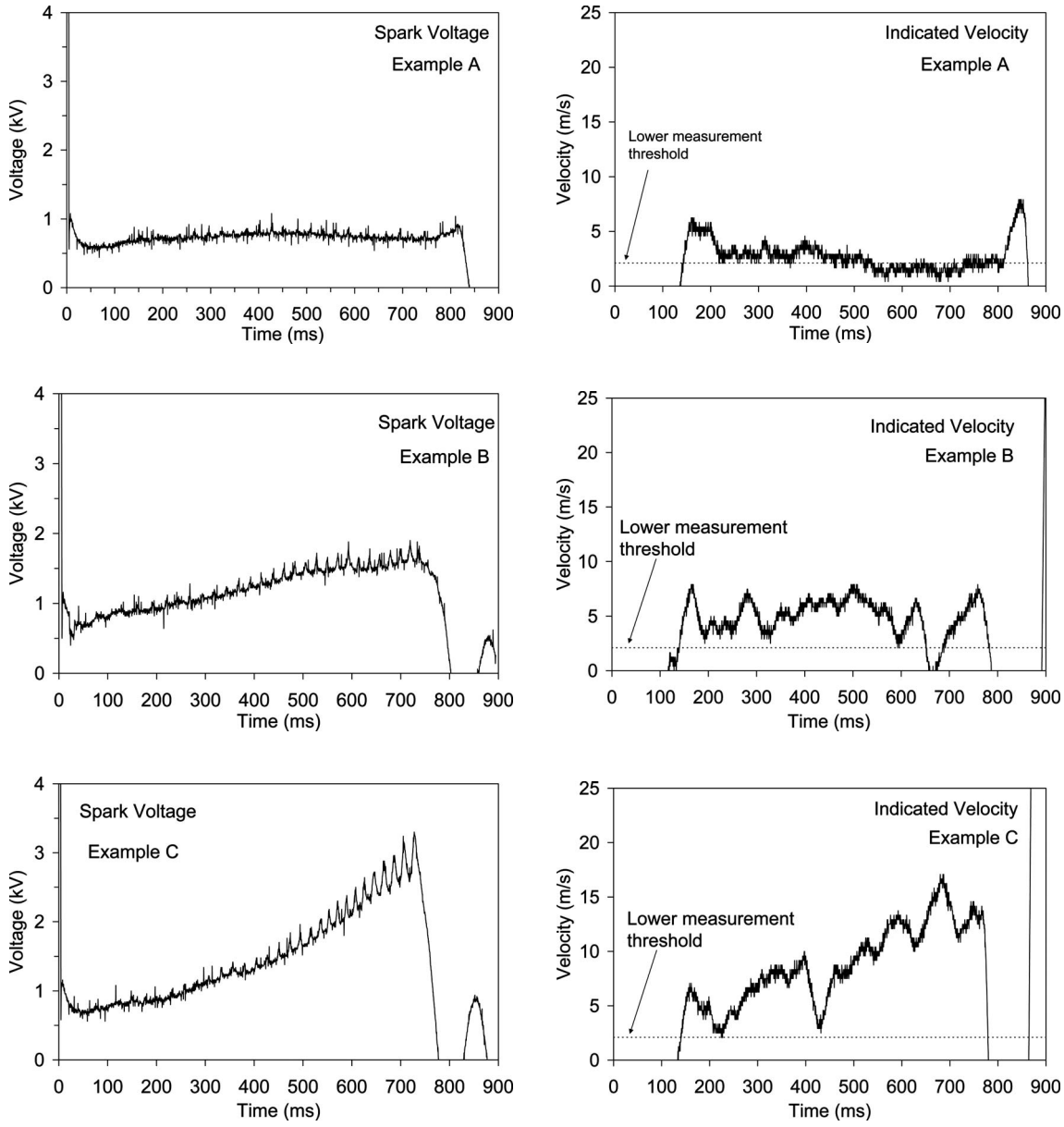

Fig. 12 Cycles without restrike events

high effective sampling rate for voltage, which permitted the average derivative of the signal to be determined easily. In contrast, the framing speed and exposure limitations of the video camera meant that the derivative of the spark length had to be determined based upon just a few video images and included errors associated with determining the length from somewhat blurred digitized images.

Similar results obtained using the improved 63.5 mm nozzle apparatus are shown in Fig. 9(*b*). In this case, there was even less scatter in the results presumably due to the relatively large, laminar flow region provided by this nozzle. There was also a remarkably linear relationship between the first voltage derivative (dV/dt) and the freestream velocity.

Figure 9(*b*) also shows that the linear fit for these data points does not pass through the origin. This observation led to further experiments, in which the spark behavior at low velocities was investigated in greater detail (Fig. 10). The error bars indicate that there was very little scatter in the data under these conditions.

It can be seen that there was a lower threshold for freestream velocity below which there is no response from the spark. In this case, there was virtually no difference in spark voltage between tests conducted without flow and those conducted at 1 m/s. This was confirmed through the analysis of the high-speed video recordings of the spark, which showed no consistent differences in the appearance of the plasma channel shape between still air and 1 m/s flow upstream of the spark plug. It can also be seen that a nonlinear transitional region existed between the lower velocity threshold and the velocity region that produced a linear dV/dt response from the spark.

It is not clear if this apparent sensitivity threshold was due to a fundamental characteristic of spark anemometry or was specific to the apparatus used in these experiments. The elongation of the plasma channel may be resisted by the restoring force of the electric field until the velocity is sufficient to overcome these forces. The threshold may also have been related to the impact of the electrodes on the flow field resulting in a stagnant region downstream of the electrodes at low freestream velocities. Further research is needed to investigate these hypotheses.

Based upon these bench test results, it was apparent that useful velocity information could be obtained from the constant current

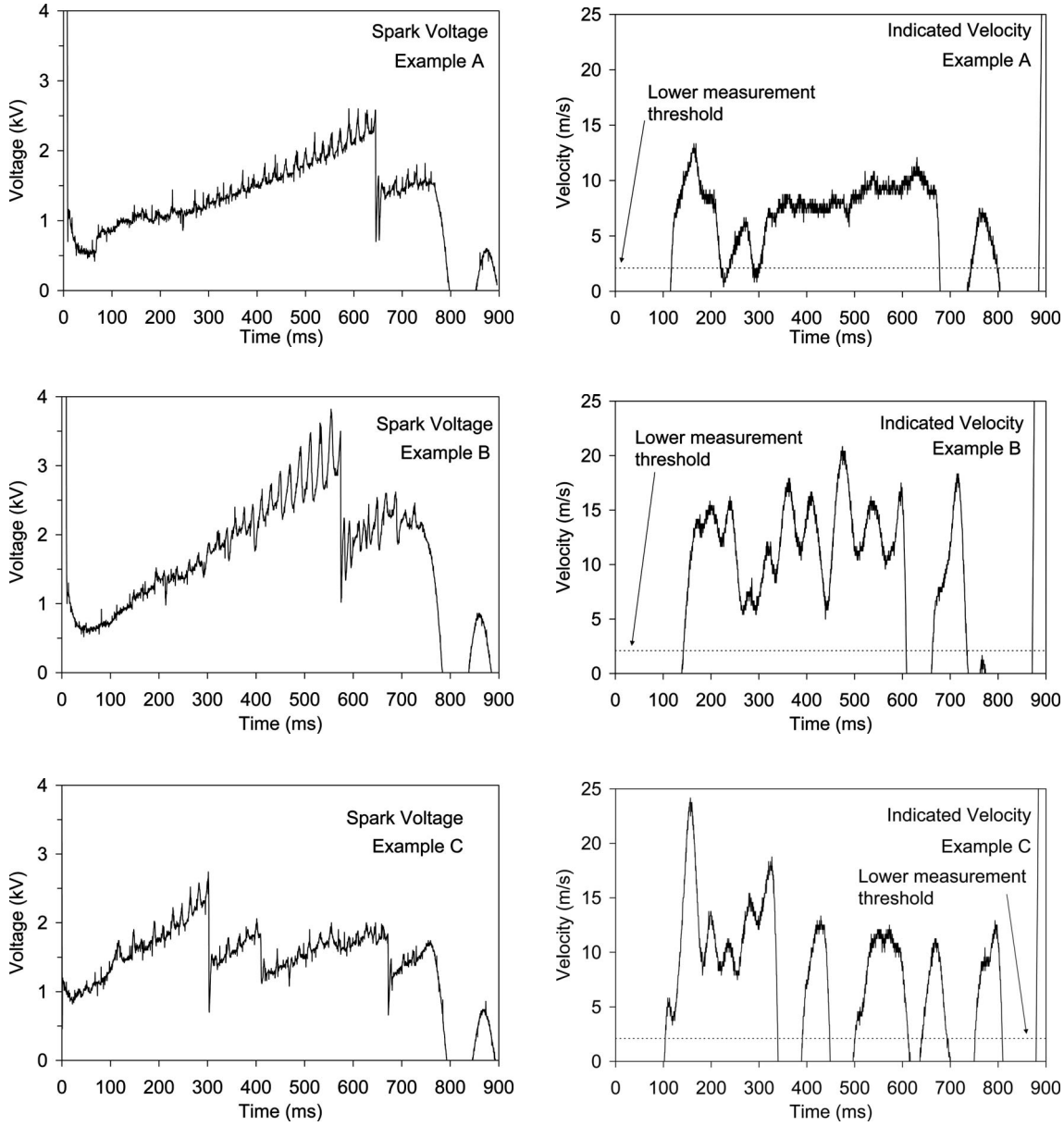

Fig. 13 Cycles with pronounced restrike events

peak anemometer based solely upon the first derivative of the spark voltage, provided that the anemometer system comprised of a spark plug and custom ignition source was calibrated under known flow conditions. The velocity being measured would also have to be great enough to exceed the response threshold of the spark anemometer, and preferably within the linear response region. As discussed earlier, a pressure correction term would be required to apply calibration data obtained at atmospheric pressure to in-cylinder measurements on a running engine.

Engine Tests. Figure 11 shows examples of signal wave forms obtained during engine tests, which were used to calculate the in-cylinder velocity. The current wave form (Fig. 11(*a*)) showed a current spike of approximately 48 mA used to initiate the spark, and the nominal 10 mA sustaining current used for the velocity measurement. Under in-cylinder conditions, the sustaining current was not as stable as in the bench tests, but the current fluctuations were relatively minor during the period of interest for the measurements.

The spark voltage (Fig. 11(*b*)) showed the abrupt voltage drop of the breakdown event, followed by a period of increasing sustaining voltage. In this example, a second abrupt drop in voltage occurred at about 550 μs, when a restrike event occurred. The high frequency spikes superimposed upon the voltage wave form were due to noise from the switching regulation of the constant current ignition system. These spikes were removed by a 5 kHz filter (Fig. 11(*c*)) prior to differentiation.

As shown by the differentiator signal (Fig. 11(*d*)), large negative signal excursions were produced by the original breakdown event and the subsequent restrike. The signal was only valid for estimating the velocity when it was a positive value during the period beginning with the establishment of a stable sustaining current at approximately 150 μs, and ending with the first occurrence of a restrike at approximately 550 μs. The window for valid measurements (termed the measurement period) for this particular wave form is shown in Fig. 11(*d*).

In the following figures, the in-cylinder velocity was calculated from the differentiator signal based upon the bench calibration data from the 63.4 mm nozzle shown earlier in Fig. 9 and cor-

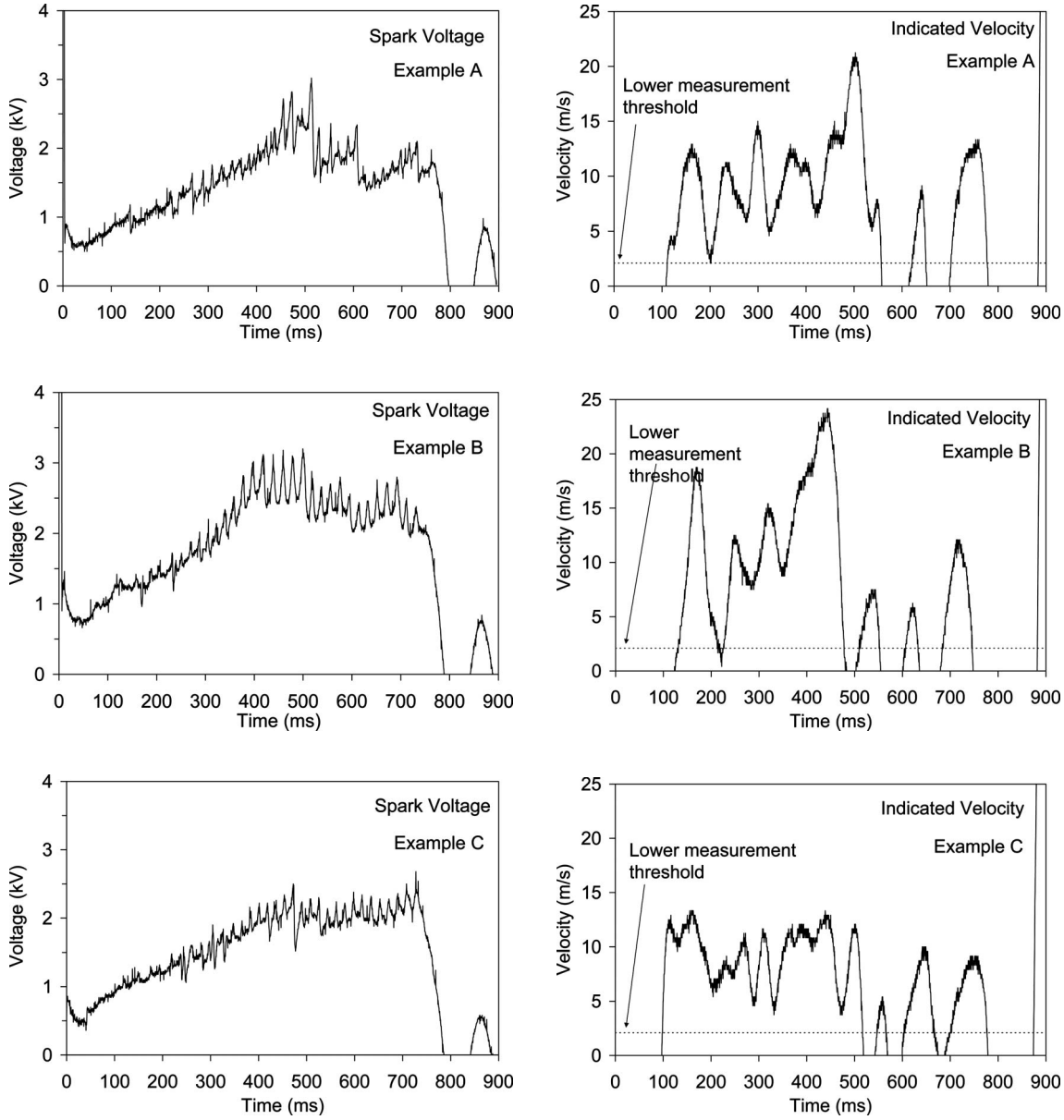

Fig. 14 Cycles with voltage plateaus due to minor restrike events

rected for pressure using data from the in-cylinder pressure transducer. A pressure exponent value of 0.51 similar to the value previously used by Kim and Anderson [4] was selected. The indicated velocity was obtained as

$$4.96\left(0.42 + \frac{dV}{dt}\left(\frac{P_{\text{cal}}}{P_{\text{cyl}}}\right)^{0.51}\right)$$

where dV/dt is the derivative of spark voltage in kV/ms, P_{cal} is the bench calibration pressure, and P_{cyl} is the cylinder pressure.

The authors recognize that the absolute accuracy of these estimates is questionable particularly in light of the absence of calibration data at elevated pressures. Nevertheless, the ability to sense even relative changes in velocity between engine configurations, operating conditions, cylinder to cylinder, and cycle to cycle may be useful for some applications. For example, Kim and Anderson [4] proposed that even approximate velocity data would have utility for cylinder-to-cylinder flow variability studies aimed at achieving balanced cylinder-to-cylinder output in production engines.

The most striking feature of the velocity data was the very high degree of variation both from cycle to cycle, and within any given cycle. In the following figures, data from individual cycles were grouped into three categories, based upon the overall behavior of the spark voltage wave form during a given cycle. All of these cycle types were common, but their relative frequency of occurrence was not quantified in this study. The figures also show the minimum velocity sensing threshold (2.1 m/s) identified in the bench test calibrations. Values below this level are invalid, and result from zero or negative differentiator signal values.

Figure 12 shows the simplest cases where the spark was sustained during its entire duration without a pronounced restrike event. As such, the available velocity measurement period was maximized, and some details of velocity changes during the cycle could be observed. Note the range of velocities recorded between different cycles arranged top to bottom from slowest to fastest. In each example, the initial indicated velocity levels are approxi-

mately 5 m/s. In Fig. 12, Example A, the velocity drops to below the detection threshold, while fluctuations above and below 5 m/s are observed in Example B. In Example C, the flow apparently accelerates or the stretching spark encounters regions of progressively higher velocity and reaches a peak indicated velocity of over 15 m/s.

Figure 13 shows examples with pronounced restrike events one or more times during the spark. These types of cycles tended to exhibit higher initial indicated velocity values and greater velocity fluctuations. This was consistent with the expectation that a spark that was stretching faster (due to higher gas velocities) would blow out and restrike earlier than a spark exposed to lower velocities. Note, however, that the peak voltage level corresponding to the first restrike event varied considerably between sparks.

These sparks showed indicated velocity values that fluctuated in the range of approximately 10–15 m/s. With earlier and more frequent restriking such as that observed in Example C, the period during which valid velocity measurements were possible was reduced to only about 200 μs.

Figure 14 shows a series of cycles where the spark voltage appeared to plateau midway through the spark event. Examination of these wave forms revealed the presence of what has been termed *minor restrike events*. In these cases, abrupt drops in the voltage occurred indicating restriking but the magnitudes of the voltage drops were much smaller than those depicted earlier in Fig. 13. In Fig. 14, these minor restrikes were most pronounced in Example A, and were barely distinguishable from the ignition wave form noise in Example D. There may have been real flow behavior such as turbulence and flow reversals affecting these signals that contributed to the plateau wave forms, but the effects of restriking and noise made it impossible to extract useful velocity data from these regions of the sparks.

The results of Figs. 12–14 show that there was no single velocity value that adequately reflected the in-cylinder flow near the spark plug in this engine. Cyclic variability must be taken into account if linkages between flow behavior and combustion characteristics are to be identified. This will require the synchronized acquisition of voltage wave forms and cylinder pressure traces from substantial numbers of consecutive engine cycles.

Within individual cycles, variations in velocity must be considered. Improvements in the measurement technique that may contribute to improved intracycle velocity measurements include reducing the intrinsic noise of the spark voltage wave forms using alternative current regulation methods, and better techniques for filtering and differentiation of the wave forms.

The ability to achieve velocity measurements over an extended period within each cycle will ultimately be limited by the difficulties caused by restriking events and the success of the techniques used to deal with them. This objective is very desirable, as continuous measurements of velocity and, hence, velocity fluctuations could yield information about turbulence characteristics. This was done by Johansson by processing laser Doppler velocimetry data from a single cylinder research engine with optical access [9,10]. Johansson found that the relatively high frequencies of the turbulence had the major influence on early combustion. Spark anemometry may ultimately provide a means of obtaining similar insights from multicylinder production engines.

Summary

The use of spark anemometry or spark voltage signals to determine flow velocities has been investigated in bench tests at atmospheric pressure, and in tests in a firing spark ignition engine. Instead of conventional, decaying current sparks, low level constant current sparks have been used in an effort to improve the performance of the measurements.

High-speed video recordings of the spark plasma channel in the bench tests have shown that with a conventional spark plug, the leading edge of the spark is connected by the flow at a velocity less than the freestream velocity upstream of the spark plug. A lower velocity threshold existed below, which there was no response from the spark. Nevertheless, there was a nearly linear relationship between the first derivative of the sustaining voltage of a constant current spark and the freestream velocity, if the velocity falls within certain limits. This makes it possible to calibrate a given spark plug and ignition system using bench tests, and apply the calibration using appropriate corrections for pressure to in-cylinder measurements in firing engines.

The engine tests conducted in the study revealed a great deal of variation in the indicated velocities both from cycle to cycle, and within any given cycle. Instances where the spark restrikes reformed after being blown out must be recognized and accounted for in order to prevent false velocity indications. The present approach can provide qualitative indications of changes to in-cylinder velocities. Further work is needed to improve the absolute accuracy of the measurements including calibration studies at elevated pressures.

Acknowledgment

The financial support of the Academic Research Program, Royal Military College of Canada, is gratefully acknowledged. The authors are also grateful to Professor A. Benaïssa for his advice and the use of his flow apparatus.

References

[1] Lindvall, F. C., 1934, "A Glow Discharge Anemometer," Trans. Am. Inst. Electr. Eng., **53**, 1063–1073.
[2] Maly, R., and Meinel, H., 1981, "Determination of Flow Velocity, Turbulence Intensity and Length and Time Scales From Gas Discharge Parameters," *Proceedings of the Fifth International Symposium on Plasma Chemical*, Vol. ISPC-5, pp. 552–557.
[3] Maly, R., Meinel, H., and Wagner, E., 1985, "Novel Method for Determining General Flow Parameters From Conventional Spark Discharge," IMechE Conf. Trans., **C67/83**, pp. 27–32.
[4] Kim, J., and Anderson, R. W., 1995, "Spark Anemometry of Bulk Gas Velocity at the Plug Gap of a Firing Engine," SAE Paper No. 952459.
[5] Pashley, N., Stone, R., and Roberts, G., 2000, "Ignition System Measurement Techniques and Correlations for Breakdown and Arc Voltages and Currents," SAE Paper No. 2000-01-0245.
[6] Maly, R., 1984, "Spark Ignition: Its Physics and Effect on the Internal Combustion Engine," *Fuel Economy in Road Vehicles Powered by Spark Ignition Engines*, V. C. Hillard and G. D. Springer, eds., Plenum, New York.
[7] Teets, R. E., and Sell, J. A., 1988, "Calorimetry of Ignition Sparks," SAE Paper No. 880204.
[8] Fansler, T. D., Stojkovic, B., Drake, M. C., and Rosalik, M. E., 2002, "Local Fuel Concentration Measurements in Internal Combustion Engines Using Spark-Emission Spectroscopy," Appl. Phys. B: Lasers Opt., **75**, pp. 577–590.
[9] Johansson, B., 1993, "Influence of the Velocity Near the Spark Plug on Early Flame Development," SAE Paper No. 930481.
[10] Johansson, B., 1994, "The Influence of Different Frequencies in the Turbulence on Early Flame Development in a Spark Ignition Engine," SAE Paper No. 940990.

The Fuel Mix Limits and Efficiency of a Stoichiometric, Ammonia, and Gasoline Dual Fueled Spark Ignition Engine

Shawn M. Grannell
e-mail: sgrannel@umich.edu

Dennis N. Assanis

Stanislav V. Bohac

Donald E. Gillespie

Department of Mechanical Engineering,
University of Michigan,
Ann Arbor, MI 48109-2133

An overall stoichiometric mixture of air, gaseous ammonia, and gasoline was metered into a single cylinder, variable compression ratio, supercharged cooperative fuel research (CFR) engine at varying ratios of gasoline to ammonia. The engine was operated such that the combustion was knock-free with minimal roughness for all loads ranging from idle up to a maximum load in the supercharge regime. For a given load, speed, and compression ratio, there was a range of ratios of gasoline to ammonia for which knock-free, smooth firing was obtained. This range was investigated at its rough limit and also at its maximum brake torque (MBT) knock limit. If too much ammonia was used, then the engine fired with an excessive roughness. If too much gasoline was used, then knock-free combustion could not be obtained while the maximum brake torque spark timing was maintained. Stoichiometric operation on gasoline alone is also presented, for comparison. It was found that a significant fraction of the gasoline used in spark ignition engines could be replaced with ammonia. Operation on about 100% gasoline was required at idle. However, a fuel mix comprising 70% ammonia/30% gasoline on an energy basis could be used at normally aspirated, wide open throttle. Even greater ammonia to gasoline ratios were permitted for supercharged operation. The use of ammonia with gasoline allowed knock-free operation with MBT spark timing at higher compression ratios and higher loads than could be obtained with the use of gasoline alone.
[DOI: 10.1115/1.2898837]

Introduction

An initial version of this work was presented at the ASME 2006 International Mechanical Engineering Congress and Exposition as IMECE2006-13048. One option for phasing out the use of petroleum-derived hydrocarbon fuels is to produce hydrogen with nuclear power, using the sulfur-iodine thermochemical process, which requires high temperature nuclear heat sources. This would enable the domestic production of a motor fuel, which does not involve carbon dioxide emissions anywhere in its life cycle. Wind or solar power could be used to make hydrogen, although their contributions are expected to be small, and biofuels are also available in limited capacity [1]. Although hydrogen gas does not have favorable energy density by volume, it can be combined with atmospheric nitrogen to make ammonia, which is stored as a liquid at a modest pressure near 10 bars. For the same energy content, liquid ammonia has 2.6 times the volume and 2.3 times the mass of gasoline. The higher efficiency, at which an ammonia fueled engine can be run, will partially offset ammonia's reduced energy density relative to that of gasoline.

Ammonia is an irritant that can cause injury if the liquid is splashed onto the skin or eyes, or by prolonged breathing of the vapor. Care must be taken to avoid spills by the appropriate design of the fill connectors on the vehicle and on the dispenser. However, ammonia is much less flammable than hydrogen. Also, ammonia, unlike hydrogen, does not require extreme pressures to contain it at a reasonable energy density. The authors have years of experience with handling liquid anhydrous ammonia, and hold the opinion that, with the right equipment, the handling, delivery, and use of liquid anhydrous ammonia can be made much less problematic than are the handling, delivery, and use of high pressure hydrogen gas.

The principal limitation on the use of ammonia as an engine fuel is the slow flame speed of ammonia/air mixtures. Ammonia can also be difficult to ignite, and it has a high autoignition temperature and narrow flammability limits. The challenge of ammonia is to make it burn completely, so that efficient engine operation with minimal power loss can be achieved. These challenges have caused ammonia to be overlooked as a solution to the hydrogen storage problem. However, the logistical and operational penalties of using hydrogen as stored by other means may delay its use even as crude oil and natural gas become more expensive than hydrogen produced by nuclear power [2]. This dual fuel investigation is intended to provide a means by which ammonia can be used as the principal fuel, while achieving engine efficiency and power, which are superior to those obtained with the use of gasoline alone.

Related Work

The use of ammonia in diesel engines has been investigated by others using various configurations and with different fuel additives to improve the engine operation [3–5]. Efforts to improve the combustion of ammonia in diesel engines have produced recommendations for the use of spark ignition, elevated compression ratios, and gaseous phase ammonia induction at a constant equivalence ratio [4]. Mozafari and co-workers gave similar recommendations [6,7].

Liquid phase ammonia induction gives better volumetric efficiency because the ammonia cools the intake mixture, and the liquid ammonia does not displace as much air. However, the theoretical efficiency gain for liquid induction is small [8], and the

Contributed by the Internal Combustion Division of ASME for publication in the JOURNAL OF ENGINEERING FOR GAS TURBINES AND POWER. Manuscript received February 7, 2007; final manuscript received February 9, 2008; published online April 28, 2008. Review conducted by Thomas W. Ryan III.

resulting compression temperature reduction and mixture nonuniformity are counterproductive to the task of improving the combustibility of the ammonia [6].

The use of high compression ratios and supercharge is known to improve the combustibility of ammonia [9], but the engine must also be able to run at light loads, including idle. Something else are also needed, even for engines that include the supercharge regime in their range of operation, because high compression ratios alone are not enough to make an engine run smoothly while idling on ammonia.

The combustibility of ammonia can be improved with the use of combustion promoters. Combustion promoters are more reactive fuels, which are used with the ammonia to improve the ignitability and flame speed. Hydrogen has been used as a combustion promoter for ammonia [8–15]. Hydrogen can be obtained by decomposing a small fraction of the ammonia into hydrogen and nitrogen in a catalyst chamber heated by the engine exhaust gases [8,10,13]. The use of this catalyst chamber, or cracker, would enable engine operation with ammonia as the only fuel. However, the decomposition yield is often inadequate and difficult to control when the entire ammonia stream is directed through the cracker [8,13]. Cornelius et al. [9], Kroch [11], and Kroch and Restieac [12] avoided the cracker problem by metering hydrogen-bearing gas mixtures into the engine separately from the ammonia. None of the references describe a comprehensive engine operating map for ammonia and a combustion promoter at any specific target combustion conditions.

Gasoline as Combustion Promoter

In this study, ammonia is to be used as the principal fuel without decomposing any of it into hydrogen and nitrogen. Gasoline is used as the combustion promoter, and ammonia is used to the maximum extent practical at each load and speed, and at a fixed compression ratio, which is also optimized. An ammonia and gasoline dual fueled engine retains the ability to be run on gasoline alone, although at a reduced maximum load from that which can be obtained with the use of some ammonia. It also avoids the problems of storing high pressure gas and/or obtaining a sufficient cracking yield. The flammability of the intake mixture is tuned by controlling the ratio of fuel mass flows.

Stoichiometric operation gives the best compromise between power density and efficiency and it is also near the flame speed maximum [14]. It was also anticipated that the postcatalyst emission cleanup point for ammonia would occur at stoichiometric, as it does for gasoline, and it did. Stoichiometric operation is the best match for the overlap of these criteria.

The stoichiometric combustion of gasoline and ammonia in 1 mole of air is shown in Eq. (1), in which (b) is a variable between 0 and 1. The equation reduces to the combustion of gasoline when $b=1$, and that of ammonia when $b=0$. (b) is the gasoline fraction, on a chemical equivalence basis. It is the fraction of the oxygen consumed by the gasoline.

$$(0.79N_2 + 0.21O_2) + 0.024bC_6H_{11} + 0.28(1-b)NH_3 \Rightarrow (0.93 - 0.14b)N_2 + (0.42 - 0.288b)H_2O + 0.144bCO_2$$

Lower heating value(LHV) energy yield: $(88.7 - 4b)$ kJ (1)

The gasoline fraction on a chemical equivalence basis and LHV energy basis are very nearly the same. From here on, all reference to the gasoline fraction is done in the LHV basis, expressed as a percentage of the total fuel energy input. Table 1 summarizes the properties of ammonia and gasoline. Ammonia is characterized by a higher knock resistance, lower flame speed, and narrower flammable equivalence ratio range than hydrocarbon fuels. The flame speed results and equivalence ratio range are for pressure=1 bar and temperature=300 °F. The octane rating for ammonia is probably an estimate, because ammonia is unlikely to burn well under the standard conditions used for research and motor octane tests.

Table 1 The properties of ammonia and gasoline

Property	Ammonia	Gasoline
Lower heating value	18.6 MJ/kg	42.45 MJ/kg
Octane rating	>130 RON[a]	92.4 $(R+M)/2$
Specific gravity	0.64 g/cm	0.73 g/cm
Stoich. A/F mass ratio	6.1	14.5
Flammable/equiv. ratio range[b]	0.72–1.46	0.55–4.24 (JP-4)
Flame speed at stoichiometric[b]	12 cm/s	52 cm/s (JP-4)

[a]Reference 16.
[b]Reference 14.

Engine and Equipment Properties

Engine. This study uses a cooperative fuel research (CFR) engine [17] with an 83.4 mm cylinder bore diameter, 114.3 mm stroke, and 625 cm^3 swept volume displacement. The cylinder head features two diametrically opposed ports at the edge of the combustion chamber. One port was used for the single Champion 3405-2 spark plug, and the other was used for the 7061B Kistler cylinder pressure transducer. The piston and cylinder head are flat, which gives the combustion chamber a pancake shape. This configuration is expected to be somewhat more knock prone, and characterized by a longer burn duration and exaggerated heat loss than those which might be achieved with a centrally located igniter and hemispherical combustion chamber.

Supercharged CFR engine operation was achieved with the use of compressed air. An actual intake compressor would have required a power takeoff, or a turbocharger would have raised the cylinder pressure during the exhaust stroke [18], thus lowering the brake and indicated thermal efficiencies a bit. No effort was made to correct for the supercharge work.

Definitions for the Pressure Signal Analysis. Equation (2) shows how the apparent heat release is calculated from cylinder pressure P and instantaneous volume V. The effective ratio of specific heats γ is calculated for each operating point from cylinder pressure and volume during compression between 50 deg and 30 deg before top center (BTC), and its typical value is 1.3.

$$dQ = \frac{\gamma}{\gamma - 1} PdV + \frac{1}{\gamma - 1} VdP \tag{2}$$

Equation (3) shows how the apparent mass fraction burned (MFB_a) is calculated from the apparent heat release. The integral starts at 30 deg BTC, where none of the operating points showed significant combustion despite a spark advance of often more than 30 deg. The total heat release is normalized to the total fuel LHV energy input per cycle Q_t.

$$MFB_a(\theta) = \frac{1}{Q_t} \int_{-30\ \mathrm{deg}}^{\theta} dQ \tag{3}$$

The MFB_a curves in Fig. 4 asymptote to an end value less than 1, typically 0.7, mostly because of the heat irreversibly lost to the combustion chamber boundaries. The 10% burn angle is the crank angle at which a MFB_a curve reaches 10% of its end value, near the lower corner of each curve. 90% burn occurs, where the curve reaches 90% of its end value, near the upper corner of each curve.

Sixty cycles were acquired for each operating point. The burn interval is the crank angle range bounded by the 10% and 90% burn angles of the 60-cycle averaged MFB_a curve. The burn duration is the crank angle width of the burn interval. The ignition delay is the crank angle distance between the spark and the 10%

burn angle of the 60-cycle averaged MFB_a curve.

The coefficient of variation of the net indicated mean effective pressure ($COV(IMEP_n)$) was used to define roughness. The coefficient of variation is the standard deviation divided by the mean. An engine would appear to be running "rough" when the $COV(IMEP_n)$ is high. Excessive roughness is defined as having a $COV(IMEP_n)$ in excess of 3%. Smooth firing occurs when the $COV(IMEP_n) \leq 3\%$.

Knock was detected in the pressure signal with a high pass filter of unity gain in the passband. The condition for incipient knock was a knock signal amplitude of 10–50 kPa for one or more cycles in a set of 60. Knock-free operation occurs when the knock signal amplitude remains below 10 kPa, which is the threshold for a knock signal that is sufficiently distinguished from noise. A knock signal amplitude of more than 50 kPa was judged to be excessive. Excessive knock was corrected by retarding the spark for operation on gasoline, or by using more ammonia and less gasoline for dual fueled operation.

Fuel Delivery. The gasoline and ammonia were stored in separate tanks, and their mass flows into the engine were controlled and measured independently. Stoichiometric operation was achieved with the use of a standard automotive exhaust gas oxygen sensor, whose characteristics were similar to the one used by Camp and Rachel [19]. The oxygen sensor reference voltage was set at 0.45 V in this study.

For operation on gasoline, the gasoline mass flow was adjusted by a control loop that responded to the oxygen sensor signal. The gasoline input was increased very slowly if a lean condition was sensed, and vice versa.

For operation on ammonia with gasoline, the gasoline mass flow was set manually and adjusted to achieve a particular combustion condition. The gaseous ammonia mass flow was slowly and automatically adjusted in response to the oxygen sensor signal to maintain stoichiometric combustion.

Ignition System. A HyFire 6 A capacitive discharge coil driver and Mallory ignition coil were used. The spark plug gap was set to 0.040 in. and left there for all operating points. The energy delivered by the coil driver to the ignition coil for each spark was nominally 135 mJ, according to the manufacturer.

Engine Intake. The CFR engine intake path consisted of these items, starting at the shop air line and working downstream: two single stage air pressure regulators, an intake air heater, a throttle body with gasoline injector and ammonia gas inlet port, and finally, a 3.5 l intake plenum at the cylinder head inlet.

An elevated intake air temperature was used to vaporize the gasoline and thereby ensure the homogeneity of the intake mixture. The air heater was adjusted such that the air temperature near the throttle body was maintained between 55°C and 60°C for all operating points. The intake mixture temperature near the cylinder head inlet port remained between 41°C and 53°C.

Operating Limits. For gasoline, an increasing spark retard away from maximum brake torque (MBT) was required to avoid knock as the load was increased. The load was increased until the knock limited spark timing reached top center (TC), or until the exhaust gas temperature became hazardous for the exhaust components (about 900°C), whichever occurred first. In either case, further attempts to increase the load beyond that point produced a diminished return on power output, rapidly decreasing efficiency and increasing exhaust gas temperatures.

For operation on ammonia with gasoline, the CFR engine was run at loads ranging from idle up to loads at which the peak firing pressures approached 100 bars. The maximum load for operation on ammonia/gasoline was not limited by knock or any other consideration besides firing pressure. Speeds of 1000 rmp, 1300 rmp, and 1600 rpm were used.

Load Characteristics. Load is represented by the net indicated mean effective pressure ($IMEP_n$). In certain load regions, the engine ran throttled, while in others it was supercharged, and normally aspirated wide open throttle (WOT) occurs at $IMEP_n \approx 700$ kPa. Idle occurs at $IMEP_n \approx 150$ kPa. Supercharged operation involves intake pressures greater than ambient, and is represented by points where $IMEP_n > 700$ kPa.

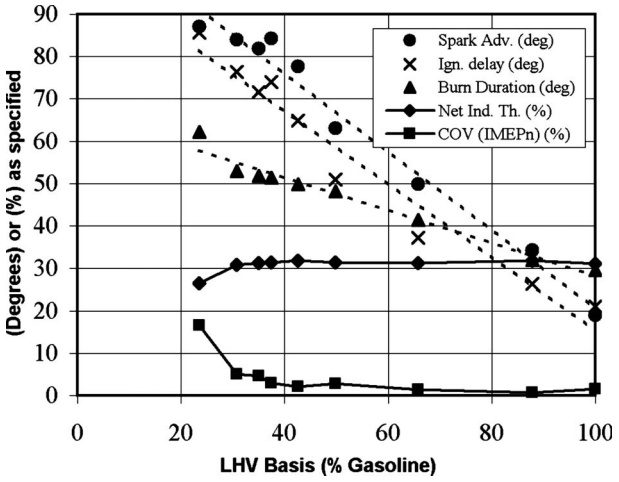

Fig. 1 Fuel mix sweep, 8:1, 1600 rpm, and $IMEP_n \sim 550$ kPa

Results and Discussion

Basic Features of Substituting Ammonia for Gasoline. The fuel mix sweep featured in Fig. 1 was obtained while running the CFR engine at 8:1, 1600 rpm, and intake pressure=80 kPa. Stoichiometric operation on 100% gasoline is featured in the rightmost data points. For operation on gasoline only at this load, MBT spark timing could not be maintained without causing the engine to knock. The gasoline input was gradually replaced with ammonia until MBT spark timing could be maintained without knock, and this occurred at 87% gasoline/13% NH_3. This MBT knock limit is one of the target combustion conditions, according to which the fuel mix was mapped as a function of load, speed, and compression ratio. The MBT knock limit sets the upper limit on the gasoline input per cycle for knock-free, smooth firing with MBT spark timing.

The replacement of gasoline with ammonia was increased further, until an excessive roughness was observed. The $COV(IMEP_n)$ curve has a large, flat region, but the roughness increased rapidly with further replacement of gasoline with ammonia beyond the corner in the curve. The corner occurred where the $COV(IMEP_n)$ was about 3%. The net indicated thermal efficiency decreases significantly when the $COV(IMEP_n)$ exceeds 5% or 10%. The rough limit is defined as the fuel mix at which the $COV(IMEP_n)$ reaches 3% in the region where further replacement of gasoline with ammonia causes the $COV(IMEP_n)$ to run away to higher values. The rough limit is the other target combustion condition, according to which the fuel mix was mapped. The rough limit sets the lower limit on the gasoline input per cycle for knock-free, smooth firing with MBT spark timing. The rough limit in Fig. 1 was at 37% gasoline/63% NH_3.

The fuel mix sweep featured in Fig. 2 was obtained at 12:1 compression ratio, 1600 rpm, and intake pressure=50 kPa. Operation on 100% gasoline at this light load was still possible at 12:1, but the spark had to be retarded far from MBT to avoid knock. The fuel mix was 58% gasoline/42% NH_3 at the MBT knock limit, and 53% gasoline/47% NH_3 at the rough limit.

The fuel mix sweep featured in Fig. 3 was obtained at 9:1 compression ratio, 1000 rpm, and WOT. It is a higher load and lower speed than that used in either Fig. 1 or Fig. 2. Operation on

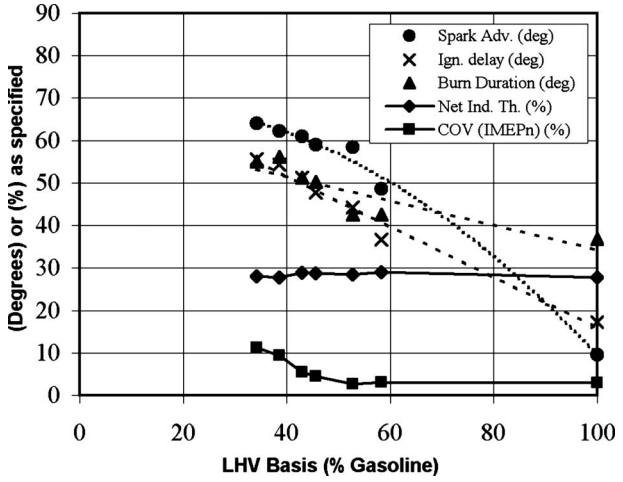

Fig. 2 Fuel mix sweep, 12:1, 1600 rpm, and IMEP$_n$~260 kPa

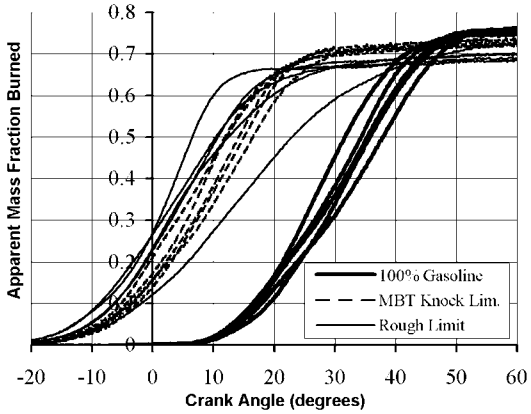

Fig. 4 Apparent mass fraction burned curves for the first five individual cycles showing the effect of ammonia at 9:1, 1000 rpm, and WOT

100% gasoline required that the spark be retarded substantially from MBT to avoid knock. The fuel mix at the MBT knock limit was 57% gasoline/43% NH_3, and the fuel mix at the rough limit was 18% gasoline/82% NH_3. The COV(IMEP$_n$) did not increase to large values with further fuel substitution beyond the rough limit but a leading edge could still be found. The COV(IMEP$_n$) curve in Fig. 3 shows that the rough limit is more difficult to find when the permitted substitution of gasoline with ammonia is high.

This leading edge could not always be found for supercharged operation at 1000 rpm and 1300 rpm. If the COV(IMEP$_n$) remained at or below 2%, then the gasoline was turned off completely. Otherwise the engine was operated with a target COV(IMEP$_n$) of 2.5%–3% for all further results obtained at the rough limit.

Figure 4 shows the apparent mass fraction burned curves for the first five individual cycles of the 100% gasoline, MBT knock limit, and rough limit points from Fig. 3. The 100% gasoline MFB$_a$ curves show retarded combustion timing because the spark had to be retarded away from MBT avoid knock. The MFB$_a$ curves for the MBT knock limit are grouped tightly and show the optimum combustion timing for best efficiency. Ammonia enables the use of MBT spark timing without knock, and this is why the ammonia is responsible for shifting the MFB$_a$ curves back near TC for the MBT knock limit.

The MFB$_a$ curves for operation at the rough limit are grouped a bit more loosely about both sides of the optimum placement. This combustion timing variation causes the cycle-to-cycle IMEP$_n$ variation. A small cycle-to-cycle ignition delay variation gets amplified into a larger combustion timing variability as the burning progresses because the burn rate is affected by the expansion of the cylinder contents during combustion. An excessive cycle-to-cycle combustion timing variability, which occurs when insufficient combustion promoter is used, cannot be compensated with spark advance. A measurable efficiency loss can occur if the overall combustion timing variability becomes too large.

Figure 5 shows the pressure-volume trace for the first five individual cycles of the 100% gasoline and rough limit points from Fig. 3. These pressure-volume curves correspond also to the 100% gasoline and rough limit MFB$_a$ curves in Fig. 4.

The pressure-volume curves for 100% gasoline show the effect of retarded combustion timing, which was required to avoid knock. The net indicated thermal efficiency was 28.4% for gasoline, whereas for the rough limit the net indicated thermal efficiency was 33%.

The rough limit pressure-volume curves show a more ideal shape that reflects the use of MBT spark timing and combustion closer to TC. The pressure variation from cycle to cycle is caused by the variation of combustion timing at the rough limit. The IMEP$_n$ differed little among the individual cycles despite the large

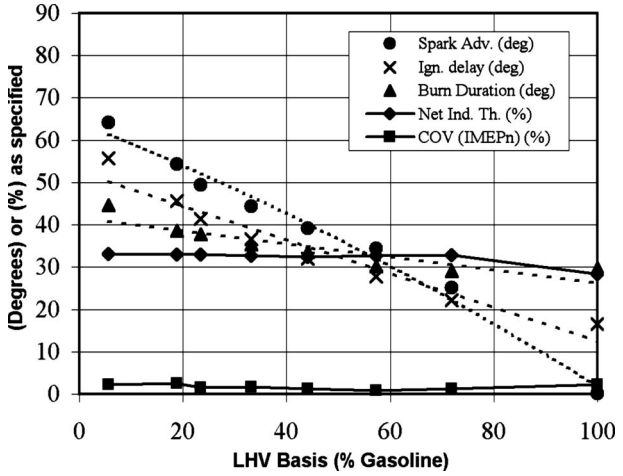

Fig. 3 Fuel mix sweep, 9:1, 1000 rpm, WOT, and IMEP$_n$ ~700 kPa

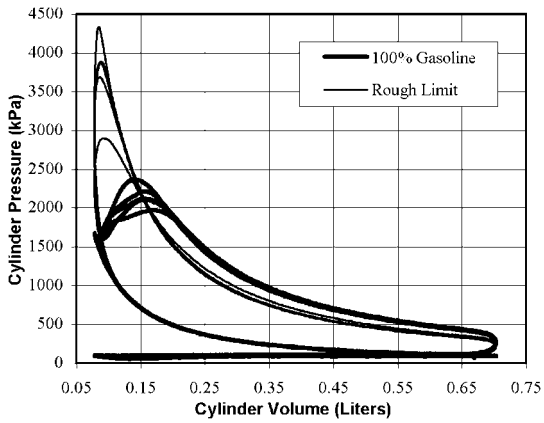

Fig. 5 Cylinder pressure curves for the first five individual cycles showing the effect of ammonia at 9:1, 1000 rpm, and WOT. The rough limit fuel mix was 82% NH_3/18% gasoline.

Table 2 The average MBT spark timing at the rough limit

	1000 RPM	1300 RPM	1600 RPM
8:1	62 deg	70 deg	76 deg
10:1	55 deg	69 deg	71 deg
12:1	51 deg	59 deg	65 deg

variation in the peak pressure above and below the optimum. The highest $IMEP_n$ yield for an individual cycle within the set of 60 cycles occurred for 1 cycle with a peak pressure near 3700 kPa.

Fuel Substitution at the Rough Limit. Operation at the rough limit seeks to maximize the extent to which gasoline is replaced with ammonia. The usefulness of ammonia as a fuel was characterized by how compression ratio, speed, and load affect the fuel composition at the rough limit. The CFR engine was run at the rough limit for 8:1, 10:1, and 12:1, at speeds of 1000 rpm, 1300 rpm, and 1600 rpm. A load sweep was done for each of the nine combinations of compression ratio and speed. Each load sweep started with marginal operation at idle with a fuel mix of nearly all gasoline. As the load was increased, the ammonia input was increased, and the gasoline input and spark advance required only small adjustments to maintain operation at the rough limit. With small corrections made to the gasoline input at each point, the engine could have been run at a constant MBT spark timing for each whole load sweep. The average spark advance for the load sweeps is shown in Table 2. All spark timing numbers are in degrees BTC.

The gasoline input per cycle for all points in a load sweep was not much larger, and often smaller, than that required at idle. The rough limit was not found for 14:1 and 16:1, for reasons that are explained later.

Figures 6 and 8 show the fuel mix at the rough limit. They contain the same data, but Fig. 6 groups the data by compression ratio, whereas Fig. 8 groups it by speed. The gasoline input was shut off completely whenever the rough limit could not be found. The points, for which the rough limit could not be found, are a special case, and these points depart discontinuously from the overall rough limit fuel mix trends. The gasoline could not be shut off for any points at 1600 rpm. The points for which the gasoline was shut off were not used to calculate the trend curves for the fuel mix at the rough limit.

The fuel mix at the rough limit has a surprisingly weak dependence on compression ratio, given its strong dependence on load. It was anticipated that combinations of load and compression ratio, for which the compressed charge energy density near TC is the same, would have the same fuel mix at the rough limit. It was expected that the rough limit fuel mix would respond to compression ratio changes as strongly as it did to load changes.

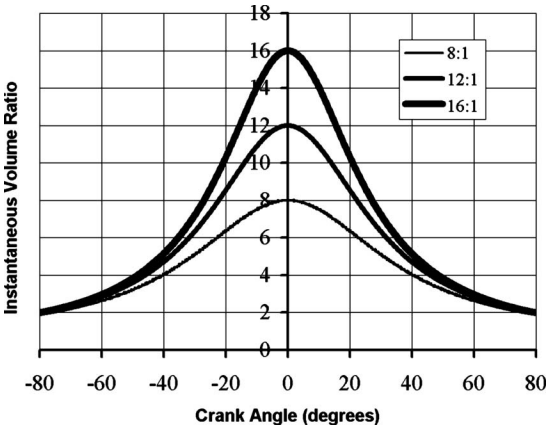

Fig. 7 The instantaneous volume ratio from BC, as a function of crank angle

Figure 7 shows the instantaneous volume ratio through which the charge was compressed from bottom center (BC), as a function of crank angle. Note that the instantaneous volume ratio at 0 deg is the compression ratio. Strong compression ratio trends should be expected for events that occur within ±20 deg. The burn interval obtained for all of the operating points at the rough limit was between about −10 deg and +40 deg crank angle, so much of the burn interval was within that ±20 deg window. Caris and Nelson obtained a similar burn interval for the same compression ratio range [20]. Both the load and the compression ratio contribute multiplicatively to the compressed charge density near TC, where much of the combustion occurred.

Ammonia's long ignition delay places the MBT spark in a crank angle region where the compression ratio has little effect. The MBT spark timing was 50 deg or more for all points at the rough limit. In this crank angle region, the instantaneous compressed charge density is proportional to load and not compression ratio. It appears that the rough limit fuel mix is determined more strongly by the compressed charge density at the spark than by the charge density near TC. The ignitability of the fuel and air mixture at the spark must be more important than the flame propagation rate through the mixture near TC, although it is likely that both contribute to the rough limit fuel mix trends.

Figure 8 shows that the gasoline requirement increases as the

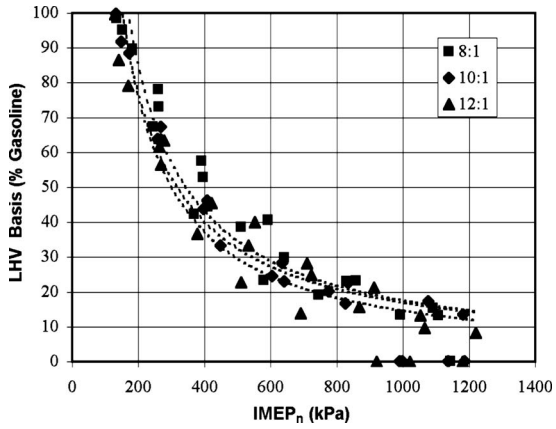

Fig. 6 Fuel mix at the rough limit, grouped by compression ratio

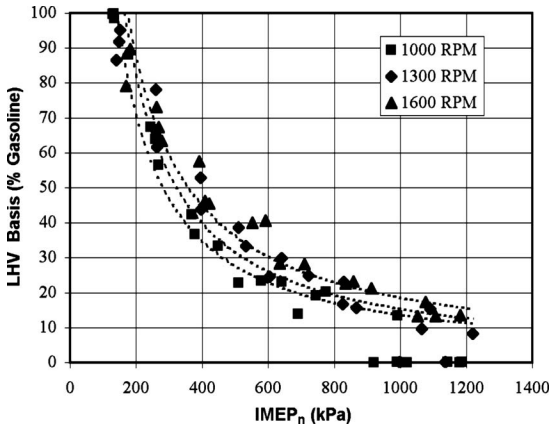

Fig. 8 Fuel mix at the rough limit, grouped by speed

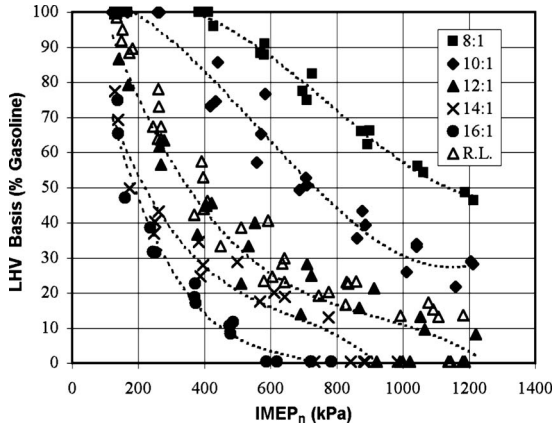

Fig. 9 Fuel mix at the MBT knock limit (solid shapes), all speeds. The hollow triangles are the 8:1 and 10:1 rough limit points from Fig. 6.

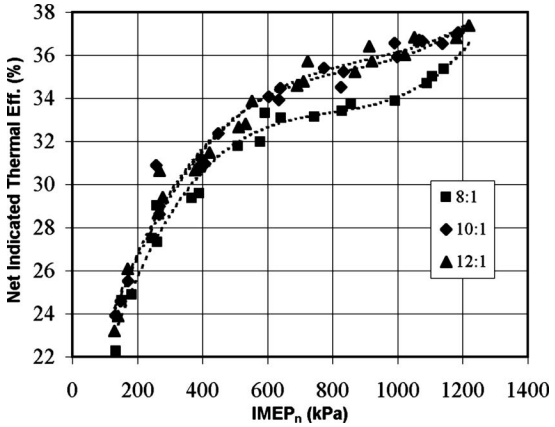

Fig. 10 Net indicated thermal efficiency for operation on ammonia with gasoline at the rough limit, all speeds

engine speed is increased. Longer ignition delay and burn duration occur with increasing speed, which increases the MBT spark advance. The increased MBT spark advance at higher speeds reduces the compressed charge density at the spark. An increased flame speed requirement near TC may also contribute to this trend.

Gasoline could probably be replaced with ammonia to a greater extent if the ignition delay and burn duration could be shortened, thereby increasing the charge compression at the ignition event. Plasma jet ignition reduces the ignition delay by about 10 deg, relative to that obtained with standard spark ignition [21]. Dual ignition also helps [9,16,22,23].

Fuel Substitution at the MBT Knock Limit. The goal of replacing gasoline with ammonia is best served by operation at the rough limit, but testing at the MBT knock limit was also done so that an acceptable fuel mix window could be established. Operation at the MBT knock limit seeks to minimize the replacement of gasoline with ammonia while using MBT spark timing and avoiding knock. An increasing substitution of ammonia for gasoline increases the overall octane rating of the fuel/air mixture.

The rough limit is a hard limit, which means that if not enough gasoline is used, then the engine will operate in an undesirable way that cannot be corrected by changing the spark advance. However, the MBT knock limit is a soft limit. If the gasoline input is greater than that specified by the MBT knock limit, then the spark can be retarded away from MBT to avoid knock, and satisfactory operation can still be achieved as long as the overall combustion timing is not delayed from the optimum by more than about 20 deg. This criterion ultimately limits how far above the MBT knock limit the engine can be run. It also limits the maximum IMEP$_n$ that can be reached when running the engine on gasoline only. For example, the spark must be retarded by 20 deg away from MBT when the engine is run on 100% gasoline at 8:1 compression ratio and IMEP$_n$=750 kPa. The same is true for 10:1 compression ratio and IMEP$_n$=600 kPa.

The solid shapes in Fig. 9 show the fuel mix at the MBT knock limit for different loads and compression ratios. The CFR engine was run at the MBT knock limit at compression ratios of 8:1, 10:1, 14:1, and 16:1, and speeds of 1000 rpm, 1300 rpm, and 1600 rpm. It was already observed that the 12:1 points from Fig. 6 had very little or no margin for error between the MBT knock and rough limits, and so they were used again in Fig. 9. There was insufficient speed dependence in the knock properties of ammonia, gasoline, and air mixtures for a significant speed trend to be shown. For a given compression ratio, the octane requirement goes up as the load is increased. For a given load, the octane requirement goes up as the compression ratio is increased. The fuel mix at the MBT knock limit is strongly dependent on both compression ratio and load because incipient knock generally occurs near peak pressure, and the peak pressure was always within the ± 20 deg window where both the compression ratio and the load have a strong effect on the compressed charge density.

Knock and Rough Limit Crossover. Smooth, knock-free, MBT combustion and the best thermal efficiencies occur when the gasoline content is greater than or equal to the minimum required at the rough limit, and less than the maximum permitted at the MBT knock limit. Figure 9 shows the placement of the rough limit points for 8:1 and 10:1 (hollow triangles) among the MBT knock limit points for all compression ratios.

A crossover, with respect to compression ratio, occurs where the permitted gasoline content at the MBT knock limit becomes less than the required gasoline content at the rough limit. For the compression ratios 8:1 and 10:1, the desired operating window exists below the solid data points for each compression ratio and within or above the region occupied by the hollow triangle points. At 10:1, this window width is about half of that at 8:1. At 12:1, the margin for error between the rough and MBT knock limits is very small or zero, *for all loads and speeds*. At 14:1 and 16:1, the desired operating window has a negative width. It was not possible to add enough gasoline to provide adequate flammability at the spark, without causing knock near TC at 14:1 and 16:1, and these points had a COV(IMEP$_n$) between 4% and 15%. For that reason, 12:1 is considered the upper compression ratio limit for an engine that runs on ammonia and gasoline. However, it is undesirable for an engine to have a vanishingly small margin of error between the MBT knock and rough limits. The fuel mix trends indicate a desired compression ratio of less than 12:1 for an ammonia and gasoline dual fueled spark ignition engine.

Net Indicated Thermal Efficiency Trends. Figures 10 and 11 show the net indicated thermal efficiency for the operation on ammonia with gasoline at the rough and MBT knock limits, respectively. All of the speeds are lumped together. For both limits, there is a significant efficiency gain when the compression ratio is raised from 8:1 to 10:1. There is a diminished return on efficiency to raise the compression ratio above 10:1.

The rough limit 10:1, 12:1 and knock limit 14:1 best fit efficiency curves coincide. There is no clear efficiency gain or loss for the entire compression ratio range from 10:1 to 16:1 when ammonia and gasoline are used in a CFR engine equipped with single ignition. Caris and Nelson found that, at high compression ratios, the burn interval got longer and occurred later as the compression ratio was raised [20]. The trade-off between heat loss and postcombustion expansion ratio is such that the MBT combustion occurs later as the compression ratio is increased. The decreased

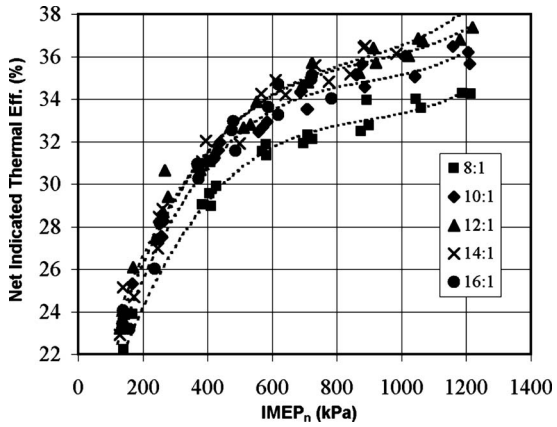

Fig. 11 Net indicated thermal efficiency for operation on ammonia with gasoline at the MBT knock limit, all speeds

combustion space increases the effect of heat loss as the compression ratio is raised, limiting the optimum compression ratio to about 16:1 [20]. In this study, the optimum compression ratio for efficiency was in the range of 10:1–14:1. The greater heat loss, caused by the CFR engine's pancake geometry, is probably why the maximum efficiency occurred at a lower compression ratio.

Figure 12 shows the net indicated thermal efficiency for 100% gasoline, 7:1–10:1 compression ratios, and all speeds. This low compression ratio range was used for gasoline because the knock constraint disallowed operating the CFR engine on gasoline near WOT for compression ratios above 10:1. No matter what fuel is used, the pumping losses due to throttling reduce the net indicated thermal efficiency for low IMEP$_n$. However, for gasoline the net indicated thermal efficiency also goes down for high IMEP$_n$ because the knock constraint requires further spark retard away from MBT with increasing load. The maximum power density and thermal efficiency achieved while operating on gasoline are both inherently knock limited. All of the gasoline operating points required spark timing retarded from MBT to avoid knock when IMEP$_n$ > 400 kPa. In this region, the net indicated thermal efficiency is better for ammonia with gasoline than for gasoline alone.

Error Analysis. Repeated measurements of the fuel mix at the rough limit show that the error is 3% for all nonzero results. For example, if the fuel mix is 40% gasoline, it is $(40 \pm 3)\%$. The main source of uncertainty was the determination of the COV(IMEP$_n$). During continuous monitoring, the COV(IMEP$_n$) would fluctuate typically between 2% and 4% when the average value was 3%. This uncertainty accounts for most of the fuel mix error, because the slope of the COV(IMEP$_n$) curves in Figs. 1 and 2 are about 0.5 near the rough limit.

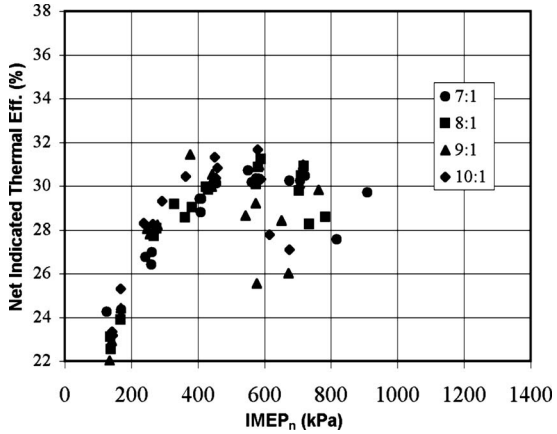

Fig. 12 Net indicated thermal efficiency for gasoline, all speeds

Repeated measurements of the fuel mix at the MBT knock limit show that the error is 10%. For example, if the fuel mix is 60% gasoline, it is $(60 \pm 10)\%$. The main source of error was the determination of the MBT spark timing, which had an uncertainty of 5 deg. The location of the MBT spark also changed as the fuel mix was varied, and there was a judgment call at each point about whether the knock occurred on the advanced or retarded side of MBT as the spark timing was varied.

Repeated measurements of the net indicated thermal efficiency show that the error is 1% for all results using ammonia with gasoline for all IMEP$_n$, and also for gasoline at IMEP$_n$ < 600 kPa. For example, when the net indicated thermal efficiency is 30%, it is $(30 \pm 1)\%$. The error is about evenly split between the fuel flow measurement uncertainty and the set-to-set fluctuation of the average IMEP$_n$.

For gasoline, when IMEP$_n$ > 600 kPa, the error is 3%. When the spark is retarded substantially to avoid knock, the variation of the knock limited spark timing is responsible for most of the variability in the net indicated thermal efficiency.

All of the net indicated thermal efficiency curves for ammonia/gasoline at 10:1–16:1 compression ratio are very closely spaced. Only the 8:1 curves are significantly different, and are lower than the curves for 10:1–16:1.

The net indicated thermal efficiency for gasoline shows a weak compression ratio trend. For the most part, the effect of increasing compression ratio was offset by the need to retard the spark further away from MBT to avoid knock.

The net indicated thermal efficiency for ammonia with gasoline at both the rough limit and the MBT knock limit becomes significantly better than the net indicated thermal efficiency for gasoline when the IMEP$_n \geq 600$ kPa and 700 kPa for 10:1 and 8:1 compression ratios, respectively.

Conclusions

Most of the gasoline burned by spark ignition engines can be replaced with ammonia when the IMEP$_n \geq 400$ kPa. A spark ignition engine cannot generally give acceptable performance while fueled by ammonia alone. However, there is a fuel mix map, as a function of load, speed, and compression ratio, which specifies the degree to which gasoline can be replaced with ammonia while yielding acceptable operation. The combustion promoter requirement is not constant, and it goes down with increasing load, and up with increasing speed. The compression ratio has a surprisingly weak effect on the combustion promoter requirement at the rough limit.

A similar, rescaled map of the rough limit should be expected when other fuels are used as combustion promoters for ammonia, or when a different engine design is used, such as the use of dual ignition or a different combustion chamber shape. There is no single, constant ratio of gasoline to ammonia that works appropriately for every combination of load and speed. For that reason, the combustion promoter and the ammonia should be stored in separate tanks and metered into the engine separately.

A compression ratio of 10:1 is recommended for the ammonia and gasoline dual fueled engine. There is a diminished return on the thermal efficiency, and also on minimizing the gasoline use at the rough limit, for compression ratios above 10:1. The margin of error between the MBT knock and rough limits becomes small when the compression ratio is increased to 12:1. Improved combustion chamber geometry should yield a slightly higher optimal compression ratio for efficiency, and also for the knock and rough limit crossovers, probably near 12:1 for both.

Ammonia's knock resistance allows engine operation at much

higher $IMEP_n$ than is possible with the use of gasoline alone. The efficiencies at high load are also better, where comparable, when ammonia is used because MBT spark timing can be used with ammonia at high $IMEP_n$. The use of ammonia with gasoline enables the continued use of MBT spark timing at combinations of load and compression ratio, which are inaccessible to gasoline.

Acknowledgment

This research is supported by the Fannie and John Hertz Foundation. The authors acknowledge Donald Gillespie for providing the initial idea to pursue this project, which then took on a life of its own with his continued guidance and help. Jeff Balis at Waukesha Engine is acknowledged for providing technical info about the CFR engine.

References

[1] Walters, L., Wade, D., and Lewis, D., 2002, "Transition to a Nuclear/Hydrogen Energy System," *World Nuclear Association Annual Symposium*, London.
[2] Schultz, K. R., 2003, "Use of the Modular Helium Reactor for Hydrogen Production," *World Nuclear Association Annual Symposium*, London, Sept. 3–5.
[3] Gray, J. T. Jr., Dimitroff, E., Meckel, N. T., and Quillian, R. D. Jr., 1966, "Ammonia Fuel-Engine Compatibility and Combustion," SAE Paper No. 660156.
[4] Pearsall, T. J., and Garabedian, C. G., 1967, "Combustion of Anhydrous Ammonia in Diesel Engines," SAE Paper No. 670947.
[5] Bro, K., and Pedersen, P. S., 1977, "Alternative Diesel Engine Fuels: An Experimental Investigation of Methanol, Ethanol, Methane, and Ammonia in a DI Diesel Engine With Pilot Injection," SAE Paper No. 770794.
[6] Mozafari, A. V., 1988, "Prediction and Measurement of Spark Ignition Engine Characteristics Using Ammonia and Other Fuels," Ph.D. thesis, University of London, London.
[7] Cooper, J. R., Crookes, R. J., Mozafari, A., and Rose, J. W., 1991, "Ammonia as a Fuel for the IC Engine," *Proceedings of the International Conference on Environmental Pollution*, Lisbon.
[8] Starkman, E. S., Newhall, H. K., Sutton, R., Maguire, T., and Farbar, L., 1966, "Ammonia as a Spark Ignition Engine Fuel: Theory and Application," SAE Paper No. 660155.
[9] Cornelius, W., Huelmantel, W. L., and Mitchell, H. R., 1965, "Ammonia as an Engine Fuel," SAE Paper No. 650052.
[10] Zavka, M., and Massagno, L., 1938, U.S. Patent No. 2,140,254.
[11] Kroch, E., 1945, "Ammonia, A Fuel for Motor Buses," J. Inst. Pet., **31**, pp. 213–223.
[12] Kroch, E., and Restieau, J. L., 1945, French Patent No. FR897181.
[13] Starkman, E. S., and Samuelsen, G. S., 1967, "Flame Propagation Rates in Ammonia-Air Combustion at High Pressure," *Eleventh Symposium on Combustion*, pp. 1037–1045.
[14] Verkamp, F. J., Hardin, M. C., and Williams, J. R., 1967, "Ammonia Combustion Properties and Performance in Gas Turbine Engines," *Eleventh Symposium on Combustion*, pp. 985–992.
[15] Luthra, S. P., Mathur, H. B., Narasimhan, T. N., and Natarajan, B., 1971, "Experimental Investigation Into the Suitability of Ammonia as a Spark Ignition Engine Fuel," J. Inst. Eng. (India), Part AG, **51**, pp. 235–241.
[16] Hodgeson, J. W., 1973, "Is Ammonia a Transportation Fuel for the Future?" ASME Paper No. 73-ICT-65.
[17] ASTM, 1956, *ASTM Manual for Rating Motor Fuels by Motor and Research Methods*, American Society for Testing Materials, Philadelphia, PA.
[18] Hu, X., and Lawless, P. B., 2001, "Predictions of On-Engine Efficiency for the Radial Turbine of a Pulse Turbocharged Engine," SAE Technical Paper No. 2001-01-1238.
[19] Camp, J., and Rachel, T., 1975, "Closed Loop Electronic Fuel and Air Control of Internal Combustion Engines," SAE Paper No. 750369.
[20] Caris, D. F., and Nelson, E. E., 1959, "A New Look At High Compression Ratio Engines," SAE Trans., **67**, pp. 112–124.
[21] Dale, J. D., and Oppenheim, A. K., 1981, "Enhanced Ignition for I.C. Engines With Premixed Gases," SAE Paper No. 810146.
[22] Graves, R. L., and Hodgeson, J. W., 1975, "Emissions From an Ammonia Fueled Spark Ignition Engine," ASME Paper No. 75-WA/DGP-2.
[23] Graves, R. L., Hodgeson, J. W., and Tennant, J. S., 1974, "Ammonia as a Hydrogen Carrier and its Application in a Vehicle," *Hydrogen Economy Miami Conference*, pp. 755–764.

Method and Detailed Analysis of Individual Hydrocarbon Species From Diesel Combustion Modes and Diesel Oxidation Catalyst

Manbae Han[1]
e-mail: manbaeh@umich.edu

Dennis N. Assanis
e-mail: assanis@umich.edu

University of Michigan,
1231 Beal Avenue,
Ann Arbor, MI 48109

Timothy J. Jacobs
Texas A&M University,
321 EPB 3123 TAMU,
College Station, TX 77843

Stanislav V. Bohac
University of Michigan,
1231 Beal Avenue,
Ann Arbor, MI 48109
e-mail: sbohac@umich.edu

An undiluted exhaust hydrocarbon (HC) speciation method, using flame ionization detector gas chromatographs, is developed to investigate HC species from conventional and low-temperature premixed charge compression ignition (PCI) combustion pre- and post-diesel oxidation catalyst (DOC) exhaust. This paper expands on previously reported work by describing in detail the method and effectiveness of undiluted diesel exhaust speciation and providing a more detailed analysis of individual HC species for conventional and PCI diesel combustion processes. The details provided regarding the effectiveness of the undiluted diesel exhaust speciation method include the use of a fuel response factor for HC species quantification and demonstration of its linearity, detection limit, accuracy, and precision. The listing of individual HC species provides not only the information needed to design surrogate exhaust mixtures used in reactor tests and modeling studies but also sheds light on PCI combustion and DOC characteristics. Significantly increased engine-out concentrations of acetylene, benzene, and toluene support the theory that net soot reduction associated with PCI combustion occurs due to the reduction of soot formation (as opposed to increased soot oxidation). DOC oxidation behavior differs depending on the combustion characteristics, which change exhaust species and temperature.
[DOI: 10.1115/1.2900728]

Keywords: gas chromatograph or gas chromatography (GC), response factor (RF), hydrocarbon (HC) speciation, diesel oxidation catalyst (DOC), premixed charge compression ignition (PCI)

1 Introduction

More stringent emission regulations of diesel vehicles have necessitated the simultaneous reduction of particulate matter (PM) and nitrogen oxides (NO_x), which can be achieved by developing new combustion strategies such as low-temperature premixed charge compression ignition (PCI) combustion and implementing aftertreatment devices. Compared to conventional diesel combustion, PCI combustion uses higher flow rates of exhaust gas recirculation (EGR) and later combustion timings via alterations to injection timing. Increased levels of EGR significantly lower combustion temperatures and assist the creation of a more premixed burn by extending ignition delay. The adjusted fuel injection timing also promotes longer ignition delays and lower combustion temperatures since much of the combustion takes place later in engine expansion stroke, compared to conventional diesel combustion [1–5]. On the other hand, PCI is prone to produce more hydrocorbon (HC) and carbon monoxide (CO) than conventional combustion [1–5] due to lower flame temperature, and local over leaning. Thus, a diesel oxidation catalyst (DOC) is necessary to oxidize these increased HC and CO concentrations [5]. Detailed HC speciation of engine-out and DOC-out HC exhaust is necessary for a more complete understanding and future development of both PCI combustion and the DOC.

Previous HC speciation of diesel exhaust has been of that produced from conventional combustion, with very little speciation analysis provided for PCI combustion. Such studies have reported the comparison of organic compounds from PCI combustion and their DOC oxidation behavior. Sluder et al. [6] found that different organic species in engine-out exhaust (e.g., formaldehyde, 1,3-cyclopentadiene, and benzene) increase at different rates when combustion is changed from a conventional to a PCI strategy, indicating a change in the fundamental combustion process. However, only light HC species were identified. Mogi et al. [7] speciated engine-out and DOC-out HCs across DOCs with different amounts of platinum (Pt) loading. Higher loading increased conversion efficiency of CO, formaldehyde, acetaldehyde, benzene, and benzo(a)pyrene, but only conventional diesel exhaust was investigated and only several HC species were measured. A more detailed quantitative analysis of PCI HC species will provide greater insight into the direction for future development of PCI combustion and DOCs.

The challenge of diesel exhaust HC speciation arises from the large HC size range of diesel fuel (C_6–C_{26}) (gasoline fuel has approximately the range of C_4–C_{10}) and the need to sample semivolatile HCs. There has been a significant amount of gasoline exhaust HC speciation [8–17] and the analysis method of it has been well established by Phases I and II of the Auto/Oil Air Quality Improvement Research Program (AQIRP) [18,19]. On the other hand, semivolatile HC analysis has not been well established. Furthermore, most diesel exhaust speciation [20–28] uses diluted exhaust gas, which simulates the natural processes that occur between ambient air and engine exhaust [29,30]. The conditions in the dilution tunnel may condense mid- and high boiling HC onto the PM. Unless the HCs are extracted from the PM and analyzed, these HCs will be inaccessible for speciation by gas chromatography (GC). Since these semivolatile species are necessary for the full understanding of PCI combustion and DOC de-

[1]Corresponding author.

Contributed by the Internal Combustion Engine Division of ASME for publication in the JOURNAL OF ENGINEERING FOR GAS TURBINES AND POWER. Manuscript received March 23, 2007; final manuscript received January 28, 2008; published online April 29, 2008. Review conducted by Thomas W. Ryan III.

velopment, an undiluted diesel engine exhaust HC speciation method was developed and is described in detail herein.

Bohac et al. [31] classified HC species composition as combustion products and DOC oxidation products to understand conventional diesel and PCI combustion modes and DOC oxidation behavior [5]. Two GCs were instrumented to identify and quantify HC species using flame ionization detectors (FIDs). The undiluted and heated exhaust gas sampling extends the highest carbon number of HC species by minimizing semivolatile HC fraction condensing on the PM. Raw exhaust gas was sampled through a series arrangement of a Tenax™ TA tube (for semivolatile HCs analyzed by GC-2) and a Tedlar bag (for volatile HCs analyzed by GC-1). About 80 HC species are quantitatively identified from the engine-out and DOC-out locations of PCI combustion exhaust. Speciated engine-out and DOC-out HCs were grouped into bins according to number of carbon atoms per HC molecule and functional HC groups such as alkenes+alkynes, aromatics, nonmethane alkanes, and methane.

This paper expands on the work reported by in Ref. [31] by providing through GC method description and by offering a more detailed analysis of individual HC species from PCI combustion exhaust. The paper demonstrates the effectiveness and validity of the direct raw exhaust gas sampling method including the determination of the fuel response factor (RF) for HC species quantification and its linearity, detection limit, accuracy, and precision. Listing of individual HC species compositions provides not only the information needed to design surrogate exhaust mixtures used in reactor tests and modeling studies but also sheds light on combustion and DOC characteristics. Acetylene, benzene, and toluene HC species are known as initiative and intermediate species to form soot during the combustion process [32]. These species' concentrations are carefully compared for each combustion mode. Furthermore individual HC species oxidation behaviors through the DOC are compared and analyzed.

2 Experimental Setup

A 1.7 L four-cylinder automotive diesel engine was used which has four valves per cylinder common rail fuel injection, a variable geometry turbocharger, a poppet-style EGR control valve, an EGR cooler, and a flapper-style intake throttle mounted downstream of the compressor to enable high rates of EGR. Low sulfur Swedish diesel fuel is used in this study. A Pt based production DOC of 0.5 L was mounted 1 m from the turbine outlet. A more detailed description of the engine and test fuel is provided in Refs. [5,33].

Raw exhaust gas from the engine was sampled by a sample cart, which is composed of (i) heated sample line to introduce exhaust gas into Tenax™ adsorbent trap (ii) Tenax™ trap (iii) mass flow controller and micropump and (iv) Tedlar bag. The heated sample line is maintained at a temperature of 190°C and the Tenax™ tube to right before Tedlar bag at 60°C in order to avoid water condensation. The heated PM filter at 190°C is located in the exhaust sample line to avoid collection of exhaust PM on the Tenax™ trap and protect emission bench.

The sample bag captures light HCs (C_1–C_8) and the Tenax trap captures semivolatile hydrocarbons ($>C_8$) although a HC overlap of about two carbon numbers exists for each. One GC is used to analyze the sample bag (GC-1) while another GC is used to analyze the Tenax trap (GC-2). Both GCs are Shimadzu GC-17A models with FIDs that are used to measure HC carbon atoms (parts per million carbon (ppm C_1)). All samples are analyzed within two hours of collection. During the time from collection to analysis sample bags are kept in lightproof outer bags and Tenax traps are sealed and kept in a refrigerator. More detailed description of GC setups and sampling conditions is listed in Tables 1 and 2.

Table 1 GC-1 instrument parameters

Sample loop	Stainless steel, 1.0 ml
Carrier gas	He (99.999% purity)
Injection port	250°C; 135 kPa g constant head pressure At start of temperature program, 5.7 ml/min column flow 25.0 ml/min split flow (4:1 split ratio) 3.0 ml/min purge flow
Precolumn	2 m × 0.32 mm, deactivated fused silica (Restek)
Main column	60 m × 0.32 mm, 1 μm dimethyl-polylsiloxane (Restek Rtx-1)
Oven temperature	−80°C at start; 20°C/min to −50°C, hold 2.5 min; 6°C/min to 236°C
Detector	FID, 300°C H_2 at 60 kPa g (99.999% purity); air at 50 kPa g (zero 0.1 grade) He make-up gas at 70 kPa g (99.999% purity)

3 Method for Raw Diesel Exhaust HC Speciation

Results from GC-1 and GC-2 are combined to obtain an overall speciation of exhaust HCs. This method yields more than 210 exhaust HC species and identifies 70% of total carbon mass through this study. Results from both GCs are combined for analysis of HC profiles from combustion mode and DOC activity studies. For the fuel used in this study, the HCs of carbon number of C_1–C_8 are partially oxidized fuel. Most HCs whose carbon number is above C_9 are unburned fuel. If a C_9–C_{19} HC is detected in the exhaust but not in the fuel, it is partially oxidized fuel and if a C_9–C_{19} HC is detected in the exhaust and in the fuel, it is considered unburned fuel.

3.1 Volatile HC Analysis (GC-1) Method for Raw Diesel Exhaust HC. GC-1 method for volatile HC species analysis was developed based on well known procedures of AQIRP in the early 1990s [18,19]. For GC-1 analysis, FID is calibrated during each sample run by adding a known concentration of propane, which does not occur in the exhaust sample, to each sample. Elution times are converted to *n*-alkane based retention indices and then HC identification is accomplished using a retention library developed by performing runs with known HC samples and from the literature [18,19]. The library for the GC-1 method is available in the literature [18,19].

3.2 Semivolatile HC Analysis (GC-2) Method for Raw Diesel Exhaust HC. For development of GC-2 method, mixtures of standard *n*-alkanes, iso-alkanes, aromatics, some alkenes, C_1, C_2-naphthalenes, cyclo-alkanes, and low sulfur Swedish diesel fuel were prepared by diluting with *n*-hexane to identify and quantify the individual HC species: retention times and *n*-alkane based indices for identification and average fuel RF for quantifi-

Table 2 GC-2 instrument parameters

Carrier gas	He (99.999% purity)
Injection port	250°C; constant velocity program (75–111 kPa g head pressure) 1.2 ml/min column flow (18 cm/s) 24.0 ml/min split flow (20:1 split ratio) 1.8 ml/min purge flow
Precolumn	2 m × 0.32 mm, deactivated fused silica (Restek)
Main column	60 m × 0.32 mm, 1 μm dimethyl-polylsiloxane (Restek Rtx-1)
Oven temperature	40°C, hold for 5 min; 6°C/min to 280°C, hold 15 min
Detector	FID, 300°C H_2 at 60 kPa g (99.999% purity); air at 50 kPa g (zero 0.1 grade) He make-up gas at 70 kPa g (99.999% purity)

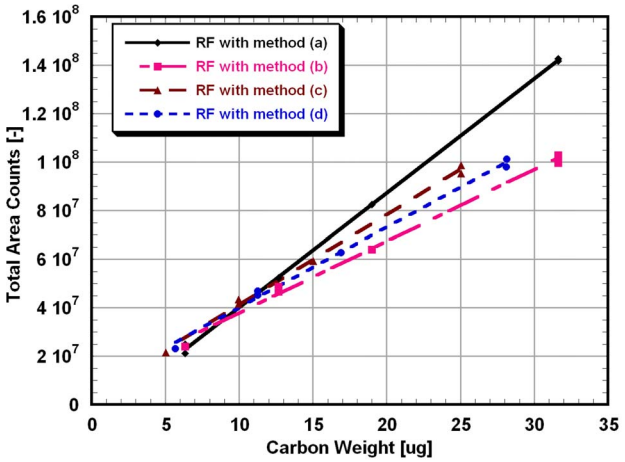

Fig. 1 RFs with respect to different calculation methods

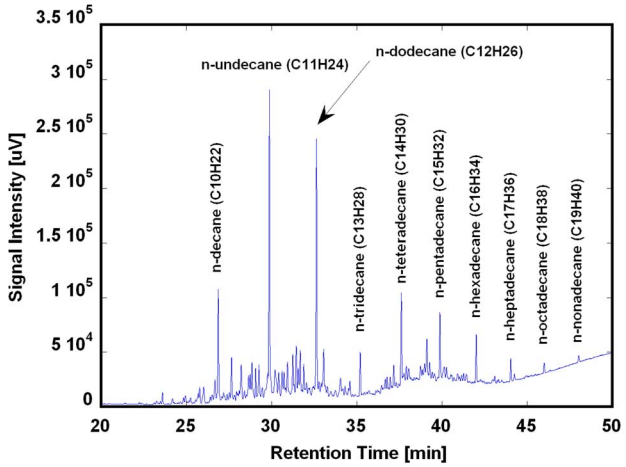

Fig. 2 Low sulfur Swedish diesel fuel chromatogram analyzed by GC-2; oven temperature profiles: 40°C for 5 min, 6°/min for 43.33 min, 300°C for 0 min; FID=300°C, injection port=250°C; split ratio 20:1, total flow=27 ml/min, and column flow =1.2 ml/min

cation. The retention times and retention indices of the standard HC compounds are saved as a retention library to identify exhaust constituents on a comparative basis. The library for the GC-2 method contains about 110 species.

3.2.1 Fuel RF Determination. Fuel RF is calculated to quantify the individual HC species' concentration of GC-2 based on C_1, which is reported as ppm C_1. Even though each HC group has a different value of RF [34], in practice, if all HCs have similar RFs within acceptable tolerance level, the same RF can be used to simplify the quantification. Hammerle et al. [23] showed that the RFs for polyaromatic HC (PAH, e.g., acenaphthalene) are lower than those of *n*-alkanes and the RFs of alkyl-PAHs (e.g., 1-methylnaphthalene) are nearly the same as those of *n*-alkanes. Of the PAHs, only acenaphthalene existed but not significant amounts in their diesel fuels, and the RF for all HC species in fuel was considered to be equivalent on a per unit weight of carbon. Low sulfur Swedish diesel fuel analysis based on ASTM D1319 test at Paragon Laboratory (Livonia, MI) showed that more than 95% is comprised of saturates and only 3% aromatics [31]. This suggests that low sulfur Swedish diesel fuel RF can be treated as equivalent on a per unit weight of carbon basis. Furthermore, the low sulfur Swedish diesel fuel analysis in GC shows that acenaphthalene is not present in the fuel.

Several different experiments to calculate the fuel RF were conducted to estimate the HC quantity in terms of carbon weight or concentration. The four ways to calculate RF were (a) RF calculated by dividing the sum of all the peak areas from fuel chromatogram (using syringe injection to the GC injection port) by the carbon weight of the fuel sample, (b) RF calculated by dividing the sum of all the peak areas desorbed from a Tenax™ trap by the carbon weight of the fuel sample, (c) RF calculated by dividing the sum of the peak areas from C_9 to C_{14} desorbed from a Tenax™ trap by the carbon weight of the fuel sample in this same carbon number range, and (d) RF calculated by dividing the sum of the peak area from C_9 to C_{13} desorbed from a Tenax™ trap by the carbon weight of the fuel sample in the same carbon number range. A fuel solution (*n*-hexane to fuel 10:1 vol/vol) was prepared, and at least three different volumes of solution were injected into the GC injection port and fuel vaporizer (Supelco) by 1 μl syringe. The syringe injection reproducibility was within 5% for the *n*-alkane solution. A least mean square linear regression method was used to calculate the RF for each method (Fig. 1). Fuel solution injected by syringe is vaporized in the glassware of fuel vaporizer where N_2 purging gas is flowing at a temperature of 120°C. Vaporized fuel HCs are adsorbed in Tenax™ tube. As shown in Fig. 1, the RF is highest for (a) method and lowest for (b) method.

The temperature of fuel vaporizer, 120°C, was not enough to vaporize all fuel HCs due to less volatility of high molecular weight HCs in the fuel, especially higher than C_{15} carbon number range. Exhaust gas flows out through the sample line of 190°C, where the exact RF must lie in between (a) and (b) method RF results. Additional experiments showed that there exist (1) transfer loss, ~12%, during sampling and desorption process and (2) temperature loss, ~8%, caused by the vaporization ability of semivolatile HCs. The estimated RF is 80% of method (a) RF. This estimated RF is only 2% different with RF of the method (d). Therefore, the method (d) RF is used for all experiments in this study.

3.2.2 Linearity and Detection Limit of GC-2. *N*-dodecane was selected as a representative HC compound to check the linearity of GC-2 method because it is one of the two most abundant compounds in the low sulfur Swedish diesel fuel. The solution of *n*-dodecane diluted with *n*-hexane was prepared with the concentration range of 0.1–30.3 μg C/μl. Using 1 μl syringe, 0.1 μl of solution was manually injected into injection port of the GC three times each concentration. The relative standard deviation of each concentration was less than 10%. Within a ±5% tolerance level of linearity, the linearity of GC-2 is guaranteed to within 0.5 ppm C_1 for lean conventional and lean PCI combustion modes and to within 3 ppm C_1 for rich PCI combustion mode. The detection limit of GC-2 was also calculated based on the ratio of signal to noise (3:1) [35], ~4 ppb C_1 for both lean conventional and lean PCI combustion modes and ~25 ppb C_1 for rich PCI combustion mode. The reason why rich PCI has a different detection limit is the necessary shorter sampling time of the exhaust gas. Rich PCI combustion produces much higher HC concentration [5,31,33] than the other combustion modes and total carbon mass deposited on the Tenax™ tube must stay within the carbon mass range of fuel RF calibration (Fig. 1).

3.2.3 Low Sulfur Fuel Analysis. Within 1 h of elution, 169 GC peaks were detected from the analysis of low sulfur Swedish diesel fuel (Fig. 2). However, diesel fuel is known to contain 1000 of individual species. Consequently, each GC peak probably represents a mixture of major and minor components. However, because of the relatively low concentrations of coeluted HC species, no attempt was made to distinguish them by using different GC columns or different detectors such as a mass spectrometer. Using

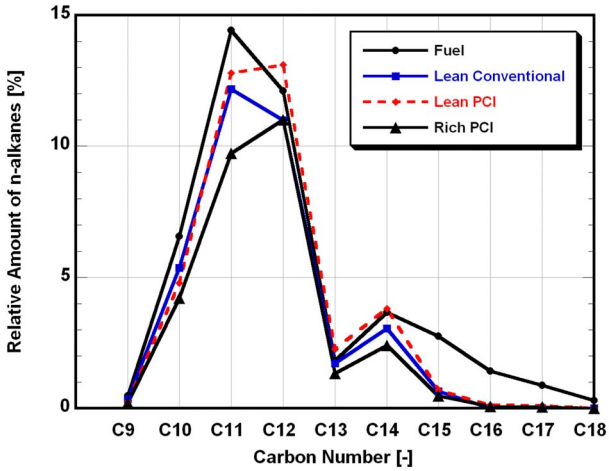

Fig. 3 Distribution of *n*-alkanes in the fuel and DOC-out exhaust samples for each combustion mode

syringe injection of fuel solution to GC injection port, the range of carbon numbers observed in low sulfur Swedish diesel fuel is approximately C_8-C_{19}.

The carbon mass lying in between C_9 and C_{13} is $77.7\pm0.7\%$ with 95% confidence level and carbon mass lying in between C_9 and C_{14} is $88.0\pm0.4\%$ with 95% confidence level. The species in the fuel were observed at the 0.01% of total carbon mass level and above. A total of 169 peaks in the fuel were resolved and the most abundant species in the fuel, *n*-alkanes, accounted for $40.5\pm0.1\%$ of the total fuel carbon mass with 95% confidence level. A total of 44 compounds were identified, which corresponds to 60% of the total carbon weight.

3.2.4 Exhaust Gas Analysis. Siegl et al. [28] used a dilution tunnel to sample DOC-out exhaust gas and compared the carbon number distribution of *n*-alkanes in the exhaust to the fuel (C_9-C_{26}) and found that the composition rapidly dropped off after C_{13} and *n*-alkanes higher than C_{15} did not appear in the exhaust. In this study, engine-out and DOC-out exhaust gas was directly sampled at 1 m downstream from the turbocharger outlet while the sample line was maintained at 190°C. This method showed that *n*-alkanes of DOC-out exhaust composition smoothly dropped off to C_{17} (Fig. 3), which was close to the highest carbon number of the fuel (C_{19}). It is supposed that the dilution causes condensation of mid- and high boiling point HC species onto PM; thus, undiluted speciation as described here is necessary if one wishes to capture a more complete analysis diesel engine exhaust HC species.

The concentration of each HC species in the GC-2 was calculated by the conversion of carbon weight to concentration by applying the ideal gas law. The volume of 1 mol of exhaust gas is obtained by applying the ideal gas law to the sampling condition of 100 kPa and 60°C.

3.2.5 Accuracy and Precision of GC Methods. The accuracy and precision of the currently developed GC methods are validated in terms of the repeatability for precision and recovery rate for accuracy. The recovery rate is defined as the ratio of GC analyzed total HC (THC) concentration divided by THC concentration analyzed by the engine exhaust emission bench.

The engine-out exhaust gas is sampled three times at 2000 rpm and 2.0 bar brake mean effective pressure (BMEP) on different days (Table 3) as a base study. Here, it is important to note that the repeatability of a HC emission measurement by emission bench or GC method indicates the repeatability of the combined engine/analyzer system at that operating condition. Repeatability of HC

Table 3 Engine operating condition and criteria for a base study of the engine-out HC repeatability measured by an emission bench and GC method

Combustion mode	Lean conventional diesel combustion
Engine rpm/load	2000 rpm/2.0 bar BMEP
Injection timing (pilot, main)	15 deg BTDC, 3 deg ATDC
Rail pressure	300 bar
Nominal fuel quantity (pilot, main)	1.2 mm^3, 8.5 mm^3
Space velocity (h^{-1})	71,000
Temperature of catalyst in ($T_{cat\text{-}in}$)	274 ± 1.5°C
$T_{cat\text{-}in}$ standard deviation	Less than 0.5°C
$HC_{cat\text{-}in}$ COV	Less than 5%
EGR rate	$29.2\pm2.0\%$

emissions analyzed by emission bench is compared to the one analyzed by GC method. Bench emission results are reference values. As shown in Table 4, THC analyzed by GC method has a COV of less than 6%, while the emissions bench shows a COV of 7%, which means that the GC method of THC analysis is equivalent to emission bench's repeatability. Three different HC groups repeatability shows COV of less than 8%, and the major HC species among the exhaust HC were selected and their repeatability varied from 2% to 14%. This repeatability level is consistent with the results of Ref. [36], less than 20%.

The THC recovery rate lies higher than 80%. In the combustion modes and DOC study, the recovery rates showed 80–95%. All the recovery rates lie in the result of Ref. [36], whose recovery rate was between 80 and 120%. In addition, the correlation between emission bench and GC analyzed HC concentration was very strong, $R^2>0.99$ (Fig. 4). The correlation of DOC conversion efficiency was also investigated during a set of DOC degreening experiments [37]. The conversion efficiency correlation during the DOC degreening showed the strong correlation ($R^2>0.99$) (Fig. 5). The repeatability, recovery rate, and strong correlation results confirm that the GC methods in this study are reasonable and successful.

4 HC Emission Profiles From Conventional and PCI Diesel Combustion Modes and HC Oxidation Behavior Through a DOC

Using the HC speciation methods described above, three operating modes are investigated: lean conventional, lean PCI, and rich PCI combustion (Table 5). A production-type Pt based DOC of 0.5 L was tested to see if the elevated HC and CO concentration of lean PCI and rich PCI combustion can be oxidized. Rich PCI also reduces NO_x and PM emissions and maintains quiet operation, and it is designed to generate at least 5% CO for aggressive lean NO_x trap (LNT) regeneration. More information of bench emission results are found in Refs. [5,31].

4.1 Engine-Out HC Emissions. Appendix A shows the major exhaust HC species present in each combustion mode; only 40 species represent more than 75% of the total carbon mass. The HCs that individually account for more than 5% of HC carbon mass are ethene, *n*-undecane, *n*-dodecane, and benzene in decreasing order for conventional combustion; *n*-undecane, *n*-dodecane, ethene, methane, and acetylene for lean PCI; and methane, acetylene, ethene, benzene, *n*-dodecane, and *n*-undecane for rich PCI. These species may be used as a synthetic surrogate for real exhaust in reactor tests or models.

Engine-out HCs from each combustion mode were speciated and grouped into bins according to number of carbon atoms per HC molecule (Fig. 6). For each bin, lean conventional has the least amount of THCs followed by lean PCI and then rich PCI. In order to look into the relative distribution, the bins, normalized by

Table 4 Summary of a base study of the engine-out HC repeatability measured by an emission bench and GC method (ppm C_1); CL denotes a confidence level

Engine w/		Test 1	Test 2	Test 3	COV	95% CL
THC	E/M bench	816	930	916	7.0%	888 ± 105
	GC-1	183	189	202	5.1%	191 ± 16
	GC-2	532	559	589	5.1%	560 ± 48
	GC total	715	748	791	5.1%	751 ± 64
	Recovery rate	88%	80%	86%		
HC group	Alkenes	136	148	145	4.4%	143 ± 11
	Aromatics	104	110	121	7.7%	112 ± 15
	Alkanes	234	243	255	4.3%	244 ± 18
Individual HC compounds	Acetylene	22.7	21.3	24.6	7.2%	22.9 ± 2.8
	Ethene	71.7	69.5	71.7	1.6%	70.8 ± 1.9
	Propene	24.3	24.8	24.3	1.2%	24.5 ± 0.5
	1-butene	13.8	15.1	14.0	4.9%	14.3 ± 1.2
	1,3-butadiene	10.8	10.7	9.2	8.8%	10.2 ± 1.5
	Benzene	17.9	23.1	23.2	14.2%	21.4 ± 5.1
	Toluene	10.1	11.2	11.9	8.2%	11.1 ± 1.5
	n-propylbenzene	8.2	9.7	10.1	10.7%	9.3 ± 1.7
	Methane	13.7	13.2	15.5	8.6%	14.1 ± 2.0
	n-decane	29.8	30.2	32.0	3.8%	30.7 ± 2.0
	n-undecane	64.4	66.7	70.8	4.8%	67.3 ± 5.5
	n-dodecane	55.2	57.1	59.6	3.9%	57.3 ± 3.7
	n-tridecane	8.1	9.2	8.5	6.5%	8.6 ± 0.9
	n-tetradecane	10.9	12.8	11.3	8.6%	11.7 ± 1.7

THC, are calculated and plotted in Fig. 7. Lean conventional and lean PCI show a similar trend, but rich PCI has a significantly higher percentage of C_1 and C_2 HCs because of the high yields of methane, ethene, and acetylene (Appendix A). The sum of C_1 and C_2 HCs accounts for 18% of THC of lean conventional, 21% of lean PCI, and 43% of rich PCI. Lean conventional and lean PCI exhaust HCs are composed of 46% and 41% partially oxidized fuel and 54% and 59% of unburned fuel, respectively. On the other hand, rich PCI HCs are composed of 64% of partially oxidized fuel and 36% of unburned fuel. The substantial increase of partially burned fuel portion of rich PCI comes from the relatively higher contribution of C_1 and C_2 HCs. Relative engine-out HC emissions with respect to HC group are summarized in Table 6. For these engine operating conditions, lean conventional combustion has relatively higher amount of alkenes and aromatics than the other two PCI modes. Lean PCI has the highest relative nonmethane alkanes and rich PCI has the highest relative acetylene and methane (Table 6).

Acetylene is known as a soot precursor species and soot can be directly formed from acetylene accumulation [32]. Highly increased concentration of acetylene as combustion mode changes from lean conventional to lean PCI to rich PCI as shown in Appendix A may reflect a limiting of the soot-forming reactions from the decreased combustion temperature and better fuel-air mixing caused by higher EGR rate and strategic injection timing. Aromatic HC species are also believed to be soot precursors [32]. The concentrations of benzene and toluene are increased with combustion mode change, especially at rich PCI. This behavior may also confirm that PCI combustion considerably freezes soot inception reactions. Other soot precursors include C_1 and C_2-naphthalene; although these species exist in the fuel, they individually account

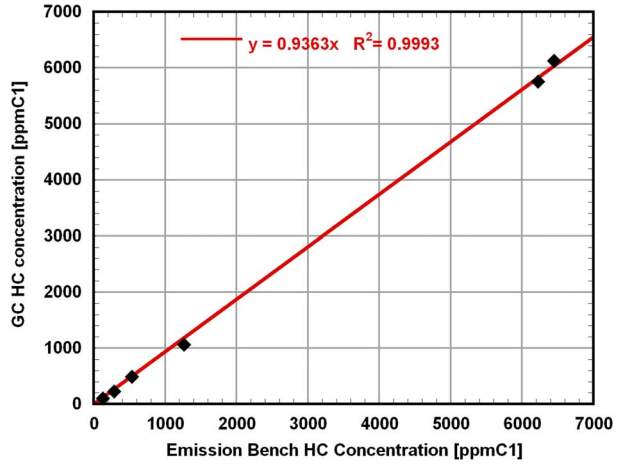

Fig. 4 Correlation between emission bench analyzed HC and GC analyzed HC concentrations from lean conventional, lean PCI, and rich PCI modes

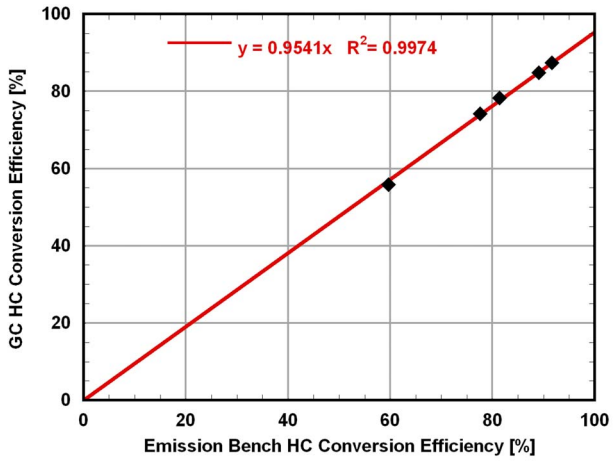

Fig. 5 Correlation between emission bench and GC analyzed HC conversion efficiency during DOC degreening experiments

Table 5 Lean conventional, lean PCI, and rich PCI engine operating modes. Some emissions are listed as pre-DOC/post-DOC; EI-PM is listed only at a pre-DOC level.

	Lean conventional	Lean PCI	Rich PCI
Speed (rpm)	1500	1500	1500
BMEP (bar)	3.94	3.89	3.62
Injection timing (CA BTDC)	5	15	25
Fuel quantity (mg/stroke)	11.2	11.3	13.3
Rail pressure (bar)	300	1,000	1,000
Combustion A/F ratio (−)	28.7	16.2	12.5
EGR (% mass)	32.7	45.3	49.1
EI-NO_x (g/kg fuel)	4.6/4.6	0.26/0.26	0.062/0.062
EI-PM (g/kg fuel)	0.49	0.070	0.008
EI-THC (g/kg fuel)	7.2/1.7	9.4/2.1	38.5/37.2
EI-CO (g/kg fuel)	29.3/0.099	116.5/1.7	669.8/669.3
Comb. noise (dB)	88	89	89
BSFC (g/kW h)	242	249	313
DOC exhaust gas temp. (°C)	290/299	283/348	254/241
Space velocity (h^{-1})	~100,000	~58,000	~54,000

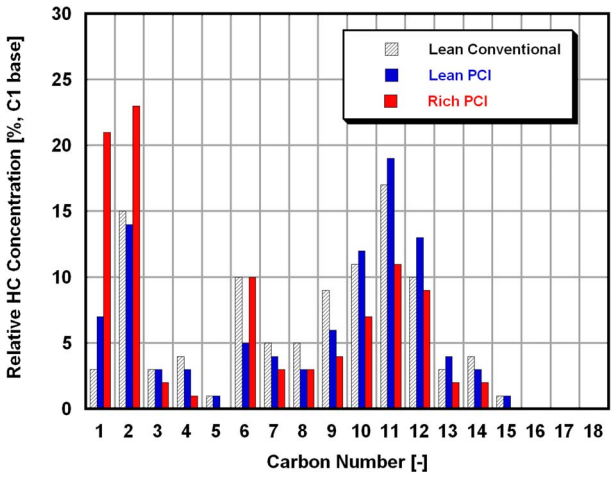

Fig. 7 Engine-out relative HC composition organized by carbon number

for less than 0.4% of the total carbon mass, as determined from the fuel speciation analysis. Furthermore, these naphthalene concentrations remain almost constant regardless of combustion modes. Siegl et al. [28] reported that these HC species amount relative to THC significantly increased during FTP-75 mode with conventional combustion using the fuel similar to 2005 US commercial diesel No. 2, higher sulfur and aromatic HC. The discrepancy between their findings and this study may come from different fuel composition, such as lower aromatic content for low sulfur fuel.

4.2 DOC-Out HC Emissions. The main DOC-out HC species, which account for higher than 5% of carbon mass (Appendix B), are methane, *n*-undecane, and *n*-dodecane for lean conventional and lean PCI, and methane, ethene, acetylene, benzene, *n*-undecane, and *n*-dodecane for rich PCI. Ethene, acetylene, and benzene found in lean conventional and lean PCI are not listed as DOC-out major HC species because acetylene and alkenes have the highest conversion efficiency followed by aromatics. The main DOC-out HC species of rich PCI are the same as engine-out major HC species because of very low conversion efficiency.

Figure 8 shows the relative HC carbon number distribution of DOC-out exhaust, which was normalized by THC. The distributions are similar to those of engine-out exhaust except that methane represents a larger fraction of THC for lean conventional and lean PCI. The carbon number distribution of rich PCI does not significantly change across the catalyst because the DOC is so inactive at this condition. Lean conventional and lean PCI conversion efficiency behaviors with regard to carbon number (Fig. 9) are nearly the same except for C_1 (methane), where lean PCI combustion produces 5% more DOC-out methane than engine-out methane.

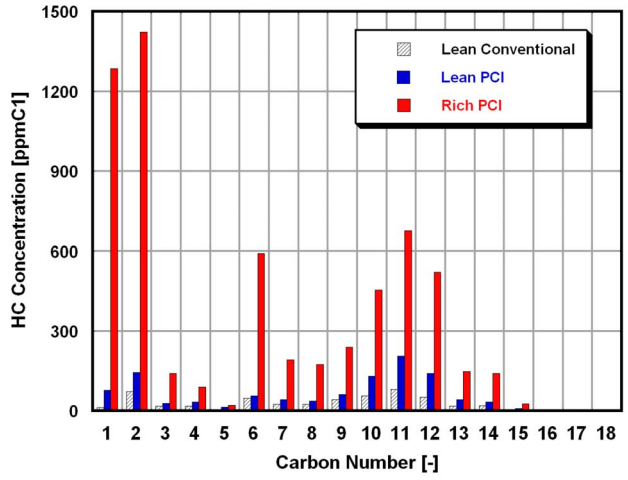

Fig. 6 Engine-out HC concentration versus carbon number

The DOC is not completely inactive for rich PCI combustion but conversion efficiency is severely reduced for the entire carbon number range. The identified HCs from each combustion mode are classified into HC groups. Conversion efficiency is similar for lean conventional and lean PCI combustion (Fig. 10). The DOC is the most effective in oxidizing CO and alkenes+alkynes and then followed by aromatics, nonmethane alkanes, and methane in lean conventional and lean PCI. Rich PCI does not exactly follow this oxidation order. Appendix B shows the conversion efficiency of the 40 major HC species. Acetylene conversion efficiency of rich PCI is still higher than 50%, but alkenes (except 1,3-butadiene with 13% conversion efficiency) have negative conversion efficiency in rich PCI (they are produced in the DOC). Methane is consumed at 4% conversion efficiency.

To prove that rich PCI combustion is ineffective to oxidize HC and CO, several experiments were performed, as discussed in detailed in Ref. [31]. The 2% of O_2 injection before the catalyst did not improve DOC performance. The lowest catalyst-in temperature of 254°C for rich PCI (290°C and 283°C for the other combustion modes) was not a reason for DOC inactivity because the catalyst-in temperature for the lean PCI mode was reduced from 290°C to 220°C by removing insulation from the exhaust but the catalyst remained active. The space velocity of lean PCI and rich PCI is almost the same and not considered to be the reason of DOC ineffectiveness in this condition. The main reason why rich PCI has nearly zero activity in the DOC is believed to be that extremely high concentrations of exhaust CO (greater than 5% by volume) are preferentially chemisorbed on the Pt sites over O and any HC specie, thus inhibiting any reaction between CO and O and/or HC and O.

The alkene yield through the DOC in rich PCI does not occur for lean conventional and lean PCI combustion. Rich PCI has quite different exhaust composition as explained in the previous section as well as quite high concentration of CO (~5.6%) and not enough O_2 (~0.9%) to oxidize all of HC and CO, which possibly makes rich PCI follow a different oxidation path than the other combustion modes. Among alkenes, ethene is the highest increased species in rich PCI combustion. The different trends of alkenes from rich PCI exhaust are believed to come from different

Table 6 Relative engine-out HC compositions of each combustion mode (% C_1 base)

	Alkynes	Alkenes	Aromatics	Methane	Nonmethane alkane
Lean conventional	4%	19%	17%	3%	27%
Lean PCI	5%	16%	13%	7%	31%
Rich PCI	12%	16%	16%	21%	19%

feedgas composition and exhaust gas temperature.

The consumed HCs of rich PCI in DOC may participate in forming oxygenated organic compounds and alkenes by cracking the long chained HC species and partial oxidation due to insufficient oxygen and low temperature [38]. Aldehyde formation through the catalyst has been reported in Refs. [7,39]. A reactor test using simulated methanol exhaust gas passing through an aged Pt/Pd catalyst observed the highest formaldehyde yield that occurred near 240°C, at the onset of light-off for both methanol and CO oxidation [39]. This temperature is close to rich PCI exhaust inlet temperature, 254°C. Mogi et al. [7] showed that a DOC with low oxidation activity promotes the formation of aldehydes in exhaust from a medium duty diesel engine.

Ethane is a by-product of DOC oxidation regardless of combustion mode. Ethane yield was also observed in a pulse flame combustor study utilizing a rich fuel-air mixture [10]. The benzene yield (~1%) in rich PCI primarily results from a competition between benzene production (dealkylation of alkyl-benzene) and benzene oxidation [10]. Negative conversion efficiency of *n*-tetradecane in rich PCI is believed to be caused by releasing the heavy HCs, which are accumulated in the DOC substrate due to a low temperature to oxidize them, not by oxidation process, where *n*-pentadecane showed the same negative conversion efficiency even though it was not listed in major HC compounds.

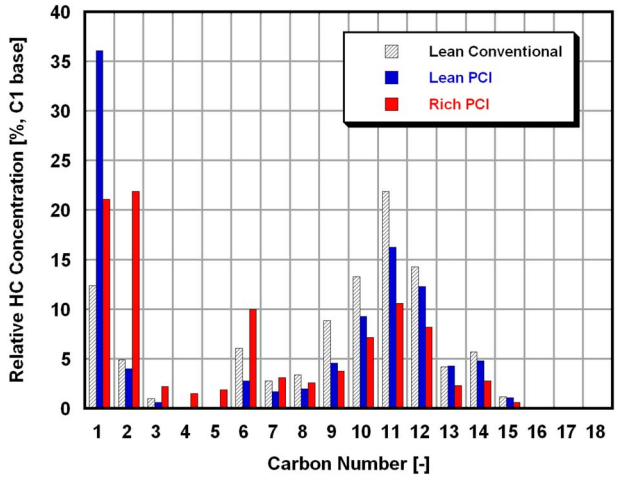

Fig. 8 DOC-out relative HC composition organized by carbon number

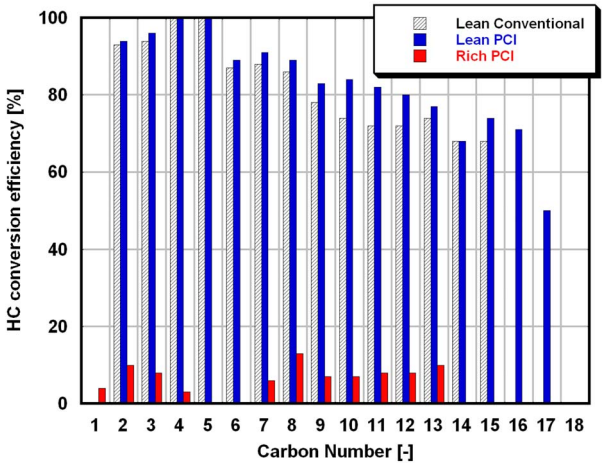

Fig. 9 HC conversion efficiency versus carbon number

5 Conclusions

For a better understanding of combustion modes and DOC activity, a method of direct diesel exhaust HC sampling and speciation technique was developed using GC-FID. The major findings of this work are as follows.

- Undiluted exhaust sampling is preferred to the dilution tunnel sampling because it reduces condensation of semivolatile HCs onto PM during the dilution process. This method increases the maximum carbon number from C_{15} to C_{17} and exhaust composition smoothly dropped off to C_{17} rather than rapidly after C_{13}–C_{15}. Engine emission repeatability measured by commercial emission bench and GC method are comparable and recovery rate is higher than 80%. The quantification limit of GC-1 and GC-2 is 0.1 ppm C_1 for lean conventional and lean PCI and is 0.5 ppm C_1 for rich PCI. The GC-FID method used in this study is believed to be successful and reasonable.
- As combustion mode changes from lean conventional to lean PCI to rich PCI, engine-out concentrations of acetylene, benzene, and toluene increase, which indicate a limiting of soot formation.
- When combustion mode is changed to rich PCI, methane and acetylene join ethene, *n*-undecane, and *n*-dodecane as major species of engine-out HC emissions. These species could be used in a synthetic exhaust used in reactor tests or modeling studies.
- The DOC differently behaves during rich PCI operation as

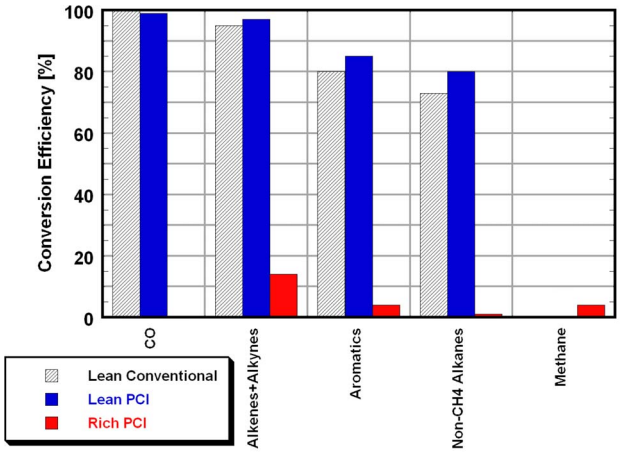

Fig. 10 Conversion efficiency of CO, alkenes+alkynes, aromatics, nonmethane alkanes, and methane

compared to the lean conventional and lean PCI cases. This shows that catalyst behavior can be highly dependent on both feedgas composition and operating temperature. Aldehyde analysis is recommended to prove the hypothesis of alhehyde formation through the DOC for rich PCI.

Acknowledgment

The authors are thankful for the technical and financial support provided by the General Motors Collaborative Research Laboratory at the University of Michigan. At GM, Dr. John Pinson and Mr. Patrick Szymkowicz offered a great deal of guidance and Dr. Keith Olson and Dr. Jong-Hwan Lee provided many technical insights. At the University of Michigan, Dr. Sergei Chernyak at the Department of Environmental Health Science is thanked for his excellent advice on the subject of GC and organic chemistry. Mr. William Northrop is thanked for his advice and analysis of catalyst formulation. Dr. Alex Knafl, Mr. Steve Busch, and Mr. Alberto López are also thanked for their support and many helpful discussions.

Nomenclature

A/F = air to fuel ratio
ASTM = American Society for Testing and Materials
ATDC = after top dead center
BSFC = brake specific fuel consumption
BTDC = before top dead center
COV = coefficient of variation
EI = emission index
FTP = federal test procedure
Pd = palladium
Tenax™ TA = a porous polymer resin based on 2,6-diphenylene oxide

Appendix A: Engine-Out Major HC Compounds From Diesel Combustion Modes

			Lean conventional		Lean PCI		Rich PCI	
HC compounds	RT (min)	RI (−)	Conc. (ppm C_1)	% of carbon	Conc. (ppm C_1)	% of carbon	Conc. (ppm C_1)	% of carbon
Methane	2.650	100.0	13.2	2.7%	78.1	7.4%	1285.9	21.0%
Ethene	2.933	156.6	55.5	11.3%	88.9	8.4%	681.8	11.1%
Acetylene	3.083	186.6	17.3	3.6%	55.6	5.3%	740.1	12.1%
Propene	5.241	290.9	16.3	3.3%	24.9	2.3%	117.7	1.9%
1-butene	10.508	392.3	6.4	1.3%	12.2	1.2%	33.6	0.5%
1,3-butadiene	10.716	396.0	7.1	1.4%	11.9	1.1%	43.1	0.7%
Benzene	14.449	653.2	24.7	5.0%	24.4	2.3%	479.9	7.8%
1,1-DMcyclopentane+ 3-Mhexane	15.307	675.8	3.3	0.7%	4.4	0.4%	14.2	0.2%
t-1,3,-DMcyclopentane	15.774	688.1	3.7	0.7%	6.9	0.7%	22.4	0.4%
Toluene	18.599	761.8	8.4	1.7%	16.2	1.5%	112.0	1.8%
Unidentified	19.299	780.1	3.2	0.6%	3.5	0.3%	18.6	0.3%
Unidentified	19.649	789.2	3.5	0.7%	6.4	0.6%	21.0	0.3%
2-Moctane+*m*,*p*-xylene	22.465	867.3	3.4	0.7%	5.1	0.5%	31.1	0.5%
o-xylene	23.265	889.7	5.1	1.0%	6.8	0.6%	31.5	0.5%
Fuel peak No. 16	25.107	945.4	4.4	0.9%	5.2	0.5%	16.7	0.3%
n-propylbenzene	25.407	954.6	8.0	1.6%	13.5	1.3%	49.7	0.8%
3-Mnonane	26.023	973.6	3.9	0.8%	5.1	0.5%	19.6	0.3%
1-decene	26.490	987.9	6.3	1.3%	5.5	0.5%	33.4	0.5%
1,2,4-TMbenzene+ *t*-butylbenzene	26.698	994.3	5.1	1.0%	10.1	1.0%	36.9	0.6%
n-decane	26.882	1000.0	17.1	3.5%	39.1	3.7%	135.4	2.2%
1-*M*-4-sopropylbenzene+ 1,2,3-TMbenzene	27.657	1026.0	6.4	1.3%	14.6	1.4%	49.9	0.8%
Fuel peak No. 40	28.232	1045.3	5.8	1.2%	13.5	1.3%	43.3	0.7%
n-butylbenzene+ 1,4-DEbenzene	28.648	1059.2	3.5	0.7%	7.1	0.7%	22.2	0.4%
Fuel peak No. 45	28.856	1066.2	3.4	0.7%	4.0	0.4%	29.7	0.5%
Fuel peak No. 46	29.065	1073.2	4.4	0.9%	9.8	0.9%	33.8	0.6%
1,4-DM-2-Ebenzene	29.273	1080.2	5.7	1.2%	14.3	1.3%	48.2	0.8%
n-undecane	29.865	1100.0	36.8	7.5%	95.0	9.0%	312.0	5.1%
1,2-DM-3-Ebenzene	30.206	1112.3	3.6	0.7%	8.1	0.8%	28.2	0.5%
Fuel peak No. 54	30.423	1120.2	4.1	0.8%	10.2	1.0%	33.3	0.5%
Fuel peak No. 55	30.623	1127.4	3.6	0.7%	8.6	0.8%	28.9	0.5%
Fuel peak No. 58	30.931	1138.5	4.7	1.0%	12.6	1.2%	41.8	0.7%
Fuel peak No. 59	31.240	1149.7	5.5	1.1%	12.2	1.2%	43.4	0.7%
Fuel peak No. 61	31.448	1157.2	7.0	1.4%	18.4	1.7%	57.8	0.9%
Cyclodecane	31.681	1165.7	4.9	1.0%	13.0	1.2%	42.5	0.7%
Fuel peak No. 65	31.890	1173.2	3.2	0.6%	8.3	0.8%	26.1	0.4%
n-dodecane	32.631	1200.0	32.7	6.6%	91.0	8.6%	358.1	5.8%
Fuel peak No. 74	33.056	1216.6	5.0	1.0%	13.9	1.3%	44.7	0.7%
n-tridecane	35.198	1300.0	5.2	1.0%	14.4	1.4%	45.6	0.7%
Fuel peak No. 105	37.164	1381.6	2.6	0.5%	5.3	0.5%	21.6	0.4%
n-tetradecane	37.606	1400.0	8.4	1.7%	14.2	1.3%	67.1	1.1%

(1) Methane to 1,3-butadiene are analyzed in GC-1 and their retention times are also referred from GC-1. The other HC species are the results from GC-2. (2) RT denotes retention time, and RI denotes retention index. (3) *M*: methyl, DM: dimethyl, TM: trimethyl, E: ethyl, and DE: diethyl. (4) Oven temperature profiles: 40°C for 5 min, 6 deg/min for 43.33 min, 280°C for 15 min; FID=300°C, injection port=250°C. Split ratio 20:1, total flow=27 ml/min, and column flow=1.2 ml/min.

Appendix B: Conversion Efficiency of Major HC Compounds From Diesel Combustion Modes

Concentration (ppm C_1) HC compounds	Lean conventional			Lean PCI			Rich PCI		
	Pre	Post	Eff. (%)	Pre	Post	Eff. (%)	Pre	Post	Eff. (%)
Methane	13.2	13.1	1%	78.1	82.4	−5%	1285.9	1237.7	4%
Ethene	55.5	3.4	94%	88.9	4.0	96%	681.8	876.2	−29%
Acetylene	17.3	0.0	100%	55.6	0.0	100%	740.1	351.8	52%
Ethane	0.0	1.7	−∞	0.0	4.5	−∞	0.0	57.7	−∞
(RT=3.150 min of GC-1)									
Propene	16.3	1.0	94%	24.9	1.4	94%	117.7	121.6	−3%
1-butene	6.4	0.0	100%	12.2	0.0	100%	33.6	36.8	−10%
1,3-butadiene	7.1	0.0	100%	11.9	0.0	100%	43.1	37.6	13%
Benzene	24.7	3.9	84%	24.4	3.8	85%	479.9	483.0	−1%
1,1-DMcyclopentane+ 3-Mhexane	3.3	0.6	82%	4.4	0.4	90%	14.2	13.3	6%
t-1,3,-DMcyclopentane	3.7	0.6	83%	6.9	0.6	92%	22.4	18.5	18%
Toluene	8.4	1.2	86%	16.2	1.6	90%	112.0	104.8	6%
Unidentified	3.2	0.7	77%	3.5	0.9	76%	18.6	12.3	34%
Unidentified	3.5	0.7	80%	6.4	0.7	89%	21.0	16.5	21%
2-Moctane+*m*,*p*-xylene	3.4	0.0	100%	5.1	0.1	97%	31.1	17.5	44%
o-xylene	5.1	1.3	74%	6.8	1.1	84%	31.5	22.7	28%
Fuel peak No. 16	4.4	0.8	83%	5.2	0.7	86%	16.7	14.6	13%
n-propylbenzene	8.0	1.5	81%	13.5	1.5	89%	49.7	41.9	16%
3-Mnonane	3.9	1.1	73%	5.1	1.3	74%	19.6	19.2	2%
1-decene	6.3	1.7	73%	5.5	1.1	80%	33.4	14.6	56%
1,2,4-TMbenzene+ *t*-butylbenzene	5.1	1.2	77%	10.1	1.5	85%	36.9	36.4	1%
n-decane	17.1	4.6	73%	39.1	6.4	84%	135.4	125.5	7%
1-M-4-isopropylbenzene+ 1,2,3-TMbenzene	6.4	1.7	73%	14.6	2.4	83%	49.9	45.7	8%
Fuel peak No. 40	5.8	1.5	74%	13.5	2.1	84%	43.3	38.3	11%
n-butylbenzene+ 1,4-DEbenzene	3.5	0.9	75%	7.1	1.3	82%	22.2	22.3	0%
Fuel peak No. 45	3.4	1.0	71%	4.0	1.6	60%	29.7	28.3	5%
Fuel peak No. 46	4.4	1.3	71%	9.8	1.9	81%	33.8	31.0	8%
1,4-DM-2-Ebenzene	5.7	1.4	75%	14.3	2.2	85%	48.2	44.9	7%
n-undecane	36.8	10.3	72%	95.0	17.1	82%	312.0	290.2	7%
1,2-DM-3-Ebenzene	3.6	0.9	74%	8.1	1.4	83%	28.2	25.5	10%
Fuel peak No. 54	4.1	1.2	71%	10.2	1.9	81%	33.3	31.3	6%
Fuel peak No. 55	3.6	0.9	75%	8.6	1.4	84%	28.9	26.5	8%
Fuel peak No. 58	4.7	1.2	74%	12.6	2.1	83%	41.8	38.9	7%
Fuel peak No. 59	5.5	1.5	72%	12.2	2.3	81%	43.4	37.0	15%
Fuel peak No. 61	7.0	1.9	72%	18.4	3.3	82%	57.8	52.0	10%
Cyclodecane	4.9	1.4	71%	13.0	2.5	80%	42.5	39.6	7%
Fuel peak No. 65	3.2	0.9	71%	8.3	1.6	80%	26.1	26.2	0%
n-dodecane	32.7	9.3	72%	91.0	17.5	81%	358.1	328.4	8%
Fuel peak No. 74	5.0	1.5	69%	13.9	3.0	79%	44.7	40.3	10%
n-tridecane	5.2	1.5	72%	14.4	3.0	79%	45.6	39.7	13%
Fuel peak No. 105	2.6	0.8	69%	5.3	1.7	67%	21.6	20.3	6%
n-tetradecane	8.4	2.6	69%	14.2	5.1	64%	67.1	71.6	−7%

(1) Methane to 1,3-butadiene are analyzed in GC-1 and their retention times are also referred from GC-1. The other HC species are the results from GC-2. (2) Ethane is a by-product through DOC reaction. (3) *M*: methyl, DM: dimethyl, TM: trimethyl, E: ethyl, and DE: diethyl. (4) Oven temperature profiles: 40°C for 5 min, 6 deg/min for 43.33 min, 280°C for 15 min; FID=300°C, injection port=250°C. Split ratio 20:1, total flow=27 ml/min, and column flow=1.2 ml/min.

References

[1] Kimura, S., Aoki, O., Ogawa, H., Muranaka, S., and Enomoto, Y., 1999, "New Combustion Concept for Ultra-Clean and High-Efficiency Small DI Diesel Engines," SAE Paper No. 1999-01-3681.

[2] Kimura, S., Aoki, O., Kitahara, K., and Aiyoshizawa, E., 2001, "Ultra-Clean Combustion Technology Combining a Low-Temperature and Premixed Combustion Concept for Meeting Future Emission Standards," SAE Paper No. 2001-01-0200.

[3] Akihama, K., Takatori, Y., Inagaki, K., Sasaki, S., and Dean, A., 2001, "Mechanism of the Smokeless Rich Diesel Combustion by Reducing Temperature," SAE Paper No. 2001-01-0655.

[4] Shimazaki, N., Tsurushima, T., and Nishimura, T., 2003, "Dual Mode Combustion Concept with Premixed Diesel Combustion by Direct Injection Near Top Dead Center," SAE Paper No. 2003-01-0742.

[5] Jacobs, T., Bohac, S., Assanis, D., and Szymkowicz, P., 2005, "Lean and Rich Premixed Compression Ignition Combustion in a Light-Duty Diesel Engine," SAE Paper No. 2005-01-0166.

[6] Sluder, C., Wagner, R., Lewis, S., and Storey, J., 2004, "Exhaust Chemistry of Low-NO_x, Low-PM Diesel Combustion," SAE Paper No. 2004-01-0114.

[7] Mogi, H., Tajima, K., Hosoya, M., and Shimoda, M., 1999, "The Reduction of Diesel Engine Emissions by Using the Oxidation Catalysts of Japan Diesel 13 Mode Cycle," SAE Paper No. 1999-01-0471.

[8] Jackson, M., 1978, "Effect of Catalytic Emission Control on Exhaust Hydrocarbon Composition and Reactivity," SAE Paper No. 780624.

[9] Siegl, W., McCabe, R., Chun, W., Kaiser, E., Perry, J., Henig, Y., Trinker, F., and Anderson, R., 1992, "Speciated Hydrocarbon Emissions From the Combustion of Single Component Fuels. I. Effect of Fuel Structure," J. Air Waste Manage. Assoc., **42**, pp. 912–920.

[10] McCabe, R., Siegl, W., Chun, W., and Perry, J., 1992, "Speciated Hydrocarbon Emissions from the Combustion of Single Component Fuels. II. Catalyst Effects," J. Air Waste Manage. Assoc., **42**, pp. 1071–1077.

[11] Hoekman, S., 1992, "Speciated Measurements and Calculated Reactivities of Vehicle Exhaust Emissions From Conventional and Reformulated Gasolines," Environ. Sci. Technol., **26**, pp. 1206–1216.

[12] Olson, K., Sinkevitch, R., and Sloane, T., 1992, "Speciation and Quantization of Hydrocarbons in Gasoline Engine Exhaust," J. Chromatogr. Sci., **30**, pp. 500–508.

[13] Nine, R., Clark, N., Mace, B., and ElGazzar, L., 1997, "Hydrocarbon Speciation for a Lean Burn Spark Ignited Engine," SAE Paper No. 972971.

[14] Siegl, W., Kaiser, E., Adamczyk, A., Guenther, M., DiCicco, D., and Lewis, D., 1998, "A Comparison of Conversion Efficiencies of Individual Hydrocarbon Species Across Pd- and Pt-Based Catalysts as a Function of Fuel-Air Ratio," SAE Paper No. 982549.

[15] Kaiser, E., and Siegl, W., 1994, "High Resolution Gas Chromatographic Determination of the Atmospheric Reactivity of Engine-Out Hydrocarbon Emissions From a Spark-Ignited Engine," J. High Resolut. Chromatogr., **17**, pp. 264–270.

[16] Bohac, S., 2003, "Reduction of Spark-Ignition Engine Hydrocarbon Emissions and the Associated Local Ozone Production Through Variable Exhaust Valve Timing," Ph.D. thesis, University of Michigan, Ann Arbor, MI.

[17] Bohac, S., Assanis, D., and Holmes, H., 2004, "Speciated Hydrocarbon Emis-

sions and the Associated Local Ozone Production From an Automotive Gasoline Engine," Int. J. Engine Res., **5**(1), pp. 53–70.
[18] Jensen, T., Siegl, W., Richert, J., Lipari, F., Loo, J., Prostak, A., and Sigsby, J., 1992, "Advanced Emission Speciation Methodologies for the Auto/Oil Air Quality Improvement Research Program—I. Hydrocarbons and Ethers," SAE Paper No. 920320.
[19] Siegl, W., Richert, J., Swarin, S., Loo, J., Prostak, A., Nagy, D., and Schlenker, A., 1993, "Improved Emissions Speciation Methodology for Phase II of the Auto/Oil Air Quality Improvement Research Program—Hydrocarbons and Oxygenates," SAE Paper No. 930142.
[20] Jemma, C., Lance, D., and Shore, P., 1992, "Speciation of Hydrocarbon Emissions from European Vehicles," SAE Paper No. 922376.
[21] Hammerle, R., Ketcher, D., Horrocks, R., Lepperhoff, G., Huthwohl, G., and Luers, B., 1994, "Emissions From Current Diesel Vehicles," SAE Paper No. 942043.
[22] Lepperhoff, G., Huthwohl, G., Luers-Jongen, B., and Hammerle, R., 1994, "Methods to Analyze Non-Regulated Emissions from Diesel Engines," SAE Paper No. 941952.
[23] Hammerle, R., Siegl, W., Herrmann, H., and Wenclawiak, B., 1995, "A Method for the Speciation of Diesel Fuel and the Semi-Volatile Hydrocarbon Fraction of Diesel-Fueled Vehicle Exhaust Emissions," SAE Paper No. 952353.
[24] Clark, N., Atkinson, C., McKain, D., Nine, R., and El-Gazzar, L., 1996, "Speciation of Hydrocarbon Emissions From a Medium Duty Diesel Engines," SAE Paper No. 960322.
[25] Gautam, M., Gupat, D., El-Gazzar, L., Lyons, D., and Popuri, S., 1996, "Speciation of Heavy Duty Diesel Exhaust Emissions under Steady State Operating Conditions," SAE Paper No. 962159.
[26] Durbin, T., Zhu, X., and Norbeck, J., 2003, "The Effects of Diesel Particulate Filters and a Low-Aromatic, Low-Sulfur Diesel Fuel on Emissions for Medium-Duty Diesel Trucks," Atmos. Environ., **37**, pp. 2105–2116.
[27] Westerholm, R., Almén, J., and Li, H., 1991, "Chemical and Biological Characterization of Particulate-, Semivolatile-, and Gas-Phase-Associated Compounds in Diluted Heavy-Duty Diesel Exhausts: A Comparison of Three Different Semivolatile-Phase Samplers," Environ. Sci. Technol., **25**, pp. 332–338.
[28] Siegl, W., Hammerle, R., Herrmann, H., Wenclawiak, B., and Luers-Jongen, B., 1999, "Organic Emissions Profile for a Light-Duty Diesel Vehicle," Atmos. Environ., **33**, pp. 797–805.
[29] Habibi, K., 1970, "Characterization of Particulate Lead in Vehicle Exhaust-Experimental Techniques," Environ. Sci. Technol., **4**, pp. 239–248.
[30] Bidleman, T., 1988, "Atmospheric Processes," Environ. Sci. Technol., **22**, pp. 361–367.
[31] Bohac, S., Han, M., Jacobs, T., López, A., Assanis, D., and Szymkowicz, P., 2006, "Speciated Hydrocarbon Emissions From an Automotive Diesel Engine and DOC Utilizing Conventional and PCI Combustion," SAE Paper No. 2006-01-0201.
[32] Tao, F., Liu, Y., RempelEwert, B. H., Foster, D. E., Reitz, R. D., Choi, D., and Miles, P. C., 2005, "Modeling the Effects of EGR and Injection Pressure on Soot Formation in a High-Speed Direct-Injection (HSDI) Diesel Engine Using a Multi-Step Phenomenological Soot Model," SAE Paper No. 2005-01-0121.
[33] Jacobs, T., 2005, "Simultaneous Reduction of Nitric Oxide and Particulate Matter Emissions From a Light-Duty Diesel Engine Using Combustion Development and Diesel Oxidation Catalyst," Ph.D. thesis, University of Michigan, Ann Arbor, MI.
[34] Lipari, F., 1990, "Determination of Individual Hydrocarbons in Automobile Exhaust from Gasoline-Methanol-, and Variable-Fueled Vehicles," J. Chromatogr., **503**, pp. 51–68.
[35] Huber, L., 2001, "Validation of Analytical Methods: Review and Strategy," http://www.labcompliance.com.
[36] Peng, C., and Batterman, S., 2000, "Performance Evaluation of a Sorbent Tube Sampling Method Using Short Path Thermal Desorption for Volatile Organic Compounds," J. Environ. Monit., **2**, pp. 313–324.
[37] Knafl, A., Busch, S. B., Han, M., Bohac, S. V., Assanis, D. N., Szymkowicz, P. G., and Blint, R. D., 2006, "Characterizing Light-Off Behavior and Species-Resolved Conversion Efficiencies During In-Situ Diesel Oxidation Catalyst Degreening," SAE Paper No. 2006-01-0209.
[38] Wagner, T., and Wyszyński, M. L., 1996, "Aldehyde and Ketones in Engine Exhaust Emissions- A Review," Proc. Inst. Mech. Eng., Part D (J. Automob. Eng.), **210**, pp. 109–122.
[39] McCabe, R. W., King, E. T., Watkins, W. L. H., and Gandhi, H. S., 1990, "Laboratory and Vehicle Studies of Aldehyde Emissions From Alcohol Fuels," SAE Paper No. 900708.

Development of a Highly Reduced Mechanism for Iso-Octane HCCI Combustion With Targeted Search Algorithm

Y. F. Tham[1]
e-mail: ytham@berkeley.edu

F. Bisetti

J.-Y. Chen

Department of Mechanical Engineering,
University of California at Berkeley,
246 Hesse Hall,
Berkeley, CA 94720

This paper describes recent development of iso-octane skeletal and reduced mechanisms for speeding up numerical simulations of homogeneous charge compression ignition (HCCI) engines. A novel targeted search algorithm is developed to systematically screen species for quasisteady state (QSS) assumption in order to reduce the mechanism size while maintaining accuracy. This new approach is especially found useful when the chemical kinetics involve complex ignition pathways. Using the iso-octane mechanism developed by LLNL, a skeletal mechanism with 215 species (Skeletal-215) and a reduced mechanism with 63 non-QSS species (Reduced-63) were constructed. Evaluations of the performances of the Skeletal-215 and the Reduced-63 were extensively conducted for the operation regimes in HCCI engine applications. Both mechanisms are found satisfactory in predicting start of combustion and minor emission species. [DOI: 10.1115/1.2900729]

1 Introduction

Homogeneous charge compression ignition (HCCI) technology has been developed to improve the emissions and efficiency of conventional engines. In a HCCI engine, chemical kinetics determines the start of combustion (SOC). To control the SOC, one may manipulate the following parameters: intake pressure, intake temperature, exhaust gas recirculation (EGR), and equivalence ratio (Φ) [1]. These parameters effectively set the initial chemical composition and thermodynamic state of the combustion charge. The effectiveness of varying individual parameter or combinations of these parameters along with fluid effects on the SOC can be explored by coupling chemistry with a CFD code, such as integrating CHEMKIN [2] with KIVA-3V [3]. For gasoline applications, the detailed iso-octane mechanism developed by Lawrence Livermore National Laboratory (LLNL) [4] may be used for accurate chemistry as the mechanism has been validated against autoignition data. Since different chain-branching reactions are responsible for ignition at different temperatures [5,6], 857 species and 3606 reactions are needed in the detailed mechanism to capture the two-stage ignition behavior of iso-octane. However, using such a large detailed mechanism in a 3D CFD engine simulation is not practical with current computing resources. This difficulty is mainly caused by both the large number of species and the stiffness of the detailed mechanism. The stiffness imposed by the detailed iso-octane mechanism requires very small time steps, making the calculations impractical. More importantly, thousands of grid points are needed to adequately describe the engine geometry. Resolving the chemical state at each grid point with 857 species would require computer memory far beyond current capacity ($\sim$30 Gbyte RAM with 1000 grid points with iso-octane based on 1D premixed flames). Therefore, the large iso-octane mechanism must be properly reduced in order to perform HCCI engine simulations.

In the past, researchers have performed HCCI engine simulations with reduced iso-octane chemistry and simplified physical models. Soyhan et al. [7,8] studied engine knock chemistry of *n*-heptane and iso-octane in a two-zone model with reduced chemistry based on a primary reference fuel (PRF) mechanism with 75 species and 510 reactions. Aceves et al. [9] showed good agreements among the multizone chemistry model predictions and the experimental data on a single-cylinder HCCI engine. With 199 species and 383 reactions, the iso-octane reduced chemistry used in the work of Aceves et al. was derived from the aforementioned detailed LLNL iso-octane mechanism [4]. Naturally, using reduced chemistry for HCCI simulations has been prevalent in the community. However, the effects of local inhomogeneities are overlooked by using the simplified physical models and SOC may not be correctly predicted [10]. This paper focuses on the development of a highly reduced mechanism from the LLNL iso-octane mechanism intended for the 3D CFD simulation with KIVA/CHEMKIN.

Reduction of Large Chemical Systems. From a numerical standpoint, the time advancement of the species composition corresponds to the solution of a system of stiff ordinary differential equations (ODEs). Without transport phenomenon, there are $N_{s,\text{detailed}}$ ODEs describing the net rate of change of the species as

$$\frac{\partial C_i}{\partial t} = \omega_{i,p} - \omega_{i,d}, \quad i = 1, N_{s,\text{detailed}} \tag{1}$$

where C_i is the species concentration, $\omega_{i,p}$ is the production rate of the ith species, and $\omega_{i,d}$ is its destruction rate. By removing species from the detailed mechanism, the computation load is reduced as the number of ODE is decreased. For a restricted regime of interest, many intermediate species can be removed from the ODE system without losing accuracy in the solution. Intermediate species can be systematically identified and removed from the ODE system via two major sequential steps [8,11]. First, a skeletal mechanism is generated from the original detailed mechanism. Further reduction of the skeletal mechanism results in a reduced mechanism.

To develop a skeletal mechanism, unimportant species and reactions for the practical combustion regime of interest are judicially removed from the detailed mechanism. The skeletal mechanism can also be described by Eq. (1) by changing $N_{s,\text{detailed}}$ to $N_{s,\text{skeletal}}$, where $N_{s,\text{skeletal}}$ is less than $N_{s,\text{detailed}}$. The computational time saving directly results from the reduction of the system size as well as the reduction in stiffness. Some current methods for

[1]Corresponding author.

Contributed by the Internal Combustion Division of ASME for publication in the JOURNAL OF ENGINEERING FOR GAS TURBINES AND POWER. Manuscript received May 2, 2007; final manuscript received January 12, 2008; published online April 29, 2008. Review conducted by Margaret Wooldridge.

developing skeletal mechanisms include the direct reduction (DR) approach [12], the directed relation graph (DRG) approach [13], and the reaction flow and sensitivity analysis [8].

To further reduce the skeletal mechanism, the quasisteady state assumption (QSSA) [8,11,14–17] can be applied to certain intermediate species. Such a reduced mechanism with QSSA can be described as:

For non-QSS species,

$$\frac{\partial C_i}{\partial t} = \omega_{i,p} - \omega_{i,d}, \quad i = 1, N_{s,\text{reduced}} \tag{2a}$$

For QSS species,

$$0 = \omega_{j,p} - \omega_{j,d}, \quad j = 1, \quad (N_{s,\text{skeletal}} - N_{s,\text{reduced}}) \tag{2b}$$

QSSA is applicable to an intermediate species when its production rate ($\omega_{j,p}$) is nearly equal in magnitude to the destruction rate ($\omega_{j,d}$), resulting in a very small net change in concentration. Concentrations of QSS species are solved by the nonlinear algebraic system described in Eq. (2*b*), whereas non-QSS species concentrations are resolved in the usual manner in Eq. (2*a*) [18]. For example, in the case of a series of reactions in propane decomposition:

$$C_3H_8 \leftrightarrow CH_3 + C_2H_5 \tag{3a}$$

$$C_2H_5 \leftrightarrow C_2H_4 + H \tag{3b}$$

C_2H_5 can be classified as a QSS species, resulting in the following net global reaction:

$$C_3H_8 \leftrightarrow CH_3 + C_2H_4 + H \tag{4}$$

As elucidated in Ref. [18], reactions in Eqs. (3*a*) and (3*b*) are equivalent to Eq. (4) by applying QSSA to C_2H_5. The concentration of C_2H_5 is solved by equating its production rate to destruction rate through (3*a*) and (3*b*), and concentrations of other species are solved by the usual manner in Eq. (2*a*). Computation time saving results from the further decrease in system size from $N_{s,\text{skeletal}}$ to $N_{s,\text{reduced}}$. Furthermore, the stiffness of the system is also decreased further as species with small lifetimes are removed [14]. However, QSS species must be chosen with caution as some species can induce large overall errors on the system [19].

The following two methods are commonly used for identifying QSS species: time-scale analysis based on computer singular perturbation (CSP) [20–23] and instantaneous error analysis for QSS species [19]. The identification of iso-octane QSS species with each method will be further discussed below.

Selection of QSS Species by CSP. In the CSP analysis, each species is classified as fast or slow mode according to its lifetime compared to a predetermined cutoff time. Species classified as fast mode have shorter lifetimes, and they are good candidates for QSSA. Although CSP identifies species that are quickly produced and consumed, it does not provide estimates of the error induced on the system when a certain species is approximated by QSSA. An investigation of iso-octane reduced mechanisms with QSS species selected by CSP has been conducted for a constant-pressure reactor with a mixture of $\phi = 0.3$ initially at $T = 800$ K and $P = 40$ atm. CSP samples were taken at different temperatures (about 12–20 points). The intervals between samples ranged from 20 deg to 30 deg at low temperature and 50 deg at high temperature. For each chemical state, species in the fast mode were separated from those in the slow mode, and species in the slow mode were grouped into non-QSS species. The final set of non-QSSA group was the union of all non-QSSA groups from all states. The cutoff lifetime was varied to generate reduced systems of various sizes. Figure 1 shows the total number of non-QSS species in reduced mechanisms versus the cutoff lifetime. Increasing the cutoff allows more species to be treated as QSS species. Correspondingly, the number of non-QSS species in the ODE system decreases but the accuracy deteriorates. For instance, if the cutoff is set at 3×10^{-4} ms, the reduced mechanism contains 145 non-QSS species. The relative error in the predicted autoignition delay times is approximately 20%. If the cutoff time is further increased, the error becomes unacceptably high. Although the reduced mechanism with 145 species is significantly smaller than the detailed mechanism with 857 species, the reduced system size is still too large for practical 3D CFD engine simulations. Thus, time-scale analysis with CSP is found to be too conservative and not optimal in identifying QSS species when the chemistry contains multiple pathways for ignition.

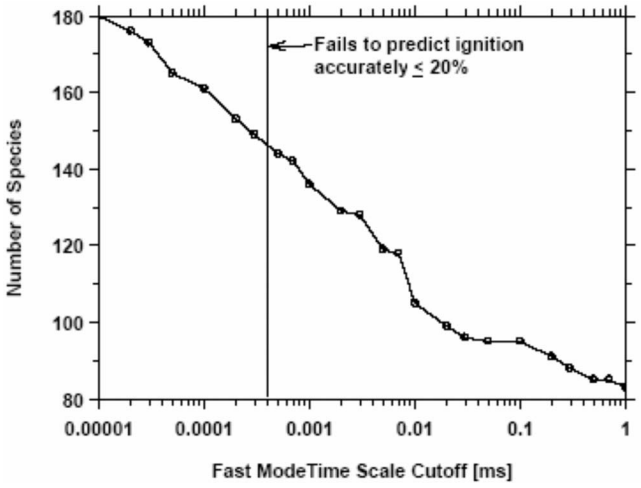

Fig. 1 Number of non-QSSA species in the reduced systems generated by CSP versus the species time-scale cutoff

Selection of QSSA Species by Instantaneous Error. The instantaneous error of making QSSA for an individual species is considered next as a criterion in selecting QSS species. The instantaneous error of QSSA is defined in Ref. [19], and the following relation can be derived:

$$E_i = [C_i]_{\text{exact}} - [C_i]_{\text{QSSA}} \tag{5a}$$

$$\approx \frac{|\omega_{p,i} - \omega_{d,i}|}{\omega_{d,i}} [C_i]_{\text{exact}} \tag{5b}$$

where $[C_i]_{\text{exact}}$ is the species concentration calculated from the starting mechanism, and $[C_i]_{\text{QSSA}}$ is the species concentration calculated from the reduced system (Eq. (2*b*)). As indicated by Eq. (5*b*), the instantaneous error is caused by the difference in the production and destruction rates of a QSS species. The relative error (RE) of a species with QSSA can be defined as

$$\text{RE}_i = \frac{|\omega_{p,i} - \omega_{d,i}|}{\omega_{d,i}} \times 100\% \tag{6}$$

During the ignition period, one may use the maximum RE as a criterion to determine if a species is a good candidate for QSSA. Thus, a species with small RE throughout the autoignition period is an excellent candidate for QSSA. However, this criterion is also found to be too conservative and problematic in choosing QSS species when chemical kinetics contains multiple ignition pathways. For instance, Fig. 2 shows the time evolution of a representative QOOH species (d-$C_8H_{17}O_2H$, the hydroperoxyoctyl radical [4]) during the first 40 ms of a constant-pressure reactor simulation. During the induction period, the production rate, is larger than the destruction rate resulting in large instantaneous errors, as shown in Fig. 3. With the different chain-branching reactions, different intermediates will have different induction periods. Thus, large instantaneous errors are expected during the induction periods occurring at various times. As an automatic procedure is necessary in the construction of reduced chemistry from a large

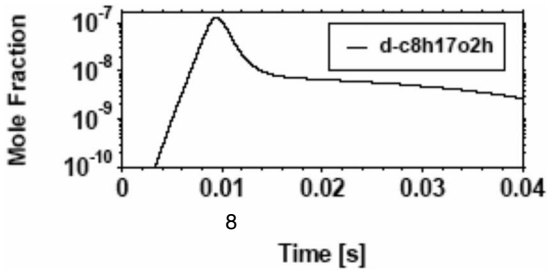

Fig. 2 Concentration of d-$C_8H_{17}O_2H$ using QSSA, with induction period in the beginning

mechanism, samples of reacting states during the autoignition period are used with Eq. (6) to determine the RE. As such, the size of the reduced system then becomes a function of sampling interval. Figure 4 shows the size of the reduced systems versus the sampling interval during the ignition period. With a large sampling time interval, few sampling states are chosen throughout the simulation. Since the likelihood of encountering the induction periods is smaller with less sampling, more intermediate species are identified as QSS species. As the sampling time interval decreases, more sampling states are chosen, the likelihood of encountering the induction periods is higher; fewer intermediate species are chosen to be QSS species. For the present iso-octane case, the reduced system fails to accurately predict autoignition when the number of non-QSS species is less than 155. The above exercise demonstrates the problematic nature of using instantaneous error as the criterion in identifying the proper set of QSS species.

In this paper, an automatic search algorithm is developed to identify the appropriate QSS species during autoignition. First, the

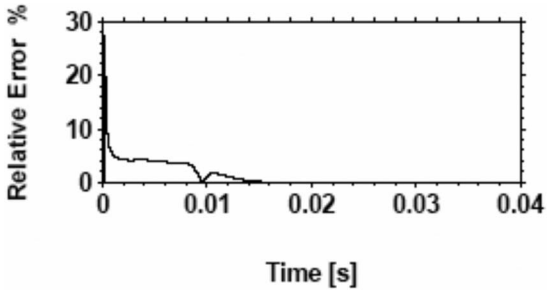

Fig. 3 QSSA instantaneous error associated with d-$C_8H_{17}O_2H$

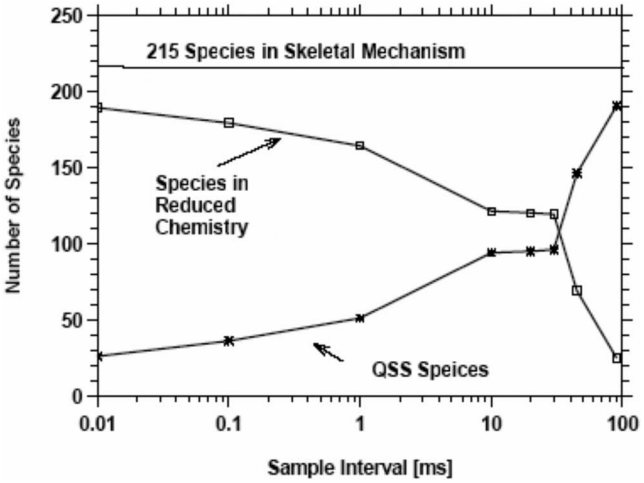

Fig. 4 Number of QSSA and non-QSSA species versus sample interval using the instantaneous error parameter

motivation and methodology for developing the automatic search are described with the objective of achieving small overall errors in mind. Next, using iso-octane as an example, a 63-species reduced chemistry is developed for gasoline HCCI combustion regime. Finally, an extensive evaluation of the performance of the reduced mechanism is presented to demonstrate the effectiveness of the new algorithm.

2 Development of Reduced Mechanism by the Targeted Search Algorithm

In this section, the concept of a newly developed search algorithm named the targeted search algorithm (TSA) is described. The development is motivated by the following observations. The introduction of QSSA (Eq. (2*b*)) induces errors in the non-QSS species compared to the original ODE system described by Eq. (1). As discussed in Ref. [19], due to the strong nonlinear coupling among species, the instantaneous errors become more difficult to assess when a group of species are approximated by QSSA. The quality of a reduced system is gauged by its accuracy in predicting certain flame behaviors. The overall impact of a group of QSS species on the accuracy of predicted global flame behaviors by the reduced system, such as autoignition delay or flame speed, often cannot be quantified until the reduced system (Eqs. (2*a*) and (2*b*)) is used for such predictions. Under certain conditions, the low temperature ignition can greatly influence the second ignition at high temperatures in a nonlinear fashion [5,6]. A 10% error in RE during the low temperature ignition often does not translate to 10% error in the high temperature ignition when the coupling is strongly nonlinear. Both the instantaneous error estimate and time-scale analysis are insufficient in determining whether or not the reduced chemistry with a certain group of QSS species can achieve the desired accuracy. Bhattacharjee et al. [24] recognized this problem and recently proposed an approach based on integer optimization via selective reaction elimination subject to global accuracy constraints.

The main idea of TSA is that during the construction phase, a reduced system derived from any complex mechanism needs to be tested under representative conditions to ensure its overall accuracy. As such, the impact of a group of QSS species on the predicted accuracy is immediately assessed in the construction phase and used to guide the selection of the appropriate group of QSS species. One important advantage of this approach is its potential to significantly reduce the size of a complex mechanism while ensuring its predictive capabilities for the targeted regime in a systematic manner. The accuracy of the reduced system is guaranteed for the targeted conditions. Alternatively, the selection of QSS species may be guided by optimization procedures using genetic algorithms [25]. Since genetic algorithms evaluate numerous possible combinations, such an approach becomes computationally expensive when the starting mechanism contains a large number of species. However, genetic algorithms are useful for fine-tuning the performance of a reduced system once it is developed with reasonable accuracy.

The first step is to identify targeted conditions under which the reduced chemistry will be used for the intended CFD simulations. For HCCI combustion, turbulence is less important than chemical kinetics in controlling SOC. Hence, the influence of turbulence on chemical states is neglected. As the current objective is aimed at modeling of gasoline HCCI autoignition, several representative HCCI preignition conditions are selected in the following manner. Figure 5 shows the operation map of a typical HCCI engine in terms of cylinder pressure versus temperature during the engine cycle with an equivalence ratio of 0.3 without EGR.

The lines represent traces of pressure-temperature relations during compression, autoignition, and expansion obtained from a multicycle engine simulation with a single-zone well-mixed reactor. Six HCCI engine conditions are chosen to represent the anticipated chemical states prior to autoignition. Point 1 represents the low temperature and pressure condition near the bottom dead

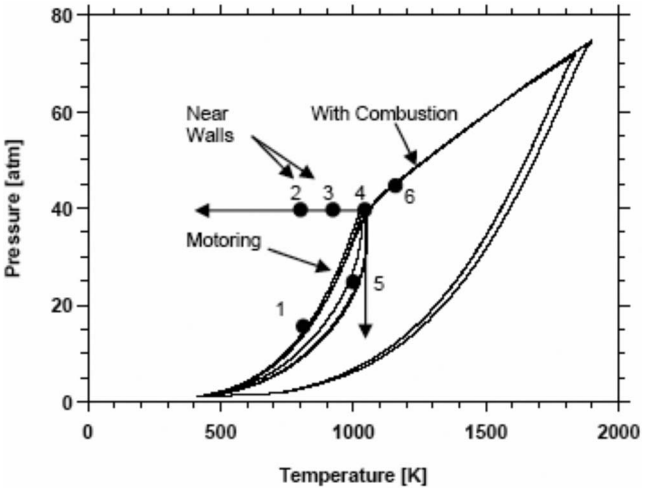

Fig. 5 The six HCCI engine reference states for testing QSSA species in the TSA

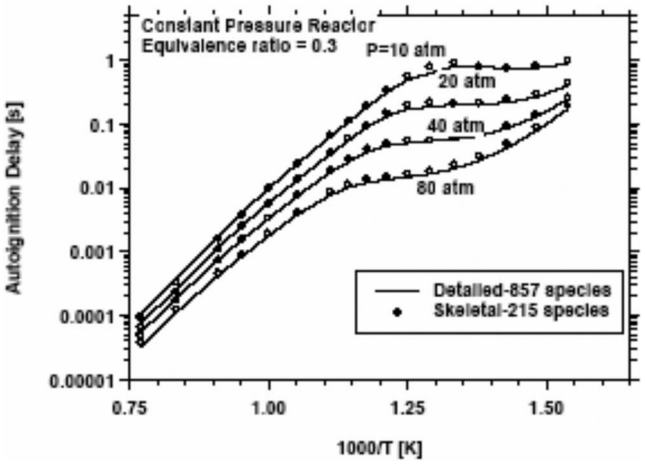

Fig. 6 Comparison of the autoignition delay times of the Skeletal-215 with the detailed iso-octane mechanism

center (BDC) at the beginning of the compression stroke. Points 2 and 3 are conditions at low temperature and high pressure representing the chemical states of the near-wall mixtures around TDC. Points 4 and 5 represent the intermediate temperature HCCI condition before autoignition takes place. Point 6 is chosen to represent the high temperature condition after TDC. The heat release rate at high temperature is relatively fast in comparison to autoignition delay. For HCCI engine applications, including high temperature heat release as one of the targets will have negligible impact on the overall results. By utilizing these six unburned initial chemical states, the predictive capability of the reduced iso-octane system is assessed during the construction phase. It is possible to include more conditions that are representatives of the regimes of interest, such as low equivalence conditions for emission purpose.

Next, a reduced mechanism is constructed and tested under the targeted conditions. First, ignition delays are calculated at isobaric and adiabatic conditions with the detailed mechanism for the targeted conditions. Then, a skeletal mechanism is created by the computer assisted reduction mechanism (CARM) [11] algorithm, where unimportant species and reactions are eliminated through careful examination of the delay data. Already reduced in size, the skeletal mechanism captures the essence of the detailed chemistry under the targeted conditions. Using the skeletal mechanism as the framework, a reduced system intended for the targeted conditions is constructed with TSA. The skeletal species are ranked according to their maximum concentrations under all targeted conditions in ascending order, as intermediate species with low concentrations are good candidates for QSSA. Fuel, oxidizer, and products with high concentrations are not considered for QSSA. Initially, the species with the lowest concentration is chosen as a candidate QSS species. Once the QSS species selection has been made, a reduced system is automatically created by CARM, where the set of algebraic equations for QSS species in Eq. (2*b*) is iteratively solved. This reduced system is used to compute autoignition delays at the targeted conditions. If the delay times are within a preset accuracy threshold (15% used in the present study) of those calculated by the detailed mechanism, the overall error induced by placing the candidate species in QSS is acceptable. Otherwise, the species will not be included in the final QSS species category. After the first QSS candidate has been tested, the next species with the lowest concentration will be placed in the QSS category, resulting in the generation and testing of another reduced system. This QSS species screening process continues until the delay times computed by the reduced system do not satisfy the preset accuracy threshold anymore. Naturally, the size of the reduced system depends on the predetermined accuracy level. Through this process, a reduced system with small overall errors for the targeted conditions is determined.

Using the LLNL iso-octane mechanism as an example, a skeletal mechanism with 215 species (referred to as Skeletal-215) and a reduced mechanism with 63 non-QSS species and 152 QSS species (referred to as Reduced-63) have been developed with satisfactory results. Reduced-63 is developed by the aforementioned TSA, with Skeletal-215 as its framework. Both mechanisms were developed for the six representative states of autoignition (Fig. 5) at equivalence ratio $\Phi=0.3$.

3 Validation of the Skeletal-215 and Reduced-63 Iso-octane Mechanisms

A comprehensive evaluation of Skeletal-215 and Reduced-63 was conducted over a wider range of HCCI conditions to assess their performances. The following test categories were conducted: autoignition delay time over a wider range of temperature and pressure, HCCI transient multicycle engine simulations with a single-zone well-mixed reactor (WMR), HCCI under very lean conditions to evaluate CO, HC, and oxygenated HC emissions, and a CFD engine simulation using KIVA-3V.

Autoignition Delay Time. Figures 6 and 7 show the comparisons of predicted autoignition delay times versus $1000/T$, where T

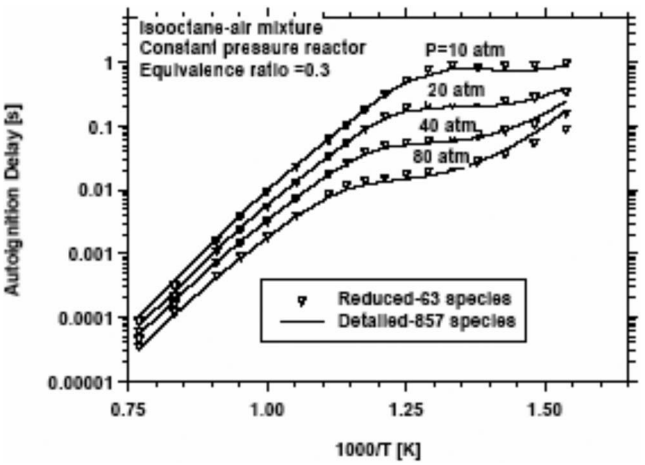

Fig. 7 Comparison of the autoignition delay times of the Reduced-63 with the detailed iso-octane mechanism

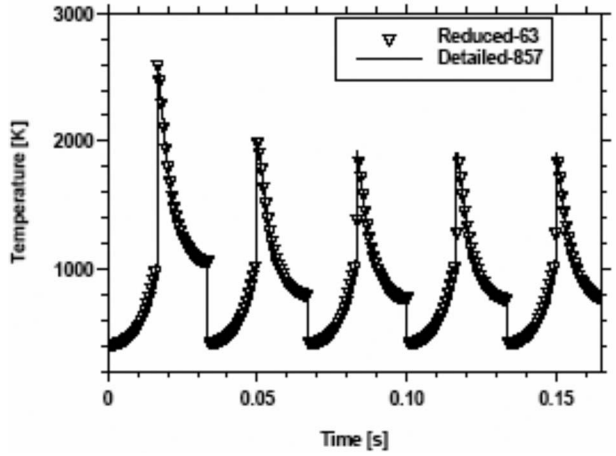

Fig. 8 Temperature trace of a transient WMR iso-octane simulation with EGR

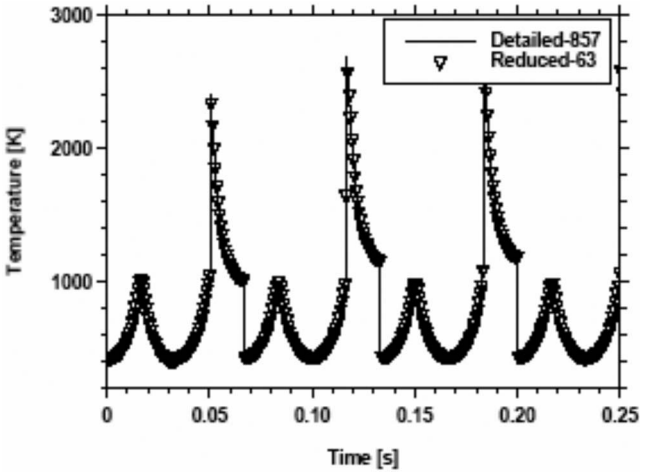

Fig. 9 Temperature trace of a transient bimodal WMR iso-octane simulation

is the initial mixture temperature. The delay times were computed for an adiabatic constant-pressure reactor at four different pressures (10 atm, 20 atm, 40 atm, and 80 atm) and equivalence ratio $\Phi=0.3$. As seen in Fig. 6, the results from Skeletal-215 show good agreement with those from the detailed mechanism over all temperature and pressure range relevant to HCCI. Thus, Skeletal-215 serves as a reliable starting mechanism for the development of reduced systems. Similarly seen in Fig. 7, the predictions from the Reduced-63 agree well with the detailed mechanism, except at low temperature (650 K) and high pressure (40–80 atm) conditions. These extreme conditions were not targeted by the TSA process as they are outside of the intended gasoline HCCI combustion regimes.

Transient Multicycle Engine Simulations With WMR. The next level of validation is performed with transient multicycle WMR simulations to test the transient performance of Reduced-63 under HCCI conditions. The calculations simulate iso-octane HCCI combustion in a cooperative fuel research (CFR) engine with a compression ratio of 16 at an engine speed of 1800 rpm with two different manifold intake pressures. The heat loss model used in these WMR simulations is based on Woschni's correlation [26]. The inlet temperature used for each cycle is 423 K, and this inlet temperature is enforced throughout all simulated engine cycles. More importantly, the effects of EGR on SOC are evaluated since no EGR is included in the targeted states during the construction. Figure 8 shows the excellent agreement of the temperature traces between Reduced-63 and the detailed mechanism for the boosted intake pressure at 2 bars. During the first cycle, the lean premixed charge ($\Phi=0.6$) was allowed to ignite without the influence of EGR. For the subsequent cycles, EGR (60% by mass) was introduced into the reactor to reduce the peak flame temperature. Similarly, Fig. 9 shows the nearly perfect agreement between results from Reduced-63 and those from the detailed mechanism under bimodal combustion conditions with the intake pressure at 1 bar. The occurrence of alternating burning and misfiring condition is merely obtained by lowering the intake pressure from 2 bars to 1 bar. The reduced mechanism is found able to accurately predict such behavior. Other HCCI conditions have also been tested (not shown), revealing good agreement. Overall, the transient WMR simulations demonstrate the capability of Reduced-63 to capture the iso-octane ignition behaviors under HCCI conditions as accurately as the detailed mechanism.

CO and HC Emissions. Operating a HCCI engine at very lean conditions is currently considered as a viable option for engine idle without a throttle plate. However, it is experimentally found that CO and unburned HC emissions increase when the equivalence ratio decreases. The predictive capability of emissions under such operating conditions with Skeletal-215 and Reduced-63 is evaluated by using a single-zone WMR simulation. Figure 10 shows a comparison of the predicted CO emissions with different mechanisms over a range of low equivalence ratios ($\Phi=0.06-0.2$).

Figure 11 presents the corresponding comparisons of predicted unburned hydrocarbon (HC) and oxygenated hydrocarbon (OHC) under the same conditions. As seen in Figs. 10 and 11, both Skeletal-215 and Reduced-63 show good agreement with the detailed mechanism.

KIVA-3V Engine Simulations. The last validation test for the reduced iso-octane systems is the comparison between KIVA-3V HCCI engine simulation results and experimental HCCI engine data [9]. Table 1 lists the relevant specifications and conditions used for the Cummins C single-cylinder engine testing. The grid and simulation parameters were taken from those used in a previous paper [9]. The mesh contains 27,575 cells with the assumption of axisymmetric geometry and without crevices. KIVA-3V uses the standard k-ε model and associated mass and heat transfer equations to model species and energy transportation, which is coupled to chemical kinetics. Details on flow solver and equations used can be found in Ref. [3]. Chemical kinetics are computed without the effect of turbulence. The simulation starts at the intake valve closing point where both temperature and pressures were adjusted

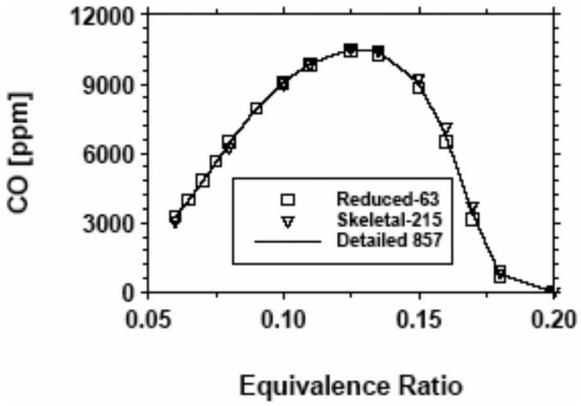

Fig. 10 Comparison of CO emissions from the WMR simulation using the detailed mechanism, Skeletal-215, and the Reduced-63

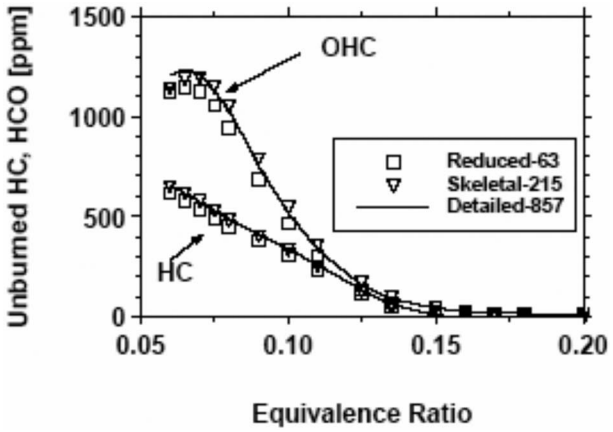

Fig. 11 Comparison of the HC and OHC emissions from the WMR simulation using the detailed mechanism, Skeletal-215, and the Reduced-63

to match the pressure traces, as done in the previous paper [9]. For Case 1, the pressure is set at 2.79 bars and the mixture temperature is 478 K. For Case 2, the pressure is 3.29 bars and temperature is 486 K. These conditions were used in the current simulation. Figure 12 shows the comparison of pressure traces from the KIVA-3V simulations with Reduced-63 and Skeletal-215, along with the experimental pressure traces. Due to the enormous computer resources required, the corresponding results with the detailed mechanism are not available. Overall, both Skeletal-215 and Reduced-63 provide quite satisfactory predictions compared to the engine pressure trace data. Table 2 shows the measured CO concentrations in the exhaust versus the predicted CO concentrations via Skeletal-215 and Reduced-63. The results from the Reduced-63 agree well with those from the Skeletal-215. Clearly, simulations underpredict the experimental CO concentrations by a factor of 4. Such underprediction in CO levels has also been observed by Aceves et al. [9], despite employing a detailed mechanism. As in conventional SI engines, CO is accumulated near cold surfaces and part of CO is trapped in the cold crevices. During the expansion stroke, the trapped CO is released from the crevices and may not be quickly oxidized enough. It is generally accepted that the underprediction is attributed to the fact that most simulations do not take into account the cold crevices in the piston ring regions.

Table 1 Parameters used for the Cummins-C single-cylinder engine experiment and simulation

	Case 1	Case 2
Engine speed (rpm)	1010	2007
Intake temperature (K)	381	413
Absolute intake pressure (bar)	2.41	3.11
Equivalence ratio (Φ)	0.346	0.348
Swirl ratio	3.6	3.6

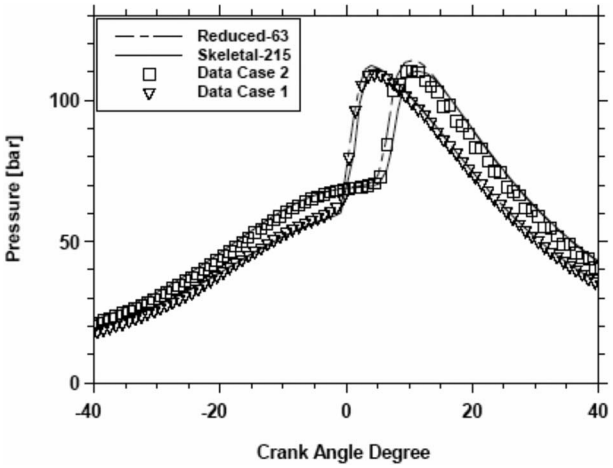

Fig. 12 KIVA-3V pressure prediction of a HCCI engine cycle with the Skeletal-215 and Reduced-63 versus experimental data

Table 2 Comparison of CO predictions from KIVA-3V with experimental measurements

	CO (exp) (g/kg)	CO (Skel-215) (g/kg)	CO (Red-63) (g/kg)
Case 1	21.7	5.18	5.91
Case 2	31.5	8.28	8.27

4 Conclusions

A new automatic search algorithm named the TSA is developed for identifying QSS species during the construction phase of reduced systems. The development was motivated by the need to account for the overall quality of SOC prediction into the developing phase of reduced systems. This is especially useful when the chemical system contains multiple ignition characteristics, making the existing methods inadequate in identifying the proper QSS species. An important first step in TSA is the identification of representative chemical states for the intended flames. If the applications are intended for flames under strong influence of turbulence, the representative states need to be identified and computed with the starting mechanism. This task remains a research topic if strong turbulence-chemistry interactions are involved. Fortunately, in HCCI engines, turbulence was found to affect the overall SOC through temperature stratification via heat transfer to cylinder walls. It is therefore possible to select proper representative conditions based on simple WMR calculations with proper heat transfer to walls. Using iso-octane as an example, the TSA was used for development of an accurate reduced system with six targeted conditions. Combining TSA and CARM enables us to automatically construct reduced systems. The performance of the resulting 63-species reduced chemistry is then further assessed over a range of HCCI conditions wider than those conditions targeted during the developing phase. In principle, all representative targets could be included in the developing phase such as low equivalence ratio cases with emissions. The performance of the reduced mechanism is found satisfactory in terms of several global flame features including autoignition delays, transient flames, and emissions under the anticipated gasoline HCCI engine regime.

Acknowledgment

This work was sponsored by the Department of Energy (DOE) Award No. F015533.

References

[1] Choi, Y., and Chen, J.-Y., 2005, "Fast Prediction of Start-of-Combustion in HCCI With Combined Artificial Neural Networks and Ignition Delay Model," Proc. Combust. Inst., **30**, pp. 2711–2718.
[2] Kee, R. J., Rupley, F. M., and Miller, J. A., 1992, "Chemkin-II: A Fortran Chemical Kinetics Package for the Analysis of Gas Phase Chemical Kinetics," Sandia National Laboratories, Report No. SAND89–8009B.
[3] KIVA3V, 1997, "A Block-Structured KIVA Program for Engines With Vertical or Canted Valves," Los Alamos Laboratory, Report No. LA-13313-MS.
[4] Curran, H. J., Gaffuri, P., Pitz, W. J., and Westbrook, C. K., 2002, "A Comprehensive Modeling Study of Iso-Octane Oxidation," Combust. Flame, **129**, pp. 253–280.
[5] Westbrook, C. K., 2000, "Chemical Kinetics of Hydrocarbon Ignition in Practical Combustion Systems," Proc. Combust. Inst., **28**, pp. 1563–1577.
[6] Roberts, C. E., Matthews, R. D., and Leppard, W. R., 1996, "Development of

a Semi-Detailed Kinetics Mechanism for the Autoignition of Iso-Octane," SAE Paper No. 962107.
[7] Soyhan, H., Amnéus, P., Mauss, F., and Sorusbay, C., 1999, "A Skeletal Mechanism for the Oxidation of Iso-Octane an n-Heptane Validated Under Engine Knock Conditions," Transactions, Journal of Fuels and Lubricants, **108**, pp. 1402–1409.
[8] Soyhan, H. S., Amnéus, P., Løvås, T., Nilsson, D., Maigaard, P., Mauss, F., and Sorusbay, C., 2000, "Automatic Reduction of Detailed Chemical Reaction Mechanisms for Autoignition Under Engine Knock Conditions," Transactions, Journal of Fuels and Lubricants, **109**, pp. 1435–1444.
[9] Aceves, S. M., Martinez-Frias, J., Flower, D., Smith, J. R., Dibble, R. W., and Chen, J.-Y., 2002, "A Computer Generated Reduced Iso-Octane Chemical Kinetic Mechanism Applied to Simulation of HCCI Combustion," SAE Paper No. 2002–01–2870.
[10] Maigaard, P., Mauss, F., and Kraft, M., 2003, "Homogeneous Charge Compression Ignition Engine: A Simulation Study on the Effects of Inhomogeneities," ASME J. Eng. Gas Turbines Power, **125**, pp. 466–471.
[11] Chen, J.-Y., 2001, "Automatic Generation of Reduced Mechanisms and Their Applications to Combustion Modeling," Transactions of the Aeronautical and Astronautical Society of the Republic of China, **33**, pp. 59–67.
[12] Wang, H., and Frenklach, M., 1991, "Direct Reduction of Reaction Mechanisms for Flame Modeling," Combust. Flame, **87**, pp. 365–370.
[13] Lu, T., and Law, C. K., 2006, "Linear Time Reduction of Large Kinetic Mechanisms With Directed Relation Graph: n-Heptane and Iso-Octane," Combust. Flame, **144**, pp. 24–36.
[14] Warnatz, J., Maas, U., and Dibble, R. W., 2001, *Combustion*, 3rd ed., Springer-Verlag, Berlin, pp. 86–88.
[15] Glassman, I., 1996, *Combustion*, 3rd ed., Academic, San Diego, p. 47.
[16] Law, C. K., 2006, *Combustion Physics*, Cambridge University Press, New York, pp. 129–131.
[17] Peters, N., *Turbulent Combustion*, Cambridge University Press, New York, p. 23.
[18] Chen, J.-Y., 1988, "A General Procedure for Constructing Reduced Reaction Mechanisms With Given Independent Relations," Combust. Sci. Technol., **57**, pp. 89–94.
[19] Turanyi, T., Tomlin, A. S., and Pilling, M. J., 1993, "On the Error of the Quasi-Steady-State Approximation," J. Phys. Chem., **97**, pp. 163–172.
[20] Massias, A., Diamantis, D., Mastorakos, E., and Goussis, D. A., 1999, "An Algorithm for the Construction of Global Mechanisms With CSP Data," Combust. Flame, **117**, pp. 685–708.
[21] Lu, T., Ju, Y., and Law, C. K., 2001, "Complex CSP for Chemistry Reduction and Analysis," Combust. Flame, **126**, pp. 1445–1455.
[22] Lam, S. H., 1993, "Using CSP to Understand Complex Chemical Kinetics," Combust. Sci. Technol., **89**(5–6), pp. 375–404.
[23] Løvås, T., Amnéus, P., Mauss, F., and Mastorakos, E., 2002, "Comparison of Automatic Reduction Procedures for Ignition Chemistry," *29th Symposium (International) on Combustion*, The Combustion Institute.
[24] Bhattacharjee, B., Schwer, D., Barton, P., and Green, W., 2003, "Optimally-Reduced Kinetic Models: Reaction Elimination in Large-Scale Kinetic Mechanisms," Combust. Flame, **135**, pp. 191–208.
[25] Montgomery, C. J., Yang, C., Parkinson, A. R., and Chen, J.-Y., 2006, "Selecting the Optimum Quasi-Steady State Species for Reduced Chemical Kinetic Mechanisms Using a Genetic Algorithm," Combust. Flame, **144**, pp. 37–52.
[26] Heywood, J. B., 1988, *Internal Combustion Engine Fundamentals*, McGraw-Hill, New York, pp. 679–680.

Characteristic Response of a Production Diesel Oxidation Catalyst Exposed to Lean and Rich PCI Exhaust

Timothy J. Jacobs
Texas A&M University,
College Station, TX 77843-3123
e-mail: tjjacobs@tamu.edu

Dennis N. Assanis
University of Michigan,
Ann Arbor, MI 48109-2121
e-mail: assanis@umich.edu

Although low-temperature premixed compression ignition (PCI) combustion in a light-duty diesel engine offers dramatic and simultaneous reductions in nitric oxides (NO_x) and soot, associated increases in unburned hydrocarbons (HC) and carbon monoxide (CO) become unacceptable. Production diesel oxidation catalysts (DOCs) are effective in oxidizing the increased levels of HC and CO under lean combustion conditions. However, the low-temperature/high CO combination under rich PCI conditions, designed as a lean NO_x trap (LNT) regeneration mode, generally renders the DOC ineffective. The objectives of this study are to characterize the oxidizing efficiency of a production DOC under lean and rich PCI conditions, and attempt to identify probable causes for the observed ineffectiveness under rich PCI. The study uses several tests to characterize the behavior of the DOC under lean PCI and rich PCI combustion conditions, including (1) steady-state feed gas characterization, (2) transient feed gas characterization, (3) air injection (4) insulated air-fuel sweep, and (5) combustion mode switching. The DOC never becomes effective under rich PCI for any of the tests, suggesting that the platinum-based catalyst may be incorrect for use with rich PCI. Furthermore, combustion mode switching between lean PCI and rich PCI (mimicking LNT loading and regeneration) demonstrates diminishing effectiveness of the DOC during and after continuous mode transitioning. [DOI: 10.1115/1.2906174]

Introduction

Diesel engines remain a viable energy-converting option by offering high thermal efficiency. However, diesel engines using conventional modes of combustion tend to have high soot and nitric oxide (NO_x) emission [1]. Low-temperature premixed compression ignition (PCI) combustion offers an opportunity to simultaneously reduce soot and NO_x (e.g., Ref. [2]), including during fuel-rich engine operation [3–5]. However, increases in hydrocarbons and carbon monoxide emissions with PCI modes create a need for diesel exhaust oxidation catalysis [5,6].

In addition to needing exhaust catalysis, PCI can also enable exhaust catalysis. For example, rich PCI can provide the necessary exhaust reductants for lean NO_x trap (LNT) regeneration. LNTs generally work by storing NO_2 during "typical" (lean) engine operation, thus requiring NO_2 release and reduction with a regeneration (rich) engine operation. Given its capability to yield carbon monoxide (CO) concentrations in excess of 5% [5], along with its inherently low soot and NO_x concentrations, rich PCI could serve as the intermittent [7] regeneration strategy. However, under such aggressive regeneration conditions, nonparticipating CO and high concentrations of HC will likely slip through the LNT and further necessitate diesel oxidation catalysis.

Diesel oxygen catalysts (DOCs) originally appeared on diesel engines to reduce the soluble organic fraction of total particulate matter (TPM) [8]. As a result, they typically had very high loadings of precious group metals in order to oxidize the liquid portion of TPM [9]. More recently, however, the growing need to oxidize HC and CO in low exhaust temperature environments [10] has continued the trend of maintaining high precious group metal loading. Since exhaust temperature is a critical parameter governing the effectiveness of a DOC, researchers have focused on (in addition to precious group metal loading) washcoat selection [11] and inclusion of HC storage substances such as zeolite [12,13] to improve low-temperature conversion efficiency. Summaries of recent DOC technology are provided in, Refs. [14–16]. In addition to the design of the catalyst itself, the exhaust gas constituents strongly influence oxidation efficiency [6,17–20].

Some literature exists coupling DOCs with low-temperature modes of combustion, such as PCI [2,6,20]. One such study by Iwabuchi et al. [2] indicates the effective DOC oxidation of increased CO and HC concentrations manifested by PCI combustion, even at temperatures around 200 °C. A complementing article founded around this study provides pre- and post-DOC hydrocarbon speciation for both lean and rich PCI conditions [6]. Knafl et al. [20] explored the light-off temperatures of a DOC fed with lean PCI engine exhaust and surrogate PCI feed gas in bench studies. This study provides similar findings under lean PCI conditions, as reported in Ref. [2]; however, it complements the literature with findings that demonstrate DOC ineffectiveness under rich PCI conditions. It also provides the basis for the follow-on study of HC speciation [6]. The objectives of this study are to characterize the oxidizing efficiency of a production DOC under lean and rich PCI conditions, and attempt to identify probable causes for the observed ineffectiveness under rich PCI.

Experimental Methodology

This experimental study was conducted on a four-cylinder direct-injection 1.7 l diesel engine with common rail fuel, exhaust gas recirculation (EGR), and variable turbocharging systems. An intake throttle, used for additional EGR control, is also in place on the engine. The engine is fully instrumented for performance and emission measurements. A production-style DOC was added 1 m downstream of the turbocharger outlet to the exhaust system for this study. The 0.5 l catalyst is platinum suspended in an alumina/

Contributed by the Internal Combustion Engine Division of ASME for publication in the JOURNAL OF ENGINEERING FOR GAS TURBINES AND POWER. Manuscript received October 24, 2007; final manuscript received November 7, 2007; published online April 29, 2008. Review conducted by Dilip R. Ballal.

silica washcoat on a cordierite ceramic monolith. The DOC is instrumented with gas temperature and gaseous emissions before and after the catalyst. The engine, catalyst, and test system are described more thoroughly in Ref. [21]. Emissions are discretely sampled between a precatalyst sample port and a postcatalyst sample port.

Injection timing is reported by the engine electronic control module. Exhaust NO_x concentrations, reported in ppm of exhaust volume, are measured using a heated chemiluminescence analyzer. Exhaust smoke concentrations, reported in filter smoke number (FSN), are measured using filter paper reflectance. Exhaust CO concentrations, reported in ppm, are measured with nondispersive infrared technique. Exhaust HC and methane (CH_4) concentrations, reported in ppm, are measured with a flame ionization technique. Temperature is measured using the standard K-type thermocouples (thermocouples are open bead, nonshielded, and located in the center of the gas stream). Reported uncertainty varies depending on the specific testing (as described in Results and Discussion section), however, generally accounts for the precision (stated by instrument manufacturer), accuracy (stated by instrument manufacturer), data sample randomness (generally over 30 data points), and test repeatability after departure from and return to the operating point.

EGR rate is the mass of EGR divided by the total trapped mass, where the mass of EGR is calculated from measured intake and exhaust CO_2 concentrations. Emission indices of NO_x (EI-NO_x) are reported in grams of NO_x per kilogram of fuel (g/kg f) and are converted from NO_x concentrations. EI-PM (g/kg f) is computed from smoke measurements (made roughly 2 m and 1 m downstream of the engine and DOC, respectively) using a correlation determined from data provided in Ref. [22]. CO and HC conversion efficiencies through the DOC are computed as the mass of oxidized species divided by the catalyst inlet mass. Space velocity is calculated as the actual exhaust volume flow rate divided by the catalyst volume. Finally, air-fuel (AF) ratio is calculated from measured exhaust species using a method prescribed by Ref. [23].

This study contains results from several testing techniques: steady-state feed gas testing, transient feed gas testing, air injection testing, insulated AF ratio sweep testing, and combustion mode switching. The specific test protocols and procedures followed for each technique are described, respectively, in Results and Discussion section.

PCI Combustion

Before providing results associated with DOC testing under PCI combustion conditions, a brief overview of PCI combustion is provided. PCI combustion is characterized by a low-temperature combustion event of a well-mixed AF mixture after a long ignition delay manifested by high levels of EGR and strategic injection timings. The concept of low-temperature combustion rises from the evidence that both soot and NO formation rates have direct dependencies on temperature. Kamimoto and Bae [24] summarized the relationship between local combustion temperature and AF ratio on soot and NO formation regimes. Although their emphasis is high-temperature combustion, the summary reveals simultaneous and substantial reductions in NO and soot at low combustion temperatures ($\sim$1500 K).

There are numerous ways to implement the PCI combustion (e.g., Refs. [2–5]). A brief and nonexhaustive summary is provided in Ref. [21]. The method followed for this study is to use high levels of EGR and (relatively) late injection timings. Three combustion modes are presented here and are the same as those in Refs. [4–6,21]. Lean conventional (lean conv) is meant to reflect a present-day European type (Euro IV) combustion mode and is also capable of meeting United States Environmental Protection Agency's (US EPA) Tier I light-duty passenger vehicle emission standards [25]. Lean PCI is meant to operate as a well-mixed low-temperature combustion mode capable of meeting US EPA Tier II Bin 5 light-duty passenger vehicle emission standards [26]. Rich PCI, also meant to operate as a well-mixed low-temperature combustion mode, is intended to operate intermittently and as needed for LNT regeneration. A summary of the three combustion modes is provided in Table 1.

Table 1 Summary of combustion modes under study

	Lean conv	Lean PCI	Rich PCI
Speed (rpm)	1500 ± 2	1500 ± 2	1500 ± 2
Fuel (g/s)	0.55 ± 0.03	0.54 ± 0.03	0.66 ± 0.03
BMEP (kPa)	409 ± 1.9	386 ± 1.9	354 ± 1.9
AF ratio	28.75 ± 0.3	16.95 ± 0.3	12.5 ± 0.3
EGR (%)	29.2 ± 0.167	43.2 ± 0.3	46.10 ± 0.3
Injection timing (°BTDC)	5	15	25

The benefits of PCI are shown in Fig. 1, where both NO_x and smoke concentrations from PCI combustion are significantly and simultaneously reduced relative to conventional combustion. The results on a mass basis are shown in Fig. 2, with corresponding US EPA Tier 2 Bin 5 regulations [26] also drawn on the figure. The conversion of g/mile standard to EI assumes a vehicle fuel economy of 36 miles/gal.

Results and Discussion

Consistently observed disadvantages of PCI combustion are increased CO and HC concentrations [2–6,21]. These increased concentrations (note that 10^4 ppm=1%) are shown on the right-hand axis in Fig. 3 for the same combustion modes summarized in Table 1. Assumed reasons for the increase in the CO and HC concentrations between lean conv and lean PCI combustion modes include low combustion temperatures (early combustion termination), low exhaust temperatures (decreased postcylinder oxidation), and low oxygen concentrations (species-limited reaction). Of course, rich PCI is intended to yield high amounts of CO; thus the overall AF ratio is nearly 15% rich of stoichiometric. In this case, low oxygen concentrations (species-limited reaction) dominate the increase in CO and HC, while low combustion and exhaust temperatures continue to contribute as well.

The DOC effectively performed ("effectively" defined as conversion efficiency greater than 50%) at both lean conv and lean PCI combustion modes. Figure 3 also shows the conversion efficiency of CO and HC through the DOC at each combustion mode.

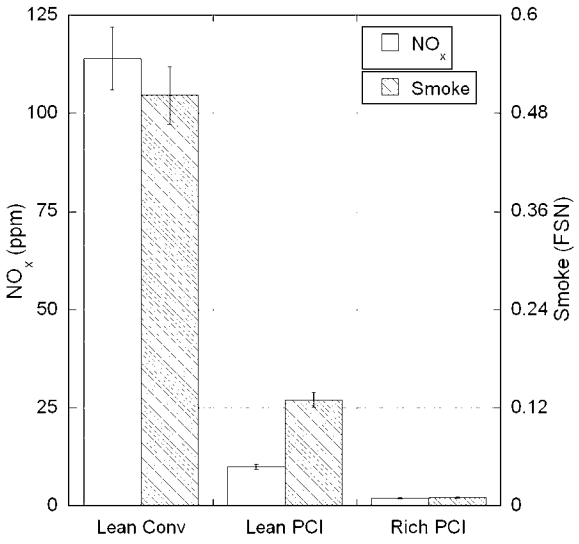

Fig. 1 NO_x and smoke concentrations at the three studied diesel combustion modes

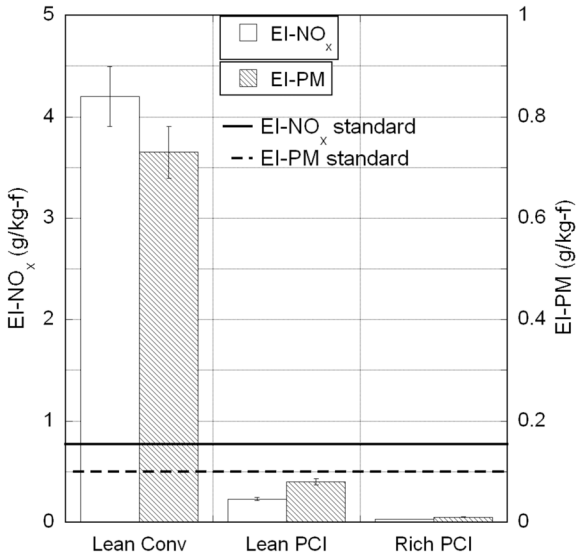

Fig. 2 EI-NO$_x$ and EI-PM emissions at the three studied diesel combustion modes. EI-NO$_x$ and EI-PM standards are based on US EPA Tier 2, Bin 5 regulations [26], assuming a vehicle fuel economy of 36 miles/gal.

Notice that the catalyst is ineffective under rich PCI conditions. Each data point in Fig. 3 is from steady-state engine and catalyst operation (as determined by steady engine and catalyst exhaust temperatures), and represents one data log averaged over 10 min (uncertainty does not include repeatability).

There are perhaps several reasons that cause the DOC to be ineffective under rich PCI. Since the DOC is a platinum catalyst, there is a high affinity to CO. Figure 3 identifies over 5% CO concentration in the catalyst feed gas. It is possible that the platinum bond sites are saturated with CO under rich PCI [17]. The activation energy of CO oxidation over the platinum catalyst is a function of temperature [17]; perhaps rich PCI's temperature falls too low to support catalytic reaction. The space velocity of the feed gas may also influence catalytic activity [27]. These possible causes are not meant to be exhaustive; however, they do provide starting points to assess the ability of the DOC to oxidize under rich PCI conditions.

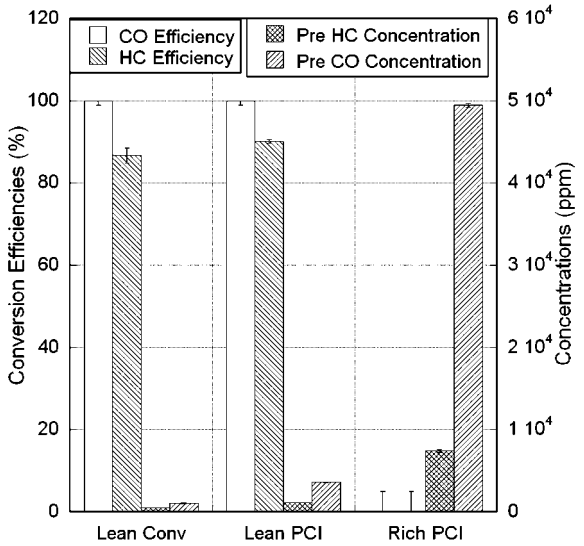

Fig. 3 HC and CO conversion efficiencies and concentrations at the three studied diesel combustion modes

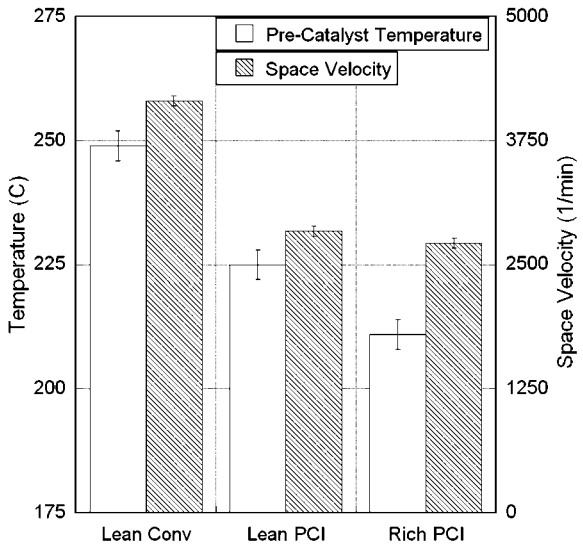

Fig. 4 Precatalyst exhaust temperature and space velocity at the three studied diesel combustion modes

Several tests associated with this study, attempting to correct the ineffectiveness of the DOC at rich PCI, include (1) evaluating the general characteristics—such as CH_4 concentration, oxygen concentration, exhaust temperature, and space velocity—of the feed gas into catalyst (steady-state testing), (2) elevating the catalyst temperature with a high-load combustion mode in an attempt to self-sustain rich PCI reactions (transient feed gas testing), (3) injecting oxygen into the catalyst feed gas to alter the CO/O_2 ratio (air injection testing), (4) artificially elevating the exhaust system temperature with insulation and performing an AF ratio sweep (insulated AF ratio sweep testing), and (5) characterizing the DOC effectiveness under pseudo-LNT storage/regeneration mode switching (combustion mode switching).

Steady-State Catalyst Characterization. Correcting the ineffectiveness of the DOC begins with characterizing the general features of the feed gas. Figure 4 indicates the feed gas temperature into the catalyst, identified as precatalyst temperature, and the feed gas space velocity. Both lean conv and lean PCI have exhaust temperatures that apparently support effective oxidation in the DOC (judging by Fig. 3), even though their respective exhaust temperatures are significantly different. Rich PCI has a significantly lower temperature from either lean conv or lean PCI. Space velocity for lean conv is significantly higher than the PCI conditions, which would tend to decrease oxidation efficiency. Thus, the lower space velocity of rich PCI is expected to assist the oxidation activity in the catalyst [27].

A known influence of HC species on CO oxidation, and vice versa, exists [19]. Furthermore, sufficient O_2 concentration is necessary for CO oxidation across a platinum catalyst [17]. Figure 5 illustrates the relative ratio of CH_4 to total HC, as well as O_2 concentration, in the catalyst feed gas for each combustion mode. Notice that PCI combustion (particularly rich PCI) has significantly increased CH_4/HC ratio relative to lean conv. More detailed analysis about this effect as well as additional HC speciation of PCI combustion are provided in Ref. [6]. The changing ratio of CH_4/HC simply and nonexhaustively suggests that PCI combustion is likely producing different HC species; it does not reveal that CH_4 is inhibiting non-CH_4 HC and CO oxidation. CH_4 has a very low reactivity, thus acts nearly inert within the catalyst (although the increased unreacted CH_4 can influence HC conversion efficiency calculation). However, rich PCI combustion could produce HC species that do inhibit CO oxidation [6].

O_2 concentration is lower with PCI because of the increased

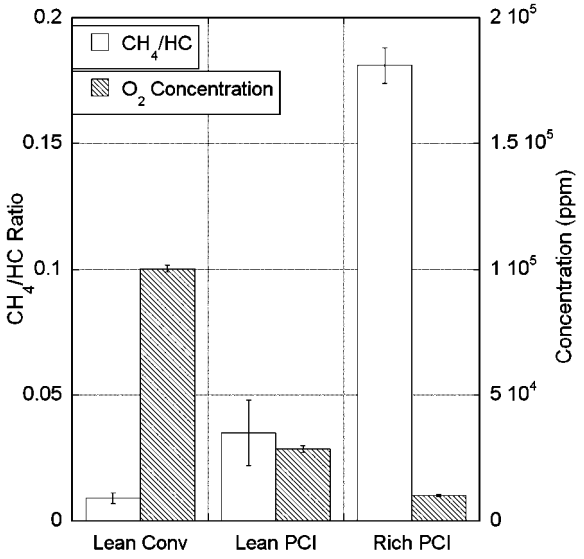

Fig. 5 CH_4/HC ratio and O_2 concentration at the three studied diesel combustion modes

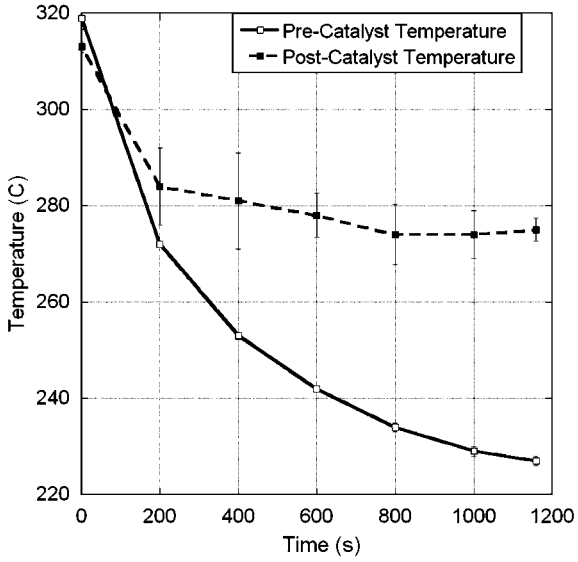

Fig. 6 Pre- and postcatalyst exhaust temperatures versus time as combustion switches from the heating mode to lean PCI (at time=0)

EGR rate needed to attain these PCI combustion modes (refer to Ref. [28] for an example development where O_2 concentrations do not lower with PCI). In spite of having a globally rich AF ratio, rich PCI still contains some significant amount of O_2 (approximately 0.8%) in the exhaust. This phenomenon is typical with direct-injection engines where crevice volume flows can trap air during combustion. In spite of some O_2 being present in rich PCI exhaust, there is likely not enough to promote oxidation over the platinum catalyst [6,17].

This characterization provides two approaches to follow in attempting to correct DOC ineffectiveness under rich PCI combustion: increasing temperature and increasing/altering O_2 concentration.

Transient Feed Gas Testing. To evaluate the influence of exhaust temperature on the DOC under rich PCI conditions, this test procedure first heated the catalyst under a high-load combustion mode, second switched the engine to either lean PCI or rich PCI, and third observed the transient temperature behavior of the catalyst as it cooled. The hope of such transient testing is to identify the catalyst temperature when the DOC becomes ineffective under rich PCI. Uncertainty includes the deviations associated with two repeats of each transient test. The data plots for this testing have time on the x axis, where time=0 is the point when the engine calibration was switched from the catalyst heating mode to a PCI mode.

The transient behaviors of precatalyst and postcatalyst exhaust temperatures versus time for lean PCI are shown in Fig. 6. Notice initially, under the catalyst heating mode (time=0), postcatalyst temperature is lower than precatalyst temperature. Confirmed by Figs. 7 and 8 (discussed in more detail later), oxidation activity occurs at this time; an exotherm, which is not large enough to overcome heat losses, as well as a high gas velocity prevent gas heating through the catalyst. However, as combustion switches to lean PCI, the precatalyst temperature begins to fall. The temperature drop is not dramatic as it takes several minutes to cool the entire exhaust system. In spite of the falling precatalyst temperature, the postcatalyst temperature maintains a high temperature manifested by the catalytic exotherm.

Pre- and postcatalyst CO and HC concentrations for lean PCI are shown in Figs. 7 and 8, respectively. Coinciding with lean PCI data shown in Fig. 3, CO completely oxidizes while typical conversions of HC are observed during the transient. Precatalyst concentrations of both CO and HC increase with time. This phenomenon is largely due to the decreasing exhaust oxidation as the exhaust system cools. Other contributors, such as changing in-cylinder heat transfer conditions, can also change both CO formation and postcombustion oxidation. It should be noted though that the controlled parameters (AF ratio, fuel flow rate, and EGR rate) did not change after mode switching occurred. The response delay between the sample port and the emission analyzers ($\sim$10 s) and the thermocouple response delay ($<$1 s) are insignificant. Postcatalyst HC concentrations increase as combustion is switched to lean PCI, likely due to the increased concentration of CH_4 (see Fig. 5).

The transient behaviors of precatalyst and postcatalyst exhaust temperatures versus time for rich PCI are shown in Fig. 9. Similar to lean PCI, precatalyst temperature cools over several minutes to its steady-state exhaust temperature (Fig. 4). Dissimilar to lean PCI, postcatalyst temperature cools over several minutes to a sig-

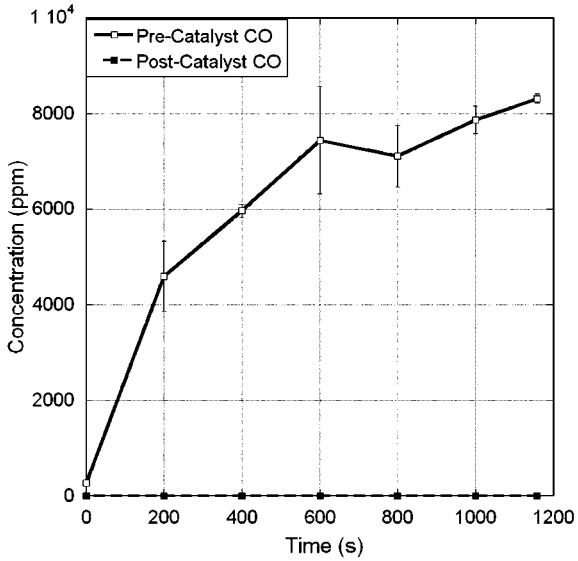

Fig. 7 Pre- and postcatalyst CO concentrations versus time as combustion switches from the heating mode to lean PCI (at time=0)

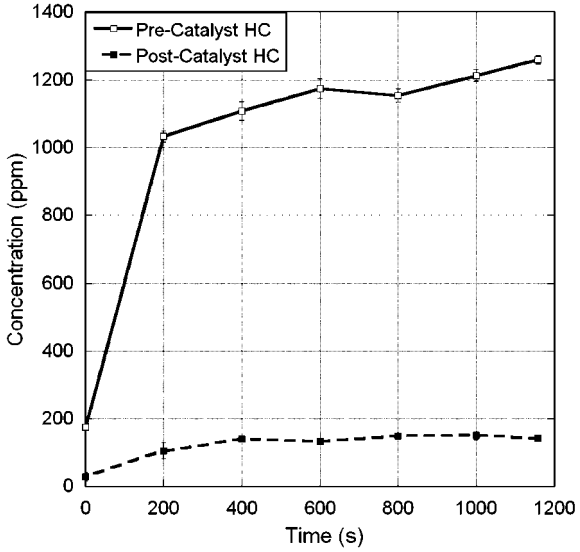

Fig. 8 Pre- and postcatalyst HC concentrations versus time as combustion switches from the heating mode to lean PCI (at time=0)

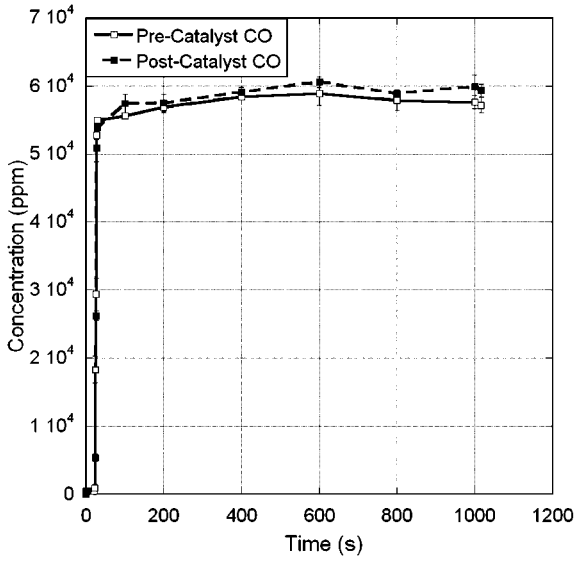

Fig. 10 Pre- and postcatalyst CO concentrations versus time as combustion switches from the heating mode to rich PCI (at time=0)

nificantly cooler temperature than the precatalyst temperature. This lack of sensible exotherm, in addition to the data shown in Figs. 10 and 11, indicates that the DOC continues to be ineffective under rich PCI.

Pre- and post-CO and HC concentrations for rich PCI are shown in Figs. 10 and 11. Immediately upon switching from the heating mode to rich PCI, the catalyst becomes ineffective. Thus, in spite of the feed gas temperature being over 300°C, the DOC is not able to effectively oxidize CO or HC under rich PCI conditions. Figure 10 suggests that the DOC could be producing CO; however, this observation is within the data uncertainty. Figure 11 reveals an initial significant amount of HC oxidation; yet, this oxidation still renders the catalyst ineffective and eventually disappears as the catalyst approaches steady state. Thus, the intended goal of establishing a local self-sustaining exothermic reaction within the catalyst at rich PCI has not been met. Furthermore, the transient data reveal that gas temperatures elevated nearly 100°C are still too low to support effective oxidation activity in the DOC under rich PCI conditions.

Air Injection Results. Since CO oxidation over a platinum catalyst strongly depends on a minimum amount of O_2 in the feed gas [17], this test evaluated the influence of air addition to the precatalyst feed gas stream while the engine operated as rich PCI. The test procedure consisted of the engine constantly running at steady-state rich PCI, while injected (nonheated) air metered through a rotameter incrementally increased precatalyst O_2 concentration. Precatalyst O_2 concentration increased from 1% to 2.2%. More details about the test setup and procedure are provided in Ref. [21].

In spite of increasing precatalyst O_2 concentration to over 2%, the oxidation activity of the DOC did not change during this air injection sweep (thus no data plots are provided). Injection of

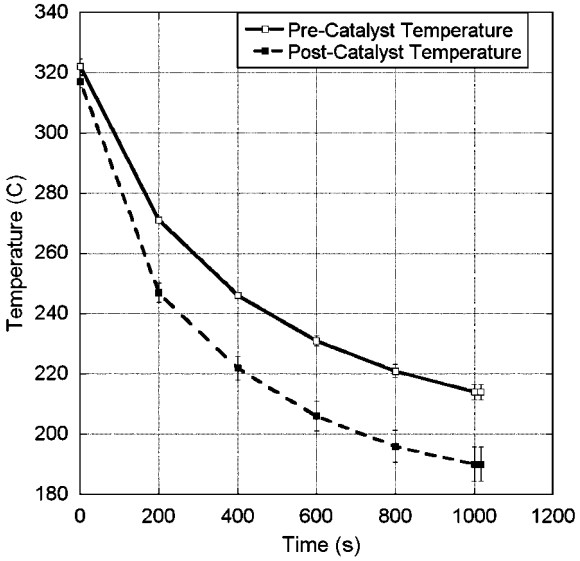

Fig. 9 Pre- and postcatalyst exhaust temperatures versus time as combustion switches from the heating mode to rich PCI (at time=0)

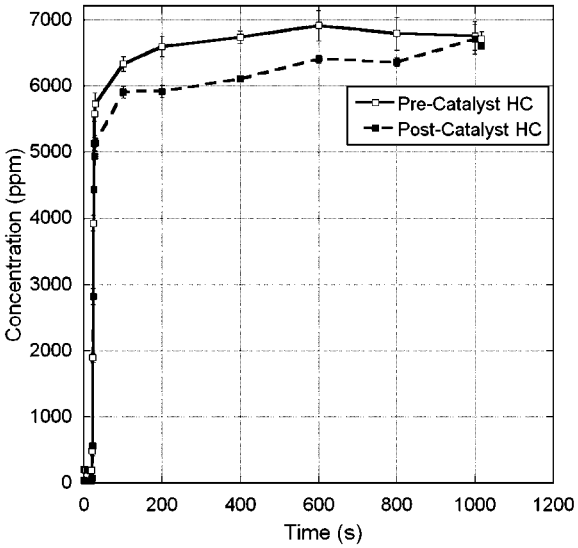

Fig. 11 Pre- and postcatalyst HC concentrations versus time as combustion switches from the heating mode to rich PCI (at time=0)

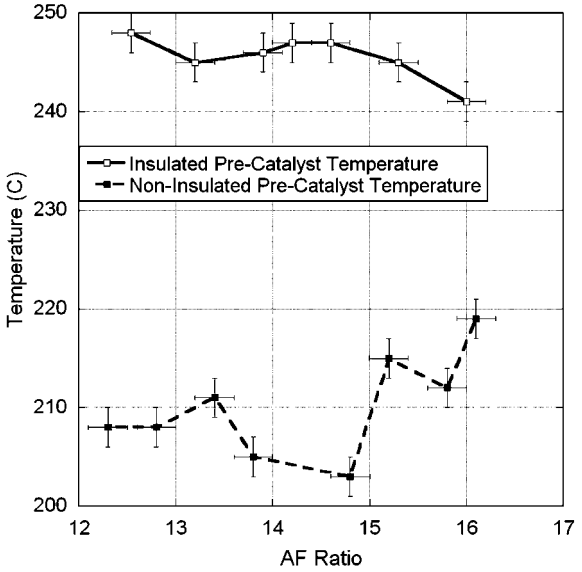

Fig. 12 Precatalyst exhaust temperatures versus AF ratio for insulated and noninsulated exhaust systems

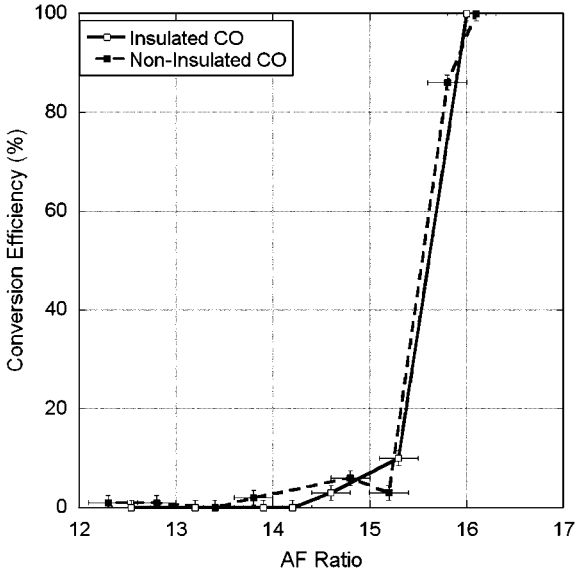

Fig. 13 CO conversion efficiency versus AF ratio for insulated and noninsulated exhaust systems

unheated air likely contributed to nonchanging ineffectiveness, as feed gas temperature decreased with increasing air injection. Furthermore, a 1% increase in O_2 may not have been enough to provide the needed concentration to promote CO activity [6,17]. Since CO inhibition on platinum is a function of both temperature and O_2 concentration [17], it may be necessary to increase both to promote DOC effectiveness. The following test attempts to evaluate (indirectly) CO/O_2 ratio and temperature on oxidation activity in the DOC.

Insulated AF Sweep Testing. It is possible that a simultaneous increase in both precatalyst exhaust temperature and O_2 concentration is needed for DOC effectiveness under rich PCI conditions. This test procedure compares the catalyst between insulated and noninsulated AF ratio sweeps. Although sweeping AF ratio alters CO and O_2 concentrations, in addition to altering combustion, the goal of this test is to assess if the DOC can be effective at any rich AF ratio. Furthermore, sweeping the AF ratio alters the CO/O_2 ratio, which along with temperature are believed to be the influencing parameters on DOC activity [17].

Precatalyst exhaust temperatures for the insulated and noninsulated cases are shown in Fig. 12. Adding insulation to the exhaust system increases precatalyst exhaust temperature by no less than 20°C and on average by 30°C. More importantly, note that the insulated precatalyst temperature is raised above the precatalyst temperature for lean PCI (approximately 225°C, see Fig. 4).

In spite of this increase in temperature (and as expected based on the results shown in Figs. 9–11), the oxidation activity of CO and HC did not change at the rich PCI condition, as shown in Figs. 13 and 14, respectively. Also note from Figs. 13 and 14, both of which are plotted against the AF ratio, that effective oxidation does not occur until the AF ratio is more than 4% lean. An increase of 30°C in exhaust temperature seems to have no effect on the oxidation activity of the DOC. It is reasonable to expect that such a temperature increase could shift the oxidation effectiveness to a significantly lower AF ratio. The observation that this temperature increase does not provide this shift suggests that a pure platinum catalyst, which has a strong affinity to CO [17–19], may be incorrect for rich PCI oxidation.

Combustion Mode Switching. All attempts to promote the DOC effectiveness at rich PCI in this study have failed. However, remembering the real role of rich PCI, this ineffectiveness could be moot if the DOC effectively responds when rich PCI is intermittently used as intended. The developmental goal of rich PCI is to create a low-NO_x/low-soot reducing exhaust environment (high CO, low O_2) for LNT regeneration [5]. This mode is intended to intermittently operate (e.g., 5 s every 60 s), where the engine operates in a lean NO-producing mode the remaining time (and thus loads the LNT). Perhaps the DOC can provide some oxidation during these short rich PCI transitions. Conversely, one transition (or a collection of transitions) to rich PCI could eventually render the DOC ineffective. To diagnose this situation, this test mimics a 60/5 (60 s lean PCI, 5 s rich PCI) LNT load/regeneration cycle over a 30 min period. The test procedure: first, stabilizes the engine and catalyst under lean PCI operation; second, starts logging under lean PCI at time=0; third, intermittently switches the engine calibration to rich PCI for a period of 5 s every 60 s; and fourth, concludes by restabilizing to lean PCI for approximately 8 min. For most of the test, HC and CO concentrations are from the postcatalyst sample port, however, for a portion of the test HC

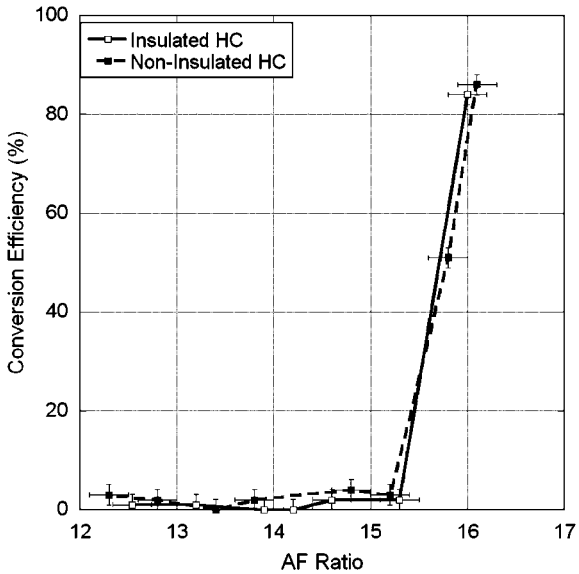

Fig. 14 HC conversion efficiency versus AF ratio for insulated and noninsulated exhaust systems

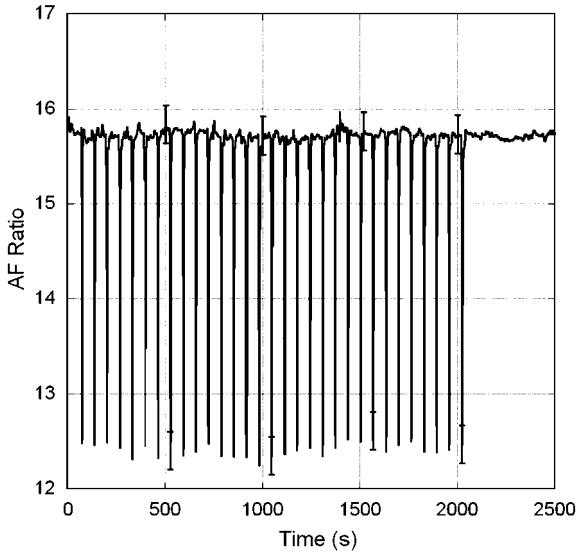

Fig. 15 AF ratio versus time for lean PCI/rich PCI mode switching. Engine operates lean PCI for 60 s, switches to rich PCI for 5 s, and returns to lean PCI.

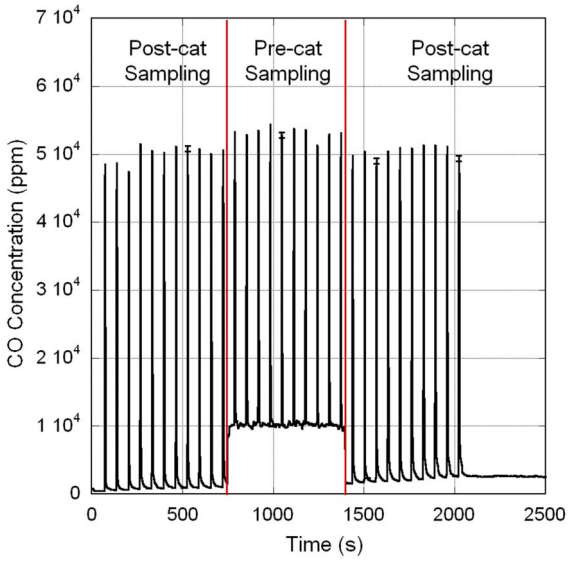

Fig. 17 Postcatalyst (and precatalyst) CO concentrations versus time for lean PCI/rich PCI mode switching. Engine operates lean PCI for 60 s, switches to rich PCI for 5 s, and returns to lean PCI.

and CO concentrations are from the precatalyst sample port. Uncertainty bars reflect only the standard uncertainty associated with instrument precision and accuracy and sample log variability; repeated tests do not exist to provide repeatability uncertainty. The response time of emission analyzers, including the time traveling through the sample line, is larger ($\sim$10 s) than the switching scheme time. Thus, there is some time delay between when emissions pass the sample port and when the emission is accurately measured. The response time of the thermocouple ($<$1 s) does not affect the stated temperature measurement.

Figure 15 illustrates the AF ratio versus time for the lean PCI/rich PCI mode switching. Note that the engine operates as rich PCI for 5 s every 60 s. There were 31 rich PCI excursions over the course of the roughly 33 min test. The corresponding postcatalyst exhaust temperatures are shown in Fig. 16. Notice that the

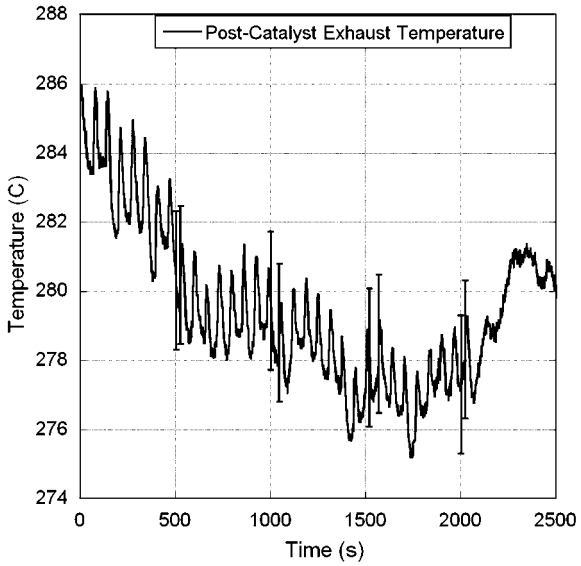

Fig. 16 Postcatalyst exhaust temperatures versus time for lean PCI/rich PCI mode switching. Engine operates lean PCI for 60 s, switches to rich PCI for 5 s, and returns to lean PCI.

temperatures match those of Fig. 6, albeit warmer at the start of the test (time=0), where the engine stabilized under lean PCI conditions.

CO concentrations versus time are shown in Fig. 17. As indicated in the figure, concentrations are reported from both the postcatalyst and the precatalyst sampling ports. Notice during the lean PCI modes the DOC is effective in oxidizing CO; although 100% conversions are not realized as in the steady-state lean PCI operation (see Figs. 3 and 7). Also notice that at the termination of lean PCI/rich PCI mode switching (time=2000 s), the postcatalyst CO concentration is higher than at the outset of the transition testing (time=0). This result suggests that the rich PCI mode may have temporarily decreased the effectiveness of the DOC. The DOC continues to be ineffective under rich PCI conditions during the mode switching. Notice that postcatalyst CO concentrations are over 4.5% during rich PCI operation. There appears to be some oxidation activity (which is better than that observed in Fig. 10) by noticing the precatalyst CO concentrations as slightly higher than the postcatalyst CO concentrations.

Similar results are observed for HC concentrations during the lean PCI/rich PCI mode switching, as shown in Fig. 18. Although the DOC is ineffective (i.e., less than 50% oxidation) at oxidizing HC, there is a significant HC oxidation activity during rich PCI excursions (more so than that reported in Fig. 11). Similar to the CO behavior, DOC effectiveness is decreased after the mode transitions (time=2000 s) relative to the start of mode transitions (time=0). Referring to Fig. 16, it appears as though the mode transitions do diminish the DOC's effectiveness; one may conjecture that continued mode transitioning might eventually render the DOC ineffective. Furthermore, the diminished effectiveness of the DOC after mode transitioning is observed as a lower steady-state temperature in Fig. 16 (after time=2000 s).

A final word about the mode transition testing again attempts to place rich PCI into proper context. A major component this study has left out is the LNT. Even during LNT regeneration, a post-LNT "cleanup" DOC likely will not see the concentrations of CO in the feed gas that have been studied here. As CO is oxidized in the LNT by NO_2, the CO concentration entering a post-LNT DOC will be significantly diminished. Hypothesizing that—because of the high CO concentrations at relatively low exhaust temperatures—CO is preferentially drawn to and occupies all

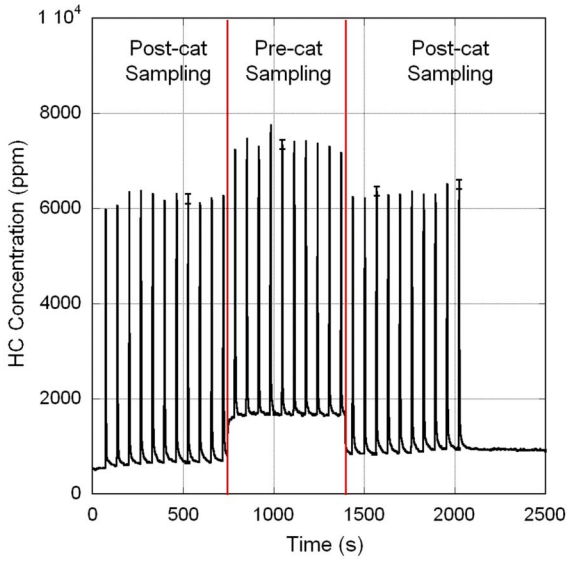

Fig. 18 Postcatalyst (and precatalyst) HC concentrations versus time for lean PCI/rich PCI mode switching. Engine operates lean PCI for 60 s, switches to rich PCI for 5 s, and returns to lean PCI.

available platinum sites in the DOC [17], reducing the feed gas CO concentration will possibly make the DOC effective in oxidizing post-LNT CO and HC. Of course, O_2 concentrations will also be sparse in the feed gas as the LNT promotes CO and HC oxidation with all available O_2; thus post-LNT/pre-DOC air injection may be necessary for post-LNT CO and HC oxidation.

Conclusions

In summary, this article reports the findings of a study that evaluates the effectiveness of a DOC in oxidizing HC and CO in lean conv, lean PCI, and rich PCI exhaust from a light-duty diesel engine. The study uses several tests—including steady-state feed gas, transient feed gas, air injection, insulated exhaust AF ratio sweeps, and mode transitioning—to improve the observed ineffectiveness of the DOC in oxidizing HC and CO under rich PCI conditions. The catalyst is platinum suspended in alumina/silica washcoat on a cordierite monolith. The study reports the following major findings.

- The DOC effectively oxidizes CO and HC under lean conditions (both lean conv and lean PCI). Effective oxidation under rich PCI is not possible even with a 100°C increase in exhaust temperature, 1% increase in O_2 concentration, or during lean PCI/rich PCI combustion mode switching.
- The AF ratio (4% fuel lean) at which the DOC becomes effective at the studied exhaust temperature (approximately 207°C) does not shift to a more fuel-rich AF ratio in spite of an approximately 30°C increase in temperature (manifested by exhaust system insulation). This observation suggests that a pure platinum catalyst, which has a strong affinity to CO at low temperatures, may be incorrect for rich PCI oxidation.
- Diminishing effectiveness of the DOC during lean PCI/rich PCI mode transitioning suggests that the DOC could eventually lose effectiveness at oxidizing CO and HC during the lean PCI operation. Furthermore, the DOC demonstrates diminished effectiveness during steady-state lean PCI operation after lean PCI/rich PCI mode transitioning. Such behavior could be observed in a pre-LNT DOC.
- Finally, it is suggested that the above results must be considered in the context of the role of rich PCI relative to a LNT and the expected feed gas into a post-LNT cleanup DOC. After passing through a LNT, the feed gas into a post-LNT cleanup DOC is expected to have significantly lower CO and HC concentrations.

Acknowledgment

The authors wish to acknowledge the technical and financial support of the General Motors Collaborative Research Laboratory (GM CRL) at the University of Michigan. The GM CRL provides the focal point for joint research between General Motors Research and Development and the University of Michigan, establishing the framework to link faculty and student expertise with long term GM needs. Particularly, the following individuals have made long-lasting positive contributions to this research study: Mr. Patrick Szymkowicz, Dr. Stani Bohac, Dr. Alex Knafl, Dr. Guntram Lechner, Mr. Bill Kirkpatrick, Mr. John Mears, Dr. Jonathan Hagena, Mr. Jerry Fuschetto, and Mrs. Linda Bnogche.

References

[1] Zelenka, P., Cartellieri, W., and Herzog, P., 1996, "Worldwide Diesel Emission Standards: Current Experiences and Future Needs," Appl. Catal., B, **10**, pp. 3–28.
[2] Iwabuchi, Y., Kawai, K., Shoji, T., and Takeda, Y., 1999, "Trial of New Concept Diesel Combustion System—Premixed Compression-Ignited Combustion," SAE Trans., **108**(3), pp. 142–151.
[3] Akihama, K., Takatori, Y., Inagaki, K., Sasaki, S., and Dean, A., 2001, "Mechanism of the Smokeless Rich Diesel Combustion by Reducing Temperature," SAE Trans., **110**(3), pp. 648–662.
[4] Jacobs, T., and Assanis, D., 2007, "The Attainment of Premixed Compression Ignition Low-Temperature Combustion in a Compression Ignition Direct Injection Engine," Proc. Combust. Inst., **31**, pp. 2913–2920.
[5] Jacobs, T., Bohac, S., Assanis, D., and Szymkowicz, P., 2005, "Lean and Rich Premixed Compression Ignition Combustion in a Light-Duty Diesel Engine," SAE Trans., **114**(3), pp. 382–393.
[6] Bohac, S., Han, M., Jacobs, T., Lopez, A., Assanis, D., and Szymkowicz, P., 2006, "Speciated Hydrocarbon Emissions From an Automotive Diesel Engine and DOC Utilizing Conventional and PCI Combustion," SAE Trans., **115**(4), pp. 41–52.
[7] Li, Y., Roth, S., Dettling, J., and Beutel, T., 2001, "Effects of Lean/Rich Timing and Nature of Reductant on the Performance of a NO_x Trap Catalyst," Top. Catal. **16/17**, pp. 139–144.
[8] Voss, K., Yavuz, B., Hirt, C., and Farrauto, R., 1994, "Performance Characteristics of a Novel Diesel Oxidation Catalyst," paper presented at the SAE International Congress and Exposition, Detroit, MI, Paper No. 940239.
[9] Farrauto, R., and Voss, K., 1996, "Monolithic Diesel Oxidation Catalysts," Appl. Catal., B, **10**, pp. 29–51.
[10] Blakeman, P., Chiffey, A., Phillips, P., Twigg, M., and Walker, A., 2003, "Developments in Diesel Emission Aftertreatment Technology," paper presented at the SAE Brazil 2003 Congress and Exhibit, Sao Paulo, Brazil, Paper No. 2003-01-3753.
[11] Kakoi, Y., Tsutsui, Y., Ono, N., Umezawa, K., and Kondo, N., 1998, "Emission Reduction Technologies Applied to High-Speed Direct Injection Diesel Engine," paper presented at the SAE International Congress and Exposition, Detroit, MI, Paper No. 980173.
[12] Ueno, H., Furutani, T., Nagami, T., Aono, N., Goshima, H., Kasahara, K., 1998, "Development of Catalyst for Diesel Engine," paper presented at the SAE International Congress and Exposition, Detroit, MI, Paper No. 980195.
[13] Andrews, G., Clarke, A., Rojas, N., Gregory, D., and Sale, T., 2001, "The Transient Deposition and Particle Changes Across a Combined Oxidation and Hydrocarbon Storage Catalyst Under Diesel Cold Start Conditions," SAE Trans., **110**(4), pp. 1212–1221.
[14] Johnson, T., 2003, "Diesel Emission Control in Review—The last 12 months," SAE Trans., **112**(4), pp. 1–14.
[15] Johnson, T., 2006, "Diesel Emission Control Technology—2003 in Review," paper presented at the SAE 2004 World Congress, Detroit, MI, Paper No. 2004-01-0070.
[16] Johnson, T., 2006, "Diesel Emission Control in Review," SAE Trans., **115**(4), pp. 1–16.
[17] Engel, T., and Ertl, G., 1978, "Elementary Steps in the Catalytic Oxidation of Carbon Monoxide on Platinum Metals," Adv. Catal., **28**, pp. 1–78.
[18] Schwartz, S., Schmidt, L., and Fisher, G., 1986, "$CO+O_2$ Reaction on Rh (111): Steady-State Rates and Adsorbate Coverages," J. Phys. Chem., **90**, pp. 6194–6200.
[19] Patterson, M., Angove, D., and Cant, N., 2000, "The Effect of Carbon Monoxide on the Oxidation of Four C6 to C8 Hydrocarbons Over Platinum, Palladium and Rhodium," Appl. Catal., B, **26**, pp. 45–57.
[20] Knafl, A., Han, M., Bohac, S., Assanis, D., and Szymkowicz, P., 2007, "Comparison of Diesel Oxidation Catalyst Performance on an Engine and a Gas Flow Reactor," paper presented at the SAE 2007 World Congress, Detroit, MI, Paper No. 2007-01-0231.
[21] Jacobs, T., 2005, "Simultaneous Reduction of Nitric Oxide and Particulate Matter Emissions from a Light-Duty Diesel Engine Using Combustion Devel-

opment and Diesel Oxidation Catalyst," Doctoral thesis, University of Michigan, Ann Arbor.
[22] Dodd, A., and Holubecki, Z., 1965, "The Measurement of Diesel Exhaust Smoke," Industry Report, MIRA Report No. 1965/10.
[23] Heywood, J., 1988, *Internal Combustion Engine Fundamentals*, McGraw-Hill, New York, pp. 148–152.
[24] Kamimoto, T., and Bae, M., 1988, "High Combustion Temperature for the Reduction of Particulate in Diesel Engines," SAE Trans., **97**(6), pp. 692–701.
[25] 1991, "Control of Air Pollution From New Motor Vehicles and New Motor Vehicle Engines: Gaseous and Particulate Emission Regulations for 1994 and Later Model Year Light-Duty Vehicles and Light-Duty Trucks; Final Rule," Fed. Regist., **56**, pp. 25723–25790.
[26] 2000, "Control of Air Pollution From New Motor Vehicles: Tier 2 Motor Vehicle Emissions Standards and Gasoline Sulfur Control Requirements; Final Rule," Fed. Regist., **65**, pp. 6697–6746.
[27] Berkmanm, M., and Katari, A., 2002, "Transient CFD: How Valuable is it for Catalyst Design?," paper presented at the SAE 2002 World Congress, Detroit, MI, Paper No. 2002-01-0064.
[28] Jacobs, T., Knafl, A., Bohac, S., Assanis, D., and Szymkowicz, P., 2006, "The Development of Throttled and Unthrottled PCI Combustion in a Light-Duty Diesel Engine," paper presented at the SAE 2006 World Congress, Detroit, MI, Paper No. 2006-01-0202.

Active Air Control System Development Using Charge Air Integrated Manifold Engine Numerical Simulation (CAIMENS)

Diana K. Grauer
Kirby S. Chapman
Ali Keshavarz

NGML,
Kansas State University,
245 Levee Drive,
Manhattan, KS 66502

This paper reports on an investigation into the transient, compressible flow physics that impact the trapped equivalence ratio. A comprehensive, variable geometry, multicylinder turbocharger-reciprocating engine computer simulation (T-RECS) has been developed to illustrate the effect of airflow imbalance on an engine. A new model, the charge air integrated manifold engine numerical simulation (CAIMENS), is a manifold flow model coupled with the T-RECS engine processor that uses an integrated set of fundamental principles to determine the crank angle-resolved pressure, temperature, burned and unburned mass fractions, and gas exchange rates for the cylinder. CAIMENS has the ability to show the transient impact of one cylinder firing on each successive cylinder. The pulsation model also describes the impact of manifold pressure drop on in-cylinder peak pressure and the pressure wave introduced to the intake manifold by uncovering the intake ports. CAIMENS provides the information necessary to quantify the impact of airflow imbalance, and allows for the visualization of the engine system before and after airflow correction. The model shows that not only does the manifold pressure drop have a significant impact on the in-cylinder peak pressure but it also has an impact on the pressure wave introduced to the intake manifold as the ports are opened. Also, each cylinder has a considerable impact on the airflow into each successive cylinder.
[DOI: 10.1115/1.2906181]

Introduction

An industry database of compressor engines identifies approximately 5600 engines on the natural gas pipeline system generating around 9,150,000 bhp [1]. Much of this equipment is very aged, though technically, there are no fundamental life-limiting aspects of the large-bore, integral engine design. Five related makes and models account for approximately 70% of the total number and total output. These are

- Cooper GMV
- Cooper GMW, V-250/V-275's, and W-330's
- Clark TCV's, TLA's (and variants), BA's, and many RA's

All of these are lean-burn, two-stroke, loop scavenged engines with various forms of aspiration ranging from pump scavenged to high pressure ratio (2.5:1) turbochargers. The Clark family represents approximately 30% of the totals while the Cooper family accounts for approximately 40%. In general, these engines utilize similar emission reduction technologies [1]. This study will focus on the Cooper GMV due to its predominance in the industry.

Technical Discussion

Historically, the turbocharged engine system has allowed the natural gas compression industry to decrease pollutant emissions by increasing airflow to the engine. Due to the physics of the turbocharged engine system, and the environments in which such engines operate, further advancement has been limited. During typical operation, the expectation and the common perception is that the corrected trapped equivalence ratio (ϕ_{se}) is not balanced between the cylinders of a given engine. Nitrogen oxide emissions directly correlate to the corrected trapped equivalence ratio written as

$$[NO_x] = f(\phi_{se}, IT) \tag{1}$$

where $[NO_x]$ is the concentration of nitrogen oxide in the exhaust, IT is the ignition timing, and the corrected trapped equivalence ratio is defined as

$$\phi_{se} = \frac{\phi_{tr}}{\eta_{se}} \tag{2}$$

The only way to achieve the same corrected trapped equivalence ratio, and therefore increase uniformity of NO_x production across the engine, is to ensure that the fuel flow rate, airflow rate, and scavenging efficiency (η_{se}) are identical for each cylinder. Only when these variables are balanced will the combustion cycle in each cylinder be balanced. Without this stability, engine NO_x production will be disproportionately increased in the richest cylinder or the engine operating range will unduly be narrow. Currently, engine balancing relies on continuity of peak pressure, peak pressure, or the peak pressure-to-cold compression pressure ratio. Engine balancing is routinely accomplished by manipulating the individual cylinder fuel valves until the target pressure or pressure ratio is achieved. This manipulation creates an imbalance in equivalence ratio between the cylinders. The imbalance in the equivalence ratio creates instability in power production from the cylinders, as well as disproportionate NO_x production within the cylinders. In the worst case scenario, some cylinders operate too lean for stable combustion and some may operate fuel rich. These "rich" burning cylinders unacceptably produce high quantities of NO_x [2], as illustrated by example in Fig. 1.

Contributed by the Internal Combustion Engine Division of ASME for publication in the JOURNAL OF ENGINEERING FOR GAS TURBINES AND POWER. Manuscript received November 5, 2007; final manuscript received November 26, 2007; published online April 29, 2008. Review conducted by Dilip R. Ballal.

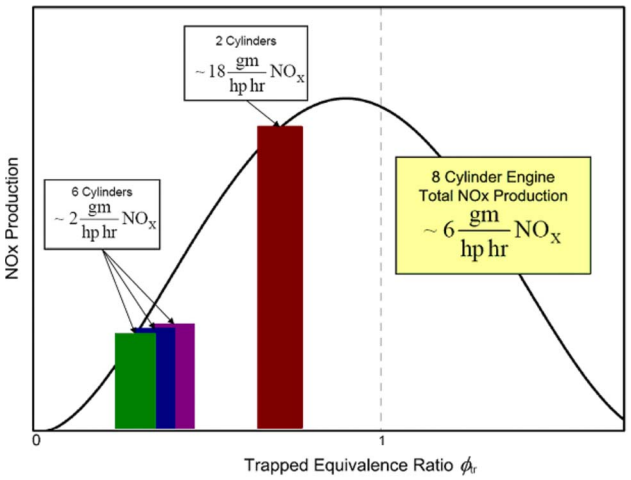

Fig. 1 Example of relative total NO_x production

Intake Manifold

In this study, the intake manifold is assumed to be a pipe with a finite diameter and length. The intake ports of five cylinders are connected through runners to this manifold. The runners are also modeled as pipe with a finite length and hydraulic diameter. Nonisothermal flow through the manifold and runners is governed by the time-dependent continuity (mass conservation), momentum, and energy equations. These are supplemented by an equation of state for homogeneous, one-dimensional, single-phase flow. By solving the resulting system of equations, the behavior of the fluid parameters can be obtained in the manifold. In this study, the goal is to develop a set of engineering models that can be used to quickly assess the transient airflow rate through the engine system. The research team elected to use one-dimensional formulations of the mass and energy conservation equations. The following equations were developed for one-dimensional, unsteady, compressible flow to include the effects of wall friction and heat transfer by Issa and Spalding [3], Deen and Reintsema [4], Thorley and Tiley [5], and Price et al. [6]. The equations are shown in partial differential form.

Conservation of mass:

$$\frac{\partial \rho}{\partial t} + \frac{\partial}{\partial x}(\rho v) = 0 \tag{3}$$

Conservation of momentum:

$$\rho \frac{\partial v}{\partial t} + \rho v \frac{\partial v}{\partial x} + \frac{\partial p}{\partial x} = -\frac{w}{A} - \rho g \sin\theta \tag{4}$$

where

$$w = \frac{f \rho v |v|}{8} \pi D$$

Conservation of energy:

$$\rho \frac{\partial h}{\partial t} + \rho v \frac{\partial h}{\partial x} - \frac{\partial p}{\partial t} - v \frac{\partial p}{\partial x} = \frac{\Omega + wv}{A} \tag{5}$$

The term Ω is the heat flow into the pipe per unit length of pipe and per unit time:

$$\Omega = -\frac{4 h_\infty A (T - T_\infty)}{D} \tag{6}$$

To obtain the gas enthalpy h in terms of p, ρ, and T, Zemansky [7] described the thermodynamic identity:

$$dh = c_p dT + \left\{ \frac{T}{\rho} \left(\frac{\partial \rho}{\partial T} \right)_P + 1 \right\} \frac{dp}{\rho} \tag{7}$$

The following equation of state is used to incorporate compressibility:

$$\frac{p}{\rho} = ZRT \tag{8}$$

The gas compressibility factor Z given by the Beatie–Bridgman equation of state (valid for $\rho \leq 0.8 \rho_{cr}$) [8]:

$$Z = 1 - \frac{\bar{\nu} c}{T^3} + \frac{B}{\bar{\nu}} - \frac{Bc}{T^3} - \frac{A}{\bar{\nu} R_u T} \tag{9}$$

where

$$A = A_0 \left(1 - \frac{a}{\bar{\nu}} \right)$$

and

$$B = B_0 \left(1 - \frac{b}{\bar{\nu}} \right)$$

Constants for air:

$$A_0 = 131.8441, \quad B_0 = 0.04611$$

$$a = 0.01931, \quad b = -0.00110, \quad c = 4.34 \times 10^4$$

These equations and identities can be combined to create a set of three equations that solve for p, ρ, and T as functions of time and thoroughly describe transient compressible gas flow. The equation set is

$$\left(\frac{\partial P}{\partial t} \right) + v \left(\frac{\partial P}{\partial x} \right) + \rho V_w^{\,2} \left(\frac{\partial v}{\partial x} \right) = \frac{V_w^{\,2}}{CpT} \left[1 + \frac{T}{Z} \left(\frac{\partial Z}{\partial T} \right)_P \right] \frac{\Omega + wv}{A} \tag{10}$$

$$\left(\frac{\partial v}{\partial t} \right) + v \left(\frac{\partial v}{\partial x} \right) + \frac{1}{\rho} \left(\frac{\partial P}{\partial x} \right) = -\frac{w}{A\rho} - g \sin\theta \tag{11}$$

$$\left(\frac{\partial T}{\partial t} \right) + v \left(\frac{\partial T}{\partial x} \right) + \frac{V_w^{\,2}}{Cp} \left[1 + \frac{T}{Z} \left(\frac{\partial Z}{\partial T} \right)_P \right] \left(\frac{\partial v}{\partial x} \right) = \frac{V_w^{\,2}}{CpP} \left[1 - \frac{P}{Z} \left(\frac{\partial Z}{\partial P} \right)_T \right] \frac{\Omega + wv}{A} \tag{12}$$

where the wave speed V_w is

$$V_w = \sqrt{\frac{ZRT}{\left\{ 1 - \frac{P}{Z} \left(\frac{\partial Z}{\partial P} \right)_T - \frac{P}{\rho CpT} \left[1 + \frac{T}{Z} \left(\frac{\partial Z}{\partial T} \right)_P \right]^2 \right\}}} \tag{13}$$

For convenience, the continuity, momentum, and energy equations are written in terms of the mass flow rate ($\dot{m}$) since the primary interests of this study are the pressure and mass flow rate as a function of time and location. Translating velocity into mass flow rate,

$$v = \frac{\dot{m}}{\rho A} = \frac{\dot{m} ZRT}{pA} \tag{14}$$

The fully implicit method is used to numerically solve the continuity, momentum, and energy equations. The implicit method is unconditionally stable and utilizes the Newton–Raphson technique to solve the set of nonlinear simultaneous equations at each time step. A thorough investigation of one-dimensional gas flow in pipes was conducted by Abbaspour [9] and Chapman et al. [10]. Abbaspour [9] also includes in-depth derivations of the conservation equations and their translation into the implicit solution scheme.

As discussed earlier and illustrated in Fig. 2, the manifold in this study is considered to be a pipe with a finite diameter and

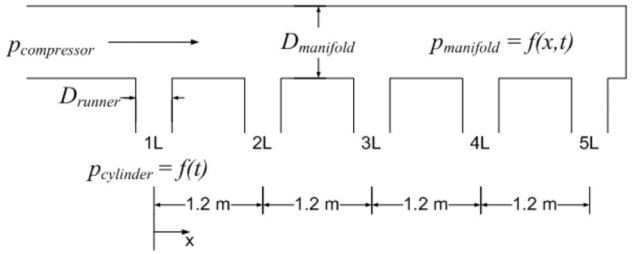

Fig. 2 Cooper GMV intake manifold model

length. Connected to this pipe are the runners, which are also modeled as pipe with a finite length and hydraulic diameter branching at 90 deg from the manifold. The cylinder runners are spaced 1.219 m (48 in.) centerline to centerline. The illustration in Fig. 2 is the left bank of the Cooper GMV intake manifold.

The cross section of the intake runners is 0.254×0.140 m^2 (10×5.5 in.^{2}), resulting in a calculated hydraulic diameter of 0.180 m (7.1 in.)

The manifold model, when subjected to known engine operating conditions (p, T, and design $\dot{m}$), which will be utilized as the boundary conditions for the model, and the geometry shown in Fig. 2 calculate the pressure distribution shown in Fig. 3. Each circle represents the location of the intake runner for each cylinder relative to intake manifold.

These data have been extensively compared to and is consistent with current literature and field test data. Abbaspour [9] also presents this comparison. This confirms that due only to the physics of the air delivery system, each cylinder is subjected to a slightly different air manifold pressure.

Port Flow

The most significant airflow restriction in a two-stroke cycle internal combustion engine is the flow through the intake and exhaust ports [11]. Typically, the minimum cross-sectional area in the intake and exhaust system occurs at the ports. To account for the pressure reduction across the intake and exhaust ports, considerable success has been realized by modeling the gas flow as one-dimensional, quasisteady, compressible flow [11]. With the upstream pressure and gas temperature known, equations for flow through a restriction can be applied. The appropriate relationship is [10]

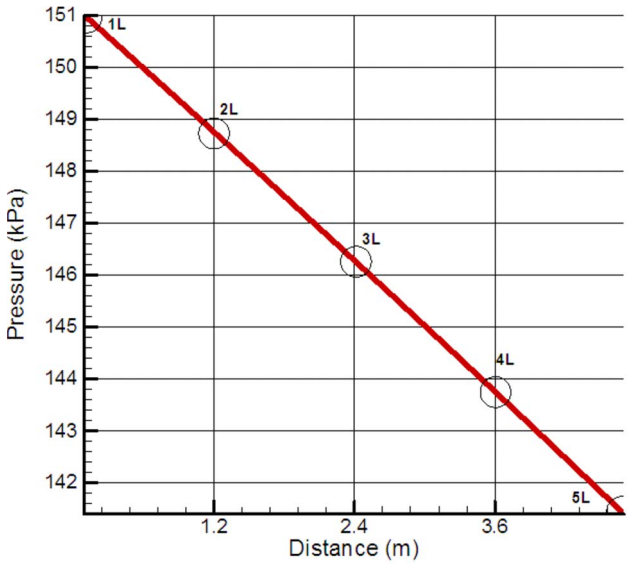

Fig. 3 Steady state Cooper GMV manifold Δp

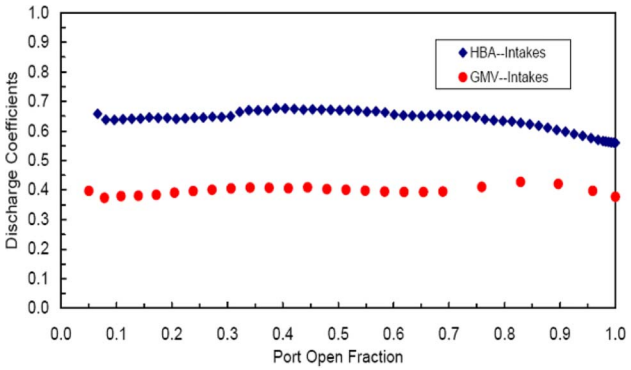

Fig. 4 Discharge coefficients for GMV and HBA intake ports

$$\dot{m}_{\text{real}} = \frac{C_D A_T p_0}{\sqrt{RT_0}} \left(\frac{p_T}{p_0}\right)^{1/\gamma} \left\{ \frac{2\gamma}{\gamma - 1} \left[1 - \left(\frac{p_T}{p_0}\right)^{(\gamma-1)/\gamma} \right] \right\}^{1/2} \quad (15)$$

The values C_D and A_T represent the discharge coefficient and the minimum area of the restriction. The subscript "0" refers to the upstream stagnation point of the restriction. For flow into the cylinder, the stagnation conditions refer to conditions in the intake manifold. For exhaust flow out of the cylinder, the stagnation conditions refer to conditions in the cylinder. Alternately, the subscript T refers to values at the restriction. This equation is only applicable to subsonic and sonic flows. The pressure ratio is defined as

$$\frac{p_0}{p_T} = \left[1 + \frac{\gamma - 1}{2} M^2 \right]^{\gamma/(\gamma-1)} \quad (16)$$

An extensive experimental investigation into port flow characteristics was conducted by Chapman et al. [12]. This study experimentally determined the port discharge coefficient C_D for large two-stroke cycle engines. The discharge coefficients shown in Fig. 4 have been utilized to calculate mass flow rate through the intake ports of the Cooper GMV. Data from the study for the Clark HBA are shown for comparison.

In-Cylinder Conditions

In order to model in-cylinder conditions, this study integrated the turbocharger-reciprocating engine computer simulation (T-RECS) into the manifold flow model. T-RECS is a design analysis tool that allows one to optimize the integration of the reciprocating engine and turbocharger air management system [13]. Specifically, the T-RECS program calculates the temperature, pressure, and intake/exhaust flow rates at various points in the turbocharged engine system. The mathematical algorithms used to determine the pressure, temperature, and mass flow rate are based on fundamental engineering principles to provide the highest reliability in the calculated values.

When coupled with the manifold model discussed in the previous section, the engine processor uses a sophisticated set of fundamental principles to determine the crank angle-resolved pressure, temperature, burned and unburned mass fractions, and gas exchange rates for the cylinder. This in turn creates a transient description of the pressure and mass flow rates seen by the intake and exhaust ports [13]. The T-RECS model operates with a forced mass and energy balance, using equations of state and chemical equilibrium.

Cylinder Activity

The intake runners and therefore the intake manifold are subject to the in-cylinder pressure variations modeled by T-RECS and illustrated in Fig. 5.

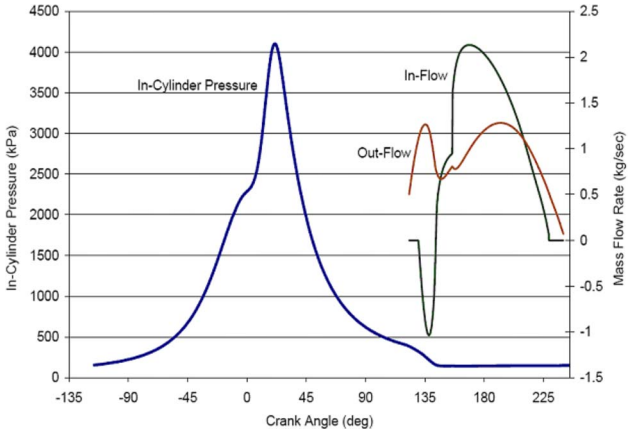

Fig. 5 T-RECS pressure and mass flow rate versus crank angle

Figure 6 is an enhanced picture of the in-cylinder pressure during the opening and closing of the ports. The in-cylinder pressure variation between intake port opening (IPO) and intake port closing (IPC) is the pressure wave that the intake manifold is subjected to during engine operation. This wave, in conjunction with the port activity, creates pulsation in the manifold.

To describe the port activity and therefore the transient conditions created by the in-cylinder pressure, cylinder firing order must be known. The timing model for the Cooper GMV is illustrated in Figs. 7 and 8.

This timing model was then used in combination with an instantaneous stroke calculation for each cylinder that allowed for visualization of the port activity. For simplicity sake, only the master rod side was considered. The instantaneous stroke (y), defined as the distance from the top of the cylinder, as described by Ferguson and Kirkpatrick[11] is

$$y = L + a - [(L^2 - a^2 \sin^2 \theta)^{1/2} + a \cos \theta] \tag{17}$$

The instantaneous stroke calculation verifies that at any time during a crank shaft revolution, there are only two cylinders open. As Cylinder 1 reaches the bottom dead center, Cylinder 4 intake ports begin to uncover. This is visualized using Fig. 9.

Results and Discussion

The overall goal of this project is the ongoing assessment of the impact of the unbalanced distribution of air in the intake manifold.

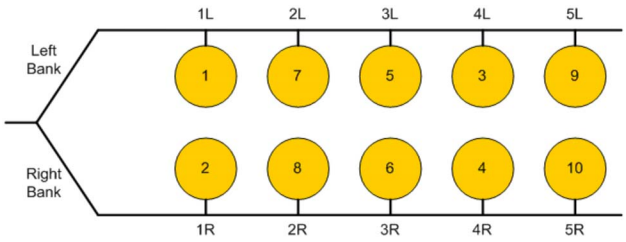

Fig. 7 Firing order for ten-cylinder GMV

Resulting from this investigation, the charge air integrated manifold engine numerical simulation (CAIMENS) has been developed. It is a multicylinder engine algorithm that models the effects of air charge imbalance between cylinders using the physical relationships from the preceding sections of this paper.

Figure 10 shows the block diagram of the CAIMENS algorithm. In order to begin calculations, engine operating parameters including average air manifold temperature and pressure, design airflow rate, and manifold geometry are entered as input parameters. These parameters are used to calculate first the steady state manifold pressure drop from cylinder to cylinder due only to geometry and the simple physics of flow through a pipe. This resultant pressure drop when fed into T-RECS allows the engine processor to calculate in-cylinder conditions for each individual cylinder. These in-cylinder pressure variations create pressure pulses in the air manifold when the piston uncovers the intake ports, which disrupt airflow to the cylinders [14].

This airflow hindrance can be assessed by analyzing the in-cylinder pressure variations that impact the manifold when the ports are uncovered and also by understanding how the variation in the manifold pressure would impact in-cylinder conditions. To more thoroughly understand the impact of each cylinder on the air delivery system and overall engine operation, a single cylinder is modeled in simplified manner first. This investigation is completed by reducing the pressure curve generated by T-RECS in Fig. 5 to the profile illustrated in Fig. 11.

The pressure profile is then input into the manifold model, which solves the pipe equations in conjunction with the boundary conditions discussed earlier (p, T, and design $\dot{m}$). The resultant pressure wave (Fig. 12) is plotted over time at the location of each cylinder in the manifold. IPO to IPC is a function of the speed of the engine. For this study, the speed of the engine is 300 rpm, resulting in an intake port uncovered to covered time of approximately 0.08 s.

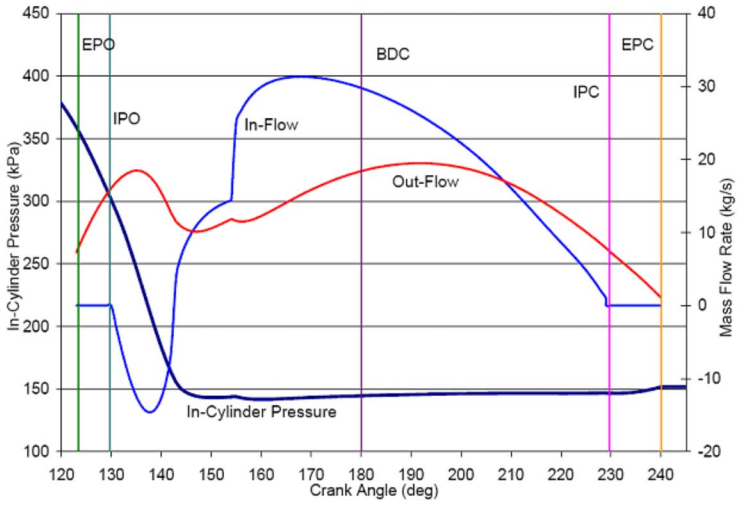

Fig. 6 In-cylinder pressure and port flow rates

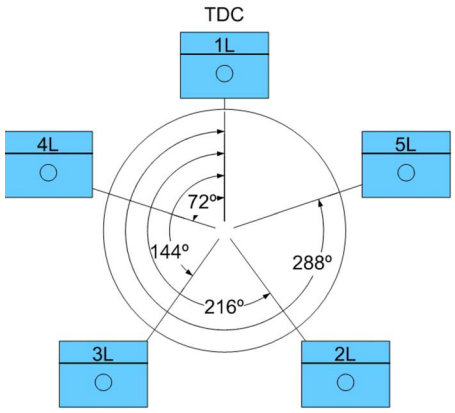

Fig. 8 Cylinder timing versus crank angle left bank of ten-cylinder GMV

It is assumed that if no other activity occurred in the manifold, the pressure wave from a cylinder decreases to the steady state air manifold pressure at the time of the port closing. This is shown in Fig. 12. At 0 m, the pressure wave closely mimics the in-cylinder pressure distribution from Cylinder 1. At every other cylinder, the results show that the pressure fluctuates with time before decreasing to the value of the steady state manifold pressure. This wave has also been compared to GMV data from an Enginuity, LLC pulsation study. The average amplitude of the manifold pulsation

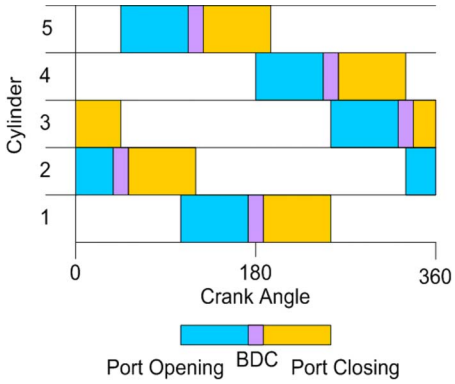

Fig. 9 Port activity overlap

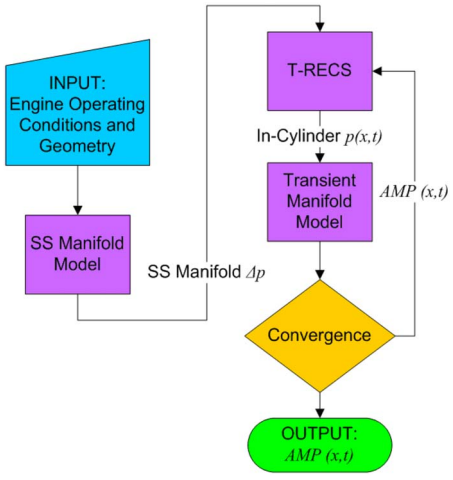

Fig. 10 CAIMENS block diagram

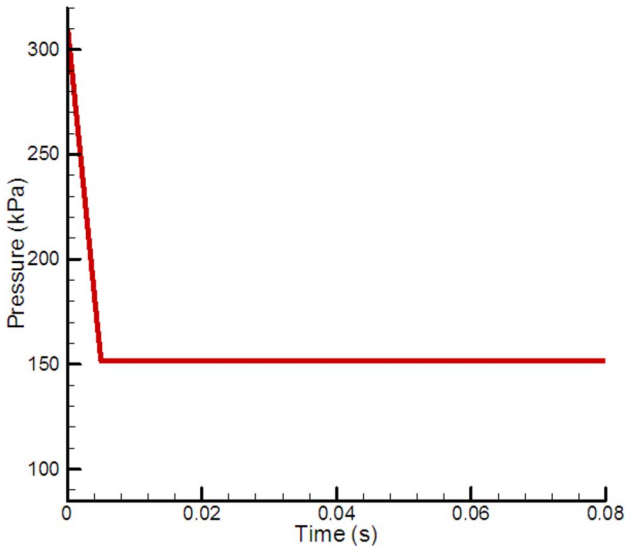

Fig. 11 Simplified in-cylinder pressure profile

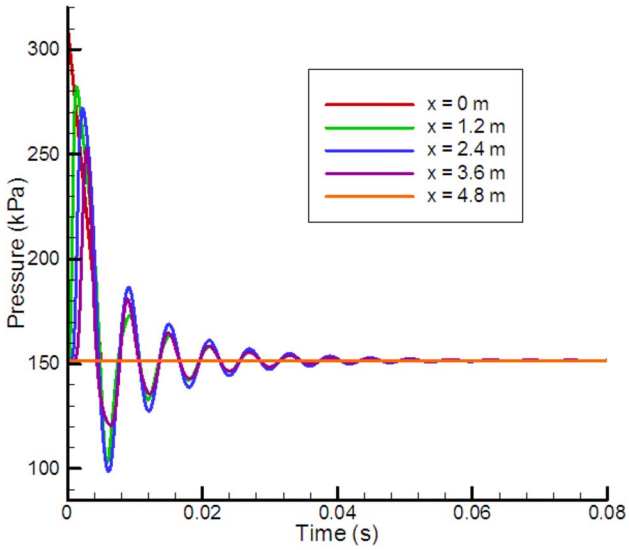

Fig. 12 Cylinder 1 fire manifold pressure distribution

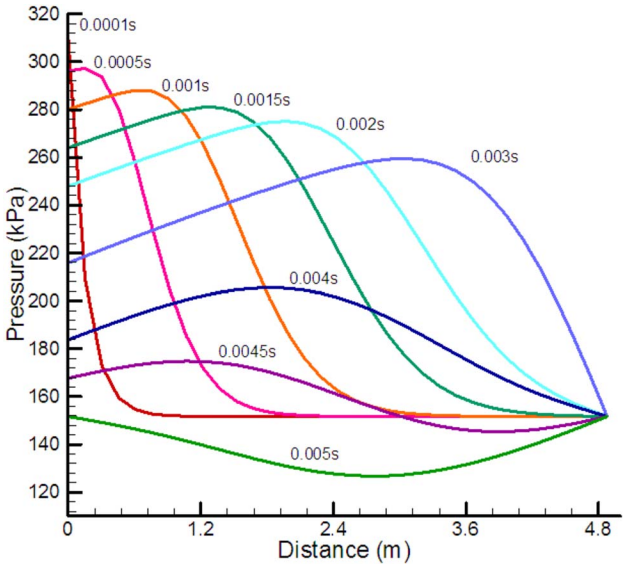

Fig. 13 Cylinder 1 fire intake manifold pressure wave propagation

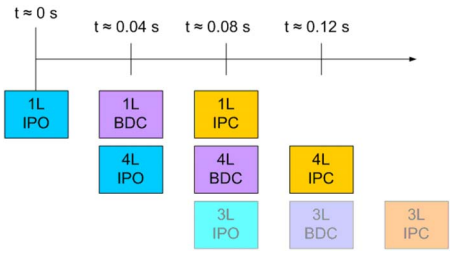

Fig. 14 Timeline for port activity

data is 13.5 kPa (4 in. Hg), which is consistent with the amplitude of the model pulse wave at each port opening (every 0.04 s).

As time progresses, the pressure wave created by Cylinder 1 propagates down the length of the manifold. This proliferation is shown in Fig. 13. As expected, the pressure decreases with time and distance. Figure 13 shows the pressure distribution in the manifold plotted at times from 0.001 s to 0.005 s. This figure demonstrates that the IPO of Cylinder 1 leads to a temporal and spatial pressure distribution throughout the manifold. Due to the nature of compressible fluids, the magnitude of the pressure wave is at times less than the steady state intake manifold pressure.

The next step is to move to a multicylinder model to assess the impact of one cylinder on the next cylinder in the firing order and timing illustrated in Fig. 14.

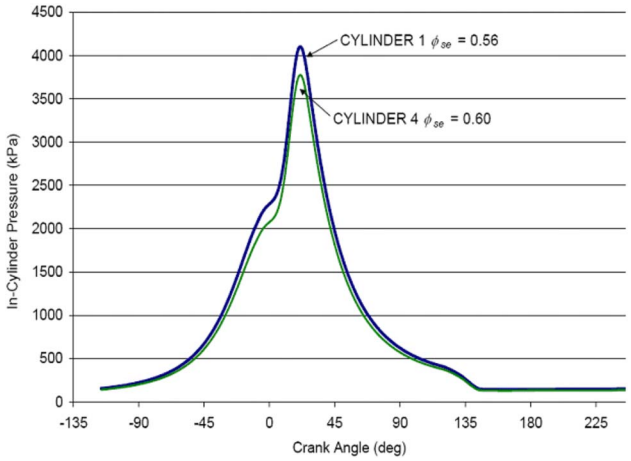

Fig. 15 T-RECS Cylinder 1 versus Cylinder 4 pressure trace

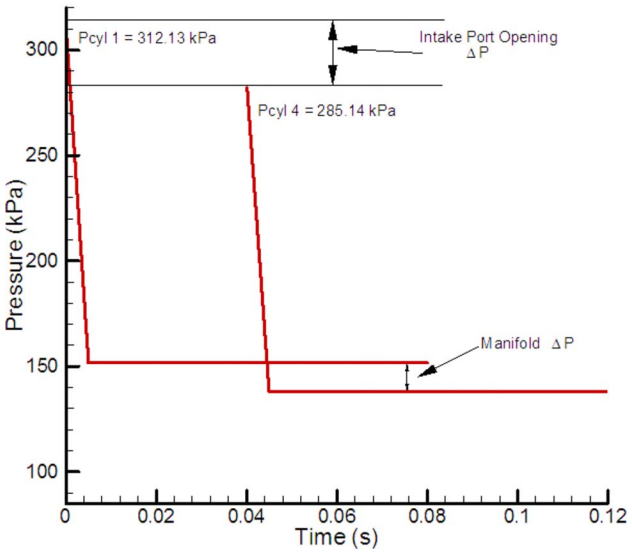

Fig. 17 Cylinder 1 versus Cylinder 4 pressure

CAIMENS manifold flow calculations show that for a 0.305 m (12 in.) diameter manifold such as the one found on a GMV engine, a pressure drop of approximately 10.3 kPa (3.05 in. Hg) occurs at steady state. Due to this pressure drop, the in-cylinder pressure at Cylinder 4, which is the second cylinder to fire in the left bank, will be less than that of Cylinder 1.

This manifold pressure drop translates into a significant change in peak pressure in the cylinder, as shown by the T-RECS pressure traces in Figs. 15 and 16. The difference in peak pressure between Cylinders 1 and 4 is approximately 200 kPa (60 in. Hg). Therefore, operators can induce a significant disruption in airflow to the cylinders by using an average peak pressure to balance the engine.

As previously discussed, the T-RECS pressure distributions for each cylinder are simplified and input into the manifold model, creating a transient pressure wave. This wave is then plotted with respect to time at each cylinder location at Cylinder 1 and Cylinder 4 firing. A comparison of Cylinder 1 to Cylinder 4 in-cylinder pressure variation when the intake ports are uncovered is shown in Fig. 17.

The wave propagation from Cylinder 4 firing is plotted with Cylinder 1 in Fig. 18. The intake ports for Cylinder 4 are uncovered from 0.04 s to 0.12 s.

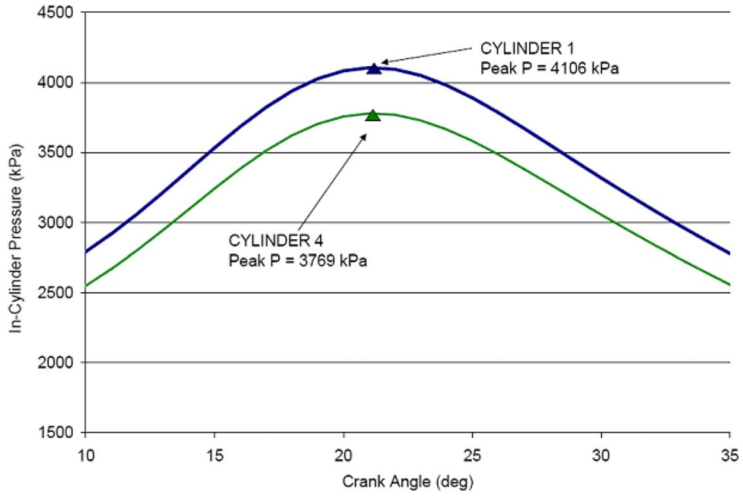

Fig. 16 T-RECS Cylinder 1 versus Cylinder 4 peak pressure

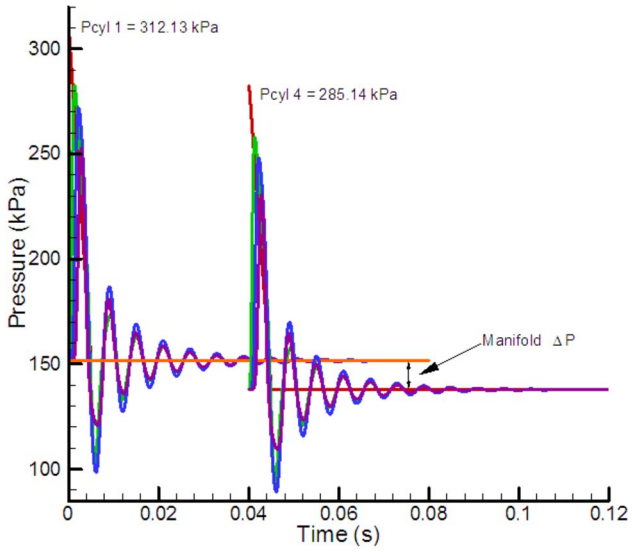

Fig. 18 Cylinders 1 and 4 pressure propagation

The port activity pressure pulse contribution to the manifold is fundamentally five separate pulse waves from each cylinder offset by 72 deg. This offset is due to the spacing of the cylinder firing (Fig. 8). Therefore, as Cylinder 1 reaches the bottom dead center, Cylinder 4 intake ports open. There are always two cylinders open to the intake manifold. Because the intake ports are uncovered for 0.08 s and there is an overlap at the bottom dead center, every 0.04 s, two different cylinder parings remove air from the intake manifold. Also, as discussed earlier, the difference in manifold pressure, due to pipe flow physics, translates into a difference in cylinder peak pressure, which further translates into a difference in pressure seen by the ports. This is also illustrated in Fig. 18.

Conclusions

As illustrated in Fig. 18, the CAIMENS model computes the transient impact of one cylinder firing on each successive cylinder. Because there are always two cylinders removing air from the intake manifold, there is a significant overlap in the pressure wave from one cylinder firing event to the next cylinder in the firing order. The pulsation model showed that not only does the manifold pressure drop have a significant impact on the in-cylinder peak pressure but it also has an impact on the pressure wave introduced to the intake manifold as the ports are opened. Also, each cylinder has a considerable impact on the airflow into each successive cylinder. CAIMENS provides the information necessary to quantify the impact of airflow imbalance and allow for the visualization of the engine system before and after airflow correction.

Acknowledgment

This paper was published with the permission of the Pipeline Research Council International, Inc. The authors would like to thank the PRCI Compressor and Pump Station Technical Committee for their ongoing guidance and encouragement throughout the development of this work. Also, the authors thank Enginuity, LLC and El Paso Corporation for contributing key information and data to the project.

Nomenclature

Symbol

A = cross-sectional area of pipe
AMP = air manifold pressure
a = crank radius
D = diameter of pipe
f = Darcy friction factor
L = rod length
$\dot{m}$ = mass flow rate
M = Mach number
p = pressure
R = universal gas constant
SS = steady state
T = temperature
t = time
$\bar{v}$ = dynamic viscosity
v = velocity in the x-direction
x = distance in the x-direction
y = instantaneous stroke
γ = ratio of specific heats
θ = angle of pipe inclination
ρ = density

Subscripts

c = critical condition
p = constant pressure
T = throat condition
0 = stagnation condition

References

[1] 2005, Pipeline Emissions Control Roadmap: Technology Pathways to Cost-Effective Year 2010 Reciprocating Engine Emission Compliance, Pipeline Research Council International, Incorporated.
[2] Nazaroff, W. W., and Alvarez-Cohen, L., 2001, *Environmental Engineering Science*, Wiley, New York.
[3] Issa, R. I., and Spalding, D. B., 1972, "Unsteady One-Dimensional Compressible Frictional Flow With Heat Transfer," J. Mech. Eng. Sci., **14**(6), pp. 365–369.
[4] Deen, J. K., and Reintsema, S. R., 1983, "Modeling of High-Pressure Gas Transmission Lines," Appl. Math. Model., **17**, pp. 268–273.
[5] Thorley, A. R. D., and Tiley, C. H., 1987, "Usteady and Transient Flow of Compressible Fluids in Pipelines—A Review of Theoretical and Some Experimental Studies," Int. J. Heat Fluid Flow, **8**(1), pp. 3–15.
[6] Price, G. R., McBrien, R. K., Rizopoulos, S. N., and Golshan, H., 1996, "Evaluating the Effective Friction Factor and Overall Heat Transfer Coefficient During Unsteady Pipeline Operation," *Proceedings of the International Pipeline Conference*, American Society of Mechanical Engineers Vol. 2, pp. 1175–1182.
[7] Zemansky, M. W., 1968, *Heat and Thermodynamics*, 5th ed., McGraw-Hill, New York.
[8] Cengel, Y. A., and Boles, M. A., 2002, *Thermodynamics: An Engineering Approach*, 4th ed., McGraw-Hill, New York.
[9] Abbaspour, M., 2005, "Simulation and Optimization of Non-Isothermal, One-Dimensional, Single/Two Phase Flow in Natural Gas Pipeline," Ph.D. thesis, Kansas State University, Manhattan, KS.
[10] Chapman, K. S., Krishnaswami, P., Wallentine, V., Abbaspour, M., Ranganathan, R., Addanki, R., Sengupta, J., and Chen, L., 2005, "Virtual Pipeline System Test Bed to Optimize the Natural Gas Pipeline Transmission System," Department of Energy, No. DEFC26-02NT41322.
[11] Ferguson, C. R., and Kirkpatrick, A. T., 2001, *Internal Combustion Engines: Applied Thermodynamics*, 2nd ed., Wiley,New York.
[12] Chapman, K., Keshavaraz, A., and Li, Y. H., 2003, "Experimentally Determined Discharge Coefficients From Large-Bore Reciprocating Engines," *Proceedings of the Internal Combustion Engine Division Conference*, American Society of Mechanical Engineers, Oct., Paper No. ICEF2003-702.
[13] Chapman, K. S., and Keshavarz, A., 2003, "Development of Turbocharger-Reciprocating Engine Simulation (T-RECS)," Gas Research Institute, No. GRI-03/0005.
[14] Bourn, G., Phillips, F., Harris, R., and Raymer, R., 2005, "Controlling Engine Air Balance Through Manifold Design—Geometric Analysis, Simulation, and Conceptual Design," *Proceedings of the Gas Machinery Conference*, Oct.

Creep-Fatigue Tests on Full Scale Directionally Solidified Turbine Blades

Xiaojun Yan

Jingxu Nie

Group 405,
School of Jet Propulsion,
Beijing University of Aeronautics and Astronautics,
Beijing, 100083, P.R.C.

A new experimental method, in which a full scale directionally solidified (DS) alloy turbine blade is loaded by a special design rig employing friction force and heated by eddy current induction, is proposed to conduct creep-fatigue life tests in this investigation. The method can take factors such as geometry, volume, especially cast procedures, etc., into creep-fatigue life assessment. Principle and design of the test rig are fully explained. Creep-fatigue tests of turbine blades made of DZ4 alloy (one type of DS alloys) were conducted and test data were analyzed. Life prediction based on test data of this investigation shows good agreement with actual flight experience of these blades. The method of this article provides a new way to estimate the potential creep-fatigue or low cycle fatigue life for turbine blades. [DOI: 10.1115/1.2901174]

Keywords: turbine blade, directionally solidified alloy, creep, fatigue, life prediction

1 Introduction

At present, almost all advanced civil and military aeroengines use directionally solidified (DS) or single crystal blades [1]. Turbine blades of aeroengine are subjected to complex mechanical, thermal, and chemical loads during service. In particular, the blades may be damaged considerably due to creep-fatigue (creep and fatigue coupled) loadings. Various methods have been proposed in predicting creep-fatigue life of turbine blades [2].

Traditional creep-fatigue life prediction methods of turbine blades are based purely on macroscopic descriptions of material behaviors and conventional finite element (FE) methods in conjunction with empirically developed failure laws. To reduce experimental costs, in most cases, tested life data of plain specimen may be used to predict "component" behavior. However, the differences between blades and plain specimens, such as geometry, volume, and especially in cast techniques for DS blades, may cause discrepancy between their mechanical performance and life distribution, and therefore may greatly affect accuracy of traditional life assessment methods [1]. To overcome the above shortcomings, the specimens can either be machined from blades or componentlike ones [3]. Compared to specimens machined from blades or componentlike ones, full scale blades are more ideal, since the specimens own the same manufacture process with real flight blades. When selecting full scale blades as specimens in life assessment tests, the most challenge work is how to simulate operating conditions of blades in laboratory. The objective of this paper is to develop such an experimental life assessment method by conducting creep-fatigue tests on full scale DS blades.

Manuscript received July 5, 2007; final manuscript received September 14, 2007; published online April 29, 2008. Review conducted by David Walls.

2 Method of Creep-Fatigue Test

Stress and temperature are two factors that dominate a turbine blade's creep-fatigue life. The combination of stress and temperature distribution will result in the most heavily damaged point, namely, the hot spot, or key section in this investigation where the hot spot locates on a blade. Generally, cracks always initiate from the location of the key section, and a blade's life is limited by the life of its key section. Therefore, creep-fatigue life of a blade can be obtained by conducting tests on the key section with properly simulating stress and temperature conditions.

For a gas turbine rotor blade with a complex geometry shape, the stress state of a point on the airfoil is mainly uniaxial condition along the centrifugal direction [4], while the stress value along the direction varies from point to point even on the same section, which means that the stress value of a point located on the pressure (concave) side is generally different from that of on the suction (convex) side. During creep-fatigue tests of the key section, not only centrifugal load but also a special moment is needed to apply on the section. Thus, the method to apply the above loads is different from that of the plain specimens.

As same as the stress, the temperature on the key section also has a distribution. It is difficult to provide a specific temperature distribution based on the present laboratory technology level. In this investigation, on the ground of scientific research, a uniform high temperature field around the dangerous area nearby the key section is provided and superposed on the stress field.

Based on the above considerations, after getting the location of the key section, the key issue of the test scheme is how to simulate the stress field of the key section and at the same time provide this area with a uniform high temperature distribution.

2.1 Location of Key Section. The location of the key section can be determined by either numerical simulation results or service/flight failure experience of the blade. The DS blade made of DZ4 alloy selected in this investigation is shown in Fig. 1. Detailed numerical simulation of stress distribution and creep-fatigue life prediction based on the development of suitable material constitutive equations can be seen in Ref. [1]. Combined with the results of numerical simulation and actual flight failures of the blade, the location of the key section is determined as shown in Fig. 1, in which the dark/red area around the key section represents a dangerous area.

2.2 Stress Field Simulation. A rig to apply load on the full scale DS turbine blade to simulate the stress distribution of the key section is designed, as shown in Fig. 2. The most distinctive characteristic of the rig is that the load from the hydraulic-servo system that transferred to the blade key section is achieved through the friction force between the rig and blade, which causes no damage to the blade. As illustrated in Fig. 2, the force from the hydraulic-servo system is firstly passed through upper Jointer 1 and adjusted pin on it, and then through upper Jointer 2, adjusted pin, out clamp, inner clamp, and last to the blade. It can be seen that there exist two contact pairs during the load transmitting path: contact between the outer and the inner clamp and contact between the inner clamp and the test blade. These two contact pairs transfer the load by means of friction force caused by the normal pressure of four long bolts. The four long bolts drill through the outer clamps and grip inner clamps closely by normal compression, which is achieved by applying torque on four nuts linked with four bolts. The required torque value applied on the nuts depends on the load acted on the blade's key section and is calculated before installation of the rig. The blade root is inserted into the disk slots on a block, which is cut from a full size turbine disk.

To ensure a complete contact between the inner clamp and the blade, two interior sides of the inner clamp are machined into a complicated surface shape just as contrary to surfaces of airfoil. Moreover, another contact pair, which is between the outer side of the inner clamp and the interior side of the outer clamp, is con-

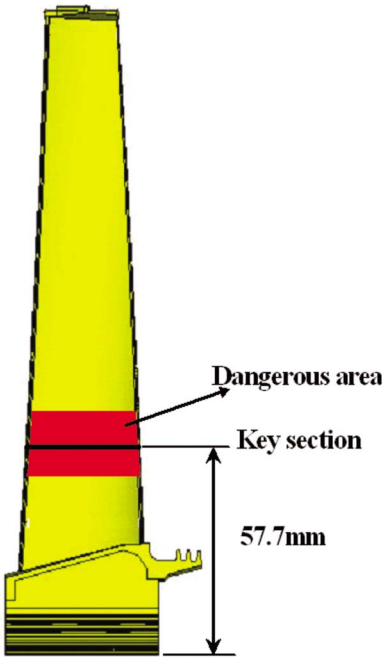

Fig. 1 Key section location

tacted with inclined planes, which makes them more closely contact with increasing load. The goal of all these measures is to prevent the specimen slipping out of the rig.

Besides loading through the friction force between contact pairs, another distinctive feature of the rig is that it can apply variable moment on the blade key section by adjusting pins. As seen in Fig. 2, there are totally four adjusting pins. The two upper jointers are linked together by two adjusting pins, which are located in two perpendicular directions, so do the two lower jointers. The jointers can move along the axis of adjusting pins, i.e., different bending moments can be obtained and applied on the key section of the blade by different combinations of four adjusting pin positions.

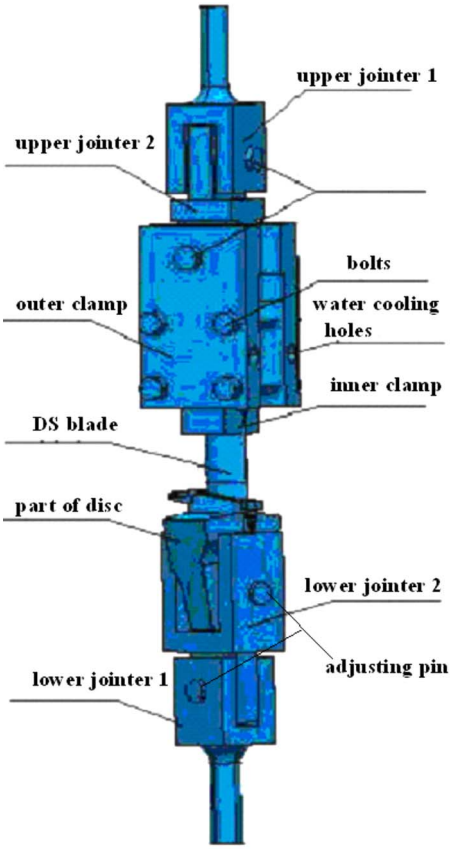

Fig. 2 Illustration of the load rig

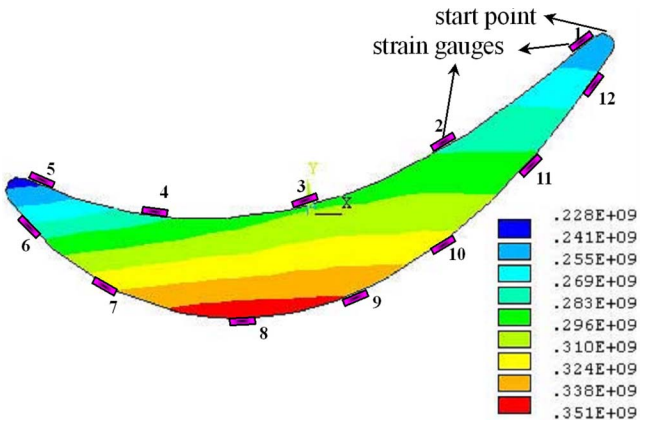

Fig. 3 Positions of paste strain gages

To verify the load capacity of the above designed rig, series of experiments were conducted. As illustrated in Fig. 3, strain gauges were pasted surrounded the key section. Before tests, positions of four adjusting pins were adjusted and then fixed by inserting thin metal spacers between two jointers. After applying a load, a strain value along the centrifugal direction of every paste point around the key section surface was recorded by a computer. Figure 4 shows a typical strain distribution around the key section surface with one of four pin position combinations. In Fig. 4, the horizontal axis represents the absolute distance from the paste gauge to the start point, which locates at the trailing edge of the key section near Gauge 1, as shown in Fig. 3. Combining positions of four adjusting pins, different moments or strain distributions can be applied on the key section. The strain distributions got from experiments can be compared to those calculated under engine's different operating conditions. The solid line in Fig. 4 shows a strain distribution of the key section under the engine's maximum aerodynamic conditions. When a specific engine's operating condition is selected to conduct a creep-fatigue test, the positions of four pins need to be adjusted until the strain distribution of the key section agrees well with that of a specific engine's operating condition, and the pins can then be fixed and begin to conduct creep-fatigue tests. It is worth pointing out that the strain value of Fig. 4 was measured at room temperature; therefore, the calculated strain values under engine operating condition have been processed to eliminate the effect of temperature.

2.3 Temperature Field Simulation. High-frequency eddy current induction furnace was selected in this investigation. As seen in Fig. 5, part of the blade was heated with induction coils. One advantage of the heating method is that it facilitates visual observation of the blade crack growth. Another merit is that it can easily be assembled with the loading rig, as shown in Fig. 2. The heated area is part of airfoil around the key section, and in this investigation, a uniform temperature distribution near the key section was simulated.

3 Tests and Results

3.1 Test Conditions. Creep-fatigue tests on full scale DS blades were conducted using a 10 ton hydraulic-servo system con-

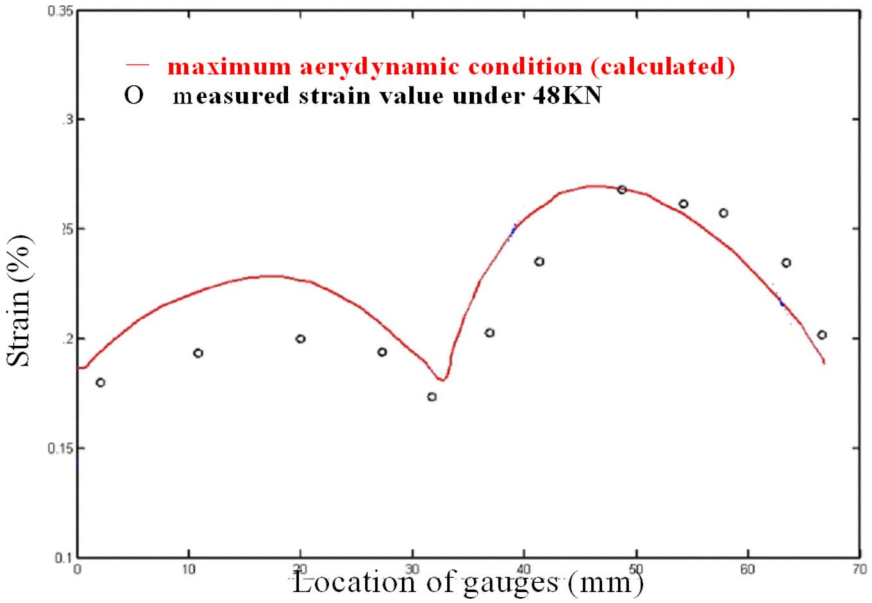

Fig. 4 Strain distribution comparison

trolled with MTS 407 panel and computer software. The full scale blade made of DZ4 superalloy as mentioned before is selected as a specimen. Furthermore, the experimental setup is just as stated above. Isothermal cycle tests with hold times $\Delta t=28$ s were carried out at 880°C. The load spectrum is shown in Fig. 6. The temperature of 880°C is a significant temperature for the DZ4 DS blade in this investigation. Since the creep-fatigue test requires long time to get a group of life data of blades, completing a creep-fatigue test of a blade may need months of time. An accelerated load spectrum $T=900$°C was used for later blade tests. The hold times of Δt at different temperatures are calculated based on the principle of equivalent damage in one cycle. Δt at 900°C is 13 s.

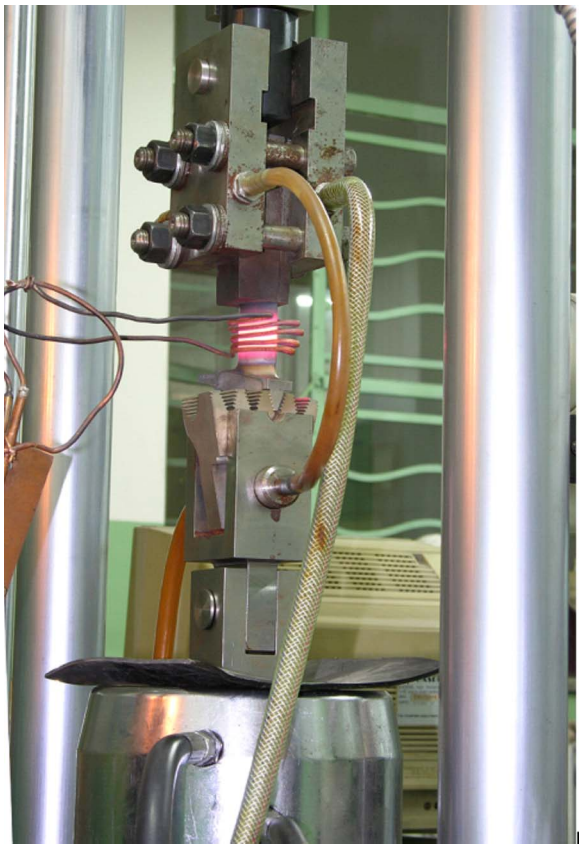

Fig. 5 Picture of conducting creep-fatigue test

3.2 Results and Analysis. Altogether, 19 creep-fatigue tested blades were conducted with a load spectrum of Fig. 6 and most of them are shown in Fig. 7, among which the number of new blades is 12 and the used ones is 7. It can be seen from Fig. 7 that all blades fractured at the location of the key section.

The life data of creep-fatigue tests on DZ4 blades are given in Table 1. It is noted that tests of new blade Nos. 1–6 were conducted at 880°C and the others were at 900°C, and sample numbers are reordered based on lifetime. For convenience of the data process, life data conducted at 900°C have been multiplied by a coefficient, which is obtained by dividing a mean value of the life data at 880°C by 900°C and converging into the corresponding data at 880°C. From Table 1, the following can be observed.

(1) The creep-fatigue life of full scale DS blades determined by the above experimental method is greatly shorter (nearly 50%) than the one predicted by the numerical simulation based on the test data of the plain specimens [1]. Therefore, the experimental method such as this investigation should be developed so that factors such as geometry, different casting procedures, etc., can be considered when predicting creep-fatigue life of DS turbine blades.

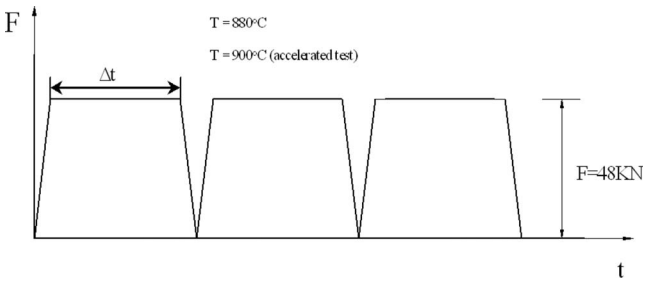

Fig. 6 Load spectrum of creep-fatigue tests

Fig. 7 Fracture blades of creep-fatigue tests

Table 1 Creep-fatigue life data of DS blades at temperature 880°C

Blade type	Sample No.	Life of creep fatigue (h, cycle)												Arithmetic average
		1	2	3	4	5	6	7	8	9	10	11	12	
New	t/h	90.40	104.88	138.05	175.15	284.27	322.55	85.83	148.61	163.31	182.87	255.80	343.76	191.29
	N/cycle	10,848	12,586	16,567	20,070	31,410	35,116	9,273	16,066	18,003	19,848	27,763	37,308	21,238
Used	t/h	47.45	54.11	165.30	173.31	192.83	235.65	294.58						166.18
	N/cycle	5,166	5,896	17,986	18,843	20,988	25,643	32,092						18,088

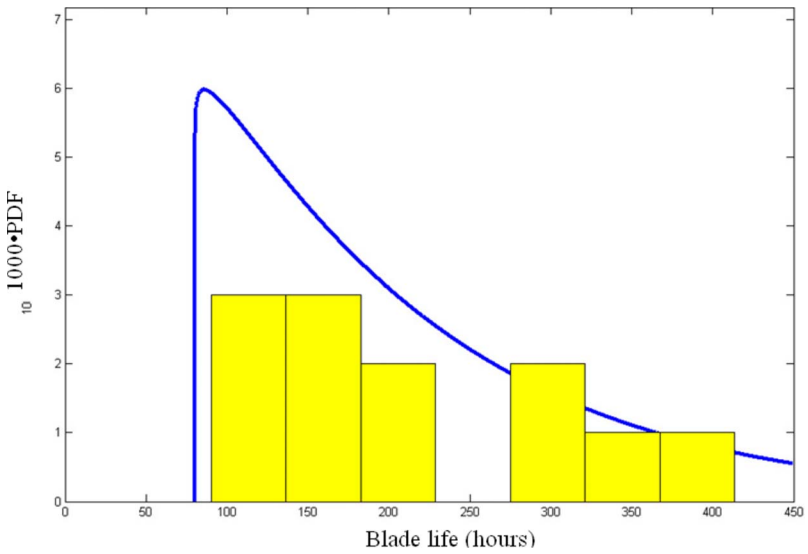

Fig. 8 Histogram and PDF of creep life (new blades)

(2) The life data of the used blades have a big scatter than the new ones. This is reasonable since the used blades have experienced different operating conditions and the accumulated damage for each used blade before tests is different.
(3) For new blades, the life scatter of normal test at 800°C (new Blades Nos. 1–6) is similar to that of the accelerated test at 900°C.

Based on the test data of Table 1, different probability models can be selected to process the data, and based on the relationship between the flight and the experimental load spectrum, the safe flight life of the tested blades can be obtained. Figure 8 shows histogram and probability density function (PDF) of new blades based on the creep lifetime using Weibull distribution model.

It is worth pointing out that the ratio of the safe creep life of new blades to used blades agrees well with the actual flight situation: The new blades fractured at flight hours two times of the used blades; moreover, after conversion between experimental and real operation conditions, the remaining life of the used blade plus their flight life is nearly equal to the life of new blades. This consistency between experimental results and flight practice can support that the experimental life obtained by the method of this investigation will play an important role in DS blade life assessments.

4 Conclusions

With a special design of the test rig, operating stress field and temperature of the key section on the DS turbine blade airfoil can be simulated in bench environment. Consistency between experimental results and flight practice of the tested DS blades supports that the experimental life obtained by the method will play an important role in DS blade life assessments. The method of this article provides a new way to estimate the potential creep-fatigue or low cycle fatigue (LCF) life for DS turbine blades, and this method can also be applicable to blades made of single crystal and generally high temperature superalloys.

Acknowledgment

This work was supported by a Foundation for the Author of National Excellent Doctoral Dissertation (FANEDD, Approved No. 200351) and a Program for New Century Excellent Talents in University of PR China (NCET-06-0178).

References

[1] Li, H. Y., 2002, "Research and Application of Anisotropic Viscoplastic Damage Uniform Constitutive Mode," Ph.D. thesis, Beijing University of Aeronautics and Astronautics, Beijing.
[2] Harrison, G. F., Tranter, P. H., Shepherd, D. P., and Ward, T., 2004, "Application of Multi-Scale Modeling in Aeroengine Component Life Assessment," Mater. Sci. Eng., A, **365**, pp. 247–256.
[3] Issler, S., and Roosb, E., 2003, "Numerical and Experimental Investigations Into Life Assessment of Blade-Disc Connections of Gas Turbines," Nucl. Eng. Des., **226**, pp. 155–164.
[4] Cross, C. J., 2000, "Multi-Axial Testing of Gas Turbine Engine Blades," *36th AIAA/ASME/SAE/ASEE Joint Propulsion Conference*, Huntsville, AL, Paper No. AIAA2000-3641.

Towards Multiplexed Fiber Delivered Laser Ignition for Natural Gas Engines

Azer P. Yalin
e-mail: ayalin@engr.colostate.edu

Sachin Joshi
e-mail: sach@engr.colostate.edu

Morgan DeFoort
e-mail: mdefoort@engr.colostate.edu

Bryan Willson
e-mail: bryan.willson@colostate.edu

Engines and Energy Conversion Laboratory,
Department of Mechanical Engineering,
Colorado State University,
Fort Collins, CO 80523

The use of laser ignition for advanced gas engines may provide benefits including extension of the lean limit and higher efficiency operation at elevated pressures. This contribution provides a short review of efforts to develop a practical laser ignition system for advanced multicylinder gas engines. The approach is to use a single laser source with fiber optic cables delivering the high power pulses from the source to the engine cylinders. The optical requirements for the fiber delivery lead us to use coated hollow core optical fibers. Characterizations and results of spark delivery tests for the fibers are presented. Single-cylinder engine test results using fiber delivered laser ignition are summarized. For multicylinder operation, a multiplexer based on a moving mirror is used to route the laser output pulses to different fiber channels (cylinders). Benchtop testing and initial engine testing of the multiplexed system are presented. [DOI: 10.1115/1.2906184]

Keywords: gas engines, ignition, laser ignition

Introduction

The first demonstration of laser ignition of an engine [1] followed relatively soon after the advent of high power pulsed lasers. Since that time, many studies have considered potential benefits of laser ignition including improved engine efficiency and stable ignition of increasingly lean mixtures (e.g., Refs. [2,3]). Our interest is primarily in large (megawatt class) stationary gas engines typically used for power generation and natural gas compression. For these engines, the drivers of efficiency and reduced pollutant emissions are leading toward increasingly lean fuel-to-air mixtures and elevated pressures. Use of laser ignition becomes increasingly favorable at elevated pressure since, in contrast to conventional spark plug ignition, the required breakdown energy decreases with pressure.

To enable laser ignition to transition to field use, practical beam delivery systems must be developed. The open beam paths used in past laboratory research are problematic owing to safety, maintenance, thermal, and vibrational concerns. For gas engines, several approaches are under investigation: (i) use of a laser per cylinder [4], (ii) use of a single laser per engine multiplexed through fibers to individual cylinders [5], and (iii) an intermediate approach in which (laser) pump light is fiber delivered to optical gain elements located on each cylinder [6]. We view that the second approach is favorable in terms of providing low cost systems; however, fiber optic delivery of laser sparks is technologically challenging. Conventional step-index silica fibers are very limited in their ability to deliver laser sparks. By using special coated hollow core fibers, we have demonstrated (for the first time) the ability to use fiber optics to deliver laser pulses to form sparks on the bench top [7] and to initiate combustion in a gas engine [5]. In a related approach we have also demonstrated spark formation from the output of fiber lasers [8], a method that may ultimately prove attractive for engine implementation. In this contribution, we review the hollow fiber efforts including development and recent testing of a multiplexed system for multicylinder ignition.

Spark Delivery With Coated Hollow Optical Fibers

The use of optical fibers for spark delivery imposes constraints on both the fiber output pulse energy and on the intensity of the refocused output light. Optical breakdown for spark formation typically requires a focused intensity of $\sim 100\ \mathrm{GW/cm^2}$ and ignition of lean mixtures requires a minimum pulse energy of approximately 10–20 mJ [2]. The intensity threshold requires delivery of high power pulses with reasonable beam quality. (The latter requirement corresponds to the ability to tightly focus the output beam as is required to form a spark.) In order to assess fiber candidates, we have performed a figure of merit analysis [8]. The analysis considers the achievable optical intensity (at the desired spark location) as a function of fiber parameters. The geometry and fiber parameters are shown in Fig. 1. The beam diameter and intensity of light at the fiber exit face are represented by d_{exit} and I_{fiber}, respectively, while the corresponding quantities at the (intended) spark location are given by I_{spark} and d_{spark}. The angular divergences of light at the fiber exit and spark location are represented with θ_{exit} and θ_{spark}, respectively. Using geometric ray-tracing optics (or embedded Gaussian concepts [8]), one finds

$$I_{\mathrm{spark}} \approx I_{\mathrm{fiber}} \left(\frac{\theta_{\mathrm{spark}}}{\theta_{\mathrm{exit}}} \right)^2 \tag{1}$$

Equation (1) shows that in order to achieve a high intensity at the intended spark location, one requires a high intensity at the fiber exit (I_{fiber}) as well as low divergence θ_{exit} at the fiber exit. The latter requirement corresponds to a high beam quality (low M^2). Furthermore, one wants high θ_{spark} at the spark location corresponding to a low $f\#$ (high demagnification) lens system. Using published values, one finds that conventional silica step-index fibers are generally unsuitable in this application [8]. On the other hand, fiber parameters for coated hollow core fibers [9] created by researchers at Tohoku University appear favorable. A cross section of the hollow fiber is shown in Fig. 2. The walls of the fiber are quartz (or glass) upon which there is a silver coating with an innermost layer of cyclic olefin polymer (COP) that serves to protect the silver layer and enhance its reflectivity.

Using the coated hollow fibers, we have demonstrated the first fiber optic delivery of nanosecond duration pulsed beams to form sparks in gases [7,8]. The tests have used the 1064 nm output of commercial Q-switched Nd:YAG lasers with pulse durations of $\sim 5-10$ ns, repetition rate of 10 Hz, and spatial beam quality $M^2 < 2$. The laser beam was launched into the fiber with a single planoconvex lens that focused the beam into the fiber. A weak helium purge was used to prevent sparking at the input of the fiber. The fiber launch angle was found to critically influence the fiber output parameters. Results for spark delivery using 2 m length fibers are presented in Table 1 (from Ref. [8]). Variables are defined as follows: The focal lengths of the launch lens and input f number are represented by f_{launch} and $f_{\#}$, respectively, the angular beam divergence at the fiber exit is given by θ_{exit}, the focal

Contributed by the Internal Combustion Engine Division of ASME for publication in the JOURNAL OF ENGINEERING FOR GAS TURBINES AND POWER. Manuscript received November 8, 2007; final manuscript received December 2, 2007; published online April 29, 2008. Review conducted by Dilip R. Ballal.

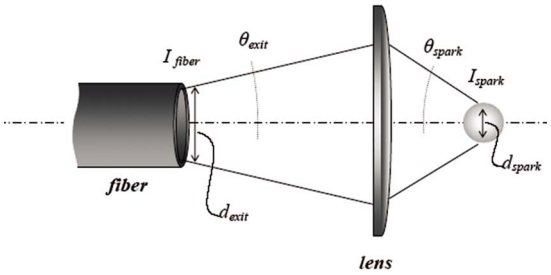

Fig. 1 Schematic diagram of light exiting fiber

spot size at the fiber input and final focused (spark) location are represented by w_{launch} and w_{focus}, the intensities at the fiber exit and final focused (spark) location are represented by I_{exit} and I_{focus}, and the beam quality of the exit beam is represented by M^2_{exit}. Also reported is the energy transmission and percentage of delivered sparks resulting in spark delivery. Of the conditions studied, we found an optimum launch *f*# of 55 (where the *f*# is defined as the focal length divided by the diameter filled on the lens) for which we had energy transmission of 86% and the sparking reliability was 98%. The experiments were performed in atmospheric pressure air. The breakdown threshold intensity for spark formation decreases with increasing pressure as $\sim P^{-n}$, where P is the pressure and n depends on the gas and lies between $\sim$0.3 and 0.9 [10], so that such configurations would readily spark at higher in-cylinder engine pressures. Effects of fiber bending were also examined [8]. It was found that fiber bending limits the output beam quality and the possibility of spark formation. At atmospheric pressure, sparks could be achieved for bend radii no smaller than $\sim$1 m, although again one should consider the pressure scaling when considering engine ignition conditions.

Single-Cylinder Engine Testing

We have used the coated hollow optical fibers for the first demonstration of fiber delivered laser ignition of a gas engine [5]. Tests were performed on a single cylinder of an in-line six-cylinder Waukesha VGF-18 engine. The hollow fiber was coated for 1064 nm, had length of $\sim$1 m, and inner diameter of 1 mm. The laser and launch optics were mounted on a robust vibration-free housing for precise laser alignment and brought to rough vacuum to avoid breakdown at the fiber launch. The engine has a nominal rating of 400 bhp continuous at 1800 rpm. The engine displacement was 18 l, with a cylinder bore of 5.98 in. and a stroke of 6.5 in.. Engine loading was achieved using a 1200 hp Midwest eddy current dynamometer. For functional testing, the engine speed was limited to 1500 rpm and load was limited to 35% of rated. Combustion pressure in each cylinder was measured using a Hi-Techniques Win600 combustion analysis system. Laser ignition system was supplied to one cylinder (No. 5). The remaining cylinders were ran with conventional spark ignition. The timing of the nonlaser cylinders was kept at the original setting, nominally 14 deg BTDC. The timing of the laser cylinder was independently controlled and retarded to 8 deg BTDC. Pressure traces of all cylinders are shown in Fig. 3 where each trace is an average of 1000 cycles. Even with the timing delayed on the laser ignition cylinder, its peak pressure was reached before all other cylinders, indicating an increased rate of heat release. Calculated mass fraction durations showed shorter early (0–10%) burn durations corresponding to elevated early flame speeds as has been observed in laboratory experiments [3]. Engine conditions were not optimized but the tests met their primary objective of showing (100%) reliability in fiber delivery, spark formation, and ignition.

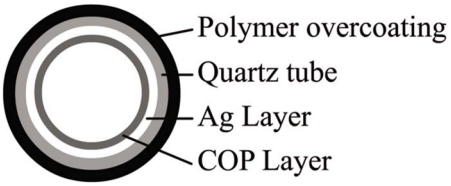

Fig. 2 Schematic diagram of coated hollow fiber

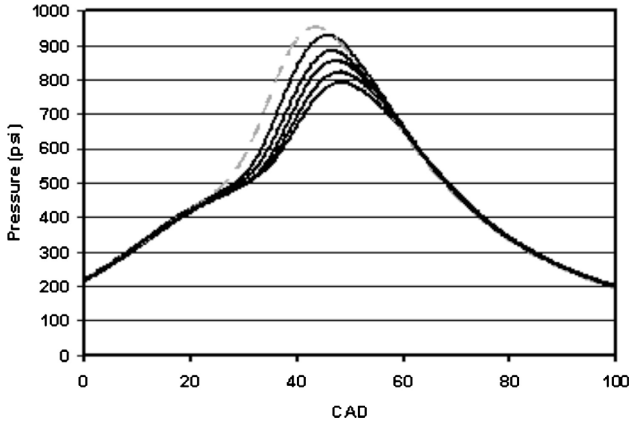

Fig. 3 Pressure curves for laser and electrical spark ignition; laser cylinder shown with dotted curve

Multiplexer Design and Testing

Fiber optic delivery affords the possibility of multiplexing the source to multiple combustion locations (e.g., engine cylinders). The switching can be done with optoelectronic methods but the current work uses simple mechanical switches (moving mirrors) owing to their lower cost and adequate performance. Two approaches based on mechanical switching are being considered: continuously rotating motors and galvanometer based mirror scanners that move to discrete positions. Either form can allow for variation in cylinder-to-cylinder timing. Figure 4 shows a schematic of the current multiplexer design based on a galvanometer scanner [11]. Figure 4(*a*) shows the laser source, galvanometer switcher, and fiber array. The multiplexer is designed for up to eight channels; however, our initial testing focuses on two channels. (The choice of two channels is to match the repetition rate of our current laser although it is emphasized that the multiplexer design would be essentially unchanged for additional channels and that higher repetition rate lasers are commercially available.) The fiber outputs are connected to optical spark plugs that mount to the engine cylinders (Fig. 4(*b*)). Within each plug, the beam

Table 1 Effect of launch geometry on 2 m long coated hollow fibers

f_{launch} (mm)	$f\#_{input}$	w_{launch} (μm)	θ_{exit} (rad)	M^2_{exit}	I_{exit} (GW/cm^2)	w_{focus} (μm)	I_{focus} (GW/cm^2)	Transmission (%)	Sparking (%)
135	35	27	0.014	21	0.58	35	120	80	$<$10
215	55	39	0.01	15	0.6	17	470	86	98
335	85	140	0.015	22	0.52	44	68	80	0

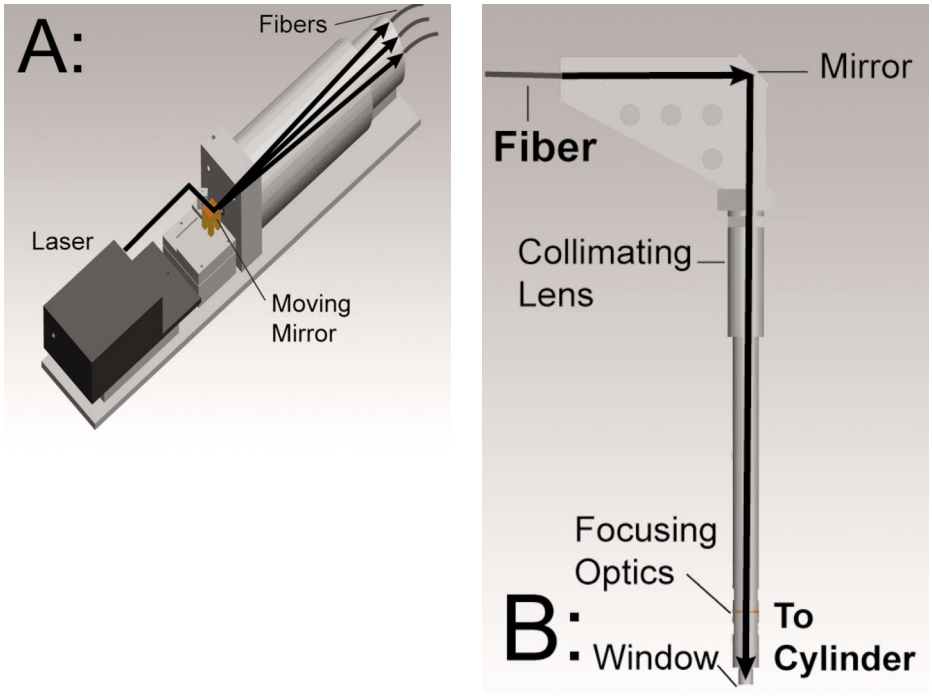

Fig. 4 Schematic of multiplexer design; black arrows show beam path; (*a*) laser source and multiplexer and (*b*) optical plug

exits the fiber and propagates within the hollow body. A mirror turns the beam 90 deg toward a collimating lens and a focusing lens (focal length of 9 mm). The turning mirror is used to accommodate bending limitations of the fibers; with this configuration, a single laser can reach multiple cylinders with relatively straight fibers. Finally, an uncoated sapphire window chosen for its mechanical and thermal properties is used as the window into the engine cylinder. The end of the optical plug has suitable spark plug threads so that it can be screwed onto the engine head.

Benchtop testing and characterization of the mutiplexer energy transmission, beam quality, and sparking were conducted [11]. The performance of the two channels was similar and is summarized in Table 2. Fiber transmission was ~85% and losses for the other optical components are roughly as expected based on standard optical surface losses. (The collimating lens was antireflection coated though the other components were not.) The energy losses are of concern in regard to the required laser source and potential optical damage to components; however, it is not relevant in terms of energy cost (efficiency penalty) since even for relatively inefficient lasers, the energy cost of ignition is insignificant. The ability to spark at engine conditions was investigated on the bench top with the aid of a high-pressure test chamber. Again, a vacuum was drawn through the entire system in order to reduce the chance of sparking on the fiber input faces. The high-pressure test chamber was filled with air and pressurized to 220 psi (roughly equivalent to the motored pressure of the Caterpillar G3516C engine). At the lean conditions studied, air and air-fuel mixtures equivalently behave in terms of assessing initial spark formation. Fiber output energies of 27 mJ (laser source energy of ~40 mJ) yielded optical intensities of ~100 GW/cm^2 at the focal spot locations. These conditions allowed 100% reliable sparking, i.e., each laser pulse produced a spark [11]. This result is taken as primary validation of desired benchtop operation of the multiplexer.

Table 2 Measured transmission (%) for individual components of the multiplexer unit

	Fiber	Turning mirror and collimating lens	Focusing optics	Total transmission	Total loss
Channel 1	83	96	85	68	32
Channel 2	87	96	79	66	34

We have also done initial dual-cylinder laser ignition tests using the multiplexed system. The tests targeted two cylinders (Nos. 8 and 10) of a Caterpillar G3516C series natural gas engine. The engine is fourstroke with a speed of 1800 rpm and 16 cylinders (the remaining 14 cylinders were ignited with conventional spark plugs). The laser cylinders (and two others) were instrumented with Kistler pressure transducers. The full multiplexer system was mounted on a rigid aluminum base plate that was vibration isolated from the engine vibration by a set of four air springs (vibration isolators). The air springs provide a low enough spring constant that the resonant frequency is much lower than the engine vibration frequency (30 Hz) and its first half frequency (15 Hz). For initial testing, the laser firing timing and the galvanometer timing and positioning were controlled with a custom LABVIEW program. The initial tests were at idle conditions (no load). Successful laser ignition was demonstrated for both targeted cylinders. Spark formation and combustion were confirmed both visually (taking photographs through the turning mirror of the plug into the cylinder) as well as by pressure traces from the Kistler transducers. Reliability was less than 100% (i.e., there were some misfires), owing to triggering and alignment problems, but the tests showed proof of principle operation.

Conclusions

Laser ignition differs from conventional spark ignition both in terms of the intrinsic spark properties and physical configuration (such as lack of electrodes). As the pressure increases, laser ignition becomes increasingly favorable and it may prove to be the preferred mode of ignition for future high-pressure gas engines. The present work concerns development and testing of a fiber delivered multiplexed laser ignition system for gas engines. Recent work has shown spark delivery by conventional solid step-

index fibers [11,12]; however, in many cases, such fibers are unsuitable. In the system presented here, each channel uses a coated hollow core optical fiber to deliver light to the corresponding engine cylinder. Characterization results for the coated hollow fibers were summarized, as was an initial single-cylinder engine test.

For multicylinder operation, a simple galvanometer based moving mirror is used to switch a single laser source to multiple channels. The multiplexed system was tested on the bench top using a high-pressure test cell to emulate engine conditions and 100% reliable sparking was observed. These results show successful operation of the multiplexer system at anticipated engine conditions. The initial system is targeted at advanced gas engines such as the Caterpillar G3516C engine. Initial dual-cylinder tests on this engine showed successful ignition of both cylinders and thus provide proof of concept for the design. The multiplexer design is readily scalable to a larger number of cylinders as long as a higher repletion rate laser is used (and such lasers are commercially available). Another potentially attractive approach that combines fiber delivery with the laser source would be to use a fiber laser system [8]. Ongoing and future work will consider life and reliability testing (including window cleanliness), parametric studies with combustion analysis, and economic assessment. Integrated diagnostics will also be considered. Laser ignition provides a window to the combustion volume and therefore can enable optical diagnostics such as fuel-to-air measurements [13].

Acknowledgment

The authors would like to thank Woodward Industrial Controls and Advanced Reciprocating Engine Systems program of US DOE for the financial support. The authors would also like to acknowledge Yuji Matsuura of Tohoku University, as well as Adam Reynolds, Keegan Thompson, and Eric Mowrer of CSU's EECL for their contributions.

Nomenclature

Variables

- BTDC = before top dead center
- CAD = crank angle degrees
- d = beam diameter
- $f\#$ = lens focal length divided by fill diameter
- I = optical intensity
- M^2 = spatial quality of the laser beam
- w = beam waist
- θ = divergence angle of beam

Subscripts

- exit = evaluated at fiber exit
- fiber = evaluated at fiber exit
- focus = evaluated at focal spot
- spark = evaluated at (desired) spark location

References

[1] Dale, J. D., Smy, P. R., and Clements, R. M., 1979, "Laser Ignited Internal Combustion Engine—An Experimental Study," Society of Automotive Engineers, SAE Paper No. 780329.

[2] Kopecek, H., Maier, H., Regider, G., Winter, F., and Wintner, E., 2003, "Laser Ignition of Methane-Air Mixtures at High Pressure," Exp. Therm. Fluid Sci., **27**, pp. 499–503.

[3] Bradley, D., Sheppard, C. G. W., Suardjaja, I. M., and Woolley, R., 2004, "Fundamentals of High-Energy Spark Ignition With Lasers," Combust. Flame, **138**, pp. 55–77.

[4] McMillian, M. H., Woodruff, S. D., Richardson, S. W., and McIntyre, D. L., 2004, "Laser Spark Ignition: Laser Development and Engine Testing," *Proceedings of ICEF2004, ASME Internal Combustion Engine Division 2004 Fall Technical Conference*, Paper No. ICEF 2004-917.

[5] Yalin, A. P., Defoort, M. W., Joshi, S., Olsen, D., Willson, B., Matsuura, Y., and Miyagi, M., 2005, "Laser Ignition of Natural Gas Engines Using Fiber Delivery," *Proceedings of ICEF 2005, ASME Internal Combustion Engine Division 2005 Fall Technical Conference*, Paper No. ICEF 2005-1336.

[6] Kofler, H., Tauer, J., Tartar, G., Iskra, K., Klausner, J., Herdin, G., and Wintner, E., 2007, "An Innovative Solid-State Laser for Engine Ignition," Laser Phys. Lett., **4**, pp. 322–327.

[7] Yalin, A. P., Defoort, M., Willson, B., Matsura, Y., and Miyagi, M., 2005, "Use of Hollow Core Fibers to Deliver Nano-Second Nd:YAG Laser Pulses for Spark Formation," Opt. Lett., **30**, pp. 2083–2085.

[8] Joshi, S., Yalin, A. P., and Galvanauskas, A., 2007, "Use of Hollow Core Fibers, Fiber Lasers, and Photonic Crystal Fibers for Spark Delivery and Laser Ignition in Gases," Appl. Opt., **46**(19), pp. 4057–4064.

[9] Matsuura, Y., Hanamoto, K., Sato, S., and Miyagi, M., 1998, "Hollow-Fiber Delivery of High-Power Pulsed Nd:YAG Laser Light," Opt. Lett., **23**(23), pp. 1858–1860.

[10] Phuoc, T. X., 2000, "Laser Spark Ignition: Experimental Determination of Laser-Induced Breakdown Thresholds of Combustion Gases," Opt. Commun., **175**, pp. 419–423.

[11] Joshi, S., Reynolds, A., and Yalin, A. P., 2007, "Multiplexed Fiber Delivered Laser Ignition of Natural Gas Engines," *Proceedings of ICEF 2007, ASME Internal Combustion Engine Division 2007 Fall Technical Conference*, Paper No. ICEF 2007-1617.

[12] El-Rabii, H., and Gaborel, G., 2007, "Laser Ignition of Flammable Mixtures via a Solid Core Optical Fiber," Appl. Phys. B: Lasers Opt., **87**, pp. 139–144.

[13] Dumitrescu, C., Puzinauskas, P., Olcmen, S., Buckley, S. G., Joshi, S., and Yalin, A., 2007, "Fiber-Optic Spark Delivery for Gas-Phase Laser-Induced Breakdown Spectroscopy," Appl. Spectrosc., **61**(12), 1338–1343.